CRANFIELD UNIVERSITY

T RÉVEILLÉ

A STUDY OF FUEL INJECTION AND MIXTURE FORMATION FOR A GASOLINE DIRECT INJECTION ENGINE

2005.

SCHOOL OF ENGINEERING

PhD Thesis

CRANFIELD UNIVERSITY

SCHOOL OF ENGINEERING

PhD Thesis

Academic Year 2004-2005

T RÉVEILLÉ

A STUDY OF FUEL INJECTION AND MIXTURE FORMATION FOR A GASOLINE DIRECT INJECTION ENGINE

Supervisor: Professor D A Greenhalgh

September 2005

This thesis is submitted in partial fulfilment of the requirements for the degree of Doctor of Philosophy

Abstract

Future requirements for lower automotive emissions have lead to the development of new internal combustion (IC) engine technologies. Gasoline Direct Injection (GDI), for example, is one of these promising new IC engine concepts. It offers the opportunity of increased efficiency through unthrottled operation. However, the realisation of this concept is critically dependent on the in-cylinder mixture formation, especially in the late injection/lean operation mode. Ideally, this would require a precise stratification of the in-cylinder fuel-air mixture in 3 distinct zones: an ignitable pocket located at the spark plug, surrounded by a stoichiometric mixture of fuel and air, encompassed by air. To enable this stratification, the GDI concept utilises advanced injector technology.

Phase Doppler Anemometry (PDA), Planar Laser-Induced Fluorescence (PLIF) and the combination of PLIF and Mie scattering in the Laser-Sheet Dropsizing (LSD) technique, have been applied to sprays in the past to obtain dropsize information and study the mixture formation process. These new GDI sprays are denser, their droplet sizes are smaller and they evaporate faster, and as such, place us at the limit of the validity of these measurements techniques.

The diagnostics were applied to a GDI spray in a pressure vessel for realistic in-cylinder conditions, ranging from supercooled to superheated environments. Tracer evaporation issues in the PLIF technique were resolved by using a dual tracer system. The study showed that the LSD technique provided good quantitative data in low evaporation regimes. In highly evaporating regimes, the technique still gave reliable dropsize data for the early stages of the injection, but was limited afterwards by vapour-phase contribution to the fluorescence signal. Variations between PDA data and LSD results also suggested a deviation of the Mie scattering signal from the assumed d^2 dependence. This was further investigated and was found to be true for small droplets ($d/\lambda<0.2$). This source of error might be improved by using a different observation angle. High density seriously compromises the accuracy of PDA, whilst its effect through multiple scattering is of second order for the LSD technique.

In low evaporating regimes, LSD has the overall advantage of being a 2-D measurement technique, and will yield data with a maximum error of 30% in dense parts of the spray where PDA data is totally unreliable. If the spray evaporates quickly, PLIF by itself is an appropriate tool for following the air-fuel mixture, because short droplet lifetimes limit the 2-phase flow behaviour of the spray.

Particle Image Velocimetry (PIV), the LSD technique and equivalence ratio LIF measurements were applied to a BMW single cylinder optical GDI engine. The early injection operation showed no particular issues. However, the results obtained in the late injection highlighted the poor mixing and inappropriate stratification.

Acknowledgements

First, I would like to thank Professor Douglas A. Greenhalgh for giving me the opportunity to work on this project. His scientific knowledge and insight on industry's needs are at the source of this study. This project was made all the more interesting by the diversity of scientific fields it involved. I am truly grateful.

Dr. James Kelman was an endless source of inspiration, both scientific and humanistic. For the discussions, the suggestions, the support and his constant availability, I am eternally grateful.

I would also like to thank Bob Wilson for being a great technician and friend, and for putting up with my Triumph Spitfire. Bob sadly died on December 1st 2003, and laboratory work was never quite the same afterwards. This thesis is dedicated to him.

Many thanks also to Dr. Glenn Sherwood for being a great experimentalist and having the patience to share an office with me.

Thanks to my friends and colleagues for making life and work in Cranfield such a pleasure. A special thanks to Adam for the 3-D drawings of the pressure vessel.

Many thanks also to Dr. Joachim Höffner's team at BMW AG in Munich. Particular thanks to Robert Eigenschenk with whom I spent most of the time in the lab. Also thanks to Dr. Matthias Hartmann for the discussions and the "nasty questions" and Dr. Martin Schenk for his knowledge of PIV and DaVis. Thanks to Peter Steil as well for arranging an evening out in ultimate driving machines for each of my stays in Munich.

The EPSRC provided the funding for this project. BMW AG supplied the optical engine, a state-of-the-art laboratory and many man-hours. I am grateful for all this financial and technical support.

Merci à mes amis, ma famille, et surtout à ma p'tite Maman, de m'avoir supporté pendant ces quelques années. Cette thèse est aussi dédicacée à Papé, mon grand-père.

And a special thanks to Bill Gates for making such wonderful operating systems…

Table of Content

Abbreviations

AFR	Air-to-Fuel Ratio
ASOI	After Start Of Injection
AESOI	After Electronic Start Of Injection
AOSOI	After Optical Start Of Injection
a.u.	arbitrary unit
CA	Crank Angle
cc	cubic centimetre
EGR	Exhaust Gas Recirculation
FAR	Fuel-to-Air Ratio
GDI	Gasoline Direct Injection
HC	Hydrocarbon
IC	Internal Combustion
imep	indicated mean effective pressure
IRO	Intensified Relay Optics
LDA	Laser Doppler Anemometry
LDV	Laser Doppler Velocimetry
LIF	Laser-Induced Fluorescence
LNT	Lean NOx Trap
LRS	Laser Rayleigh Scattering
LSD	Laser-Sheet Dropsizing
MDRs	Morphology Dependent Resonances
MP	Measurement Point
Nd:YAG	Neodynium-Yttrium-Aluminium-Garnet
NOx	Nitrous Oxyde
PDA	Phase Doppler Anemometry
PDF	Probability Density Function
PDS	Planar Droplet Sizing
PFI	Port Fuel Injection
PIV	Particle-Image Velocimetry
PLIEF	Planar Laser-Induced Exciplex Fluorescence

PLIF	Planar Laser-Induced Fluorescence
ppm	parts per million
PTU	Programmable Timing Unit
RPM	revolutions per minute
SCR	Selective Catalytic Reduction
SCV	Swirl Control Valve
SI	Spark Ignition
SMD	Sauter Mean Diameter
SRS	Stimulated Raman Scattering
TDC	Top Dead Centre
TWC	Three-Way Catalyst
UV	Ultra Violet
2-D	Two-Dimensional

List of Figures

List of Tables

PART I

OVERVIEW AND BACKGROUND

Chapter 1

Introduction

In this chapter, the concept of direct-injection spark-ignition engines is introduced, along with its potential to increase efficiency and therefore reduce emissions, especially in the stratified/lean burn mode. First, a brief review of thermodynamics and combustion fundamentals relevant to lean burn and direct-injection are given. This is followed by the description of several combustion concepts for direct injection and the issues that this technology faces. The objectives of the work and an outline of the thesis complete the chapter.

1.1. Engine Basics

1.1.1. Emissions

Irremediably, the exhaust gases of a gasoline engine contain mainly water (H_2O) and carbon dioxide (CO_2), with small amounts of nitrogen oxides (NOx), carbon monoxide (CO) and unburned hydrocarbons (UHC).

Before 1970, no legislation limited the amount of any of these emissions. However, as CO and UHC became known as a risk to human health, the USA was the first to limit these sources of pollution through legislation. More accurate control of the fuel was sufficient to avoid these emissions.

Later on, NOx was discovered to be the source of smog when it interacts with sunlight and HC. Exhaust gas after-treatment with 3-way catalysts (TWC) allowed to meet the new NOx and HC regulations.

More recently, CO_2 has been regarded as a source of pollution, because it is a greenhouse gas which is considered to contribute to global warming. The European Commission has undertaken to reduce CO_2 emissions by 8% between 1990 and 2012, in compliance with the Kyoto protocol. With this in mind, the main automotive companies are aiming to limit average CO_2 emissions from vehicles sold in Europe to 140 g/km in 2008 (compared with 164 g/km in 2002) and a further reduction to 120 g/km by 2012 is also being considered. For a petrol engine, CO_2 emissions can only be reduced by improving the fuel consumption. Because the engine manufacturers do not want to compromise on engine performance, they have only one solution: increase the gasoline engine's efficiency.

1.1.2. Combustion Basics

By definition, an air/fuel mixture is stoichiometric when the exact amount of air is supplied to burn the fuel completely. In theory, the end products of a stoichiometric combustion of a hydrocarbon fuel in air will be CO_2, H_2O and N_2.

$$C_xH_y + \left(\frac{x}{2} + \frac{y}{4}\right)(O_2 + 3.76 \cdot N_2) \rightarrow xCO_2 + \frac{y}{2}H_2O + 3.76 \cdot \left(\frac{x}{2} + \frac{y}{4}\right)N_2$$

Equation 1-1: Ideal stoichiometric combustion of a hydrocarbon fuel

In practise, the fuel might not have sufficient time to burn completely before the exhaust valve(s) open, especially in the transient conditions, when air-to-fuel ratio (AFR), spark timing and Exhaust Gas Recirculation (EGR) may not be properly matched. Quenching of the flame in the later phase of the expansion stroke - when the combustion is especially slow - is a source of unburned hydrocarbon and carbon monoxide emissions. Another source of UHC emissions is engine oil left in a thin film on the cylinder wall, piston and cylinder head. These oil layers can absorb and desorb hydrocarbons before and after combustion thus permitting a fraction of fuel to escape the combustion process unburned. Fuel trapped in crevices too narrow for the flame is also a source of UHC (Heywood 1988).

Also, for combustion temperatures above 2000K, CO_2, O_2 and H_2O molecules are dissociated to CO, O and H_2. The molecular oxygen then reacts with the nitrogen of the

air. This leads to the formation of small quantities of nitrogen oxides, mainly of nitric oxide (NO) and small amounts of nitrogen dioxide (NO_2). The formation of NO increases with the temperature of the burnt gases.

Catalytic converters can remove NO from the burnt gases by reduction using CO and H_2. They also oxidise CO and hydrocarbons into CO_2 and H_2O.

Today's engines are all equipped with 3-way catalysts to reduce the unwanted CO, UHC and NOx. However, these catalysts require a stoichiometric mixture for optimal conversion. If an engine is going to be run lean, the oxygen-rich environment will not allow an efficient reduction of NOx. Therefore, the engine has to run sufficiently lean in order to form only acceptable quantities of nitrous oxides.

1.1.3. Engine Thermodynamics

In 1862, French engineer Alphonse Beau de Rochas patented the principle of a 4-stroke internal combustion engine with a cycle consisting of 2 isentropic and 2 isochoric curves. His idea was that more work could be retrieved if the air/fuel mixture was compressed before the combustion. 14 years later, German engineer Nicolaus Otto built the engine, known as the spark ignition engine.

The cycle is illustrated in *Figure 1-1*:

- $1 \rightarrow 2$ Constant pressure intake
- $2 \rightarrow 3$ Adiabatic and reversible compression
- $3 \rightarrow 4$ Adiabatic combustion at constant volume
- $4 \rightarrow 5$ Adiabatic and reversible expansion
- $5 \rightarrow 6 \rightarrow 7$ Exhaust

The efficiency of this theoretical cycle is:

$$\eta = \frac{W_e}{m_f \cdot Q} = 1 - \frac{1}{r_c^{\gamma-1}}$$

Equation 1-2

where r_c is the compression ratio and γ is the specific heat ratio. W_e is the recovered work, and is represented by the blue area.

Equation 1-2 states that the efficiency of the cycle can be improved by increasing the compression ratio, and by decreasing the specific heat ratio.

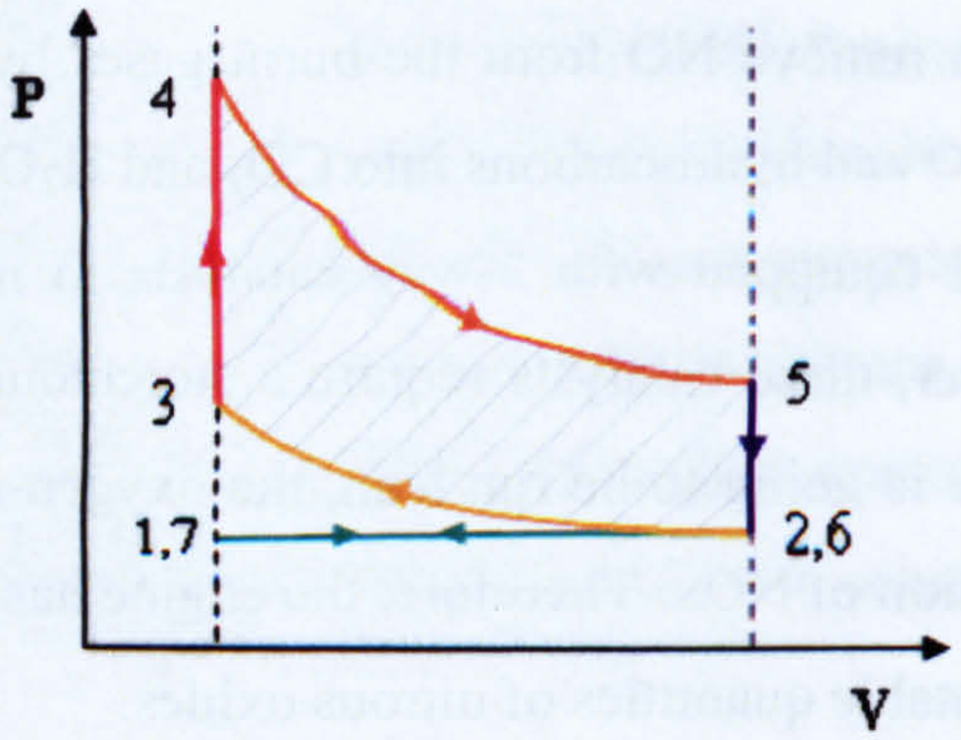

Figure 1-1: Clapeyron diagram of a theoretical 4-stroke SI engine cycle

Most petrol engines operate with homogeneous, near stoichiometric air/fuel mixture in order to perform the complete combustion of the pre-mixed charge. To run such an engine at part load, the amount of fuel is reduced. The amount of air must also be reduced to keep the mixture stoichiometric. That is usually done by throttling with a butterfly valve. This throttling induces pumping losses - represented by the green area of the PV diagram of a throttled cycle (see *Figure 1-2*).

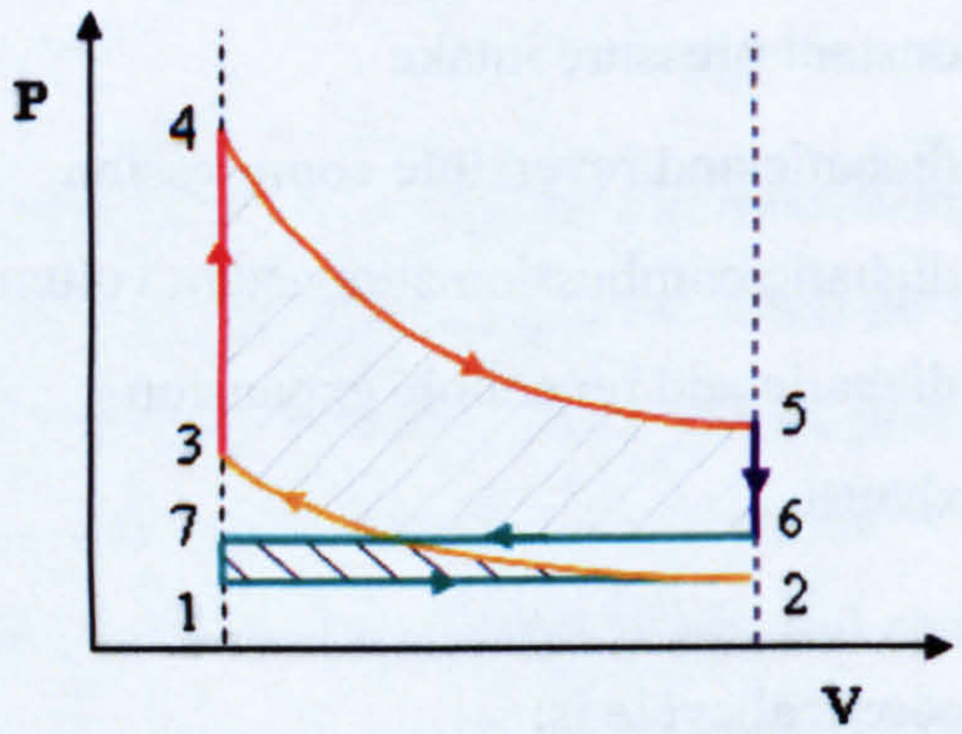

Figure 1-2: Clapeyron diagram of a theoretical throttled cycle

If an engine could be operated at part load without throttling the air, its efficiency would be increased. However, not throttling the air implies that the engine must run on an overall lean air/fuel mixture.

1.2. Lean Burn Combustion in SI engines

1.2.1. Lean Operation

Typically, the stoichiometric air-to-fuel ratio (AFR) is 14.6 for petrol engines.

An engine will run with a homogeneous lean charge, within the lean operation limit. Beyond that limit, the mixture will fail to ignite, leading to unacceptable UHC emissions, and cycle-to-cycle fluctuations in torque which will affect the driveability and smoothness.

However, even within that limit, as the mixture is leaned out, the time to establish the flame kernel, the flame propagation period and the fluctuations in indicated mean effective pressure (imep) all increase (Young 1981). For slow burning cycles, the mixture might not be completely burnt before the exhaust valve opens, leading to a rapid increase in UHC emissions and fuel consumption (Quader 1976). Therefore, the slowest burning cycle actually defines the practical (or stable) lean operation limit for a homogeneously lean operating engine.

Furthermore, in order to optimise torque in SI engines, the bulk of the heat release must occur at a specific time in the cycle. The variations in flame propagation implies that for faster burning cycles, the heat release will occur too soon, and for the slower burning cycles it will occur too late. This leads to a reduction of torque and power, thus a reduction in efficiency.

Further dilution may cause flame extinction before the exhaust valve is open, or before the flame has propagated across the chamber.

1.2.2. Extending the Lean Operation Limit

As seen previously, leaning out the mixture reduces flame propagation speed: the slower burning rates limit the engine's lean operation. The factors that influence the flame development and propagation are:

- compression ratio
- spark location
- mixture formation
- turbulence level

They have the potential to extend the lean operation limit.

Increasing the compression ratio increases the charge's temperature, thus helping combustion. It also reduces the fraction of residual gases, which limit the lean operation (Quader 1974). However, the compression ratio can only be increased to the knock limit. This is determined by the engine's geometry and the fuel's octane rating.

Rapid combustion can also be helped by placing the spark plug in a central position, or adopting a twin sparkplug strategy.

Increasing the turbulence level will increase the burning rate, provided that the flame is not extinguished through too much stretching or increased heat transfer. A practical way of creating turbulence in the cylinder is by introducing kinetic energy during the intake stroke, which will be converted to turbulence during the compression stroke.
Swirl, or air that rotates around the cylinder axis, will result in turbulence generation throughout the cycle (Liou and Santavicca 1983, Hall and Bracco 1987). Swirl can be generated by helical inlet ports (like the ones in the Honda V-TEC engine), by shrouded valves or by asymmetric inlet (Pajot 2000). Above a certain level, swirl does not significantly improve the lean limit (Inoue et al. 1993).
Tumble, or air that rotates round a horizontal axis, generates turbulence in the second part of the compression stroke (Haddad and Denbratt 1991, Kiyota et al. 1992). Tumble can be obtained with 4-valve configurations.

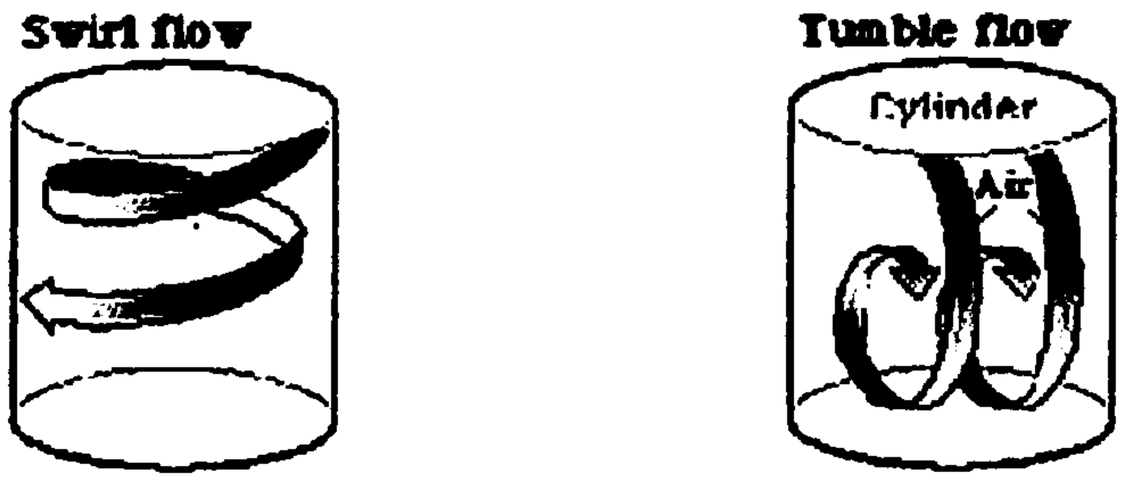

Figure 1-3: Swirl and Tumble flows

Squish is also a source of turbulence which helps the development of the flame, as long as the spark plug is located in the squish flow (Gatowski and Heywood 1985). Tumble

ratios above 2.5 tend to increase misfires and imep fluctuations, for part load and ultra lean mixtures (Iwamoto et al. 1992).
For a fixed valve timing and lift, turbulence is a function of engine speed. If adequate levels of turbulence are generated at low engine speeds, this may lead to excessive turbulence levels at high RPM. High fluctuations in flow might then cause flame extinction due to excessive stretch.

The issue with lean burning is the flame development. The variations in flame development are mainly caused by variations in laminar flame speed (Keck et al. 1987). Flame speed is a function of the ignition process and mixture strength influences the ignition (Pischinger and Heywood 1988, Le Coz 1992).
The lean operation for homogeneous mixtures is therefore limited by the weak mixture at ignition. This leads to the concept of fuel stratification in order to produce an ignitable pocket near the spark plug at the time of ignition.

1.2.3. Stratification

Three Japanese manufacturers developed lean burn engines. All used the same strategy: at low RPM and load, the engine runs with a lean air/fuel ratio for maximum fuel economy. As the combustion temperature is low, NOx output is also low: the catalyst just oxidises HC and CO. At higher load, the engine reverts to homogeneous stoichiometric mixing for increased power and the catalyst also reduces the NOx.

Toyota's lean-burn engine operates with an AFR of 25 below 4800 RPM and below 75% of maximum torque. At higher speed and load, it reverts back to a stoichiometric mixture, and runs at full load with an AFR of 12.5. The cylinder head features a 4-valve per cylinder pent-roof configuration with separated dual intake ports. One is a helical port shape, and the other is straight, containing a swirl control valve (SCV). To increase volumetric efficiency, a small passage between the two ports allows a small air flow to the straight when the SCV is closed. A twin spray fuel injector injects into both ports. It is claimed that the fuel is finely atomised by the swirling flow in the helical port and the high speed flow in the straight port, resulting in a homogeneous charge.

The Honda V-TEC engine follows the same concept: it operates with an AFR of 22 below 3000 RPM and at low load. At high load or above 3000 RPM, the engine reverts to homogeneous stoichiometric combustion. The engine also has a 4-valve pent-roof head with a central spark plug. One of the inlet valve controls a high swirl port, in order to insure high turbulence. In the lean mode, only this inlet valve opens fully, while the other opens about 1mm briefly to avoid fuel build-up. At full load, both valves open fully for good volumetric efficiency. With double injection in the lean operation mode, it is claimed that the charge is stratified near the spark plug at ignition (Horie et al. 1993, Hardalupas et al. 1995, Berckmüller 1996).

Although both lean burn port-injection engines follow the same strategy (i.e. swirl intake and sequential injection), it is noteworthy that Toyota's engine is claimed to be a homogeneous charge engine (Shimuzu et al. 1992) while Honda's engine is stratified charged. However, Berckmüller (1996) signals that the measurements on the Toyota engine can be deceptive as only 1 region was measured.

In 1992, Mitsubishi began producing the Mitsubishi MVV (Mitsubishi Vertical Vortex) 3-valve per cylinder engine. It used the combination of tumble and injection of fuel through one port to stratify the mixture. It is claimed that the absence of swirl maintains the stratification during the compression stroke. The exhaust valve situated opposite the fuel intake valve is replaced by the spark plug, thus positioning the latter near the axially stratified charge (see *Figure 1-4*). Using tumble instead of swirl reduces the pumping losses. The lean-burn MVV engine can achieve complete combustion with an air-fuel ratio as high as 25.

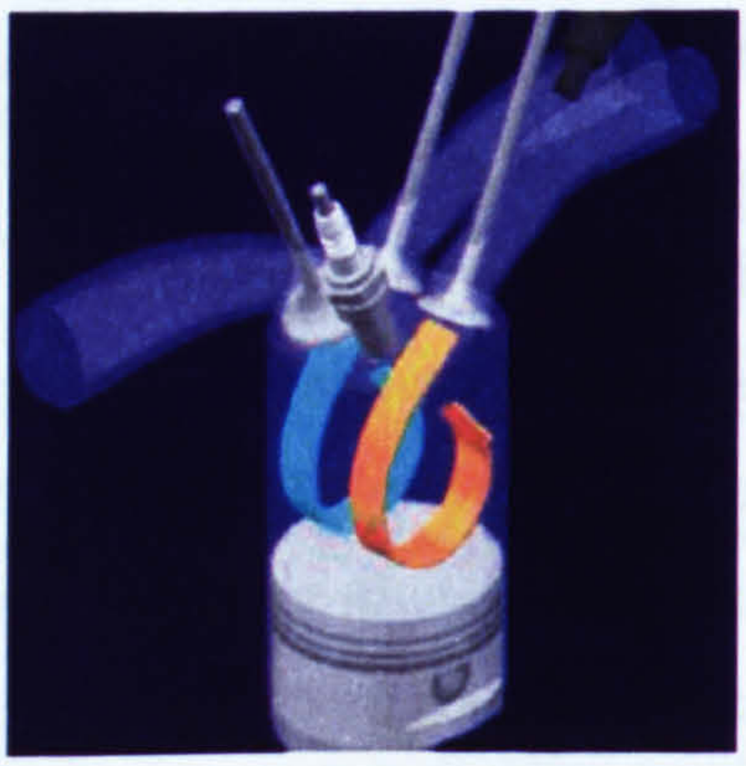

Figure 1-4: Mitsubishi MVV 3-valve tumble-guided stratified lean-burn engine

One of port fuel-injection's (PFI) limitations is that the fuel can only enter the cylinder when the intake valves are open. By directly injecting fuel into the cylinder, the injection process is no longer limited to valve opening, but can be extended through the whole cycle, and more interestingly, during the compression stroke. The advantage of direct injection is that the fuel can be placed in the combustion space in a more controlled manner than with conventional port injection systems: this gives it a greater potential for charge stratification

1.3. Gasoline Direct Injection

1.3.1. Development

Since the 1920's, attempts have been made to develop hybrid internal combustion engines that would combine the best features of petrol and diesel engines.

During World War II, Daimler-Benz, in conjunction with Bosch and the Reich Air Ministry experimented with direct injection. The primary aim was to eliminate fuel starvation during steep dives and improve performance for air combat. The result was the DB 601 family of engines, which equipped various fighters and bombers of the Luftwaffe, its most famous association being with the Messerschmitt Me 109 in the Battle of Britain. Direct fuel injection into the cylinders was provided by means of a twelve-unit high-pressure pump mounted between the cylinder blocks where it was fed by a Graitzin transfer pump. The high-pressure leads between the pump and the cylinders were of equal length. This fuel injection system proved to be very smooth and accelerated rapidly when the throttle was opened.

In 1954, Mercedes-Benz introduced the world's first four-stroke direct injection gasoline engine in a production car. It had a 3-litre, in-line 6-cylinder engine with a Bosch direct mechanical fuel injection. The engine produced 215 horsepower, and gave the car a top speed of 160 mph.

However, these DI engines operated with homogeneous stoichiometric mixtures. The idea behind GDI today is that directly injecting into the cylinder allows a better control of the fuel location within the cylinder, therefore giving it a greater potential for mixture

stratification. This should allow GDI to extend the AFR of lean-burn gasoline engine to values higher than 25, and reach equivalence ratios similar to those of Diesel engines. If the gasoline engine can be run unthrottled, then the reduction of the pumping losses will enable it to increase the efficiency and therefore reduce fuel consumption: theoretically, GDI has the potential to reduce the fuel consumption by 20 to 25 % at low speeds and loads compared to homogeneous stoichiometric operation (Karl et al. 1996).

In 1996, Mitsubishi launched the first stratified spark-ignition direct injection engine, called GDI (Gasoline Direct Injection). This engine was said to reduce fuel consumption by over 15%, without compromising on driveability.

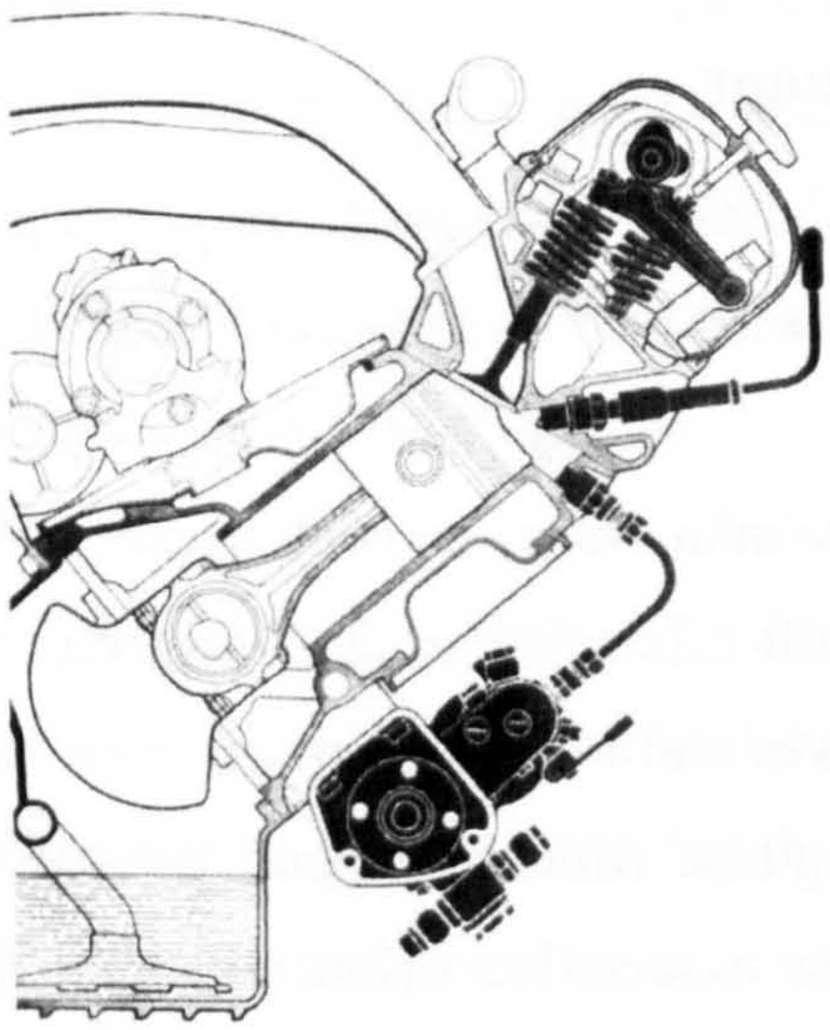

Figure 1-5: Cutaway section of the 1954 Mercedes 300SL direct injection engine

1.3.2. Advantages of GDI

The GDI concept is meant to increase the efficiency of the petrol engine and therefore reduce the fuel consumption. In turn, this reduces the CO_2 emissions. This increase in efficiency is possible through 4 main features:

- Higher compression ratio
- Increased ratio of specific heat (γ)
- Reduction of pumping losses
- Less heat losses

By injecting the fuel directly inside the chamber, the charge is cooled inside the cylinder as it evaporates. In PFI engines, the cooling starts in the intake manifold, but the charge is then warmed up as it travels through the port before reaching the cylinder. Therefore, with GDI, the temperature of the charge at the time of compression is lower than that of a PFI engine. Because its temperature is lower than that of a PFI charge, it can be compressed more before it spontaneously ignites. This enables to increase the compression ratio, thus increasing the cycle's efficiency.

Because the charge is leaned out, the mixture contains a higher ratio of diatomic molecules (N_2 and O_2). This increases the ratio of specific heats, which increases the efficiency (see *Equation 1-2*).

Running lean with very high AFRs enables to control the engine power output by varying the amount of fuel without having to throttle the air. This reduces the pumping losses, increasing to the cycle's efficiency at part load.

The increase in efficiency also comes from the presence of excess fresh air in the stratified mode. This reduces the heat and exhaust losses due to lower temperature in the cylinder during the combustion and expansion stroke.

Direct injection can also improve cold-start hydrocarbon emissions and engine transient response because it avoids the deposition and build-up of fuel in the intake ports of conventional PFI engines. However, for most engine operating conditions, direct-injection has higher engine-out smoke and HC emissions than their PFI counterparts.

1.3.3. GDI Combustion Chamber Concepts

The idea of direct injection is to create a perfect, stratified charge by forming a richer cloud in the vicinity of the spark plug. The challenge is to control precisely the amount, size and distribution of the fuel droplets to suit varied driving conditions, and to do this reliably over the life of the vehicle.

Within a few milliseconds, the fuel spray must be atomised in very fine droplets, and be completely evaporated before ignition. At the same time, it is absolutely crucial that the

mixture at the spark location is optimal at the time of ignition. Otherwise, the combustion is not efficient, and the pollutant output increases.

Three different concepts have been developed to obtain the stratified mixture for direct injection combustion systems:

- Wall-guided
- Air-guided
- Spray-guided

In reality, for the three concepts, the stratification is achieved by a combination of these mechanisms.

In the wall and air-guided systems, the spark plug is usually located centrally, and the injector is to the side. Fuel is injected at a distance from the spark location at pressures typically around 100 bar, and is redirected towards the spark plug by a secondary mechanism. In the case of wall-guided systems, the piston crown has a bowl shape that redirects the fuel towards the spark plug. Mitsubishi's GDI engine (see Figure 1-6) features upright straight intake ports rather than horizontal intake ports used in conventional engines. The upright straight intake ports direct the airflow down at the curved-top piston, which redirects the airflow into a strong reverse tumble for optimal fuel injection.

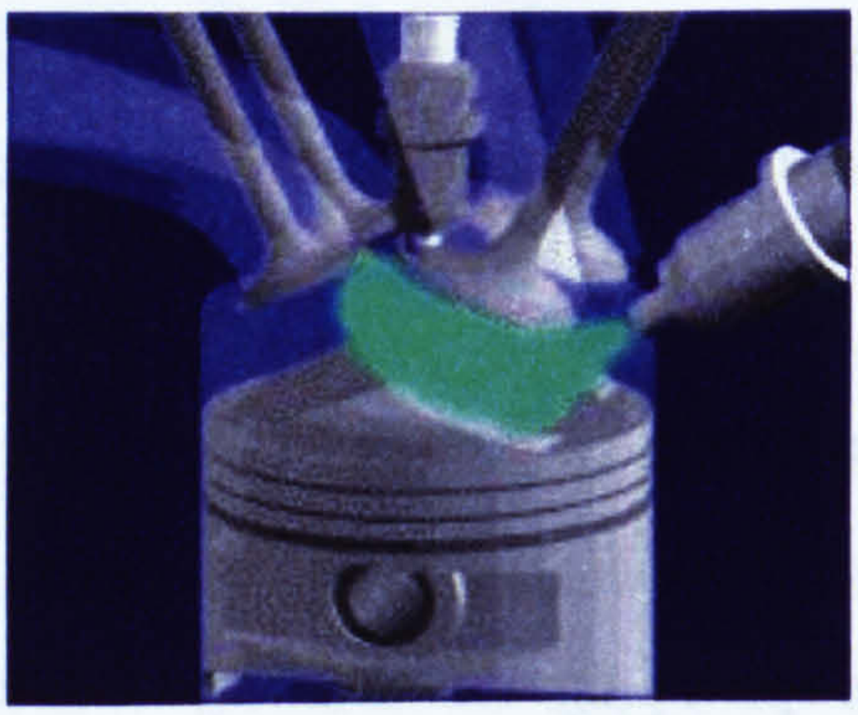

Figure 1-6: Mitsubishi GDI wall-guided system

Audi's FSI (Fuel Stratified Injection) technology (see Figure 1-7) is an air-guided system. A vortex is created inside the combustion chamber by a tumble flap in the

intake manifold combined with a specially-shaped piston crown. The injected fuel is redirected by the air motion towards the centrally placed spark plug. The FSI engines range from a 1.6 Litre in-line 4 cylinder engine with a compression ratio of 12:1 to the latest 3.2 Litre V6 engine with a compression ratio of 12.5.

Figure 1-7: Audi FSI air-guided system

The spray-guided system, where the fuel is injected directly towards the spark gap location was investigated as early as 1972 (Simko et al.). Such systems suffered from two main problems: spark plug fouling and poor combustion robustness. However, with the progress in injector technology, and the introduction of Piezo-electric injectors, spray-guided systems are now knowing renewed interest (Matsumoto 2004). These injectors operate at higher pressures than the 1st generation GDI injectors. Their response time is quicker, more precise and the droplet sizes are much smaller.

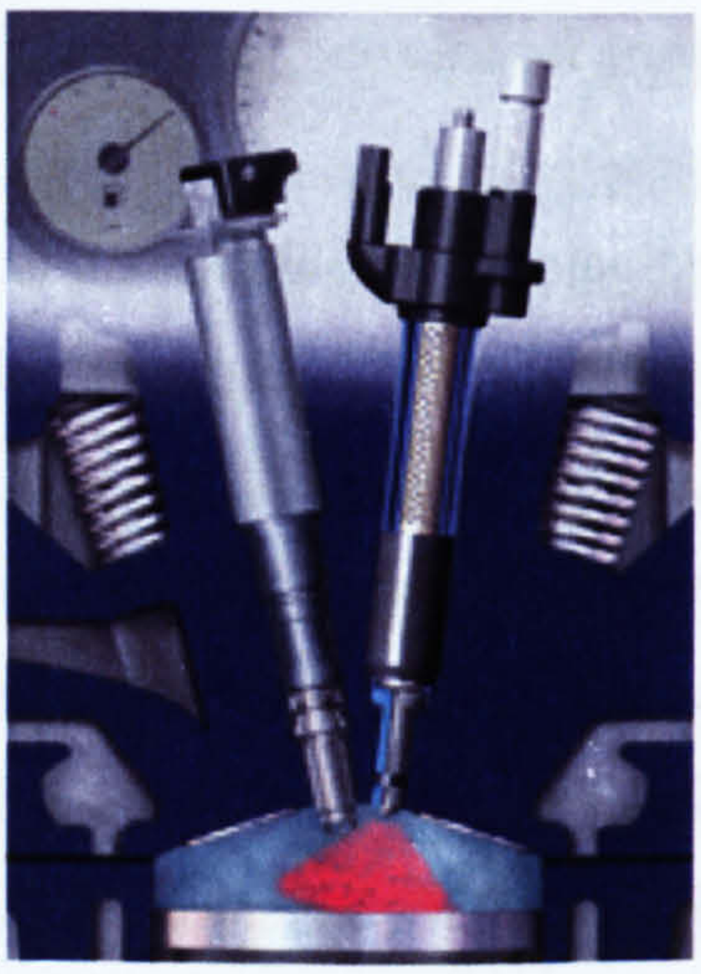

Figure 1-8: Spray-guided system with Piezo-electric injector

1.3.4. Issues

1.3.4.1. Emissions

The difficulty in GDI is that the charge must remain stratified while the mixing process occurs. Paradoxically, the presence of the fuel must be short enough not to diffuse and long enough to mix properly.

The stratified charge preparation relies on mixing of the air and the spray just enough to obtain an ignitable mixture underneath the spark plug, surrounded by air or an extremely lean mixture. This inevitably results in rich regions inside the ignitable pocket and leaner regions at the periphery. Both regions are subject to incomplete combustion, which is the first source of HC emissions.

The first generation of GDI designs (wall-guided systems) used a bowl to direct the spray towards the spark plug. The impingement of the fuel on the piston results in the formation of a liquid fuel film that constitutes the second source of HC emissions (Karlson and Heywood 2001). Frank and Heywood (1991) had found little changes in HC emissions with changes in piston temperature, and concluded that fuel wetting of the piston surface was not a significant source of HC emissions. However, they acknowledged that they used a high volatility fuel. Stanglmaier et al. (1999) studied the influence of wall wetting location for HC emissions and found that the wetting of the cylinder liner on the exhaust side was the strongest contributor, followed by the wetting on the piston top, and finally the wetting of the liner under the intake valves being the best case. Depositing 10% of the total fuel mass on the top of the piston results in a 30 to 70% increase in HC emissions for idle and part load conditions (Li et al. 1999).

Sandquist et al. (2000) investigated these hydrocarbon emissions and confirmed that over-mixing at the boundaries of the air/fuel mixture cloud and under-mixing both in the spray centre and on the surface of the piston bowl are the dominant mechanisms. There is a fuel injection timing optimum that minimises the sum of HC from over-mixing and under-mixing. As the mixing time is reduced, carbon monoxide (CO) and soot emissions increase. Drake et al. (2003) confirmed this and found that wall wetting was only responsible for 15% of UHC emissions for a swirl injector and 2% for a multihole injector in a wall-guided system. They found that most of the fuel-film mass

evaporates during the cycle and burns as pool fires. The fuel-films are the dominant source of smoke emission with 10% of the fuel-film mass converted to emitted smoke for the swirl injector. Smoke emissions are very small when using the multihole injector, which is consistent with the decrease in fuel-film.

With stratified-charge combustion, the rich regions produce high temperatures which are favourable for NOx formation in the presence of excess air. Replacing the excess air with EGR can reduce NOx, but is limited by the fact that EGR reduces laminar flame speed (Metghalchi and Keck 1982, Rhodes and Keck 1985) and is therefore detrimental to the combustion process.

1.3.4.2. Catalysts for GDI engines

The idea behind GDI is to decrease CO_2 emissions, but this must not compromise on HC or NOx emissions. The 3-way catalysts equipped on PFI engines are only efficient at reducing NOx under stoichiometric operation. Therefore, an adequate system must be developed for GDI engines in order to run under both homogeneous and lean burn conditions.

Lean NOx catalytic converters currently come in two varieties: the Selective Catalytic Reduction (SCR) and the Lean NOx Trap (LNT).

The Lean NOx Trap is equipped of a 3-way catalyst and a NO_2 trap. This trap is made of an alkaline earth compound (such as barium or strontium) or an alkali metal compound (such as potassium) which adsorb the NO_2 and form a stable metal nitrate. Under lean conditions, the catalyst oxidises NO to produce NO_2 which is adsorbed by the trap along with the NO_2 resulting from the in-cylinder combustion. When the device is full, the engine reverts to a stoichiometric combustion and the NO_2 is reduced to N_2. The storage-type converter is controlled by a mapped operating characteristic and by temperature. When the storage device is saturated, the engine's mixture is made richer for a short time (typically for 2-3 seconds each minute). This raises the temperature of the exhaust gas, so that the NO_2 is released and reduced in the 3-way catalyst.

Originally, the Selective Catalytic Reduction concept was used on stationary sources using ammonia or urea as the reducing agent. The Selective Catalytic Reduction using

hydrocarbons (SRC-HC) has the advantage that the catalyst utilizes hydrocarbon species present in the exhaust stream for NOx reduction. The reaction can be supplemented with additional hydrocarbons either via secondary injection into the cylinder or direct injection into the exhaust stream.

Lean NOx traps (LNTs) are currently the technology of choice for treating the NOx emissions from lean-burn SI engines because of their higher efficiency. However, the sulphur tolerance of aged LNTs is much lower than that of the fresh LNTs. Moreover, the aged LNTs are more difficult to desulphate relative to the fresh ones. Long-term use of this type of NOx catalytic converter in Europe, where the sulphur content of petrol is 200ppm, would result in almost total loss in effectiveness. The robustness of the LNT still needs to be improved. With the help of the newly established low sulphur fuel to be introduced in the European and the U.S. markets, the widespread application of LNT technology will become more promising (Li et al. 2001).

1.4. Summary

One method to reduce CO_2 emissions from SI engines is to improve their efficiency. This can be achieved by operating with a lean mixture. In the late 1980's Japanese manufacturers launched stratified charge port-injection engines. It was clear that direct injection could extend the stratification by allowing injection during the compression stroke. The improvements in fuel injection technology as well as advances in the understanding of the processes involved in mixture preparation and stratified charge combustion have allowed the realisation of the concept. In 1996, the technology became commercially available with Mitsubishi's GDI engine: the first generation of stratified charge direct injection SI engines with a wall-guided system.

Compared to port injection SI engines, HC emissions were thought to be improved because of the absence of wall wetting in inlet ports. However, the wetting of the piston and the cylinder walls during the injection and mixing process are important issues. Also, the stratification in the late injection, lean burn mode requires refinement, because the mixing time is poor, which irremediably creates inhomogeneous regions prone to bad combustion. By re-introducing spray-guided direct injection and using the lean burn concept in the future, the gasoline engine fuel consumption will come even closer to the supreme economy of a modern diesel.

1.5. Aims of this Thesis

The mixture formation process for the lean operation mode is therefore a key issue to its further development. It is essential to obtain a perfectly stratified charge with an optimal stoichiometry in a localised mixture near the spark plug. If zones of the mixture are too rich, soot will be produced and if too lean, misfire or hydrocarbon (HC) emissions will occur. Further, it is critical to avoid the mixture having excessive wall contact or impacting crevices which can enhance HC emissions. Understanding the mixture formation process in detail requires an accurate knowledge the spray formation (i.e. droplet sizes and their evolution during injection as they evaporate). The Laser Sheet Dropsizing (LSD) technique is an important new laser diagnostics tool with the potential to study such a system. Combined with other 2-dimensional, non-intrusive diagnostics to measure droplet speed and local AFR, this would give development engineers a powerful tool for rapidly characterising sprays. The aim of the thesis was to develop such a tool. This requires the improvement and validation of the LSD technique for highly evaporative sprays. The diagnostic is combined with Particle Image Velocimetry (PIV) and Planar Laser-Induced Fluorescence (PLIF) to measure drop size, speed and fuel distribution in a BMW GDI optical research engine.

1.6. Outline of this Thesis

This thesis is organised in 4 parts. *Part I* includes *Chapter 1* and *2* to provide background information on GDI's potential to meet future legislation and presents the different laser techniques used in SI engines to better understand and improve the mixing process. *Part II* (*Chapters 3-5*) concerns the development of the Laser Sheet Dropsizing (LSD) technique for an evaporating GDI spray. *Part III* (*Chapter 6*) is the application of the LSD technique to an optical engine, along with other laser techniques for a complete characterisation of the spray. *Part IV* contains the conclusion and discussion of this work, along with the references and appendices.

Chapter 2 reviews the various laser diagnostics used to study and characterise spray development and mixture formation inside engines and gives examples of applications. An intensive study of fluorescence for the development of the LSD technique is found in *Chapter 3*. This includes a study of liquid-phase fluorescence and the determination

of the best fuel/tracer system regarding absorption, temperature and evaporation issues. *Chapter 4* describes the experimental set-up that enabled to study a GDI spray in realistic engine conditions using both Phase Doppler Anemometry (PDA) and the LSD technique. *Chapter 5* presents and compares the results obtained from the LSD and the PDA technique in order to validate and find the limitations of the LSD technique for different realistic conditions. In *Chapter 6*, the LSD technique is applied to an optical engine, along with PIV and AFR measurements for a complete 2-dimensional study of the spray development. The conclusions of the thesis work are discussed in *Chapter 7*.

Chapter 2

Laser Diagnostics in Spark Ignition Engines

The importance of in-cylinder fluid motion and the need for visualisation and measurement has been recognised since the early days of engine research. In-cylinder flow was studied by Clerk as early as 1921 using a low speed optical engine designed by Ricardo.

The combustion phenomenon is a direct result of the in-cylinder air-fuel mixing and the ignition, therefore any information on mixture strength distribution, spray size distribution and velocities could prove useful. Combustion chambers are harsh environments, with usually limited access, which makes measurements difficult. Laser-based diagnostics allow for non-intrusive measurements within these systems. With high power lasers, improved imaging systems, imaging techniques and optical engines, non-intrusive measurements methods have developed greatly. This has allowed a greater understanding of the in-cylinder phenomenon.

This chapter first presents light scattering theory, followed by a review of various laser diagnostics that are used to study and characterise sprays and the air-fuel mixing process.

2.1. Light Scattering Techniques

Light scattering is a term referring to physical processes involving the interaction of light and matter. This interaction partially "deflects" the incident light in directions deviated from the incident direction.

The passage of light through a medium induces vibrations which give rise to secondary waves. In a perfectly homogeneous medium, the secondary waves are equally scattered

in all directions: their sum is a wave that has the same propagation direction as the incident light. Molecules in a liquid or a gas induce small variations in refractive index, therefore creating a non homogeneous medium. As a result, the secondary waves do not cancel each other out, and the resulting light is scattered in different directions to that of the incoming light.

A droplet can be seen as a collection of antennas that emit (scatter) an incident electric field. This scattering depends on the size and shape, the observation angle (scattering angle), the response of each antenna (composition), and the polarisation state and wavelength of the incident wave.

Scattered signals can be either elastic or inelastic. The elastic scattering is an interaction without an energy loss (or exchange) between the light and the matter within a droplet: after the interaction, the liquid drop is at the same state of energy as it was initially, and the energy in the light exiting the interaction point is equal to the energy of the incident light. This restriction of equal energy does not prohibit a change in direction, but according to Planck's law, it prohibits a change in frequency.

$$E = h \cdot \nu \Rightarrow \Delta E = h \cdot \Delta \nu$$

Equation 2-1: Planck's law

where E is the energy and ΔE is the energy variation, ν is the frequency and $\Delta \nu$ is the frequency variation and h is Planck's constant.

In the case of an elastic scatter (i.e. when there is no energy exchange - $\Delta E = 0$) there is no frequency change ($\Delta \nu = 0$). On the other hand, an inelastic process describes a permanent energy exchange and involves a frequency shift. In practice, the two types of scattering may take place simultaneously.

2.1.1. Laser Rayleigh Scattering (LRS)

LRS is the elastic scattering of incident laser light with particles smaller than the wavelength of the light. From a quantum mechanics point of view, LRS occurs when a photon collides with a molecule, exciting it to a higher energy state. The molecule then relaxes back to the original state, emitting a photon of the same wavelength.

For a sphere of radius r much smaller than the wavelength of the light ($r << \lambda$), Rayleigh deduced that the intensity of scattered light is proportional to r^6 / λ^4.

Usually, Rayleigh scatter is detected at 90°, and allows to measure species concentration. If the pressure and species are known, the density measurement can be converted to temperature (Dibble and Hollenbach 1981).

Since LRS is an elastic process it suffers from background light of the same wavelength. That includes Mie scatter from particles, which, for a 1μm droplet, is about 20 orders of magnitude higher than the Rayleigh scattering. Scattering from optics and other surfaces are also an issue.

Arcoumanis and Enotiadis (1991) used LRS and showed that the fuel concentration in the combustion chamber of a port-injected spark-ignition engine was affected by the injection time and duration.

Zhao et al. (1993) used LRS with a 532nm laser light sheet in a motored optical SI engine. They used Freon-12 and propane to study the mixing process, and found that the concentration distribution was non-homogeneous at the time of ignition.

Espey et al. (1997) obtained quantitative 2-D images of fuel vapour concentrations in an evaporating and combusting diesel spray, using a 532nm laser light sheet in an optical single cylinder DI Diesel engine. They estimated the error to be around 20%.

2.1.2. Spontaneous Raman Scattering (SRS)

When a photon collides with a molecule, it transfers its energy and excites the molecule to a higher energy state. Generally, both rotational and vibrational energies of the molecule are affected through the collision with the photon. In the case of SRS, the energy of the photon is more than can be stored by rotation or vibration in the molecule, but not enough to allow the molecule to reach the first electronic state. The molecule is therefore excited to a highly unstable virtual state and drops back almost immediately to a stable energy level, emitting a photon in the process. If the final level is the same as the original level, Rayleigh scatter is observed. If the final level is higher than the original level, the energy transfer is called Stokes Raman, and is red shifted. If the final level is lower than the original level, the result is the emission of a photon of lower wavelength, referred to as anti-Stokes Raman.

Raman scattering is an inelastic process which allows species and temperature measurements. The scattered light is collected and its intensity and spectral characteristics measured with a spectrometer. The species concentration is obtained from the intensity and the temperature from the spectral distribution.

SRS was first applied to IC engines in 1979 when Johnston obtained AFR measurements in a DI stratified charge engine from the ratio of signals of the fuel (Propane) and N_2 at different crank angles.

Because of the small Raman scattering section, interference from other light scattering processes can be a serious problem to the technique. For this reason, little progress was made in the development of SRS during the 1980's (Zhao and Ladommatos 1998).

More recently, Miles and Dilligan (1996) measured major species (H_2O, CO_2, O_2 and fuel (C_3H_8)) in the Sandia transparent research engine. The residual gas mole fraction was obtained.

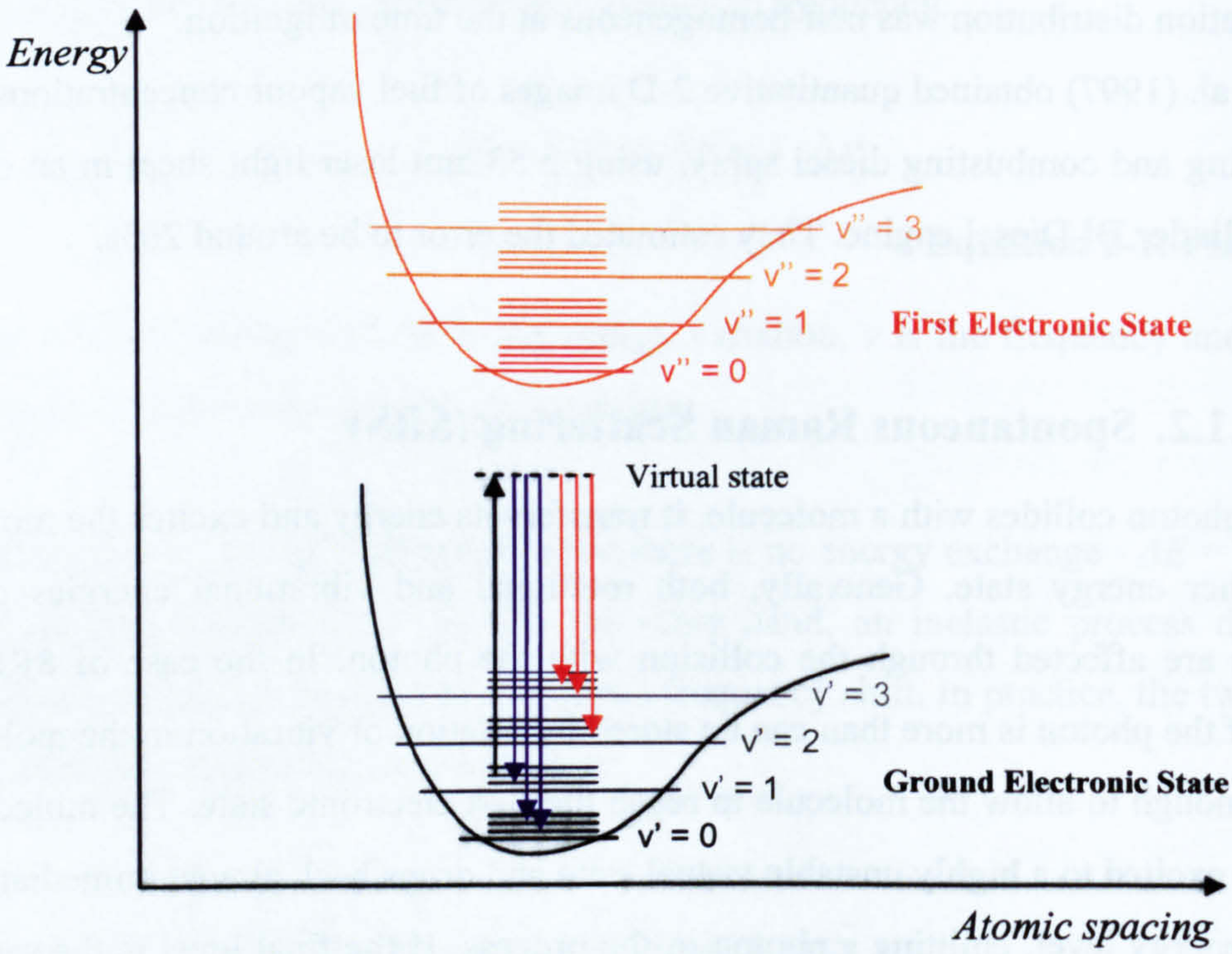

Figure 2-1: Raman scattering energy levels: Stokes (red) and anti-Stokes (blue)

Knapp et al. (1997) performed SRS in one of the cylinders of a 4-cylinder SI engine. They measured single-cycle and cycle-averaged concentrations of H_2O, O_2 and Iso-Octane (C_8H_{18}) relative to N_2 at different temperatures to take into account the temperature dependence of the Raman cross sections. By normalising the fuel and air

signals, the AFR measurement obtained from single shots eliminated pulse-to-pulse laser variation and window fouling. A precision better than 4% was obtained in the low load case and better than 3% in the high load case.

Miles (1999) describes a simultaneous multipoint single laser shot SRS measurement system applied to an optical engine.

Since SRS measures AFR directly, it can be applied to situations where EGR gas exists and has been accorded renewed interest. The drawback of the technique has been the low signal strength, but with the new high power UV lasers, this is less of a problem.

2.1.3. Mie scattering

Mie scattering is an elastic process which appears if the scattered particles are large compared with the incident wavelength (i.e. $d>>\lambda$). If light is scattered by particles that are smaller than the light's wavelength, the phenomenon is Rayleigh scattering.

The Mie scattering process is based on a change of the electrical and magnetic properties inside and in the vicinity of the scatterer. Due to the large size of the particles, the scattering process is a due to reflections, refraction and diffraction. The exact solution for scattering of electromagnetic waves from a spherical dielectric body was first obtained by Gustav Mie in 1908. The field of radiation resulting from the interaction between a single droplet and an incident light beam can therefore be calculated using the Mie-Lorenz theory. The resulting effects on the emitted light are changes in phase, amplitude and polarisation.

For Mie scattering, the mathematical solution of the Lorentz-Mie equation is a function of droplet diameter, scattering angle, refractive index of the droplet, polarisation and wavelength of the incident beam (Bohren and Huffman 1983).

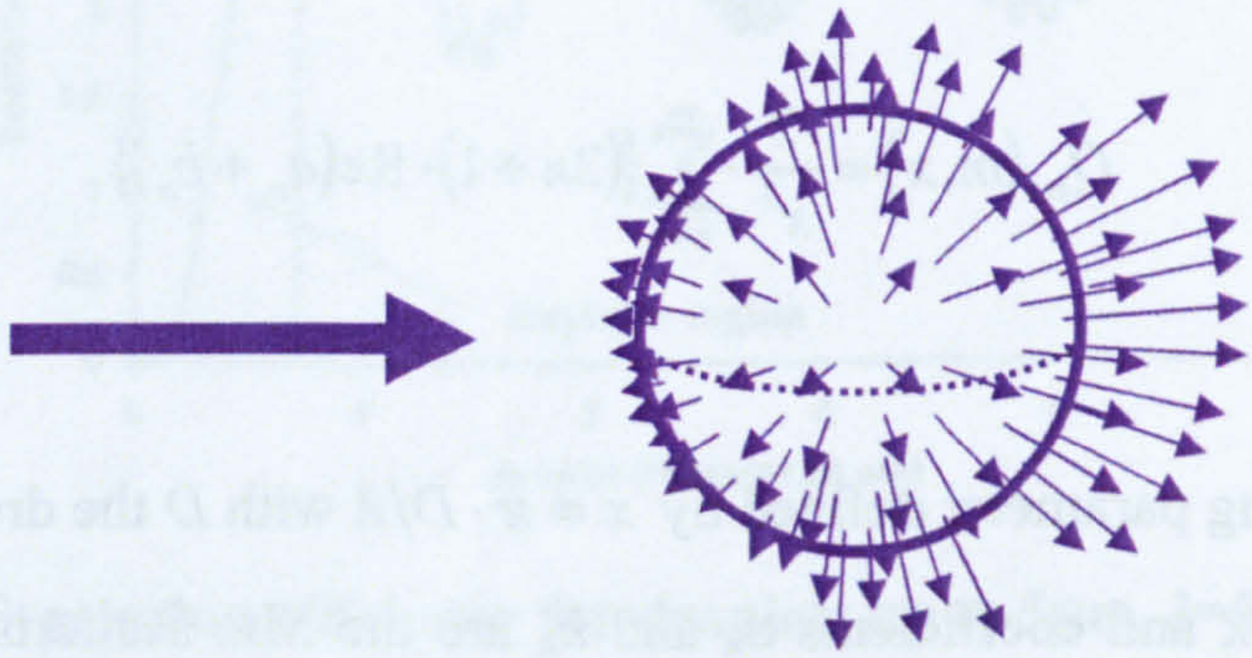

Figure 2-2: Scattered light from a droplet

2.1.3.1. Total scattered signal

A droplet redirects (scatters) light proportionally to its scattering cross section (σ_{scatt}):

$$I_{s,total} = C \cdot I_{laser} \cdot \sigma_{scatt}$$

Equation 2-2

where I_{laser} is the intensity of the incoming light and C is a proportionality constant.

The Mie scattering efficiency for a droplet is its ability to redirect power. It is defined as the scattering cross section divided by the cross-sectional area:

$$Q_{scatt} = \frac{\sigma_{scatt}}{\sigma} = \frac{4}{\pi} \cdot \frac{\sigma_{scatt}}{D^2}$$

Equation 2-3

Combining *Equation 2-2* and *Equation 2-3* gives an expression of the total scattered intensity as a function of diameter:

$$I_{s,total} = C' \cdot I_{laser} \cdot Q_{scatt} \cdot D^2$$

Equation 2-4

The scattering and extinction efficiencies are provided by the Lorenz-Mie theory (Bohren and Huffman 1983):

$$Q_{scatt}(m,x) = \frac{2}{x^2} \cdot \sum_{n=1}^{\infty} \left\{ (2n+1) \cdot \left[|a_n|^2 + |b_n|^2 \right] \right\}$$

Equation 2-5

$$Q_{ext}(m,x) = \frac{2}{x^2} \cdot \sum_{n=1}^{\infty} \left\{ (2n+1) \cdot \mathrm{Re}(a_n + b_n) \right\}$$

Equation 2-6

where x is the sizing parameter defined by $x = \pi \cdot D/\lambda$ with D the droplet diameter. m is the refractive index and coefficients a_n and b_n are the Mie scattering coefficients, and can be found explicitly in Van de Hulst (1957) or Bohren and Huffman (1983).

The absorption efficiency is then defined by:

$$Q_{abs} = Q_{ext} - Q_{scatt}$$

Equation 2-7

In case of absorption, the refractive index must be used in its complex form:

$$m = m_{\mathrm{Re}} - im_{\mathrm{Im}}$$

Equation 2-8

The real part (m_{Re}) corresponds to the refractive index (i.e. the ratio of the speed of light to the phase velocity in the medium). The imaginary part (m_{Im}) expresses attenuation or absorption of the light as it propagates through the medium.

Le Gal (1999) computed the scattering efficiency as a function of droplet diameter for a 532nm incident wavelength and non absorbing droplet of refractive index $m=1.44$. His results (see *Figure 2-3*) demonstrated the features of Mie scatter found in Conwell et al. (1984):

- Q_{scatt} sharply increases as the droplet diameter increases from the Rayleigh limit ($D<\lambda$)
- Q_{scatt} approaches the geometrical optics limit of 2 as the diameter becomes large
- The spectrum consists of rapid oscillations superimposed on a slowly varying background.

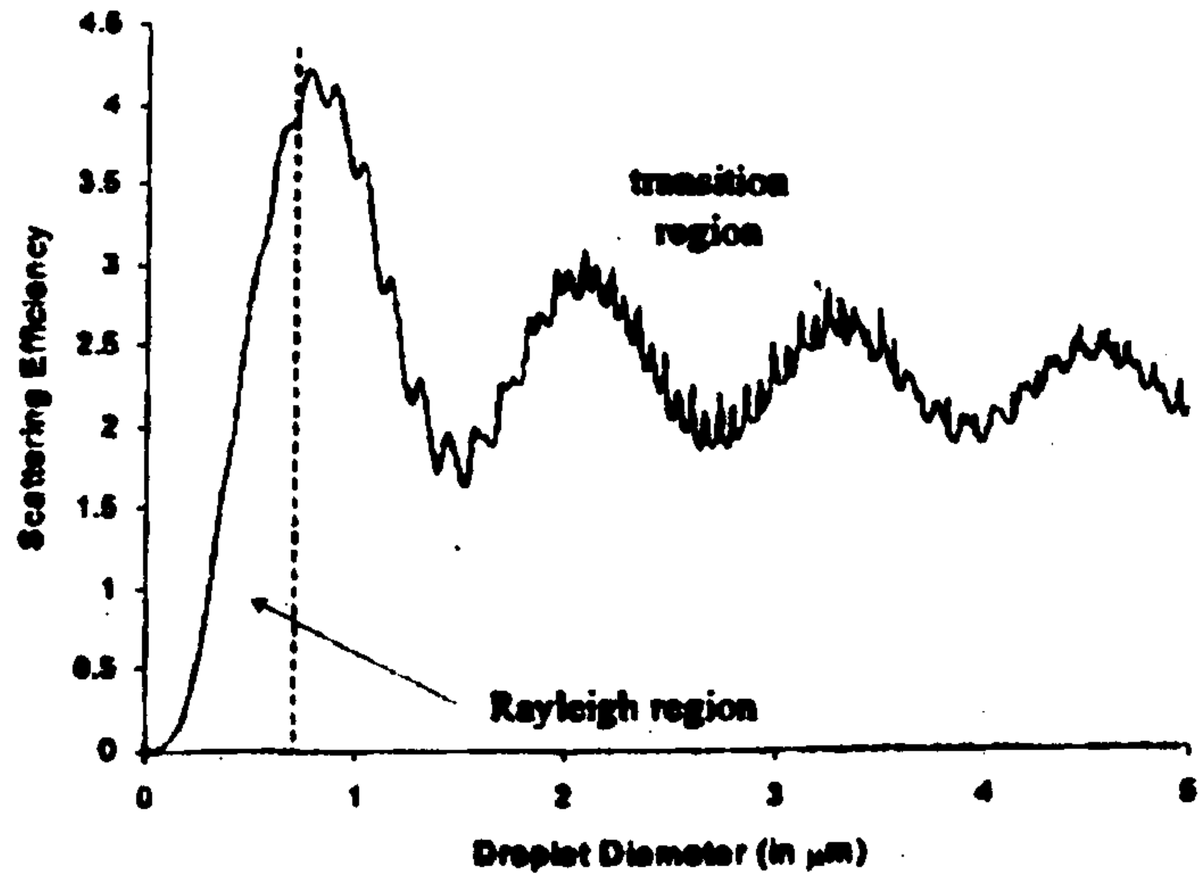

Figure 2-3: Scattering efficiency for droplets up to 5μm, λ=532nm, m=1.44 (Le Gal 1999)

These low frequency oscillations are due to interferences between refracted and diffracted light (Knight et al. 1992). Each peak occurs at regular intervals and can be associated with a resonance which correspond to Morphology Dependent Resonances (MDRs) and are discussed further in this chapter.

The result also suggests that for diameters above a few microns, the Mie scatter intensity could vary as a function of the diameter squared.

The FarField Mie scattering LightLab software developed by Valley Scientific, Inc. was used to determine the scattering efficiency as a function of droplet diameter for a 266nm incident wavelength. A refractive index m=1.4 was used to simulate scattering from non absorbing Iso-Octane droplets.

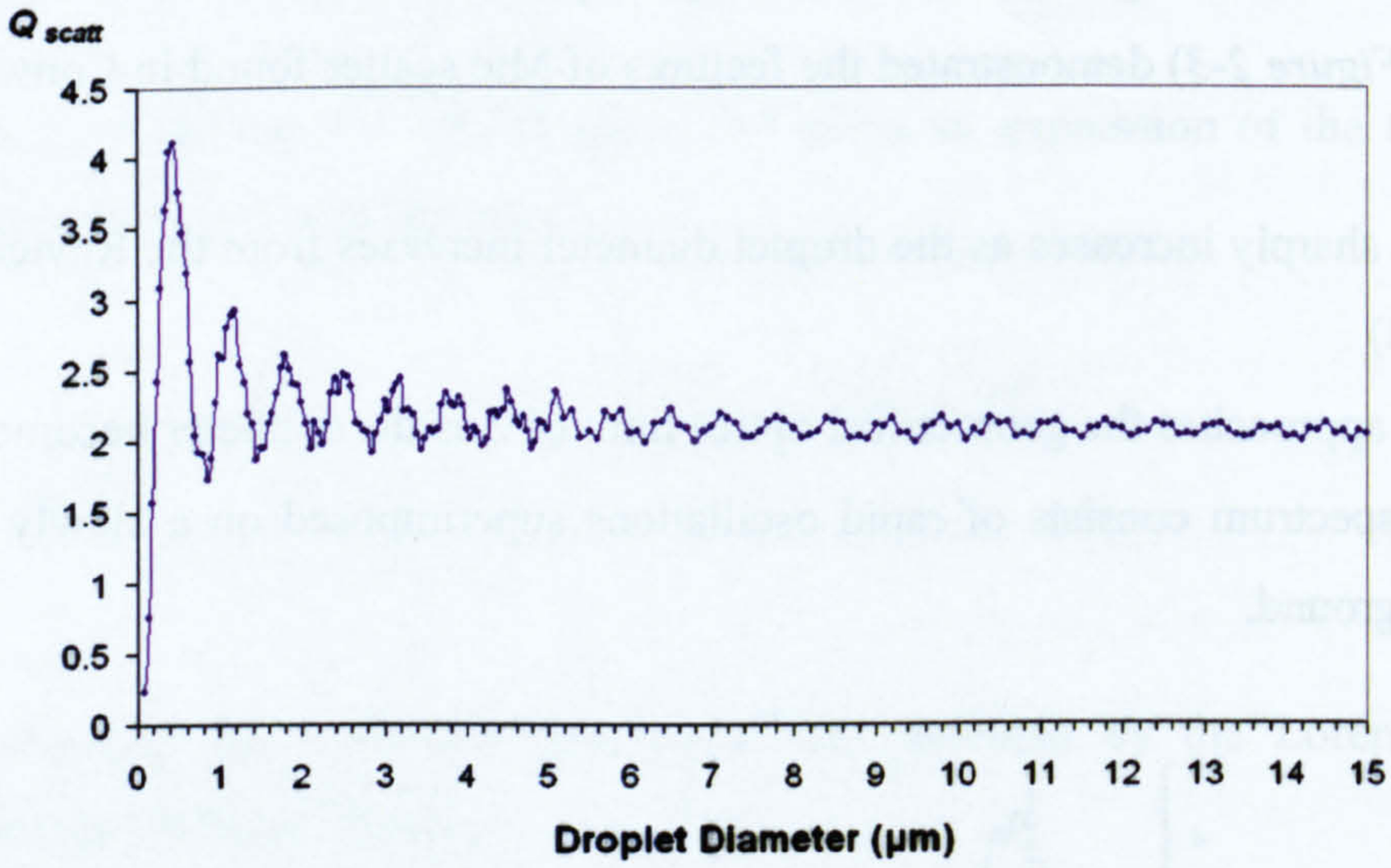

Figure 2-4: Scattering efficiency, λ=266nm, m=1.4

As expected, when the wavelength is halved, the characteristics of the Mie scattered intensity occur at half the diameter sizes. This suggests that the total scattered intensity will deviate from surface dependence by a maximum of 5% for droplets larger than 6µm.

2.1.3.2. Mie scattering as a function of angle

As seen previously, the total scattered light is proportional to the surface area. However, the scattered intensity is not evenly distributed. *Figure 2-5* is the polar diagram (in a logarithmic scale) for the scattering intensity of 266nm light by a 10μm droplet. The figure shows three important results:

- The intensity of the forward scattered light (θ=0°)is much larger than the backscatter or any other direction
- The characteristics of the intensity distribution changes very strongly with observation angle
- The intensity distribution from two polarisations can be very different.

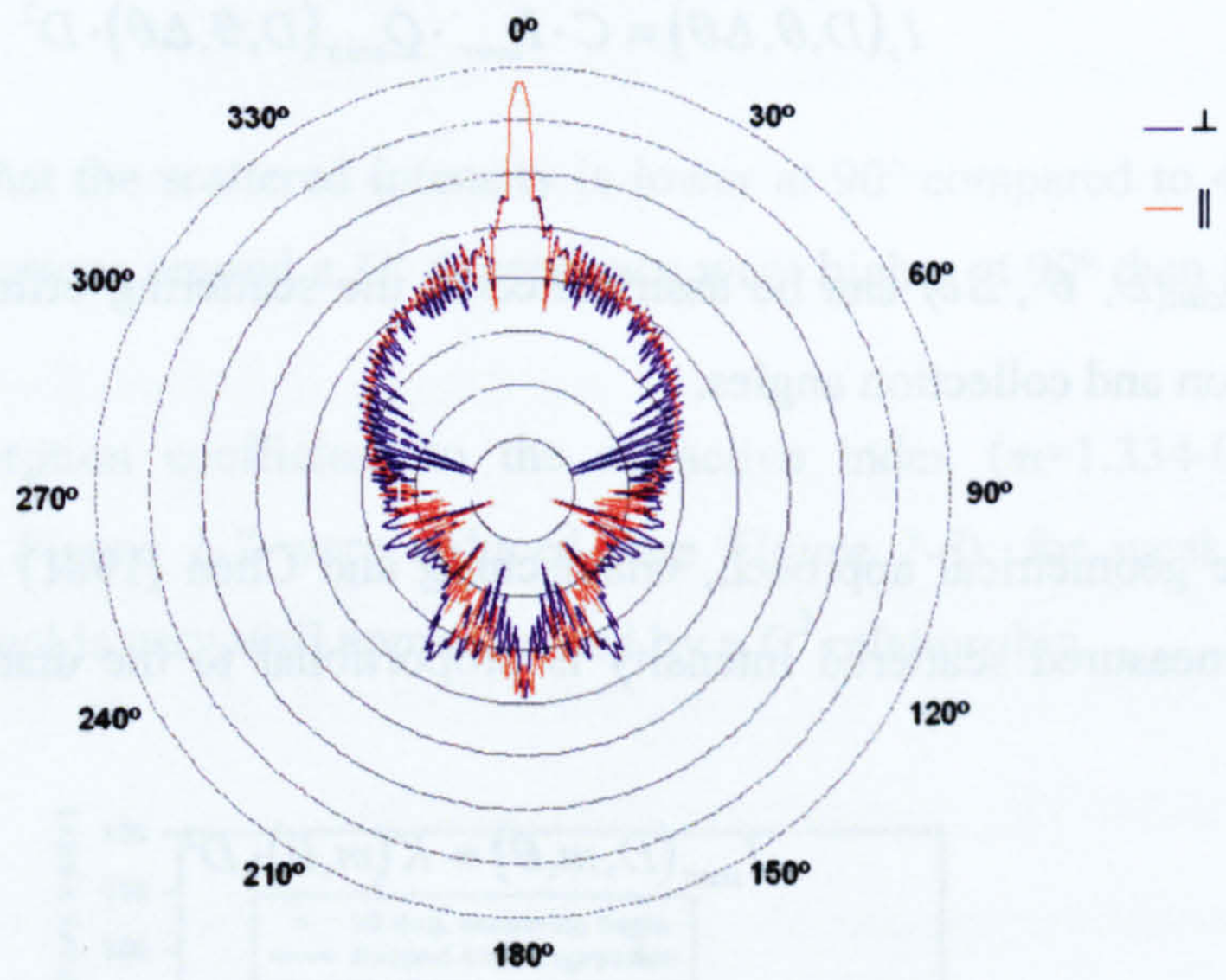

Figure 2-5: Polar diagram (log scale) of Mie scattering for a 10μm droplet

If the scattered light from a droplet of diameter D is observed at an angle θ with a collection angle of $\Delta\theta$ (see *Figure 2-6*), the intensity will be:

$$I_s(D,\theta,\Delta\theta) = C \cdot I_{laser} \cdot F(D,\theta,\Delta\theta) \cdot Q_{scatt} \cdot D^2$$

Equation 2-9

where F represents the proportion of light scattered within the collection angle. At a given wavelength, F is a function of droplet diameter, observation angle and collection angle.

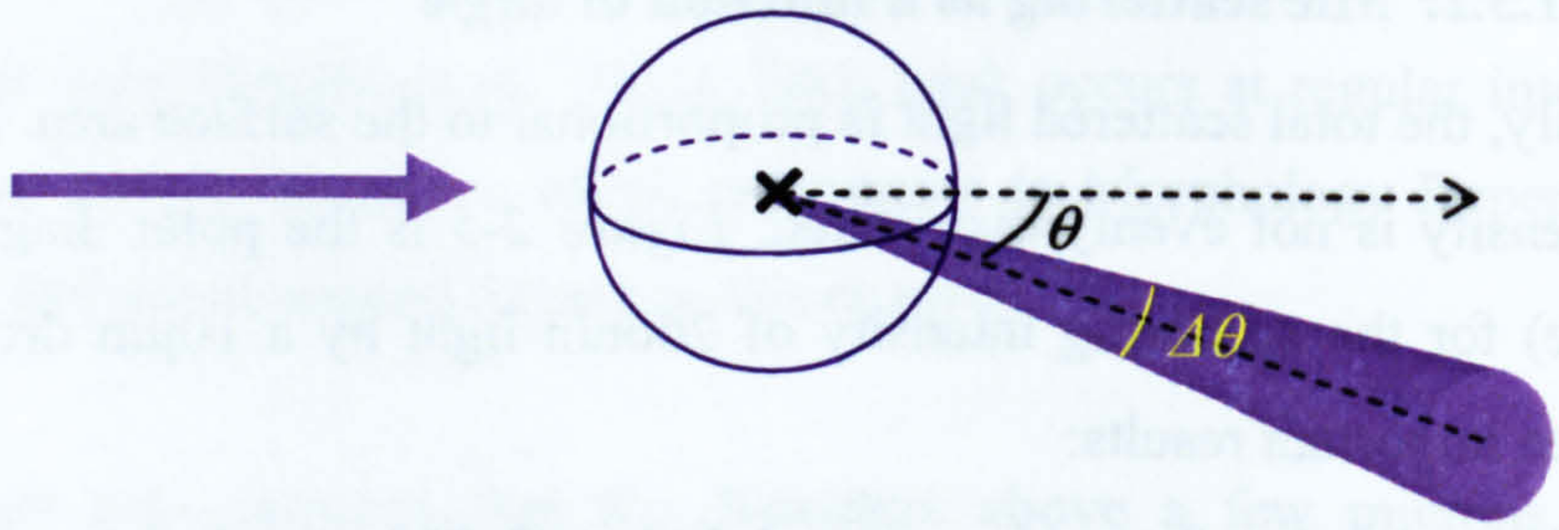

Figure 2-6: Mie scattering observed at an angle

In their notations, Yeh et al. (1993a, 1993b) combine F and Q_{scatt} in a single term and write *Equation 2-9* as:

$$I_s(D,\theta,\Delta\theta) = C \cdot I_{laser} \cdot Q_{scatt}(D,\theta,\Delta\theta) \cdot D^2$$

Equation 2-10

where $Q_{scatt}(D, \theta, \Delta\theta)$ can be assimilated to the scattering efficiency for the specific observation and collection angles.

Using the geometrical approach, Glantschnig and Chen (1981) demonstrated that the average measured scattered intensity is proportional to the diameter of the spherical scatterer:

$$I_{scatt}(D,m,\theta) = K(m,\theta) \cdot D^2$$

Equation 2-11

where $K(m,\theta)$ is a constant depending on the refractive index (m), the collection angle (θ) and the geometry of the scattering set-up.

Equation 2-11 is correct, as long as the receiver's f-number is small enough to average over the angular fluctuations resulting from the interference between the reflected and refracted light (Bachalo and Houser (1984)).

Sankar et al. (1997) modelled the scattering intensity based on the Mie-Lorenz theory in order to predict the variation of scattered signal with droplet size.

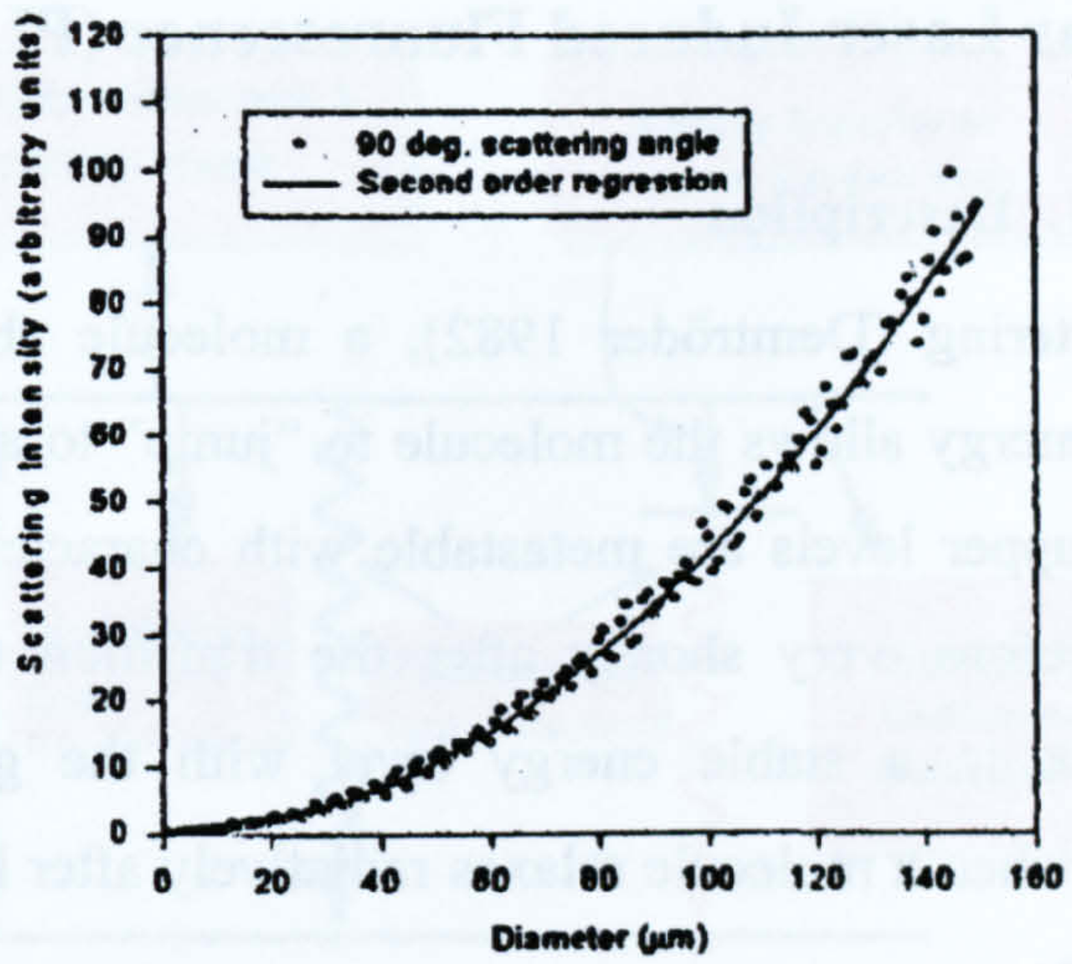

Figure 2-7: Computed variation of scattered light intensity with diameter for a 90° collection angle and no absorption (Sankar et al. 1997)

The authors found that the scattered intensity is lower at 90° compared to 45° or 145° angles. Also the variations around a D^2 dependence were higher at 90° than for the two other angles.

By adding an absorption coefficient to the refractive index (m=1.334-0.001i) the oscillations seen in *Figure 2-7* were reduced (see *Figure 2-8*): for weak absorbing droplets, the Mie signal is very well approximated by a D^2 relationship.

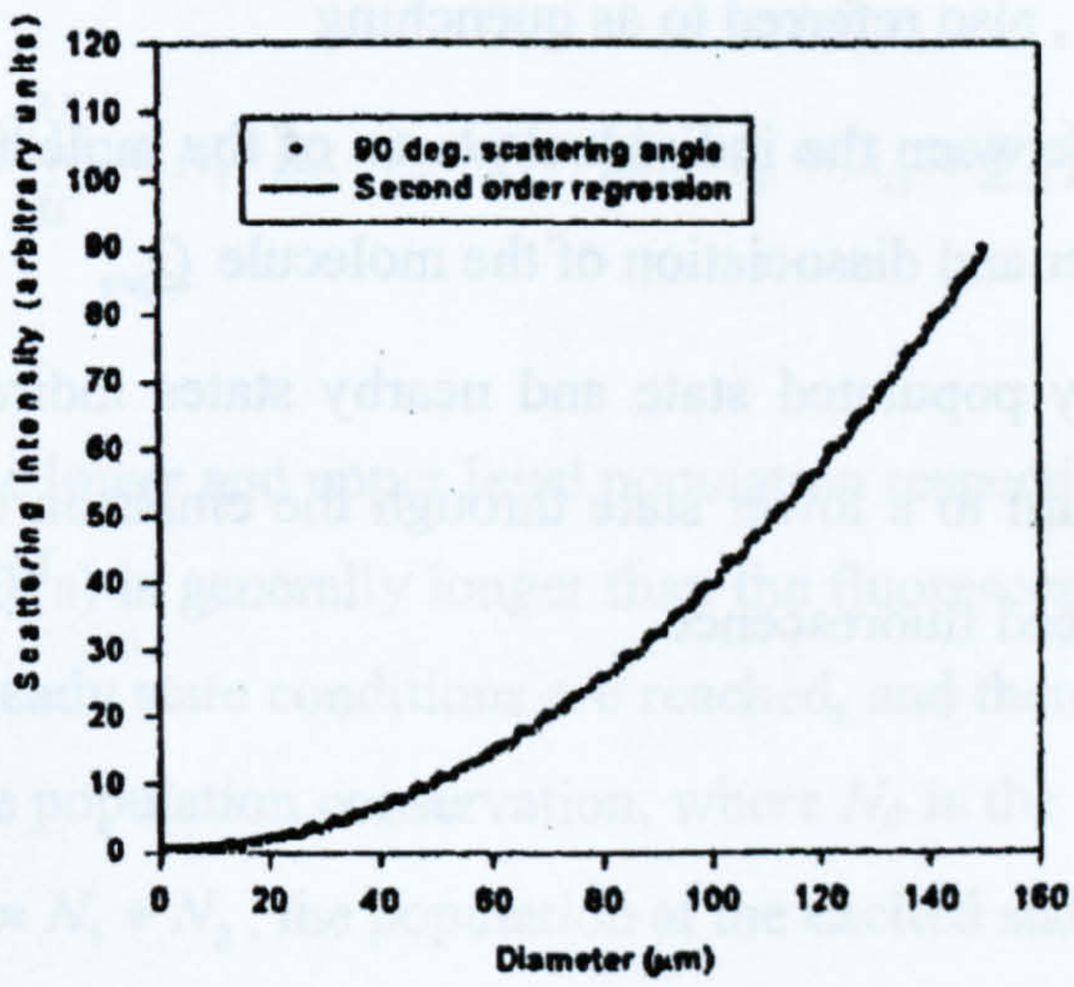

Figure 2-8: Computed variation of scattered light intensity with diameter for a 90° collection angle and weak absorption (Sankar et al. 1997)

2.1.4. Planar Laser-Induced Fluorescence (PLIF)

2.1.4.1. Description

In fluorescence scattering (Demtröder 1982), a molecule absorbs a photon of the incident light. This energy allows the molecule to "jump" to a higher electronic level. The states of these upper levels are metastable with characteristic lifetimes of about 0.1ns to 10μs. Therefore, very shortly after the transition to the upper level, the molecule drops back to a stable energy level with the ground electronic state. Fluorescence occurs when a molecule relaxes radiatively after having been excited to a higher electronic state.

For a simple two level energy system, following the excitation from state 1 to state 2 ($B_{12} \cdot I_\nu$), a molecule can undergo 5 important processes:

- The molecule returns to its original quantum state by laser-induced stimulated emission $B_{21} \cdot I_\nu$
- The molecule can absorb another photon and reach a higher state, eventually reaching an ionized level $B_{2i} \cdot I_\nu$
- Inelastic collisions with other molecules can produce vibrational and rotational transfers $Q_{vib,rot}$. In many cases, these collisions result in electronic energy transfers Q_{elec}, also referred to as quenching
- Interactions between the individual atoms of the molecule can produce internal energy transfer and dissociation of the molecule Q_{pre}
- The originally populated state and nearby states indirectly populated through collisions return to a lower state through the emission of light A_{21}, producing the laser induced fluorescence

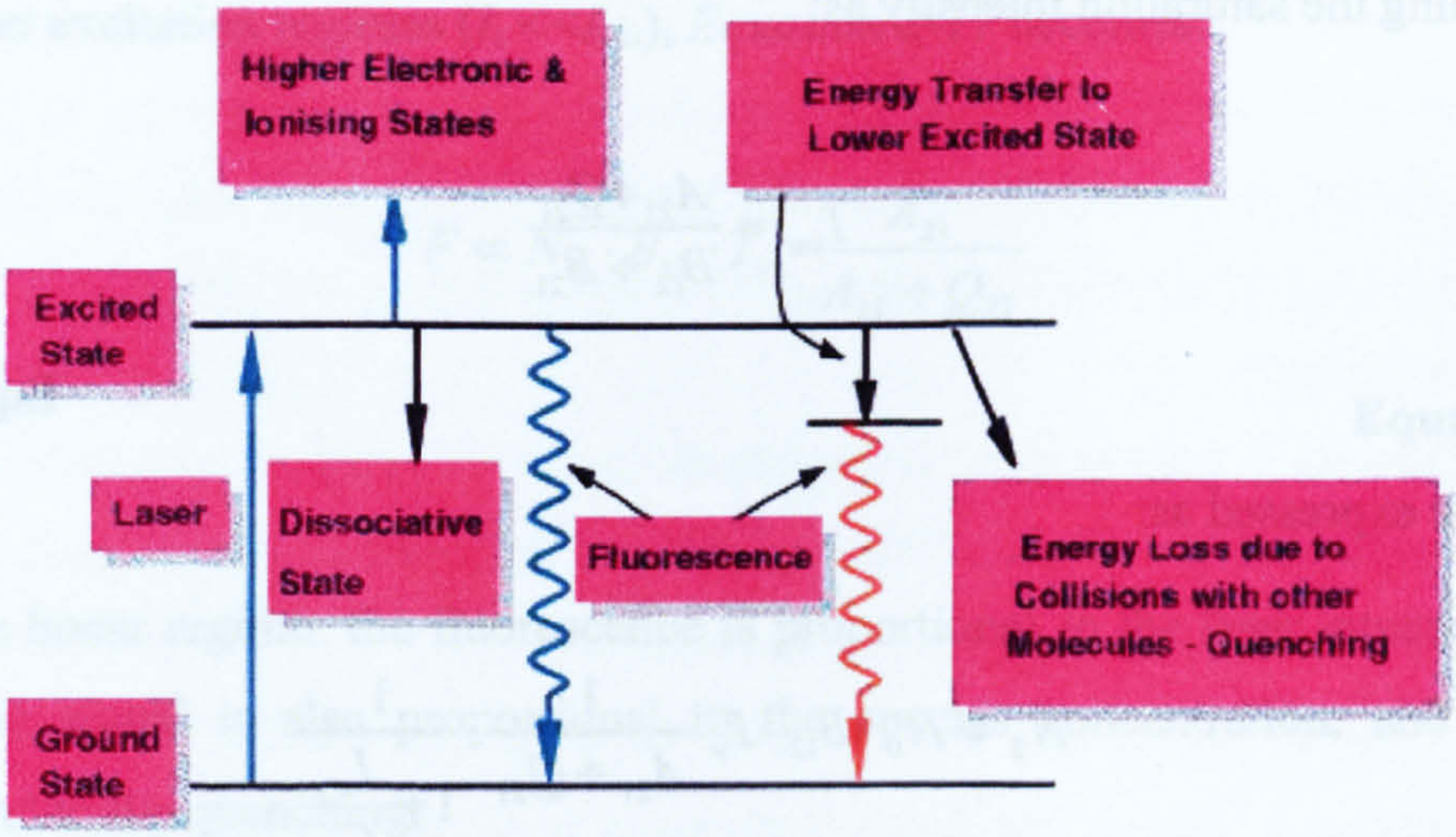

Figure 2-9: Two energy level diagram for molecules excited by a laser source (Seitzman and Hanson 1993)

Considering a two energy level system, where A_{21} is the Einstein coefficient for spontaneous emission (fluorescence), B_{12} and B_{21} the Einstein coefficients for stimulated excitation and emission respectively and Q_{21} is the total quenching factor (i.e. a combination of the pre-dissociation quenching factor Q_{pre}, the collisional or electronic quenching factor Q_{elec}, and the intermolecular collisional quenching $Q_{vib,rot}$), the rate of change of the population at the excited level is given by:

$$\frac{dN_2}{dt} = N_1 \cdot B_{12} \cdot I_\nu - N_2 \cdot \left(B_{12} \cdot I_\nu + A_{21} + Q_{21}\right)$$

Equation 2-12

where N_1 and N_2 are the lower and upper level population respectively.

As the laser pulse (~10^{-8}s) is generally longer than the fluorescence lifetime (~10^{-9}s), it can be assumed that steady state conditions are reached, and therefore *Equation 2-12* is equal to zero. With the population conservation, where N_0 is the initial total population at the lower level, $N_0 = N_1 + N_2$, the population at the excited state can be written as:

$$N_2 = N_0 \cdot \frac{B_{12} \cdot I_\nu}{A_{21} + Q_{21} + \left(B_{12} + B_{21}\right) \cdot I_\nu}$$

Equation 2-13

By defining the saturation intensity as:

$$I_{sat} = \frac{A_{21}+Q_{21}}{B_{12}+B_{21}}$$

Equation 2-14

N_2 can be expressed as:

$$N_2 = N_0 \cdot B_{12} \cdot I_\nu \frac{1}{A_{21}+Q_{21}} \cdot \frac{1}{1+\frac{I_\nu}{I_{sat}}}$$

Equation 2-15

The fluorescence is proportional to the upper state population multiplied by its probability to fluoresce:

$$F \propto N_2 \cdot A_{21}$$

Equation 2-16

The fluorescence can therefore be expressed as:

$$F \propto N_0 \cdot B_{12} \cdot I_\nu \cdot \frac{A_{21}}{A_{21}+Q_{21}} \cdot \frac{1}{1+\frac{I_\nu}{I_{sat}}}$$

Equation 2-17

In the saturation regime ($I_\nu >> I_{sat}$), the fluorescence intensity is:

$$F \propto N_0 \cdot B_{12} \cdot \frac{A_{21}}{B_{12}+B_{21}}$$

Equation 2-18

The fluorescence signal is independent of both the laser fluence and the quenching: the signal is directly related to the species concentration. However, it is very difficult to reach saturation when performing PLIF.

At low laser excitation regimes ($I_v << I_{sat}$), *Equation 2-17* becomes:

$$F \propto N_0 \cdot B_{12} \cdot I_v \cdot \frac{A_{21}}{A_{21} + Q_{21}}$$

Equation 2-19

This is the linear regime: the fluorescence is proportional to the laser intensity. In this regime, the signal is also proportional to the species concentration, and inversely proportional to the quenching.

In the linear regime, if the quenching rate is low ($Q_{21} << A_{21}$), the fluorescence signal becomes:

$$F \propto N_0 \cdot B_{12} \cdot I_v$$

Equation 2-20

If the quenching rate is high ($Q_{21} >> A_{21}$), *Equation 2-15* becomes:

$$N_2 = N_0 \cdot B_{12} \cdot I_v \cdot \frac{1}{Q_{21}}$$

Equation 2-21

and the fluorescence signal becomes:

$$F \propto N_0 \cdot B_{12} \cdot I_v \cdot \frac{A_{21}}{Q_{21}}$$

Equation 2-22

In these conditions, the fluorescence signal is proportional to the laser intensity and the species concentration.

2.1.4.2. PLIF applied to IC engines

The wide application of PLIF in IC engines is mainly due to the strength of the fluorescence process, relative to those of Raman or Rayleigh scattering. Also, PLIF can

be used to image fuel location in both the liquid and vapour phase (Tait and Greenhalgh 1992).

For in-cylinder measurements, two different strategies have been adapted: natural fluorescence from the species of interest or fluorescence obtained from an added dopant (also called tracer).

Most of the early fluorescence work carried out in IC engines was performed in the linear non-quenching regime. In these conditions, the fluorescence signal is proportional to the laser intensity and the species concentration.

Naturally fluorescing species like OH were excited to look at flame front (Felton et al. 1988, Suntz et al. 1988). For fuel visualisation in IC engines, gasoline was first used because it contains fluorescing compounds. However, these different compounds each have individual fluorescence properties and for that reason, quantitative measurements are not possible. For quantitative measurements, Arnold et al. (1990) used a specific tracer in the fuel (acetaldehyde). Lawrenz et al. (1992) studied various tracers to replace the gasoline fuel by a single compound fluorescent fuel. They found Ethylmethylketone (EMK – or 2-Butanone) to be the best and measured AFR using throughout the intake and compression stroke and found appreciable inhomogeneities in fuel distribution. Baritaud and Heinze (1992) introduced Iso-Octane as a single component fuel, doped with biacetyle to obtain the fluorescence. Since, many fuel studies in IC engines have used various tracers with Iso-Octane. The choice of added tracers to visualise the fuel is discussed in *Chapter 3*. Berckmüller et al. (1994) used 3-Pentanone to visualise the fuel vapour and measure crank-angle resolved AFR in a lean burn Honda V-TEC transparent engine and found that there was substantial cycle-to-cycle variations in local fuel concentration at the spark electrodes.

LIF has also been used to measure oil film thickness, as early as 1974 by Smart and Ford. Shaw et al. (1992) developed an optical fibre based LIF measurement system and determined oil film thickness at the piston ring / cylinder liner interface.

Until this point, tracers had been selected for their non-quenching behaviour in oxygen. If the tracer was quenched by oxygen (e.g. TriEthylAmine -TEA- which has a high fluorescence yield but is strongly quenched), experiments were carried out in a Nitrogen environment.

Reboux et al. (1994) showed that quenching in the vapour phase, which had been considered as an unwanted effect could, on the contrary, be used for quantitative determination of AFR. If the quenching rate is directly proportional to the concentration of oxygen ($Q_{21} = k \cdot [O_2]$), a linear relation exists between the fluorescence intensity and the fuel-to-air ratio (FAR):

$$F \propto \frac{N_0}{Q_{21}} \propto \frac{[fuel]}{[O_2]} \propto \Phi$$

Equation 2-23

Frieden and Sick (2003) measured Oxygen distribution using toluene and 3-pentanone tracers. Because the fluorescence spectra of the two tracers are distinct, their signals can be easily separated. In addition, toluene's fluorescence is quenched in oxygen, whereas 3-pentanone's is not. The ratio of their signals can be used to extract O_2 concentration. By knowing the amount of fuel and the amount of air, the distribution of the 3rd species (EGR) can then be obtained.

$$\left.\begin{array}{l} F_{pent} \propto [fuel] \\ F_{tol} \propto \dfrac{[fuel]}{[O_2]} \end{array}\right\} \Rightarrow \frac{F_{pent}}{F_{tol}} \propto [O_2]$$

One issue with this technique is that the signal is inversely proportional to the species that is being measured.

One of the issues with PLIF is that the fluorescence from the liquid or vapour phase of a single component cannot be spectrally separated. This is because the fluorescence spectra of organic molecules dissolved in non-polar solvents are virtually identical to the spectra of the same molecules in the vapour phase. To overcome this, Melton (1983) introduced Laser Induced Exciplex Fluorescence (LIEF). The technique uses a mixture of two monomers, one serving as an electron donor (*D*) and the other as an electron acceptor (*A*). When *A* and *D* are excited (to *A** and *D** respectively) and fluoresce, they can bind with the opposite ground state monomer to form a third fluorescent species *(A-D)** which is bound in the excited state but not in the ground state. The newly formed

species is called the excited state complex or *exciplex*. The probability that *A* and *D* form an exciplex is influenced by temperature and concentrations of the donor and acceptor. By adequately choosing the concentration of the donor and the acceptor, it can be assured that the liquid-phase fluorescence is predominantly characterised by the red-shifted emission from the exciplex, whereas the vapour phase fluorescence is dominated by the emission of the monomers *A* and *D*.

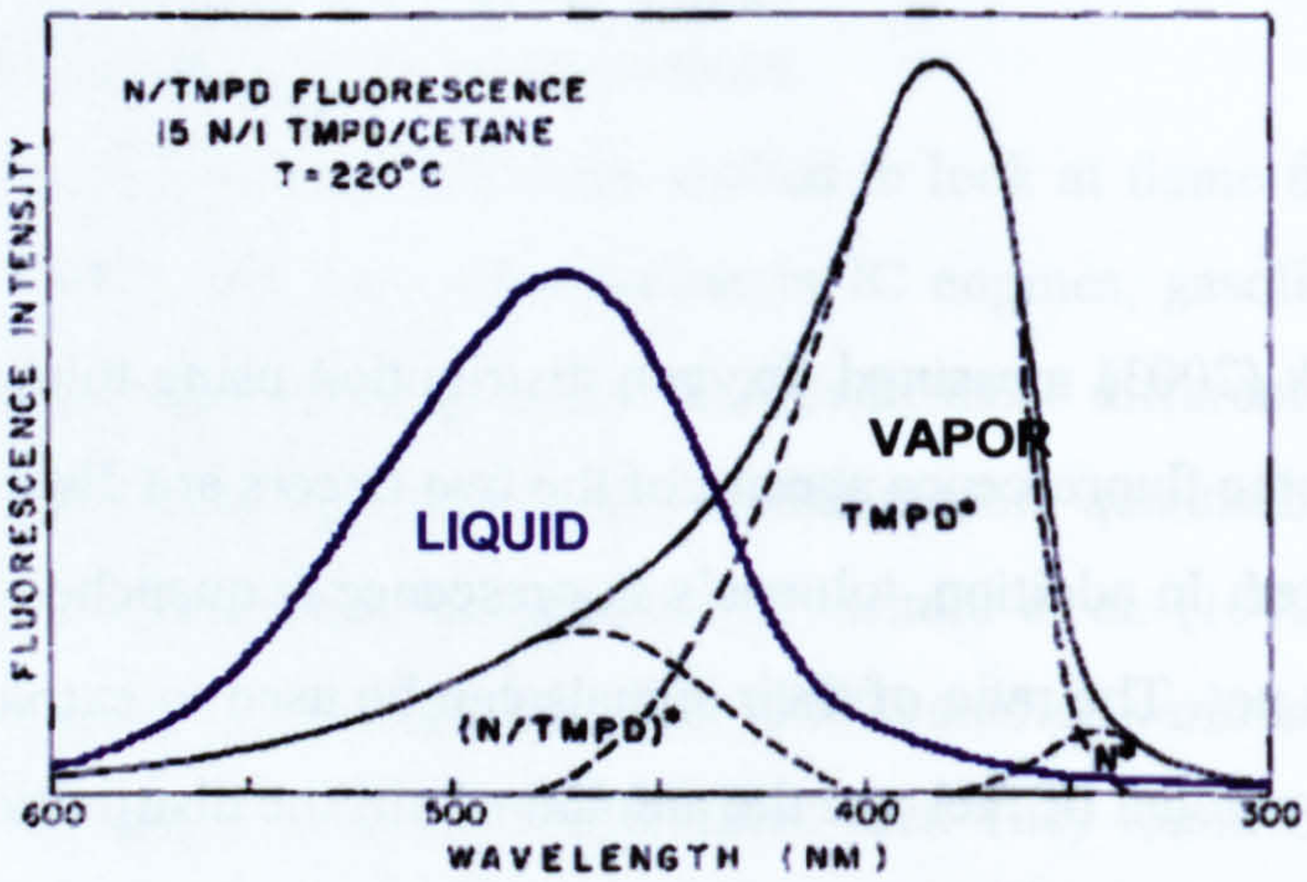

Figure 2-10: Spectra of 10% Naphtalene, 1% TMPD, 89% cetane mixtures in the ligand and vapour phases - T=220°C (Melton 1983)

The first exciplex system for LIEF was developed by Melton (1983) and applied to droplets. The mixture consisted of 10 to 15% naphthalene combined with 1% tetramethyl-p-phenylene diamine (TMPD) in a synthetic diesel fuel (hexadecane). Melton and Verdieck (1985) later used a 2.5% Naphtalene / 1% TMPD exciplex mixture in 96.5% hexadecane (cetane) to study the vapour and liquid phase mixing of a Delavan hollow cone injector. *Figure 2-10* shows the spectral separation of the liquid phase fluorescence of the exciplex with the vapour phase fluorescence.

Melton (1993) proposed exciplex systems with boiling points matching those of gasoline fuel. They were based on tertiary alkyl amines like TriEthylAmine (TEA) and *n*-PropylDiEthylAmine (NPDEA) mixed with electronegatively substituted benzenes like Fluorobenzene (FBZ) and 4-FluoroToluene (4FT). Fröba et al. (1998) introduced TriEthylAmine (TEA) and Benzene as a new fluorescent tracer system for LIEF. A mixture of 2% TEA and 3.4% Benzene was used in Iso-Octane. This tracer mixture has two advantages: it predominantly forms an exciplex in the liquid phase, and it is also

quenched by oxygen. This allowed to simultaneously separate the liquid and vapour phase fluorescence whilst using the quenching behaviour to determine FAR

2.1.5. Morphology Dependent Resonances (MDR)

Morphology Dependent Resonances (MDRs) of spherical and smooth non-spherical particles are reviewed by Hill and Benner (1988). MDRs in microspheres are responsible for the ripple structure observed in Mie scattering (see *Figure 2-3*). They are also responsible for the large optical feedback necessary for the lasing (Serpengüzel et al. 1992).

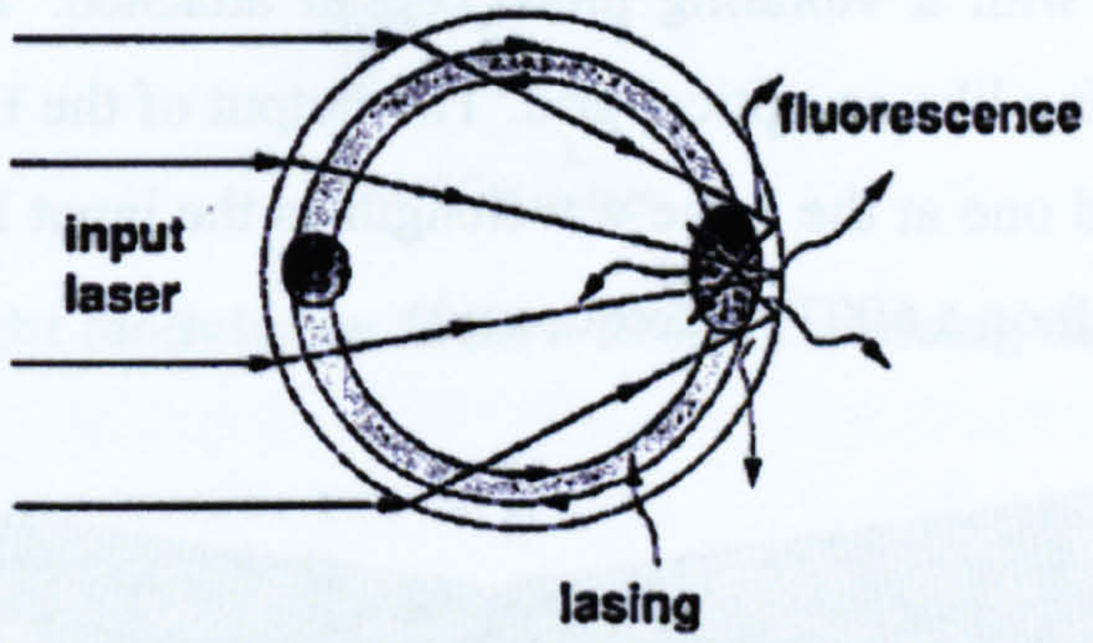

Figure 2-11: Spatial distribution of the internal intensity in a microsphere (Serpengüzel et al. 1992)

An interpretation of MDRs is that of rays propagating around the droplet's surface. MDRs are usually treated as standing waves that can be decomposed into two counter-propagating waves that are contained by total internal reflection and travel around the droplet rim (see *Figure 2-11*). For the correct droplet size, the waves may return to their starting point with their initial phase and constructive interference takes place. The structure due to the constructive interference is correlated to the morphology of the drops, hence the usage of the term morphology dependent resonance.

Resonance peaks have been observed in elastic and inelastic scattering, and can modify the emission from a micro-droplet. Resonant effects are only likely to be important if the spacing between MDRs exceeds the emission line width of the fluorescent molecules (Hill et al. 1996). In practice, resonance peaks are dampened by surface imperfections and droplet shape. Inhomogeneities in refractive index near the surface of an evaporating droplet will also dampen resonance peaks (Knight et al. 1992).

2.2. Velocity Measurements

2.2.1. Laser Doppler Anemometry (LDA)

Laser Doppler Anemometry (LDA) - or Laser Doppler Velocimetry (LDV) - was pioneered by Yeh and Cummins (1964) and is described in detail by Durst et al. (1981). It is a point measurement technique.

A probe volume is created by splitting the laser beams in two equal intensity beams and crossing them at an angle. At first, beam splitters were used, and the interference pattern of the coherent light resulted in fringes. Later, a Bragg cell was used as a beam splitter. It is a glass crystal with a vibrating piezo crystal attached. The vibration generates acoustical waves acting like an optical grid. The output of the Bragg cell is two beams of equal intensity and one at the same wavelength as the input beam, the other slightly shifted (a 40MHz shift on a 600THz frequency).

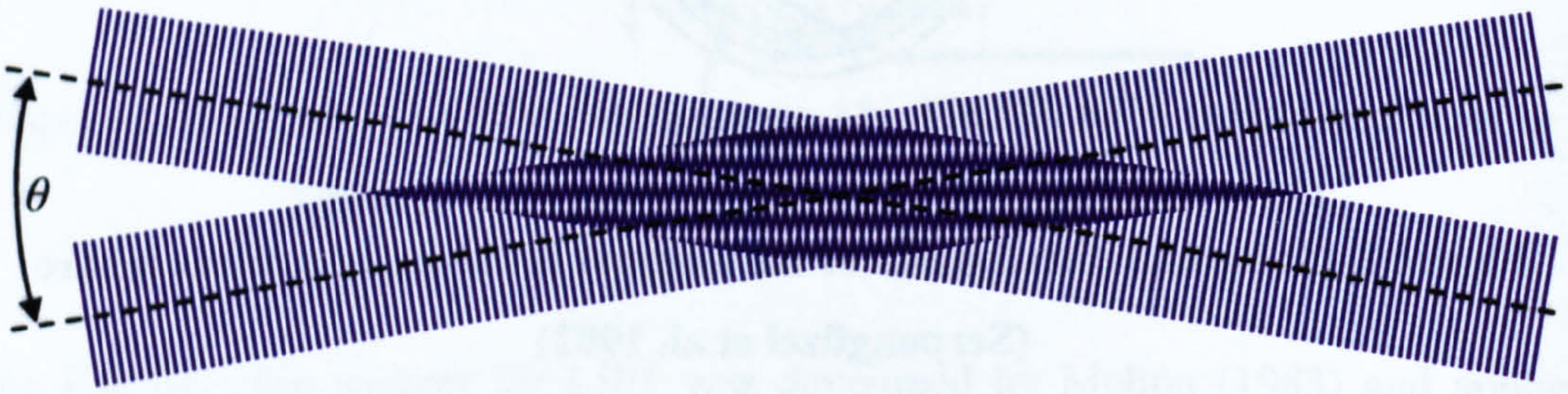

Figure 2-12: Interference fringes

The fringe spacing d_f is given by:

$$d_f = \frac{\lambda}{2 \cdot \sin\theta}$$

Equation 2-24

The frequency shift obtained by the Bragg cell makes the fringe pattern move at a constant velocity (V_{shift}). Particles which are not moving will generate a signal of the shift frequency f_{shift}. The velocities V_{pos} and V_{neg} will generate signal frequencies f_{pos} and f_{neg} , respectively.

When a single droplet crosses the interference fringes in the probe volume, it scatters intensity-modulated light. The rate of intensity variation (i.e. the Doppler frequency - f_D) indicates the time the droplet takes to travel the distance between two fringes. The droplet's velocity component normal to the fringes and relative to the fringe velocity is:

$$V_r = d_f \cdot f_D$$

Equation 2-25

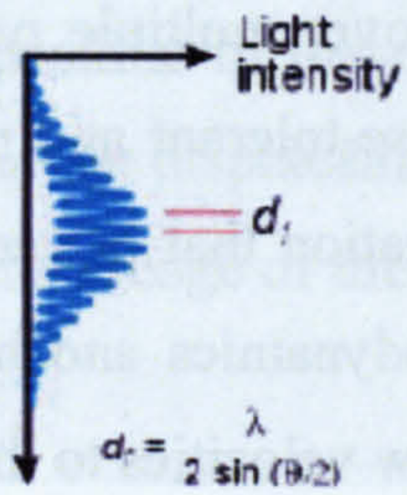

Figure 2-13: light modulation from a droplet crossing the fringe pattern

The actual velocity of the particle is:

$$V = V_{shift} + V_r$$

Equation 2-26

2.2.2. Particle Image Velocimetry (PIV)

In 1921, in-cylinder- flow was studied by Clerk using a low speed optical engine designed by Ricardo. At this early stage the flow was visualised using smoke, and allowed Clerk to confirm the turbulent behaviour of the in-cylinder flow and also to disprove Otto's theory that the charge was stratified.

In 1937, studies, undertaken by Lee, employed a number of innovations. In particular, pieces of feather were introduced in the flow as tracers and the motion was recorded using a high-speed cine camera and an intense light source. By manually matching the location of the seeds in consecutive frames, velocity was determined. It was the early form of Particulate Tracking Velocimetry (PTV). With CCD cameras, photographs are now digitised and tracking algorithms automate the process.

Correlation-based Particle Image Velocimetry (PIV) does not require the matching of individual droplets. Instead, it determines average motion of groups of particles contained within a small area called the interrogation region. The overall frame is divided into regions and the correlation function is computed over each region, yielding a velocity vector per interrogation region. It is possible to calculate average velocity maps, instantaneous or average vorticity maps, turbulence intensity maps and spatial correlation maps.

Compared to PTV, the averaging over multiple particle pairs within an interrogation region makes the measurement noise-tolerant and robust. This measurement technique gives access to quantitative information that is very useful for the characterisation of flows. It can be used both in aerodynamics and hydrodynamics, and the measurable velocity range extends from very low velocities to the supersonic regime.

While LDA is limited to the point measurements, PIV is used to extract 2-dimensional velocity fields. Due to the short laser pulse duration, each image contains the instantaneous position of the particles. The local velocity in the flow is measured by determining the displacement of the particles between two laser pulses (images). If the seeding density is sufficiently high, a two-dimensional velocity map of the illuminated region can be generated.

When the pairs of images are recorded on the same frame, the analysis is carried out by auto-correlation: the displacement is determined by shifting the image relative to itself and summing the product of the corresponding pixels for each shift. This sum goes through a maximum when the shift matches the displacement. For each square interrogation region of width w, the correlation function for each shift (i,j) is given by:

$$R(i,j) = \sum_{x=-\frac{w}{2}}^{x=\frac{w}{2}} \sum_{y=-\frac{w}{2}}^{y=\frac{w}{2}} I(x,y) \times I(x+i, y+j)$$

Equation 2-27

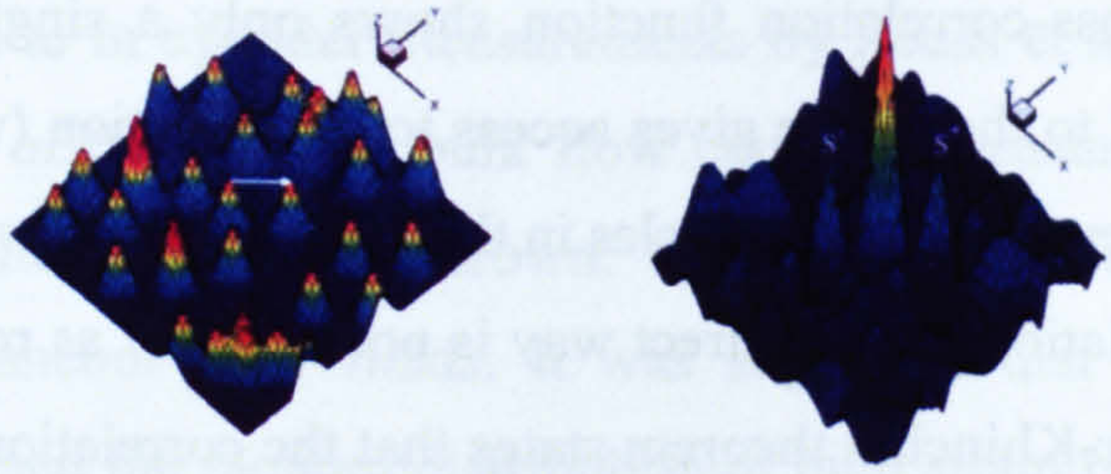

Figure 2-14 – Single frame - double exposure and Auto-correlation analysis

The auto-correlation function shows a central peak (i.e. *R(0,0)* is the maximum) and two symmetric secondary peaks. The position of these secondary peaks with respect to the centre of the analysis window gives the displacement of the particles. The symmetry of the correlation function prevents knowledge of the direction of displacement, which has to be determined from the flow.

To eliminate the ambiguity, the two particle images can be recorded on different frames. The analysis is then carried out by cross-correlation: the determination of the displacement is done by shifting the second image relative to the first image and summing the product of the corresponding pixels for each shift. This sum reaches its maximum when the shift is equal to the displacement. In discrete terms, the cross-correlation is given by:

$$R(i,j) = \sum_{x=-\frac{w}{2}}^{x=\frac{w}{2}} \sum_{y=-\frac{w}{2}}^{y=\frac{w}{2}} I_1(x,y) \times I_2(x+i, y+j)$$

Equation 2-28

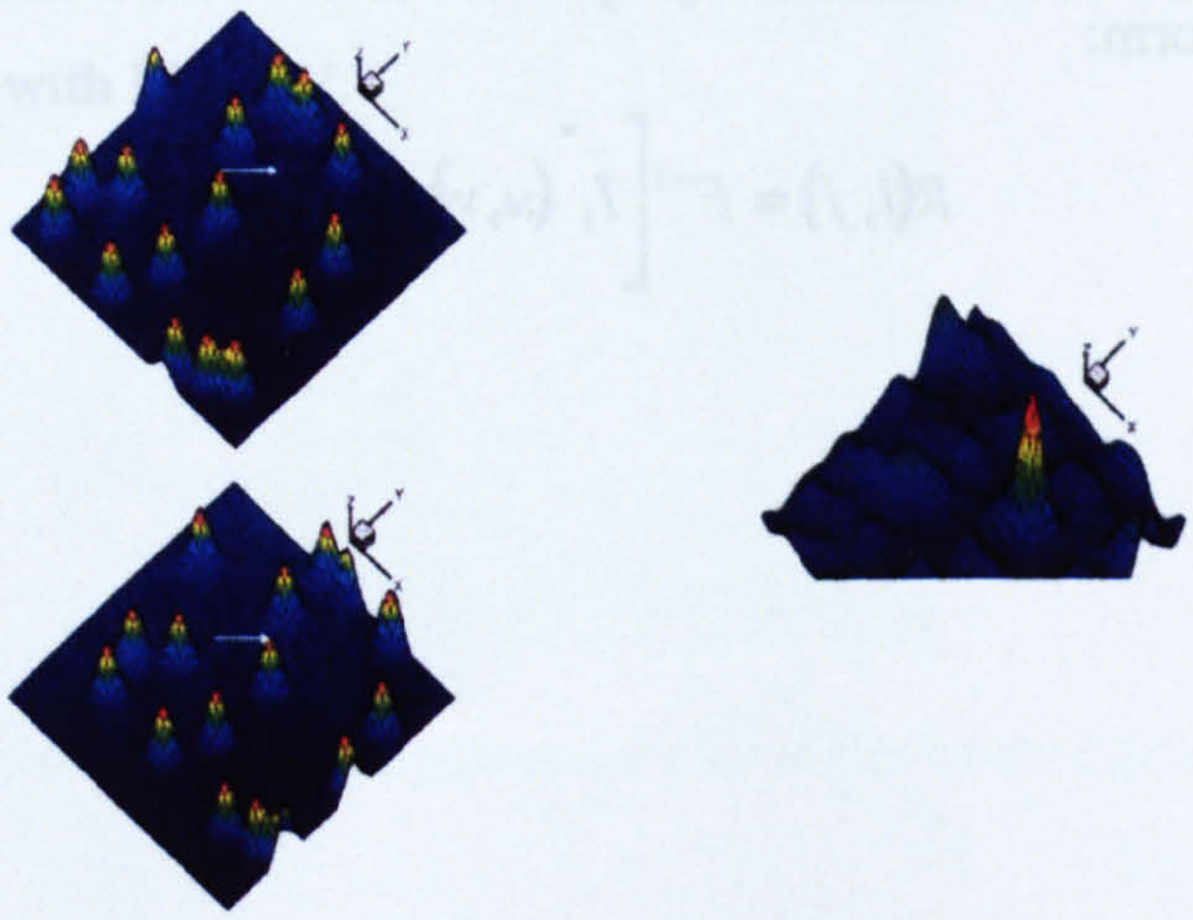

Figure 2-15 – Double frame – double exposure and Cross-correlation analysis

In this case, the cross-correlation function shows only a single intense peak whose position with respect to the centre gives access to the direction (with no ambiguity) and length of the displacement of the particles in the analysis window (see *Figure 2-15*)
Evaluating the correlations in the direct way is not efficient as regards computing time. However, the Wiener-Khinchin theorem states that the correlation of two signals f and g ($f \otimes g$) in the temporal domain can be computed as a multiplication in the frequency domain:

$$f \otimes g = F^{-1}\left(\tilde{f}^{*} \times \tilde{g}\right)$$

Equation 2-29

where $\tilde{f}$ and $\tilde{g}$ are the Fourier transforms of f and g respectively, $\tilde{f}^{*}$ is the complex conjugate of $\tilde{f}$ and F is the inverse Fourier transform.

Using the Fast Fourier Transform (FFT) is far more efficient: the auto-correlation (where f=g=I) can be quickly calculated by 1 forward transform and 1 inverse transform:

$$R(i,j) = F^{-1}\left[\left|\tilde{I}(u,v)\right|^{2}\right]$$

Equation 2-30

The cross-correlation (f=I_1 and g=I_2) can be obtained quickly with 2 forward transforms and 1inverse transform:

$$R(i,j) = F^{-1}\left[\tilde{I}_1^{*}(u,v) \times \tilde{I}_2(u,v)\right]$$

Equation 2-31

PIV was first applied to in cylinder measurements by Reuss et al. (1989) in a motored engine. The velocity of the swirling bulk flow could be measured in a portion of the engine cylinder, parallel to the piston crown. Vorticity structures and strain rates were derived from instantaneous flow fields. It was suggested that the magnitude of the observed strain rates and the random distribution of high strain regions could affect the early flame growth and therefore contribute to cyclic variations in engine performance.

Nino et al. (1993) demonstrated PIV in a fired 2-stroke engine with high swirl inlet configuration. Instantaneous and ensemble averaged velocity fields parallel to the piston crown and velocity fluctuations could be obtained in the unburned gas.

Reeves (1994) measured the instantaneous velocity field in a motored 4-valve engine. Illumination of a plane parallel to the cylinder axis through a piston window allowed the study of large scale tumble vortices.

Pajot (2000) made turbulence velocity measurements in a port injection RENAULT engine and also showed that the axis of tumble and swirl movement were not respectively exactly horizontal and vertical.

Hentschel et al. (1999) studied droplet PIV of a swirl injector. They used 2 Excimer lasers (308nm) for the measurements in a pressure chamber, and a double pulse frequency-doubled Nd:YAG laser (532nm) for the engine experiments. They found that in some cases, the droplet velocities could only be obtained on the edge area due to the high density inside the spray.

Yamakawa et al. (2001) studied simultaneously the spray and air motion around the spray. They injected a solution of water and Rhodamine into the air and used a 532nm light source. The scattered light from the spray droplets was separated from the fluorescence of the Rhodamine in the air. Spray velocities were obtained by Mie scatter PIV and air motion with LIF PIV.

2.3. Size Measurement

The droplet size distribution is directly related to the spray's atomisation and vaporisation process. The quality of the air-fuel mixing is critically dependent on these factors. Early development of sizing techniques include freezing drops (Longwell 1943) or molten wax techniques (Joyce 1949). The first technique used an alcohol bath kept at the temperature of dry ice, which was cold enough to freeze the drops. This enabled to sample the droplets. The second technique used the fact that molten wax has the same properties as kerosene, and was fed through aero injectors, and would solidify at the exit. Since then, non intrusive methods have greatly developed.

2.3.1. Laser diffraction

Low-angle laser light scattering (LALLS, commonly called laser diffraction) systems typically pass a laser beam of known wavelength through a suspension of the material to be analyzed and measure the angular distribution and intensity of the forward-scattered (diffracted) light by the particles in suspension. A theoretical model, based on diffraction of particles with particular properties and grain-size distribution, is then fitted to the actual diffraction results. When the first laser diffraction instruments were launched, the constraints of most commonly available computers meant that the instruments used an approximation of Mie light-scattering theory known as the Frauenhofer approximation to produce particle size analyses. However the full the solution of the light scattering of spheres as predicted by Gustav Mie can now be applied.

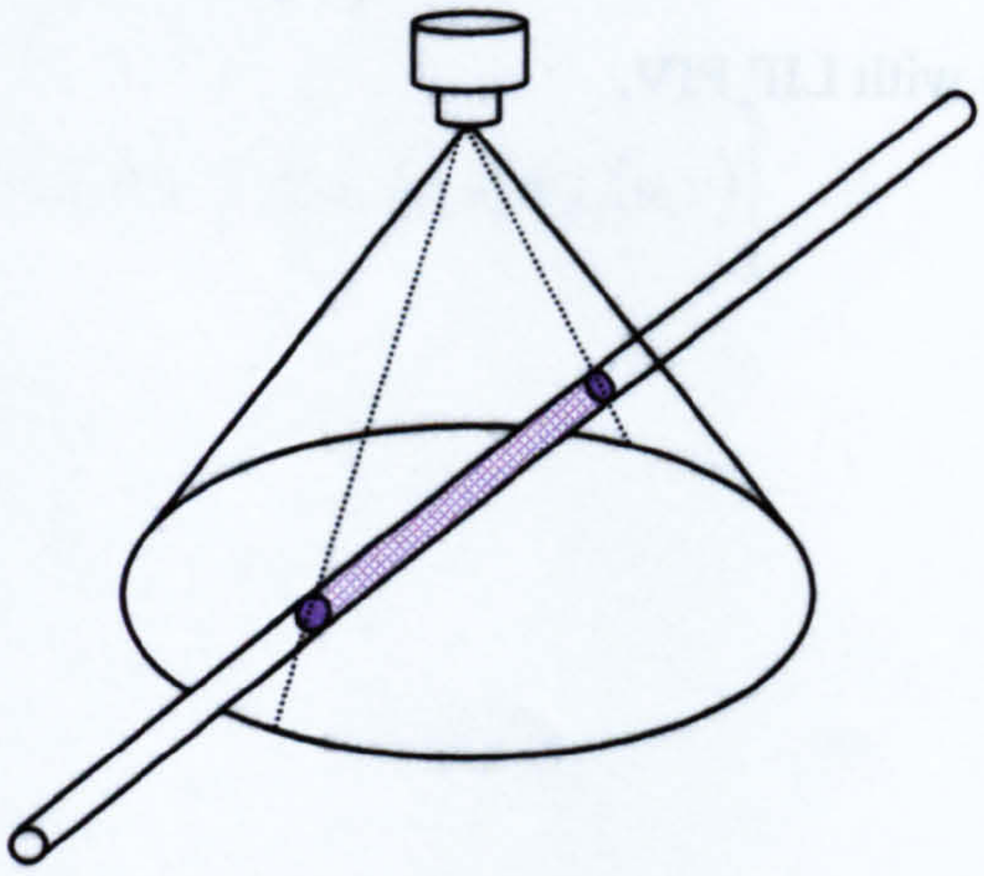

Figure 2-16: Measurement volume for the line-of-sight scattering technique

This line-of sight technique uses forward scattered light from moving particles. The detected light is not sensitive to refractive index or shape, and therefore is only a function of size (Swithenbank 1976). The measurement of this angular light distribution is the basis of the optical particle sizer manufactured by Malvern Instruments Ltd.

The technique measures the forward scattered light of a cloud of particles in a laser beam. Not only is the measurement averaged over the light path (line-of-sight technique), it is also averaged over the beam diameter, which gives this method limited spatial resolution. However, if the spray is axisymetric, the averaged measurements of optical extinction and droplet size distribution can be deconvoluted into radial variations of drop size distribution and number density (Hammond 1981).

2.3.2. Interferometric Particle Imaging

This technique is based on the principle of defocused imaging of Mie scattering from transparent droplets. The interference of reflected and refracted light results in fringe patterns (see *Figure 2-17*) which contain the information about the size of the droplet in the spacing of the fringes.

It goes by various names: PMSI - Planar Mie Scattering Interferometry, PII – Planar Interferometric Imaging, PPIA – Planar Particle Image Analysis, ILIDS – Interferometric Light Imaging for Droplet Sizing.

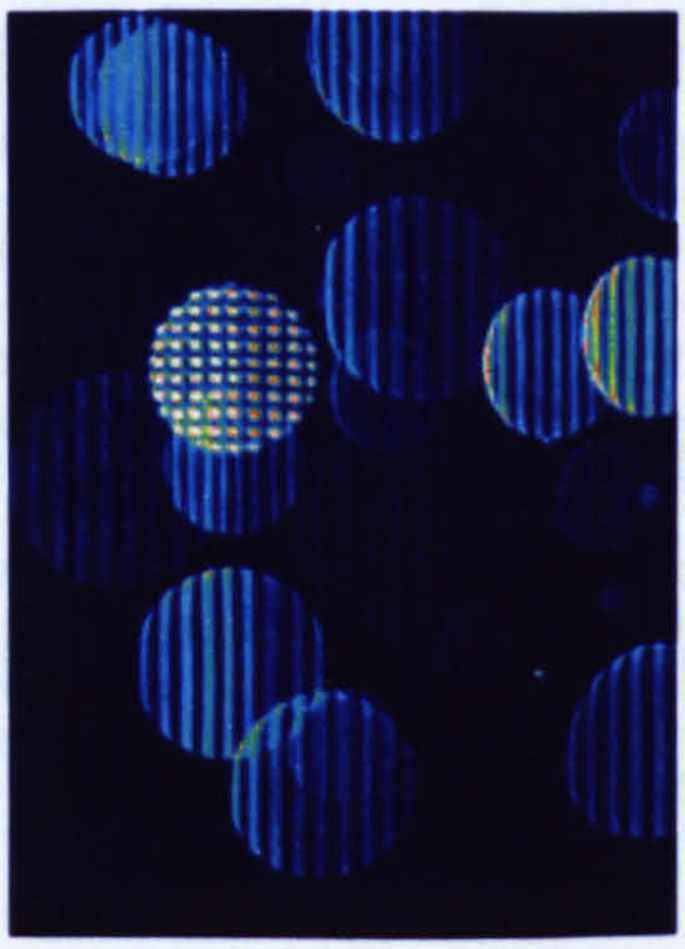

Figure 2-17: Interference pattern in out-of-focus imaging of droplets

The technique was pioneered in 1986 by König et al. They focused a laser beam onto a stream of monodisperse droplets and measured the resulting fringe pattern in the far field. They recognised the potential for accurate drop size measurements.

Van de Hulst and Wang (1991) proposed that the droplets give two glare points in the focussed plane, and that it is possible to determine the diameter from the distance between the 2 glow spots. However, this would require high magnification to resolve them, and this technique would offer no advantage over direct particle imaging.

These two points act as 2 spherical emission sources. Their overlap creates parallel fringes, and can be seen in the defocused plane.

Using geometrical optics, Hesselbacher et al. (1991) demonstrated that the diameter and the fringe spacing were linked, and described the relationship between particle diameter d and number of fringes N by:

$$d = \frac{2 \cdot \lambda \cdot N}{\alpha} \cdot \frac{1}{\cos\left(\theta/2\right) + \frac{m \cdot \sin\left(\theta/2\right)}{\sqrt{m^2 - 2 \cdot m \cdot \cos\left(\theta/2\right) + 1}}}$$

Equation 2-32

where m is the refractive index, λ is the laser wavelength, θ and α are the scattering and collecting angle respectively.

Glover et al. (1995) extended the technique to a light sheet and applied it in an engine to a spatially sparse spray. Pajot and Mounaïm (1998) successfully obtained dropsize data from the non-dense part of a spray in an SI engine, but the denser part of the spray was not measurable due to the overlapping of the circular interferogram.

Koboyashi et al. (2000) further improved the technique by optically compressing the circular fringe images using an anamorphic system consisting of two cylindrical lenses. This not only avoids signal overlap but also increases signal-to-noise ratio of the captured interferential image. They obtained an error of less than 3% for arithmetic mean diameter.

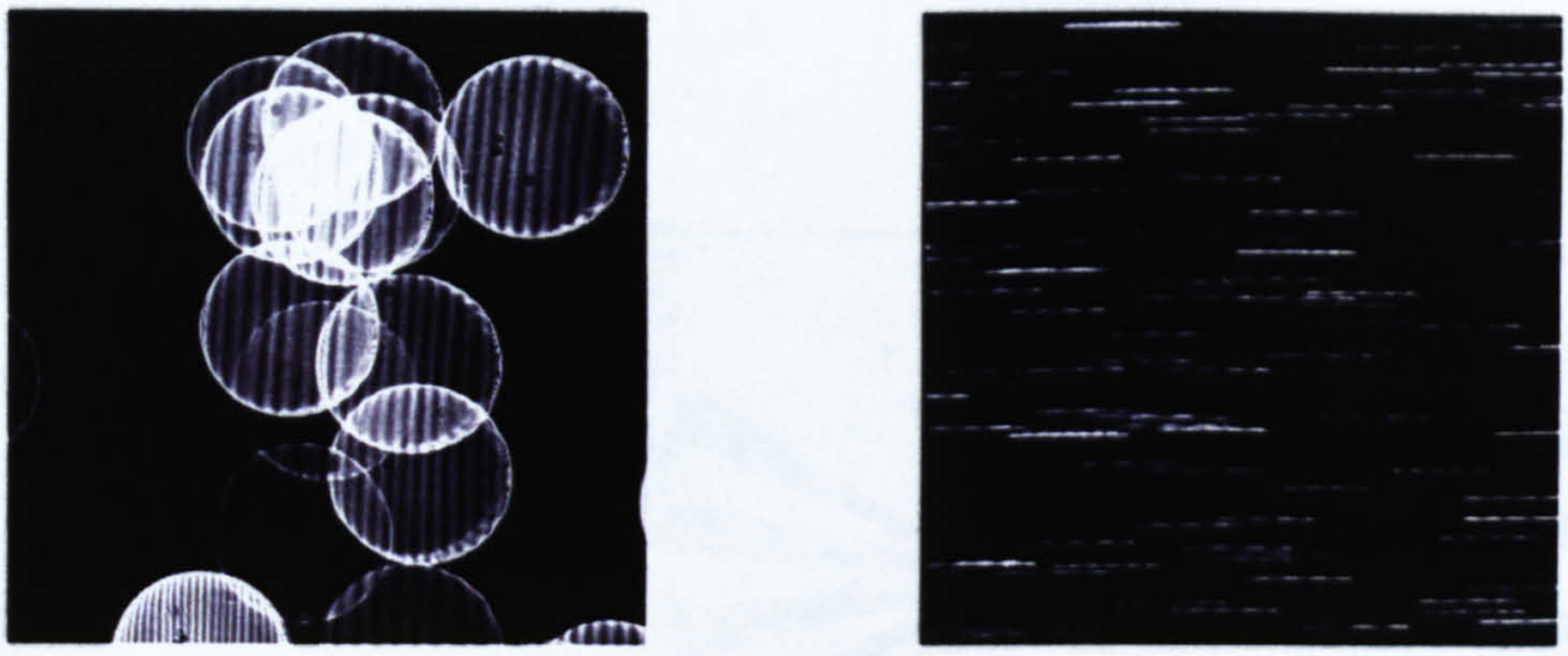

(A) (B)

Figure 2-18: Interferometric image (Maeda et al. 2000) using

(A) Conventional technique – 15 droplets

(B) Compression Optics - >100 droplets

Maeda et al. (2000) combined the compression technique with double-pulsed images and simultaneously measured drop size and velocity.

The technique shows great promise but only manages to capture parts of the spray: typical imaging is 10mm × 10mm on a 1008 × 1018 pixel camera (Maeda et al. 2003). Commercial instruments are available from Dantec (FlowMap Particle Sizing System) and LaVision (SizeMaster).

2.3.3. Phase Doppler Anemometry (PDA)

The basic principle of this method was proposed by Durst and Zaré in 1975 and by Bachalo in 1980 as an extension of Laser Doppler Anemometry (LDA). The technique uses the phase angle between adjacent Doppler signals for drop size measurement.

When a droplet crosses a fringe pattern formed at the intersection of two focused laser beams, it acts as a lens and forms a magnified version of the fringes at the two detectors (see *Figure 2-19*).

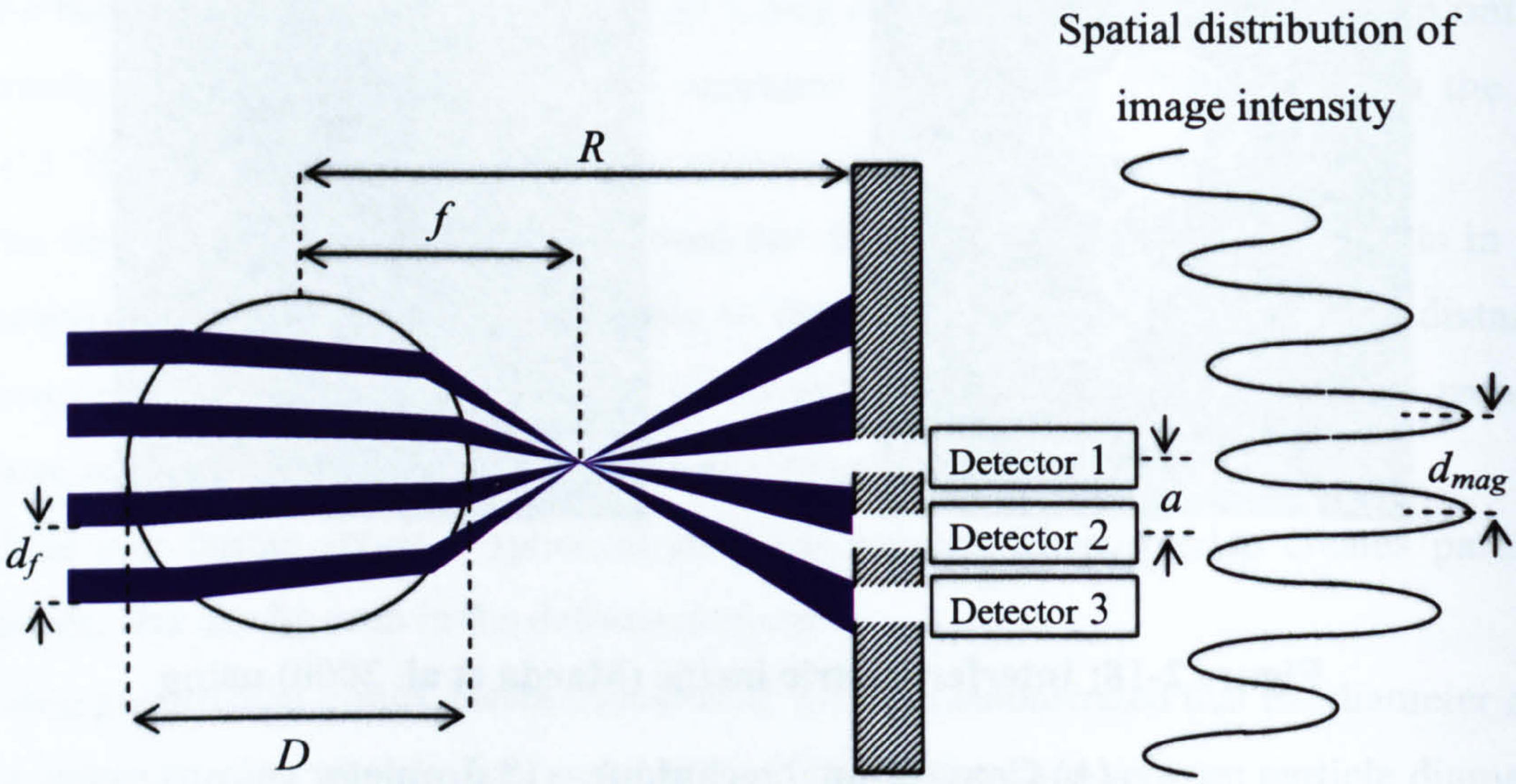

Figure 2-19: PDA sizing principle (figure is not to scale: in practice, R>>f)

A stationary sphere of diameter D will project magnified fringes at a distance R from the centre of the droplet. If f is the focal length of the sphere, considered as a thick lens, and d_f is the object fringe spacing, then the measured spacing of the image fringes d_{mag} is given by:

$$d_{mag} = (R - f) \cdot \frac{d_f}{f}$$

Equation 2-33

As $R >> f$, *Equation 2-31* can be simplified to:

$$d_{mag} \approx R \cdot \frac{d_f}{f}$$

Equation 2-34

For a sphere of refractive index n, considered as a thick lens for small scattering angles:

$$f = \frac{n}{n-1} \cdot \frac{D}{4}$$

Equation 2-35

If the particle moves, the fringes will appear to rotate about the focal point of the the thick lens. A detector at a given point will therefore see an oscillating pattern of light and dark fringes. If another detector is seperated by the distance a, the signal will be out of phase from the first detector by an angle:

$$\Phi = 2\pi \cdot \frac{a}{d_{mag}}$$

Equation 2-36

Combining *Equation 2-34*, *Equation 2-35* and *Equation 2-36* we obtain :

$$\Phi \approx \pi \cdot a \cdot \frac{n}{n-1} \cdot \frac{\sin\theta}{R \cdot \lambda} \cdot D \propto D$$

Equation 2-37

One complication with PDA is that the light from a droplet is both refracted and reflected and the phase difference from these two scattering mechanisms is not necessarily the same. The solution is to use polarised laser light and to arrange for the detectors to be close to Brewster's angle $\Phi_b = 2 \cdot \text{Arctan}(1/n)$ at which refraction dominates reflection. In practice the phase-diameter relationship is near linear between 30° to 80°, with the best linearity at Brewster's angle normally a maximum in the scattering at the angle of 1st refraction often referred to as the rainbow angle.

A second issue concerns the compromise between accuracy and range afforded by a total phase angle of 2π. To overcome this limitation, normally 3 detectors are used, yielding two different separations between pairs so that the wider-separated pair phase angles greater than 2π can be measured without ambiguity. This arrangement also increases the redundancy of the measurement and permits validation of the measurement.

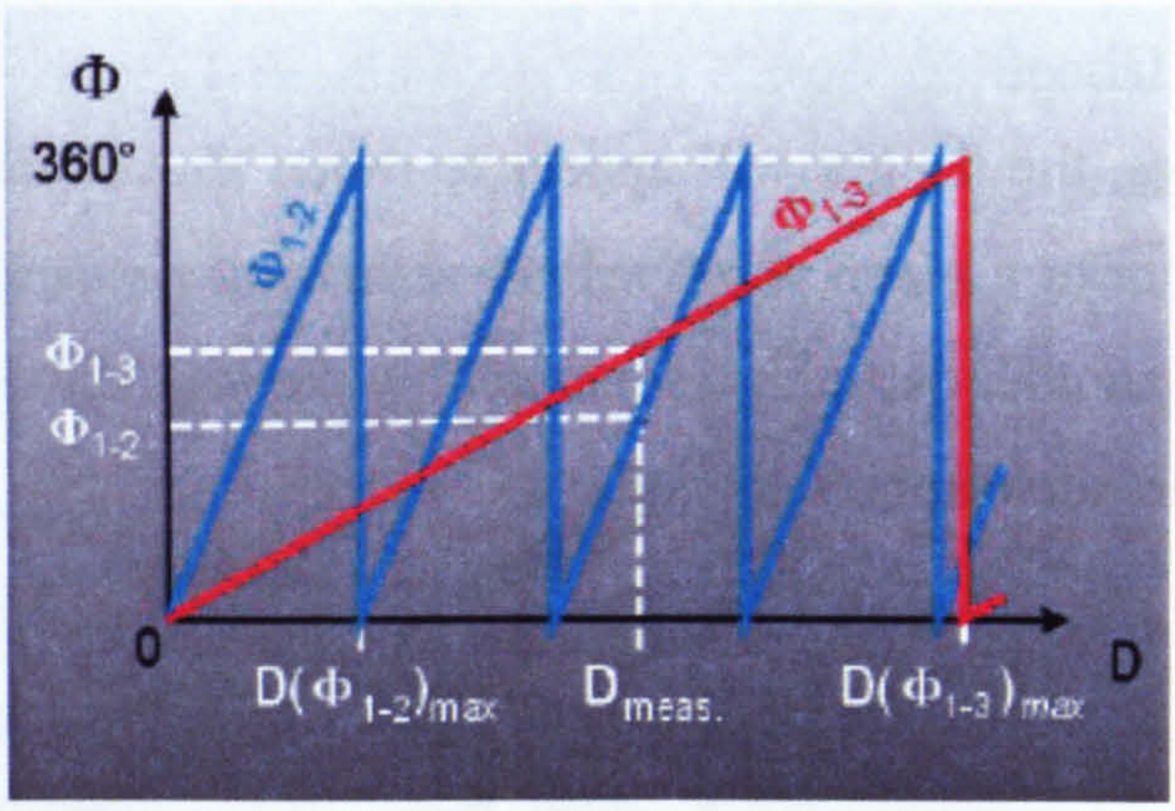

Figure 2-20: Calibration curves for detectors' phase shifts (1-2 and 1-3)

Signals are typically processed using a dedicated signal processor and in particular a covariance processor which can simultaneously measure phase and frequency from a Doppler burst. More recently, commercial manufacturers have developed discrete Fourier transform processors. These offer higher bandwidth and hence velocity range, higher accuracy, and reduced dead-time.

A major uncertainty with the PDA is caused by the measurement volume effect (MVE). This is due to the beams' Gaussian profile and is also referred to as the trajectory effect: if a large particle penetrates the probe volume, the intensity profile of the incident beams causes a non-uniform illumination of the particle and induces reflected and refracted rays which may have roughly the same intensities on the detectors (see *Figure 2-21*). For dominating reflected light, this effect results in considerable errors in size measurement.

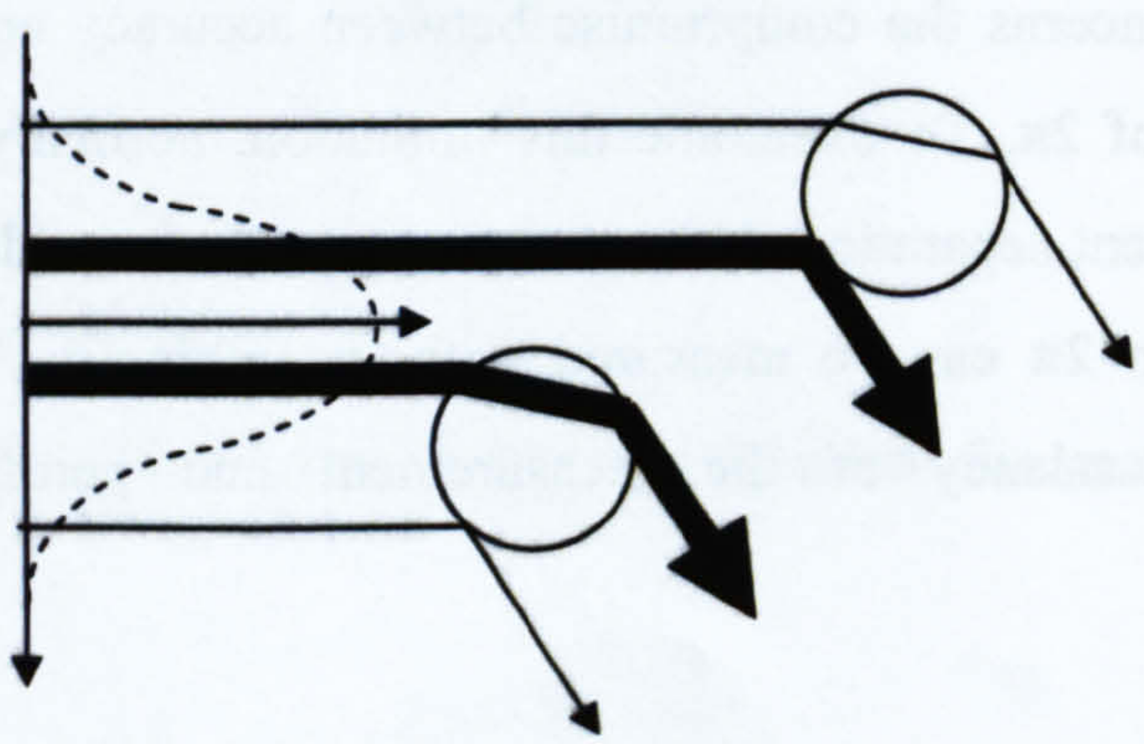

Figure 2-21: Trajectory effect due to beam profile

Using geometric optics, Sankar et al. (1992) showed that the measurement of a 45µm droplet placed in a measurement volume with a 80µm waist might result in an underestimation as large as 67% of the true diameter. One way to minimise the distribution effect is to increase the size of the measurement volume. However, this increases the probability of multiple occupancy. Another method is to use an additional detector (Gréhan et al. 1992).

The slit aperture can also suppress completely the light scattering property selected for calculating the particle diameter. If a particle crosses the right part of the volume (see *Figure 2-22*), the refracted light will be suppressed. If this was the chosen scattering mechanism, the equipment will determine a wrong drop size.

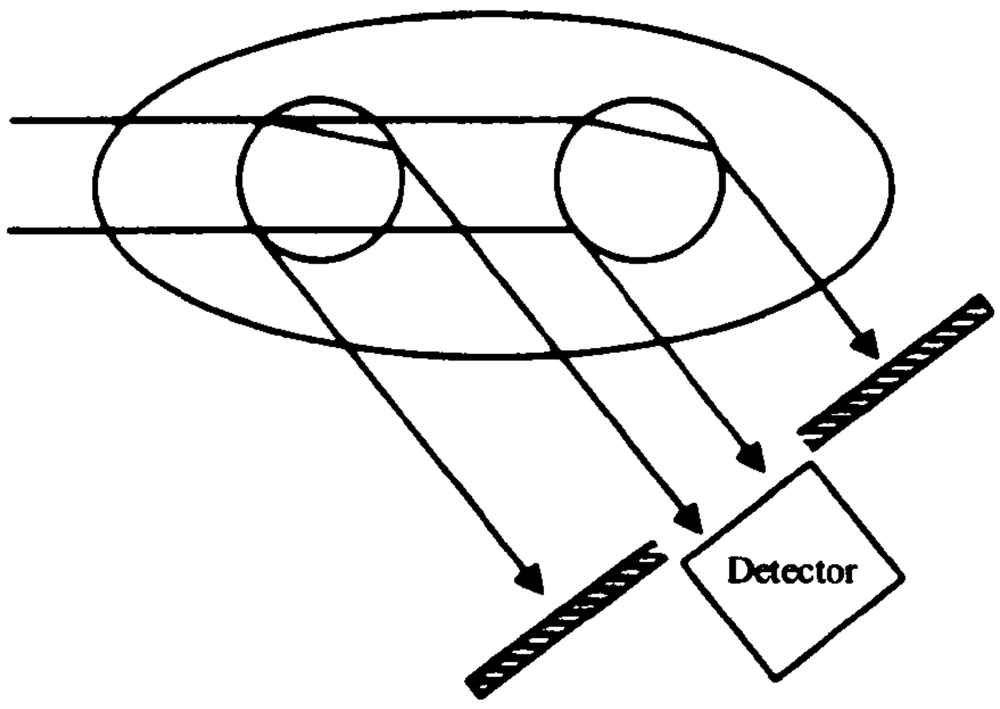

Figure 2-22: The slit effect

Durst et al. (1994) showed that the non uniform illumination effect due to the image boundary of the spatial slit filter in the receiving optics is even more critical than the Gaussian beam defect.

In spray applications, the PDA system is usually set up to receive refracted light. Due to the trajectory and slit effect, reflected light can damage the measurement. Aizu et al. (1993) proposed the Planar PDA (PPDA) system which consists in a 90° rotation of the transmitting and receiving optics.

Tropea et al. (1994) proposed the dual-mode PDA. This four beam system basically combines two detectors of the standard PDA (SPDA) with two detectors of the Planar PDA in a single receiving unit (see *Figure 2-23*). The comparison of the droplet size obtained with the SPDA and PPDA allows to validate the measurement.

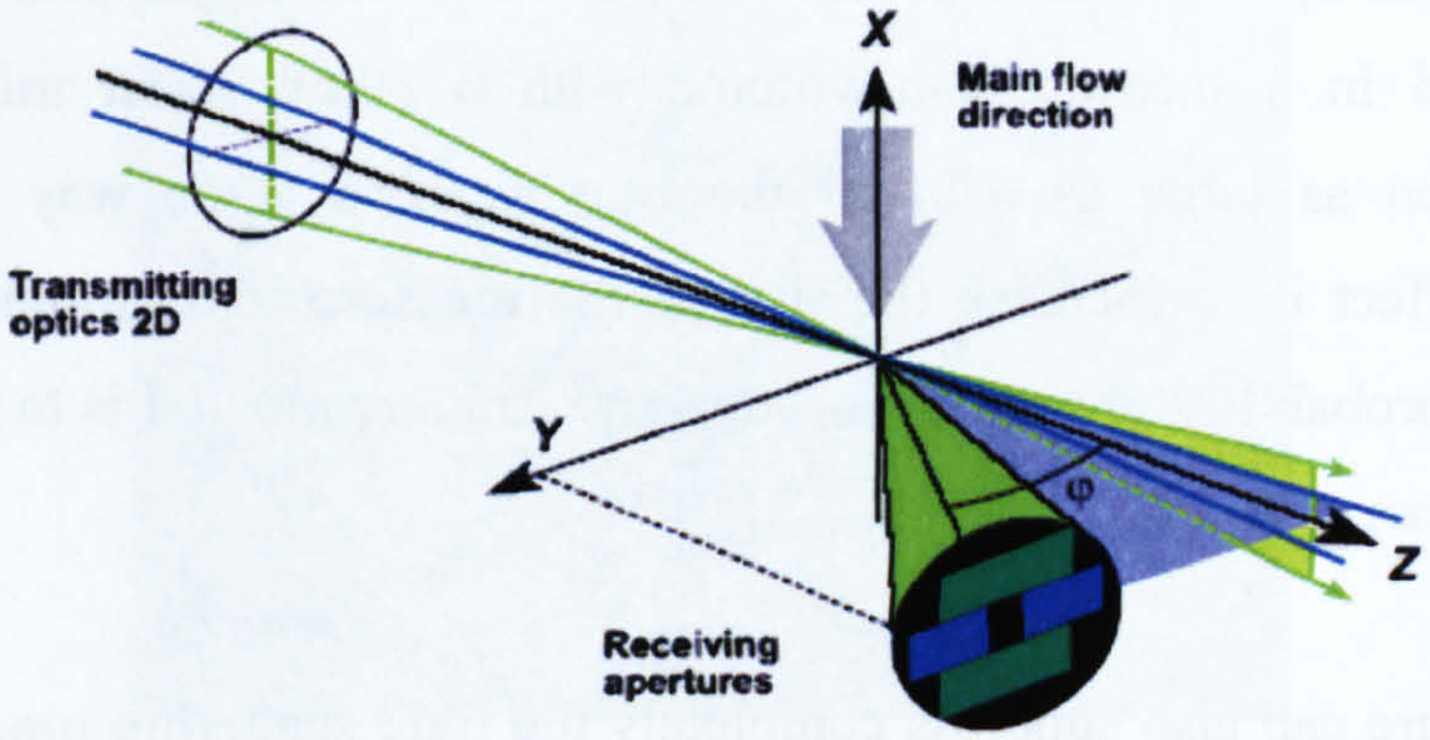

Figure 2-23: Dantec Dual-mode PDA

PDA in dense spray cannot provide reliable data (Wigley 1994). This is partly due to the fact that PDA cannot make reliable measurements when more than one drop enters the measurement volume. Also, in dense sprays, random scattering and attenuation due to numerous droplets crossing the incident and reflected/refracted light is also an issue.

Wigley et al. (1999) improved the PDA system by reducing the measurement volume and increasing the power (120mW and 250mW per beam at 488 and 514nm respectively) and measured velocities and drop sizes in a GDI injector (Wigley et al. (2002).

2.3.4. Laser Sheet Dropsizing (LSD)

For a given number (N) of droplets, the Sauter Mean Diameter (SMD or D_{32}) corresponds to the diameter of a drop that would have the same ratio of volume-to-surface area as that of the N droplets. This diameter is frequently specified because it allows the calculation of the total area of an atomised volume of liquid. It is also the most useful value for determining the rate of evaporation. Therefore, lower SMDs indicate better atomisation of the fuel.

$$D_{32} = \frac{\int_0^\infty \frac{dn}{dD} \cdot D^3 \cdot dD}{\int_0^\infty \frac{dn}{dD} \cdot D^2 \cdot dD} \qquad D_{32} = \frac{\sum_i n_i \cdot D_i^3}{\sum_i n_i \cdot D_i^2}$$

Equation 2-38: Definition of the Sauter Mean diameter (continuous – discrete)

Theoretically, the ratio between the LIF and Mie scatter signal from liquid droplets can be used to extract the SMD. The technique originated in 1993 from Yeh et al. and was applied on a diesel injector. Sankar et al. (1996) developed a similar technique - Planar Drop Sizing (PDS) - which was applied to a Delavanan swirl injector. Le Gal (1999) developed the Laser Sheet Dropsizing (LSD) technique which uses the same principle as Sankar et al. (1996) with a UV light source from a Nd:YAG laser. An in depth review of the principle can be found in *Chapter 3*.

The basic principle of the LSD technique uses the property that the LIF and Mie scatter signals from a low absorbing droplet (k) are volume and surface dependent respectively. The local ratio of the two signals will therefore be proportional to SMD:

$$D_{32}(i,j) \propto \frac{I_{LIF}(i,j)}{I_{Mie}(i,j)}$$

Equation 2-39

Le Gal (1999) verified the volume and surface dependence of the LIF and Mie scattering signals respectively using a TSI droplet generator. He later applied the technique to a Delavan pressure-swirl atomiser spray and found good agreement with results obtained with PDA.

Park et al. (2002) verified the technique with a droplet generator using unleaded gasoline and also found good agreement for the d^3 and d^2 dependence of the LIF and Mie scatter signals respectively. They applied the technique to a GDI swirl type injector and determined the calibration constant using PDA. They found that the characteristics of the injector varied with injection pressure.

Zimmer et al. (2002) applied the technique to an industrial oil burner and found that droplet clusters form in high density regions. They identified flow structures using PIV, possibly explaining this cluster formation.

Domann and Hardalupas (2003) and Charalampous et al. (2004) have proposed recent improvements to the technique, which are discussed in *Chapter 5*.

PART II

DEVELOPMENT OF THE LASER SHEET DROPSIZING (LSD) TECHNIQUE

Chapter 3

Development of Laser Sheet Dropsizing for Evaporative Sprays

The Laser Sheet Dropsizing (LSD) technique is based upon the combination of elastic Mie scatter and inelastic scatter (LIF) of illuminated droplets. Mie scattering is a very robust technique for liquid-phase imaging, but the behaviour of fluorescence in an evaporative spray is less obvious. The feasibility of the LSD technique is strongly dependent on the accuracy of PLIF in the evaporating liquid phase. In this chapter, the requirements and selection of an appropriate tracer/fuel system are discussed. Temperature and Pressure dependence are investigated along with evaporation calculations. This is followed by the description of a dual imaging set-up along with the calibration procedures required for the LSD technique.

3.1. Principle

Because the fluorescence and the Mie scatter are volume and surface effects respectively, theoretically, the ratio between the LIF and Mie scatter signal from liquid droplets can be used to extract the Sauter Mean Diameter.

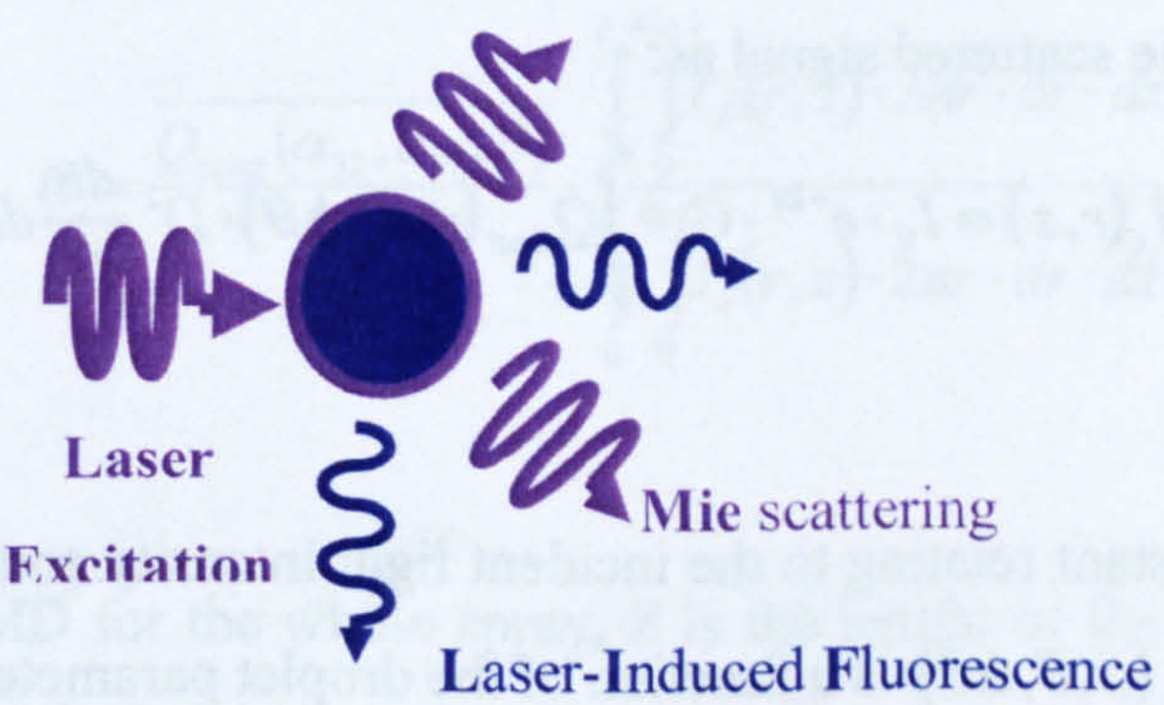

Figure 3-1: Light scattering from an absorbing droplet

3.1.1. Early development

Yeh et al. (1993a, 1993b) were the first to use the intensity ratio of simultaneous LIF and Mie scatter signals to measure Sauter Mean Diameter (SMD). They applied the technique on an axisymetric spray.

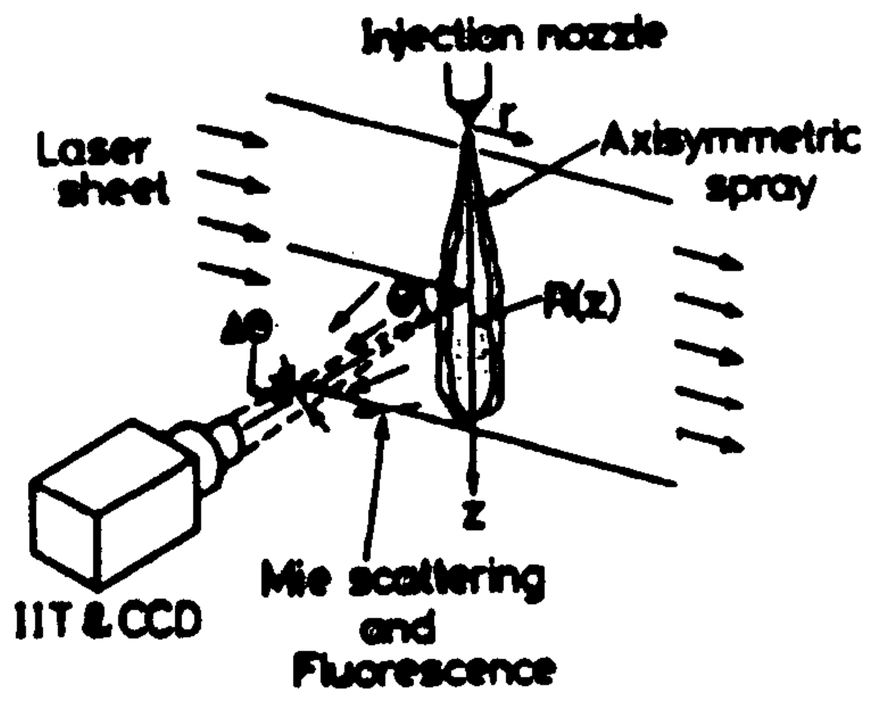

Figure 3-2: Experiment schematics - Yeh et al. (1993a).

They assumed that the LIF intensity was proportional to droplet volume for droplets smaller than 80μm. At location (r,z) the fluorescence is given by:

$$I_f(r,z) = I_0 \cdot e^{-kx} \cdot C_1 \cdot \int_0^{\infty} D^3 \frac{dn}{dD} dD$$

Equation 3-1

where I_o is the incident laser intensity and will be attenuated by kx according to Beer-Lambert's law, x is the distance from the incident spray edge and k the attenuation coefficient. C_1 is a constant value that includes the absorption coefficient, the quantum yield and the detection system's characteristics.

They defined the Mie scattered signal as:

$$I_s(r,z) = I_0 \cdot e^{-kx} \cdot C_2 \cdot \int_0^{\infty} Q_{scatt}(\alpha,\theta,\Delta\theta) \cdot D^2 \frac{dn}{dD} dD$$

Equation 3-2

where C_2 is the constant relating to the incident light intensity and the detection system characteristics. $Q_{scatt}(\alpha,\theta,\Delta\theta)$ is a function of the droplet parameter $\alpha = \pi \cdot D/\lambda$.

By assuming a particle size distribution, they defined an average scattering coefficient:

$$\overline{Q_{scatt}(\alpha_{32},\theta,\Delta\theta)} = \frac{\int_0^\infty Q_{scatt}(\alpha,\theta,\Delta\theta)\cdot D^2 \frac{dn}{dD} dD}{\int_0^\infty D^2 \frac{dn}{dD} dD}$$

Equation 3-3

where $\alpha_{32} = \pi \cdot D_{32}(r,z)/\lambda$ and $D_{32}(r,z)$ is the local Sauter Mean Diameter and is given by:

$$D_{32} = \frac{\int_0^\infty D^3 \frac{dn}{dD} dD}{\int_0^\infty D^2 \frac{dn}{dD} dD}$$

Equation 3-4

By combining *Equation 3-1*, *Equation 3-2*, *Equation 3-3* and *Equation 3-4* they obtained:

$$D_{32}(r,z) = \frac{\overline{Q_{scatt}(\alpha_{32},\theta,\Delta\theta)}}{C} \cdot \frac{I_f(r,z)}{I_s(r,z)}$$

Equation 3-5

where $C = C_1/C_2$.

By assuming that the spray was axisymetric, they integrated *Equation 3-5* cylindrically over the spray to extract a value of the constant *C*:

$$C = \frac{\overline{Q_{scatt}(\alpha_{32},\theta,\Delta\theta)}}{D_{32}} \cdot \frac{\int_0^Z \int_0^{R(z)} I_f(r,z)\cdot 2\pi r \cdot dr \cdot dz}{\int_0^Z \int_0^{R(z)} I_s(r,z)\cdot 2\pi r \cdot dr \cdot dz}$$

Equation 3-6

where D_{32} is the SMD for the whole spray, Z is the height of the spray and $R(z)$ is the radius of the spray at the height z.

They then used an empirical equation to determine the SMD for the whole spray (D_{32}) and, which enabled the calculation of $\overline{Q_{scatt}(\alpha_{32},\theta,\Delta\theta)}$.

The local SMD ($D_{32}(r,z)$) was then determined using an iterative process on *Equation 3-5* as $\overline{Q_{scatt}(\alpha_{32},\theta,\Delta\theta)}$ is a function of ($D_{32}(r,z)$).

They applied the technique using TMPD in a base fuel and the fluorescence was generated using a Nd:YAG laser at a wavelength of 355nm. They collected the light at 90°and separated the LIF from the Mie scatter using a doubling prism and filters.

This technique is self-calibrating if the spray's overall SMD is known and the spray can be assumed axisymetric. The determination of the local SMD also requires the local droplet size distribution and in many cases, it is unknown.

3.1.2. The Laser Sheet Dropsizing principle

Le Gal (1999) developed the Laser Sheet Dropsizing (LSD) technique based on the same principle. However, whereas the approach by Yeh et al.(1993) used the exact Mie scatter signal - which takes into account the variation of the scattering coefficient (Q_{scatt}) for different droplet sizes - the LSD technique simplifies this by assuming that the scattering coefficient is constant (i.e. the Mie scatter signal collected at 90° is simply a function of the diameter squared).

Under low absorption conditions, fluorescence is expected to be proportional to liquid volume or liquid mass distribution (Talley et al. 1996, Domann and Hardalupas 2000) and the LIF signal from a droplet k can therefore be expressed as:

$$I_{f,k} = C_1 \cdot I_{laser,k} \cdot d_k^3$$

Equation 3-7

where $I_{laser,k}$ is the laser power which excites droplet k.

Sankar et al. (1997) showed that for weak absorption, the Mie scatter signal can be well approximated by:

$$I_{s,k} = C_2 \cdot I_{laser,k} \cdot d_k^2$$

Equation 3-8

where C_1 and C_2 are constants independent of the droplet size or laser power.

If both images are captured on a CCD, the spray image is digitised into in small windows, as seen in *Figure 3-3*.

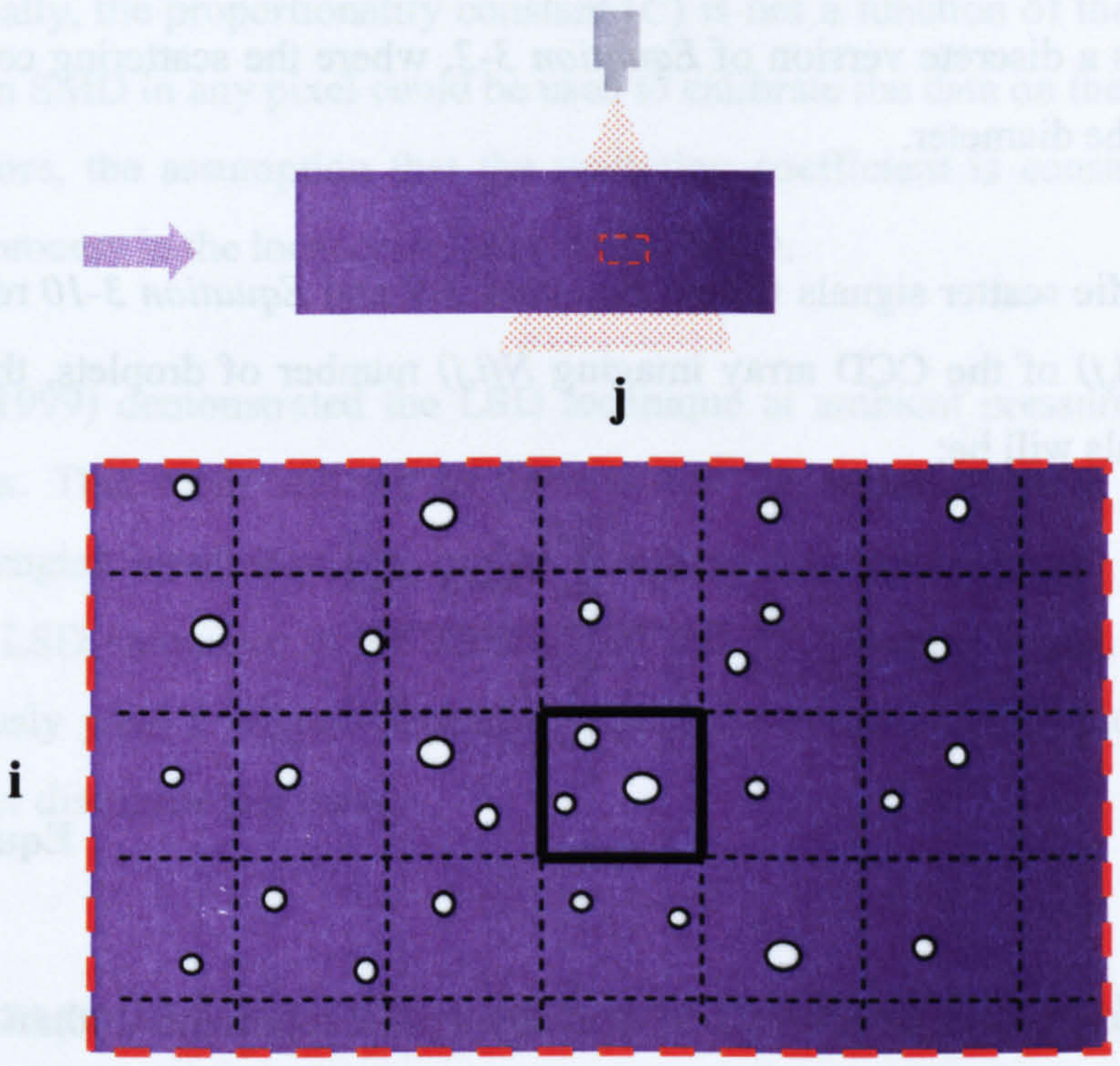

Figure 3-3: Droplet distribution of the spray, as seen by the CCD chip

The intensity of pixel (i,j) corresponding to the fluorescence of *N(i,j)* droplets can be expressed as:

$$I_f(i,j) = \sum_{k=1}^{N(i,j)} I_{f,k} = \sum_{k=1}^{N(i,j)} \left(C_1 \cdot I_{laser,k} \cdot d_k^3 \right) = C_1 \cdot \sum_{k=1}^{N(i,j)} \left(I_{laser,k} \cdot d_k^3 \right)$$

Equation 3-9

Equation 3-9 corresponds to the discretisation of *Equation 3-1.*

Because the droplets within a pixel are randomly placed, the scattered light lacks coherence and will not interfere (Sankar et al. 1996). The intensity of pixel (i,j) from the Mie scattering of *N(i,j)* droplets can be written as:

$$I_s(i,j) = \sum_{k=1}^{N(i,j)} I_{s,k} = \sum_{k=1}^{N(i,j)} \left(C_2 \cdot I_{laser,k} \cdot d_k^2 \right) = C_2 \cdot \sum_{k=1}^{N(i,j)} \left(I_{laser,k} \cdot d_k^2 \right)$$

Equation 3-10

Equation 3-10 is a discrete version of *Equation 3-2*, where the scattering coefficient is independent of the diameter.

If the LIF and Mie scatter signals follow *Equation 3-9* and *Equation 3-10* respectively, for each pixel *(i,j)* of the CCD array imaging *N(i,j)* number of droplets, the intensity ratio of the signals will be:

$$\frac{I_f(i,j)}{I_s(i,j)} = \frac{C_1 \cdot \sum_{k=1}^{N(i,j)} \left(I_{laser,k} \cdot d_k^3 \right)}{C_2 \cdot \sum_{k=1}^{N(i,j)} \left(I_{laser,k} \cdot d_k^2 \right)}$$

Equation 3-11

For low absorption and small pixel sizes (typically a pixel represents 100µm × 100µm), the laser absorption is negligible: the laser power can be assumed homogeneous within the pixel (i.e. $\forall k \in [1, N(i,j)] \; I_{laser,k} = cst$). Also, if the images are recorded simultaneously, the laser intensity is the same for both scatterings. Therefore, the ratio can be written as:

$$\frac{I_f(i,j)}{I_s(i,j)} = \frac{C_1}{C_2} \cdot \frac{\sum_{k=1}^{N(i,j)} d_k^3}{\sum_{k=1}^{N(i,j)} d_k^2} = C \cdot D_{32}(i,j)$$

Equation 3-12

where $C = C_1/C_2$

The local SMD is given by:

$$D_{32}(i,j) = \frac{1}{C} \cdot \frac{I_f(r,z)}{I_s(r,z)}$$

Equation 3-13

Equation 3-13 shows that the uneven distribution of laser fluence across the CCD chip is eliminated by the ratio of the signals pixel by pixel, and that the result is proportional to Sauter Mean Diameter.

Theoretically, the proportionality constant (C) is not a function of the pixel. Therefore, the known SMD in any pixel could be used to calibrate the data on the whole CCD chip. Furthermore, the assumption that the scattering coefficient is constant eliminates the iterative process in the local calculation of the SMD.

Le Gal (1999) demonstrated the LSD technique at ambient pressure and temperature conditions. This work will try to demonstrate the technique in a GDI spray under realistic engine conditions, i.e. higher pressures and temperatures. The critical issue with the LSD technique is the accuracy of the fluorescence signal, and its ability to continuously yield a volume-dependent signal for evaporating droplets. The following subchapter discusses this issue.

3.2. Laser-Induced Fluorescence for the LSD technique

3.2.1. Fluorescent Tracers

Since the introduction of Iso-Octane as a single component fuel, the application of LIF has seen the use of various fluorescing tracers for fuel distribution measurements in transparent engines. Tracers such as Acetaldehyde (Arnold et al. 1990), Biacetyl (Baritaud and Heinze 1992) and Acetone (Wolff et al. 1994) were used. Recent work suggests the widespread use of 3-Pentanone. This tracer's popularity is due to its almost matching boiling point with Iso-Octane (101.7°C and 99.2°C respectively). Qualitative work using 3-Pentanone is reported amongst others by Neij et al. (1994), Ossler and Aldén (1997), Steeper and Stevens (2000). Berkmüller et al. (1994) and Stojkovic and

Sick (2001) performed quantitative measurement of local AFR measurements. Stojkovic and Sick (2001) also used the ratio of LIF and Mie scattering signals to determine SMD. However, recent study by Davy et al. (2003) has demonstrated that 3-Pentanone's boiling point is deceptive, and that under engine evaporating regimes, the fluorophore does not perform its required task: tracing the fuel.

In the engine, the fuel/tracer system is subject to evaporation, rises in pressure and temperature and finally combustion. In order for the fluorescent dye to properly act as a tracer for the Laser Sheet Dropsizing technique, it must follow certain requirements.

The tracer should:

- Absorb at the laser wavelength
- Co-evaporate with the fuel
- Be soluble in the fuel / Consumed during combustion

The tracer's fluorescence should:

- Yield sufficient signal
- Be volume-dependent
- Be independent of temperature / pressure
- Not quench

Of the commonly used fluorophores, the first 3 properties enabled to select 5 potential tracers. The likelihood of co-evaporation was done by selecting tracers with boiling points close to that of iso-octane:

- 3-Pentanone
- 2-Hexanone
- Toluene
- Fluorobenzene
- TEA

Compound	Formula	Molecular Weight (g/mol)	Boiling Point (°C)	Density (g/cm^3)	Heat of vaporisation (J/g)
Iso-Octane	C_8H_{18}	114.23	99.2	0.6919	269
3-Pentanone	$C_5H_{10}O$	86.14	101.7	0.8138	388
2-Hexanone	$C_6H_{12}O$	100.16	127.6	0.812	363
Fluorobenzene	C_6H_5F	96.1	84.7	1.02	324
Toluene	C_7H_8	92.14	110.6	0.867	360
TEA	$C_6H_{15}N$	101.19	89.5	0.725	306

Table 3-1: Properties of Iso-Octane and various tracers

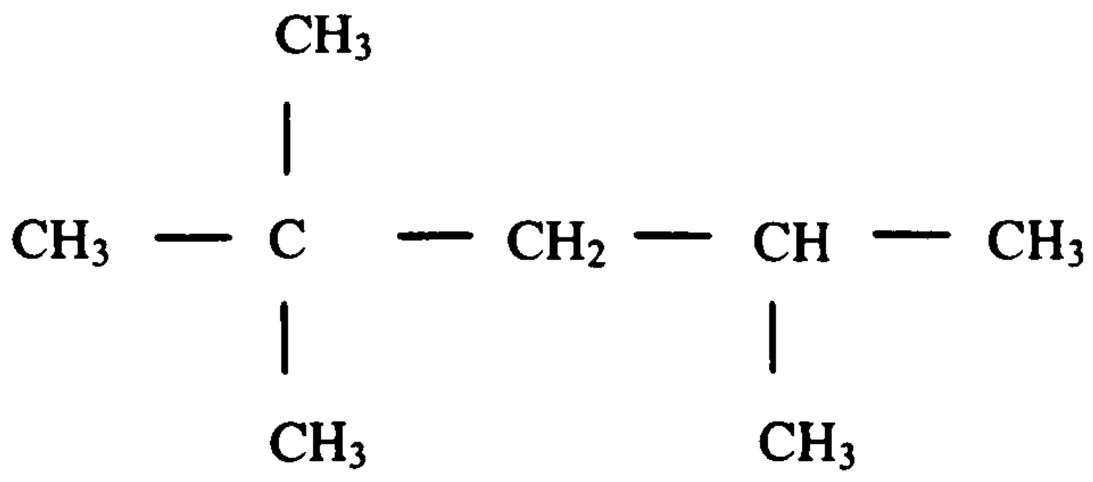

Figure 3-4: Iso-octane

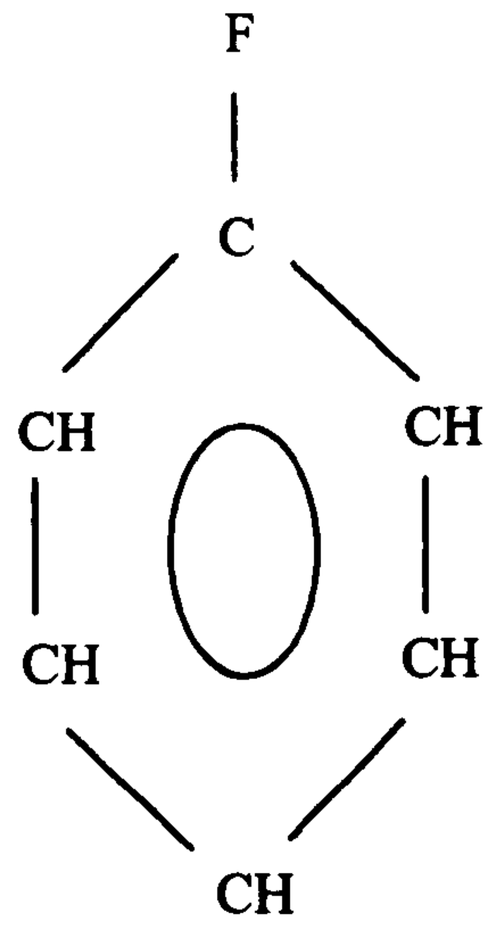

Figure 3-6: Fluorobenzene

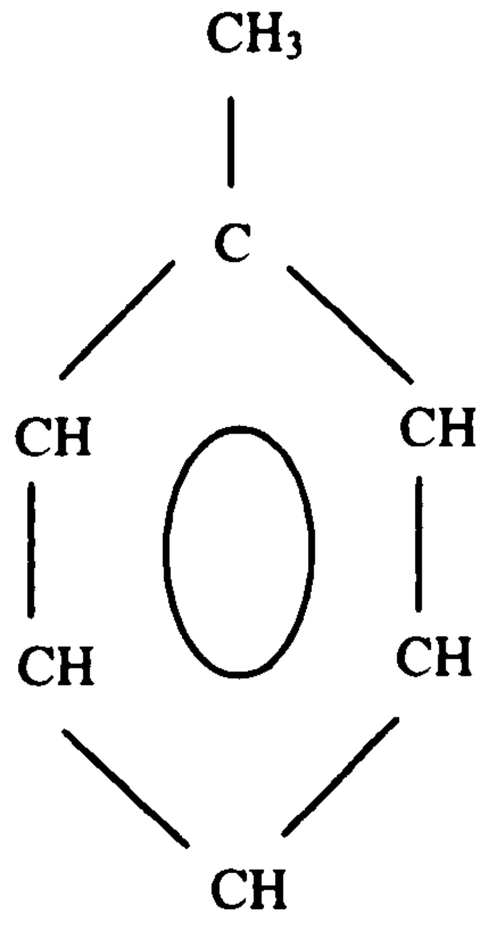

Figure 3-5: Toluene

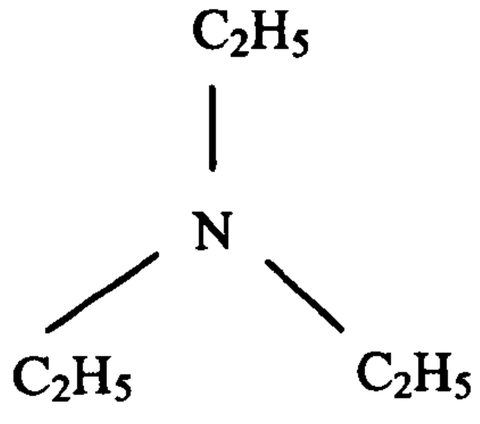

Figure 3-8: TEA

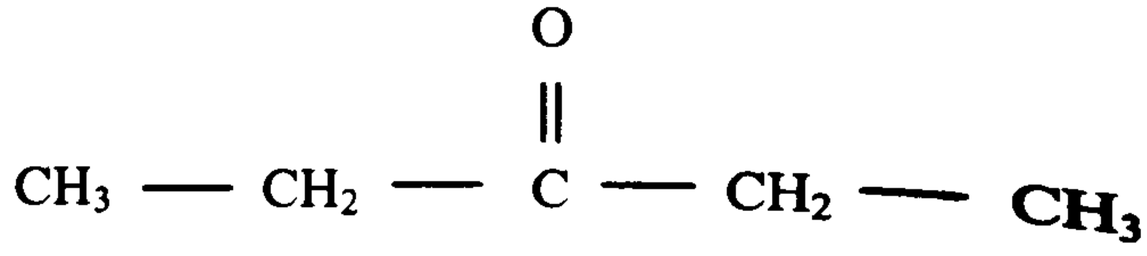

Figure 3-7: 3-Pentanone

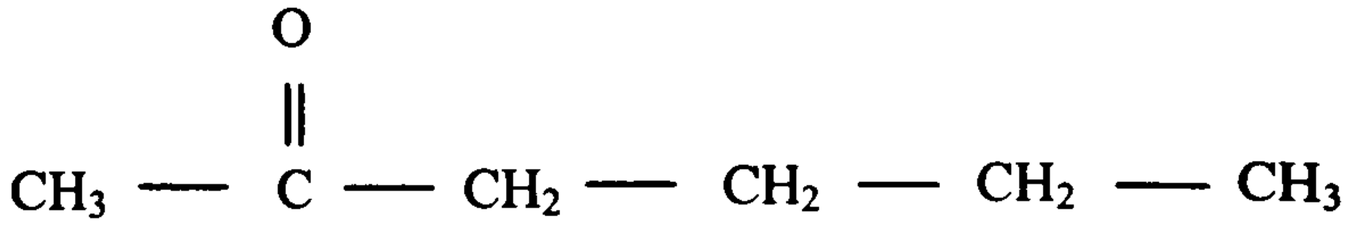

Figure 3-9: 2-Hexanone

3.2.2. Absorption measurements

In order to fluoresce, the tracer must absorb at the excitation wavelength. In order for the fluorescence to be volume dependent, the entire volume of the droplet must be homogeneously illuminated. This requires an optimal absorption.

Beer-Lambert law gives the theoretical behaviour of light as it passes through an absorbing medium:

$$I = I_0 \cdot e^{-\varepsilon \cdot c \cdot d}$$

Equation 3-14

where I_0 is the incident light energy, I is the energy after travelling the distance d, c is the concentration and ε is the molecular absorptivity (or extinction coefficient).

Parker (1964) uses a more practical form of this equation with a base 10 logarithm and defines the optical density (or absorbance) as:

$$A = \log\left(\frac{I}{I_0}\right) = \varepsilon \cdot c \cdot d$$

Equation 3-15

where c is expressed in $mol.L^{-1}$, d in cm and ε in $L.mol^{-1}.cm^{-1}$.

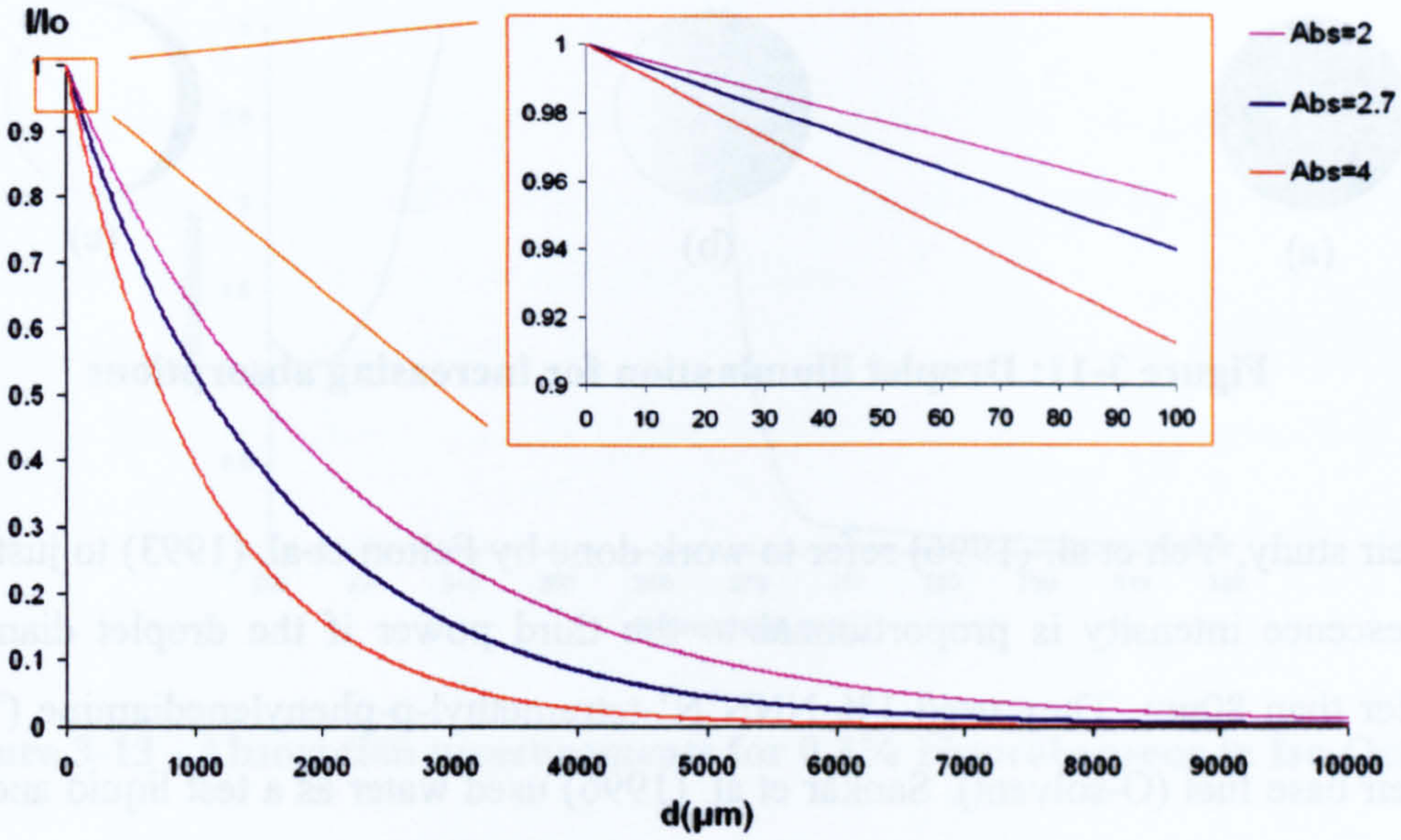

Figure 3-10: Light extinction for different absorbances

Using a droplet generator and different dye concentrations, Le Gal (1999) showed that the LIF signal is proportional to d^n, where n varied from 3.2 to 2 and found that an absorbance of 2.7 gave a diameter cubed LIF signal.

In the extreme case of a highly absorbing droplet, the incoming light will be completely absorbed near the surface (see *Figure 3-11(c)*). The bulk of the fluorescence will appear to coming from the surface, thus yielding a fluorescence signal proportional to surface area, hence n=2.

In the case of low absorption, the droplet's volume is homogeneously illuminated and the fluorescence signal is volume dependent (see *Figure 3-11(a)*). However, if the tracer concentration is too low, the droplet may exhibit amplified stimulated emission (ASE), where the droplet acts as a cavity with gain greater than 1. Fluorescing systems with low quantum gain, for example low quantum efficiency or less efficient internal reflection (lower refractive index relative to medium) are likely to show less pronounced ASE and have n nearer 3.

Domann and Hardalupas (2000) computed the LIF signal in a droplet and showed that it was unevenly distributed and that the d^3 dependency was accurate for low tracer concentrations.

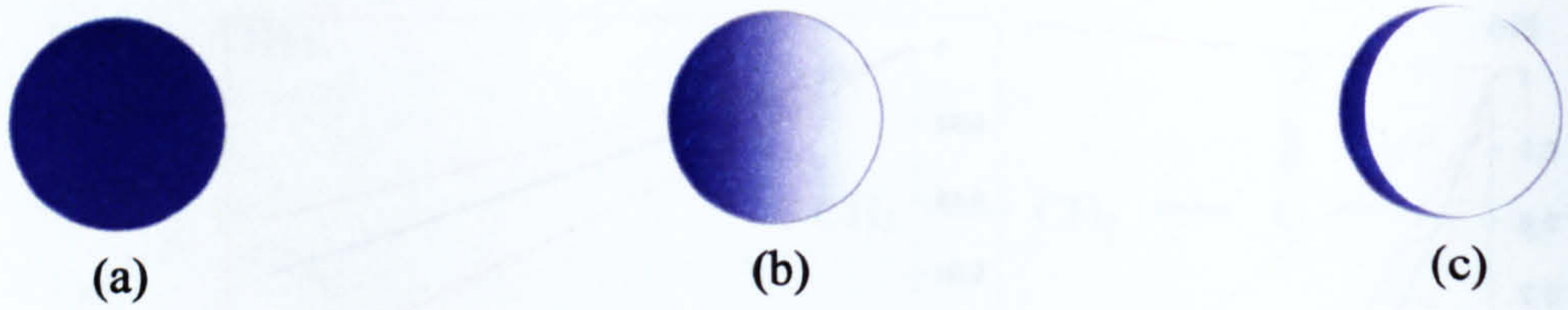

Figure 3-11: Droplet illumination for increasing absorptions

In their study, Yeh et al. (1996) refer to work done by Felton et al. (1993) to justify that fluorescence intensity is proportionnal to the third power if the droplet diameter is smaller than 80μm. They used 1% NNN'N'-tetramethyl-p-phenylenediamine (TMPD) in their base fuel (O-solvent). Sankar et al. (1996) used water as a test liquid and added small amounts of fluorescein-di-sodium salt to obtain a low absorbing tracer system. These small concentrations will typically give low absorption mediums. *Figure 3-10* shows that such small mediums will only absorb a fraction of the incoming light, and the illumination within the droplet will be quasi-homogeneous.

In order to accurately determine the appropriate tracer concentrations, the absorbances of various fuel/tracer systems for different dye concentrations were measured using a PERKINS-ELMER Lambda 7 UV/VIS Spectrophotometer.

The absorbance measurements were done in a 1cm path-length fused silica cuvette. The following graphs represent absorbance as a function of wavelength. The red dot represents the ideal point (i.e. A=2.7 at λ=266nm).

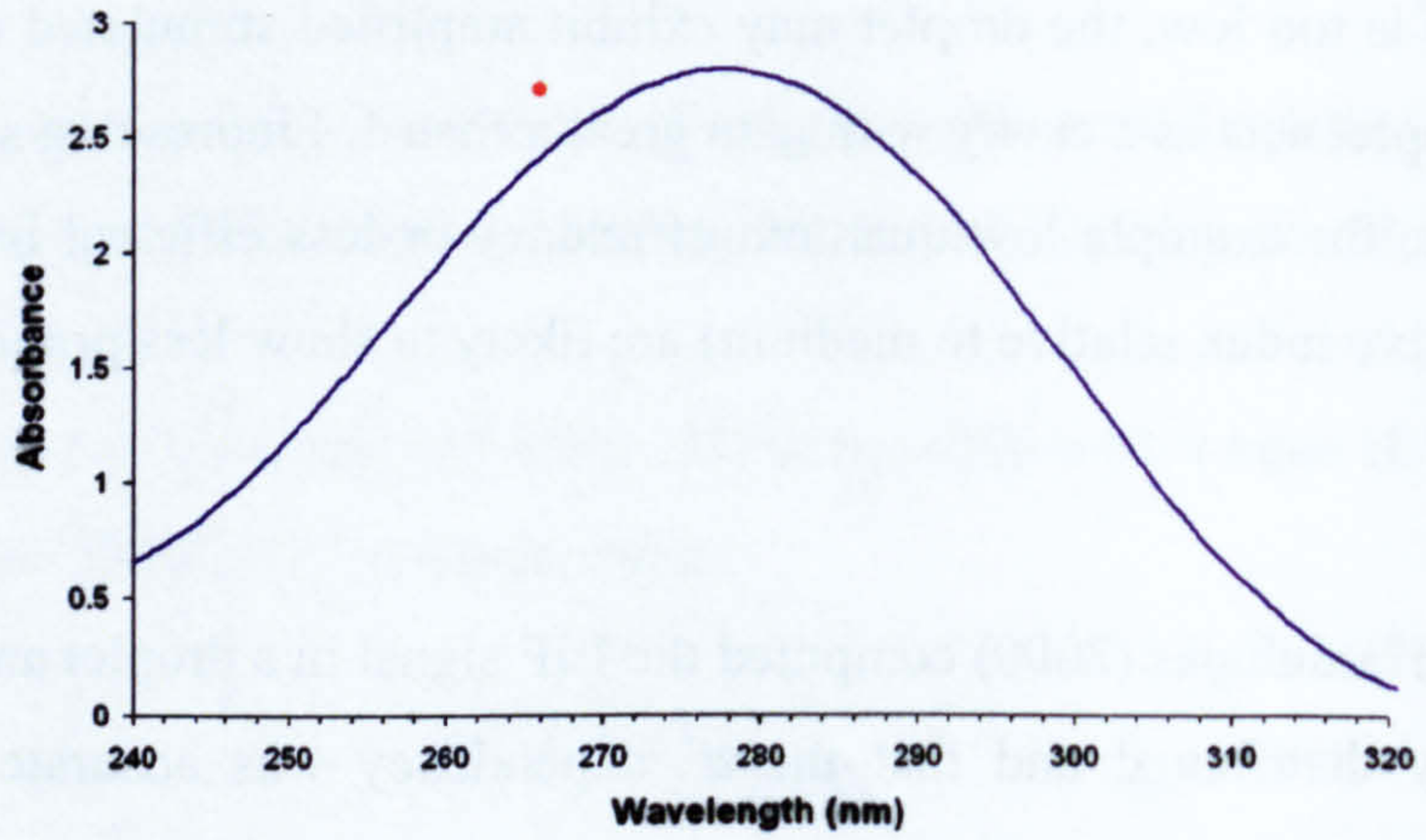

Figure 3-12: Absorption measurement for 1% 3-Pentanone in Iso-Octane

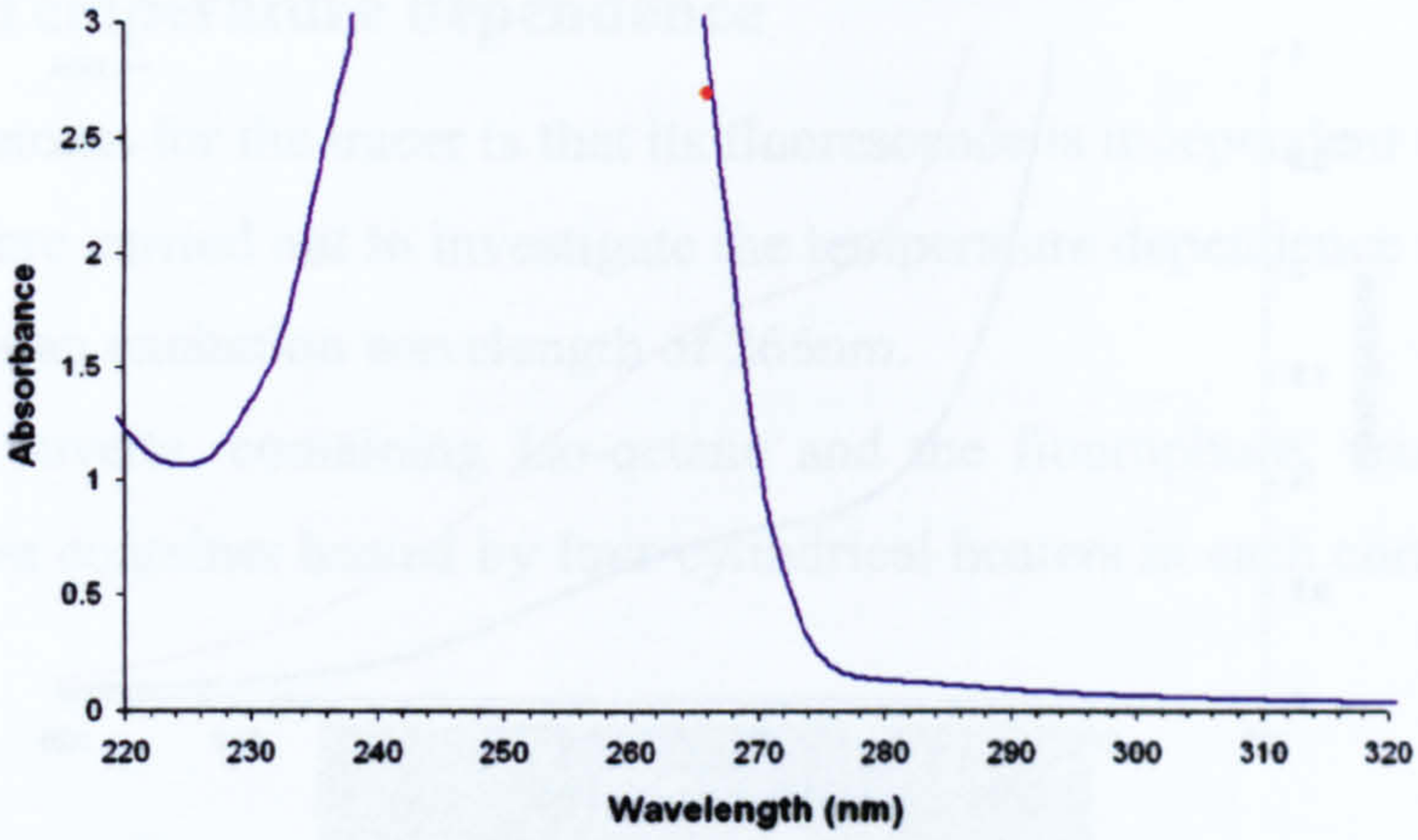

Figure 3-13 - Absorption measurements for 0.3% Fluorobenzene in Iso-Octane

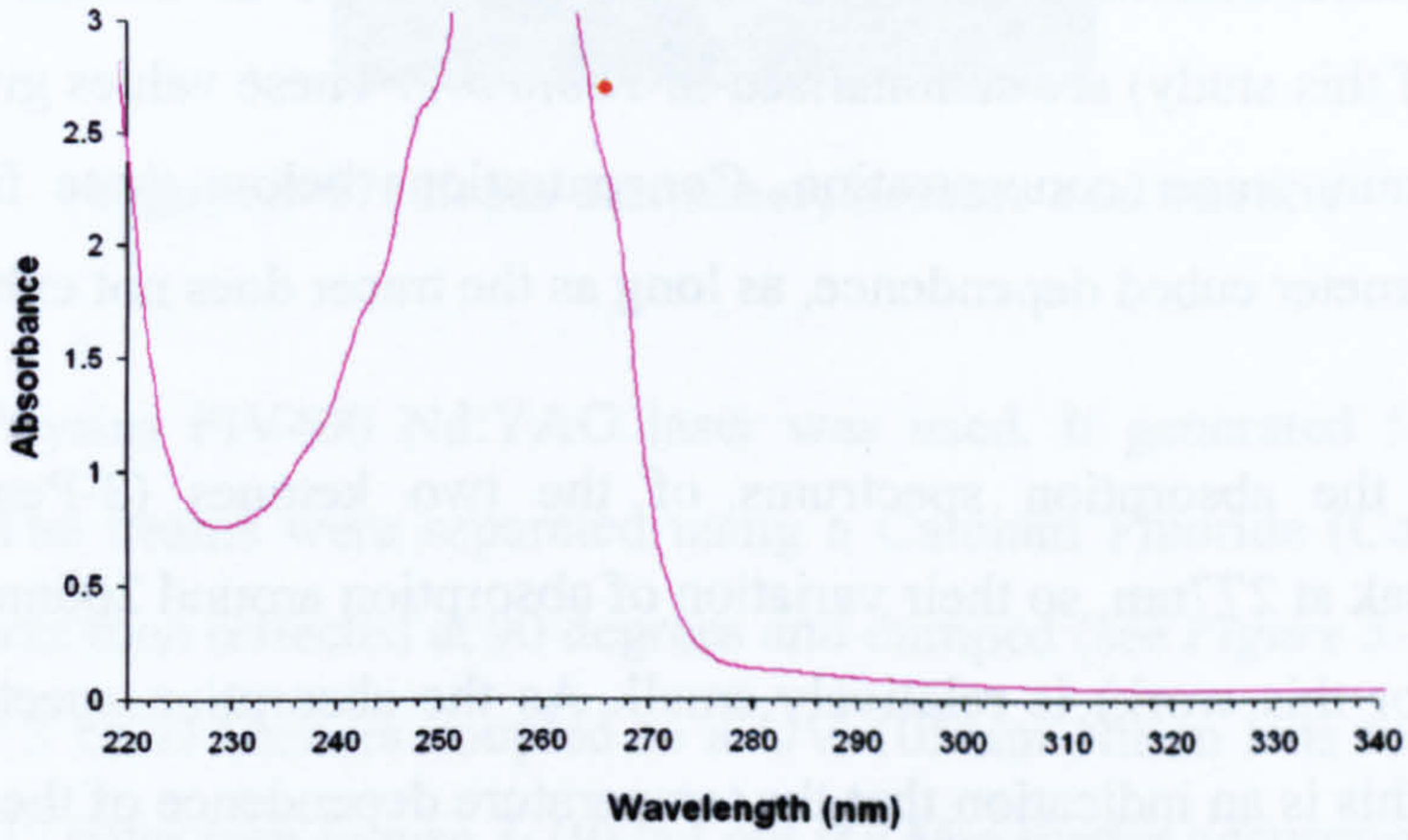

Figure 3-14 - Absorption measurements for 0.2% Toluene in Iso-Octane

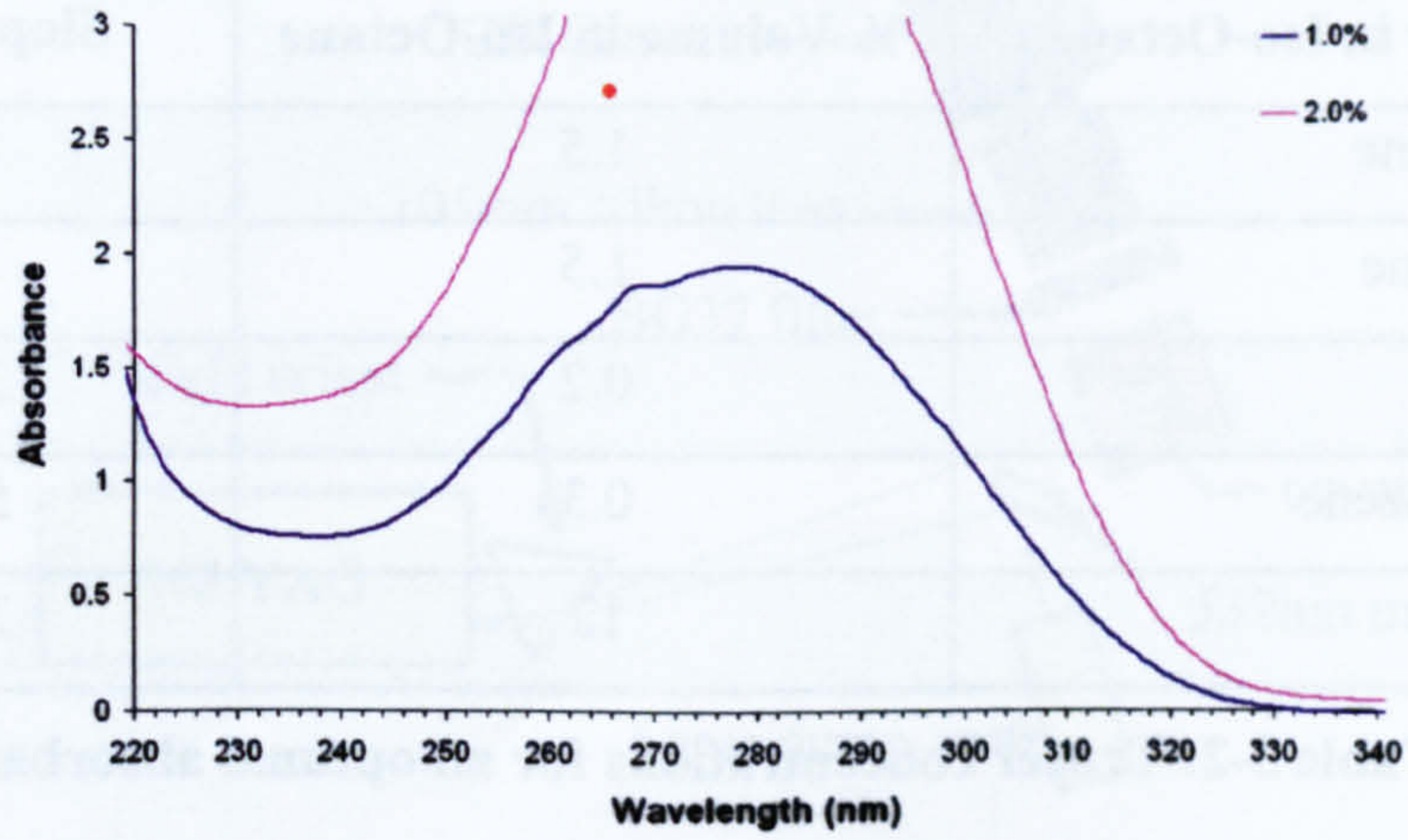

Figure 3-15: Absorption measurements for 2-Hexanone in Iso-Octane

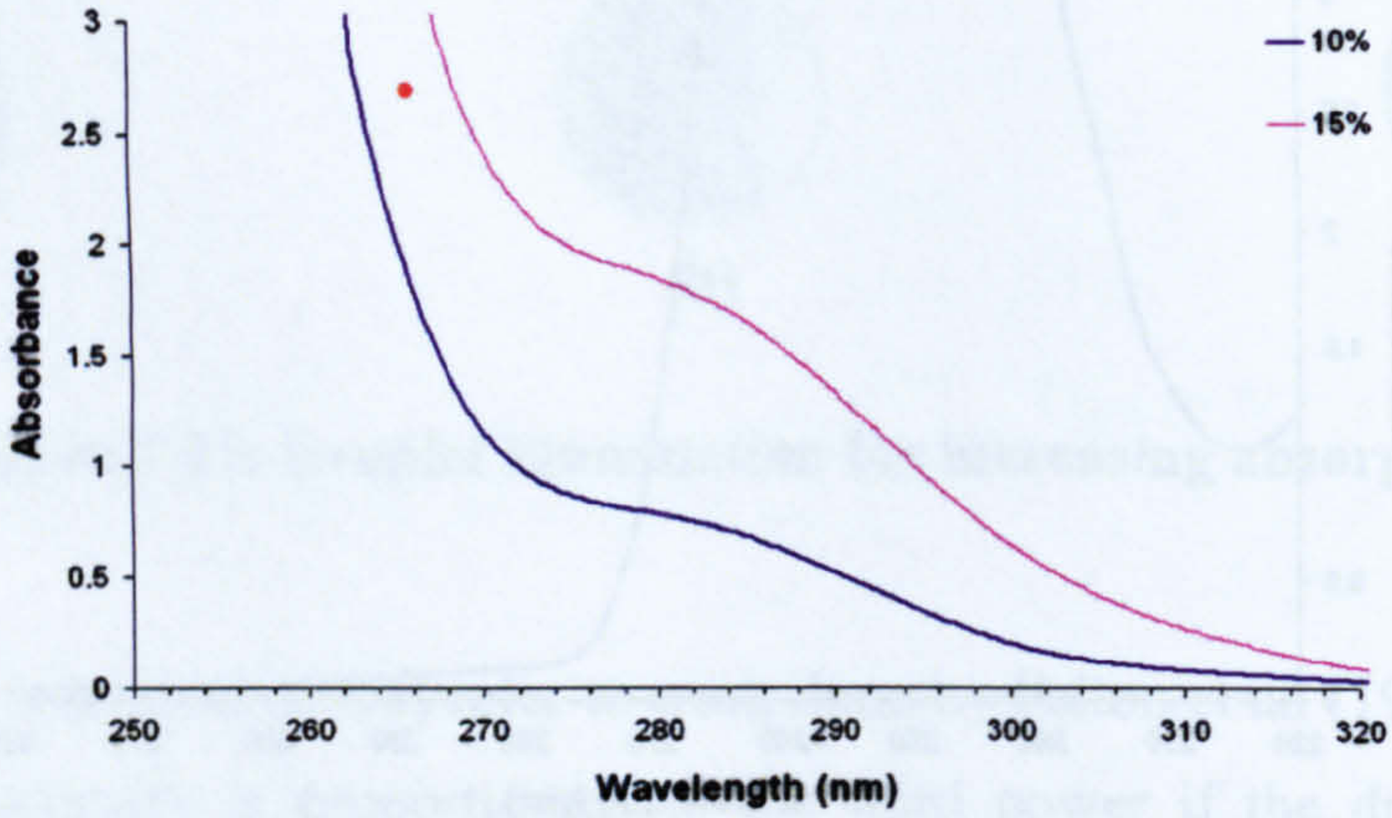

Figure 3-16: Absorption measurements for TEA in Iso-Octane

The tracer concentrations which give a 2.7 absorbance at 266nm (the excitation wavelength of this study) are summarised in *Table 3-2*. These values give an indication of the maximum tracer concentration. Concentrations below these figures will still satisfy the diameter cubed dependence, as long as the tracer does not exhibit ASE.

Furthermore, the absorption spectrums of the two ketones (3-Pentanone and 2-Hexanone) peak at 277nm, so their variation of absorption around 266nm (the excitation wavelength for this work) is relatively small. As the absorption spectrum shifts with temperature, this is an indication that the temperature dependence of the fluorescence of these two compounds is likely to be weak.

Tracer in Iso-Octane	% Volume in Iso-Octane	Slope (nm^{-1})
3-Pentanone	1.5	6%
2-Hexanone	1.5	6%
Toluene	0.2	25%
Fluorobenzene	0.3	50%
TEA	12	25%

Table 3-2: Tracer concentrations for an optimal absorbance

3.2.3. Temperature dependence

Another requirement for the tracer is that its fluorescence is independent of temperature. Experiments were carried out to investigate the temperature dependence of liquid-phase fluorescence for an excitation wavelength of 266nm.

A fused silica cuvette, containing Iso-octane and the fluorophore, was inserted in a rectangular brass container heated by four cylindrical heaters in each corner (see *Figure 3-17*).

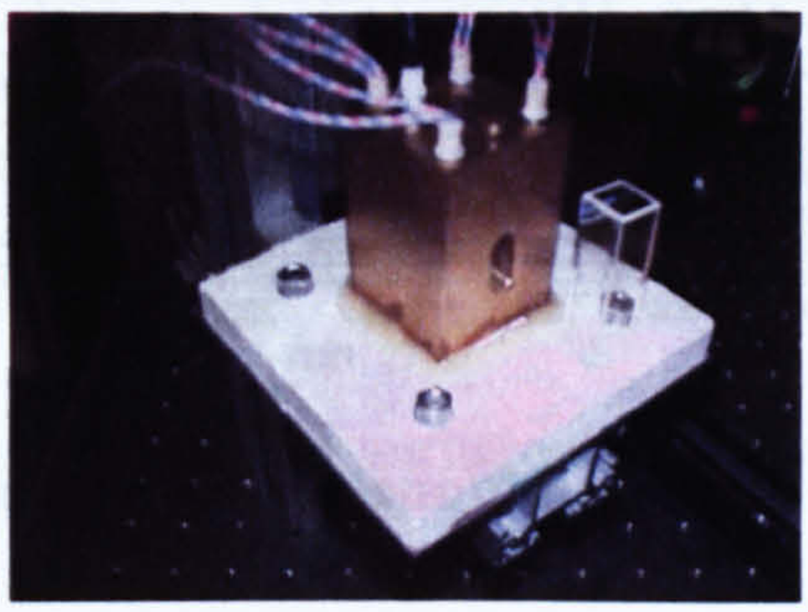

Figure 3-17: Brass container, heaters and cuvette

The Spectra Physics PIV400 Nd:YAG laser was used. It generated 532 and 266nm wavelengths. The beams were separated using a Calcium Fluoride (CaFl) prism. The 532nm beam was then reflected at 90 degrees and dumped (see *Figure 3-18*).

A Flowmaster 3 CCD Camera coupled to a UV 105mm Nikon lens recorded the LIF images. A BG37 filter (see *Figure 3-19*) cut out the Mie scatter occurring at 266nm.

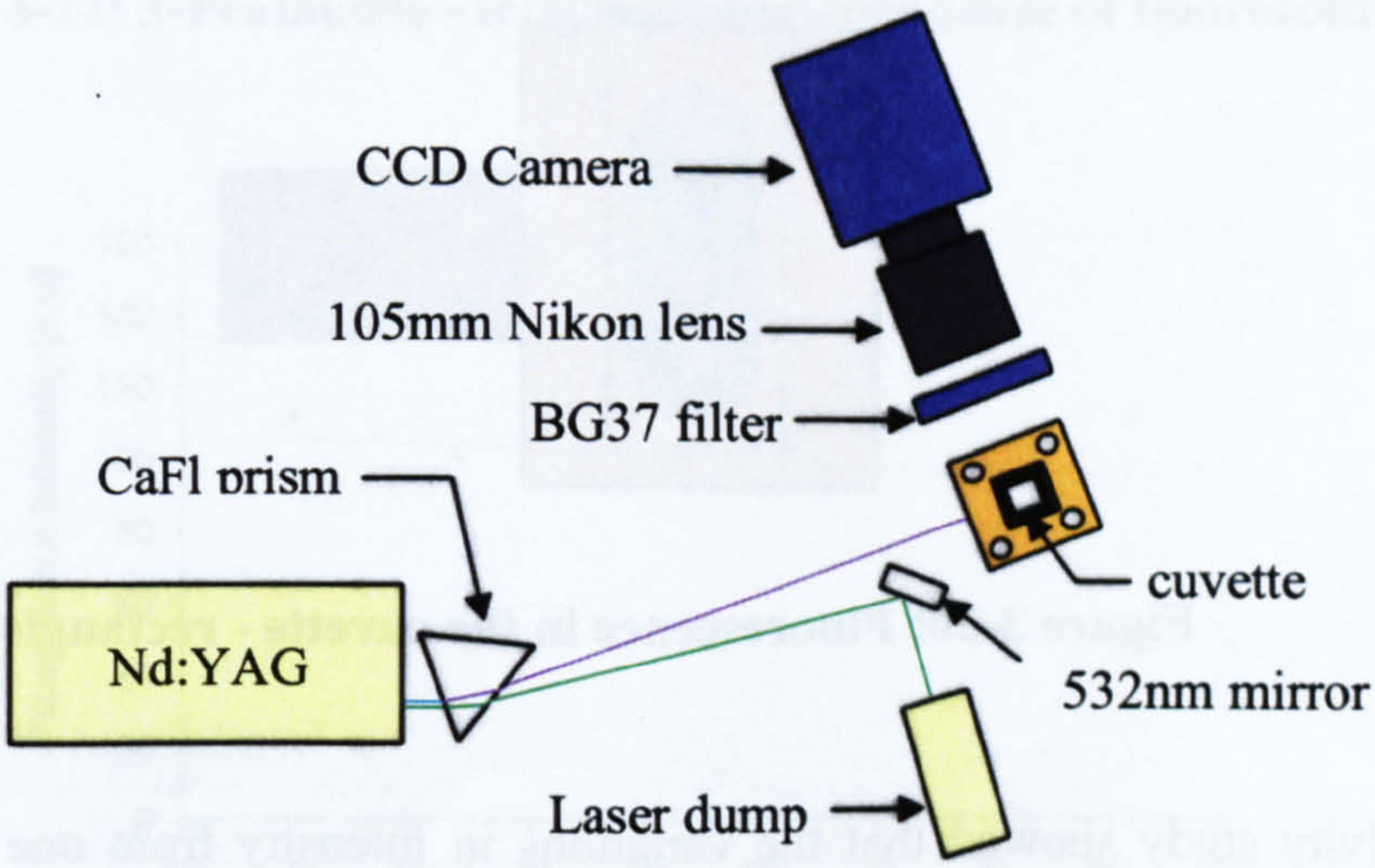

Figure 3-18: Experimental set-up for temperature dependence of LIF

The computer was the experiment master and the Davis imaging software from LaVision used to trigger the laser and the camera. The image processing was also done with Davis.

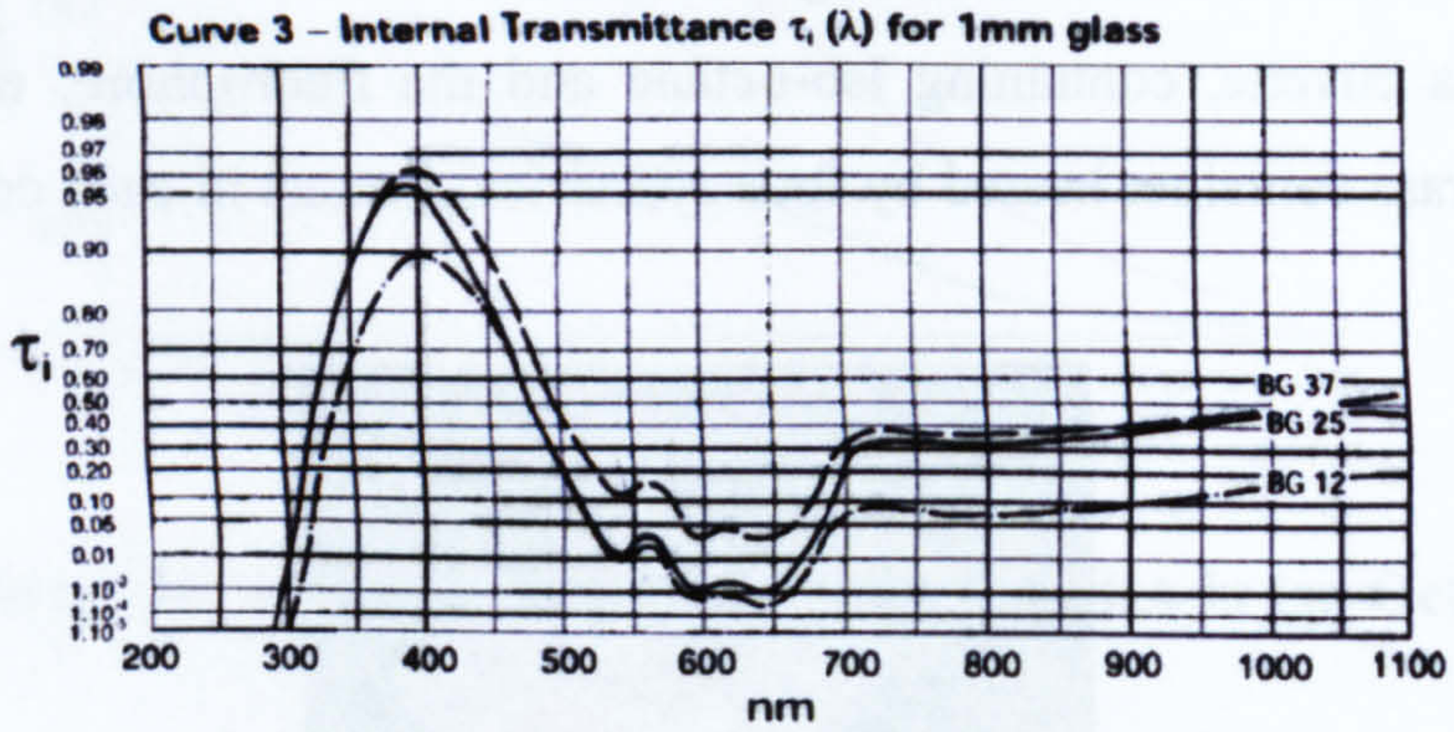

Figure 3-19: Transmittance curve for the BG37 filter

The heaters were turned on and off with a switch, and the temperature of the brass container was measured by a thermocouple. The container was heated and maintained at a stable temperature for 1 minute before the images were recorded, in order to allow the fuel/tracer mixture to reach that temperature. 60 images were recorded. To eliminate laser fluctuations while the laser warms up, only the last 30 images were averaged to give a final image. 2 rectangles within the image were selected and the average intensity within each rectangle was extracted.

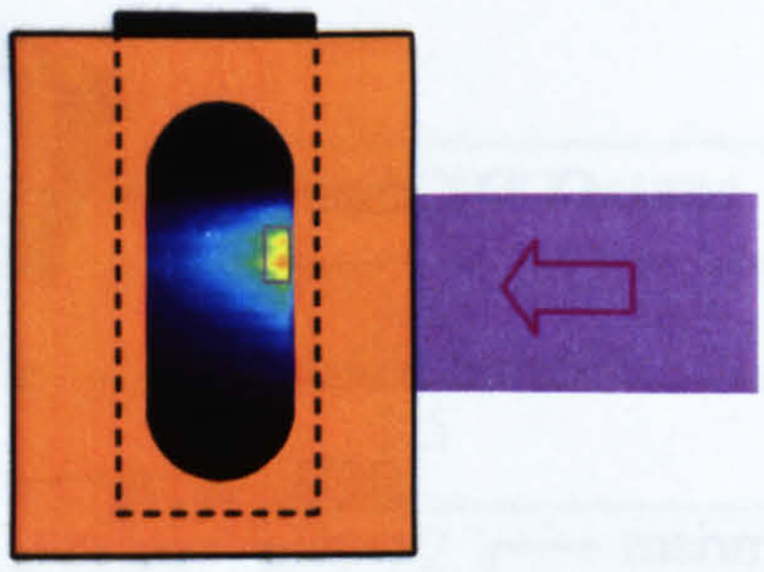

Figure 3-20: Fluorescence in the cuvette - rectangle

A sensitivity study showed that the variations in intensity from one rectangle to the other were identical (see *Figure 3-21*).

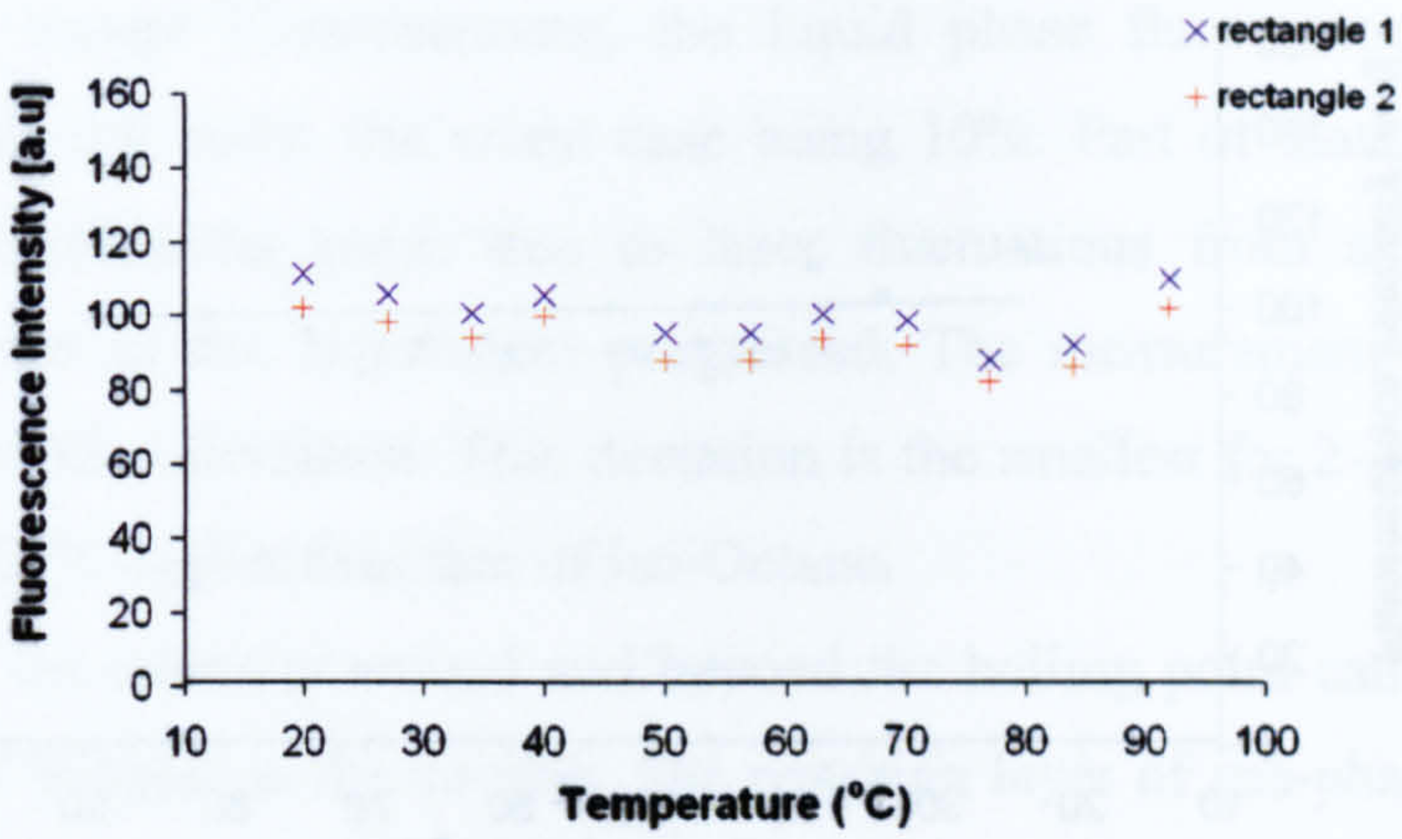

Figure 3-21: Intensity variation in 2 different rectangles

The following set of graphs present the variation of fluorescence intensity at various temperatures.

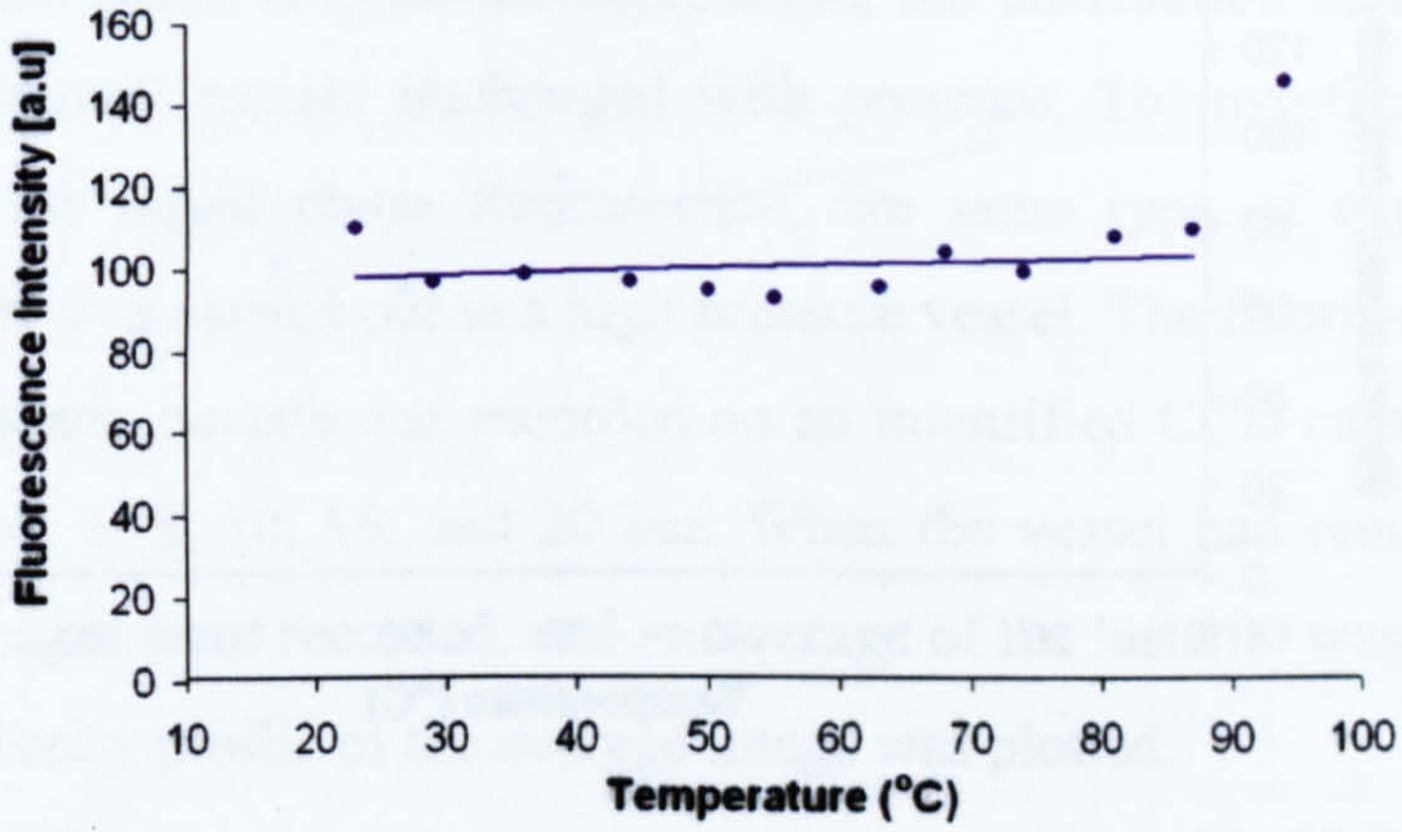

Figure 3-22: 3-Pentanone - temperature dependence of fluorescence

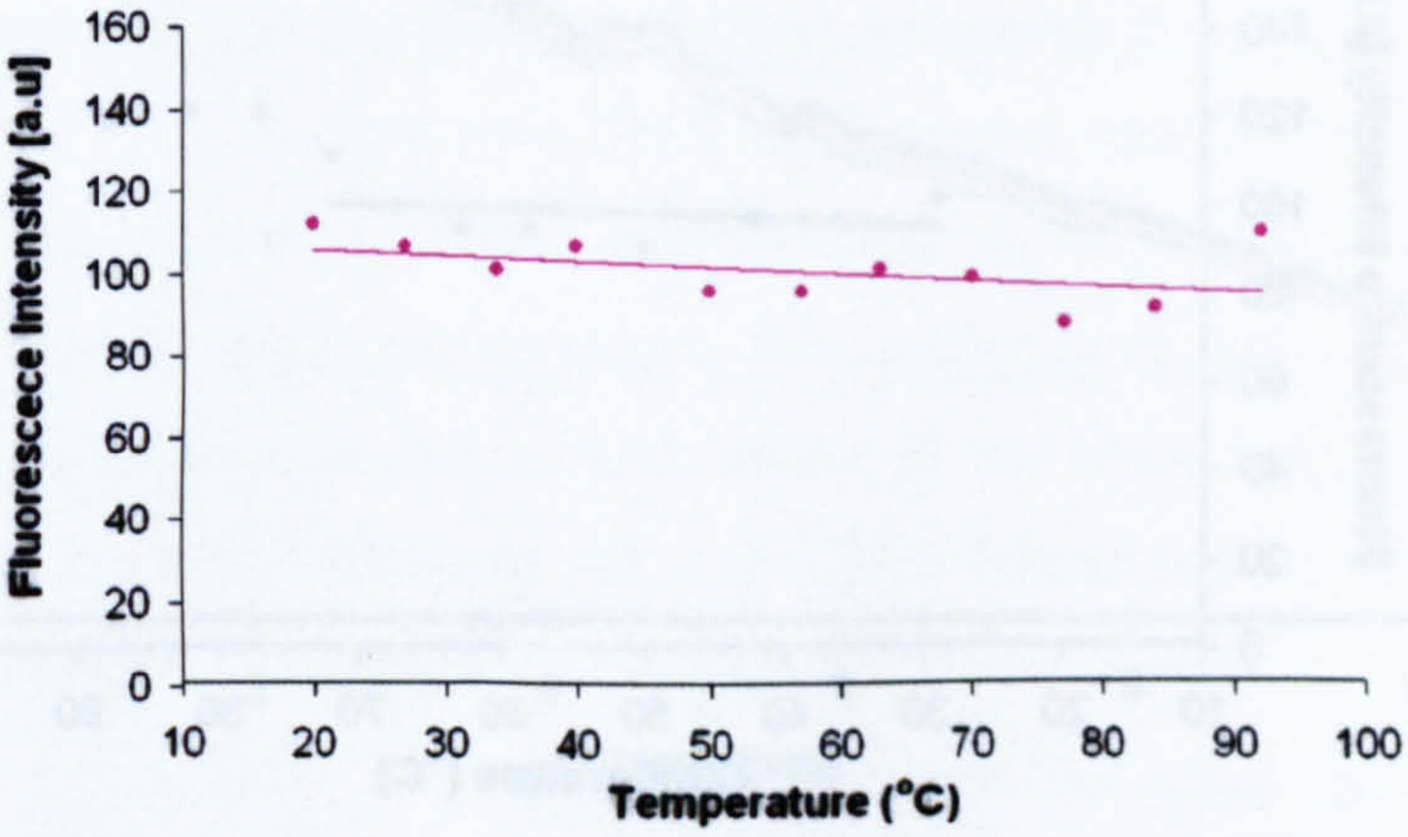

Figure 3-23: 2-Hexanone - temperature dependence of fluorescence

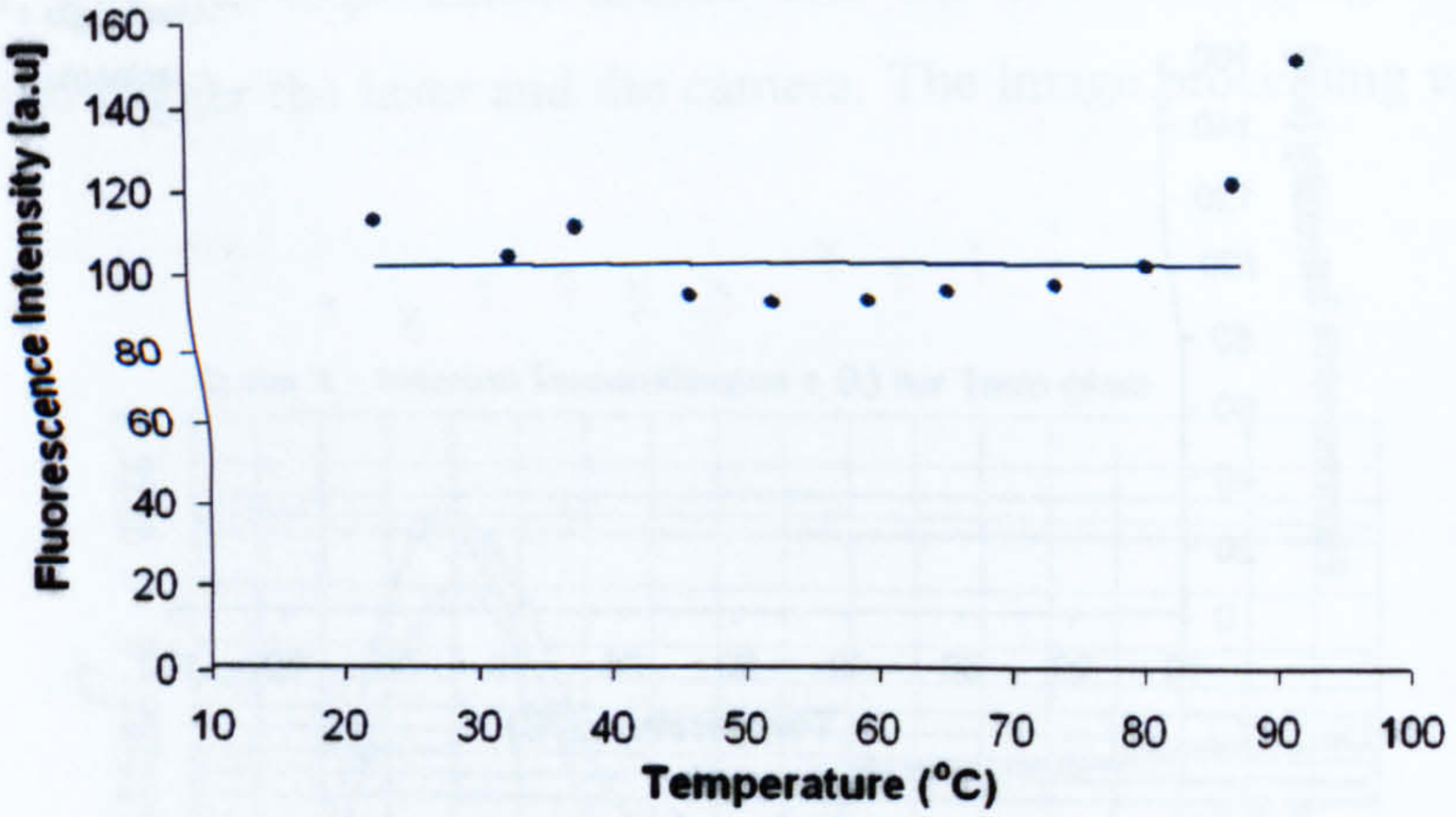

Figure 3-24: Toluene - temperature dependence of fluorescence

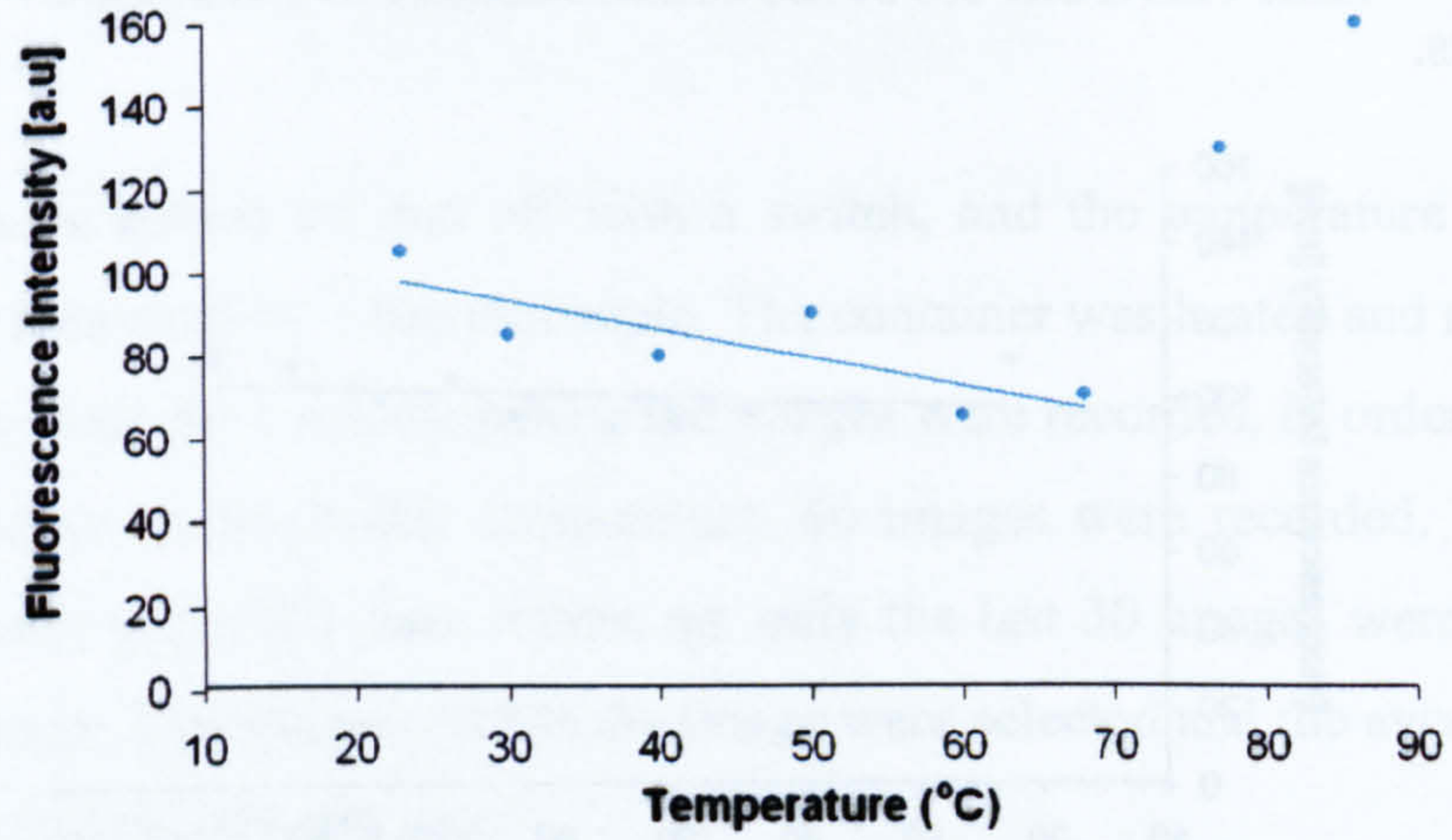

Figure 3-25: Fluorobenzene - temperature dependence of fluorescence

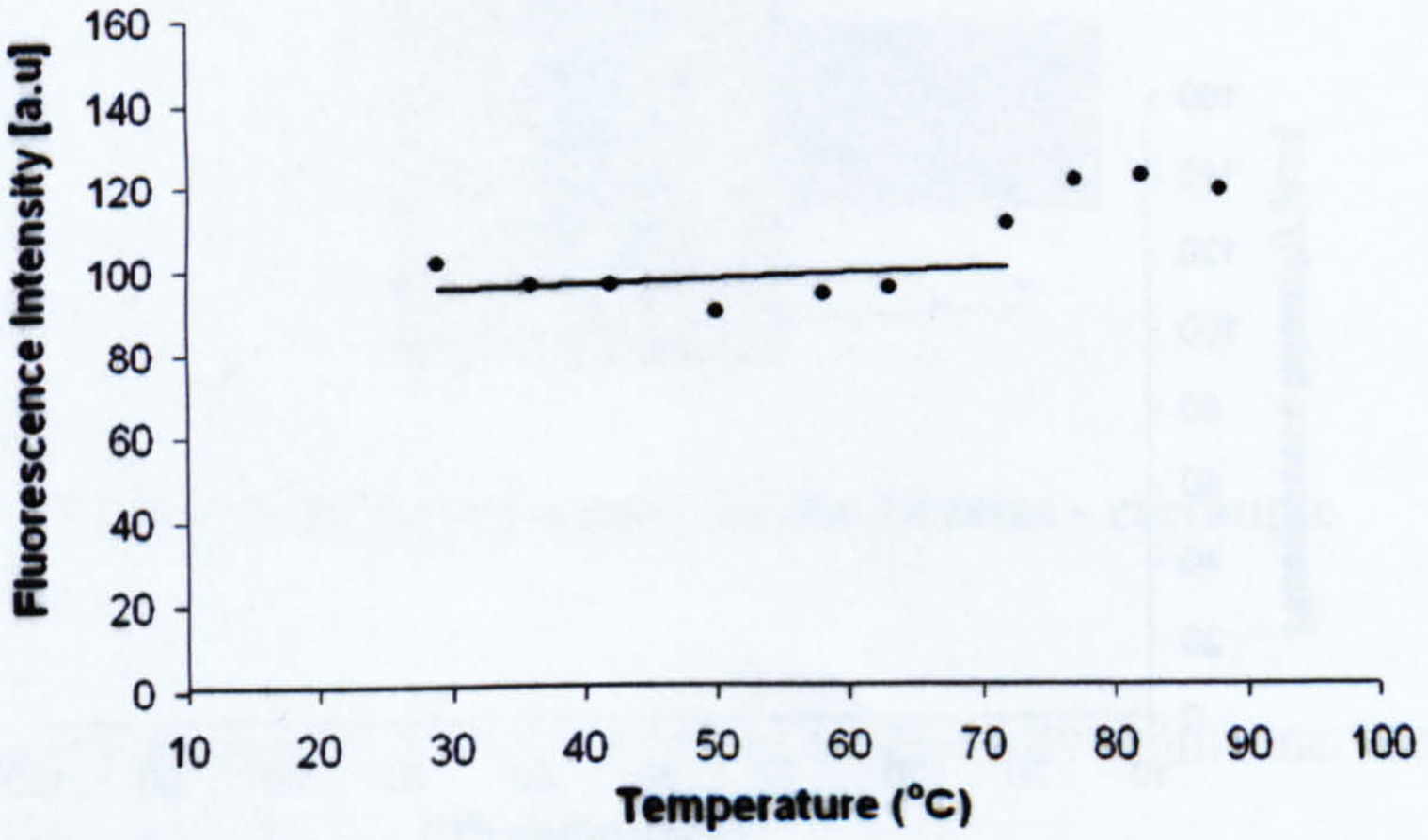

Figure 3-26: TEA - temperature dependence of fluorescence

For all tracers, except Fluorobenzene, the liquid phase fluorescence showed little change below boiling point, the worst case being 10%. Part of that variation can be attributed to experimental error, due to laser fluctuations from shot to shot, and deviation in power as the experiment progressed. The measurement points closer to 100°C show a positive deviation. This deviation is the smallest for 2-Hexanone, whose boiling point is 25°C higher than that of Iso-Octane.

The increase of the intensity around and beyond the boiling point can be attributed to the formation of bubbles in the cuvette. The resulting layer of gas-phase decreases the absorption. This in turn increases the laser power at the measurement volume and therefore the fluorescence intensity.

3.2.4. Pressure dependence

Because the liquid phase is quasi-incompressible, the distribution of the tracer within the liquid fuel should remain unchanged with pressure. To investigate the pressure dependence of the liquid phase fluorescence, the same type of experiment as the temperature study was carried out in a high pressure vessel. The fluorescence of the fuel tracer within a quartz cuvette was recorded on an intensified CCD camera. 5 Pressures were investigated: 1, 5, 10, 15, and 20 bar. When the vessel had reached the desired pressure, 200 images were recorded, and an average of the last 100 was calculated. The fluorescence intensity profile of the average image was plotted.

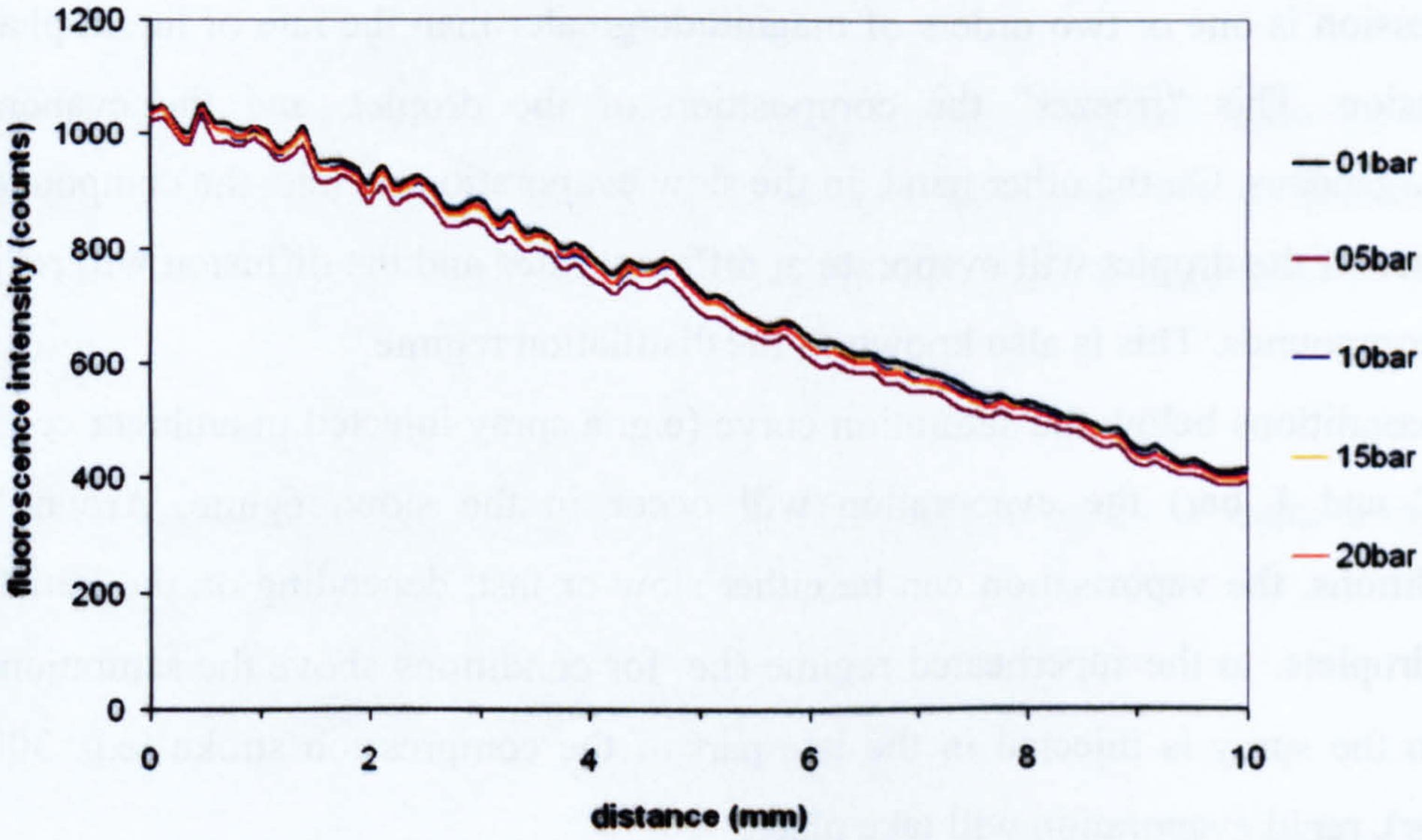

Figure 3-27: Fluorescence intensity profile across the cuvette for 3-Pentanone

As expected, the variation of the profile was weak. A first experiment had consisted in taking images at increasing pressures (1, 5, 10, 15 and 20bar). It was observed that the profiles were very similar, but decreasing with pressure. The experiment was reiterated by choosing another order for the pressures (1, 10, 20, 15 and 5bar), and it was found that the decrease of the profile's intensity was actually a function of time. This decrease is due to the breaking down of the ketone bond (C=O) from the repetitive UV excitation (Tait 1994).

The deviation of the profile from the Beer-Lambert's law can be attributed to the honeycomb structure which was clearly visible with the intensifier used.

All the tracers tested verified that the liquid phase fluorescence is independent of pressure.

3.2.5. Tracer evaporation

3.2.5.1. Background

The fluorescence signal of a droplet is a function of the tracer volume (concentration) within the droplet. In order to maintain the diameter cubed dependence of the LIF signal, the tracer's relative concentration should not change during evaporation. It is absolutely crucial that the tracer evaporates at the same rate as the fuel.

Two extreme regimes of droplet evaporation must be considered (Law 1982). In the rapid evaporation (also referred to as diffusion-limited evaporation), the rate of surface regression is one or two orders of magnitude greater than the rate of liquid-phase mass diffusion. This "freezes" the composition of the droplet, and the evaporation is homogeneous. On the other hand, in the slow evaporation regime, the compounds at the surface of the droplet will evaporate at different rates and the diffusion will redistribute the compounds. This is also known as the distillation regime.

For conditions below the saturation curve (e.g. a spray injected in ambient conditions - 25°C and 1 bar) the evaporation will occur in the slow regime. Around boiling conditions, the vaporisation can be either slow or fast, depending on the initial size of the droplets. In the superheated regime (i.e. for conditions above the saturation curve), when the spray is injected in the late part of the compression stroke (e.g. 300°C and 10bar), rapid evaporation will take place.

3-Pentanone has been the preferred tracer for AFR measurements because of its close matching boiling point with Iso-Octane (99.2°C vs. 101.7°C at 1 bar) and because its fluorescence is well characterised (Ghandi and Felton (1996), Grossman et al. (1996). However, Le Coz et al. (1994) reported that the molar fraction of 3-Pentanone in the vapour phase was twice that of the liquid phase for a 5/95 mixture in Iso-octane, and suggested the use of 2-Hexanone because of its lower volatility. Davy et al. (2003) also indicated that 3-Pentanone is not a suitable tracer at low concentrations due to its preferential evaporation when mixed with Iso-octane, even though it's boiling point is higher. This is because 3-Pentanone and Iso-Octane form an azeotrope.

An azeotrope is a mixture of liquids that has a constant boiling point and thus cannot be separated by distillation. Ethanol (boiling point 78.5°C) and water (boiling point 100°C) form a binary azeotrope having a boiling point of 78.2°C and a composition that is 95.6% ethanol. Therefore, a mixture of 95% ethanol and 5% water will co-evaporate.

In the case of non-azeotropic mixture, a close matching boiling point will be beneficial. However, for mixtures which form an azeotrope, the concentrations should match the azeotropic mixture. However, if that mixture has a too high absorbance, than it will not be suitable.

3.2.5.2. Vapour-Liquid Equilibrium Calculations

3.2.5.2.1. The model

To characterise and calculate the differential evaporation of various tracer systems in Iso-Octane, a model using the gamma-phi method following the guidelines from Malanowski and Anderko (1992) was developed for flash calculations at a fixed temperature.

The liquid vapour equilibrium (VLE) of any component within a multi-component mixture is given by:

$$y_i \cdot P \cdot \Phi_i = x_i \cdot \gamma_i \cdot P_i^o$$

Equation 3-16

where:

y_i: vapour mole fraction of component i

P: equilibrium pressure

Φ_i: fugacity coefficient/correction factor for the non-ideality of the vapour phase of compound i

x_i: liquid mole fraction of component i

γ_i: activity coefficient of component i

P_i^o: vapour pressure of pure component i

For low pressures, the fugacity coefficient can be considered equal to 1.

The activity coefficients can be estimated using the Wilson (1964) equation:

$$\ln \gamma_i = -\ln\left[\sum_{j=1}^{n} x_j \cdot \Lambda_{i,j}\right] + 1 - \sum_{k=1}^{n} \frac{x_k \cdot \Lambda_{k,i}}{\sum_{l=1}^{n} x_l \cdot \Lambda_{k,l}}$$

Equation 3-17

At infinite dilution, the activity of component *i* over component *j* is extrapolated from the case where the molar fraction of component *i* is 1 and the molar fraction of *j* is 0.

This leads to:

$$\ln \gamma_{i,j}^{\infty} = -\ln \Lambda_{i,j} - \Lambda_{j,i} + 1$$

Equation 3-18

$$\ln \gamma_{j,i}^{\infty} = -\ln \Lambda_{j,i} - \Lambda_{i,j} + 1$$

Equation 3-19

Parameters $\Lambda_{i,j}$ are found from simultaneous solution of the above relations for two components at infinite dilution.

The activity at infinite dilution can be found using the Modified Separation of Cohesive Energy Density model (MOSCED) proposed by Thomas and Eckert (1984). It is based on the assumption that forces contributing to the cohesive energy density are additive. Forces included are dispersion, orientation, induction and hydrogen bonding. The five parameters associated to these forces are the dispersion parameter λ, the induction parameter q, the polar parameter τ, and the acidity and basicity parameters (respectively α and β). These modifications affect the activity coefficients in a symmetric way, contrary to experiment. Thomas and Eckert introduce two more parameters (ψ and ξ) to account for asymmetry effects resulting from differences in polarity and degree of hydrogen bonding respectively. These two are functions of other parameters.

The activities at infinite dilution are given by:

$$\ln \gamma_{i,j}^{\infty} = \frac{\upsilon_i}{RT} \cdot \left[(\lambda_i - \lambda_j)^2 + \frac{q_i^2 \cdot q_j^2 \cdot (\tau_i - \tau_j)^2}{\psi_j} + \frac{(\alpha_i - \alpha_j) \cdot (\beta_i - \beta_j)}{\xi_j} \right] + d_{j,i}$$

Equation 3-20

where υ_i is the liquid molar volume at 20°C in $cm^3.mol^{-1}$ and is given by:

$$\upsilon = \frac{M}{\rho}$$

Equation 3-21

with M the molecular weight in $g.mol^{-1}$ and ρ the density in $g.cm^{-3}$.

d_{ij} is the Flory-Huggins combinatorial term to account for differences in molecular size:

$$d_{ij} = \ln\left(\frac{\upsilon_j}{\upsilon_i}\right)^{aa_j} + 1 - \left(\frac{\upsilon_j}{\upsilon_i}\right)^{aa_j}$$

Equation 3-22

Parameters α, β, τ, ψ, ξ and aa are temperature dependent:

$$\alpha = \alpha_0 \cdot t^{0.8}$$

Equation 3-23

$$\beta = \beta_0 \cdot t^{0.8}$$

Equation 3-24

$$\tau = \tau_0 \cdot t^{0.4}$$

Equation 3-25

The subscript 0 refers to 20°C.

$$\psi = POL + 0.011 \cdot \alpha \cdot \beta$$

Equation 3-26

$$\xi = 0.68 \cdot (POL - 1) + \left\{3.4 - 2.4 \cdot \exp\left[(-0.023) \cdot (\alpha_0 \cdot \beta_0)^{1.5}\right]\right\}^{t^2}$$

Equation 3-27

$$POL = q^4 \cdot \left|1.15 - 1.15 \cdot \exp\left(-0.02 \cdot \tau^3\right)\right| + 1$$

Equation 3-28

$$aa = 0.953 - 0.00968 \cdot \left(\tau^2 + \alpha \cdot \beta\right)$$

Equation 3-29

Having determined the activities and the saturated pressures (for a fixed liquid fraction), the equilibrium pressure is:

$$P = \left(\sum_{i=1}^{n} y_i\right) \cdot P = \sum_{i=1}^{n} \left(y_i \cdot P\right) = \sum_{i=1}^{n} \left(x_i \cdot \gamma_i \cdot P_i^o\right)$$

Equation 3-30

The vapour fraction of a component *i* can then be calculated as:

$$y_i = \frac{x_i \cdot \gamma_i \cdot P_i^o}{P}$$

Equation 3-31

3.2.5.2.2. The parameters

The parameters required for the MOSCED calculation were taken from the literature (Reid et al. 1987). All but one compound were found in a table. The parameters for 2-Hexanone were estimated by the following equations:

$$\alpha_0 = C_\alpha \cdot \left(\frac{4.5}{3.5 + N_C}\right) \cdot \left(1 + \frac{N_C - 1}{100}\right)$$

Equation 3-32

$$\beta_0 = C_\beta \cdot \left(\frac{4.5}{3.5 + N_C}\right) \cdot \left(1 + \frac{N_C - 1}{100}\right)$$

Equation 3-33

$$\tau_0 = C_\tau \cdot \left(\frac{4.5}{3.5 + N_C}\right) \cdot \left(1 + \frac{N_C - 1}{100}\right)$$

Equation 3-34

where N_C is the number of carbon atoms in the molecule. For ketones, $C_\alpha = 0$, $C_\beta = 4.87$ and $C_\tau = 3.93$.

For saturated compounds, $q_0 = 1$.

The values of the different parameters are found in *Table 3-3*.

	v_0	λ_0	τ_0	q_0	α_0	β_0
Iso-Octane	165.1	7.84	0.00	1.00	0.00	0.00
3-Pentanone	105.8	7.86	2.77	1.00	0.00	3.43
2-Hexanone	123.3	7.85	1.95	1.00	0.00	2.42
Toluene	106.3	8.45	1.56	0.90	0.15	1.60
TEA	139.0	7.52	0.53	1.00	0.00	4.98

Table 3-3: MOSCED parameters for various compounds at 20°C

The vapour pressures are usually not well documented for values above the boiling point at atmospheric conditions. However, the data for Toluene is almost complete for temperatures ranging from 0°C to the critical point (318°C). *Figure 3-28* represents the

staturation curve of Toluene. The values for the different series are obtained using the Antoine equation which expresses the vapour pressure P (in bar) as function of the temperature T (in Kelvin):

$$\log(P) = A - \frac{B}{T + C}$$

Equation 3-35

where A, B and C are the Antoine parameters determined empirically. These parameters are usually defined for a specific temperature range.

The extrapolation of the data points between *Series 1* and *2* and *Series 2* and *3* fit well. Also, *Series 3* can be extrapolated to the critical point. These features were used to approximate the saturation curves for the other compounds.

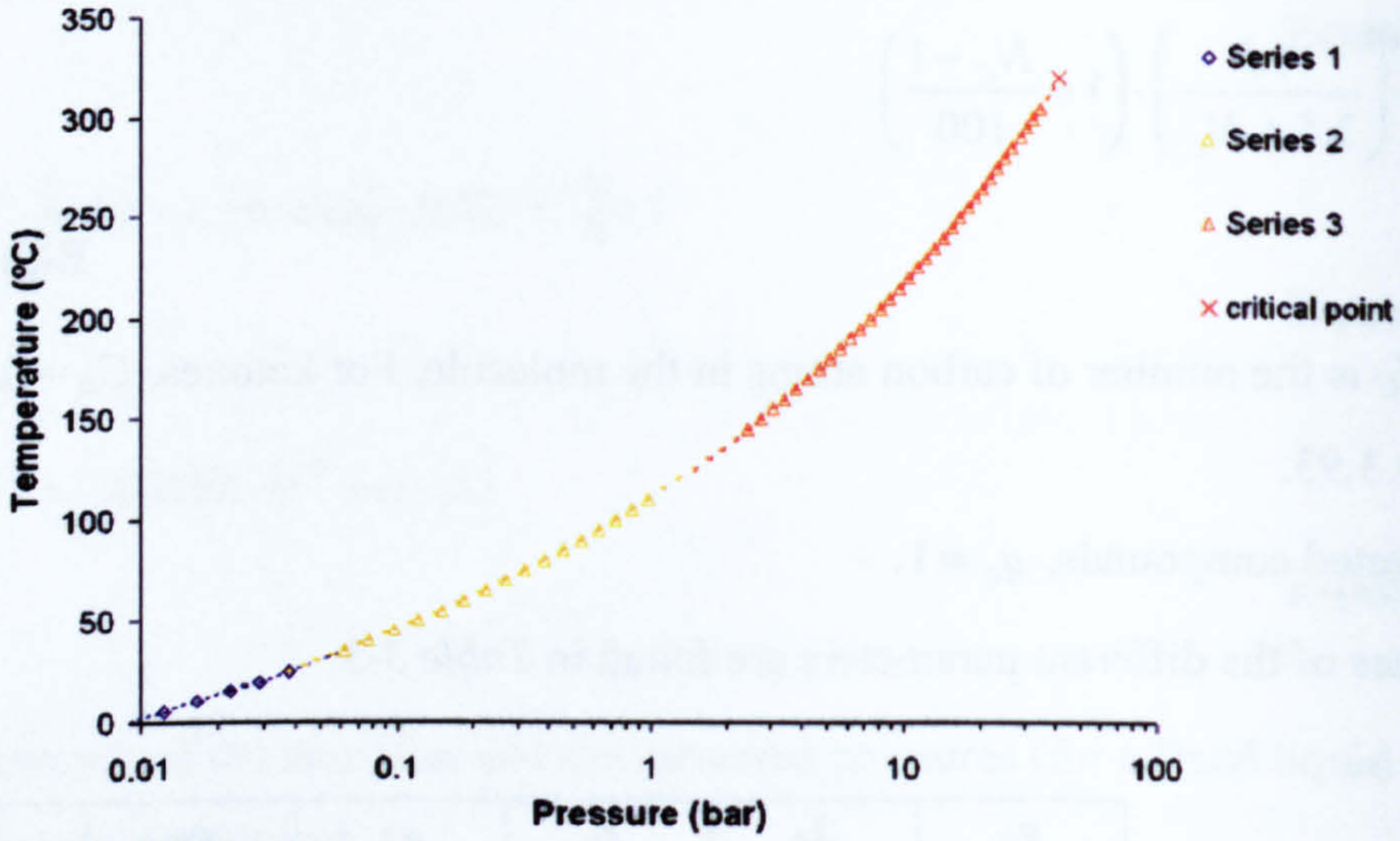

Figure 3-28: Saturation curve for Toluene

The critical points can be found in the CRC Handbook of Chemistry and Physics and the Antoine parameters for some temperature ranges were found in the NIST Chemistry WebBook. The other saturation points were determined using the generalised enthalpy diagram. The saturation curves are represented in *Figure 3-29*, and the vapour pressures at 4 different temperatures can be found in *Table 3-4*.

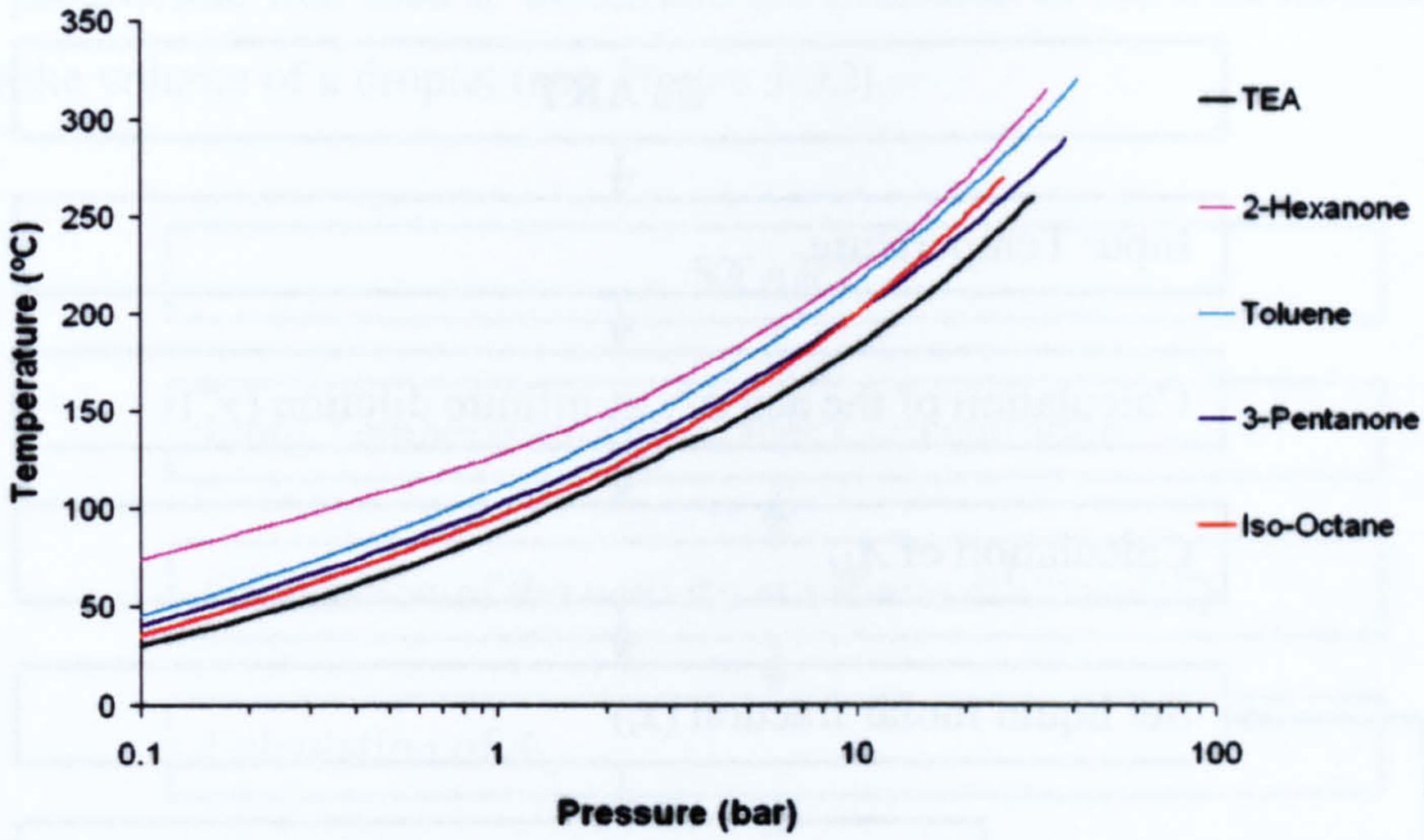

Figure 3-29: Saturation curves for various compounds

	50°C	100°C	150°C	200°C
Iso-Octane	0.19	1.13	3.97	9.80
3-Pentanone	0.15	0.95	3.56	9.79
2-Hexanone	0.03	0.34	2.03	6.49
Toluene	0.12	0.74	2.75	7.46
TEA	0.26	1.38	5.03	13.24

Table 3-4: Vapour pressures (in bar) at 4 different temperatures

3.2.5.2.3. The programme

A programme was written in C++ to calculate the equilibrium pressure and vapour molar fraction as a function of liquid molar fraction of the tracer system (see *Figure 3-30*). The calculation was done for liquid molar fractions ranging from 0 to 1 in step of 0.001. This allowed to build the vapour-liquid equilibrium diagram and understand the evaporative behaviours of the tracers in Iso-Octane.

The programme was validated by tracing the 3-Pentanone boiling and condensation curves for 50°C (see *Figure 3-31*) and comparing them with the ones from Davy et al. (2003). In their work, Davy et al. (2003) used empirical data from Fuchs et al. (1984) which use slightly different vapour pressures than the ones obtained from the literature. For the purpose of the validation, those vapour pressures were used.

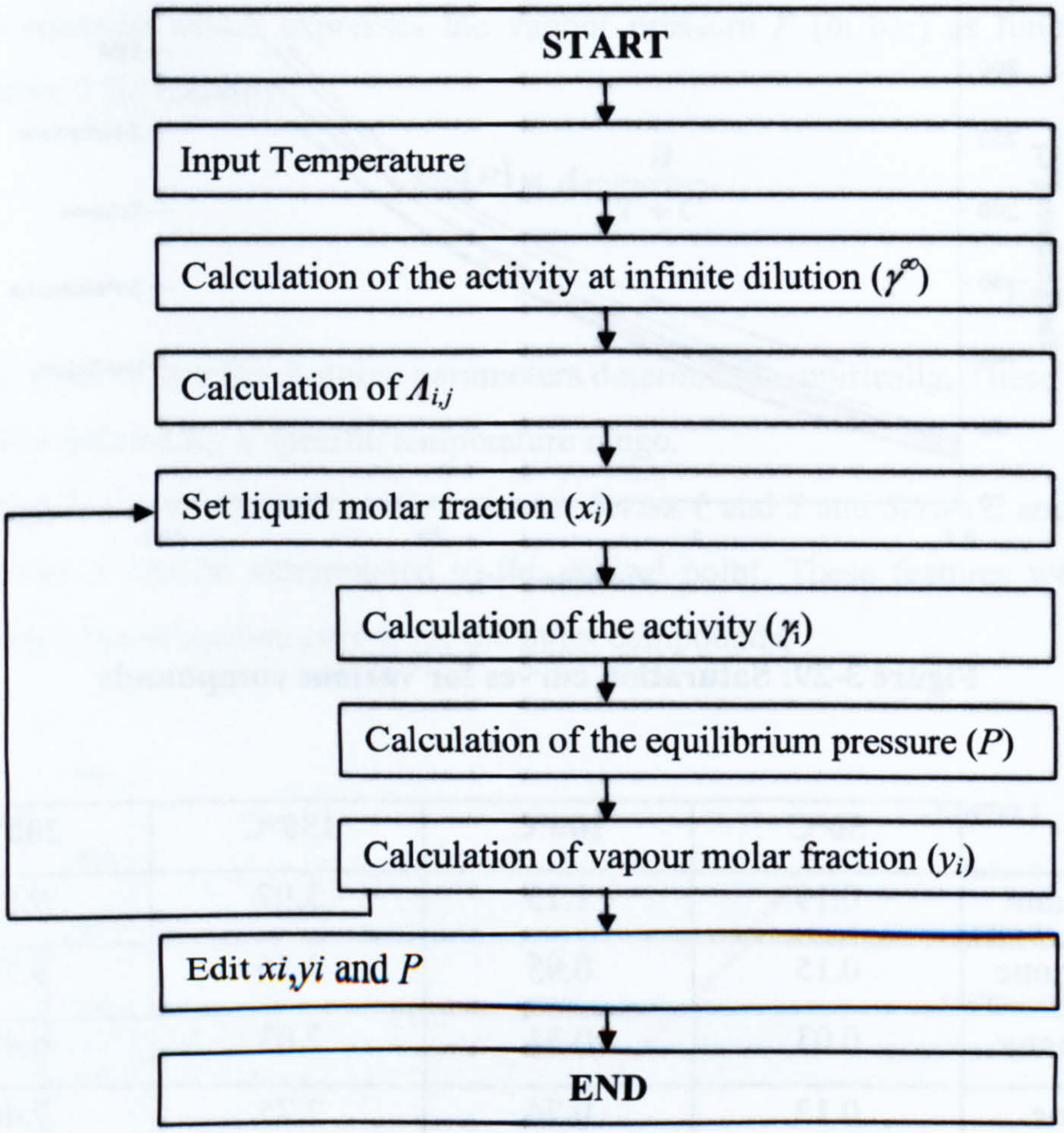

Figure 3-30: Programme structure for the distillation calculations.

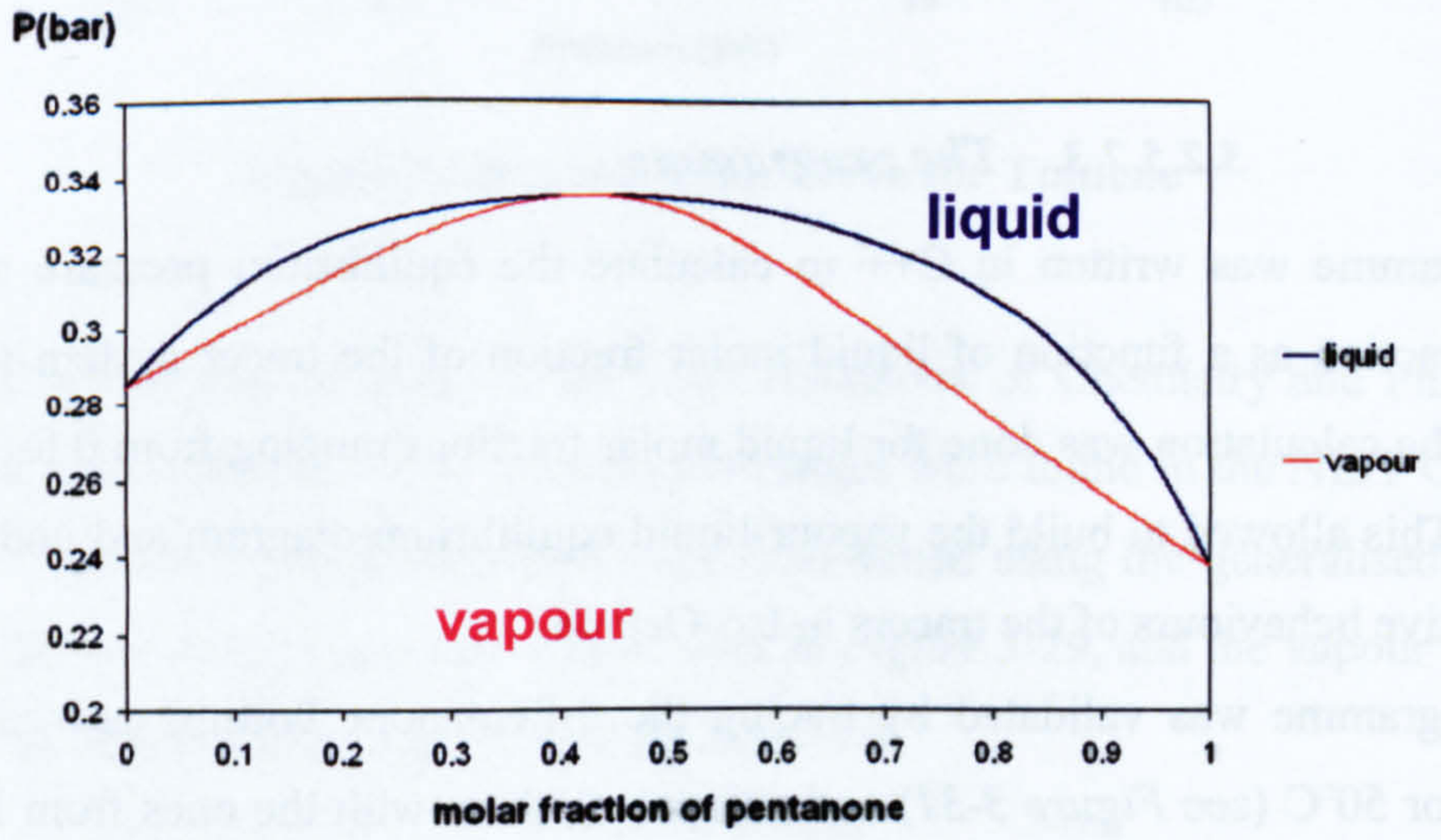

Figure 3-31: Vapour-liquid equilibrium diagram for the 3-Pentanone/Iso-Octane system at 50°C

A second programme was used to determine the evolution of the fluorescence intensity relative to the volume of a droplet (see *Figure 3-32*).

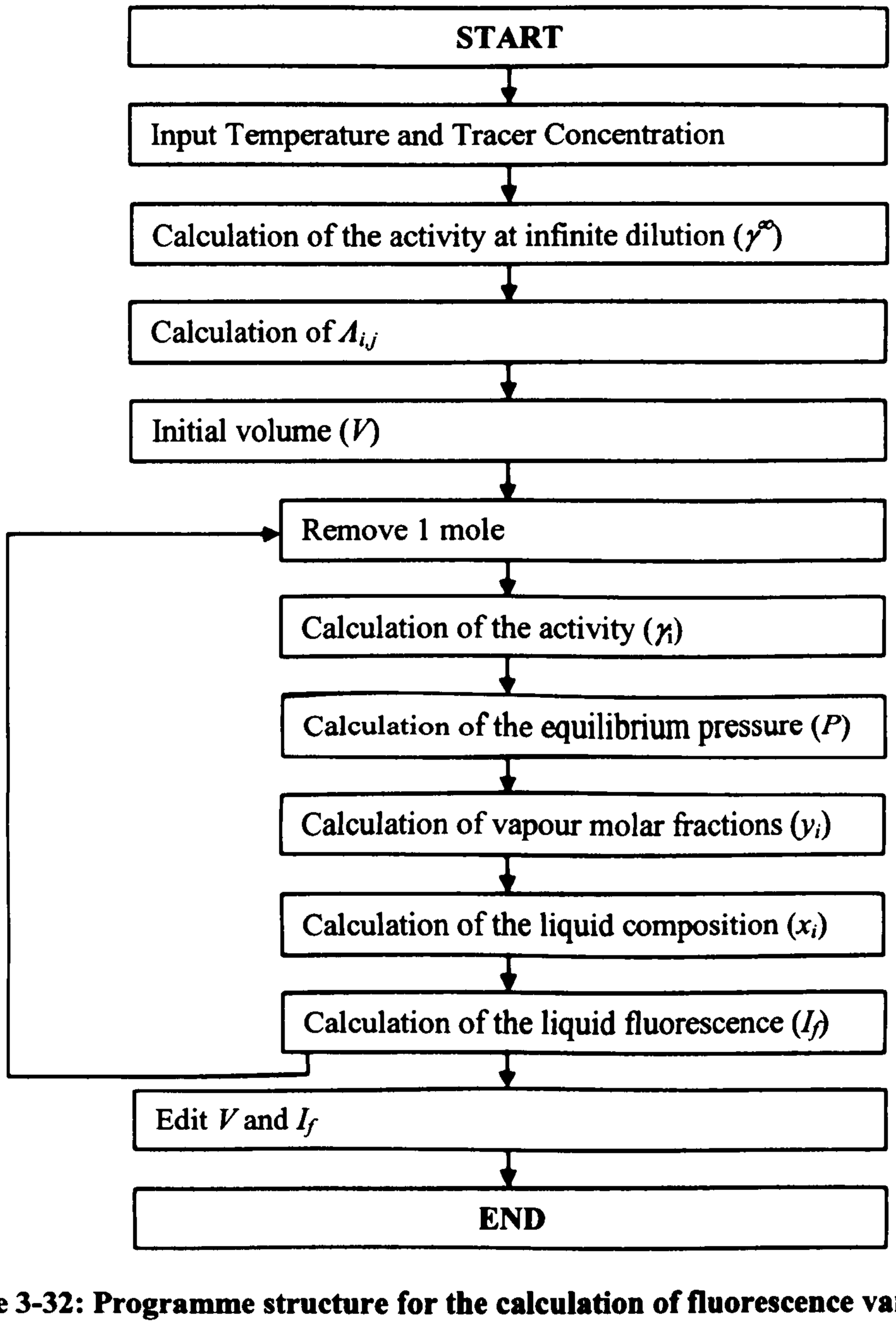

Figure 3-32: Programme structure for the calculation of fluorescence variation in an evaporating droplet

The calculation consisted of 1000 steps, corresponding to the removal of 1 mole from a 1000 mole droplet. For each numerical step, the vapour molar fraction of the removed mole was determined to recalculate the composition of the liquid-phase mixture. Assuming that the fluorescence is not quenched and that the droplet is homogeneously

illuminated droplet (volume dependent signal), the fluorescence intensity was directly proportional to the tracer concentration in the remaining volume.

3.2.5.3. Results for single tracer systems

For each tracer, two graphs are plotted.

The first graph presents the vapour molar fraction as a function of the liquid molar fraction. This indicates whether the tracer or the Iso-Octane is preferentially expelled . It also allows to notice if the tracer/fuel mixture forms an azeotrope, and if so, at which mixture concentration.

The second graph presents the fluorescence of a droplet as a function of the volume, as the droplet evaporates. For the purpose of this programme, the fluorescence is proportional to the tracer concentration (i.e. there is no quenching). The fluorescence and the volume have initial values of 100[a.u.].

3.2.5.3.1. 3-Pentanone

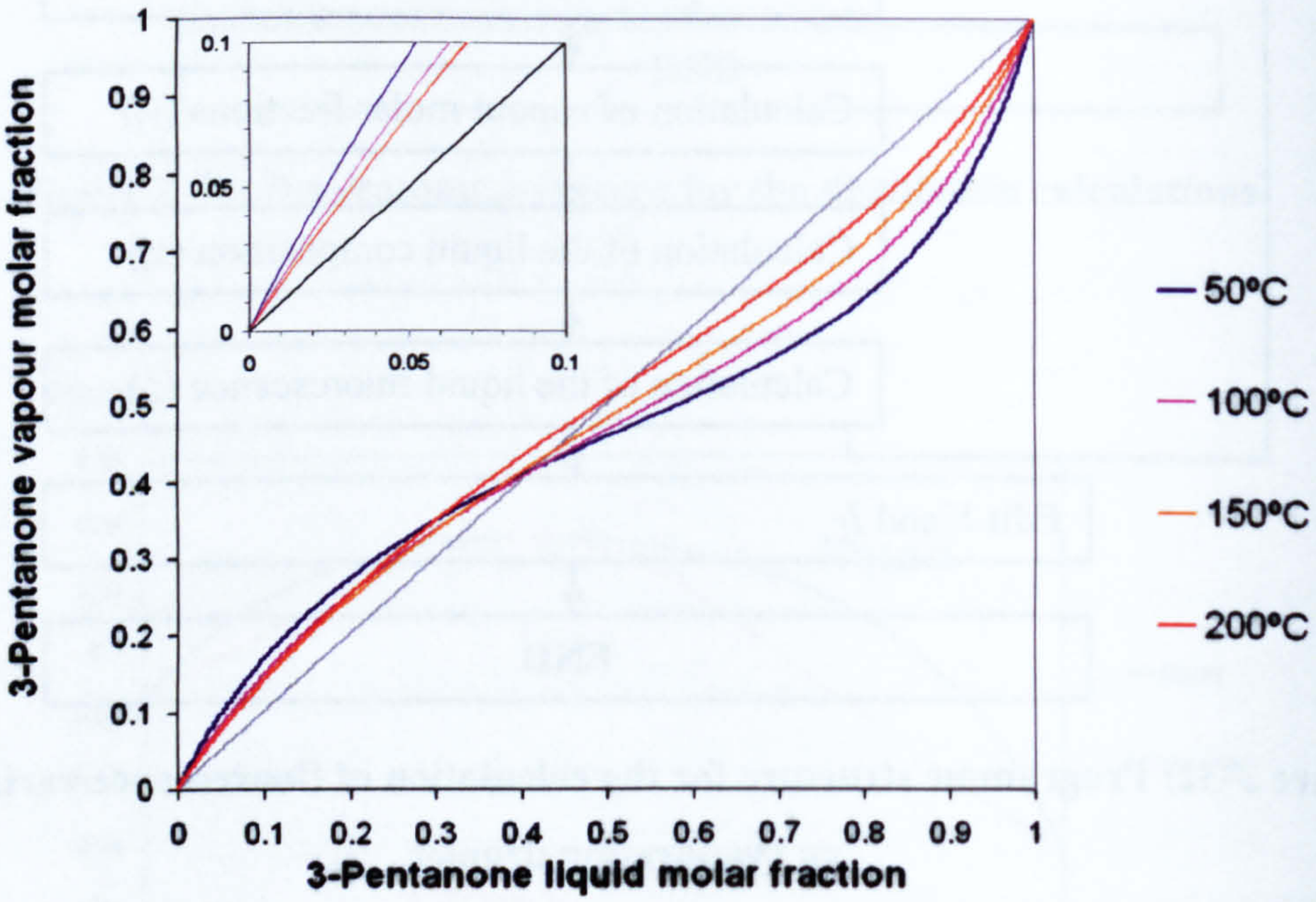

Figure 3-33 : Liquid-vapour equilibrium of 3-Pentanone in Iso-Octane for different temperatures

Figure 3-31 showed that the boiling and condensation curves go through an extremum (a maximum in the case of 3-Pentanone and Iso-Octane), characteristic of a (positive) azeotrope. *Figure 3-33* shows the azeotrope's shift with temperature: at 50°C, the azeotropy is for a 40/60 mixture whilst at 200°C the azeotrope corresponds to a 60/40 mixture.

However, the azeotrope occurs at high concentrations of 3-Pentanone which are not suitable for the volume dependence fluorescence of the droplets studied.

At low tracer concentrations, the mixture will preferentially evaporate the 3-Pentanone, even though its boiling point is higher.

A 2% 3-Pentanone liquid composition will have a vapour composition of 4.1 % at 50°C and 3.1 % at 200°C.

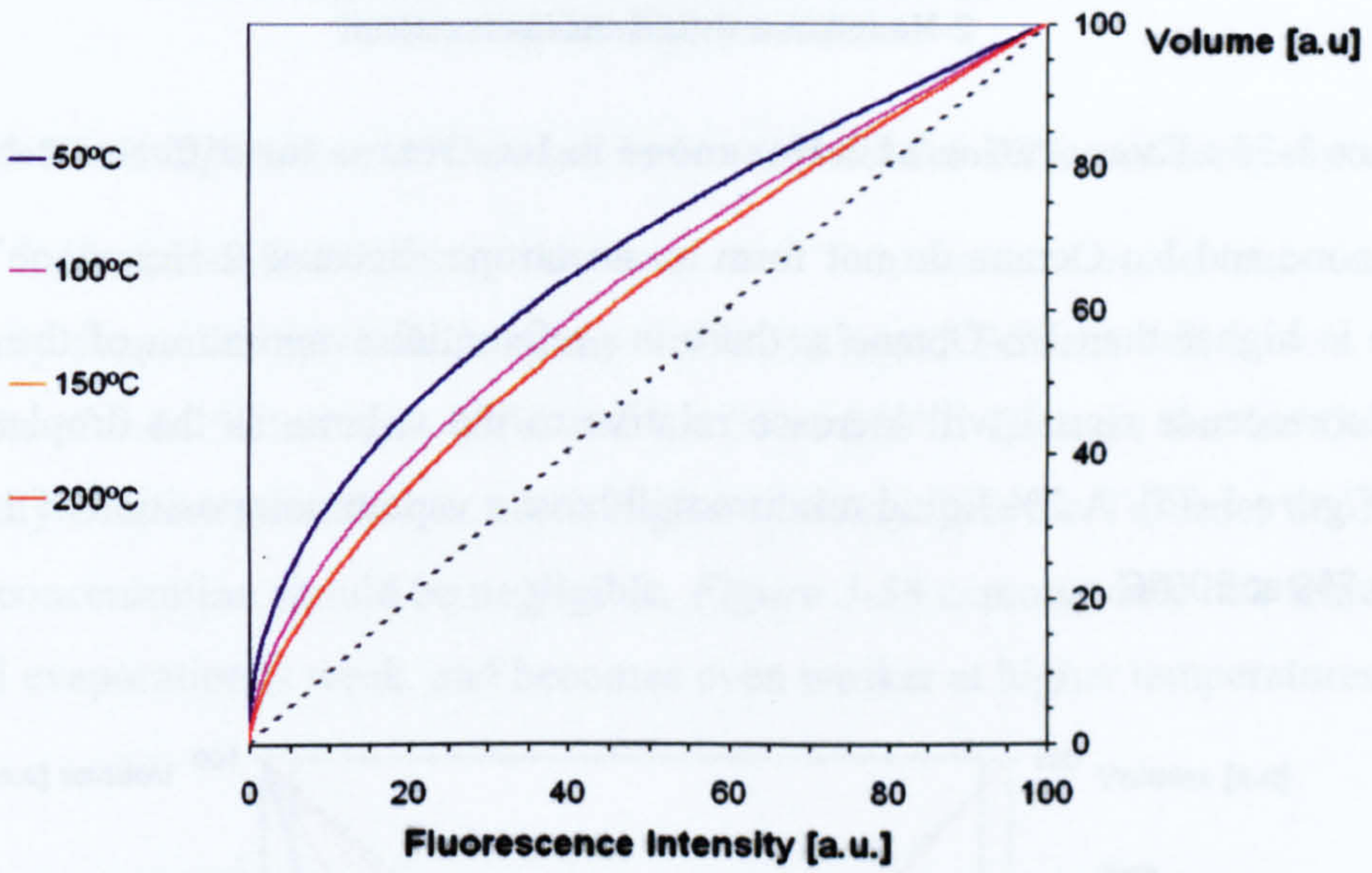

Figure 3-34: Fluorescence vs. Volume for an evaporating droplet containing 2% 3-Pentanone

Figure 3-34 demonstrates the importance of differential evaporation. When the droplet has half evaporated, the fluorescence intensity has decreased by 80%, already yielding an error greater than 50%. The differential evaporation decreases with temperature, but would still be unsatisfactory for slow evaporation regimes.

3.2.5.3.2. 2-Hexanone

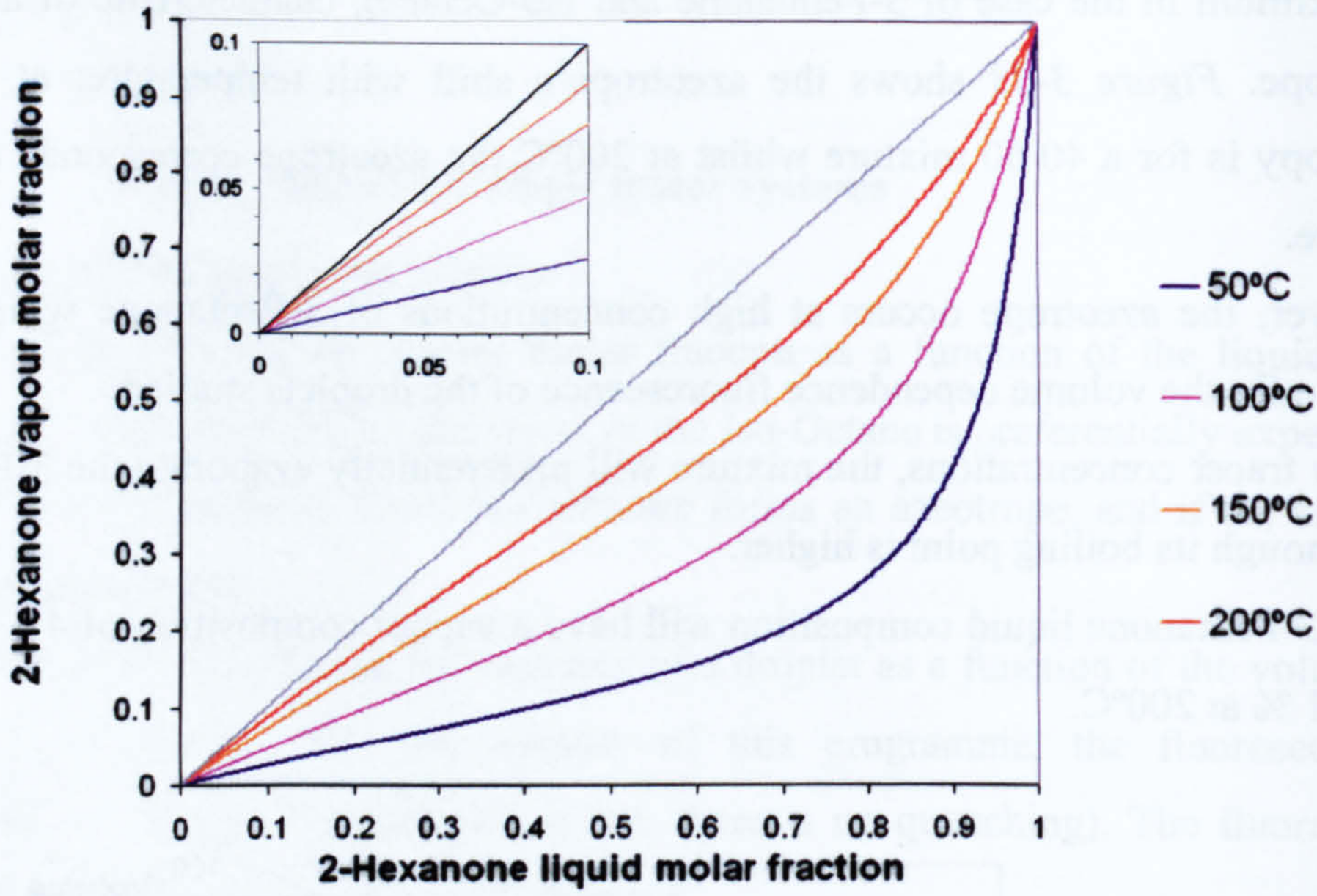

Figure 3-35 : Evaporation of 2-Hexanone in Iso-Octane for different temperatures

Hexanone and Iso-Octane do not form an azeotrope. Because 2-Hexanone's saturation curve is higher than Iso-Octane's, there is preferential evaporation of the Iso-Octane: the fluorescence signal will increase relative to the volume as the droplet evaporates (see *Figure 3-35*). A 2% liquid mixture will have a vapour composition of 1.1% at 50°C and 1.7% at 200°C.

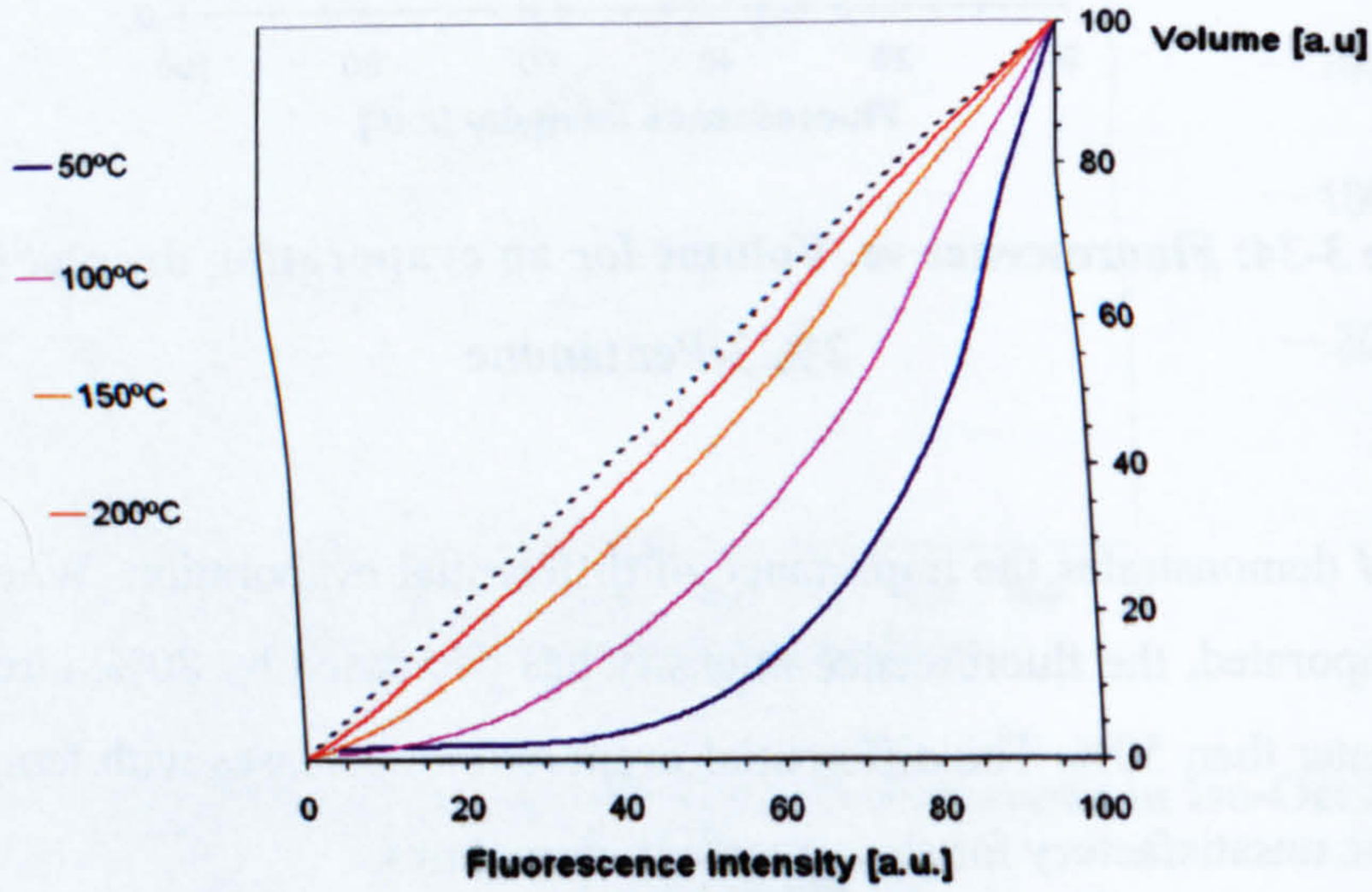

Figure 3-36: Fluorescence vs. Volume for an evaporating droplet containing 2% 2-Hexanone

3.2.5.3.3. Toluene

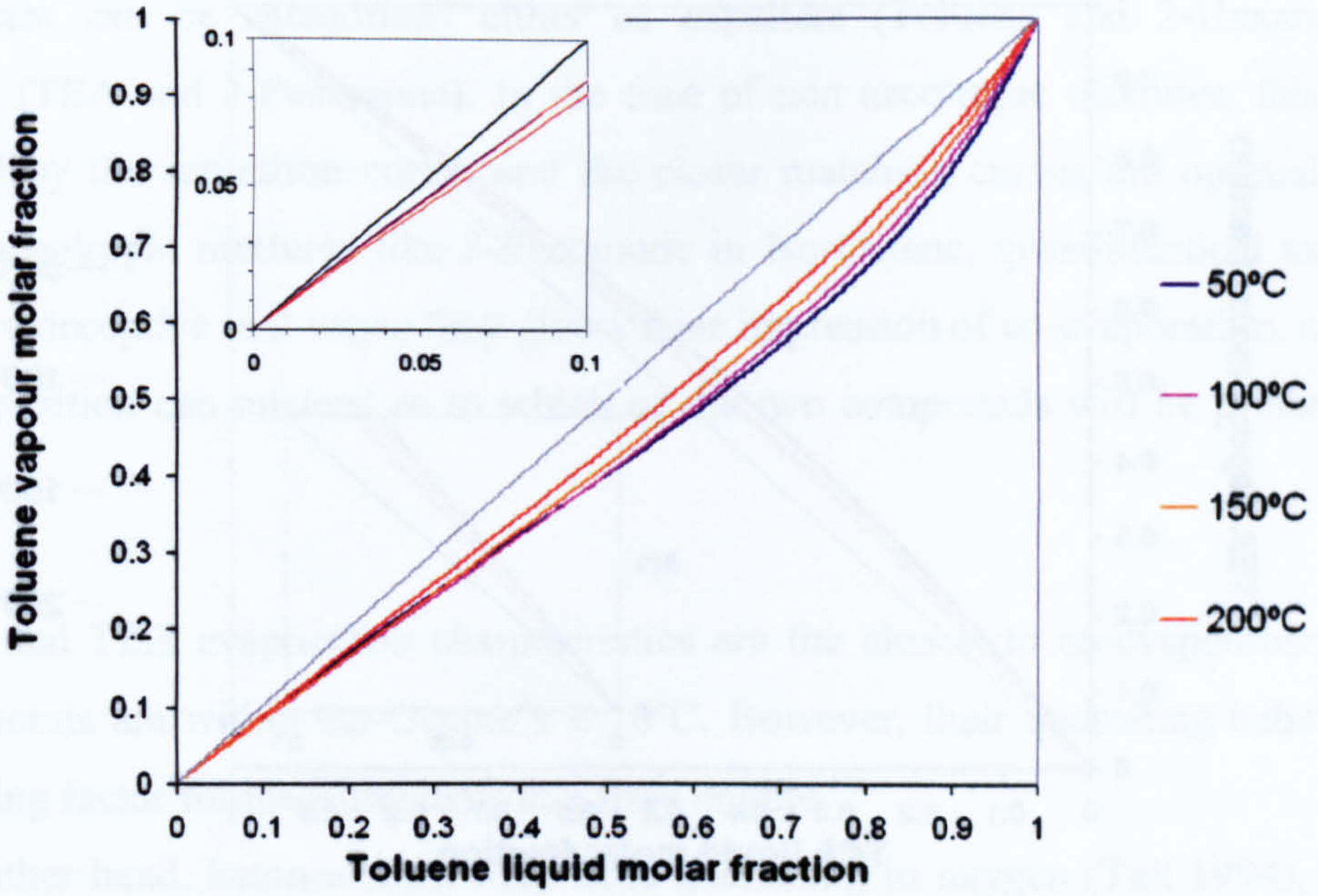

Figure 3-37: Evaporation of Toluene in Iso-Octane for different temperatures

Like the 2-Hexanone/Iso-Octane mixture, the Toluene/Iso-Octane mixture will preferentially evaporate the fuel. A mixture of 0.3% liquid Toluene will have a vapour composition of 0.44 % tracer at 50°C and 0.4 % at 200°C. Because the Iso-Octane is preferentially evaporated and is in much higher quantity than the Toluene, the relative change in concentration should be negligible. *Figure 3-38* demonstrates this feature: the differential evaporation is weak, and becomes even weaker at higher temperatures.

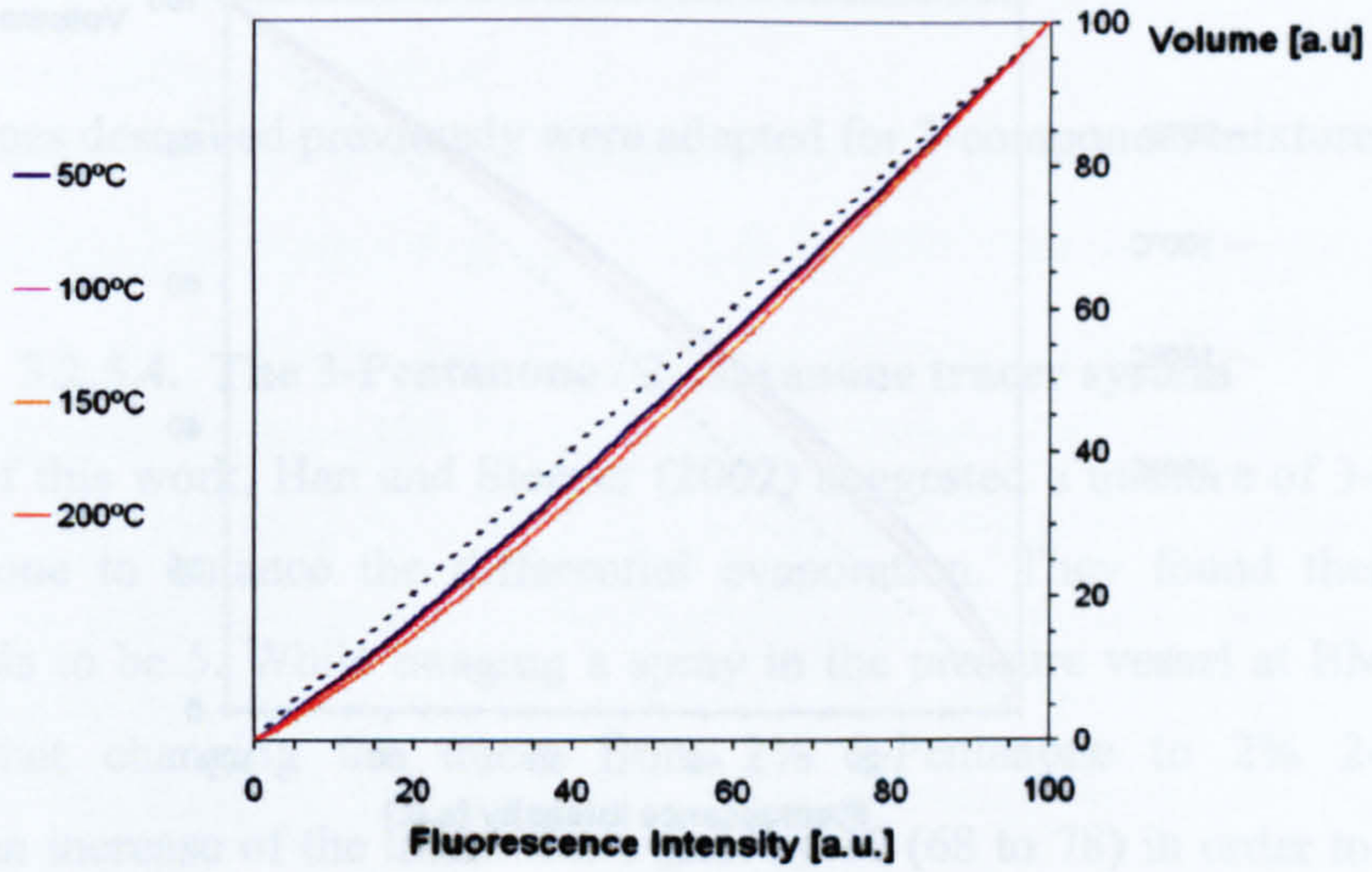

Figure 3-38: Fluorescence vs. Volume for an evaporating droplet containing 0.3% Toluene

3.2.5.3.4. TEA

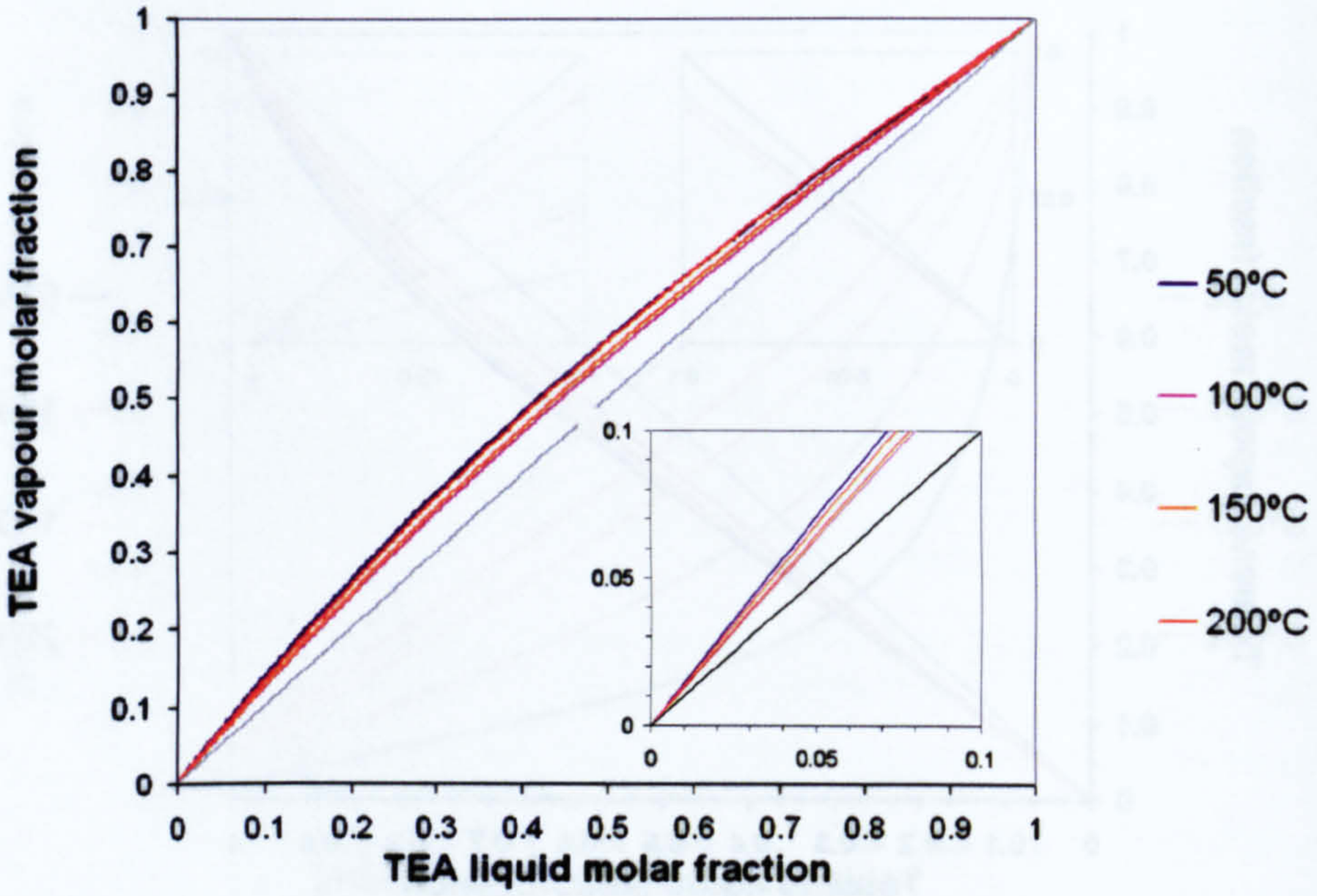

Figure 3-39 : Evaporation of TEA in Iso-Octane for different temperatures

TEA does not form an azeotrope in Iso-Octane (see *Figure 3-39*). Because of its lower saturation curve relative to Iso-Octane, TEA will be preferentially evaporated. A 3% TEA liquid mixture will have a vapour composition of 4.3% and 4% at 50°C and 200°C respectively. The differential evaporation is weaker than for 3-Pentanone (see *Figure 3-40*).

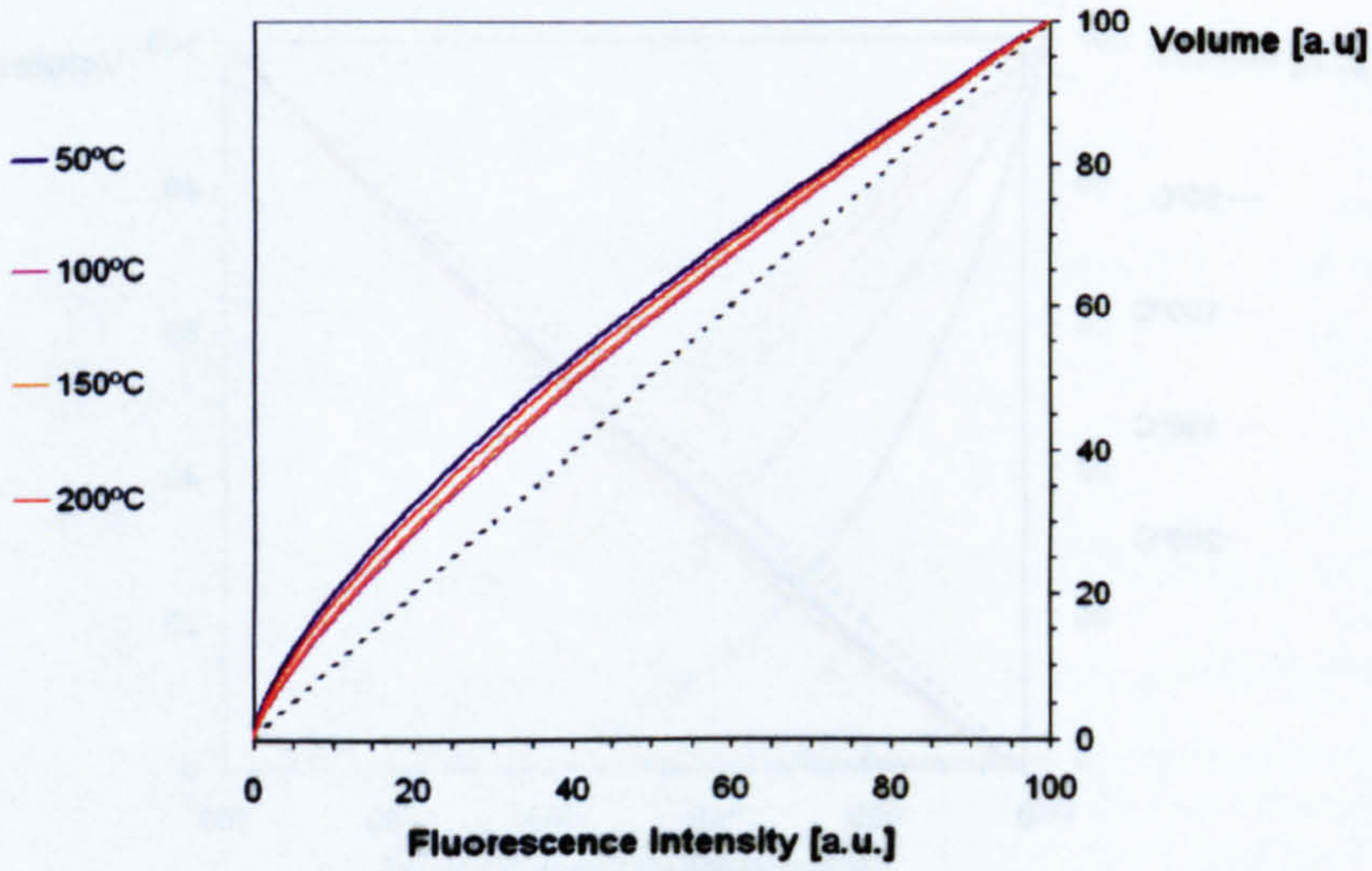

Figure 3-40: Fluorescence vs. Volume for an evaporating droplet containing 3% TEA

3.2.5.3.5. Conclusion

The tracers can be categorised either as expellers (Toluene and 2-Hexanone) or expulsed (TEA and 3-Pentanone). In the case of non azeotropic mixtures, this can be predicted by the saturation curve, and the closer matching curves are optimal. In the case of azeotropic mixtures like 3-Pentanone in Iso-Octane, quasi-identical saturation curves are deceptive in 2 ways: they give a false impression of co-evaporation, and their relative position can mislead as to which of the two compounds will be preferentially expelled.

Toluene and TEA evaporation characteristics are the closest to co-evaporation. Their boiling points are within Iso-Octane's ± 10°C. However, their quenching behaviour is the limiting factor for measurements in a fired engine.
On the other hand, ketones show very little quenching in oxygen (Tait 1994), so they are more appropriate from that point of view for the LSD technique. However, as has just been shown, 3-Pentanone and 2-Hexanone do not satisfy co-evaporation behaviours. Nevertheless, because they exhibit opposite expulsion behaviours, the combination of these 2 tracers could balance out the differential evaporation.
However, the two tracers don't have the same quantum yield: even if a dual tracer system evaporates homogeneously, the fluorescence will not be an adequate indication of the volume. A compromising tracer composition should be possible to optimise the tracer system's fluorescence with an evaporating droplet.

The programmes described previously were adapted for 3-component mixtures.

3.2.5.4. The 3-Pentanone / 2-Hexanone tracer system

At the time of this work, Han and Steeper (2002) suggested a mixture of 3-Pentanone and 3-Hexanone to balance the differential evaporation. They found their ratio of quantum yields to be 5. While imaging a spray in the pressure vessel at BMW AG, it was found that changing the tracer from 2% 3-Pentanone to 2% 2-Hexanone necessitated an increase of the intensifier's gain by 10 (68 to 78) in order to match the fluorescence intensity. From the intensifier's data sheet, the ratio of quantum yields was calculated to be 4.3.

The two ketones have similar absorption/absorbance spectrums. As seen previously, both tracers could be used individually at a concentration of 2% in Iso-Octane. Therefore, the dual tracer system could also have a concentration of 2%. The evaporation of a droplet was simulated for 5 mixtures of 3-Pentanone and 2-Hexanone in 98% Iso-Octane. These mixtures ranged from 3-Pentanone to pure 2-Hexanone.

For convenience, a mixture of *x*% 3-Pentanone, *y*% 2-Hexanone *z*% Iso-Octane is referred to as x/y/z.

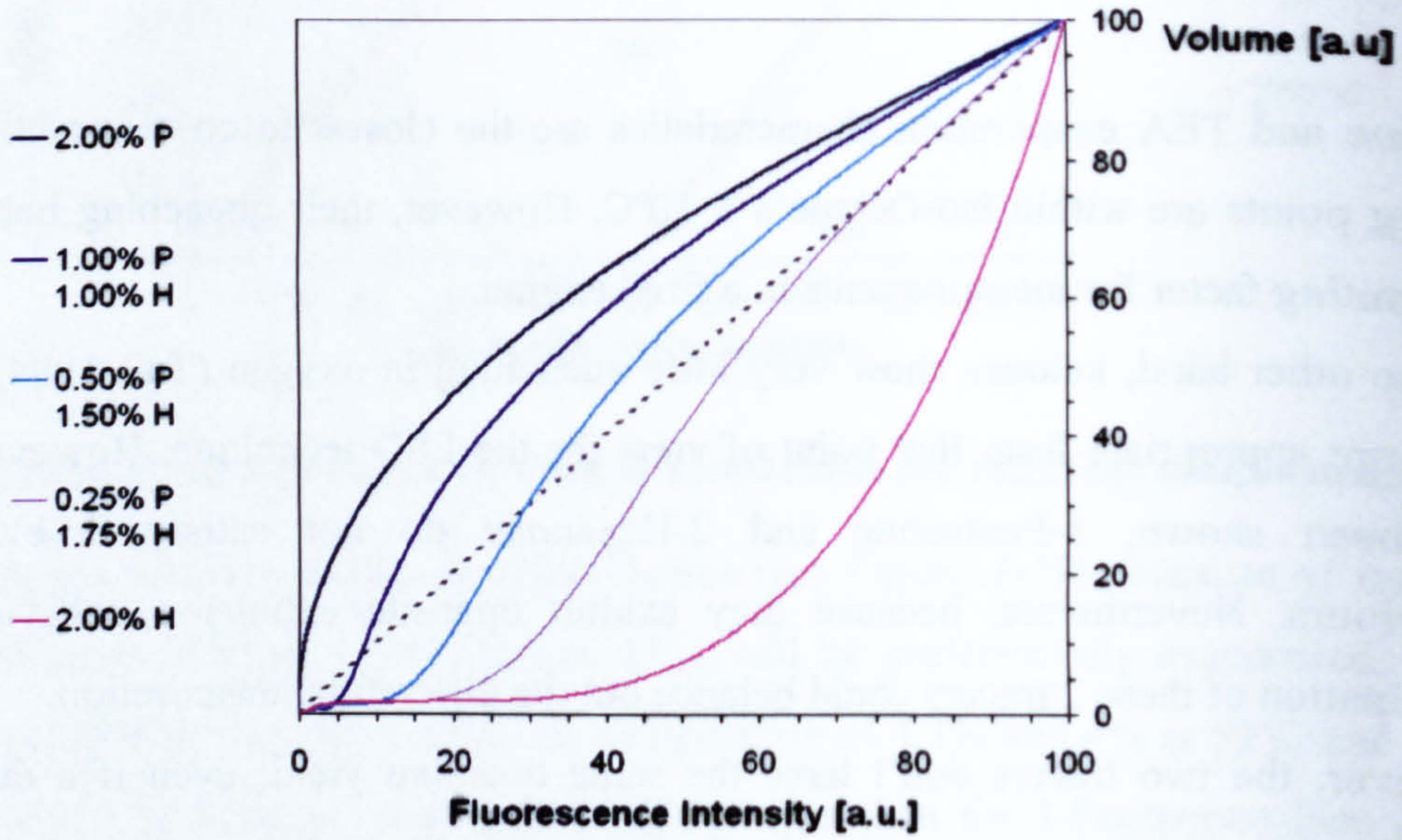

Figure 3-41: Fluorescence vs. Volume for an evaporating droplet at 50°C containing various 3-Pentanone / 2-Hexanone mixtures in 98% Iso-octane

At 50°C, the 0.25/1.75/98 mixture balances perfectly the co-evaporation and the quantum ratio for the first 40% of the volume evaporation, but yields an increasing discrepancy afterwards.

With a 0.5/1.5/98 mixture composition, at the start of the evaporation, the fluorescence signal is underestimating the droplet size by a maximum error of 13%. At the lower end of the evaporation, the signal is overestimated by a maximum of 33%.

The LIF from a 1/1/98 mixture will underestimate the volume during most of the evaporation with a maximum error of 42% and will overestimate the rest of the evaporation

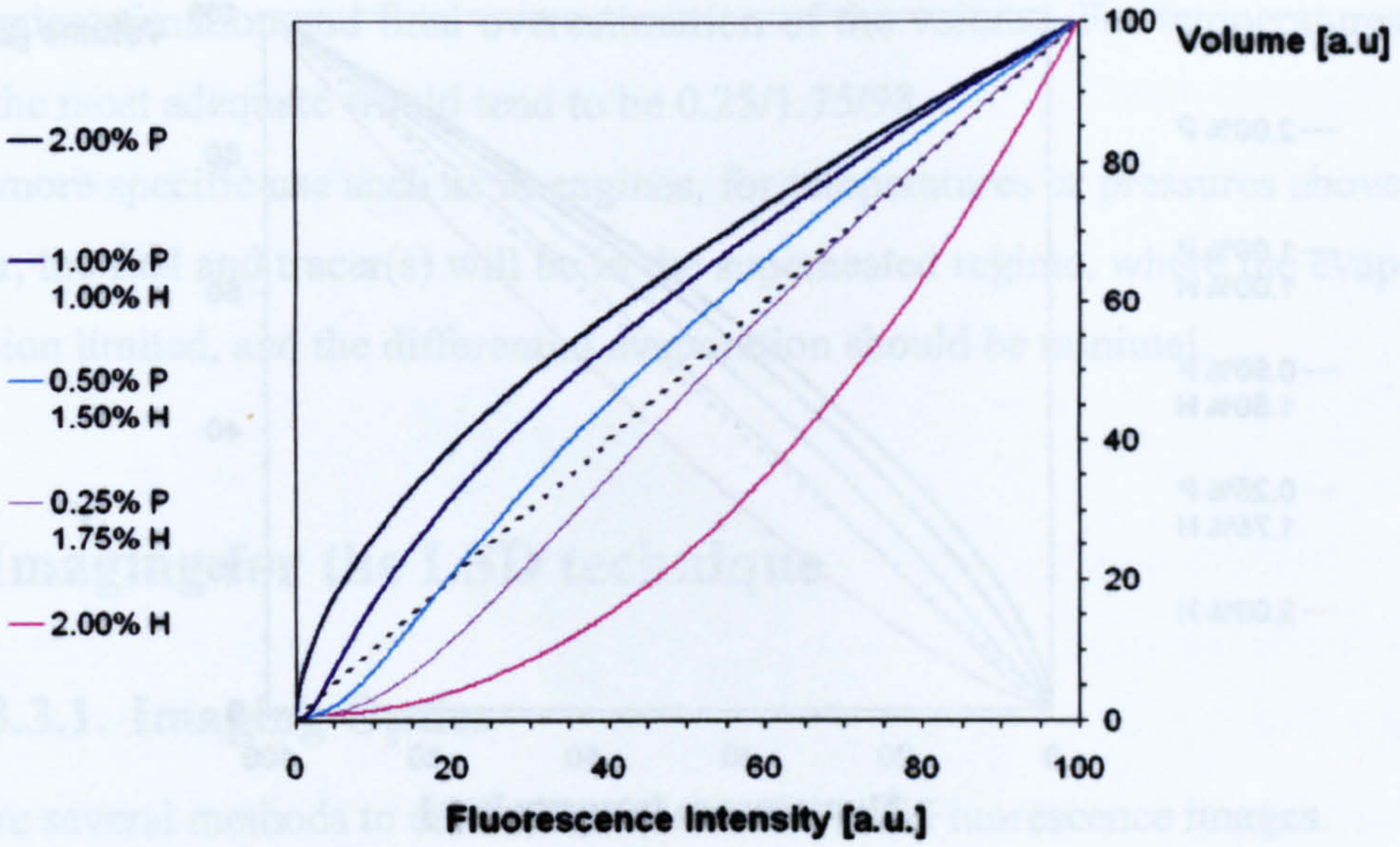

Figure 3-42: Fluorescence vs. Volume for an evaporating droplet at 100°C containing various 3-Pentanone / 2-Hexanone mixtures in 98% Iso-octane

As the temperature is increased to 100°C, the curves for the single tracers get closer to the $y=x$ line, signifying that the compromise for the tracer system is much more open (see *Figure 3-42*).

The 1/1/98 mixture still exhibits a 39% underestimation of the volume, but the 0.5/1.5/98 mixture is precise within 11% for 85% of the volume evaporation. Once again the 0.25/1.75/98 mixture is perfect for the first half of the evaporation, but the excess 2-Hexanone makes this mixture's behaviour overestimate the volume by a factor of 3.6 for the rest of the evaporation.

As the temperature is further increased, (see *Figure 3-43* and Figure 3-44), the narrowing of the curves around the $y=x$ line is still improved. At 150°C, the 1/1/98 and 0.5/1.5/98 mixtures underestimate the volume throughout the whole evaporation, with maximum errors of 51% and 22% respectively. The error with the 0.25/1.75/98 mixture is within 4% for most of the evaporation and only increases within the last 5% of the remaining volume.

At 200°C, the 0.25/1.75/98 mixture is optimal, with a worst-case underestimation and overestimation error of 17% and 1.6% respectively.

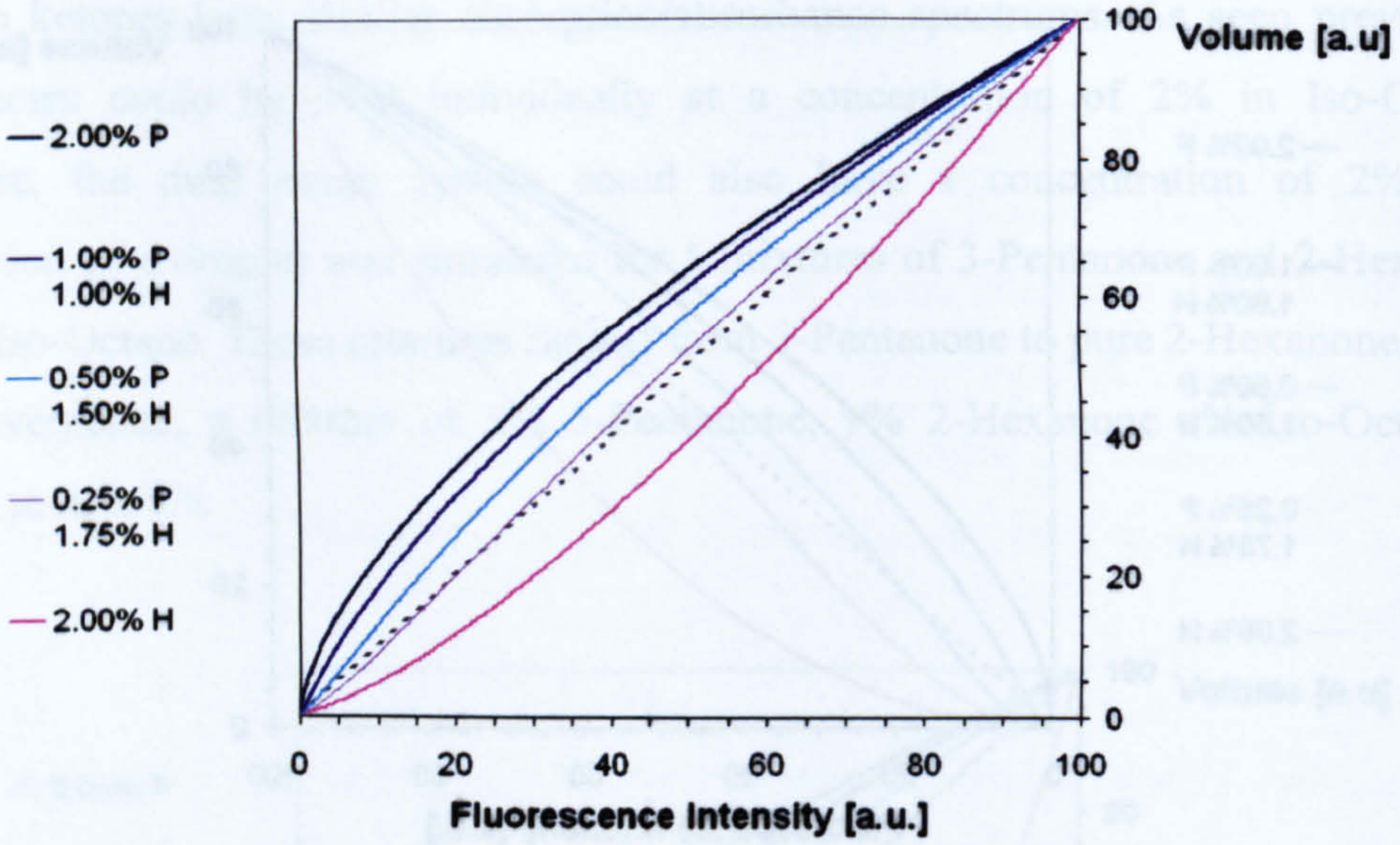

Figure 3-43: Fluorescence vs. Volume for an evaporating droplet at 150°C containing various 3-Pentanone / 2-Hexanone mixtures in 98% Iso-octane

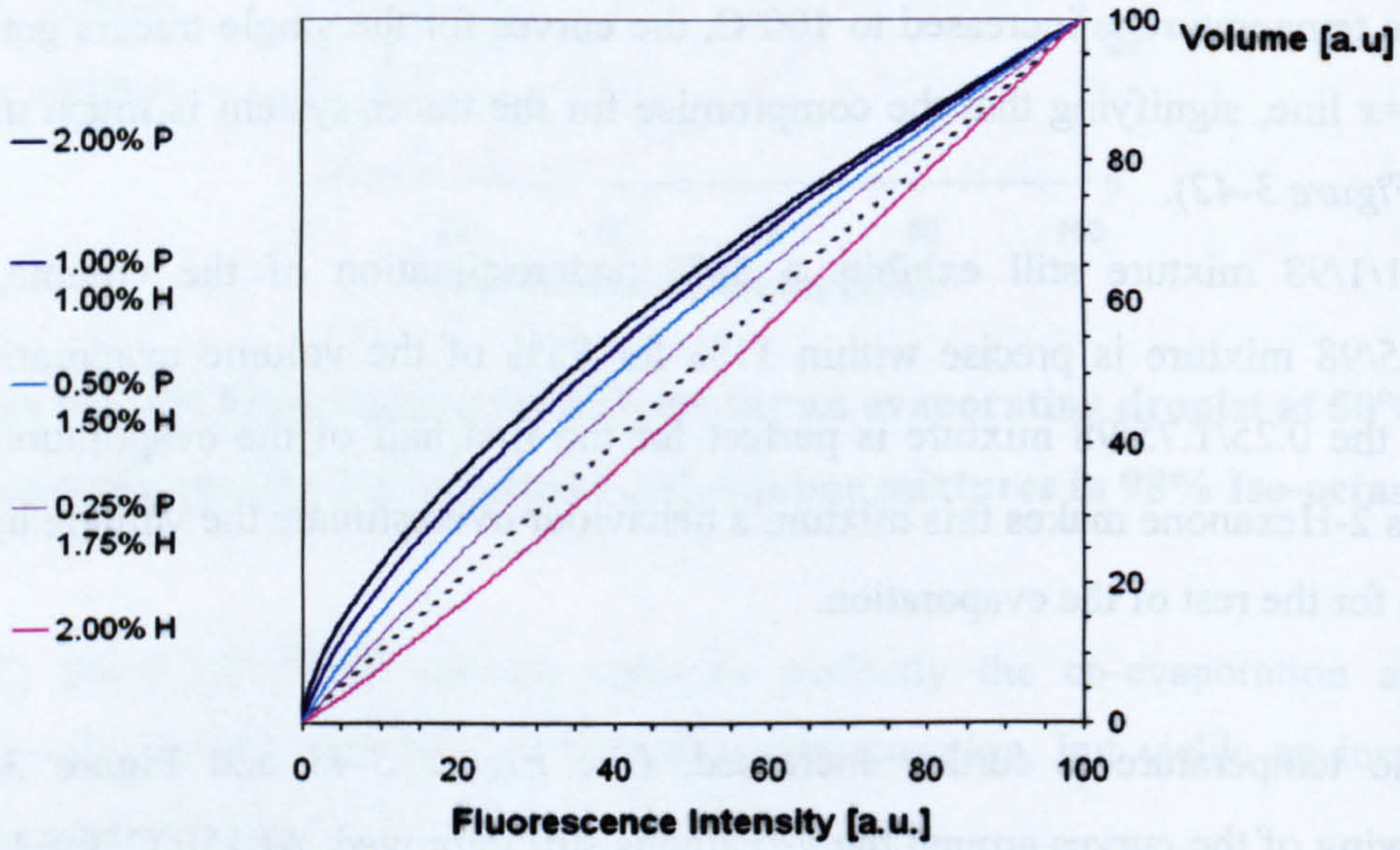

Figure 3-44: Fluorescence vs. Volume for an evaporating droplet at 200°C containing various 3-Pentanone / 2-Hexanone mixtures in 98% Iso-octane

In the case of a non-quenching environment, Toluene would be the obvious simple choice as regards tracer evaporation. In the presence of oxygen, depending on the temperature, the optimal 3-Pentanone / 2-Hexanone tracer system will vary slightly. Below 100°C, the 0.5/1.5/98 mixture is the best compromise between the fluorescence's

initial underestimation and final overestimation of the volume. For temperatures above 150°C, the most adequate would tend to be 0.25/1.75/98.

But for more specific use such as in engines, for temperatures or pressures above 200°C and 5bar, the fuel and tracer(s) will be in the superheated regime, where the evaporation is diffusion limited, and the differential evaporation should be minimal.

3.3. Imaging for the LSD technique

3.3.1. Imaging Optics

There are several methods to collect the Mie scatter and Fluorescence images.

The most appropriate is to collect them simultaneously. The easiest – and most expensive – method requires the use of 2 intensified cameras, one for each image. A cheaper option is to use one camera onto which both images can be recorded. This single camera technique requires image separation optics. The following paragraphs presents several ways to achieve this.

3.3.1.1. The stereoscopic imager

The stereoscopic imager is a very compact design that consists of two front apertures with mirrors to redirect the incoming light out a third aperture situated in the back (see *Figure 3-45*)

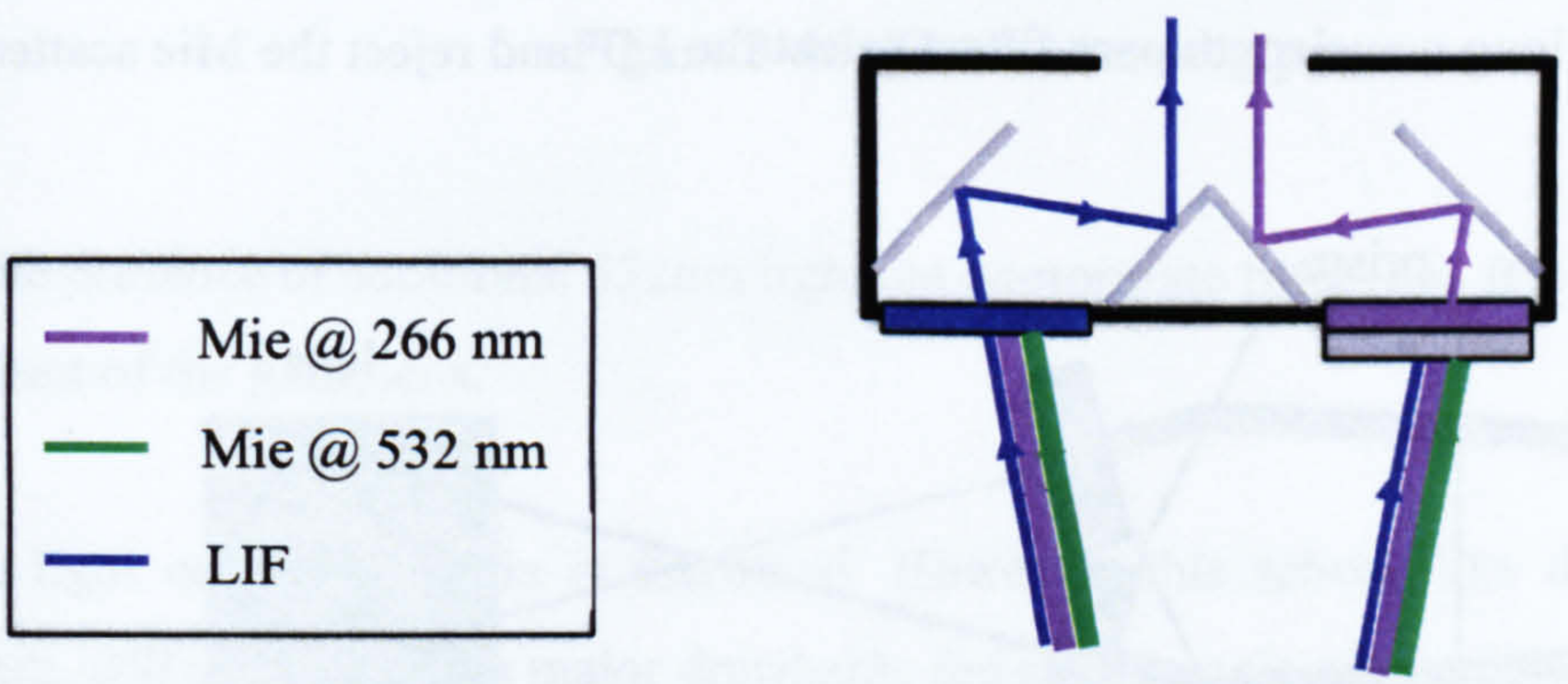

Figure 3-45: The stereoscopic beam splitter with its filters

On the front left aperture, a BG 4 band pass filter can be fitted to select the LIF and reject the Mie scatter.

On the other front aperture, a 266nm interference filter selects the Mie scatter signal only. A neutral density (ND) filter is added to the interference filter to attenuate the Mie signal, in order to obtain LIF and Mie intensities of the same order of magnitude on the CCD chip.

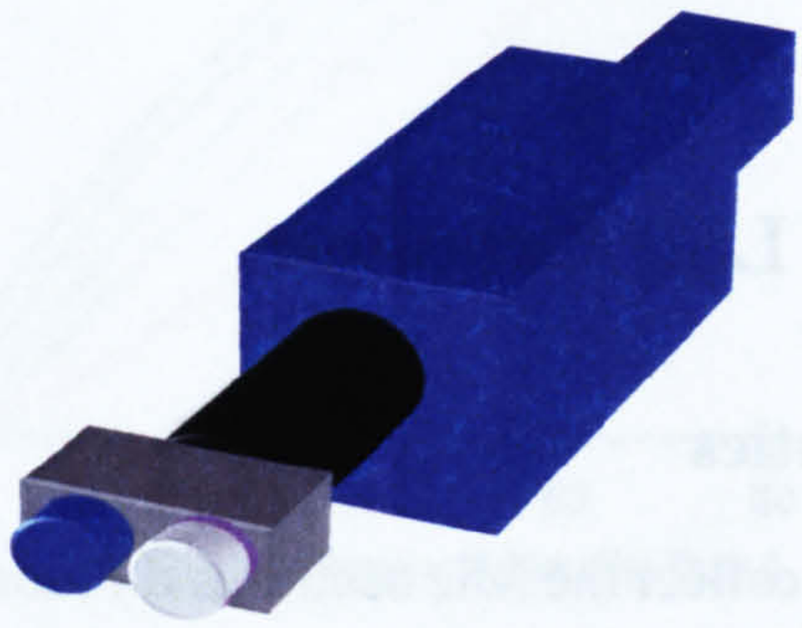

Figure 3-46: The stereoscopic imager, lens, intensifier and camera set-up

However, one of the drawbacks of this imaging system is the small size of its mirrors, which gives a weak light collection (10% efficiency). As the LIF signal is already weak, this type of imager is not suitable for our experiments.

3.3.1.2. The prism set-up

The following optical set-up by Park et al. (2002) uses a doubling prism. On one half, a band pass filter and a ND filter selects and attenuates the Mie scatter signal. On the other half, two long wavelength pass filters select the LIF and reject the Mie scatter (see *Figure 3-47*).

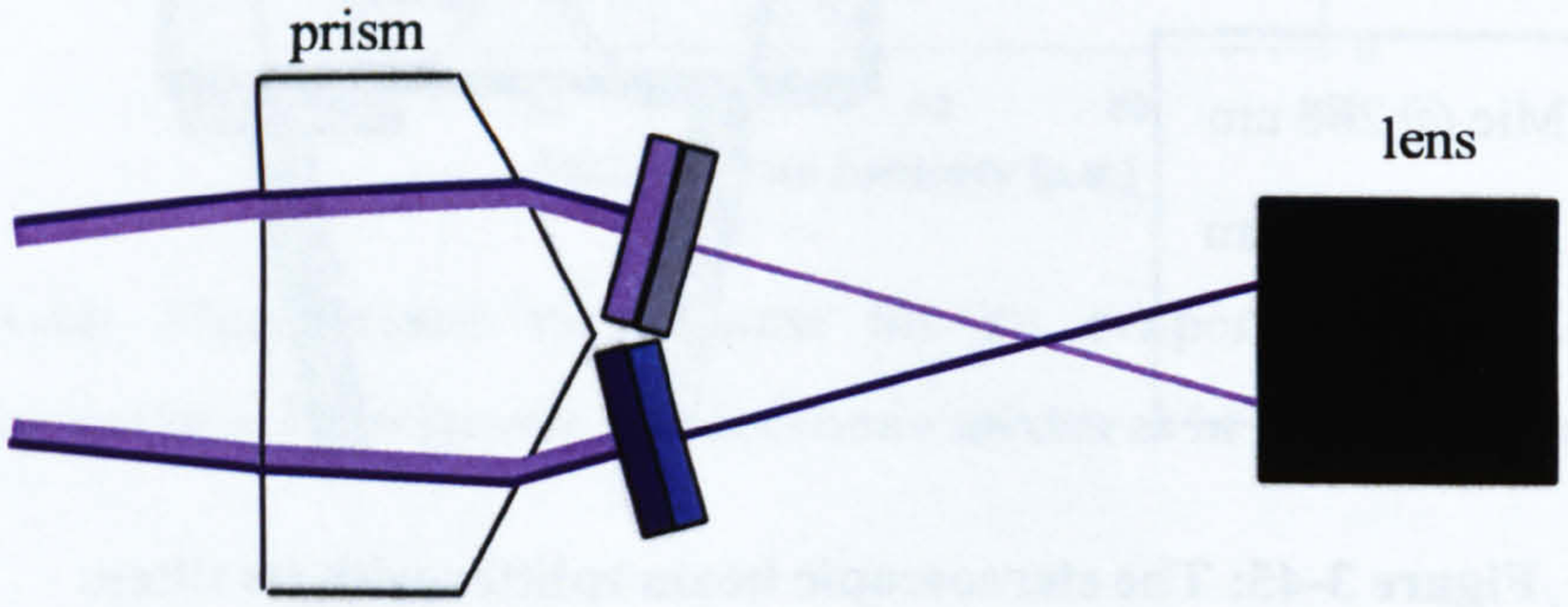

Figure 3-47: The prism separation

In the presence of 532nm light, an appropriate filter can be added to the two long-pass filters.

The stereoscopic imager and the prism share a common drawback: they both reject half of the intensity from each signal. This is an issue, considering the weak fluorescence intensity of 2-Hexanone and 3-Pentanone.

3.3.1.3. The 2 lens set-up

This set-up is adapted from the separating optics used by Kelman and Masri (1994). It uses two lenses. A glass lens focuses the fluorescence on the intensifier and rejects the Mie scatter. The Mie scatter signal is collected on a different path. It is redirected into the intensifier using dichroic mirrors and focused using a quartz lens of longer focal length (because the optical path is longer than that of the fluorescence).

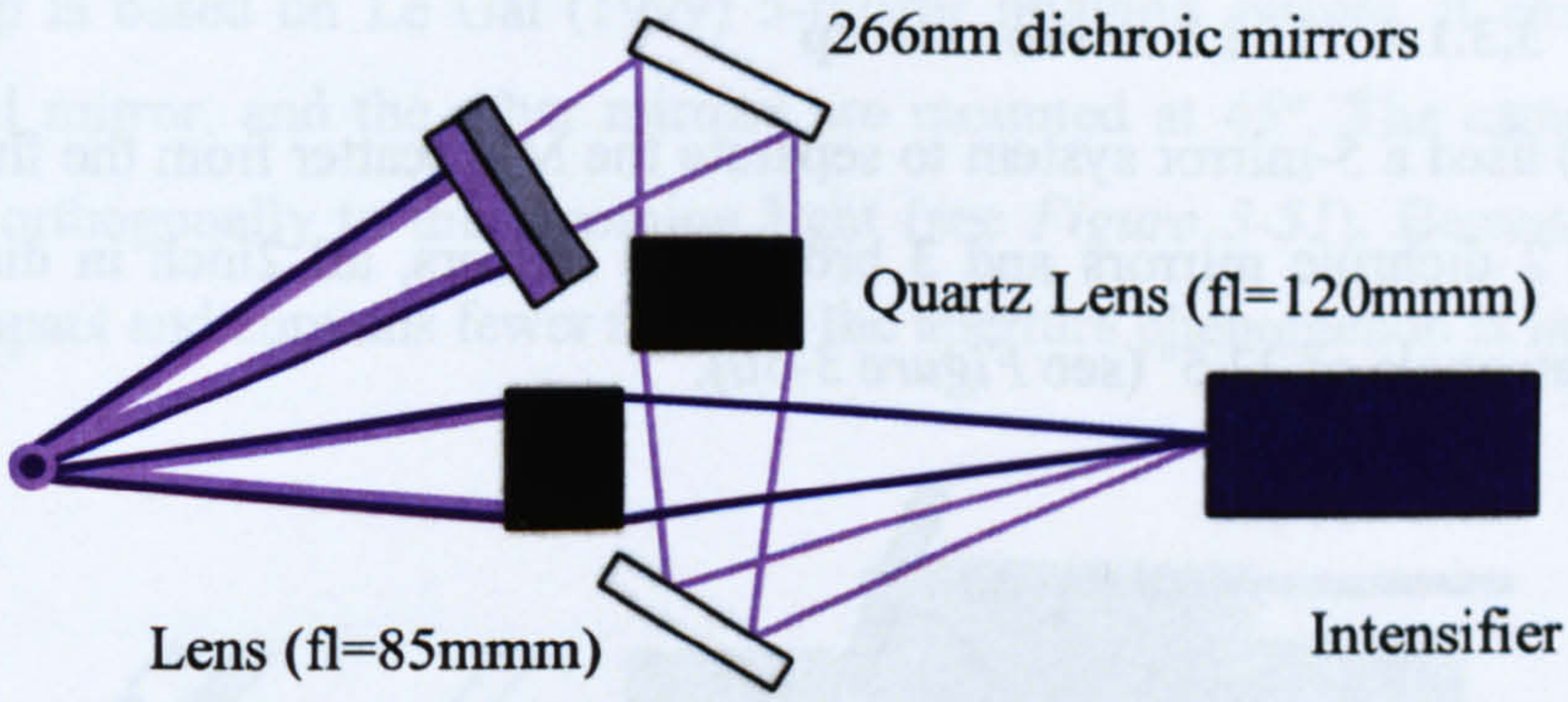

Figure 3-48: The 2-lens set-up

In the presence of additional 532nm light, an appropriate filter (e.g. BG4) can be located in front of the glass lens.

The light collection angle is increased. However, this set-up, like the two previous others, still suffers from a major drawback: the stereoscopic view of the object. Because the two light paths are not the same, in a dense spray, the signal collected through the Mie path does not go through the same parts of the spray as the signal collected for the LIF path (see *Figure 3-49*). This induces error that cannot be quantified.

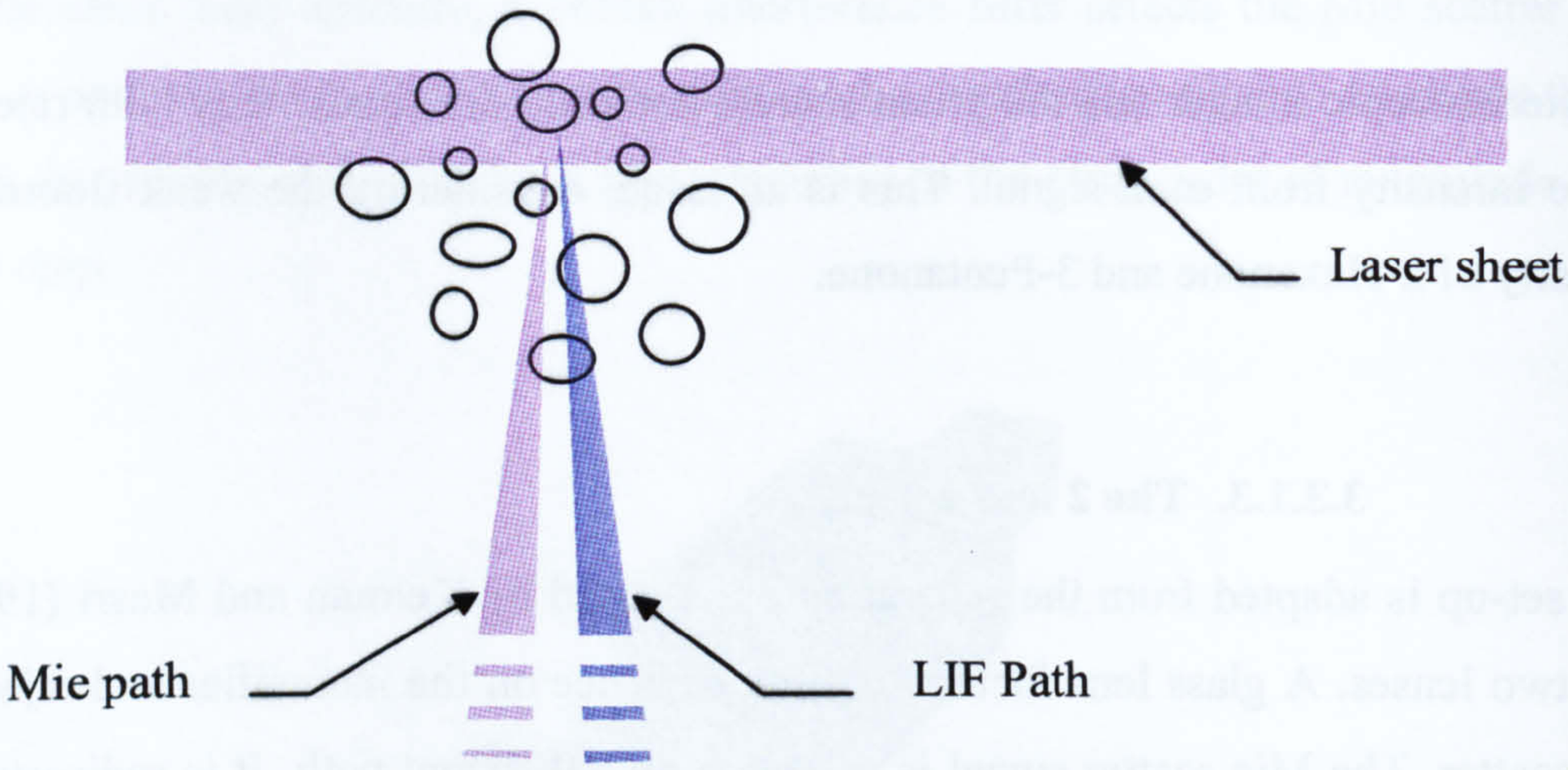

Figure 3-49: Stereoscopic imaging - Different light paths in dense sprays

3.3.1.4. The 5 mirror set-up

Le Gal (1999) used a 5-mirror system to separate the Mie scatter from the fluorescence. It consists of 2 dichroic mirrors and 3 broadband mirrors, all 2inch in diameter and positioned at an angle of 22.5° (see *Figure 3-50*).

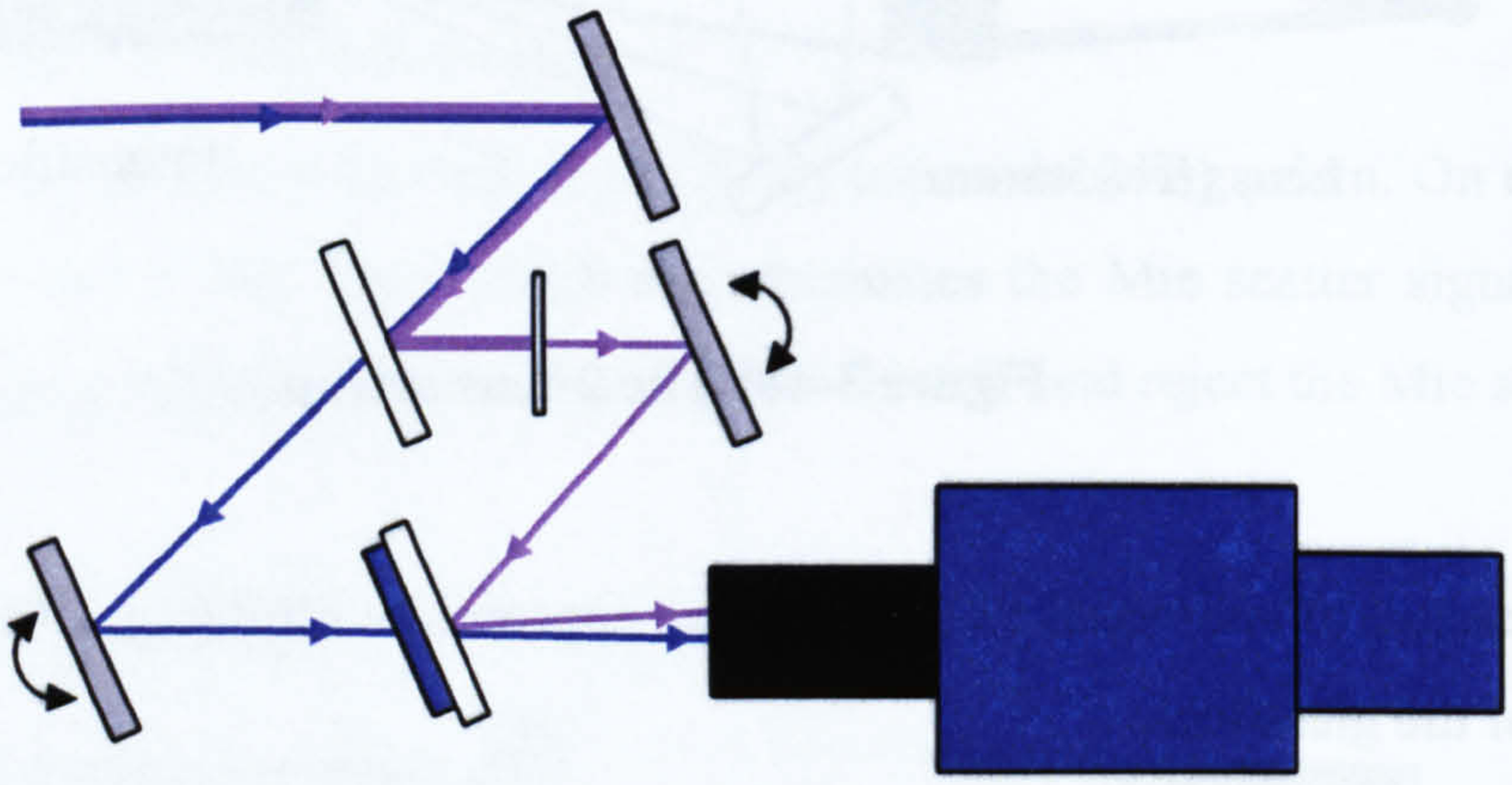

Figure 3-50: The 5-mirror set-up

In this setup, the light is reflected off a broadband mirror. It comes onto a 266nm dichroic mirror (quartz glass with a 266nm coating) which reflects the Mie signal and lets the LIF through. Both signals are then reflected on two different broadband mirrors on adjustable mounts. The signals rejoin at the second dichroic mirror where the Mie signal is reflected and the LIF signal goes through. Both signals have been separated using the adjustable mirrors, but they originate from the same light path. Another

advantage of the set-up is that the camera is positioned parallel to the incoming light path.

A neutral density filter is in the Mie signal path to attenuate the signal's intensity in order to match the weaker LIF intensity.

A BG4 filter is in the LIF path to cut out the eventual Mie scatter that could have been transmitted through the dichroic mirrors. It also cuts out 532nm Mie scattering because the laser sheet contains both second and fourth harmonics (532 and 266nm).

However, this set-up is too long: the mirrors represent increasingly smaller apertures as they are further away from the camera.

3.3.1.5. The 4 mirror set-up

This setup is based on Le Gal (1999) 5-mirror imaging system. It abandons the first broadband mirror, and the other mirrors are mounted at 45°. The camera is therefore mounted orthogonally to the incoming light (see *Figure 3-51*). Because this set-up is more compact and contains fewer mirrors, the aperture phenomenon is improved.

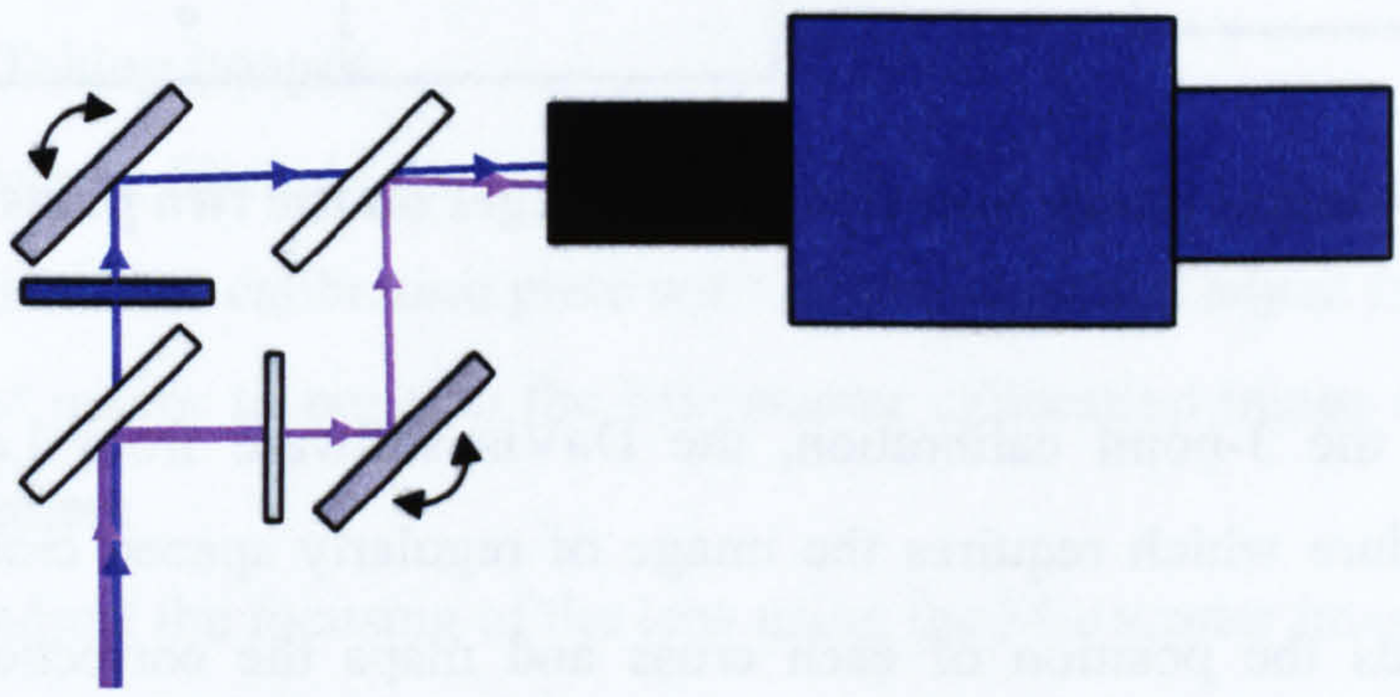

Figure 3-51: The 4-mirror set-up

However, because the mirrors are mounted at 45° instead of the previous 22.5°, their effective surface is narrower, and the set-up must be finely tuned for imaging.

For this reason, the same short set-up was designed with 3-inch mirrors.

3.3.2. Geometric Calibration

The LSD technique requires the ratio of fluorescence and scattered light from the same droplets. From an imaging point of view, the technique requires that the intensity from a pixel in the LIF image is divided by the intensity of a geometrically corresponding pixel in the Mie scatter image. In other words, the two scattering images must be superimposed. However, the use of a single camera with a 4 mirror set-up will rotate, translate and project the images in the separation process. Therefore, a geometric calibration of the camera is required to superimpose the LIF and Mie scatter image perfectly: each part of the CCD chip must have its own calibration to rotate, de-warp and translate the image so that the two will superimpose in order to match for the division in the LSD technique.

The simplest method requires the illumination of three non-aligned points. By finding their pixel co-ordinates, the rotation, relative warping and translation can be obtained.

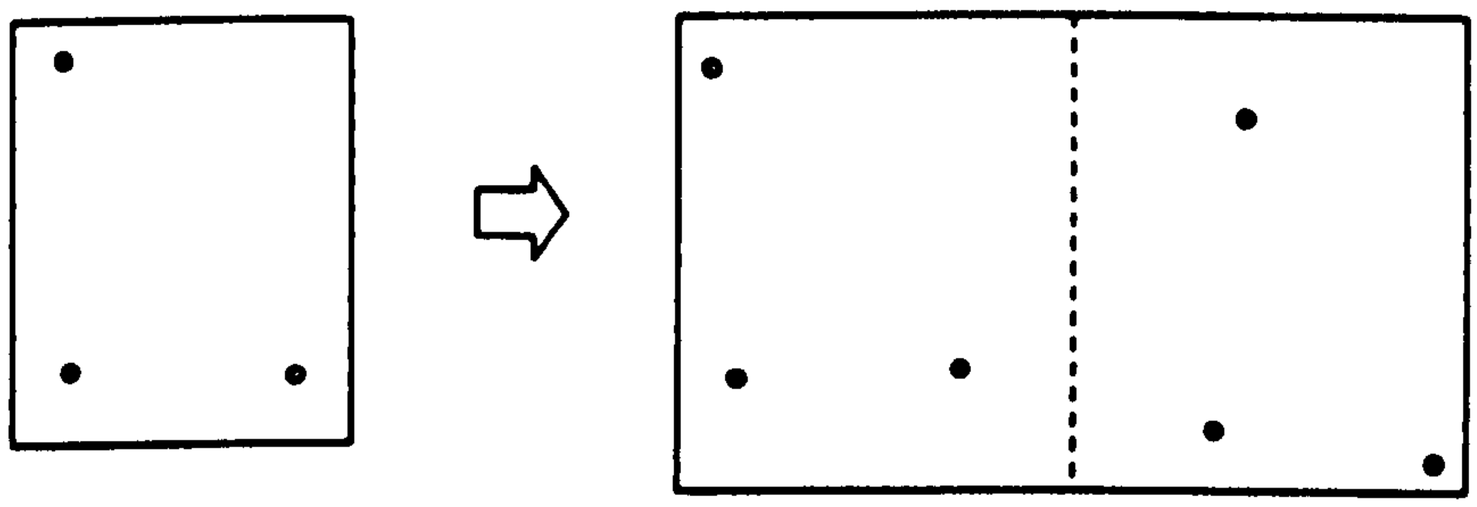

Figure 3-52: Original image and separated images on the two parts of the chip

Instead of using the 3-point calibration, the DaVis software from LaVision has a calibration procedure which requires the image of regularly spaced crosses (or dots). The software finds the position of each cross and maps the correction so that the corrected image looks like the original image.

3.3.3. Calibration procedure

In a first step, the optical system must be set up. This requires the adjustment of the 4-mirror system, the focusing of the lens and the camera should have a resolution of approximately 100μm/pixel.

This can be done by the following sequence:

Install the system

- Install the calibration plate in the imaging plane.
- Install the 4-mirror and camera system
- Check that all mirrors are at 45°

Calibration plate illumination

- Illuminate the calibration plate with a lamp
- Take images
- Adjust the *LIF mirror* to position the calibration image on one half of the camera

Camera and lens rough adjustment (using the LIF path)

- Adjust the camera's distance and focusing to obtain a resolution of approximately 100μm / pixel
- Stop taking images
- Decrease the Intensifier Gain back to 0

Mie scatter path mirror adjustment

- Block off the LIF path
- Start Taking Images
- Remove all filters in the Mie scatter path.
- Illuminate the calibration plate with 266nm light and adjust Intensifier Gain
- Adjust mirror to position the Mie scatter calibration image on the other half of the camera
- Fine adjust the focusing of the lens using the Mie scatter image.

Following the adjustment of the mirrors, the following step consists in imaging the spray in realistic conditions in order to determine the ND filters required for the attenuation of the Mie scatter signal. The adjustment mirrors can also be tuned to eliminate overlap of noise or reflections from one image onto the other's spray image.

With the correct filters in place and the mirrors adjusted, the calibration plate should be re-inserted and calibration images for the Mie scatter and LIF path must be recorded. It was found that illuminating the calibration plate with the laser light sheet provided both

a Mie scatter and fluorescence image of the calibration plate. The fine adjustment of the light sheet at an incoming small angle was absolutely crucial, as was the quality of the calibration plates. An aluminium plate or sheet was used at the other end of the calibration plate to reflect and diffuse the light for optimal illumination.

Chapter 4

Experimental Setup for LSD Validation

To investigate the validity of the LSD technique for a highly evaporating GDI spray, measurements were carried out in Munich in the Benzin-Direkt-Einspritzung Optischer Prüfstand (BDE-OP – Gasoline Direct Injection Optical Test Bed) at BMW AG. This chapter presents and describes the test rig. It consists of two pressure vessels: the first vessel enabled simultaneous measurements of Mie scatter and LIF images on a GDI spray and to apply the LSD technique. The second vessel allowed acquisition of PDA data for the same spray in order to compare the two techniques.

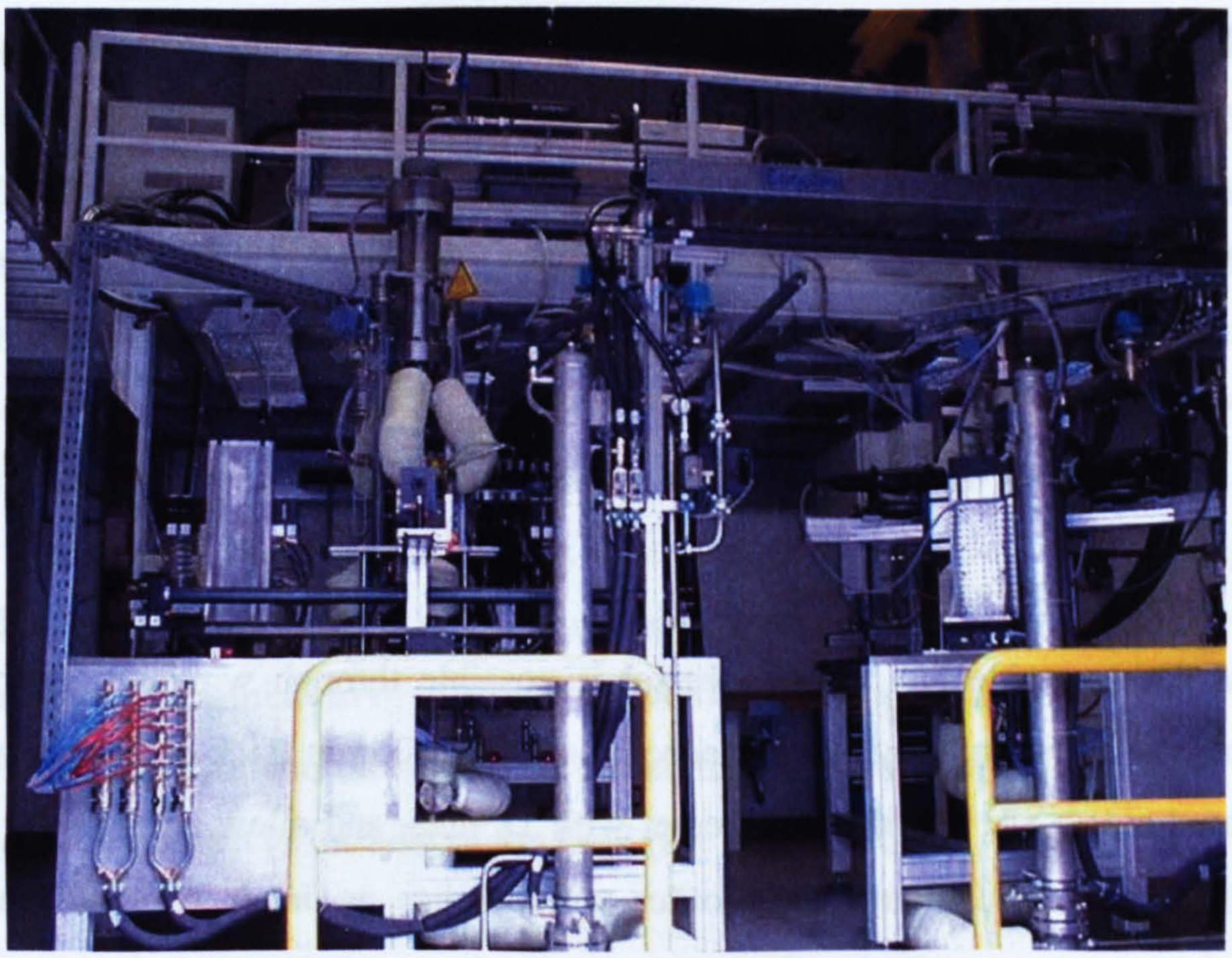

Figure 4-1 : View of the 2 Pressure Vessel rigs (Photo: BMW AG)

4.1. The test rig

The test rig is a 1.5 million Euro facility composed of 2 fully automated pressure vessels for laser diagnostics on injectors: one allows for 2-D imaging of LIF and Mie scatter, the other is for PDA.

The design of the vessel is by RWTH Aachen's ITM department headed by Professor Peters. The automation of the test rig is by Sonplas. The imaging system and software for the Mie scatter/LIF vessel is from LaVision and the system for the PDA vessel was originally from TSI and was later replaced by Dantec.

The vessels enable the simulation of various temperature and pressure conditions under which injectors have to operate. To do so, the inside of the vessels are pressurised and heated with continuous flow of Nitrogen. The maximum operating conditions are 400°C and 35bar.

4.1.1. Vessel design

The basic design of each vessel consists of two concentric cylinders (see *Figure 4-2*). The outer cylinder is 60mm thick to resist to pressures up to 35bar. It is closed at the top and bottom. The pressure tightness is ensured by rubber O-rings which are water cooled. The inner cylinder is 105mm in diameter and 260mm high. It contains the Nitrogen flow and the injector spray. It is open to the outer cylinder, so that it is not subject to pressure differentials. Its main role is to insulate the thick outer cylinder in order to reduce the thermal inertia of the system: this allows the experiment to proceed from one set of Pressure and Temperature conditions to the next without having to cool down or warm up the bulk of the pressure vessel.

4.1.2. Optical Access

Optical access inside the pressure vessel is possible through windows. Both vessels have inserts in the outer cylinder to accommodate for 35mm thick outer side windows. Window holders are bolted to the vessel with 12 nuts, and allow an apparent window aperture of 60mm×140mm. Each outer window has an inner window counterpart inserted in the inner cylinder. Both vessels also have a bottom window to allow for imaging from below.

Figure 4-2: Cutaway section of the Mie/LIF Pressure vessel - inner/outer cylinder, windows and window holders

4.1.3. Vessel Conditioning

Liquid Nitrogen is stored in a pressurised 3000 Litre tank. It is delivered to the vessels by evaporation, thus avoiding using an expensive and high maintenance pump. In order to operate the rig continuously, a valve and a throttle (one upstream and one downstream of the vessel) control the pressure inside the chamber while continuously purging the gas flow. For chamber pressures below 2.5bar, a suction pump is activated in order to produce a sufficient pressure difference between the inlet and the outlet of the vessel to maintain a permanent purging gas flow.

The temperature conditioning is done by passing the Nitrogen flow through heaters before it enters the vessel. A first set of heaters is used for the 25-150°C temperature range. For temperatures above 150°C, a second set of heaters is used, and the Nitrogen flow has to be at a minimum of $60Nm^3/h$ to avoid damaging them.

To allow for space around the top of the vessel, the nitrogen enters the chamber through 3 pipes which connect to the side of the head (see *Figure 4-3*).

4.1.4. Injector

The injector is inserted and held in the injector mount. Originally, the pressure vessel's design only allowed positioning of the injector mount on top of the chamber, injecting downwards. The vessel design was modified to have the possibility to operate with a motorised side mount, allowing automatic rotation of the injector. Therefore, the injector can sit either on the top of the chamber and inject downwards, or can be installed on the side, injecting towards the side windows. Whichever position is not occupied by the injector is replaced by a blank.

The injector temperature is conditioned by a silicon oil conditioned heating/cooling unit. The injection is triggered by the Test-rig computer. A timing signal is sent to the injector driver, which delivers the appropriate power signal to the injector.

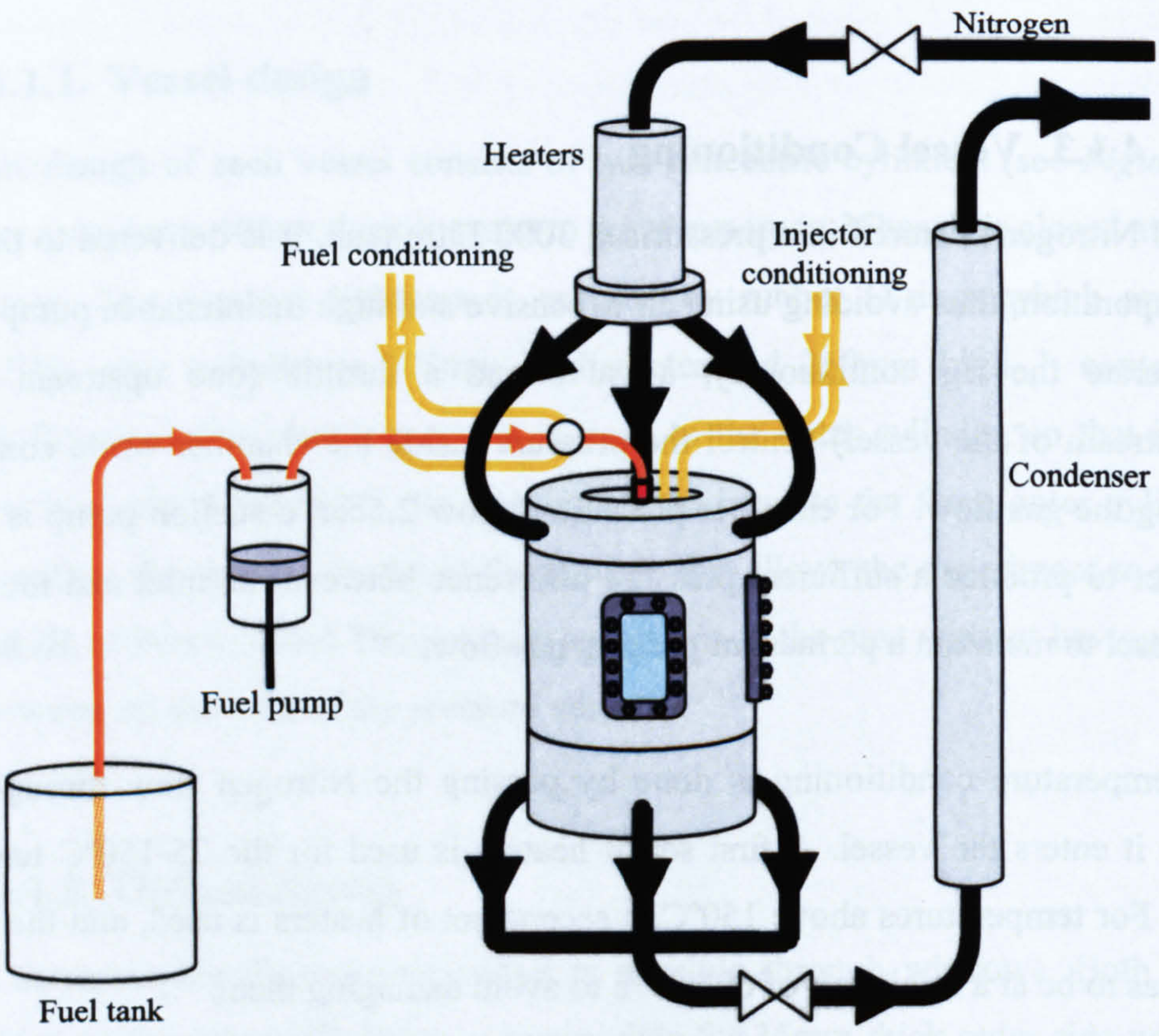

Figure 4-3: Schematics of the pressure vessel

4.1.5. Fuel

Fuel is drawn from the fuel tank by a piston pump. Once the pump is full, it can pressurise the fuel up to a maximum pressure of 200bar. The pressure is maintained by a moving the pump piston with a fast stepping motor. This enables the delivery of fuel at a constant pressure - therefore pulsation-free, contrary to a rotating pump system.

Before entering the injector, the fuel is conditioned by another silicon oil bath in the pump and in a cross-flow heat exchanger near the injector.

At the exit of the vessel, the nitrogen/fuel mixture passes through heat exchangers, condensers and an active carbon filter to retrieve the UHC.

4.2. The "Mie/LIF" Pressure Vessel

This vessel allows for laser sheet diagnostics.

4.2.1. Fuel

This vessel has two separate fuel lines: one for pure iso-octane only and another for an iso-octane/tracer mixture. The non-tracered and tracered fuel are contained in 2 different tanks. In order to minimise contamination, each tank has a separate fuel line containing its individual pump and pipes. The pipes only rejoin 10cm upstream of the injector. Excess fuel or purged fuel is dumped in a third tank.

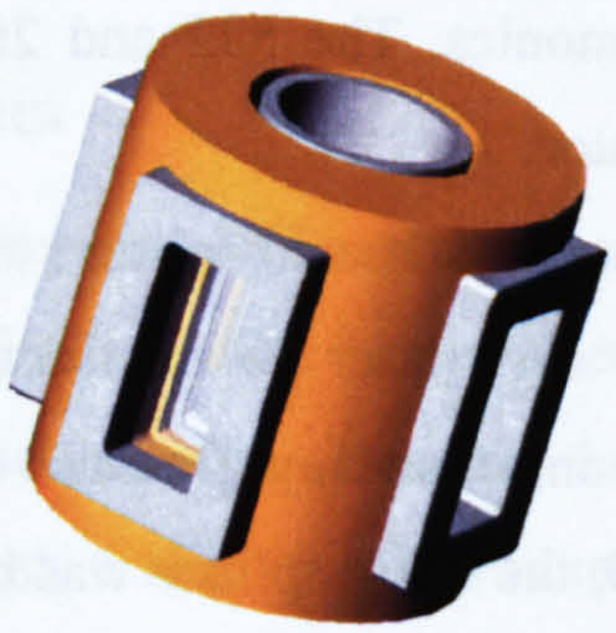

Figure 4-4: The "Mie/LIF" pressure vessel and its 3 side windows

4.2.2. Optical access

Optical access inside the pressure vessel is possible through 4 windows (3 rectangular side windows and 1 round bottom window). The two diametrically opposed side windows allow two opposed laser sheets to enter and exit the chamber. The third side window and the bottom window allow for the imaging.

4.2.3. Laser and sheet forming optics

The laser used is a PIV 400 Nd:YAG from Spectra Physics. It is a twin cavity laser having independent control between cavities. Each cavity consists of an oscillator and amplifier mounted in series. Both are made up of a flashlamp, rod and reflective cavity. The flashlamps are triggered at a fixed rate of 10Hz (with an allowed tolerance of ±10%) to build up the energy. This energy is released by a Q-switch: this changes the polarisation of the back plate and allows the light to pass through. For maximum power output, the laser requires an optimal delay between the flashlamp trigger signal and the Q-switch signal - typically around 180µs for this laser. Therefore, the laser cannot fire on demand.

The fundamental output beams (1064nm) are combined with beam steering optics and fed through two doubling crystals to form 532nm and 266nm beams. Typical energies are round 400mJ/pulse at 532nm and 60mJ/pulse at 266nm.

In the laser head, a first mirror allows the dumping of the fundamental immediately, reflecting the 2^{nd} and 4^{th} harmonics. The 532 and 266nm beams are then redirected through a 532nm beam attenuator.
The beam is then divided with a 50/50 beam splitter, to form two opposing laser sheets. This allows to obtain a more even laser power through the spray, as opposed to an attenuated sheet that traverses only one way. Because the coating had degraded and the ratio was of the order of 90/10, the beam splitter was replaced by a 266 mirror, and the laser sheet entered the vessel through the left side window only. This was possible because the laser attenuation in the LSD technique is not critical, as the ratio of two scattering images cancels it out.

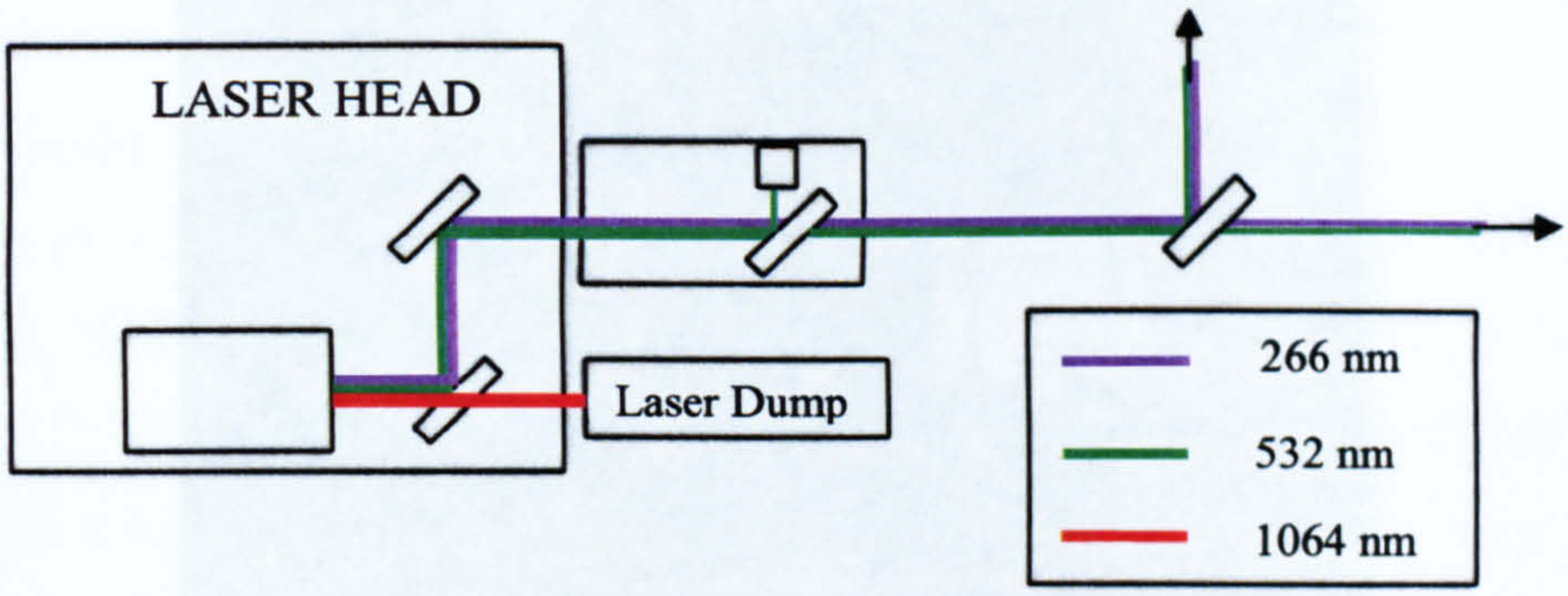

Figure 4-5: The laser set-up

The 266nm mirror directs the beam upwards. A finely adjustable 45° mirror then redirects it into the sheet forming optics. This consists of 2 pairs of concave and convex fused silica cylindrical lenses: 2 to focus the sheet horizontally at the centre of the pressure vessel, and 2 to expand the sheet vertically. The lenses are located on a slider which is encased in a black cylinder. Circular knobs slide the lenses backwards and forwards for the adjustment of the laser sheet. The sheet-forming optics can be rotated 90° to form a either a vertical or horizontal light sheet, and are mounted on a motorised vertical translation stage, allowing to move the sheet up and down.

The laser sheet was positioned at the centre of the chamber, below the injector tip. The sheet was focused at the middle of the vessel by looking at the sheet profile at the entry and exit of the chamber. The sheet was centred on the windows, so that is was perpendicular to the chamber.

4.2.4. Imaging system

The separation of the Mie scatter and LIF was done using the 4-mirror set-up with 3 inch mirrors (see *Chapter 3, §3.3.1.5*). The 4-mirror set up was positioned on a sliding rail located in the axis of 2nd side window. Because the camera needed to be mounted orthogonal to the incoming light, a sliding rail was mounted on a vertical translation stage, for the positioning and adjustment of the camera (see *Figure 4-6*).

Imaging was done using the DaVis software from LaVision. The images were recorded using a 12 bit FlowMaster 3 CCD camera coupled to a gated IRO image intensifier with a Halle $f2$ 100mm achromatic fused silica lens.

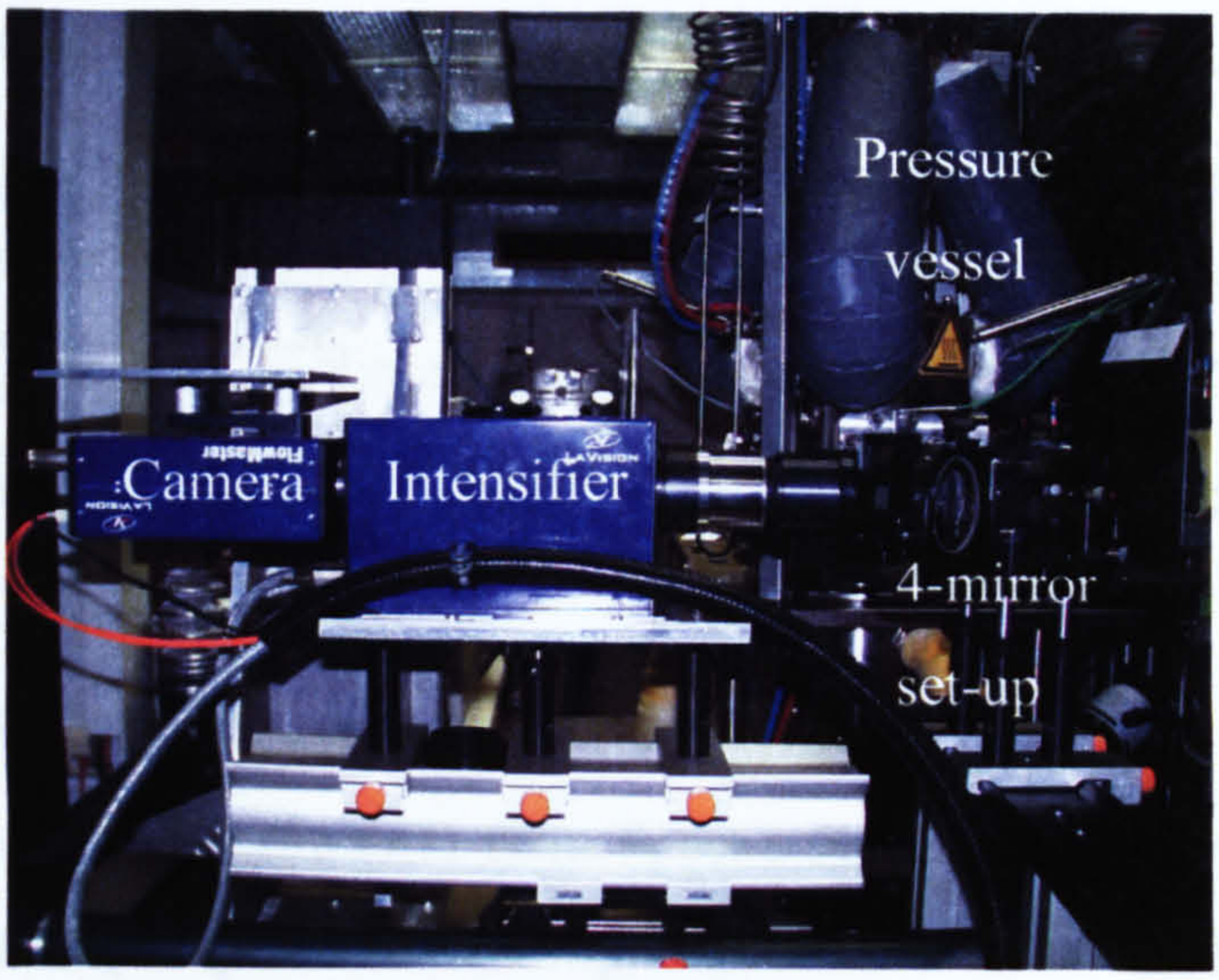

Figure 4-6: Imaging Set-up (Photo: BMW AG)

4.2.5. Timing and Synchronisation

The injection is triggered by the Test-rig computer. The Imaging computer uses this signal to trigger its Programmable Timing Unit (PTU). The PTU sequence synchronises the laser (Flashlamp and Q-switch), Intensifier and Camera exposure, so that the images occur at a specific time after the start of injection (see *Figure 4-8*). The user sets the imaging times in the window illustrated in *Figure 4-7*.

Each injector has a specific "dead time" which corresponds to the delay between the triggering - or electronic start of injection (ESOI) - and the actual start of fuel injection - also called optical start of injection (OSOI). This "dead time" is a combination of an electronic delay between the trigger signal input to the injector driver and the signal it sends to the injector and a mechanical delay due to the needle lift.

The DaVis software requires the input of this parameter. This allows it to determine the PTU delay so that the imaging can correspond to timings after the actual start of injection (i.e. OSOI).

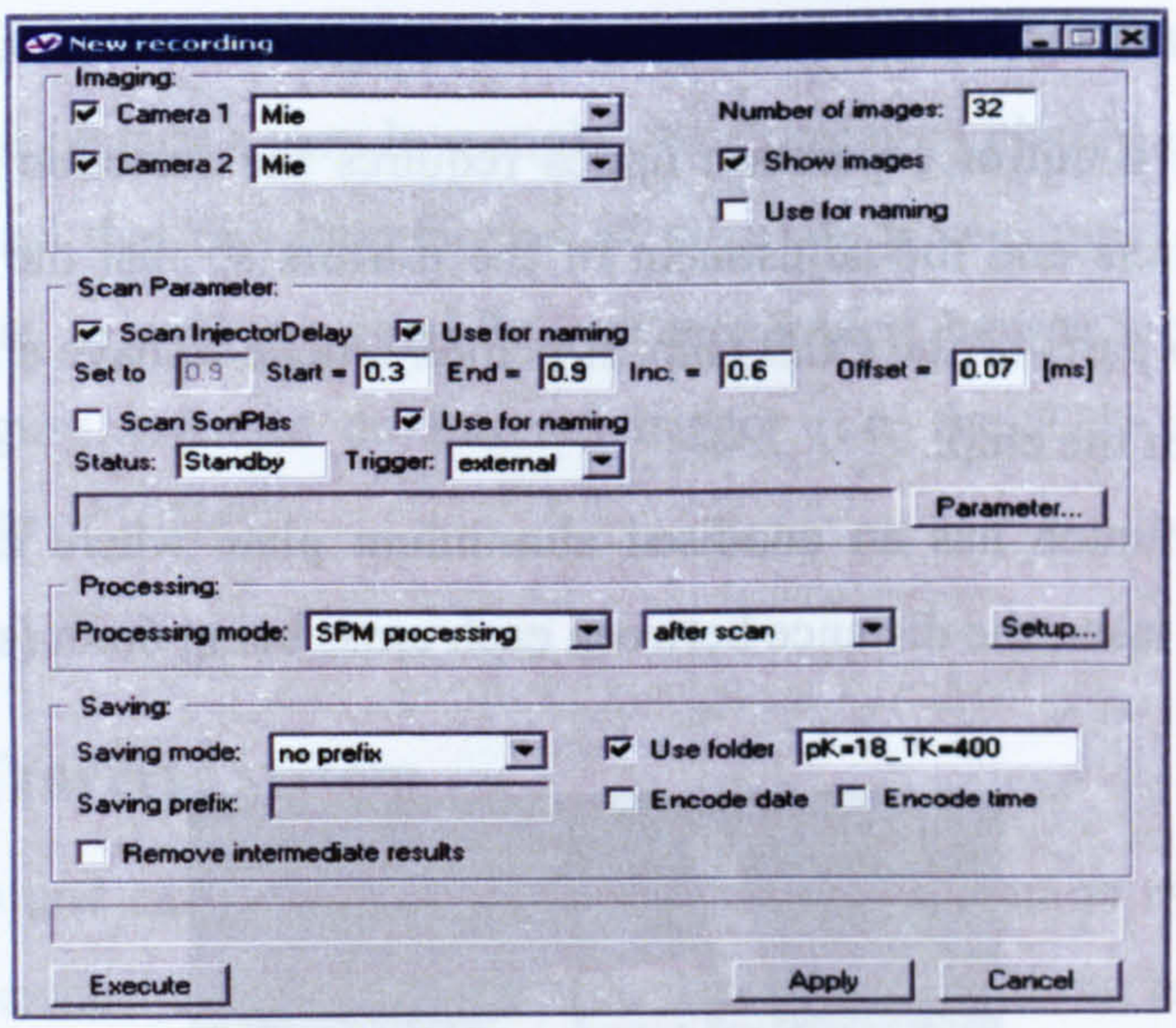

Figure 4-7: Window for the imaging timings

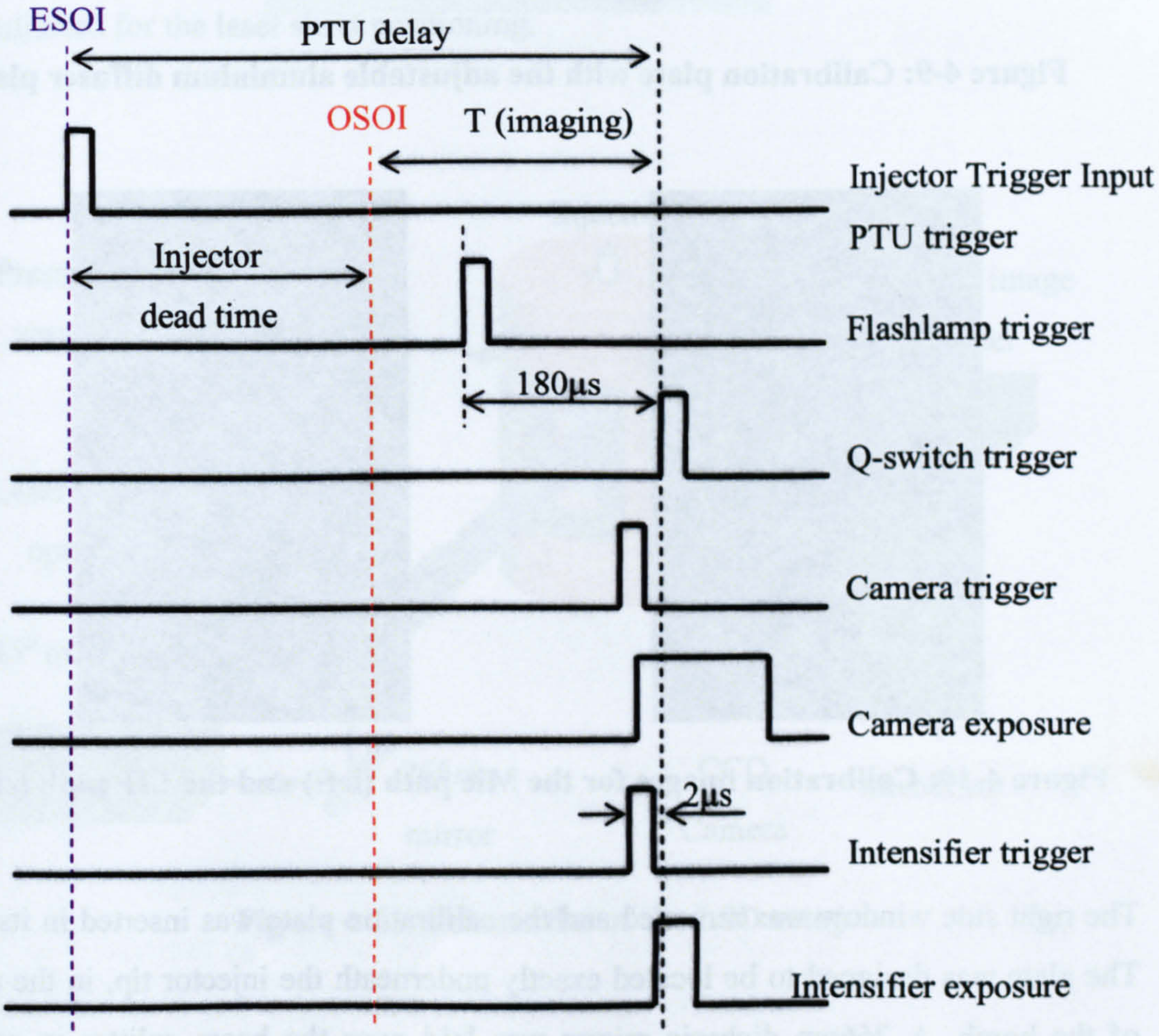

Figure 4-8: PTU synchronisation sequence (not to scale)

4.2.6. Spatial Calibration

The set-up of the 4-mirror separation optics requires the selection of band-pass and neutral density filters and the adjustment of the mirrors so that the LIF and the Mie images are on two parts of the CCD chip. It is then crucial to have a spatial calibration of the two halves of the chip.

The test rig in Munich has an anodised aluminium plate where crosses have been marked out with a laser, the distance between each cross being 6mm (see *Figure 4-9*).

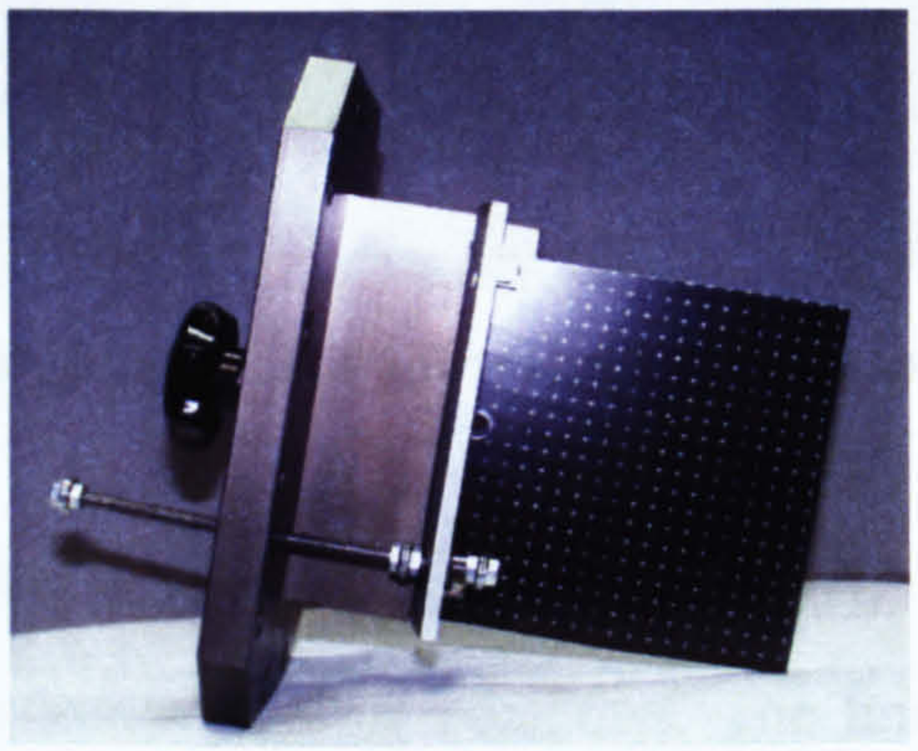

Figure 4-9: Calibration plate with the adjustable aluminium diffuser plate

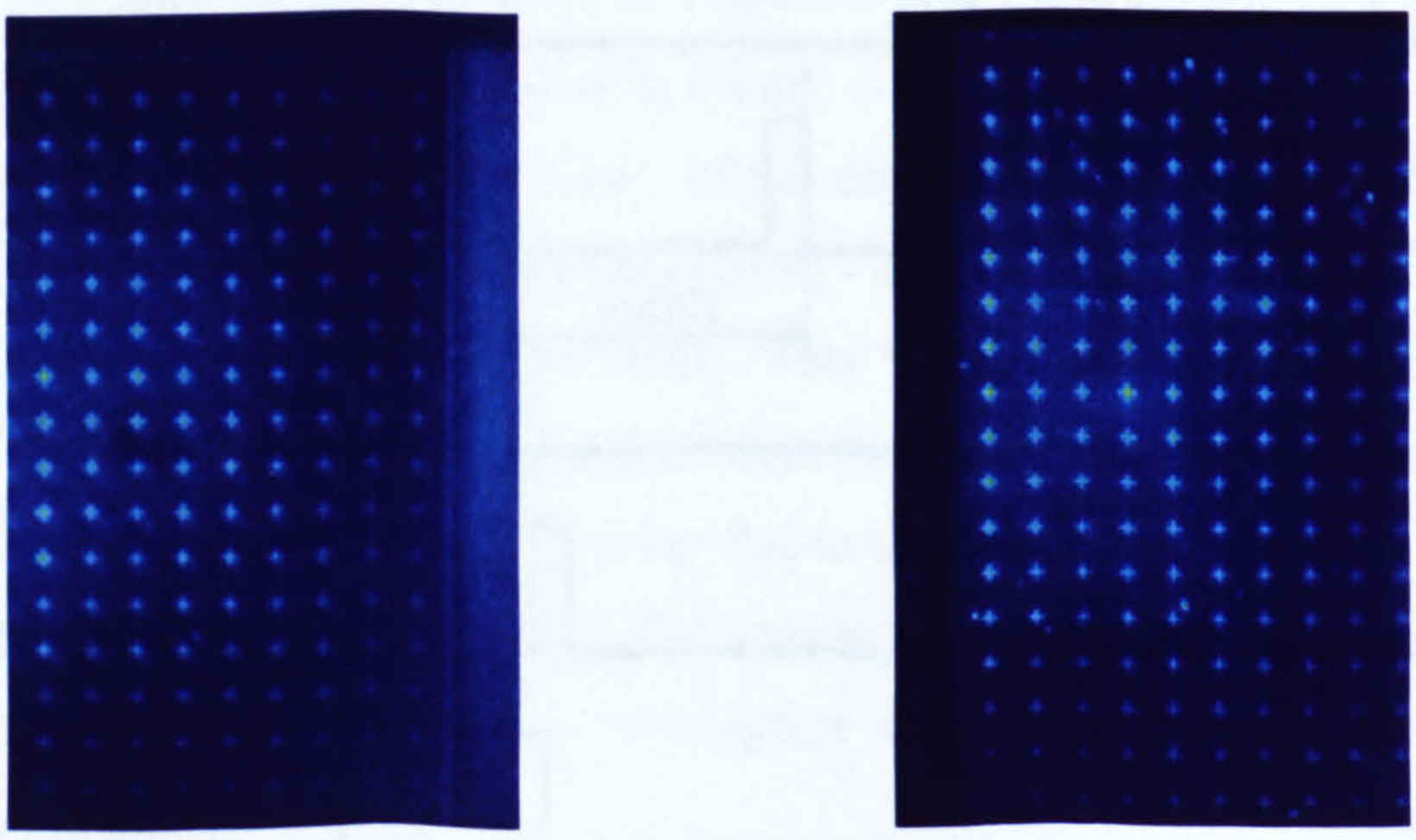

Figure 4-10: Calibration images for the Mie path (left) and the LIF path (right)

The right side window was removed and the calibration plate was inserted in its place. The plate was designed to be located exactly underneath the injector tip, in the middle of the bomb. A 266nm dichroic mirror was laid over the beam splitter in order to redirect the 266nm laser light through the left sheet-forming optics. The adjustment

knobs on the top 45° mirror situated before the sheet-forming optics allowed to direct the sheet onto the plate at a very low angle. An aluminium plate was used to scatter the light. It was found that this illumination of the plate gave a good 266nm Mie scatter image of the plate, as well as a good fluorescence image. Images were taken by running the DaVis imaging software on internal trigger (i.e. the PTU is triggered by the computer at a rate of 10Hz).

4.2.7. Traverse system

The laser optics and camera system are mounted on a common motorised translation stage, so that the sheet can be moved inside the chamber without requiring re-focusing or re-calibrating. To ensure positional accuracy, each time the rig is switched on, the translation stages must be referenced. The Test-rig computer performs this by moving the traverses to the end of the stage. Only afterwards can the traverse be moved freely. For these experiments, measurements were done in a single plane, so the traverse was only adjusted for the laser sheet positioning.

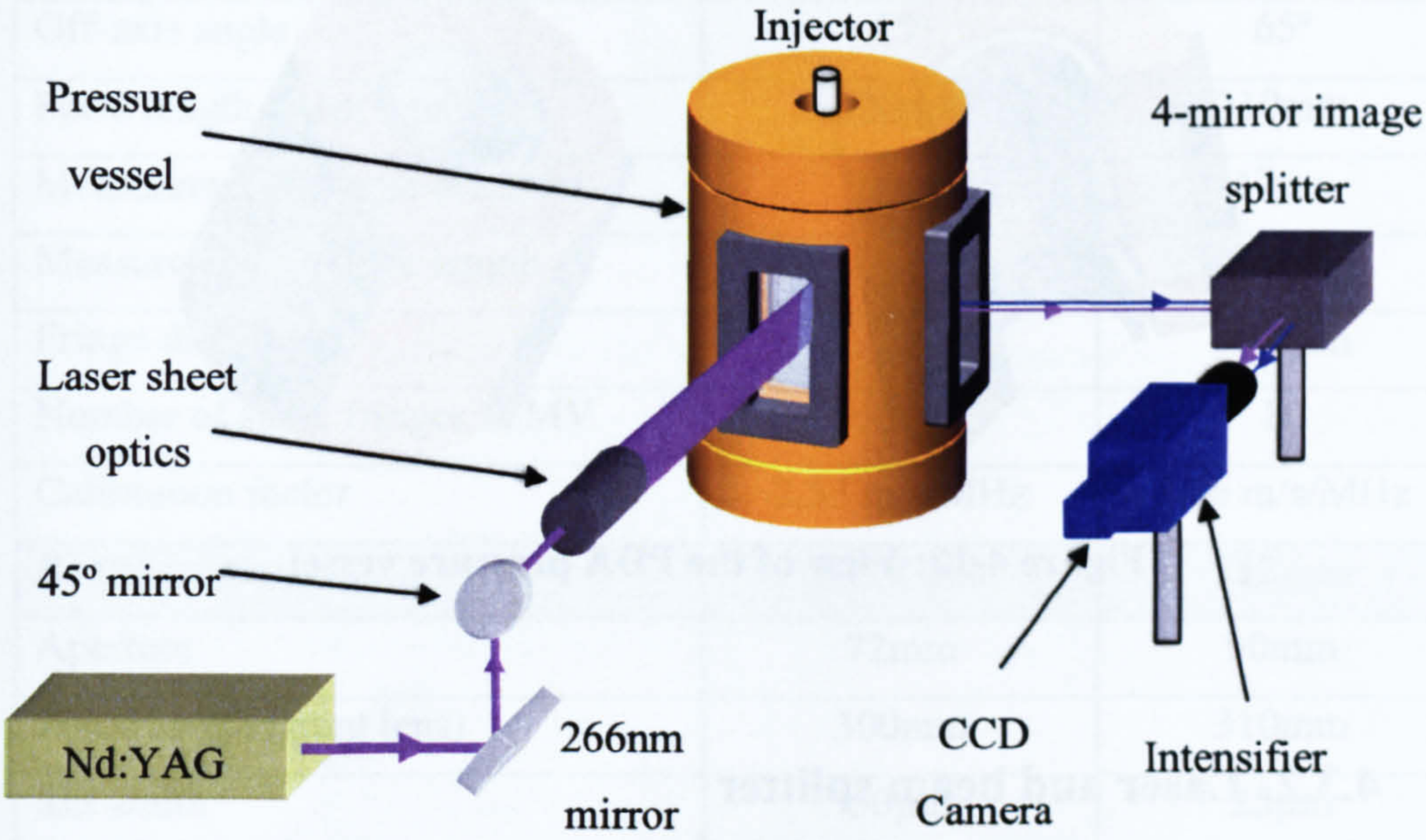

Figure 4-11: Schematics of the LSD setup

4.3. PDA pressure vessel

This vessel is actually equipped with a Dual PDA enabling to measure 2 component velocities and diameter. Originally, the diagnostics system was from TSI, consisting of a Fibre Coupler, transmitting and receiving optics, a Photodetector Module (PDM 100) and the Multibit Digital Processor (FSA 4000) controlled by the PC-based software package called Flow Sizer. The experiments were carried with this system. Later, a DualPDA system from Dantec was installed, with a new fibre coupler, transmitting ad receiving optics, Photodetector Module (detector Unit), Processor (BSA P80) and software (BSA Flow Software) which enabled to renew part of the experiment with a different system.

4.3.1. Optical Access

The PDA pressure vessel has two side windows, at an angle of 115° (i.e. PDA is done using refraction at an off-axis angle of 65°. The transmitting (or sending) and receiving optics are each located in front of a window.

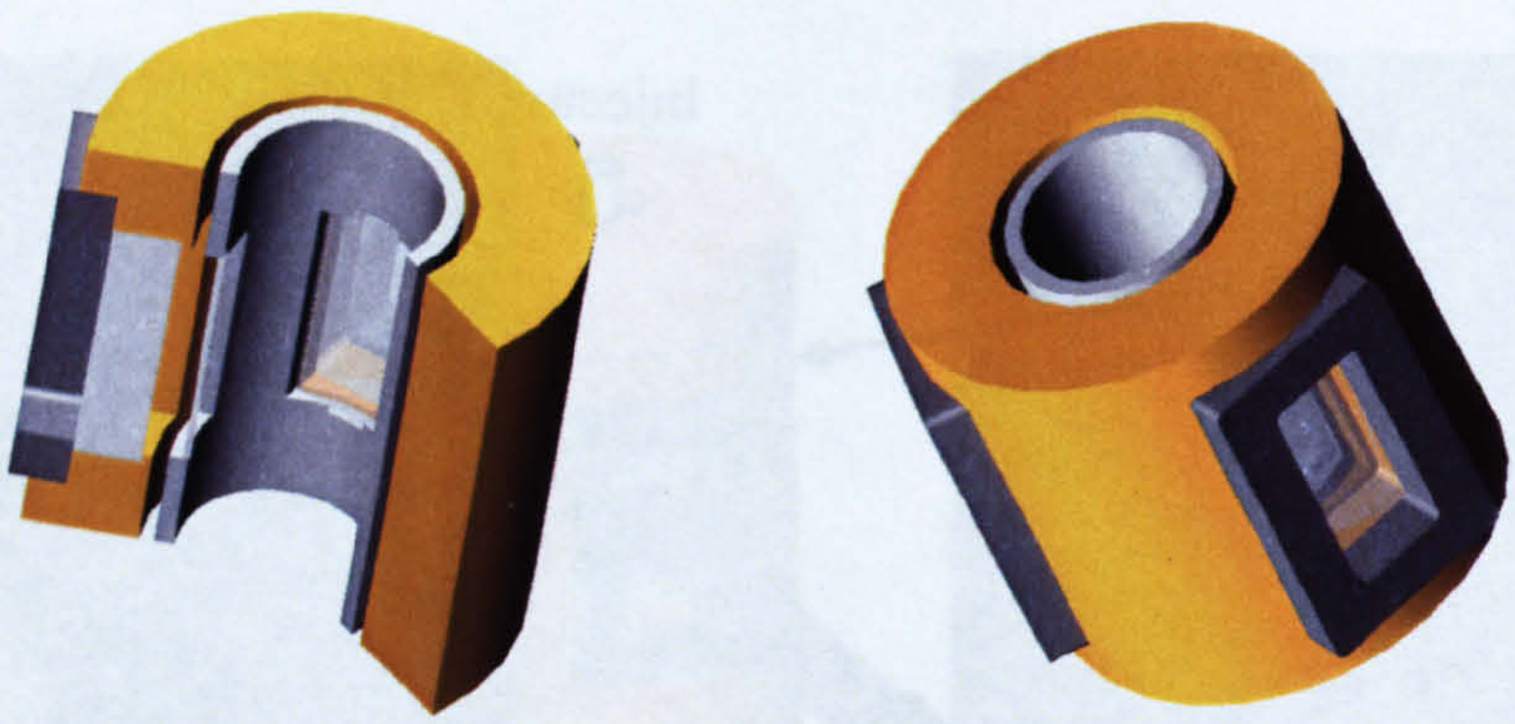

Figure 4-12: View of the PDA pressure vessel

4.3.2. Laser and beam splitter

The laser is an Innova Model 305C 5W Argon Ion Laser from Coherent.

The laser light goes through a Bragg cell. This device splits in the beams in equally intense beams and adds a 40MHz optical shift frequency onto the 1st order beam. The beams of orders 0 and 1 are extracted and fall onto a prism. This splits the light into the

discrete Argon ion wavelengths. The most intense green (514nm) and blue (488nm) beams are redirected with mirrors into the fibre coupling. From there, they reach the Transmitting optics.

4.3.3. Measurement volumes

The 2 pairs of beams interfere and form 2 measurement volumes which must be superimposed. This requires the beams to intersect at the same point. To adjust the intersection of the beams, the sending optics were removed from the mount and pointed towards a wall. A 4mm focal length spherical lens was placed at the intersection to magnify the image of the beams and allow optical adjustment.

The sizes of the measurement volumes for the TSI and Dantec system are found in *Table 4-1*.

PDA system	**TSI**	**Dantec**
Transmitter	**XRV 208-6.3**	**112mm Fiber**
Beam distance	60mm	75mm
Beam diameter	2mm	4.5mm
Off-axis angle	65°	65°
Focal length (front lens)	300mm	310mm
Measurement volume diameter	98µm	47µm
Measurement volume length	980µm	390µm
Fringe distance	2.58µm	2.16µm
Number of static fringes in MV	38	10
Calibration factor	2.58 m/s/MHz	2.16 m/s/MHz
Receiver	**RCV 208**	**112mm**
Aperture	72mm	90mm
Focal length (front lens)	300mm	310mm
Slit width	50µm	25µm

Table 4-1: PDA parameters

4.3.4. Timing

For each new injection, the PDA system requires a temporal reference to determine the time at which an event occurred after the start of injection. This reference is the injector trigger from the Test-rig computer, i.e. the electronic start of injection.

The user can also set a window at which the events are validated, (e.g. from 1ms ASOI to 3ms ASOI).

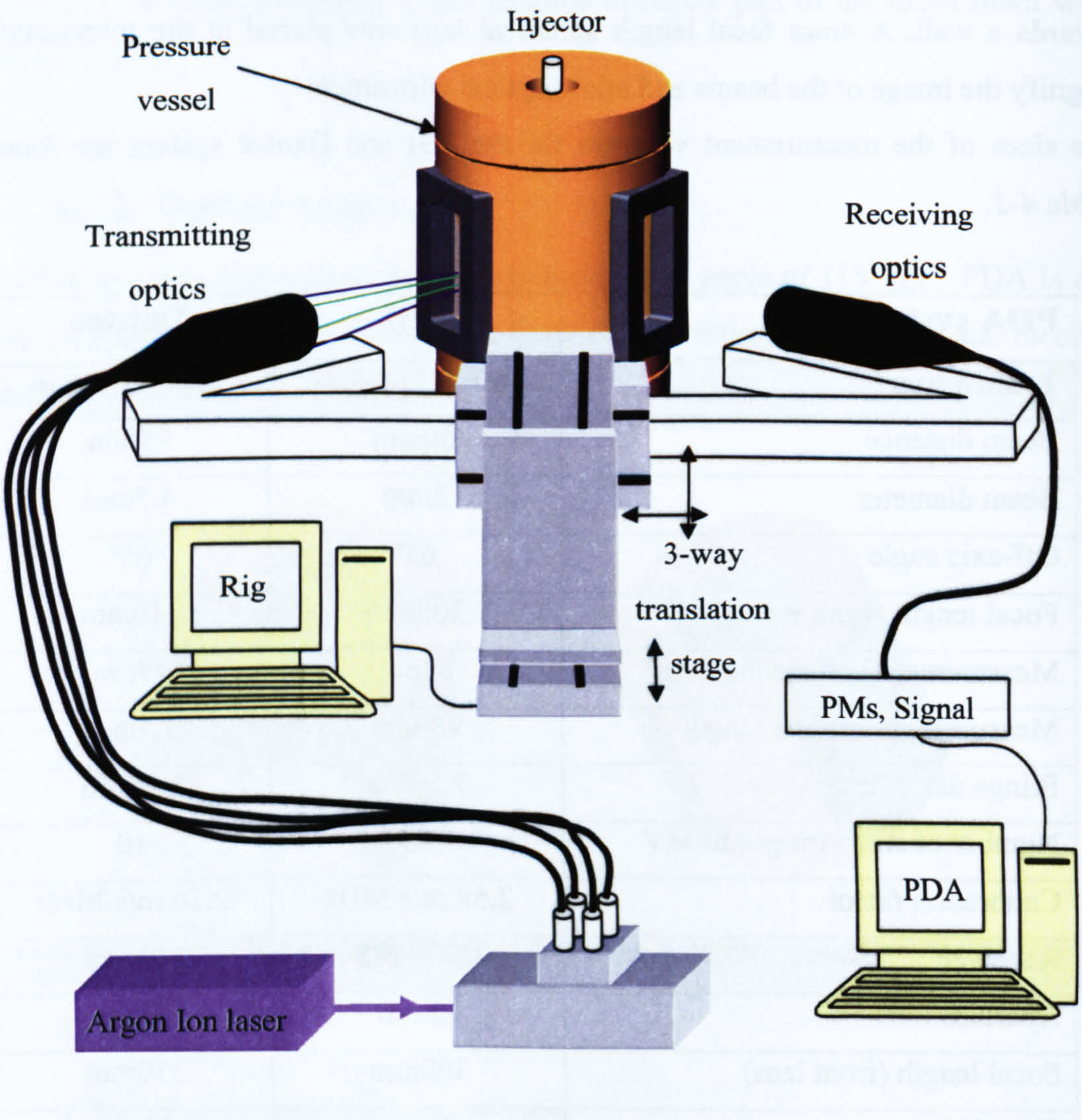

Figure 4-13: Schematics of the PDA vessel

4.3.5. Traversing system

The transmitting and receiving optics are mounted on the same horizontal aluminium beam. This beam is mounted on a three-way translation stage to allow for displacement in all directions. The stage is motorised and the coordinates are input to the Test-rig computer. In the same way as the other vessel, the stage must go to a reference point before being operated. The point of origin is set manually at the injector tip. This is done by inserting a specific blank with a small needle in replacement of the injector mount. The design is such that the tip of the needle is at the location of the injector tip. The traverse system is adjusted so that the measurement volume hits the tip of the needle. The precision is ±250μm.

4.3.6. Tuning

A monodisperse spray from a water nebuliser was used for the fine adjustment of the system. It allowed an accurate positioning of the receiving optics, by checking the collected data along with the collection rate (typically 90% and more).

4.4. Test rig operation

The test-rig can be operated either manually or in automatic mode.

Each vessel is controlled by its individual Test-rig computer. This computer controls the conditioning of the vessel and the fuel, the movement of the traverses and also triggers the injector: it is the experiment master.

Each rig then has a specific computer for the laser diagnostics which run as slaves.

4.4.1. Manual mode

The manual mode allows set-up of the experiment and adjustment of the optics for the injection measurements. In this mode, the user sets all the parameters remotely. The conditioning of the vessel (Pressure, Temperature and Flux) is done using the windows shown in *Figure 4-15*. The user fills the fuel pump by opening and closing a series of valves and inputs the pressure (see *Figure 4-16*). The injection is triggered using the window illustrated in *Figure 4-14* in which the user inputs the injection duration and repetition rate.

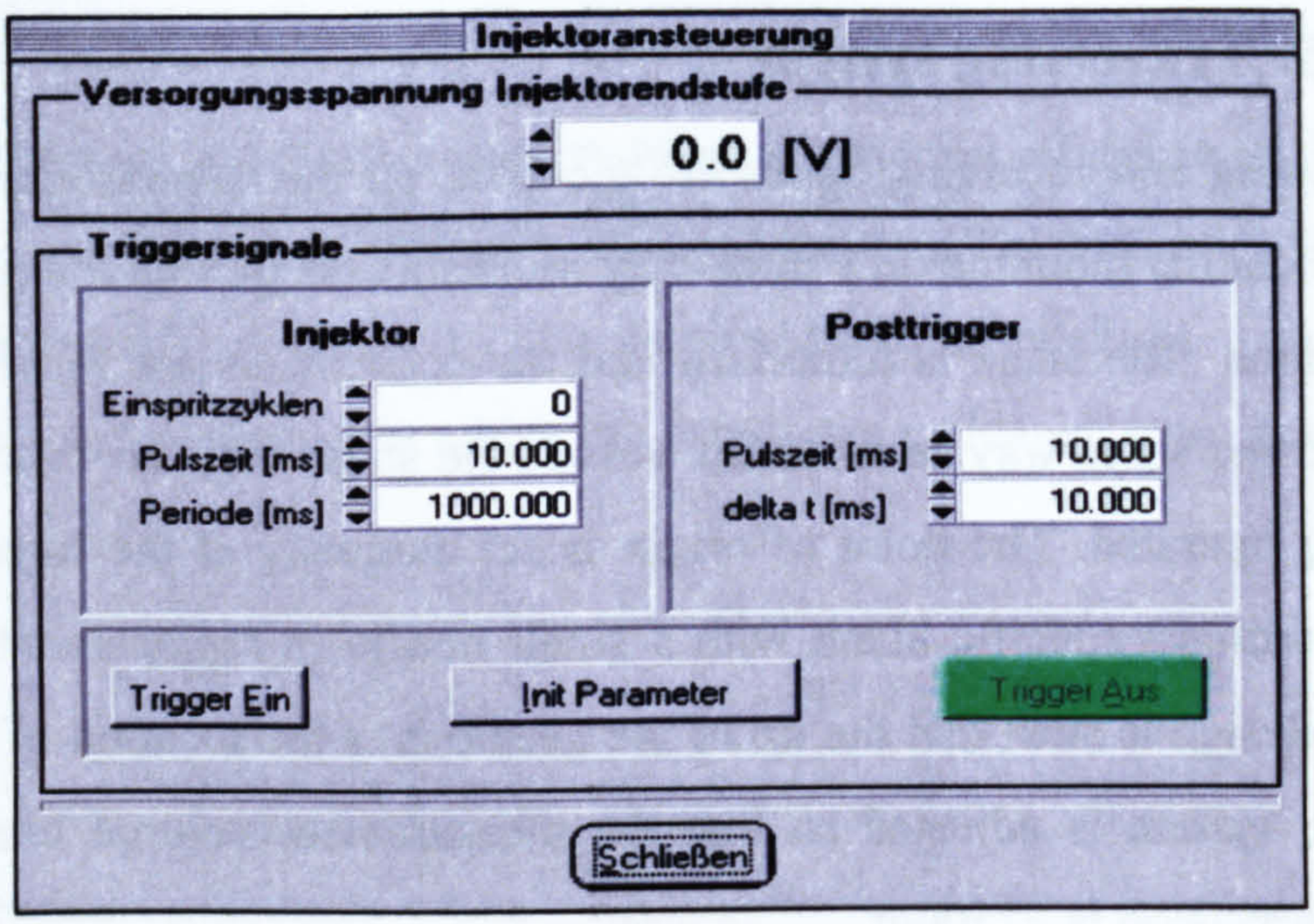

Figure 4-14: Injector Trigger

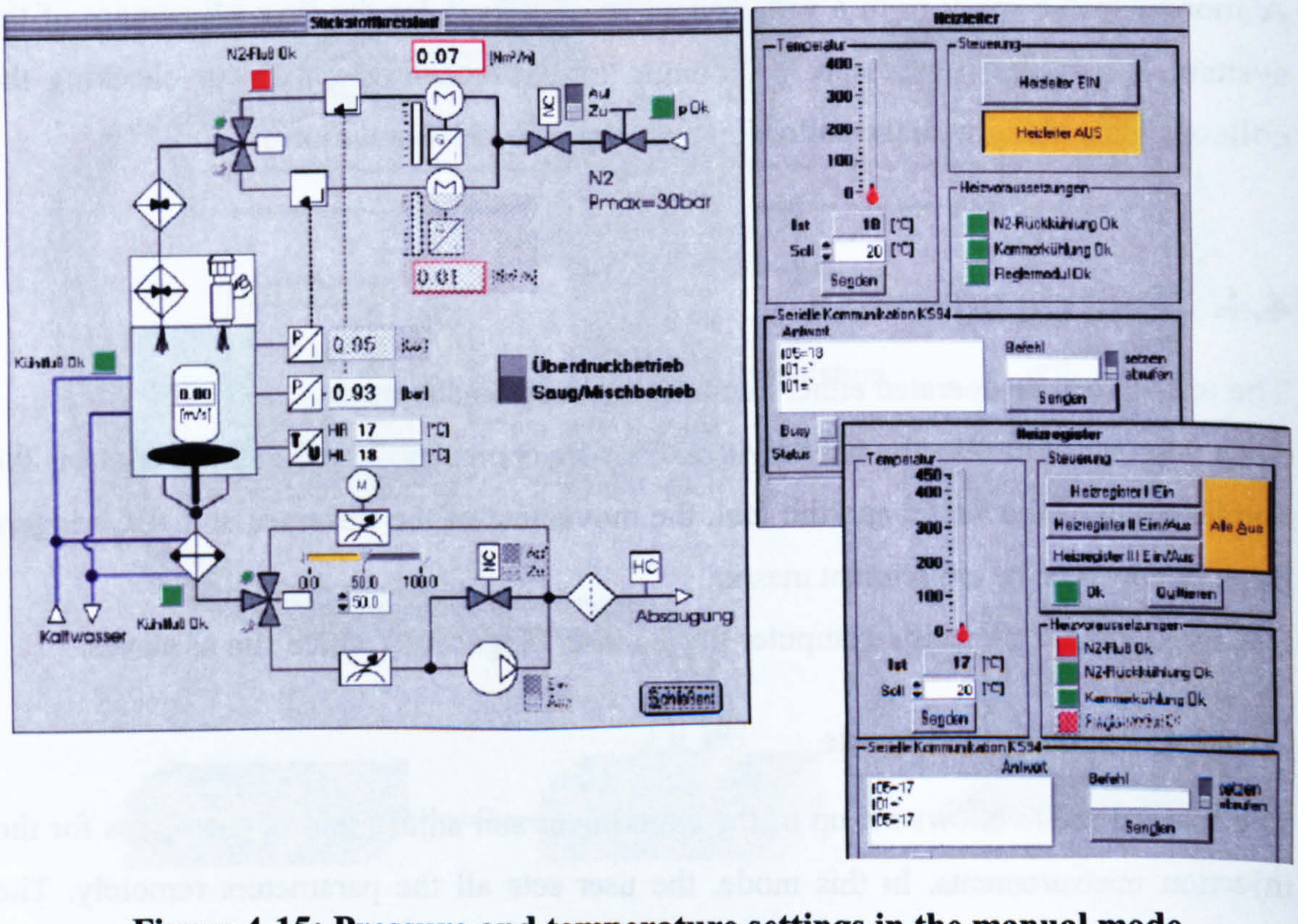

Figure 4-15: Pressure and temperature settings in the manual mode

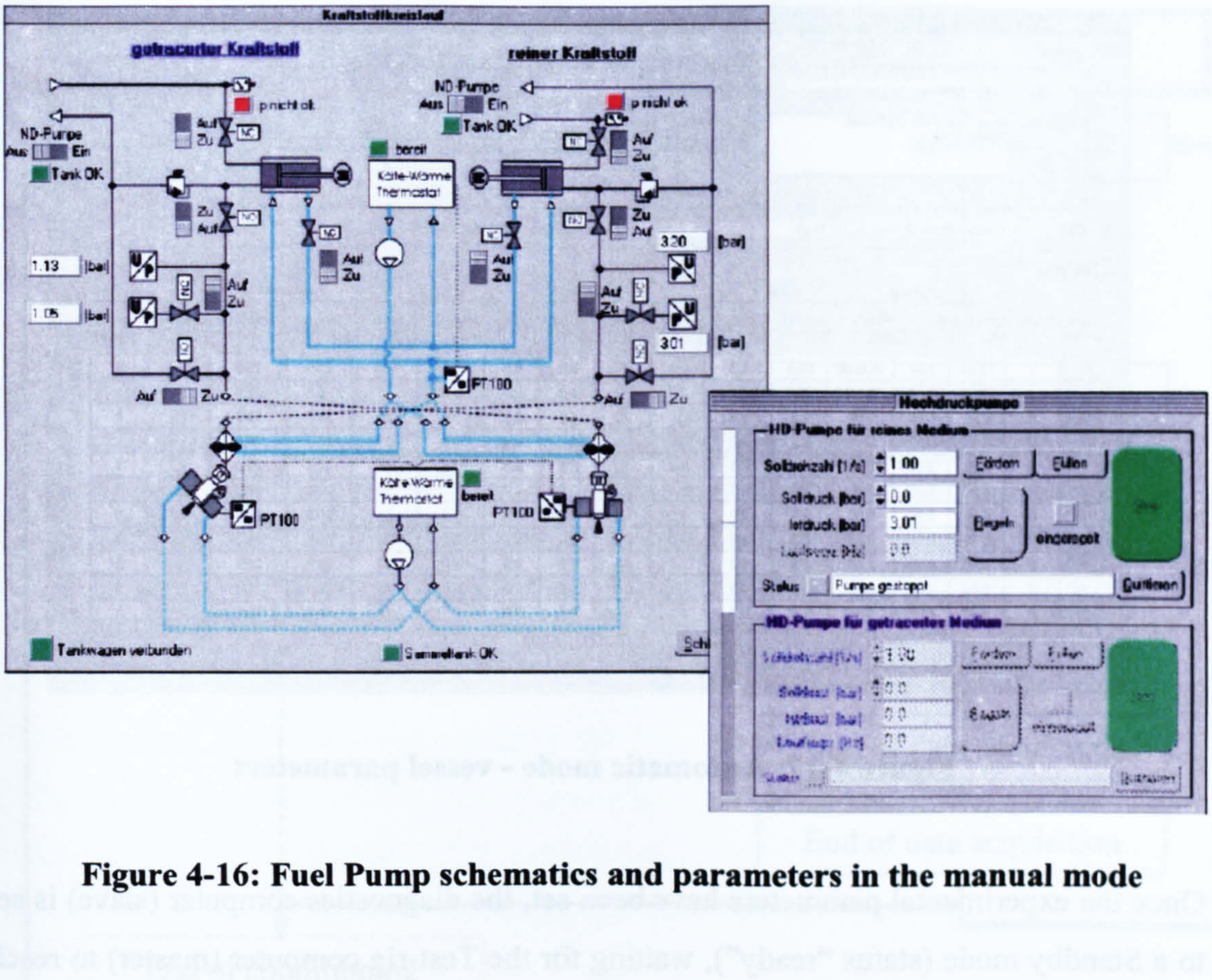

Figure 4-16: Fuel Pump schematics and parameters in the manual mode

4.4.2. Automatic mode

Once the setup is complete, the rig can be operated in automatic mode.

In this mode, the user inputs the vessel's conditioning parameters in a line on the Test-rig computer (see *Figure 4-17*). Each line represents one set of measurements.

The parameters are:

- the vessel's Pressure and Temperature
- the fuel's Pressure and Temperature
- the translation stage's position
- the injector voltage, injection time and frequency

There is a serial communication protocol to exchange data between the two PCs, consisting of 4 commands (status, start, break, end) and 3 statii (ready, busy, error): the Test-rig computer (master) continuously sends commands to the diagnostics computer (slave) and checks the slave's status. Each command has to be answered within a few seconds, otherwise the test-rig PC (master) will switch the rig off.

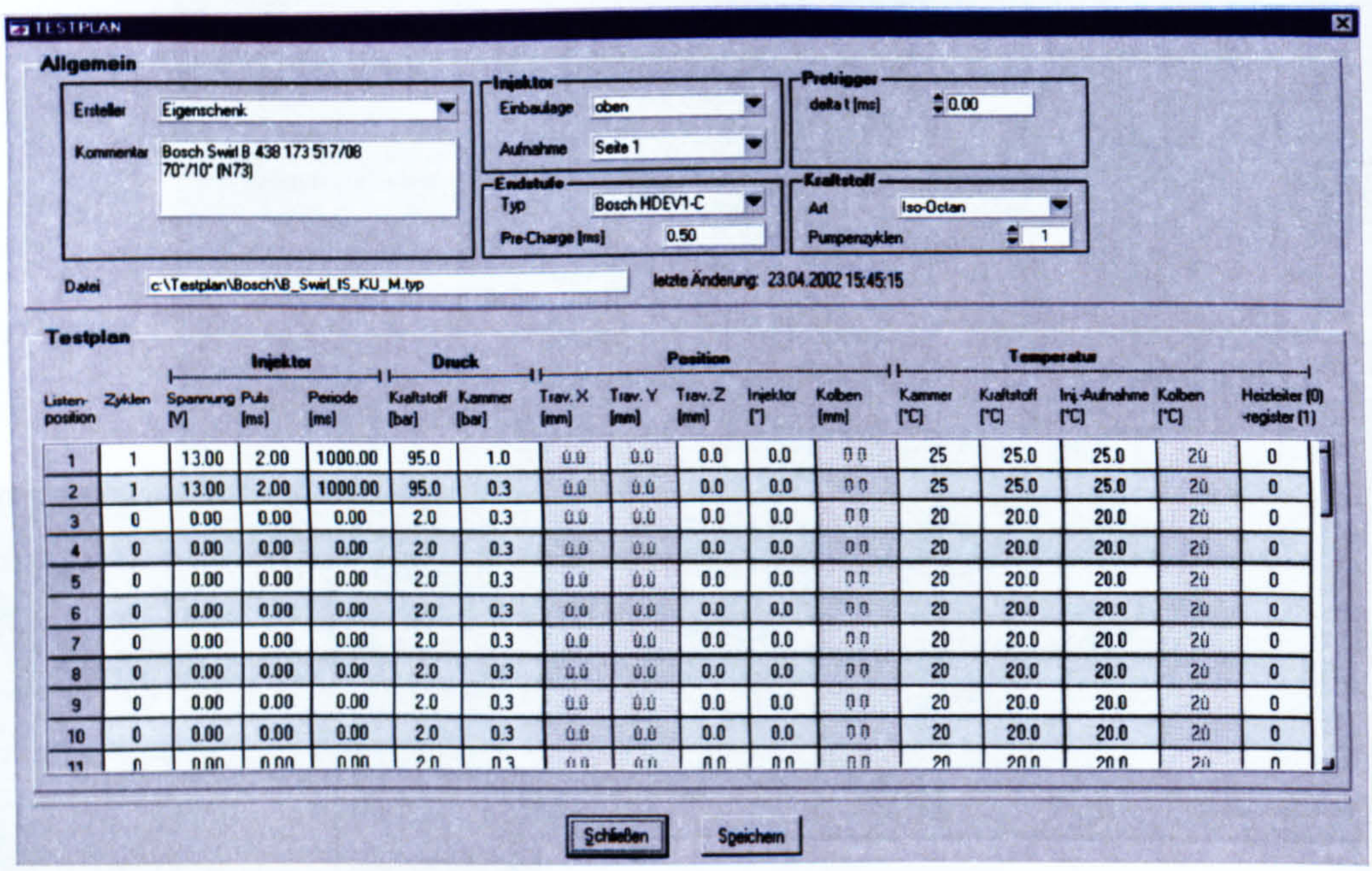

Figure 4-17: Automatic mode - vessel parameters

Once the experimental parameters have been set, the diagnostics computer (slave) is set to a Standby mode (status "ready"), waiting for the Test-rig computer (master) to reach the conditioning parameters of the vessel. The conditioning sequence starts with the release of Nitrogen into the chamber. First, the valves stabilise the pressure and the purging flow. The heaters then heat up the Nitrogen whilst the valves are continuously adjusted to maintain the pressure and the flow. When the nitrogen has reached a stable temperature, the fuel is conditioned to the desired temperature. Once the conditioning is stabilised (± 3%), the fuel pump is filled. When the pump has reached the desired pressure, the master computer tells the slave computer it is ready to start. As soon as the slave is ready, it gets a new command, and measurements can begin. At this point the slave status becomes "busy". The injection proceeds until the diagnostics computer has finished the data acquisition for this conditioning line. At this point, the slave computer changes its status to "ready" and the Test-rig computer moves to the next conditioning parameters. The end of the measurements is indicated by a *0* at the beginning of the next line. At that point, the rig releases the pressure and maintains a flux until the heaters are cooled down.

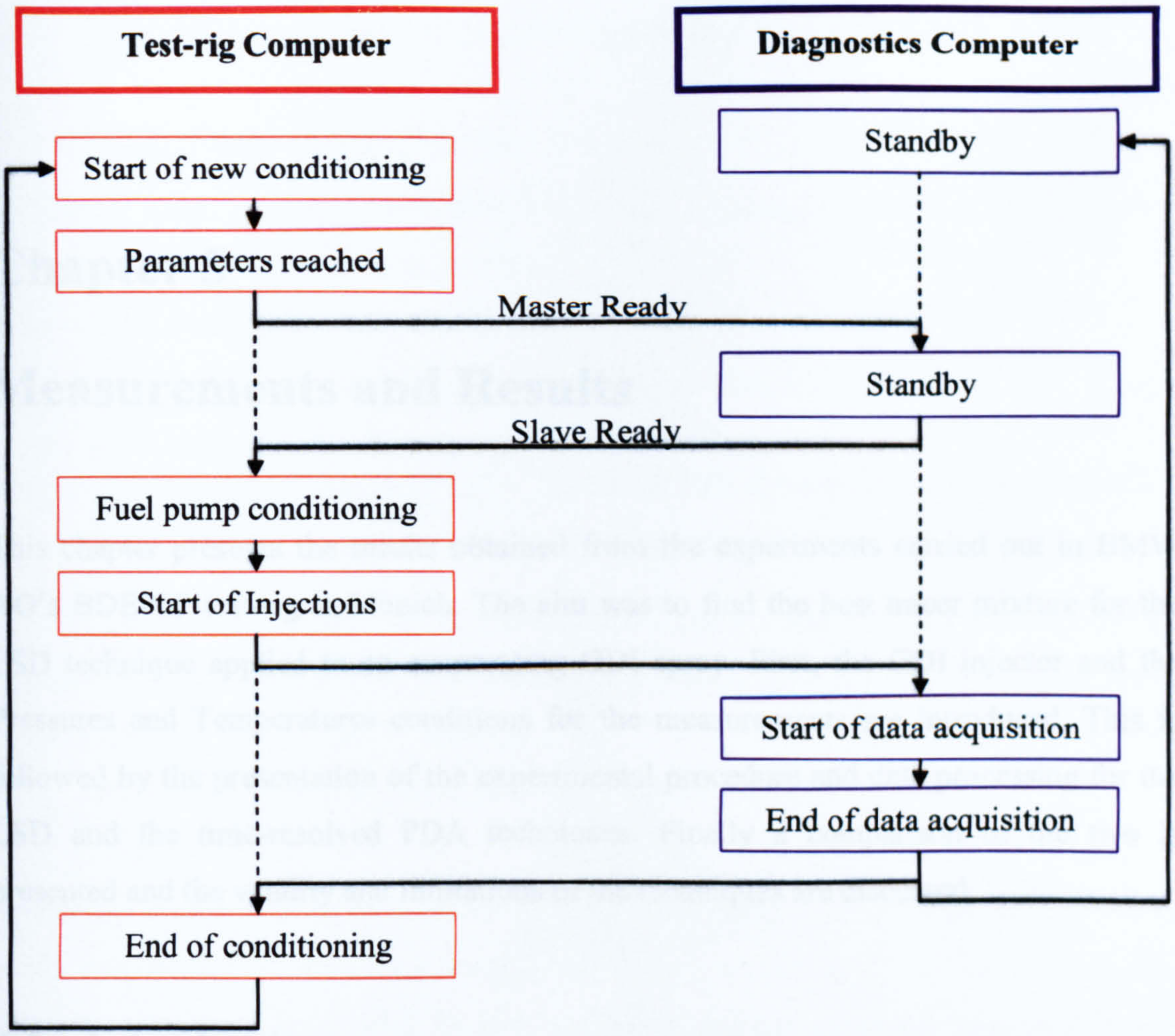

Figure 4-18: Schematics of the Master-Slave computer communication in the automatic mode

In the meantime the rig-PC has 15 threads running to control the rigs hardware and is surveying 6 safety loops. The rig-PC is also connected to an I/O-profibus delivering data from sensors (temperature, pressure, fuel levels, water flow, etc.), pneumatic valves, actors and pumps. In addition to the profibus, the rig-PC is connected by TCP/IP with 10 units controlled with a serial RS232 or RS485 interface such as gas flow valves and throttles, silicon oil conditioners. Timings and the pump control is done by a separate controller connected via a CAN bus to the PC. Above all there is a SPS acting as profibus master. Safety features are all SPS controlled.

Chapter 5

Measurements and Results

This chapter presents the results obtained from the experiments carried out in BMW AG's BDE-OP test-rig in Munich. The aim was to find the best tracer mixture for the LSD technique applied to an evaporating GDI spray. First, the GDI injector and the Pressures and Temperatures conditions for the measurements are introduced. This is followed by the presentation of the experimental procedure and data processing for the LSD and the time-resolved PDA techniques. Finally a comparison of the two is presented and the validity and limitations of the techniques are discussed.

5.1. Introduction

A GDI spray from a swirl injector was investigated at 5 different Pressures and Temperatures. These conditions were chosen to represent both realistic in-cylinder conditions and different boiling regimes (see *Figure 5-1*).

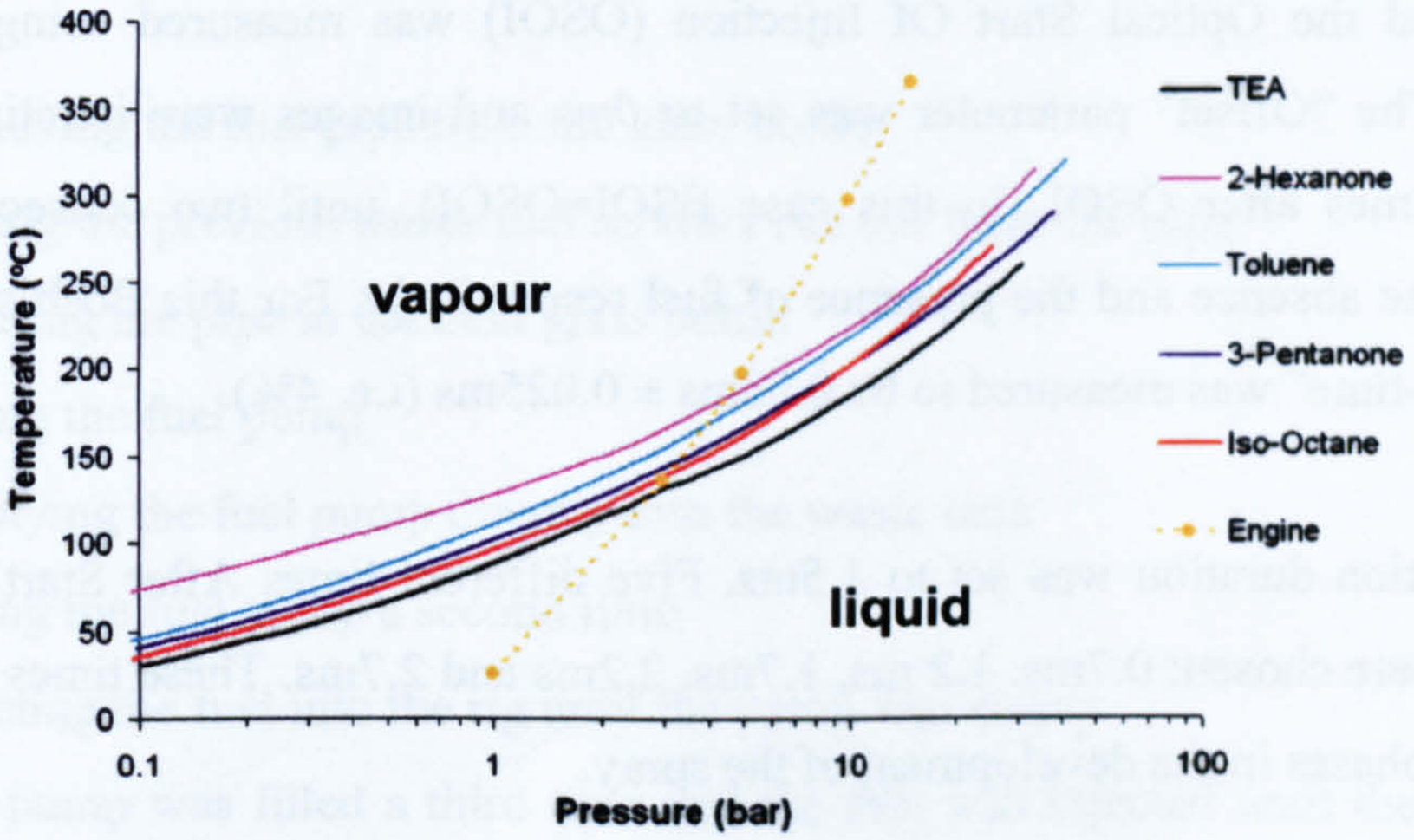

Figure 5-1: Saturated Pressures of various compounds - Engine conditions

These conditions are:

- 01bar - 25°C
- 03bar - 135°C
- 05bar - 195°C
- 10bar - 295°C
- 15bar - 360°C

The injector used in this work was the Bosch 70°/0° high pressure swirl injector. It is a needle-type injector, with an axisymetric spray (γ=0°) and a cone-angle of α=70°.

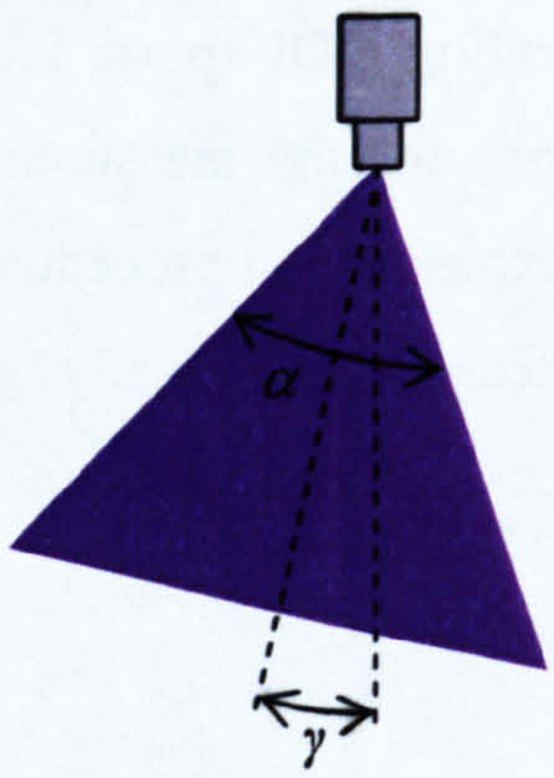

Figure 5-2: Injector α and γ angles

The delay between the electronic injection signal (or Electronic Start Of Injection – ESOI) and the Optical Start Of Injection (OSOI) was measured using Mie scatter images. The "Offset" parameter was set to *0ms* and images were iteratively taken at various times after OSOI (in this case ESOI=OSOI), until two consecutive images showed the absence and the presence of fuel respectively. For this Bosh swirl injector, the "dead-time" was measured to be 0.68ms ± 0.025ms (i.e. 4%).

The injection duration was set to 1.5ms. Five different times After Start Of Injection (ASOI) were chosen: 0.7ms, 1.2 ms, 1.7ms, 2.2ms and 2.7ms. These times represent the different phases in the development of the spray.

5.2. LIF/Mie scatter measurements for the LSD technique

5.2.1. Fuel/tracer systems

5 different tracer systems were tested, 4 of which consisted of different mixtures of 3-Pentanone and 2-Hexanone in Iso-Octane:

- 2.0% Pentanone – 98% Iso-Octane
- 1.0% Pentanone – 1.0% Hexanone - 98% Iso-Octane
- 0.5% Pentanone – 1.5% Hexanone - 98% Iso-Octane
- 2.0% Hexanone - 98% Iso-Octane

As will be discussed at the end of the chapter, these 4 tracer systems were limited by vapour contribution to the fluorescence signal. An Exciplex system developed by Fröba et al. (1998) was used as the 5th tracer mixture:

- 2% TEA – 3.4% Benzene – 94.6% Iso-octane

To change the fuel/tracer mixture, the tank must be completely emptied and washed to avoid contamination. The tank was not designed specifically for this. Instead, the mixtures were prepared in glass bottles, and the pipe from which the mixture is drawn from the tank was inserted into the bottle.

For each change in the tracer system, a sequence of operations was carried out to ensure sure that the next measurement campaign did not contain residuals from the previous mixture. This consisted of:

- Removing the fuel pipe from the glass bottle
- Letting the previous tracer/fuel mixture run out from the pipe
- Inserting the pipe in the next glass bottle
- Filling the fuel pump
- Emptying the fuel pump directly into the waste tank
- Filling the fuel pump a second time
- Injecting the fuel into the rig until the pump was empty
- The pump was filled a third time and the fuel was injected until the pump was empty.

The images of the injection after the 3rd pump filling showed a stable fluorescence signal, suggesting that the previous fuel was completely evacuated from the system.

With the new fuel in place, images were recorded. The LIF intensity varied from the previous mixture, due to the difference in fluorescence yield and tracer concentrations. The LIF path contained a BG4 filter to attenuate any 266nm light and Mie scatter from the 532nm light present in the pressure vessel. In the case of the Exciplex mixture, the liquid phase fluorescence was selected using the WG335 long-pass filter, rejecting the spectrum below 335nm. The Mie scatter light path was accordingly attenuated so that the Mie scatter intensity matched that of the LIF signal. The filters used are found in *Table 5-1*.

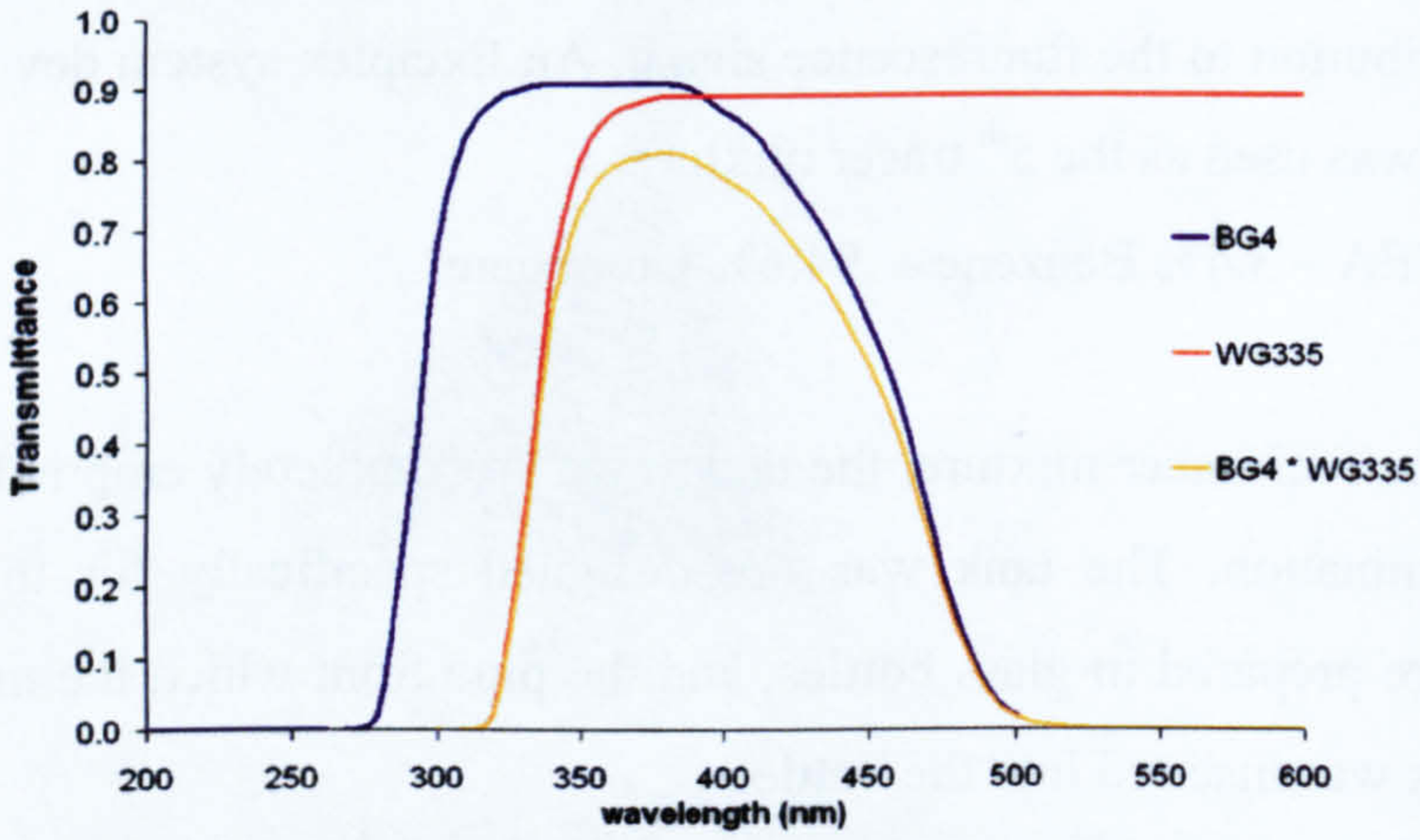

Figure 5-3: Transmittance of the BG4 and GG400 filters and their combination

Tracer composition	ND filter	Filter in LIF path
2.0% Pentanone	3 + 0.2 ~ *3.3*	BG4
1.0% Pentanone 1.0% Hexanone	3 + 0.6 ~ *3.6*	BG4
0.5% Pentanone 1.5% Hexanone	3 + 0.6~ *3.6*	BG4
2.0% Hexanone	3 + 1 ~ *4*	BG4
2.0% TEA 3.4% Benzene	3 + 1+ 0.3 ~ *4.3*	BG4 WG335

Table 5-1: Filters for the different tracer systems

The alignment of the 4-mirror setup and the intensified camera was done for the first tracer mixture. For the other mixtures, only the filters had to be changed. Each filter change modified the light paths. Therefore, a new spatial calibration was carried out for each new mixture.

5.2.2. Experimental Settings

Because of the limited capacity of the fuel pump, 80 images were recorded for each of the 5 timings. This allowed the experiment to proceed with the recording of the 5 different sets in a single run, without having to refill the pump and interrupt the experiment.

An injection frequency of 1Hz was chosen. A frequency of 2Hz was tested, but the fluorescence image suffered from contamination by vapour remains from the previous injection.

The calibration images enable the positioning of the Mie scatter and LIF images in identical locations in two separate images. It also determines the resolution of the image. The injector tip was set as the reference point. This procedure involved determining the pixel co-ordinates of the tip, and its accuracy was within 1 pixel, i.e. 100μm.

	Bosch 70°/0° Swirl Injector
Fuel Pressure	80 bar
Injection duration	1.5ms
Injection Frequency	1 Hz
Start of imaging	0.7ms ASOI
End of imaging	2.7ms ASOI
Increment	0.5ms
Number of timings	5
Injector dead-time	0.68ms
Images recorded	80

Table 5-2: Injection and imaging parameters

5.2.3. Experimental Procedure

With the calibrated optical system in place and the laser sheet adjusted, the parameters for the test-rig computer and the imaging computer were set. The first step required the adjustment of the laser. This consisted in:

- Warming up the laser for 20 minutes
- Optimising the laser power by adjusting the doubling crystals
- Letting the laser run for another 15 minutes
- Checking the laser power and adjusting if necessary

Once the laser power was stable, the imaging computer was set to the "Ready" status by setting the software to "External trigger" and pressing the "Start" button.

The measurement was then initiated by pressing the "Start" button on the test-rig software.

The laser power was monitored on-line. If the case of large laser fluctuations, the laser power could be readjusted.

Between two sets of measurements (i.e. when the pressure vessel was conditioned to the next set of Pressure and Temperature), the laser power was checked and adjusted if necessary.

5.2.4. Image Processing

For each measurement condition, the intensifier was set to a fixed gain. A background image was recorded with the laser firing inside the pressure vessel, without injection. This background image was automatically subtracted to the images.

For each time step, the dual images were then averaged, separated and corrected for geometrical alignment.

An additional background value was subtracted to account for spray-induced background. This value was determined by averaging the intensity of a selected region around the spray for each image.

The images were then masked by setting all intensities below a threshold (typically 10 counts) to 0.

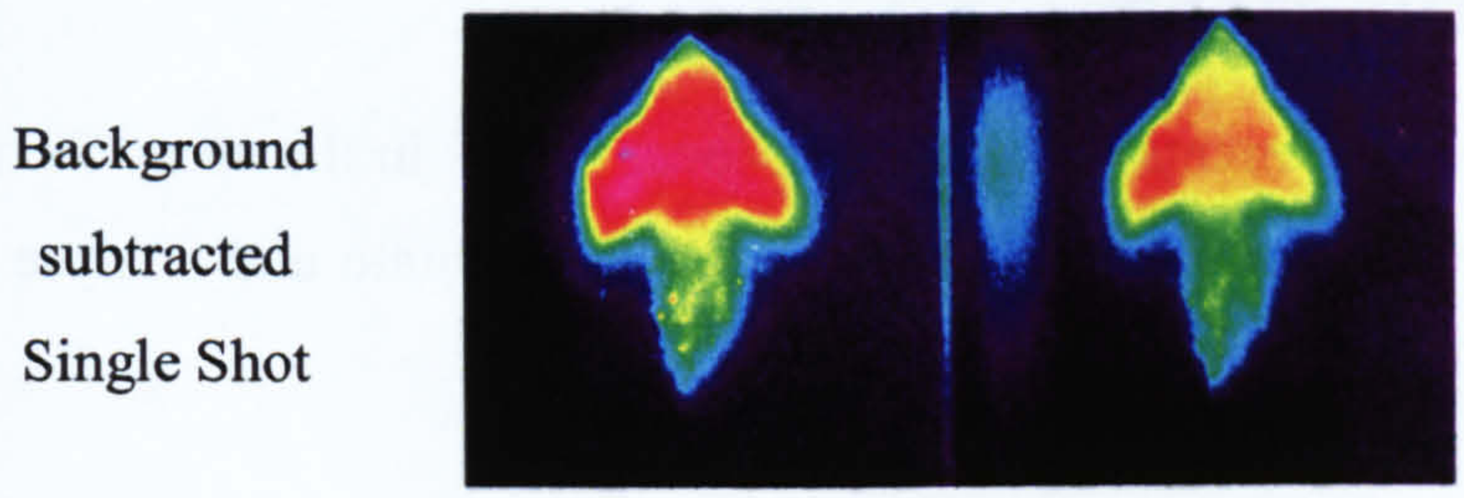

Figure 5-4: Image processing of the Mie scatter (left) and LIF (right) images

Because the spray was nearly axisymmetrical, the data from one half of the spray was extracted. Due to the interference of side reflections with the left part of the fluorescence image, the right half of both images was chosen. However, the mirrors in the system invert the images from right to left. Therefore, the data extracted in the right half of each image corresponded to the half spray, left of the injector tip.

The average LIF and Mie scatter images can be found in *Appendix A*.

5.3. PDA Measurements

The aim of the PDA experiments was to obtain local SMDs in the spray for the same five Pressure and Temperature conditions, in order to calibrate and analyse the data obtained from the LSD measurements.

5.3.1. Measurement grid

Measurements were carried out along a grid, with a vertical spacing of 5mm. The horizontal spacing varied in order to obtain a minimum of 50 measurement points for each condition.

To minimise the distance travelled through the spray, the measurement volume was moved in the "*(0,y,z) , y<0* " vertical half plane, located below the injector tip and closest to the receiving optics. However, the measurements in the "Mie/LIF" pressure vessel were performed in the "*(0,x,z) , x<0* " half plane. Therefore, the injector was rotated 90° anti-clockwise for the PDA measurement.

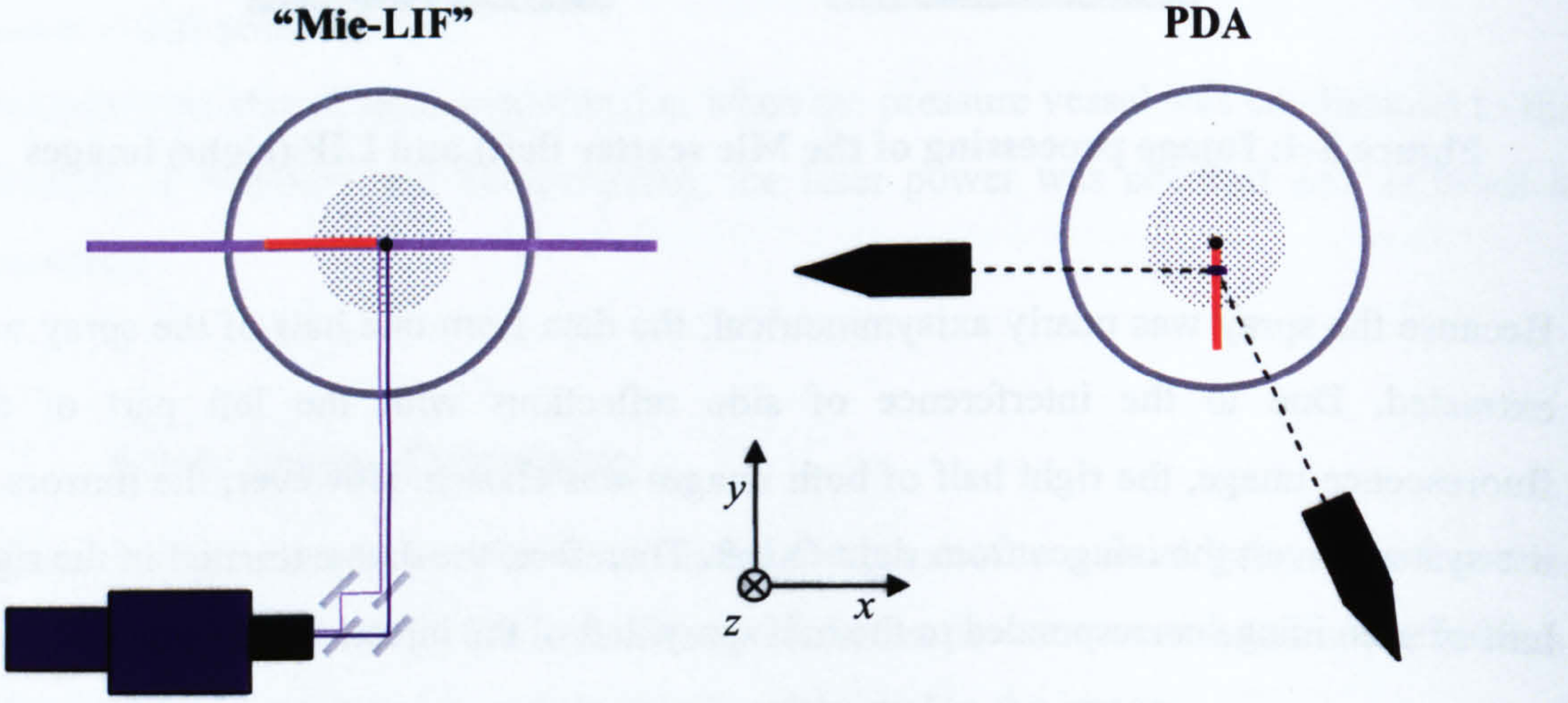

Figure 5-5: Measurement half planes (red) for the LSD and PDA techniques

	1bar 25°C	3bar 135°C	5bar 195°C	10bar 295°C	15bar 360°C
Grid - V×H (mm×mm)	4 × 5	3 × 5	3 × 5	2.5 × 5	2 × 5
Measurement points	64	74	56	54	49

Table 5-3: Grid size and measurement points

The grid size intervals and the measurement points were determined using the Mie scatter images previously obtained for the same spray.

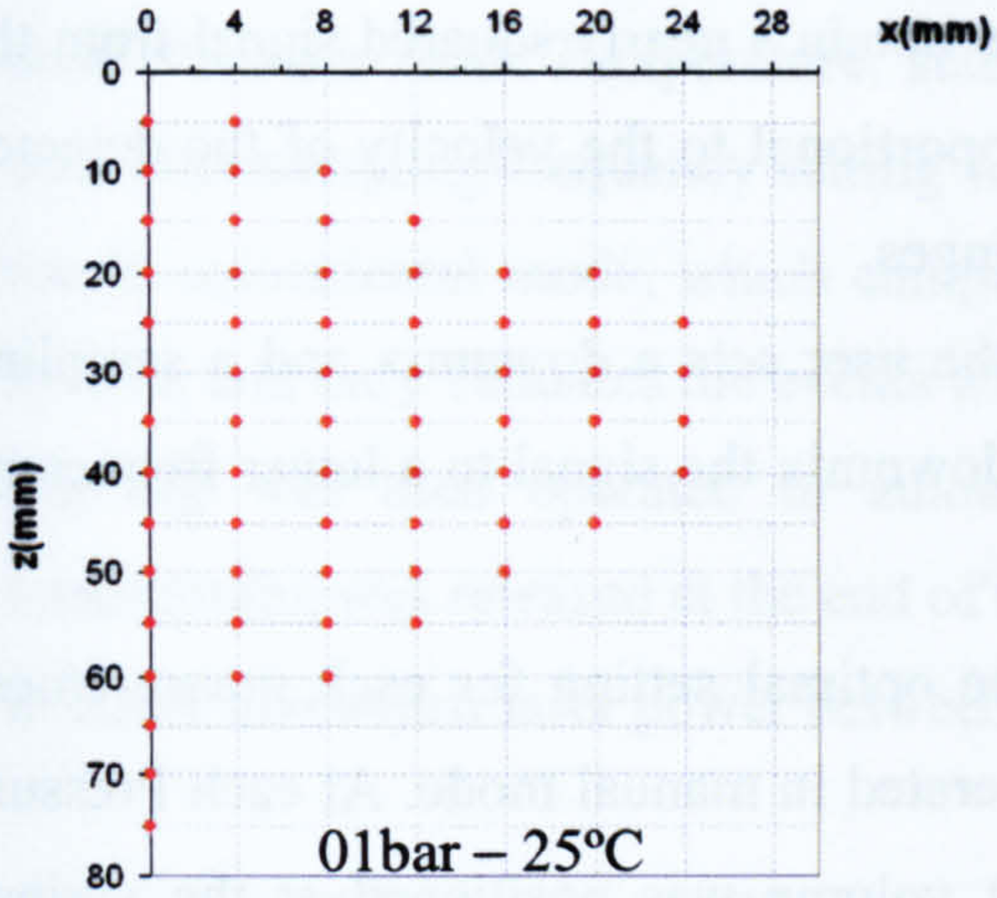

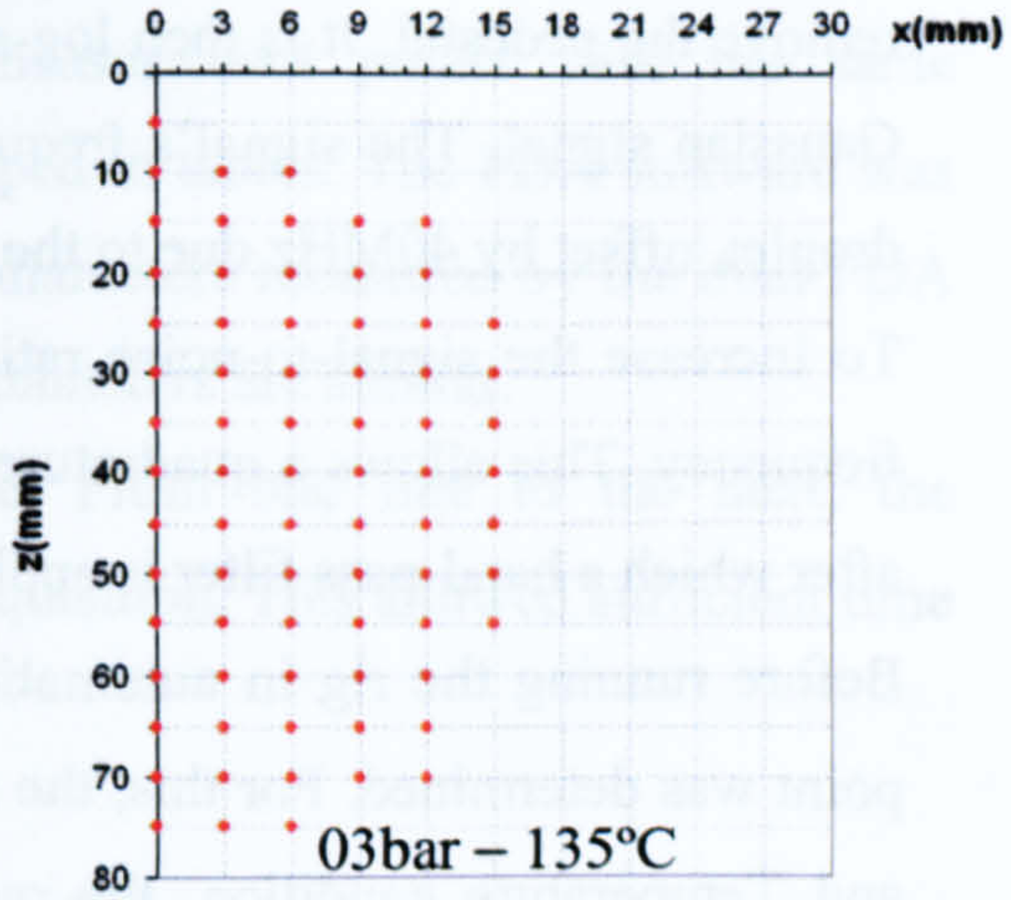

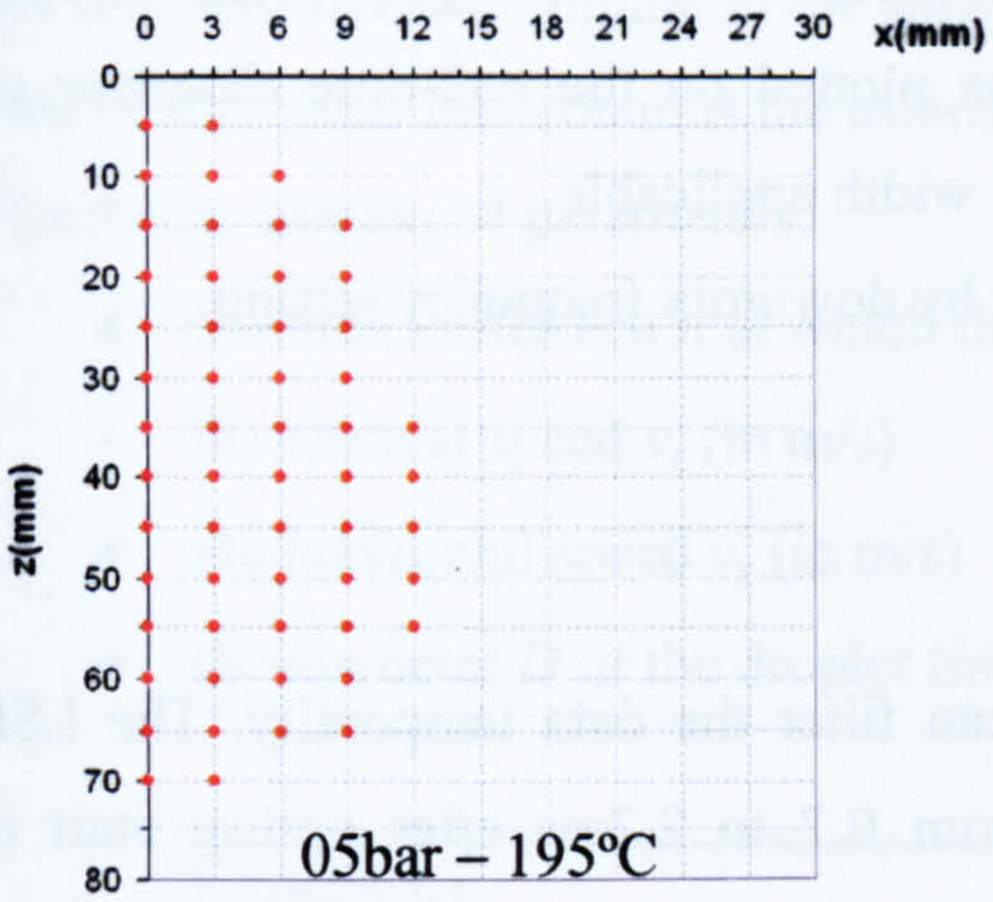

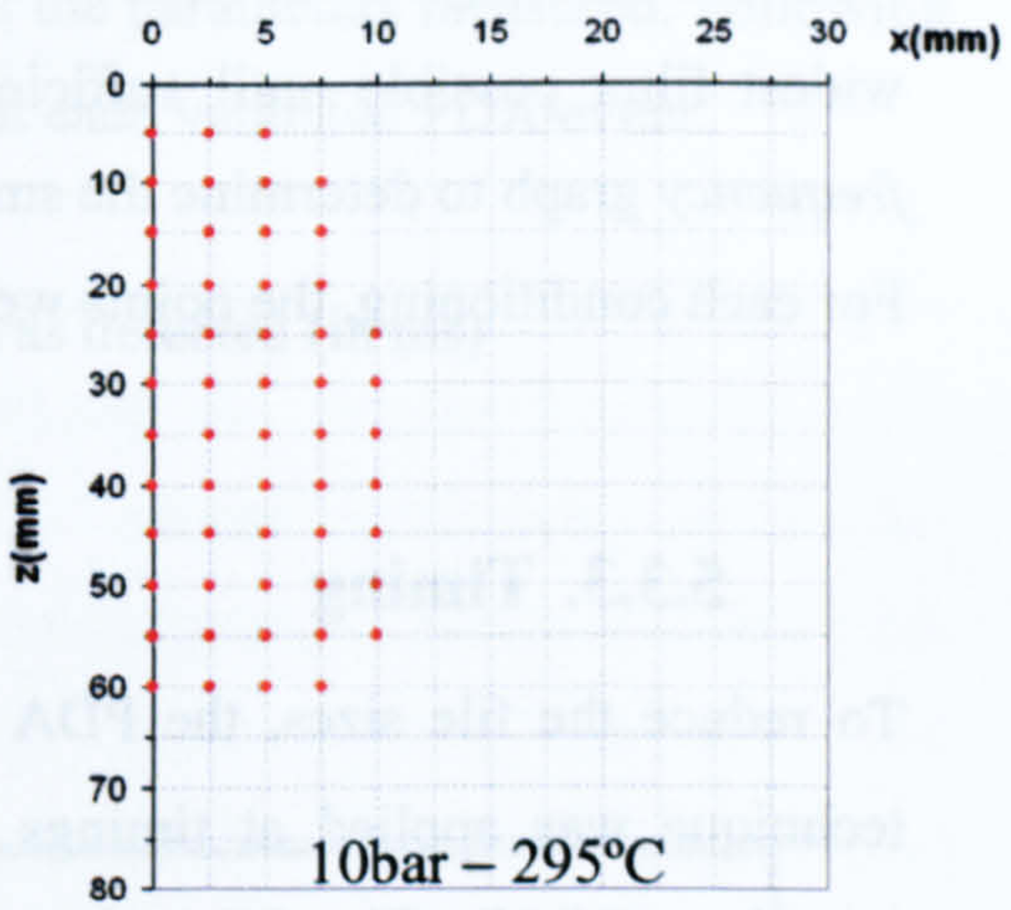

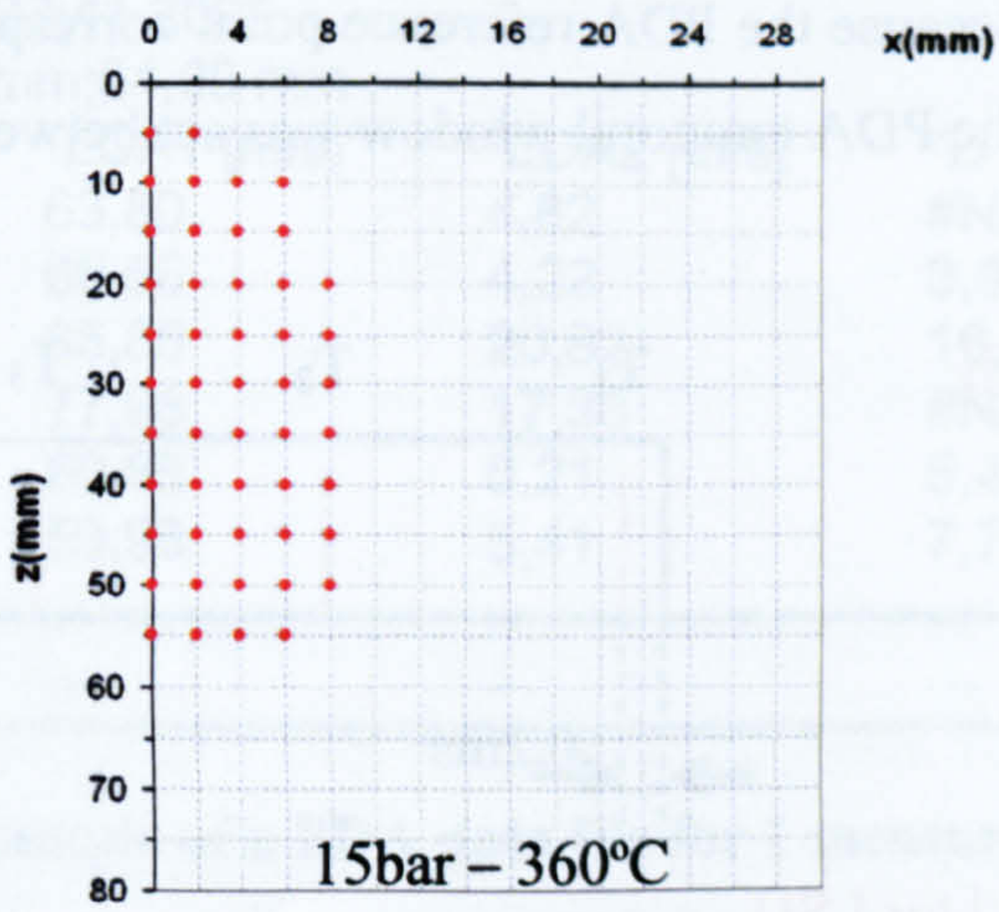

Figure 5-6: Measurement points in the grid

5.3.2. Downmix / Sampling frequency settings

The photodetectors transfer the light into an electrical signal which is read out by the digital processor. The incoming raw signal from the PMs is first high-pass-filtered to remove the pedestal. It is then log-amplified to obtain a nearly squared signal from the Gaussian signal. The signal's frequency is proportional to the velocity of the detected droplet, offset by 40MHz due to the moving fringes.

To increase the signal-to-noise ratio (SNR), the user sets a downmix and a sampling frequency. This allows a quadrature mixer to downmix the signal to a lower frequency, after which a band-pass filter is applied.

Before running the rig in automatic mode, the optimal setting for each measurement point was determined. For this, the rig was operated in manual mode. At each Pressure and Temperature condition, the measurement volume was positioned at the various locations of the grid. At each location, PDA measurements were performed with the widest filter possible until sufficient data was plotted on the real-time *diameter vs. frequency* graph to determine the smallest filter width applicable.

For each conditioning, the points were grouped by downmix frequency setting.

5.3.3. Timing

To reduce the file sizes, the PDA software can filter the data temporally. The LSD technique was applied at timings ranging from 0.7 to 2.7ms after optical start of injection (OSOI). The PDA data was therefore filtered around that range, with a tolerance of 0.2ms. Because the PDA reference point corresponds to the electronic start of injection (ESOI), the PDA temporal window was set between 1.18 and 3.58ms.

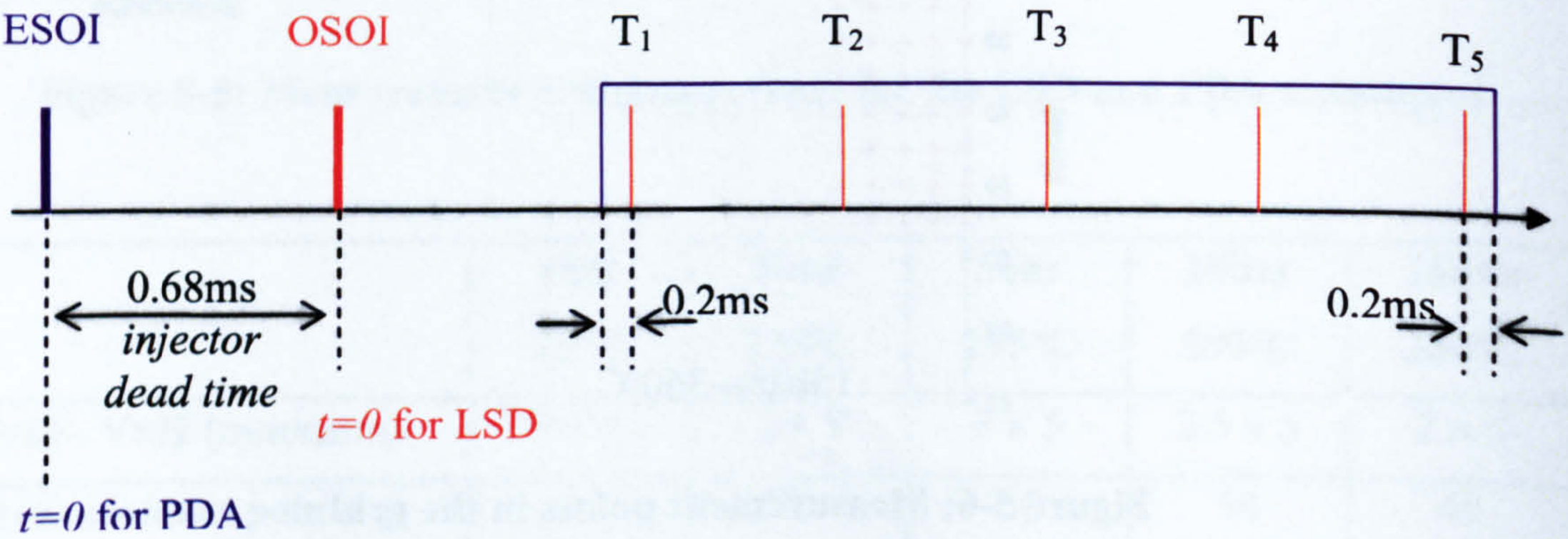

Figure 5-7: Trigger and Temporal filter (blue) for the PDA data acquisition

5.3.4. Measurement procedure

The Argon-Ion laser was first warmed up and the power was then adjusted.

The measurement positions were input in the test-rig computer's conditioning table. For each Pressure and Temperature setting, the measurement points with the same downmix/sampling frequency setting were regrouped in tables. The PDA software was run in coincidental mode, which compares the 2 diameters measured by the dual PDA system, and only validates the events where both diameters are similar.

The rig was then operated in automatic mode. From one line to the next, the conditioning was released at the end of the data acquisition. This allowed sufficient time to check and adjust laser power between two runs.

At the end of the run, the software creates a file. A 5-line header indicates the position of the measurement volume in the spray as well as the parameters measured. Following the header, each line contains the information about each validated PDA event.

Each line contains 4 parameters:

- the time t after ESOI at which the droplet was detected (in ms)
- the vertical speed v_z (in m/s)
- the horizontal speed v_y (in m/s)
- the diameter D of the droplet (in µm)

DXEX v1
C:\PDA-Messungen\B_Swirl_r=0-16.lda
Thu Mar 25 16:23:41 2004
0,00 mm;-4,00 mm;64,00 mm

"Time [ms]"	"LDA1 [m/s]"	"LDA2 [m/s]"	"D [um]"
1,228	63,80	4,82	#N/A
1,231	60,66	4,22	3,9
1,237	85,85	20,82	16,4
1,238	77,98	17,38	#N/A
1,246	60,85	6,21	5,4
1,248	59,96	5,41	7,7
...	...	...	...
...	...	...	...

Figure 5-8: Example of a PDA data file for 1 measurement point

The PDA data was used to calculate the SMD of droplets for the five timings at each measurement point.

5.3.5. Time selection

The LSD technique freezes the spray and allows the measurement of the SMD of droplets present in one pixel at a specific time (e.g. T = 1.2ms AOSOI). On the other hand, the PDA measurement technique does not freeze the spray: it analyses the passage of a droplet through the measurement volume, and indicates the time at which the event occurred. These two techniques are intrinsically different. Therefore, the PDA data must be carefully selected to match the LSD measurement. One method of freezing the PDA data in time could consist of selecting the events which occurred specifically at that time. However, a more appropriate way of matching the PDA data to the LSD experiment is to select the droplets which would be present in the LSD measurement volume at the time of interest. Because the pixels are binned 2 by 2, the actual LSD measurement volume is larger than the PDA's. Therefore, droplets detected by the PDA system just before or after the time of interest (e.g. 1.204ms or 1.997ms) might be located within that volume at the time of interest (1.2ms).

The measurement volume has the shape of an elongated rugby ball, of horizontal and vertical axis measuring ~900µm and ~100µm respectively. Due to the slit in the receiving optics (50µm for the TSI system), the effective measurement volume is a cylinder of diameter ~100µm and a height of 50µm (see *Figure 5-9*).

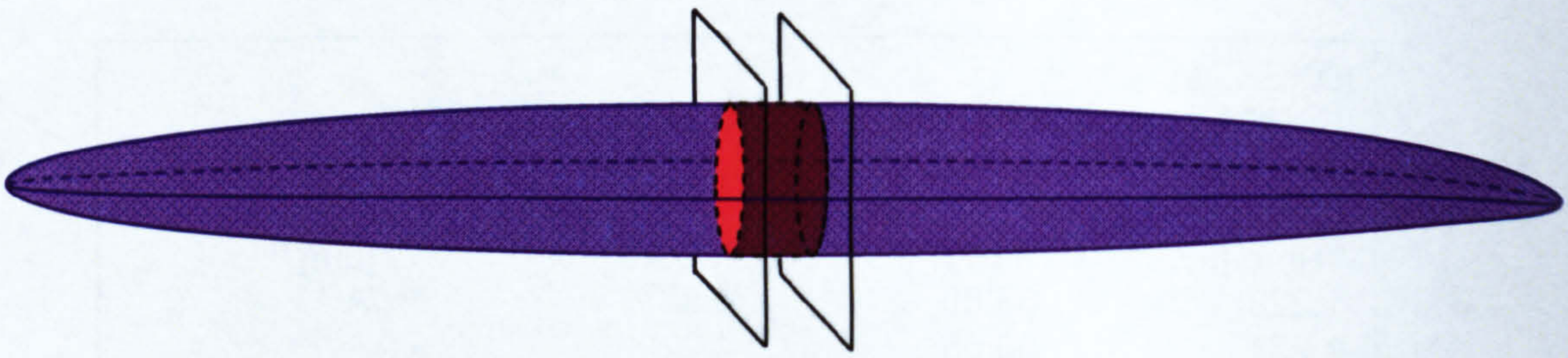

Figure 5-9: PDA measurement volume

For each event, the PDA data provides the horizontal and vertical speeds of the droplet (v_y and v_z respectively). Assuming that the droplet's speed remains constant over small distances, the location of a droplet shortly before and after the event can be determined (see *Figure 5-10*). If a droplet is spotted before or after our time of interest (at $T'=T \pm \delta t$), between T and T', the droplet will have had a horizontal and vertical displacement $\delta y=v_y.\ \delta t$ and $\delta z=v_z.\ \delta t$ respectively. If these displacements are both smaller than 100µm,

the droplet was present at the time of interest in the measurement volume used for the LSD experiment.

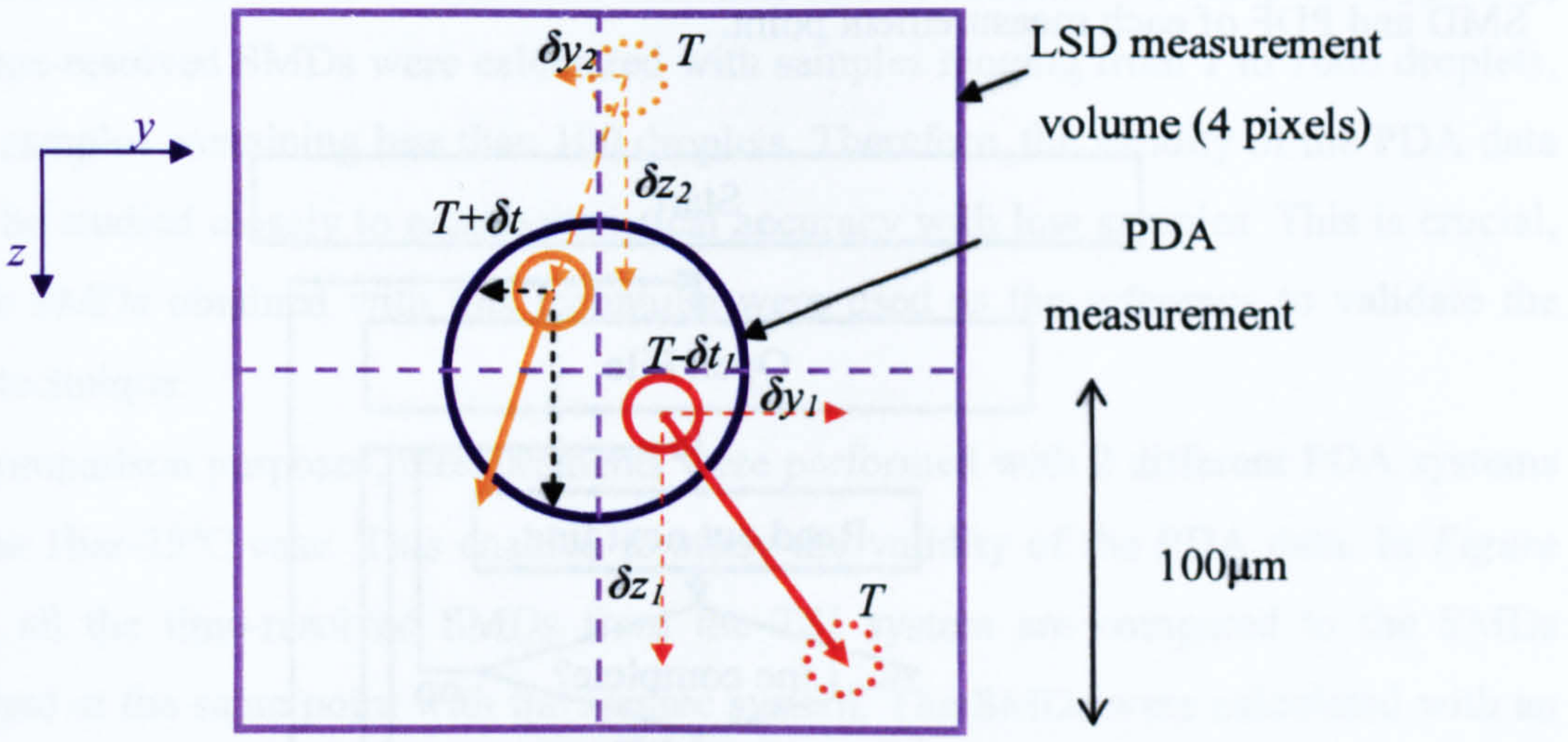

Figure 5-10: Cutaway section of the measurement volumes

However, the distance criterion chosen for the time-resolved data can be an issue. In a highly evaporating environment, or for very small droplets, the diameter may evolve within the allowed displacement. Also, as the sampling size is changed, it is possible that erroneous diameters appear or disappear, thus creating large variations in SMD. For this reason, the SMD data was time-resolved using 3 displacement tolerances: 50, 100 and 150µm. The 100µm displacement was used as the reference, the two others served as indicators of the accuracy/stability of that reference. The variation in SMD was used as a criterion for selecting the final data and was defined as:

$$\Delta\phi = \max\left(\frac{\left|SMD_{50\,\mu m} - SMD_{100\,\mu m}\right|}{SMD_{100\,\mu m}}, \frac{\left|SMD_{150\,\mu m} - SMD_{100\,\mu m}\right|}{SMD_{100\,\mu m}}\right)$$

Equation 5-1

5.3.6. Data processing

A programme was written in C++ in order to extract time-resolved SMD from the PDA data. The programme consists of reading out a line, verifying that the line is valid, and separating it in the 4 parameters: time, vertical speed, horizontal speed and diameter).

The velocity data then allows to check whether the distance travelled between the event and a time of interest is within the distance criteria. If so, the diameter is stacked in an array. At the end of the file, this array then allows the calculation of the time-resolved SMD and PDF of each measurement point.

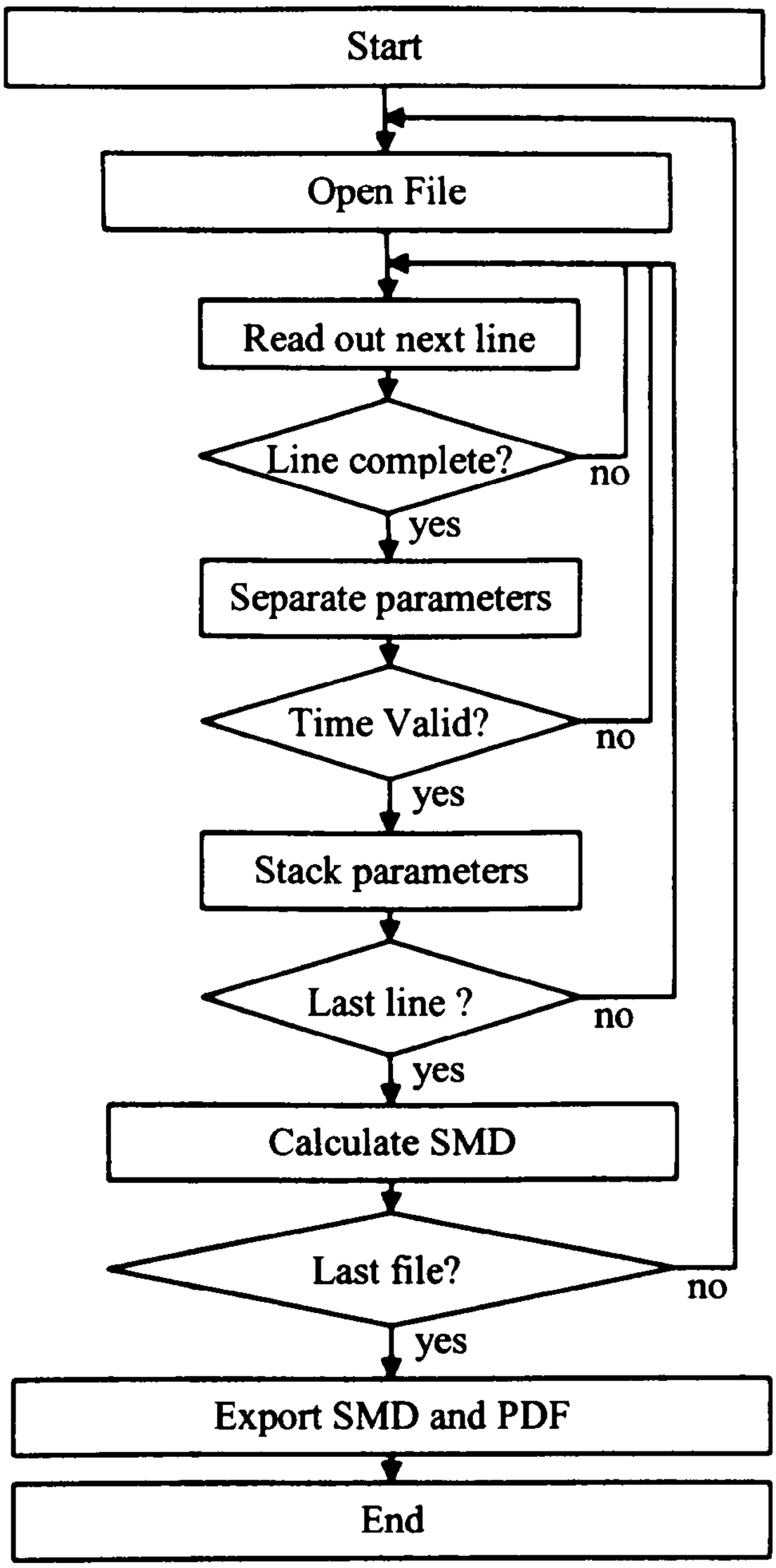

Figure 5-11: Program Structure for PDA data Processing

The SMD values and corresponding sample sizes were transferred to a spread sheet and were placed in a table, representing their position in the half spray (see *Appendix B*).

5.3.7. PDA accuracy

Because the spray was very dense, the validation rate and therefore the number of samples obtained was low. The time selection further reduced the samples. Typically, the time-resolved SMDs were calculated with samples ranging from 1 to 1000 droplets, most samples containing less than 100 droplets. Therefore, the validity of the PDA data must be studied closely to ensure statistical accuracy with low samples. This is crucial, as the SMDs obtained with this technique were used as the reference to validate the LSD technique.

For comparison purposes, measurements were performed with 2 different PDA systems for the 1bar-25°C case. This enabled to study the validity of the PDA data. In *Figure 5-12*, all the time-resolved SMDs from the TSI system are compared to the SMDs obtained at the same point with the Dantec system. The SMDs were calculated with an allowed displacement of 100µm. The diagonal indicates is the $y=x$ line, and the dotted lines above and below indicate +15% and -15% variation respectively. The colours indicate the time ASOI.

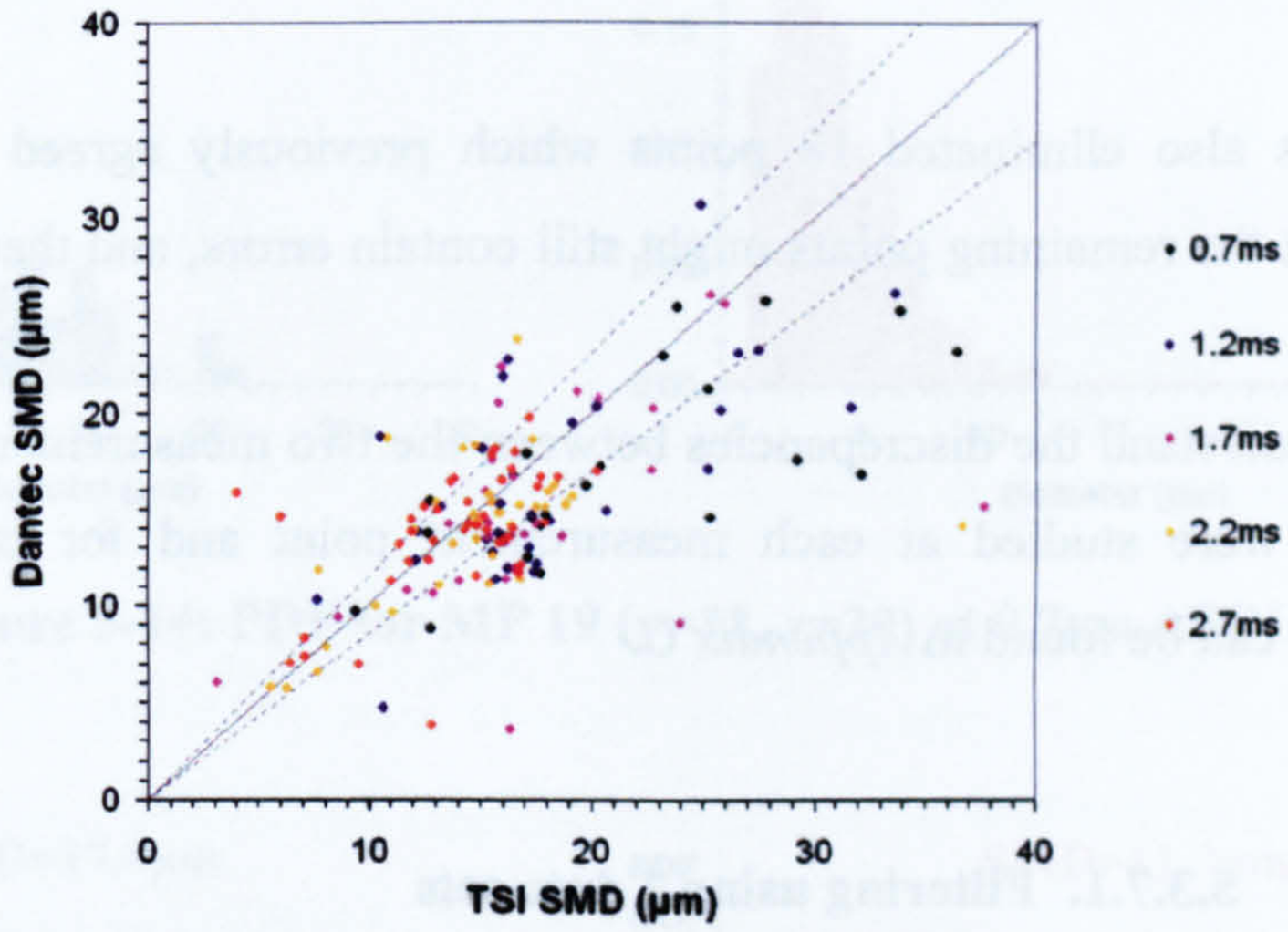

Figure 5-12: TSI-Dantec SMD variations for all measurement points

The comparison shows that out of the 166 points compared, only 75 (~½) agree within 15% variation. This raises 3 issues: is the PDA data reliable? When both TSI and Dantec data are available, can they be filtered to ensure reasonable accuracy? How can one ensure accuracy when only TSI data is available?

By selecting the data where both SMDs showed less than 15% variation for the three distance criteria (i.e. $\Delta\phi$ <15%), most of the points outside the 15% deviation are eliminated (see *Figure 5-13*).

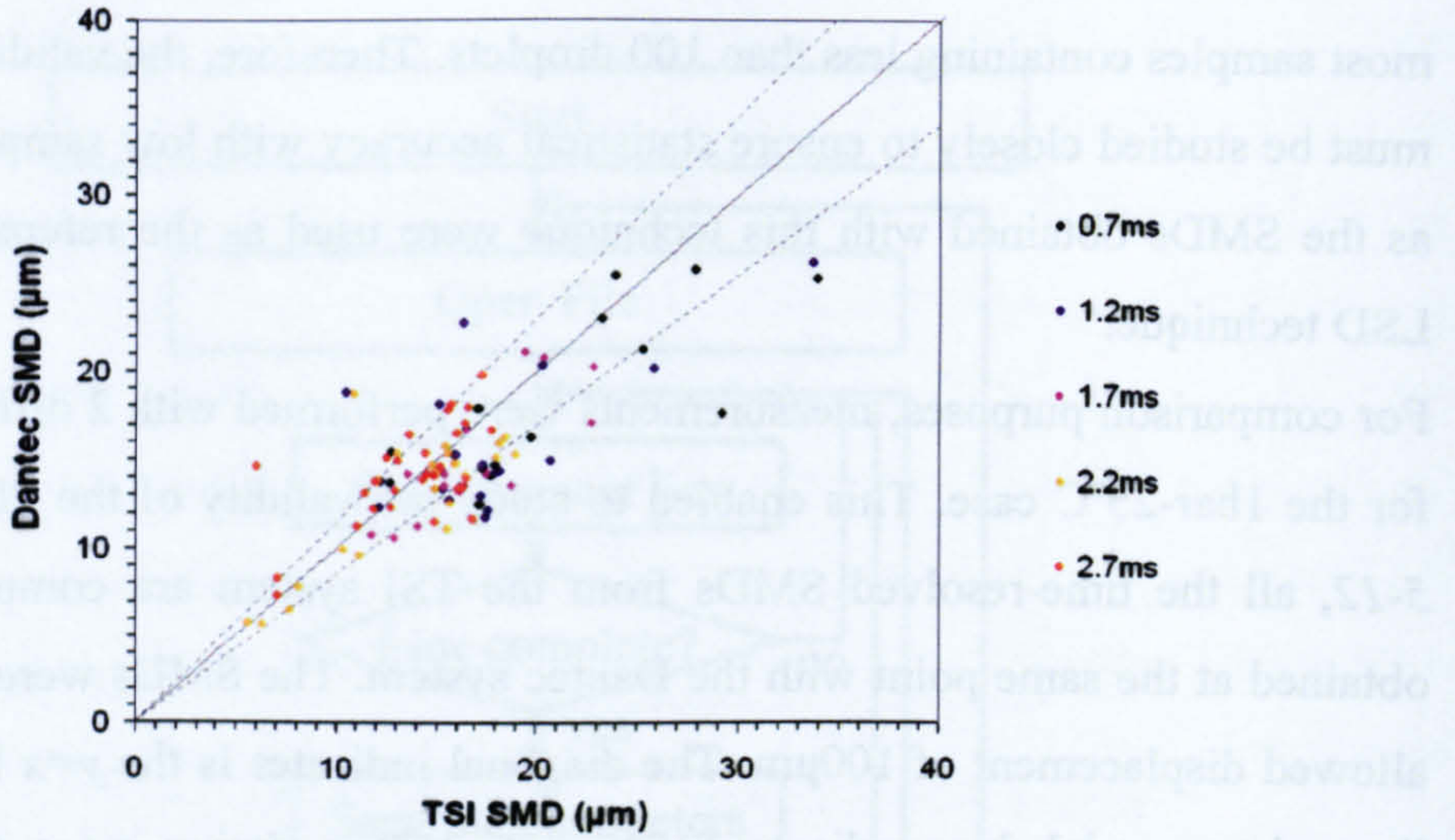

Figure 5-13: TSI-Dantec SMD variations for all measurement points with $\Delta\phi$ <15%

This process also eliminated 18 points which previously agreed within 15%. This suggests that the remaining points might still contain errors, and that further filtering is required.

To better understand the discrepancies between the two measurements, the droplet size distribution were studied at each measurement point and for each timing. These distributions can be found in *Appendix C*.

5.3.7.1. Filtering using 2 data sets

The TSI and Dantec data can be considered reliable if both measurement systems give similar droplet size distributions for the same point. Because of the number of distributions, a study was carried out to determine the parameters which could be used to automatically filter/eliminate the measurements which yielded different size distributions. A few distributions at different measurement points (MP) are represented below to illustrate the different cases encountered. The blue distributions are obtained from TSI data and the red distributions from the Dantec system.

Three types of cases were found:

1. the distributions and SMDs both do not match
2. both distributions and SMDs match
3. the SMDs match but the distributions are different

A variable representing the variation of SMD was defined as:

$$\Delta SMD = \frac{SMD_{Dantec} - SMD_{TSI}}{SMD_{TSI}}$$

Equation 5-2

In case n°1, illustrated by MP 19 (see *Figure 5-14*) and MP 49 (see *Figure 5-15*), the ΔSMD are 31% and 33%. These measurements can be eliminated by setting a maximum allowed value for ΔSMD.

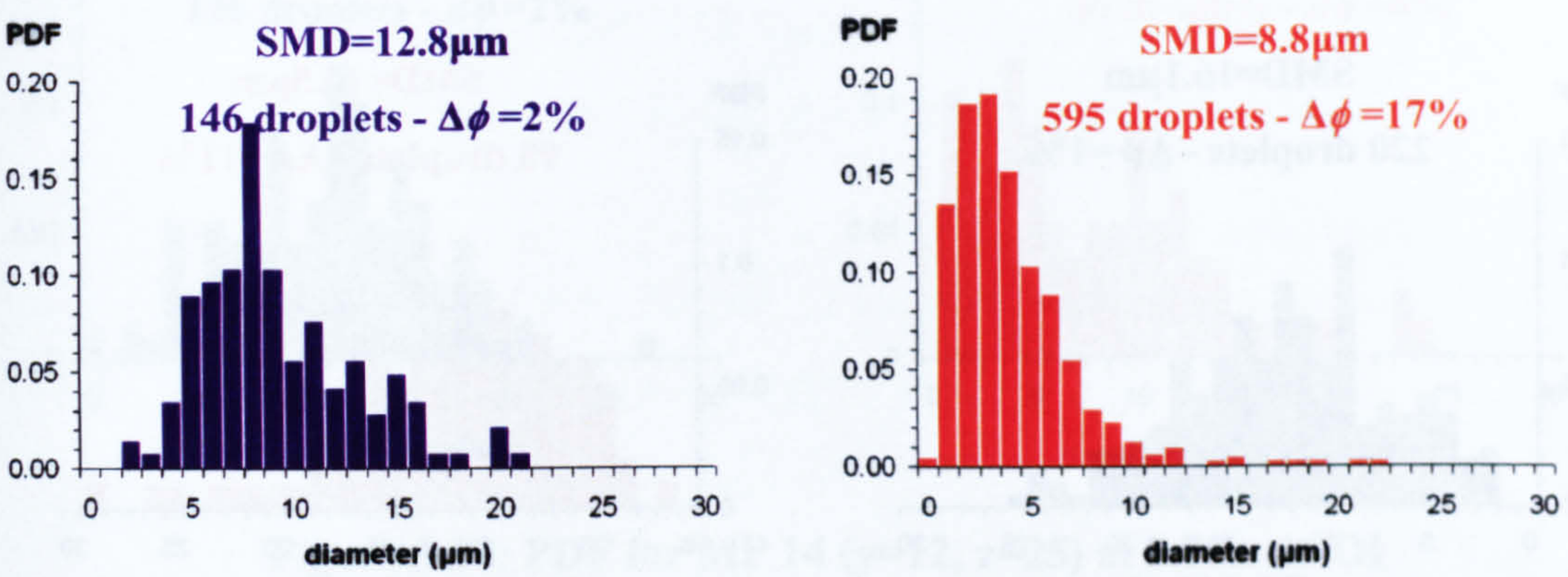

Figure 5-14: PDF for MP 19 (y=12, z=20) at 0.7ms ASOI

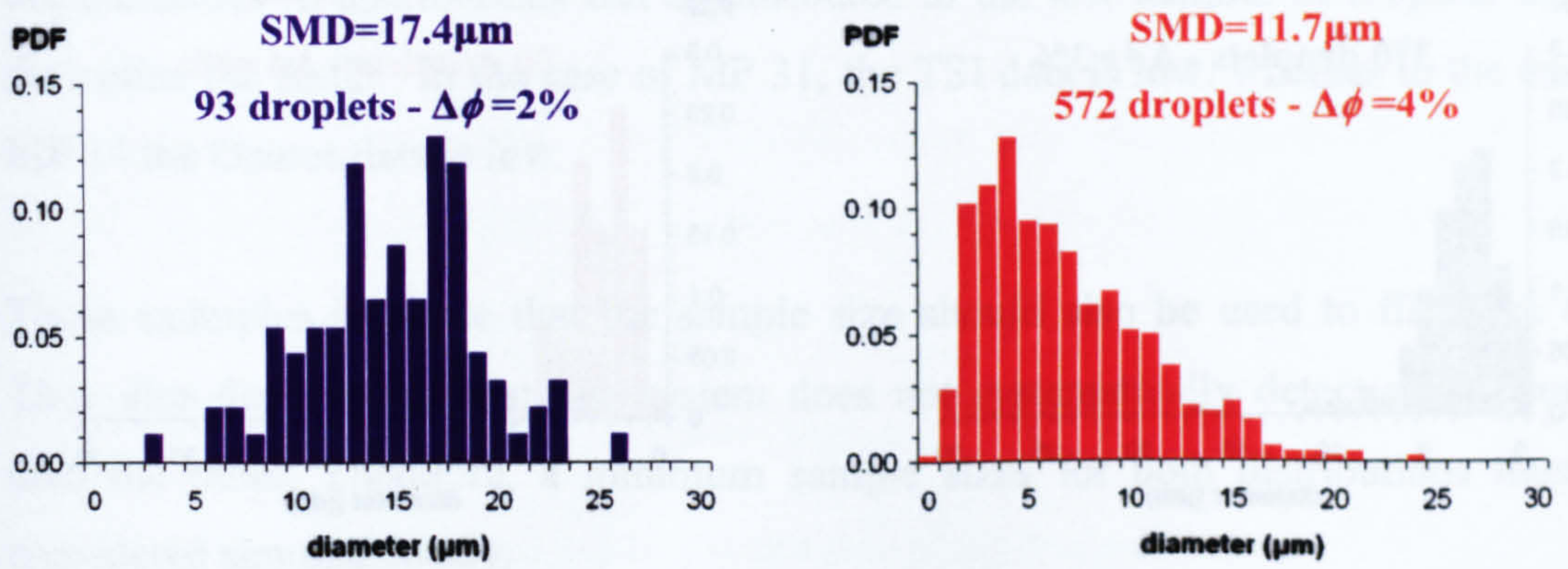

Figure 5-15: PDF for MP 49 (y=16, z=30) at 1.2ms ASOI

An issue arises when the SMDs are similar. For this case, another variable must be used to separate the measurement points with different distributions from those with similar distributions.

It was found that matching SMDs which had both been calculated from higher sample sizes showed similar distributions (see *Figure 5-16*, *Figure 5-17* and *Figure 5-18*).

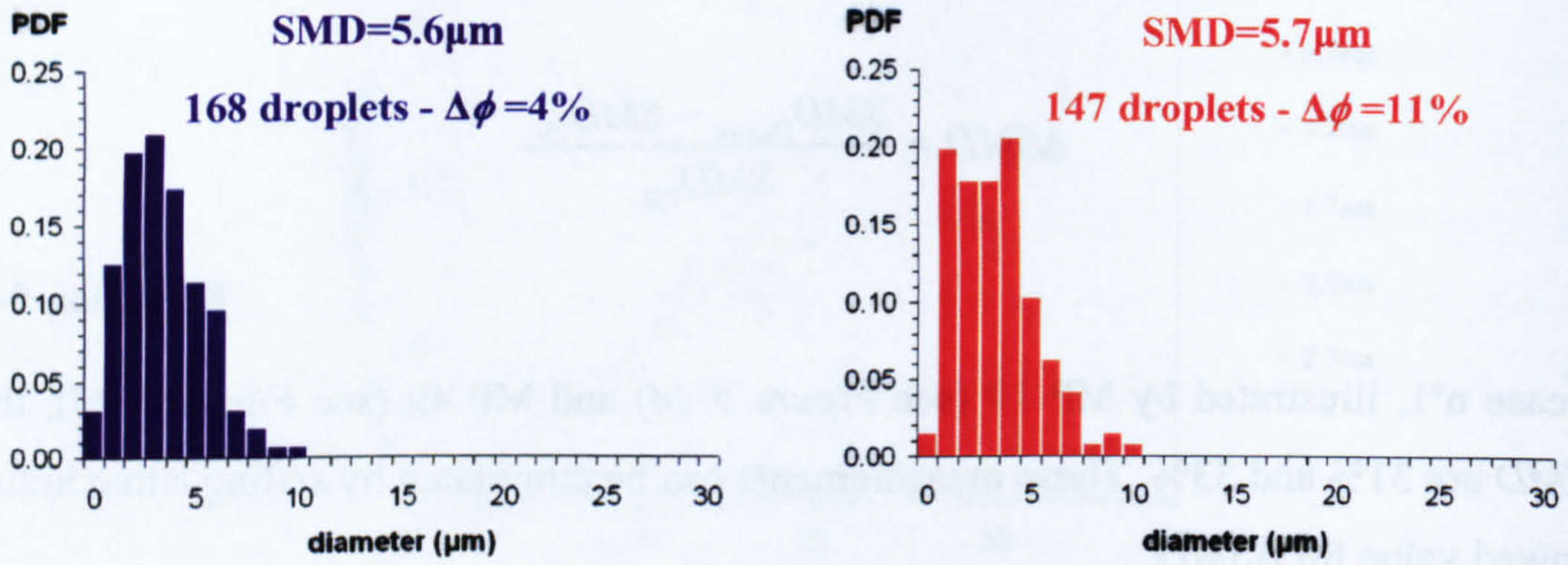

Figure 5-16: PDF for MP 2 (y=0, z=10) at 2.2ms ASOI

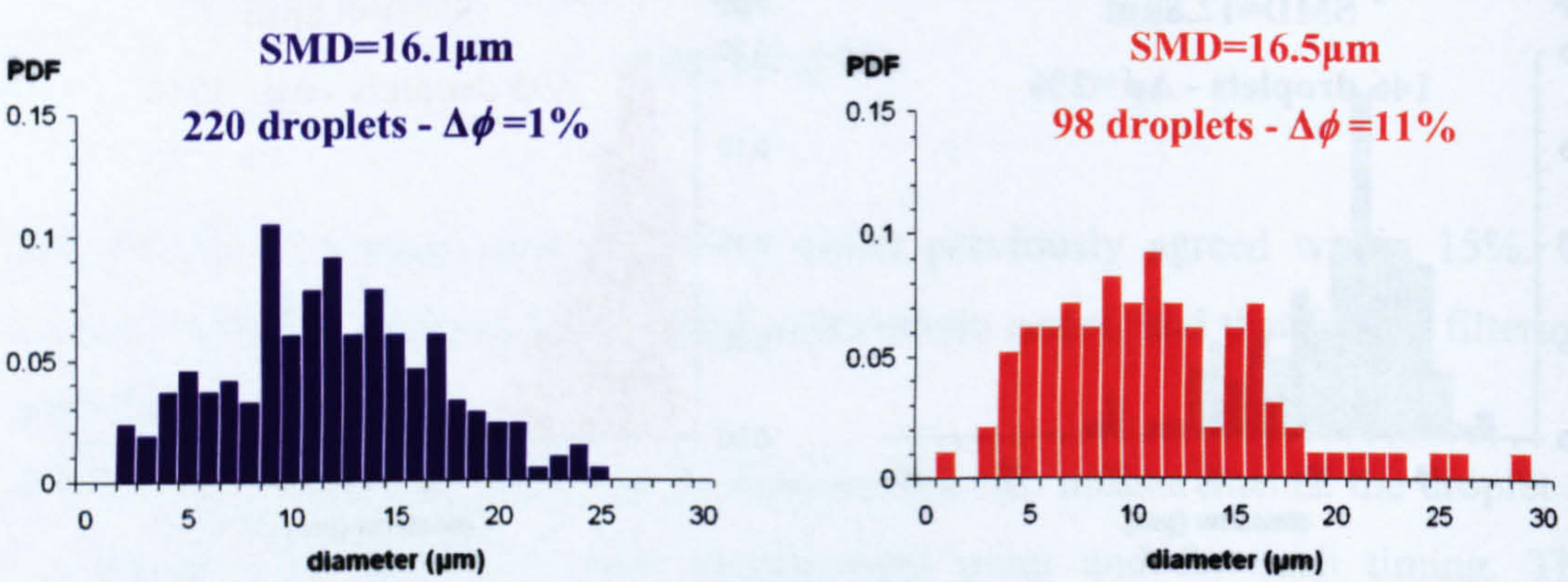

Figure 5-17: PDF for MP 62 (y=8, z=60) at 2.7ms ASOI

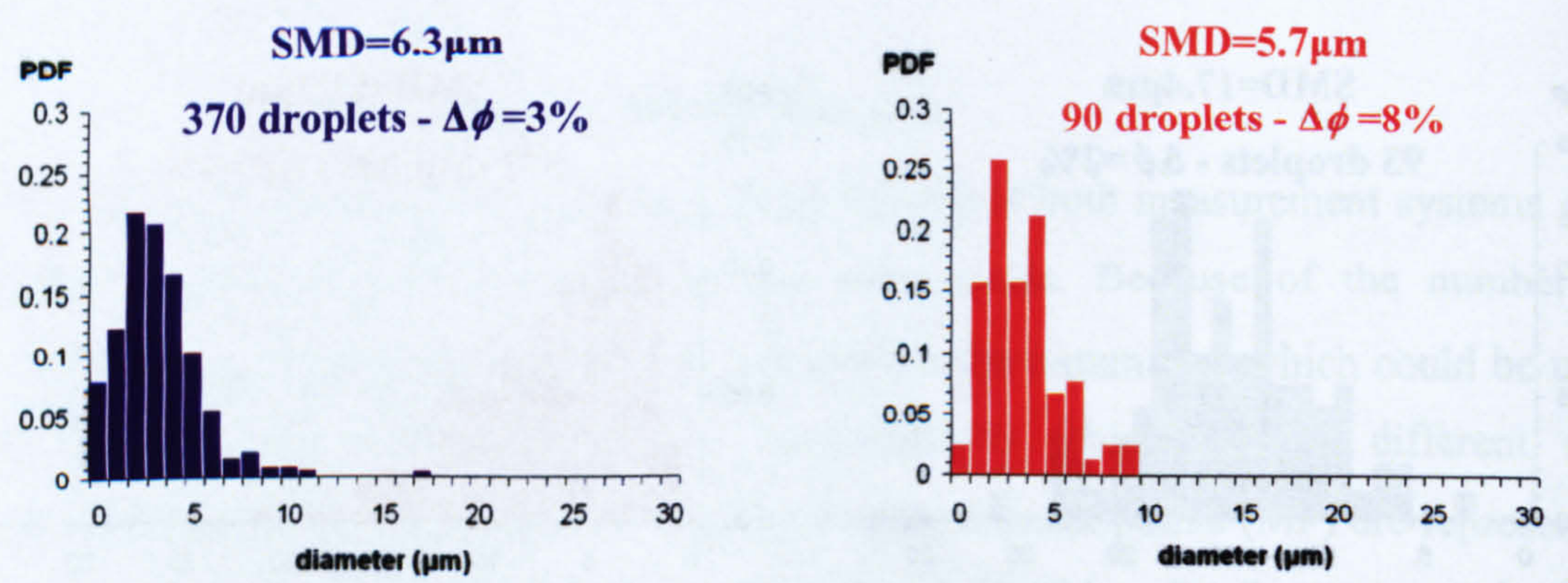

Figure 5-18: PDF for MP 1 (y=0, z=5) at 2.2ms ASOI

On the other hand, when at least one of the two sample sizes was low, the distributions were different (see *Figure 5-19* and *Figure 5-20*).

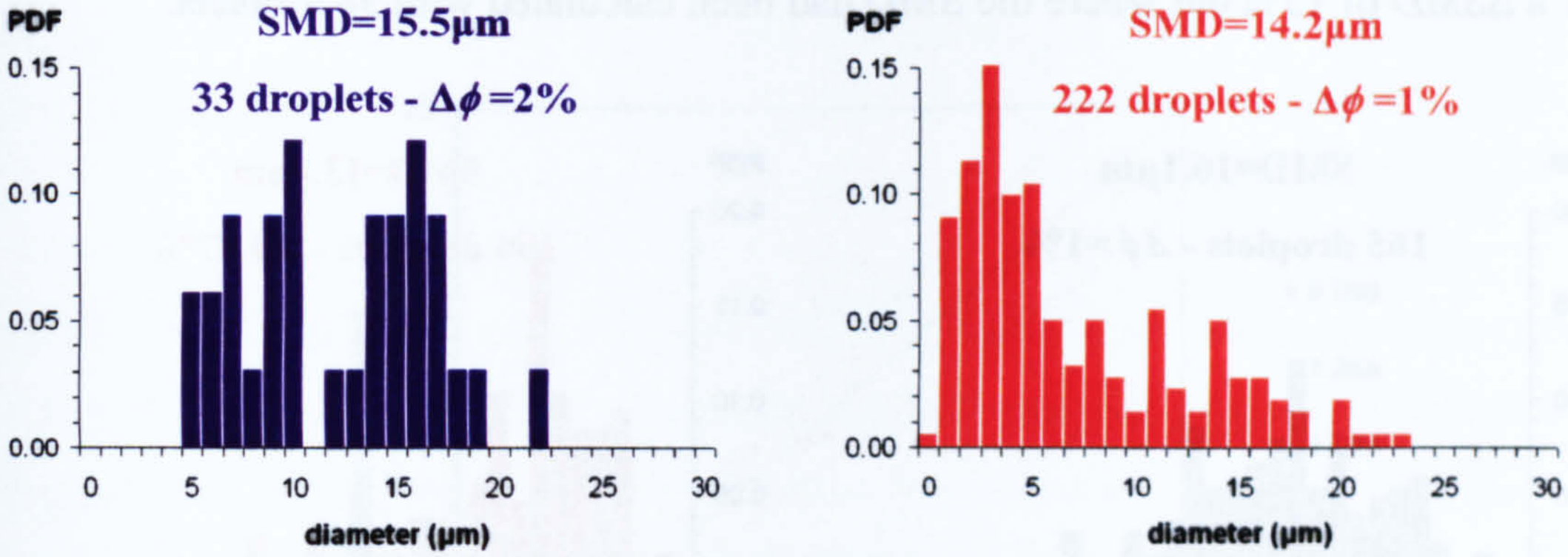

Figure 5-19: PDF for MP 31 (y=12, z=35) at 1.7ms ASOI

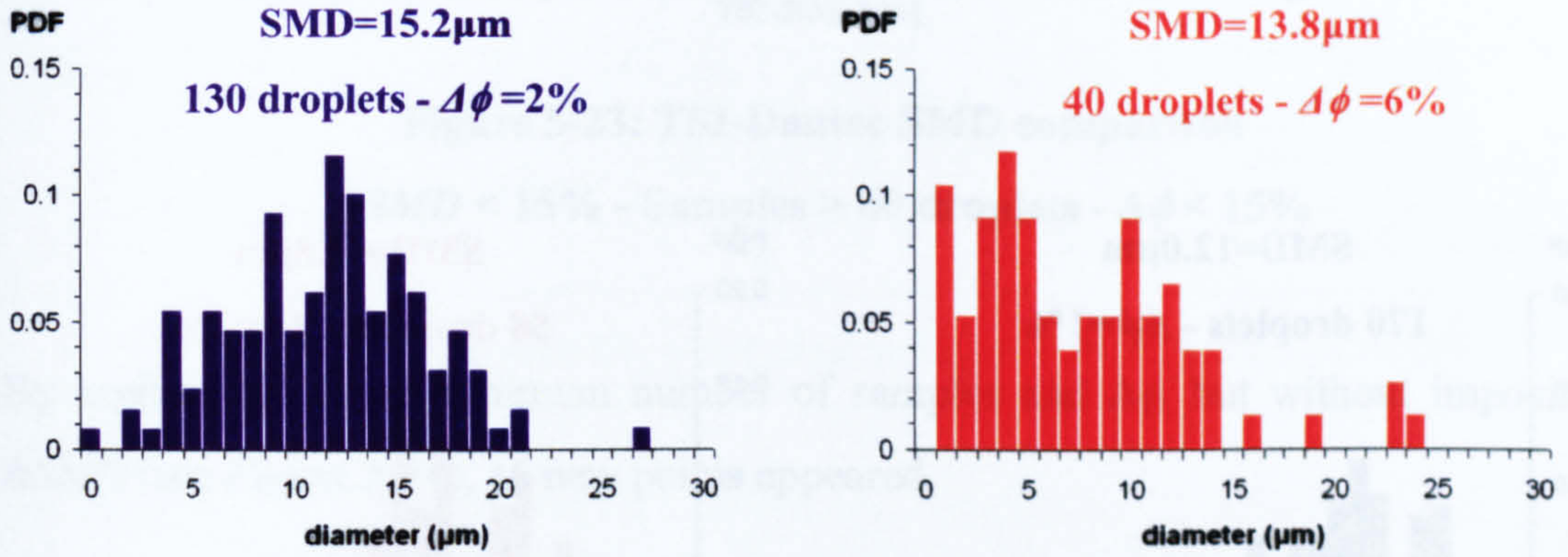

Figure 5-20: PDF for MP 14 (y=12, z=25) at 2.7ms ASOI

For both these cases, the SMDs were similar within 9%, and the $\Delta\phi$ were both low. The dissimilarities in distributions can be attributed to the low number of droplets used to determine the SMD. In the case of MP 31, the TSI data is low, whereas in the case of MP 14 the Dantec data is low.

These examples illustrate that the sample size should also be used to filter the data. They also demonstrate that one system does not systematically detect more droplets than the other. Therefore, a minimum sample sizes for both distributions must be considered simultaneously.

Measurement point MP 60 (see *Figure 5-21*) showed the case where the distributions were different for high sample sizes (>100) with a ΔSMD of 17%.

On the other hand, MP 12 (see *Figure 5-22*) showed the case of different distributions for a ΔSMD of 15% but where the SMD had been calculated with 58 droplets.

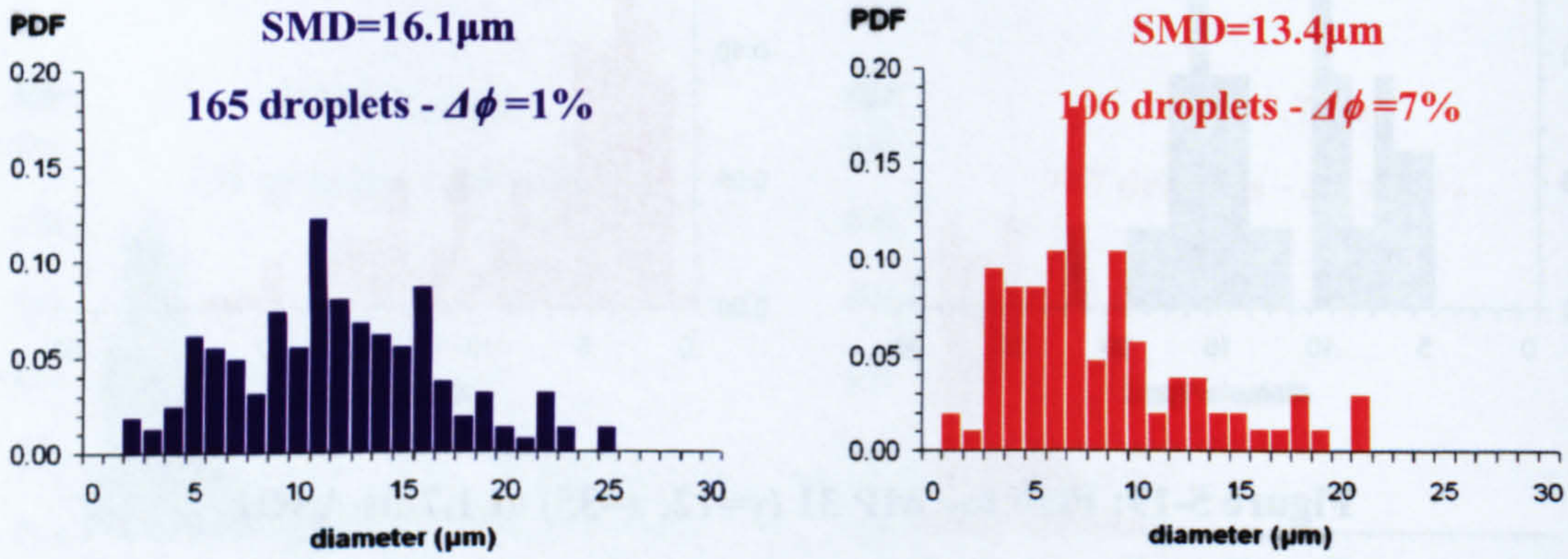

Figure 5-21: PDF for MP 60 (y=12, z=55) at 2.7ms ASOI

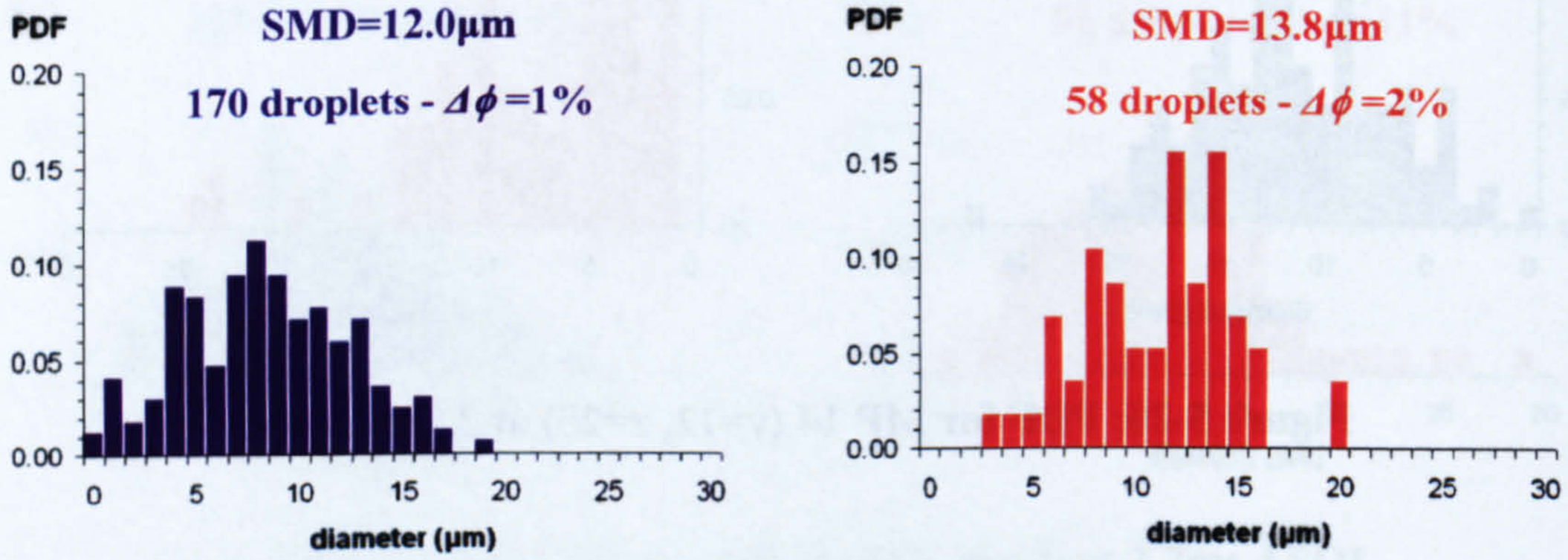

Figure 5-22: PDF for MP 12 (y=4, z=25) at 2.7ms ASOI

By setting the highest allowable value of ΔSMD and $\Delta\phi$ to 15% and the minimum sample size to 60 droplets, the remaining data (21 points) had matching SMDs and distributions.

5.3.7.2. Filtering using 1 data set

Figure 5-23 illustrates the PDA points validated with $\Delta SMD < 15\%$, $\Delta\phi < 15\%$ and a minimum sample size of 60 droplets.

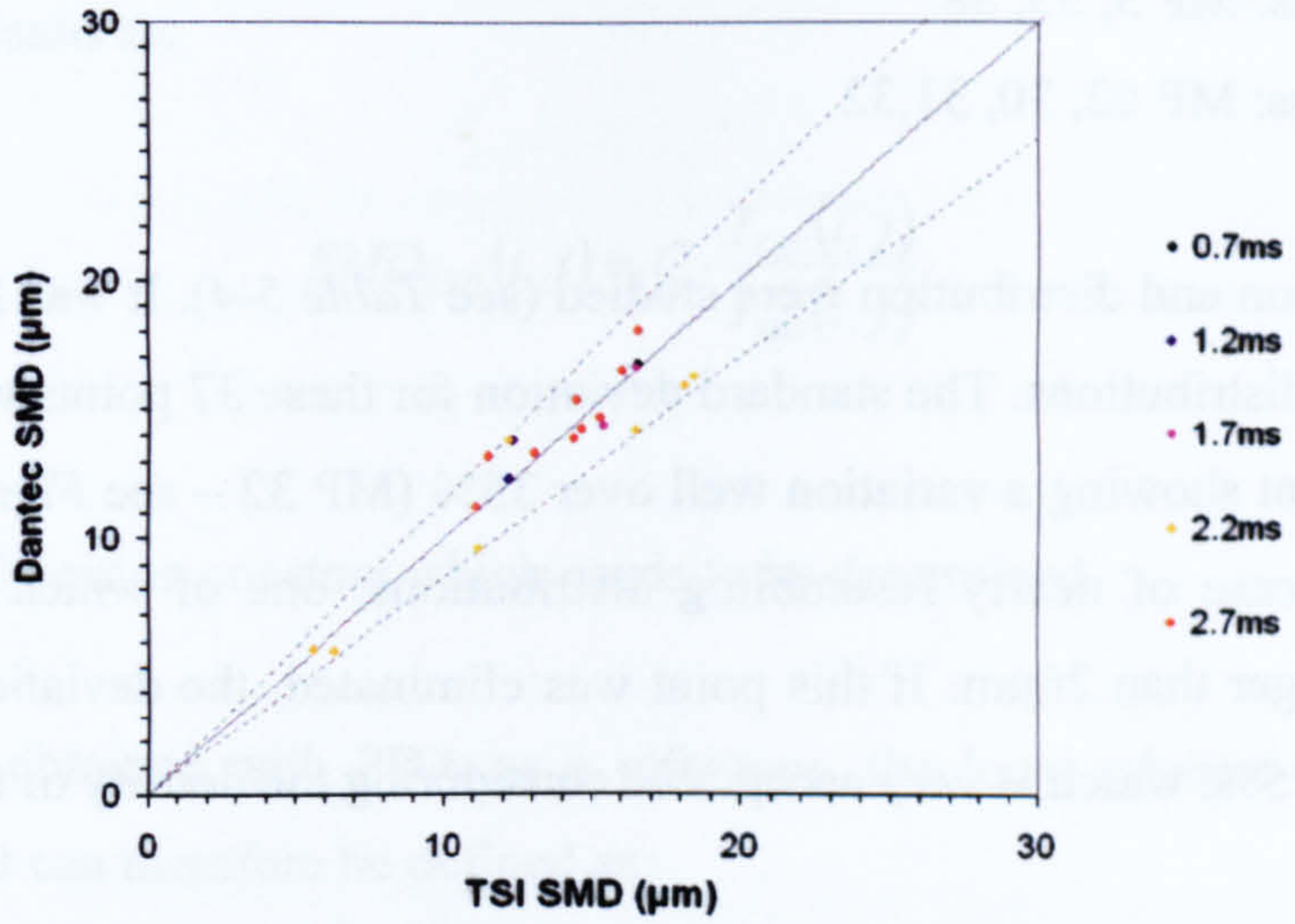

Figure 5-23: TSI-Dantec SMD comparison

$\Delta SMD < 15\%$ - Samples > 60 droplets - $\Delta\phi < 15\%$

By keeping the same minimum number of samples and $\Delta\phi$, but without imposing a ΔSMD (see *Figure 5-24*), 16 new points appeared.

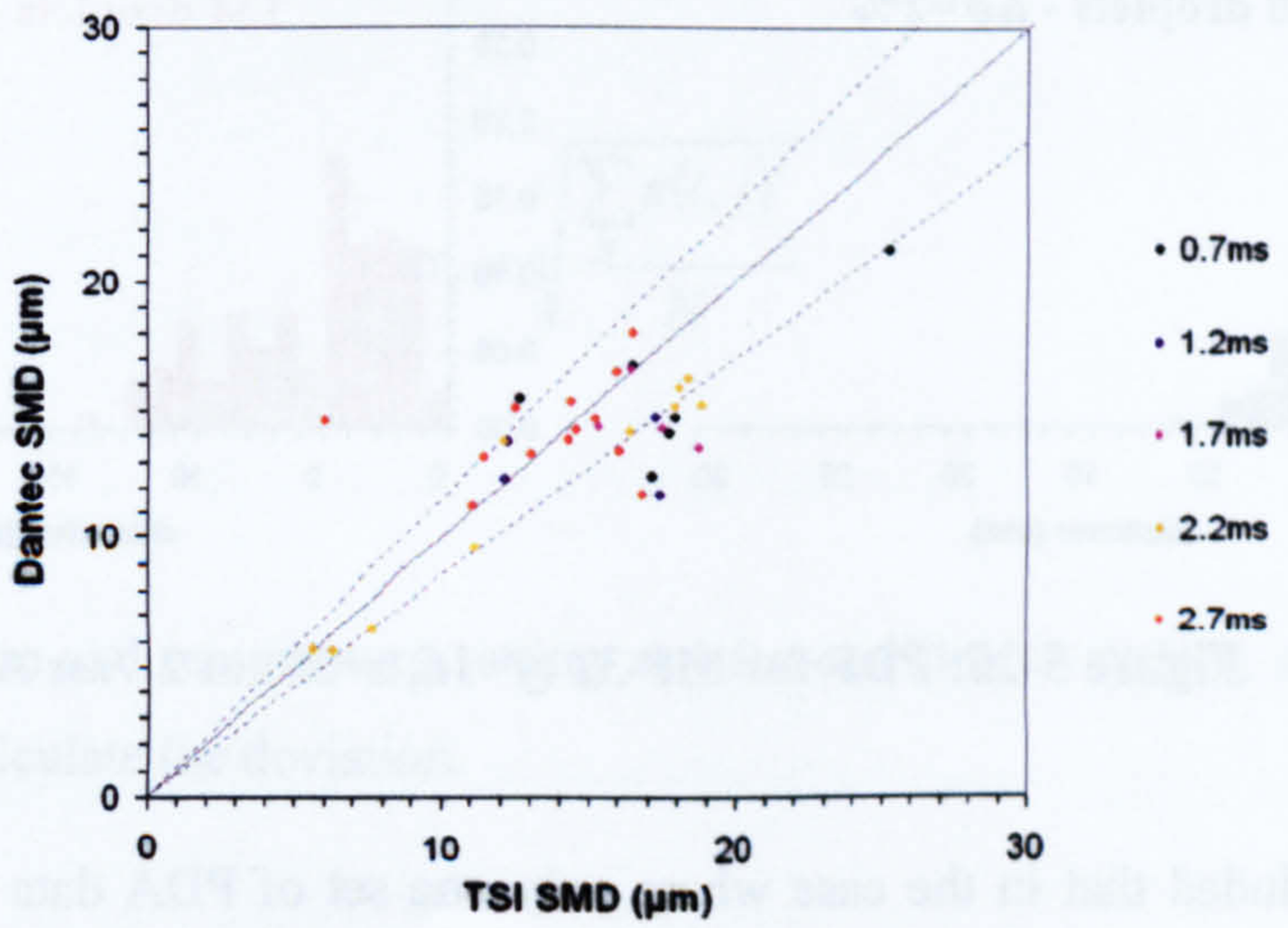

Figure 5-24: TSI-Dantec SMD comparison

Samples > 60 droplets - $\Delta\phi < 15\%$

These points were identified as:

- 0.7ms: MP 29, 34, 23, 24, 14
- 1.2ms: MP 30, 49
- 1.7ms: MP 35, 36,
- 2.2ms: MP 3, 55, 58
- 2.7ms: MP 62, 30, 31,32

Their variation and distribution were studied (see *Table 5-4*). It was found that 78% had resembling distributions. The standard deviation for these 37 points was 27%. However, the only point showing a variation well over 35% (MP 32 – see *Figure 5-25*) displayed the unique case of nearly resembling distributions, one of which contained isolated samples bigger than 26µm. If this point was eliminated, the deviation of the 36 points dropped to 15%, which is very acceptable considering the density of the spray.

ΔSMD	0-15%	15-20%	20-25%	25-35%	30-35%	+35%
Number of points	21	8	3	2	2	1
Matching Distribution	21	4	3	0	1	?

Table 5-4: PDA data points for Samples > 60 droplets and $\Delta\phi < 15\%$

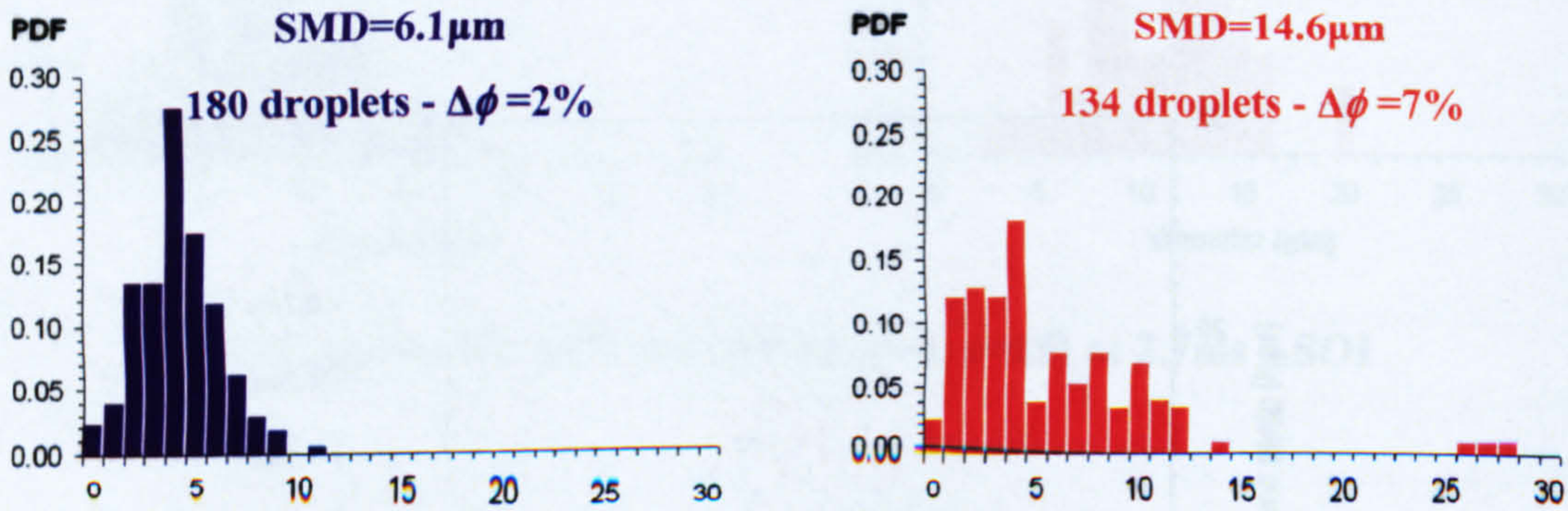

Figure 5-25: PDF for MP 32 (y=16, z=35) at 2.7ms ASOI

It was concluded that in the case where only one set of PDA data was available, the SMDs selected as references would be the ones calculated with a minimum of 60 droplets, and with a $\Delta\phi < 15\%$.

5.4. LSD - PDA Comparison

5.4.1. Calibration Constant

Theoretically, the division of the LIF and Mie scatter intensity is proportional to SMD. This can be expressed as:

$$SMD_{LSD}(i,j) = C \cdot \frac{I_{LIF}(i,j)}{I_{Mie}(i,j)}$$

Equation 5-3

where C is the calibration constant which needs to be determined.

Using the SMD obtained with PDA as a reference, the local relative error in SMD measured by LSD can therefore be defined as:

$$\varepsilon(i,j) = \frac{SMD_{LSD}(i,j) - SMD_{PDA}(i,j)}{SMD_{PDA}(i,j)}$$

Equation 5-4

For N points, the most appropriate calibration constant is obtained by minimising the relative errors. This can be done by minimising the error's deviation from zero:

$$\sigma_{\varepsilon} = \sqrt{\frac{\sum_{N} \varepsilon(i,j)^2}{N}}$$

Equation 5-5

For every pressure and temperature setting and for each tracer system, a spread sheet was created to calculate the deviation.

The sheets consisted of:

- SMD and sample size for a distance criteria of 50μm from TSI data
- SMD and sample size for a distance criteria of 100μm from TSI data
- SMD and sample size for a distance criteria of 150μm from TSI data
- SMD and sample size for a distance criteria of 50μm from Dantec data (only at 1bar-25°C)
- SMD and sample size for a distance criteria of 100μm from Dantec data (only at 1bar-25°C)
- SMD and sample size for a distance criteria of 150μm from Dantec data (only at 1bar-25°C)
- LIF data
- Mie scatter data

The spreadsheet was structured so that the data could be filtered by selecting

- the minimum number of droplets in the PDA samples
- a maximum value for ΔSMD (only at 1bar-25°C)
- a maximum value for $\Delta\phi$

For the 1bar-25°C case, the reference SMDs were calculated by averaging the SMDs obtained from the TSI and Dantec systems:

$$SMD_{PDA}(i,j) = \frac{SMD_{TSI}(i,j) + SMD_{Dantec}(i,j)}{2}$$

Equation 5-6

For a given calibration constant, the spread sheet would give:

- The deviation (σ_ε)
- The number of points compared
- A plot of the filtered SMDs obtained with PDA versus the SMDs obtained with the LSD technique.

Calibration constants were determined by minimising the deviation.

For a given tracer system, the calibration constant should be constant. Due to the confidence in the PDA data for the 1bar-25°C case, it was obvious that the calibration constant should be determined using the LSD data obtained in the 1bar-25°C case.

Tracer composition	Calibration Constant (C)	PDA-LSD Deviation (σ_e)
2.0% Pentanone	18	25%
1.0% Pentanone 1.0% Hexanone	23	23%
0.5% Pentanone 1.5% Hexanone	34	22%
2.0% Hexanone	27	26%
2.0% TEA 3.4% Benzene	78	32%

Table 5-5: Calibration Constant for the different tracer systems

5.4.2. Results

The results are presented as a comparison of the SMD obtained from the PDA data plotted against the SMD obtained with the LSD technique. The continuous grey line represents the $y=x$ line (i.e. where PDA and LSD agree). The doted lines around the grey line are variations. In the 1 bar-25°C case, these lines represent ±15%. For all other cases, they represent ±20%.

The colours indicate the time ASOI.

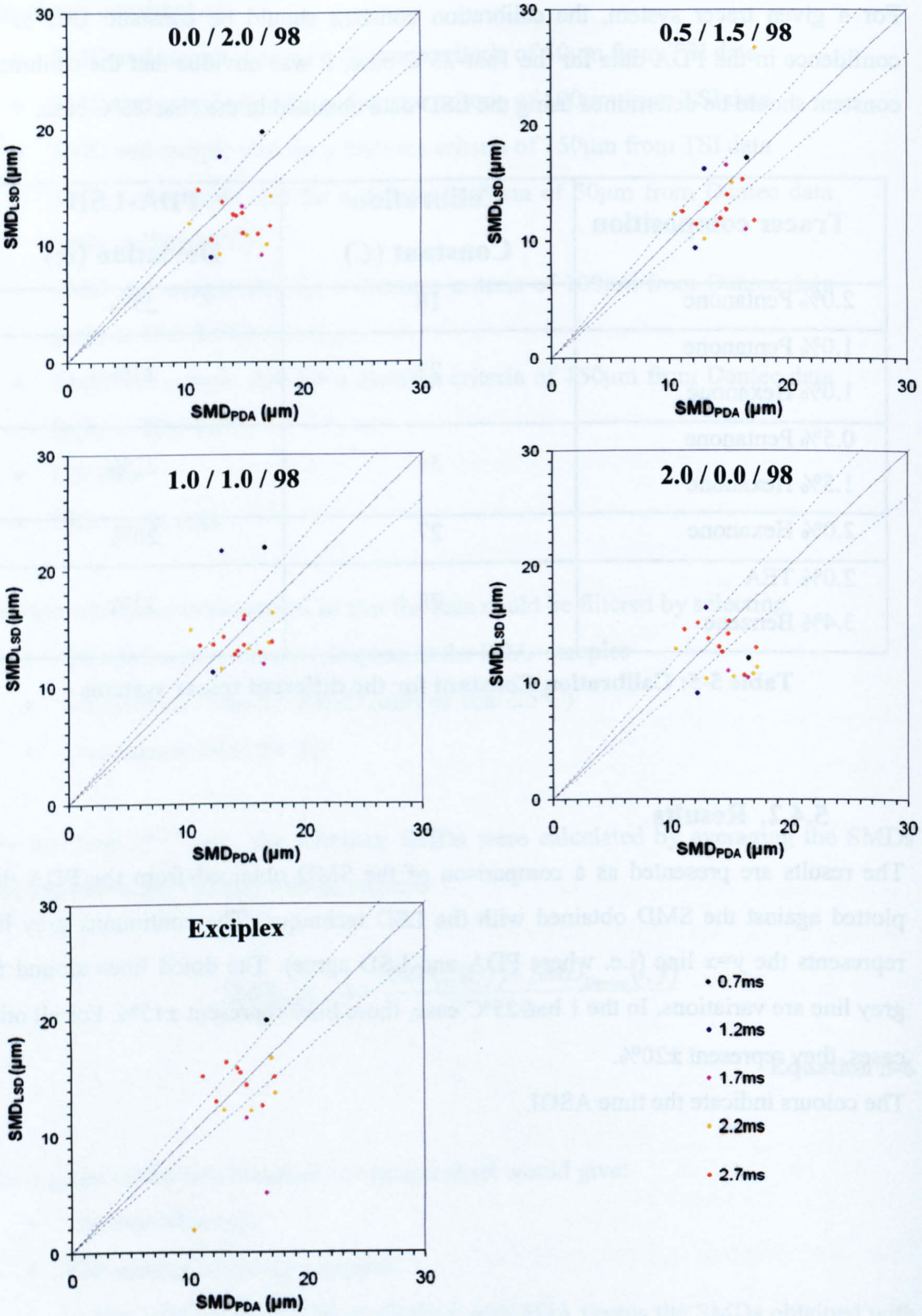

Figure 5-26: PDA-LSD comparison at 1bar – 25°C

x / *y* / *z* ⇔ *x*% 3-Pentanone – *y*% 2-Hexanone – *z*% Iso-Octane

Exciplex ⇔ 2% TEA – 3.4% Benzene – 94.6% Iso-Octane

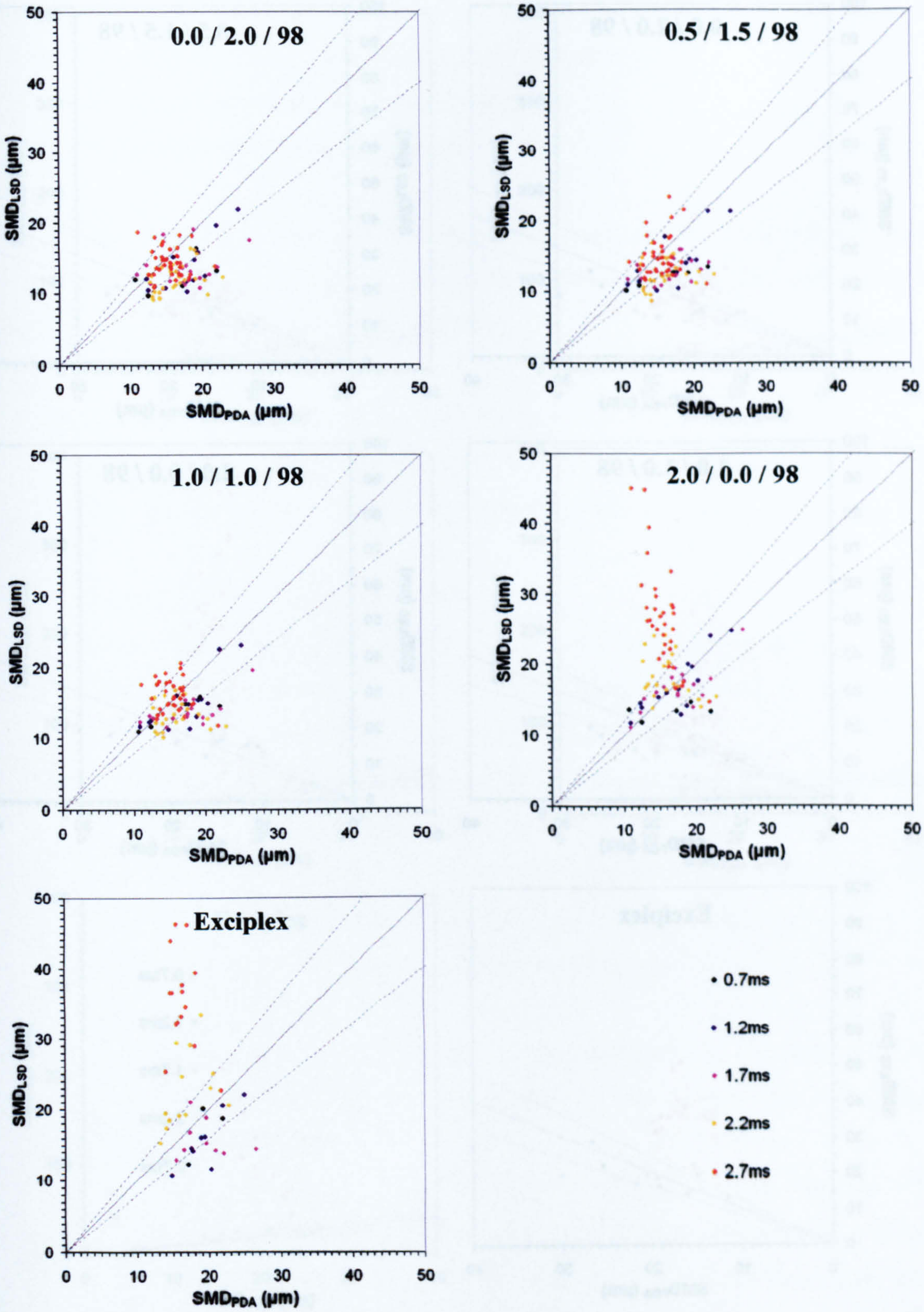

Figure 5-27: PDA-LSD comparison at 3bar – 135°C

$x / y / z$ ⇔ x% 3-Pentanone – y% 2-Hexanone – z% Iso-Octane

Exciplex ⇔ 2% TEA – 3.4% Benzene – 94.6% Iso-Octane

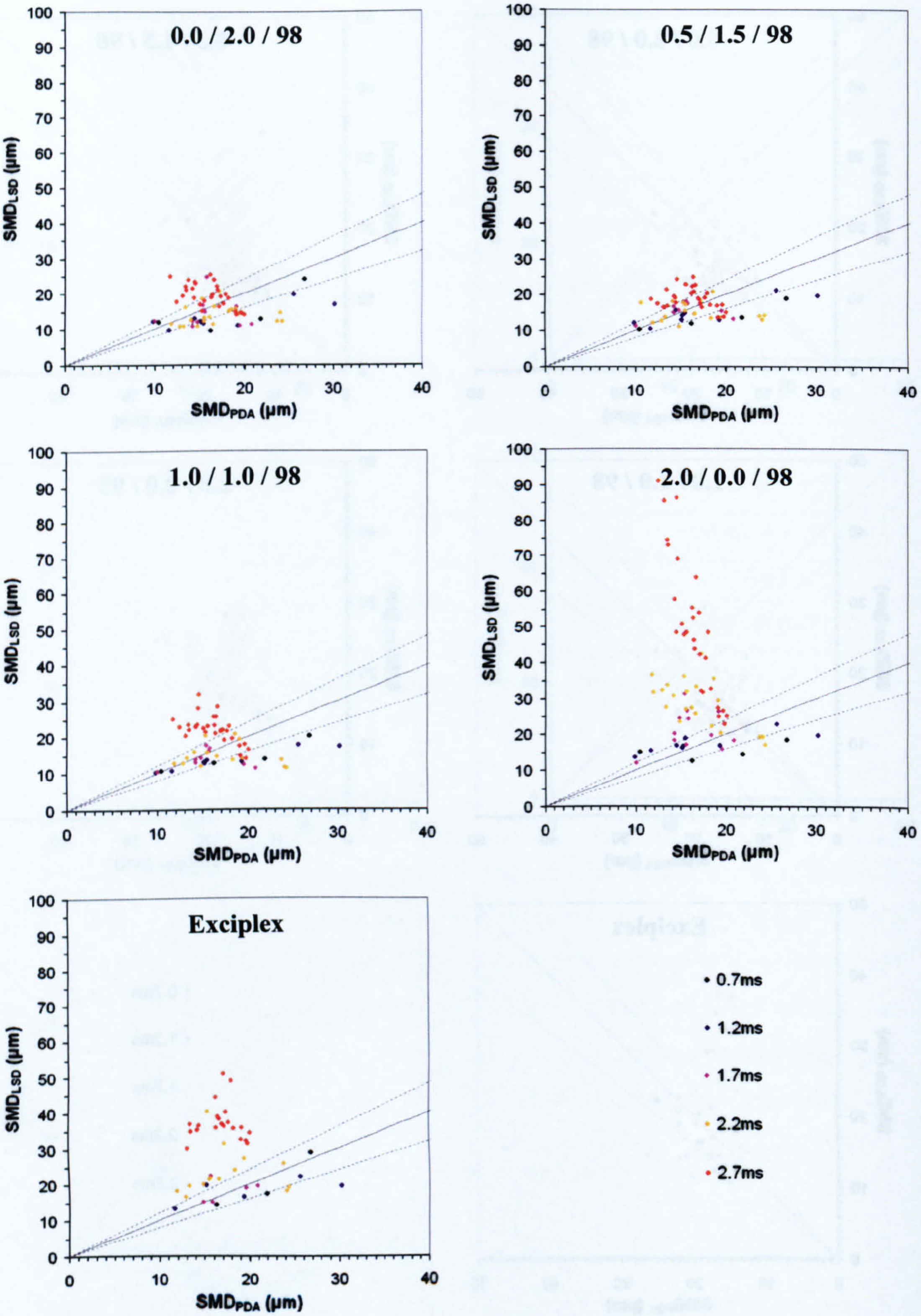

Figure 5-28: PDA-LSD comparison at 5bar – 195°C

x / *y* / *z* ⇔ *x*% 3-Pentanone – *y*% 2-Hexanone – *z*% Iso-Octane

Exciplex ⇔ 2% TEA – 3.4% Benzene – 94.6% Iso-Octane

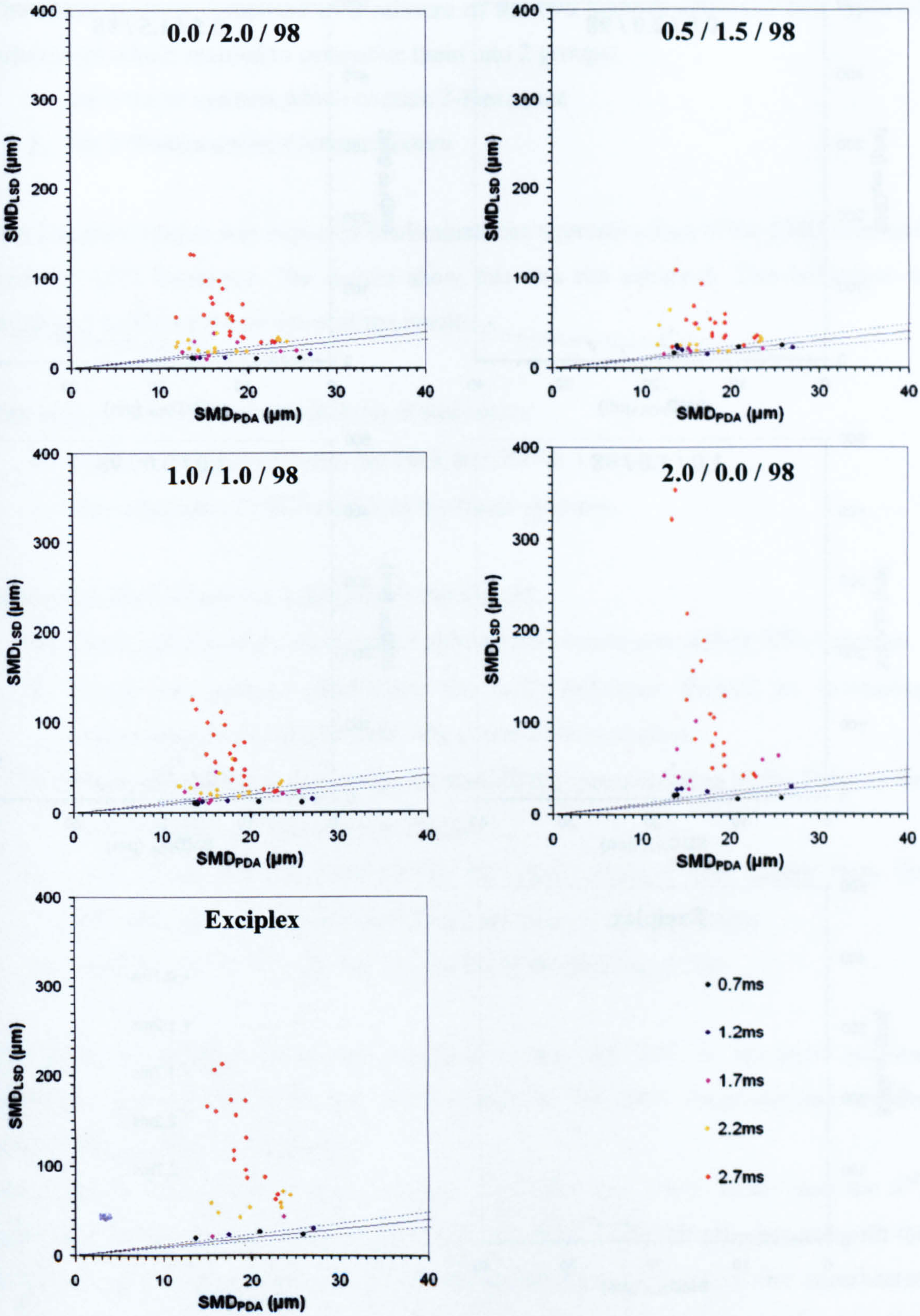

Figure 5-29: PDA-LSD comparison at 10bar – 295°C

x / y / z ⇔ x% 3-Pentanone – y% 2-Hexanone – z% Iso-Octane

Exciplex ⇔ 2% TEA – 3.4% Benzene – 94.6% Iso-Octane

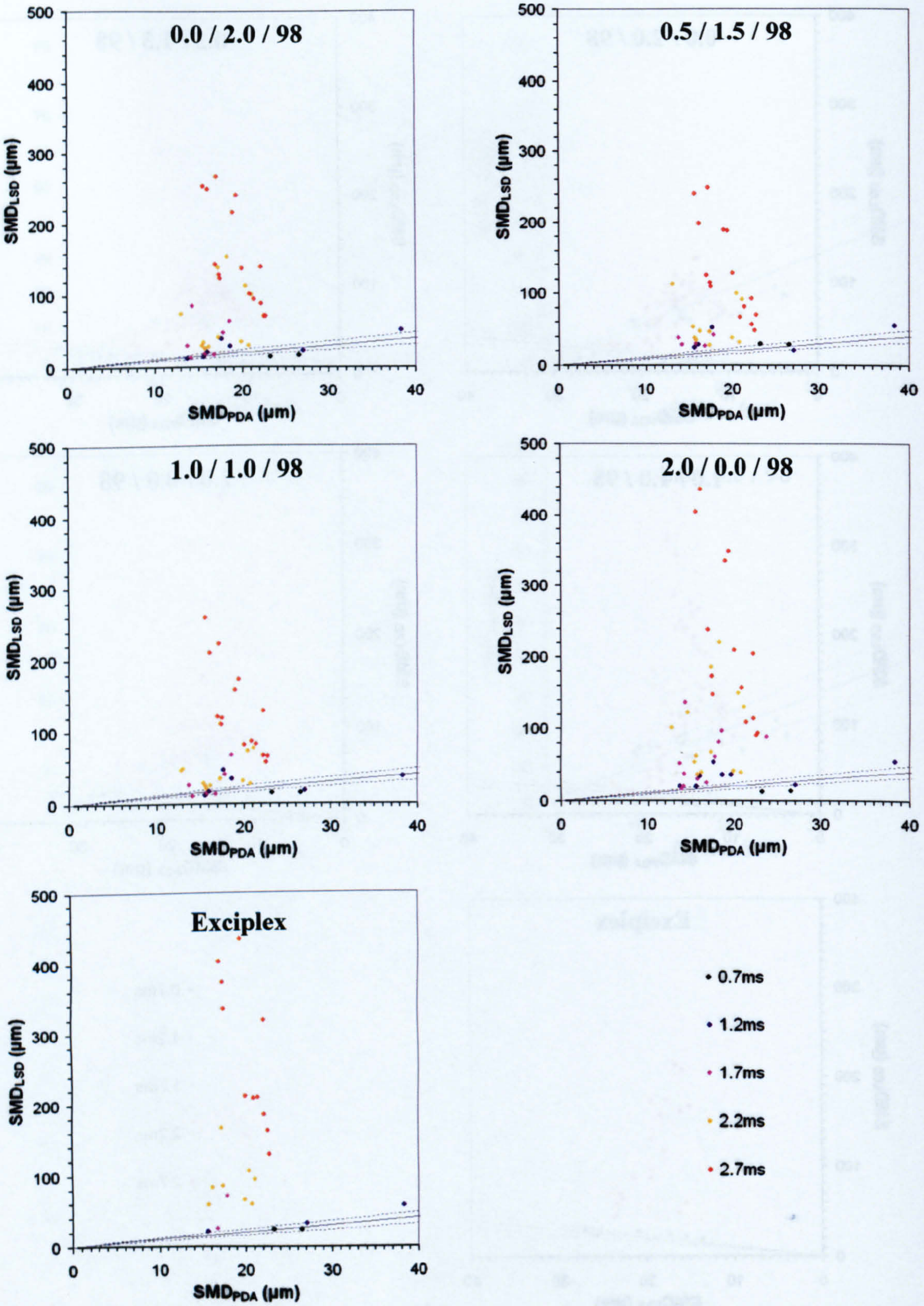

Figure 5-30: PDA-LSD comparison at 15bar – 360°C

x / *y* / *z* ⇔ *x*% 3-Pentanone – *y*% 2-Hexanone – *z*% Iso-Octane

Exciplex ⇔ 2% TEA – 3.4% Benzene – 94.6% Iso-Octane

The tracer systems composed of a mixture of the two ketones displayed two types of behaviours which enabled to categorise them into 2 groups:

1. the 3 tracer systems which contain 2-Hexanone
2. the 3-Pentanone/Iso-Octane mixture

The Exciplex system was expected to eliminate the overestimation of the SMD obtained with the LSD technique. The results show this was not achieved. This behaviour is explained further in the analysis of the results.

The analysis is carried out by looking at two issues:

- the discrepancies between the PDA and the LSD results
- the variations of LSD relative to the tracer systems.

Generally, the 5 following behaviours were noticed:

- Good agreement for all tracers at atmospheric conditions, within 30% variation.
- Above atmospheric conditions, the LSD technique showed an increasing overestimation of the SMD for later stages of the injection.
- The LSD technique showed an increase of the overestimation of the SMD as the environment became more superheated
- From 3bar-135°C to 10bar-295°C, the SMD obtained were higher from the Exciplex and 3-Pentanone/Iso-Octane mixtures at the later stages
- At 15bar and 360°C, the overestimation of the SMD level out.

For all tracer mixtures, the results obtained at 1bar and 25°C do not show extreme variations between the PDA and LSD technique. The best tracer systems are the 1.0/1.0/98 and 0.5/1.5/98 mixtures.

At 3bar and 135°C, the 1st group matches the PDA data much better than the 2nd, especially in the later phases of the injection. The best results are still obtained with the 1.0/1.0/98 and 0.5/1.5/98 mixtures. As the conditions evolve toward the superheated regime, the discrepancies between PDA and LSD results worsen as the injection progresses. Also, for the 5bar – 195°C and 10bar – 295°C cases, the variations in SMD between group 1 and 2 increase. However, at 15bar and 360°C, all systems show the same order of variation.

5.5. Analysis

The discrepancies between the results obtained with the LSD technique and the PDA technique can be caused by three factors:

- The LIF signal
- The Mie scatter signal
- The PDA data

The variation of LSD data relative to the different mixtures can only be explained by the LIF or Mie scatter signals. Because the tracer concentrations in Iso-Octane were very weak (only a total of 2% for the 3-Pentanone / 2-Hexanone mixtures), the spray (i.e. the droplets' evolution) was expected to be independent of the fuel mixture. Therefore the variation in SMD from one mixture to another can be attributed predominantly to the fluorescence.

To better understand these variations in fluorescence, 3 issues must be examined:

- fluorescence yield
- vapour phase contribution to the LIF signal
- evaporation regime

5.5.1. Fluorescence yield

The fluorescence is proportional to the amount of tracer and also to the fluorescence yield. The behaviour of 3-Pentanone's fluorescence in various environments is well documented for several UV excitation wavelengths (Wolff et al. (1995), Grossman et al. (1996), Fujikawa et al. (1997), Ossler and Aldén (1997), Koch and Hanson (2003) - see *Figure 5-31*).

However, 2-Hexanone's fluorescence behaviour is not documented. Han and Steeper (2002) have also looked at mixtures of ketones (3-Pentanone and 3-Hexanone) to produce co-evaporating tracer systems. They studied the fluorescence of two tracer systems for a 266nm excitation wavelength and found that the normalised fluorescence of the mixture containing only 3-Pentanone decreased less than the fluorescence of the tracer system containing a mixture of the two ketones (see *Figure 5-32*). This suggests that the fluorescence of 3-Hexanone decreases more with temperature than with 3-Pentanone. The same can be assumed between 2-Hexanone and 3-Pentanone.

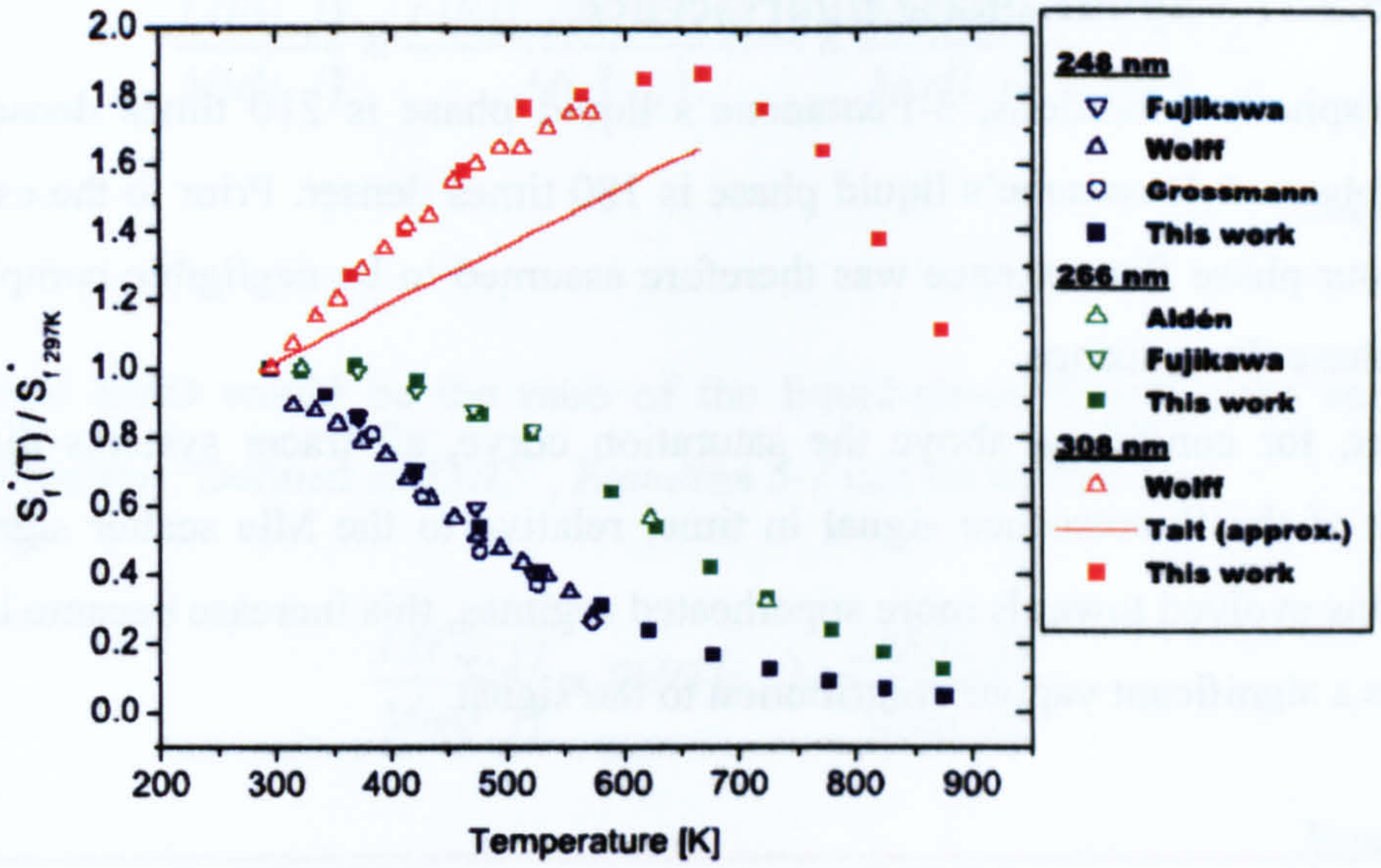

Figure 5-31: Temperature dependence of 3-Pentanone Fluorescence in atmospheric Nitrogen - Koch and Hanson (2003)

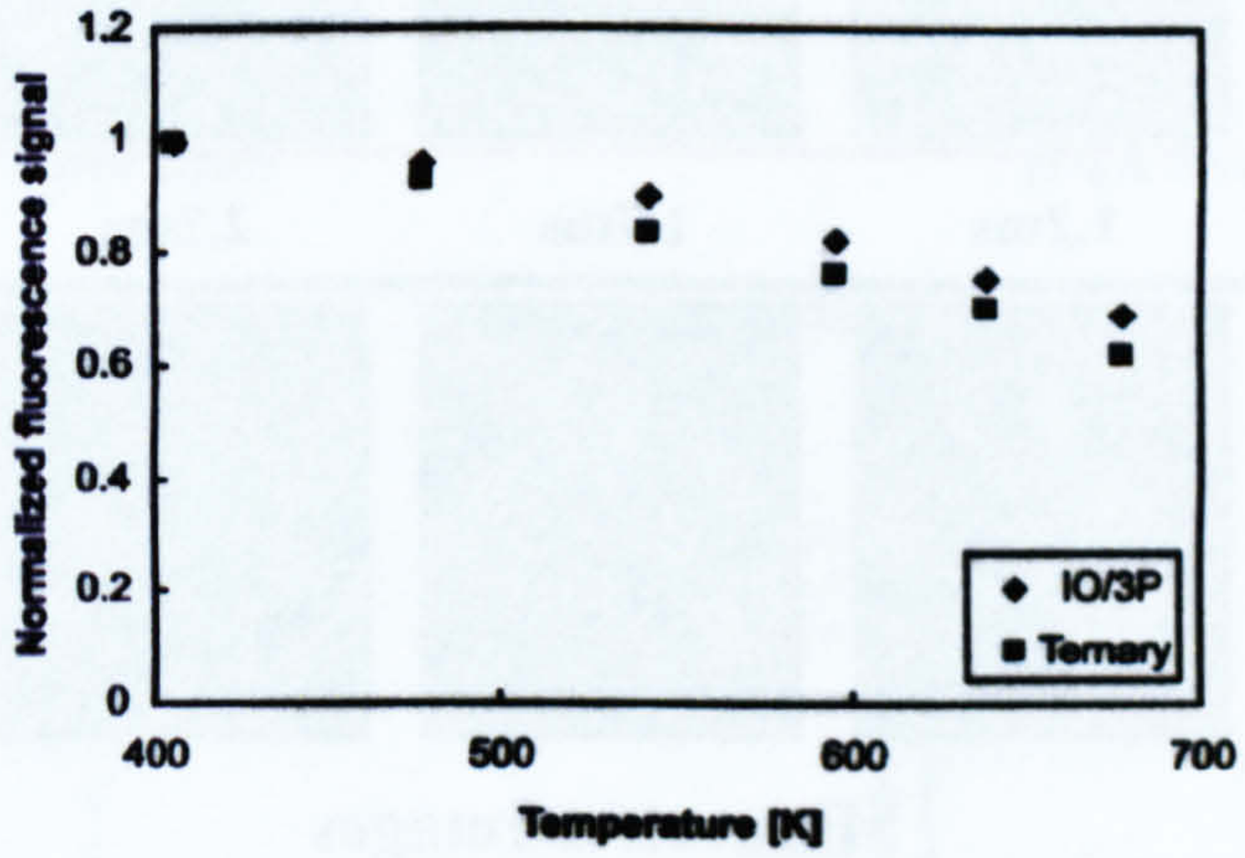

Figure 5-32: Fluorescence and Temperature for a 266nm excitation wavelength Han and Steeper (2002)

IO/3P ⇔ Iso-Octane / 3-Pentanone

Ternary ⇔ 90% Iso-Octane / 10% 3-Hexanone / 1% 3-Pentanone

These graphs suggest a decrease of fluorescence with temperature. They do not justify the increase of the LIF signal.

5.5.2. Vapour phase fluorescence

At atmospheric conditions, 3-Pentanone's liquid phase is 210 times denser than the vapour phase. 2-Hexanone's liquid phase is 180 times denser. Prior to the experiments, the vapour phase fluorescence was therefore assumed to be negligible compared to the liquid-phase fluorescence.

However, for conditions above the saturation curve, all tracer systems displayed an increase of the fluorescence signal in time, relative to the Mie scatter signal. As the conditions evolved towards more superheated regimes, this increase became larger. This suggests a significant vapour contribution to the signal.

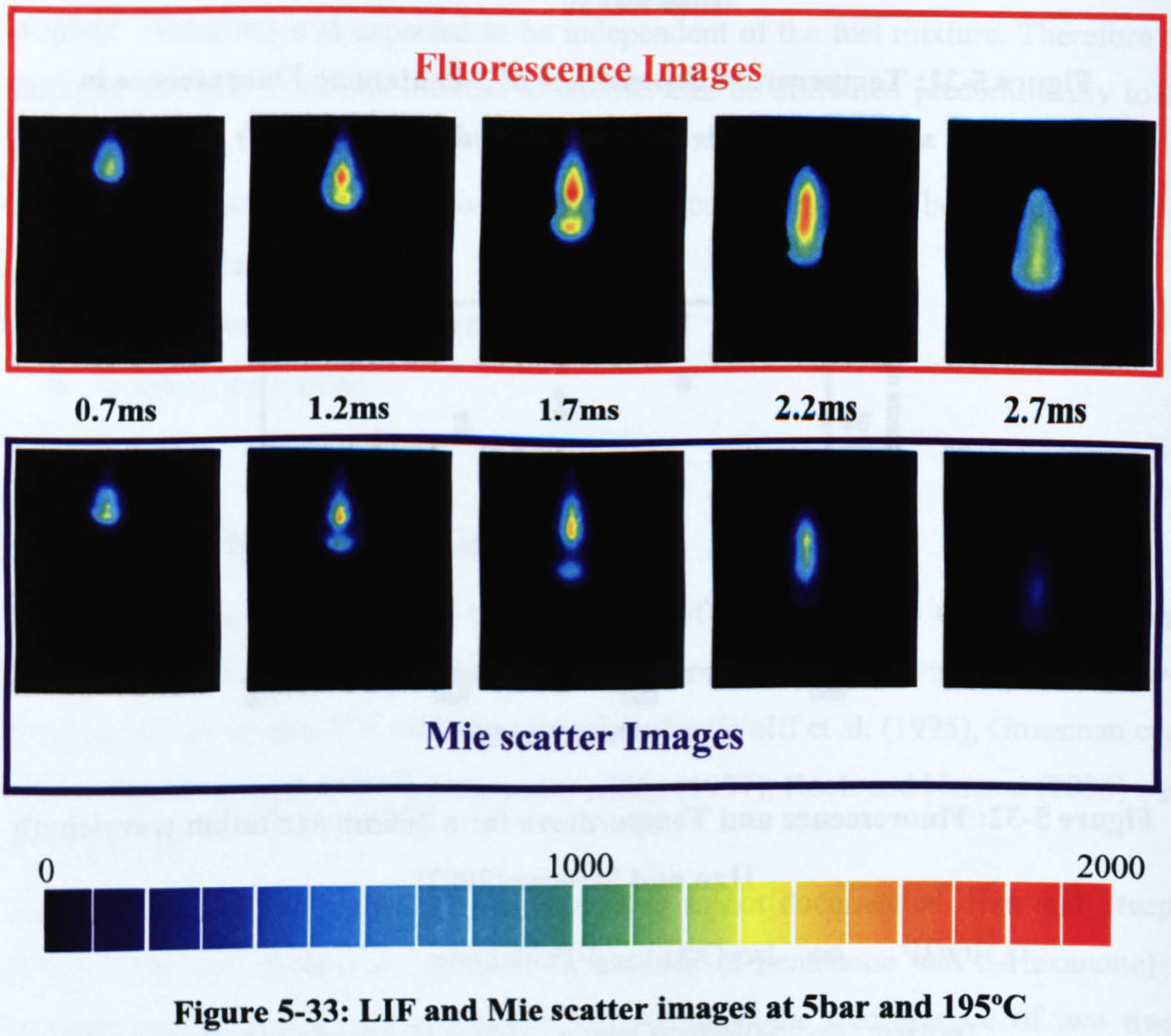

Figure 5-33: LIF and Mie scatter images at 5bar and 195°C

If the local fluorescence signal is separated in a liquid phase and a vapour phase signal, the local ratio of the fluorescence and the Mie scattering intensities in the LSD technique is:

$$\frac{LIF(i,j)}{Mie(i,j)} = \frac{LIF_l(i,j)+LIF_v(i,j)}{Mie(i,j)} = \frac{LIF_l(i,j)}{Mie(i,j)} + \frac{LIF_v(i,j)}{Mie(i,j)}$$

Equation 5-7

The desired SMD would be the ratio of the liquid-phase fluorescence and the Mie scatter intensities. Defined as *SMD'*, *Equation 5-7* can be written as:

$$\frac{LIF(i,j)}{Mie(i,j)} = SMD'(i,j) + \frac{LIF_v(i,j)}{Mie(i,j)}$$

Equation 5-8

Figure 5-34 is an illustration of *Equation 5-8*. At 1bar and 25°C (i.e. low evaporation conditions), the vapour fluorescence is negligible, and the ratio of scattering intensities is close to the SMD determined by PDA.

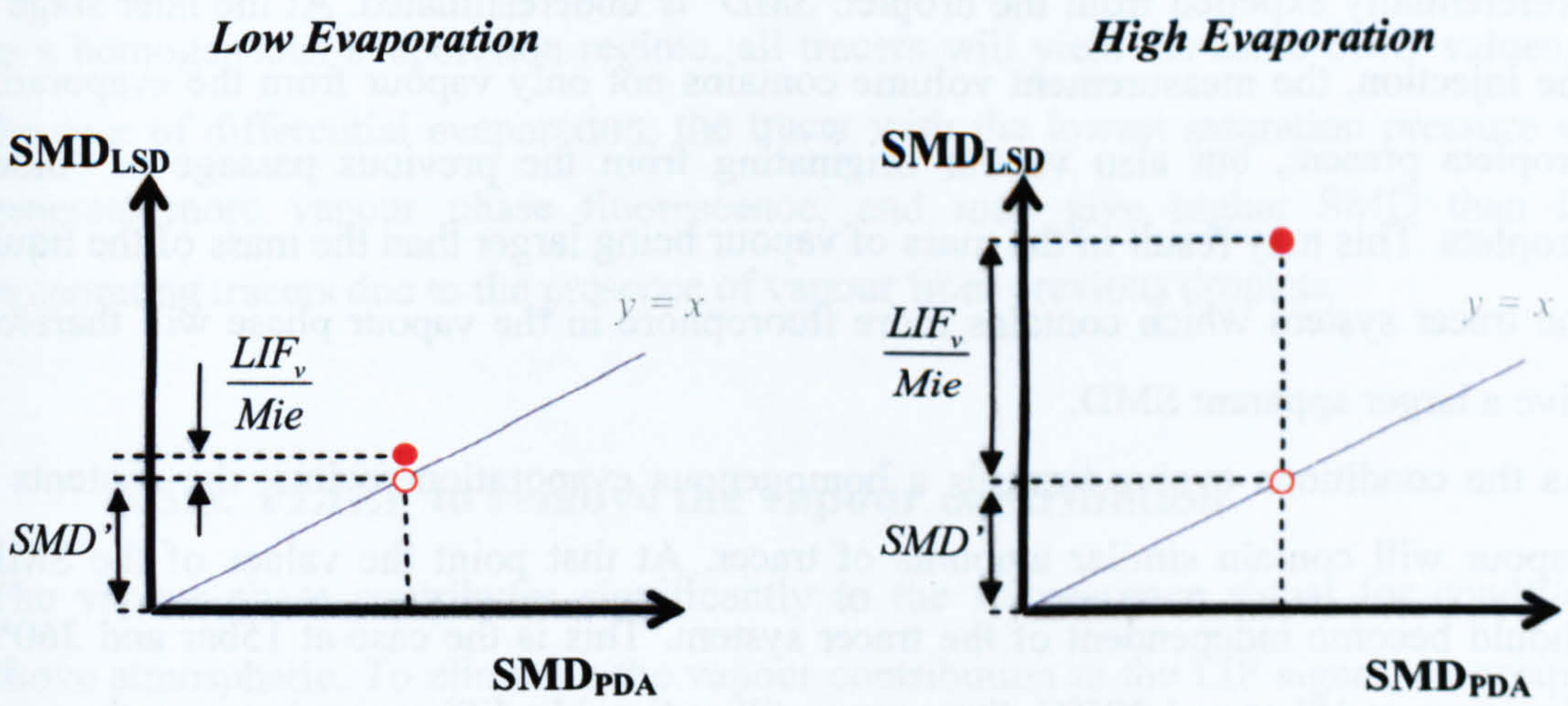

Figure 5-34: Vapour contribution in the estimation of the SMD

5.5.3. Evaporation regime

When the vapour contribution to the fluorescence signal is at least of the same order as the liquid LIF, the second term of *Equation 5-8* cannot be neglected.

In the case of a 2-Hexanone/Iso-Octane mixture, for slow evaporation, the relative tracer concentration increases in the droplet. Therefore *SMD'* is expected to be

overestimated. Any additional fluorescence intensity from the presence of vapour in the measurement volume will increase the overestimation (see *Figure 5-35*).

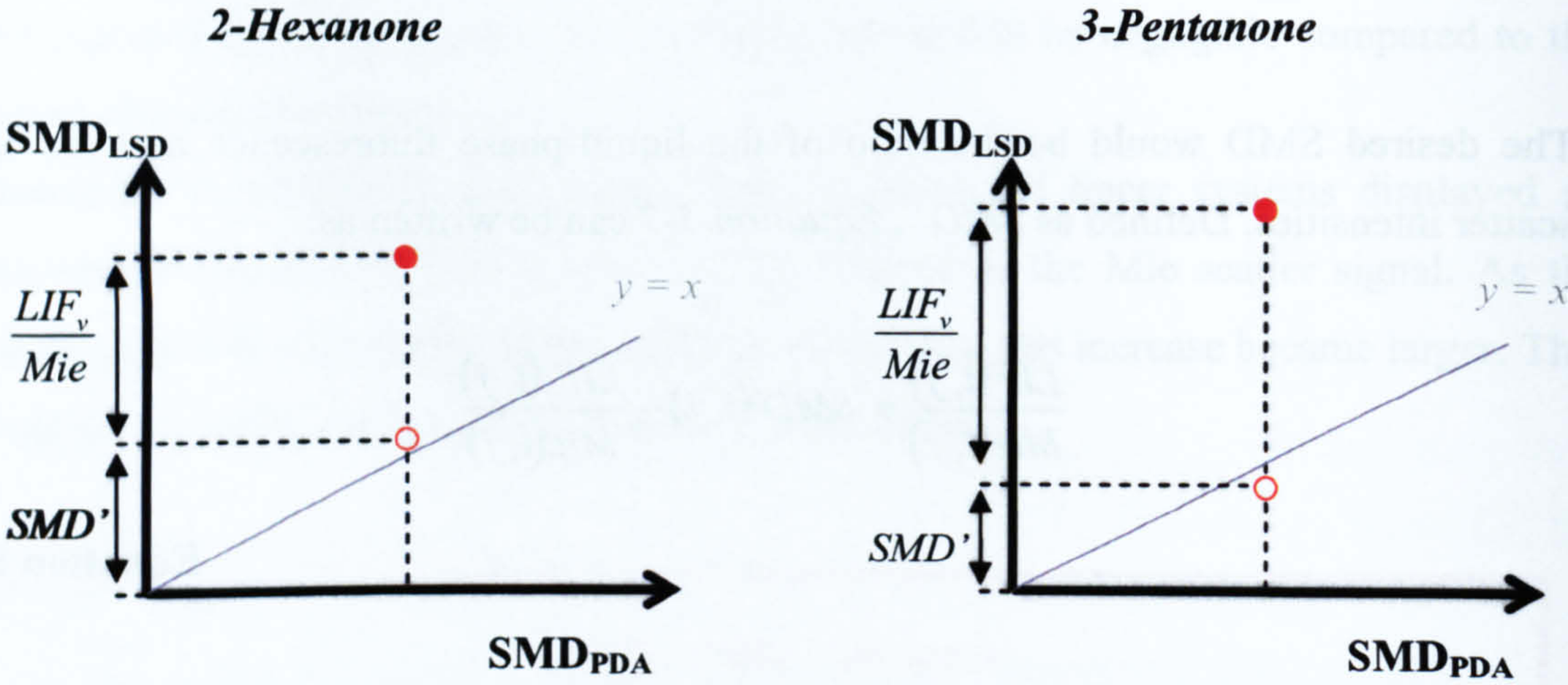

Figure 5-35: Differential evaporation and vapour phase contribution

With the 3-Pentanone/Iso-Octane mixture, in the case of slow evaporation, the tracer is preferentially expelled from the droplet: *SMD' is* underestimated. At the later stage of the injection, the measurement volume contains not only vapour from the evaporating droplets present, but also vapour originating from the previous passage of "older" droplets. This may result in the mass of vapour being larger than the mass of the liquid: the tracer system which contains more fluorophore in the vapour phase will therefore give a larger apparent SMD.

As the conditions evolve towards a homogenous evaporation regime, the contents of vapour will contain similar amounts of tracer. At that point the values of the SMDs should become independent of the tracer system. This is the case at 15bar and 360°C. However, at 10bar and 295°C, there were still noticeable differences between the tracer systems containing 2-Hexanone and the 3-Pentanone/Iso-Octane mixture. This suggests that even though the environment is superheated, the droplet's warming-up phase is not negligible, which limits the evaporation rate and allows for diffusion/differential evaporation.

5.5.4. Conclusion

The work undertaken with tracer systems composed of various mixtures of 3-Pentanone and 2-Hexanone (i.e. 2 ketones with opposite vaporisation characteristics) showed that the LSD technique works well at atmospheric conditions. This is because the evaporation is weak, and the vapour can diffuse. This allows the amount of tracer in the vapour phase to be sufficiently low not to contribute significantly to the fluorescence signal. In this case, the ratio of LIF to Mie scatter signal is proportional to the ratio of Volume to Surface of the liquid phase, thus yielding close SMD, within 30% variation.

With the increase in pressure and temperature, the technique still gives reasonable results for the early stage of the injection because the vapour content of the spray is not significant enough. However, the technique fails to deliver accurate SMD at the later phases of the injection. The increase in pressure causes the spray to collapse and limits the diffusion of the vapour. The rise in temperature generates vapour more quickly. These two phenomena explain the increase of the presence of tracer in the vapour phase, which increases the fluorescence signal relative to the Mie scattering signal.

In a homogeneous evaporation regime, all tracers will yield the same SMD values. In the case of differential evaporation, the tracer with the lowest saturation pressure will generate more vapour phase fluorescence, and may give higher SMD than less evaporating tracers due to the presence of vapour from previous droplets.

5.5.5. PLIEF to remove the vapour contribution

The vapour phase contributes significantly to the fluorescence signal for conditions above atmospheric. To eliminate the vapour contribution to the LIF signal, an exciplex system was tested. The system showed similar results for the 1bar – 25°C, where evaporation is not an issue. However, at 3 bar and above, the values of SMD increased in a similar way as the 3-Pentanone/Iso-Octane mixture.

As the temperature is increased, the monomers' - i.e. the vapour phase's - emission spectrum is red-shifted. Furthermore, Kornmesser et al. (2001) showed that the fluorescence yield of the monomer increases by a factor of 4 between 20 and 100°C (see *Figure 5-37)*. Also, both TEA and Benzene have much lower boiling points than the

other tracers and Iso-Octane itself (85 and 80°C respectively). The vapour phase will therefore contain much more tracer than with the other mixtures.

These 3 effects contribute to amplifying the fluorescence in a spectral range that is not eliminated because the filter was not sufficiently selective. Therefore, the experiments should be carried out by selecting the fluorescence which occurs above 400nm.

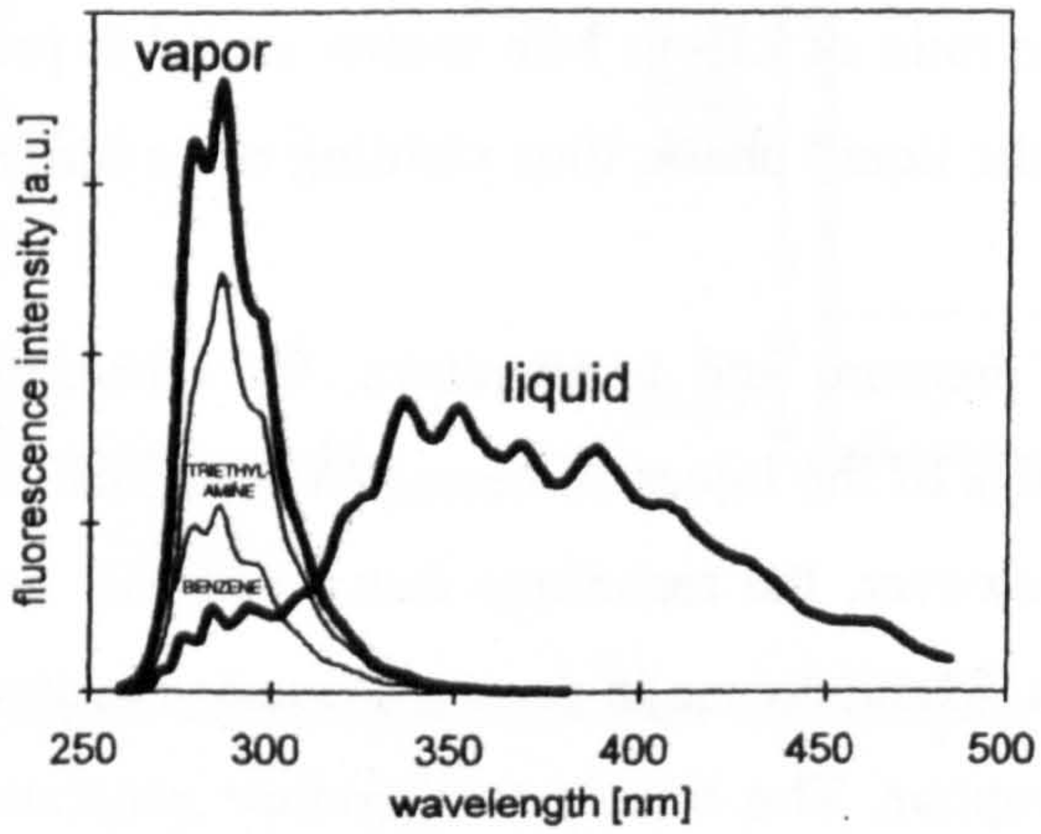

Figure 5-36: Liquid-vapour emission spectra for the LIEF - Fröba et al. (1998)

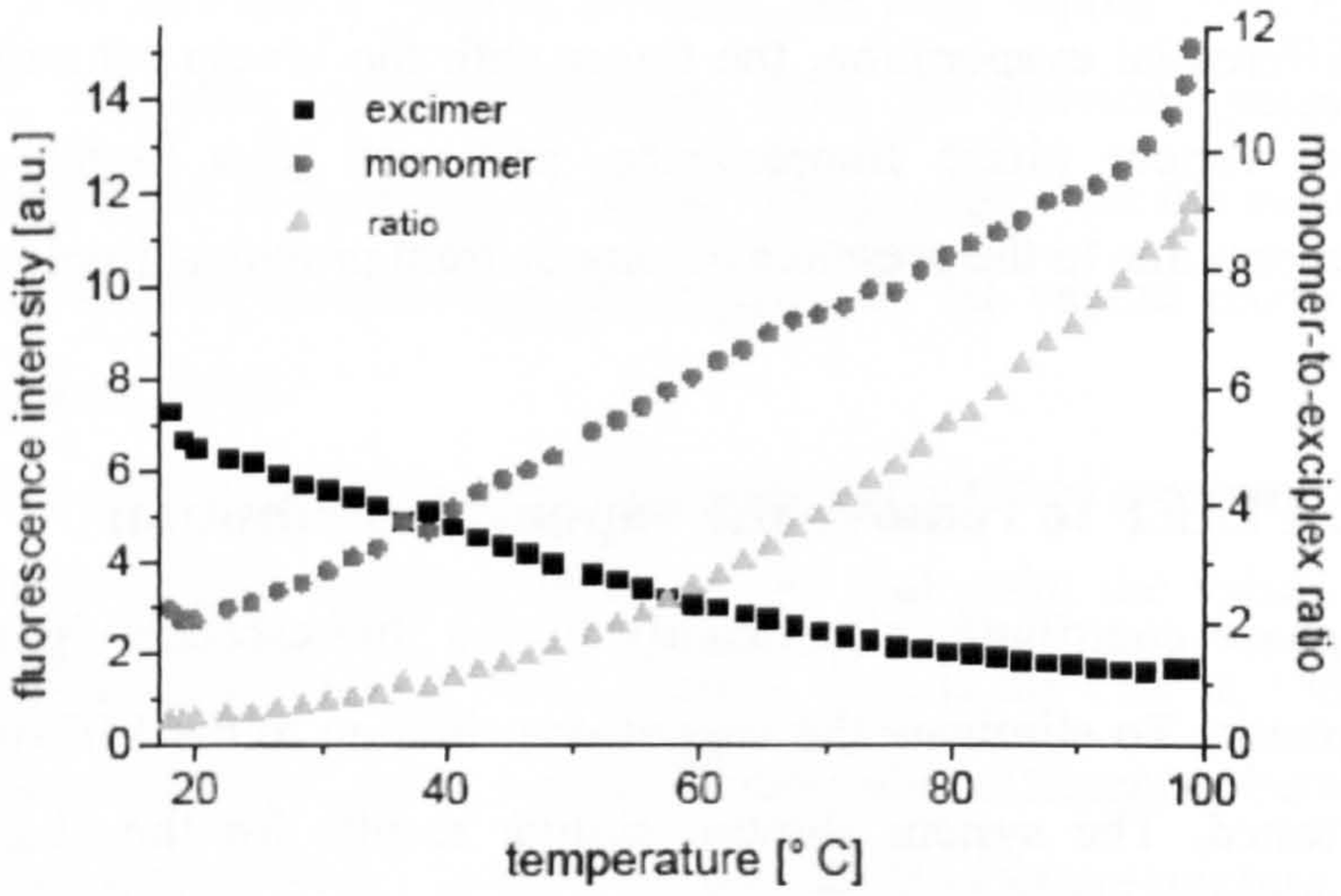

Figure 5-37: Relative fluorescence intensities of the TEA/Benzene exciplex and monomer in Iso-Octane (Kornmesser et al. 2001)

5.5.6. PDA – LSD discrepancies

The work shows that at atmospheric conditions, the evaporation is low and the tracer systems behave in a similar way. These conditions were expected to give matching results between the LSD and the PDA techniques. However, there are variations between the SMD obtained with the PDA and LSD technique.

Le Gal (1999) suggested that for dense sprays, the multiple scattering effects between the laser sheet and collecting optics was responsible for the deviations of the LIF and Mie scatter signals from their d^3 and d^2 dependence respectively. It is believed that the multiple scattering is of second order, because it affects both signals: the effect of additional intensity caused by multiple scattering is attenuated in the ratio of the fluorescence and Mie scattering signals.

Other problems lie in the fact that PDA is not an accurate tool for measuring dense sprays. The best measurements are done in parts of the spray where the number of droplets is sufficiently low to limit multiple occupancy. However, in these parts of the spray, the fluorescence and Mie scattering signals are low, and their SNR is high, yielding erroneous SMD. Therefore, where the PDA data provides reliable data, the LSD technique can not, and vice-versa.

The variations in the results can be attributed to imperfections in the fluorescence signal, multiple scattering and the PDA technique. The validity of the surface dependence of the Mie scatter signal, however, was never questioned following the findings of Bachalo (1984) and the work by Sankar et al. (1996) where numerical work had showed that "for absorbing droplets, the scattered light intensity is proportional to the droplet diameter, especially for droplets greater than about 1μm in diameter".

Figure 5-38 shows numerical simulations by Domann and Hardalupas (2003) of Fluorescence and Mie scatter signal intensities using an excitation wavelength of 514.5nm (Argon-Ion), scattering at 90° and a collection angle of 3.8°. The graphs show large variations of the Mie scatter signal from the d^2 dependence (in red) for droplets smaller than 100μm in diameter. This suggests at best a good agreement for droplet diameters smaller than 50μm for an excitation wavelength of 266nm. On the other hand, the fluorescence signal agrees well with a d^n law. They found that n=2.996 for an absorbing droplet, which implies that the fluorescence signal will deviate from the droplet volume by a maximum of 2.5% for droplet diameters smaller than 50μm.

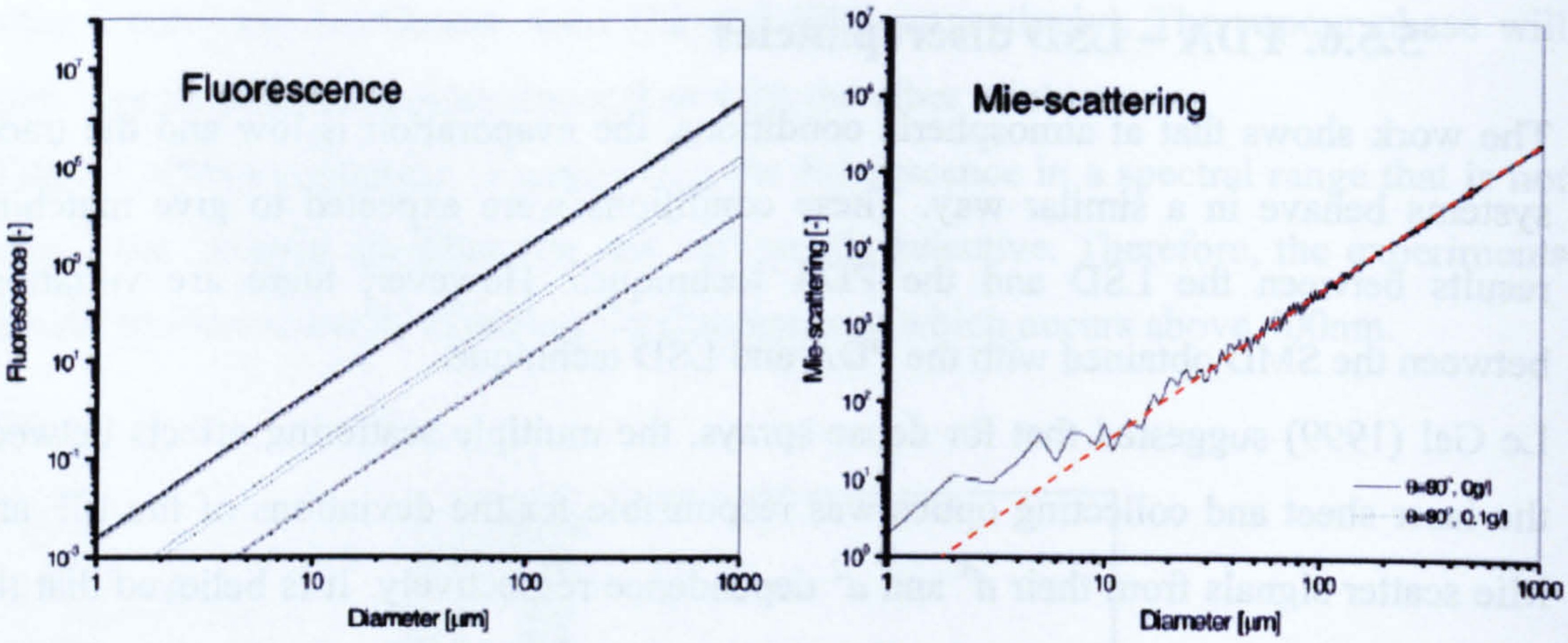

Figure 5-38: Fluorescence and Mie scatter intensity as a function of diameter (Domann and Hardalupas 2003)

Following this, they numerically calculated the SMD obtained for single droplets using the ratio of the LIF and Mie scatter signals. By comparing it to the real SMD (in this case, the diameter), they obtained the calibration constant (K). *Figure 5-39* displays the calibration constant as a function of size. K_{fit} represents the calibration constant if both signals followed the ideal volume and surface relationship. In the 20-50µm range, the error will be as high as 30%. The plot also suggests that the discrepancies worsen as the diameters get smaller.

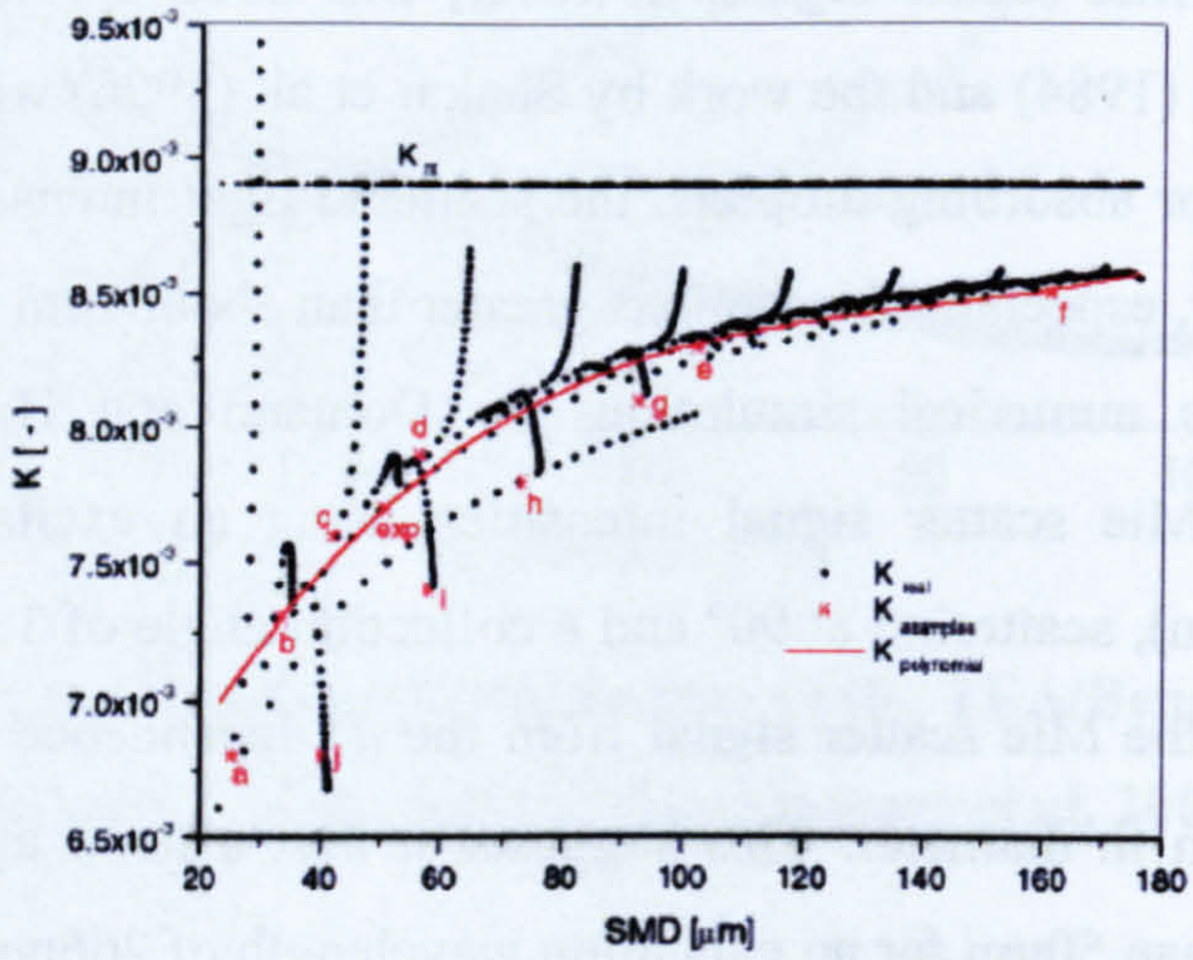

Figure 5-39: Calibration constant for monodisperse droplets (Domann and Hardalupas 2003)

Figure 5-40 illustrates the errors that these variations create when the SMD is measured for different distribution of droplets. The error is smaller for distributions containing large droplets. In the case of the Bosch Swirl injector in this study, the distributions were usually of the Rosin-Rammler or Log-normal type, with a maximum droplet diameter of 50μm, similar to distribution (a) in *Figure 5-40*. This distribution gives an error of 31%.

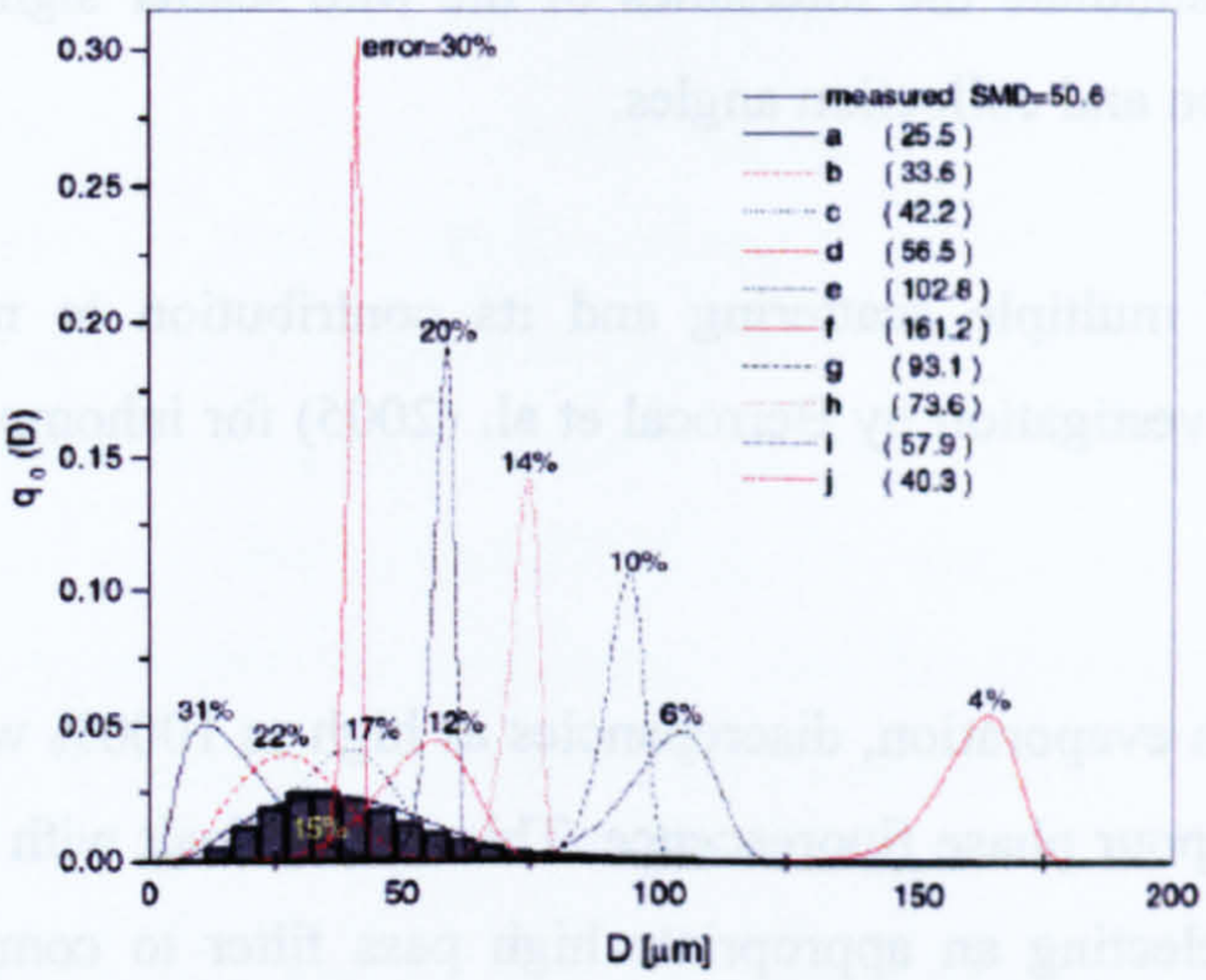

Figure 5-40: Error in Measured SMD for different size distributions (Domann and Hardalupas 2003)

The comparison of the SMDs obtained with the LSD and the PDA techniques showed variations of this order of magnitude.

5.6. Summary

PDA measurements were carried out on a spray to study the validity of the LSD technique for in-cylinder conditions.

Even though the PDA data was not necessarily reliable because of the nature of the spray, several issues were identified.

The most important issue arises from the previously assumed result that the Mie scattering signal follows a d^2 dependence. However, as was discussed, for the range of droplet diameters in this particular spray, the Mie scatter signal will deviate strongly

from that surface dependence, because the proportion of light emitted towards the collection optics varies strongly from one size droplet to the other. The integration of the signal over a droplet size distribution will attenuate these variations. Determining the calibration constant using PDA data from a similar droplet distribution will further reduce the discrepancies. Charalampous et al. (2004) have carried out such work using the geometrical approach and found the best accuracy was obtained for a 60° observation angle. Further studies could include computational work using the Mie scatter theory to simulate the intensities of the Mie scatter signal and determine the optimal observation and collection angles.

The influence of multiple scattering and its contribution to measurement error is currently under investigation by Berrocal et al. (2005) for inhomogeneous polydisperse turbid media.

In the case of high evaporation, discrepancies as high as 1000% were found, due to the contribution of vapour phase fluorescence. This can be dealt with by using an Exciplex system and by selecting an appropriate high pass filter to completely eliminate the monomers' fluorescence.

In the case of high evaporation at high pressures, the increase in the SMD obtained with the LSD technique is actually an indication of vapour apparition, and can be used to compare evaporation rates between injectors.

Experimentally, the best tracer system was the 3-Pentanone / 2-Hexanone / Iso-Octane mixture at proportions of 0.5 / 1.5 / 98 by volume. The maximum error was 30% up to 5bar and 195°C. Above these conditions, the vapour phase contribution to the fluorescence signal is non negligible. However, in highly evaporating conditions, the droplet life-times are short because of their small sizes. In this case, the location of the vapour phase is more relevant to the combustion process.

PART III

ENGINE SPRAY VISUALISATION MEASUREMENTS

Chapter 6
Engine Measurements

Several laser diagnostics techniques were applied to a GDI optical engine to characterise the spray for two injection strategies: early/homogenous injection and late/stratified injection. These diagnostics include PLIF measurements to determine equivalence ratio, simultaneous Mie scatter / LIF images in the LSD technique for calculating SMD, and PIV measurements using Mie scattering to determine droplet velocities. This chapter presents the optical engine and the experimental set-up. The set-up for each technique is described, and the results are analysed.

6.1. Experimental Set-Up

6.1.1. Engine configuration

These experiments were carried out on a BMW single-cylinder research engine with optical access. The engine is composed of a Ricardo crank casing, an elongated engine block, an elongated piston, a fused silica annulus and the cylinder head (see *Figure 6-1*) and has a displacement of 499cc.

The block has a 45° mirror mounted inside. The piston is elongated and hollow with intake and exhaust side walls removed, enabling the positioning of the 45° mirror directly under the cylinder axis. This allows optical access of the combustion chamber through a fused silica window located in the piston top. Previously, a bowl-shaped piston with a small centred window was used for wall/air-guided mixing. For these experiments, the piston is flat, allowing a large diameter window (50mm) and therefore favouring optical access rather than in-cylinder mixing (see *Figure 6-2*, *Figure 6-3*, *Figure 6-4* and *Figure 6-5*).

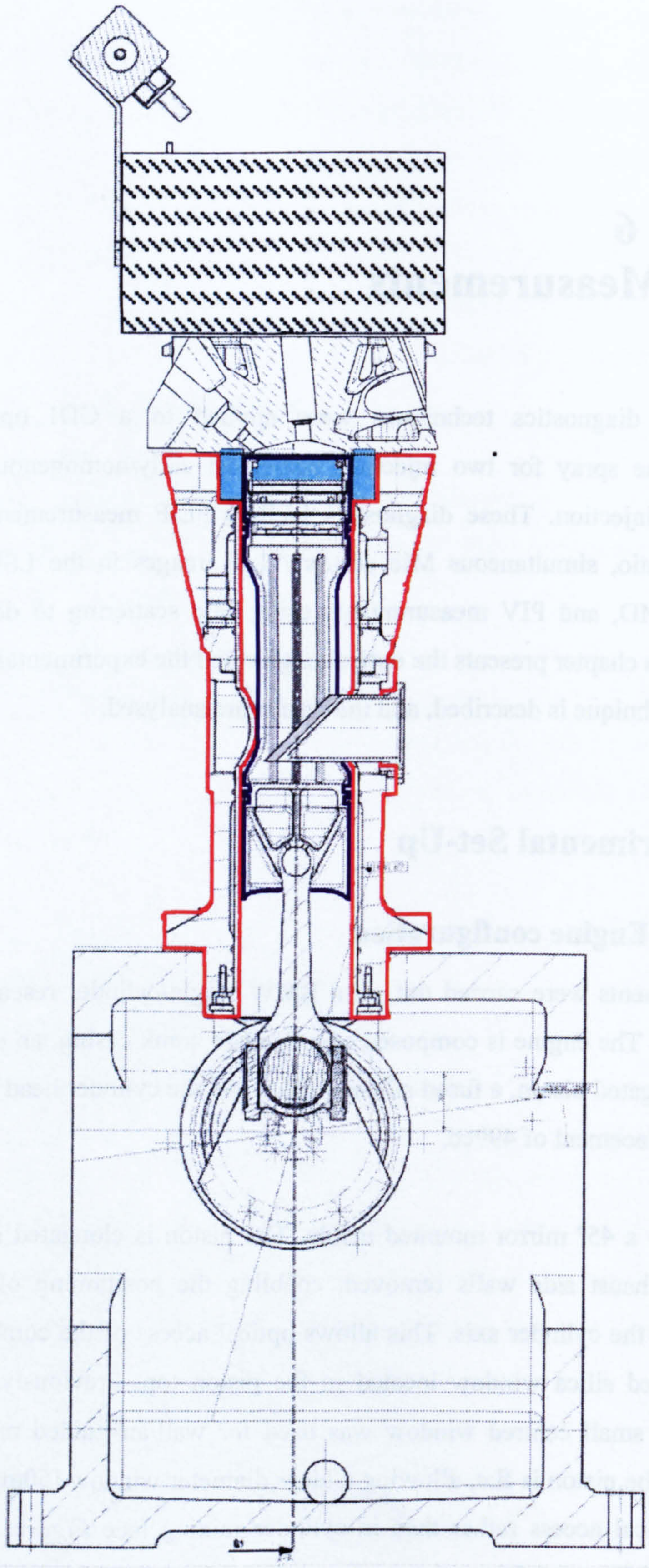

Figure 6-1: Single cylinder optical research engine

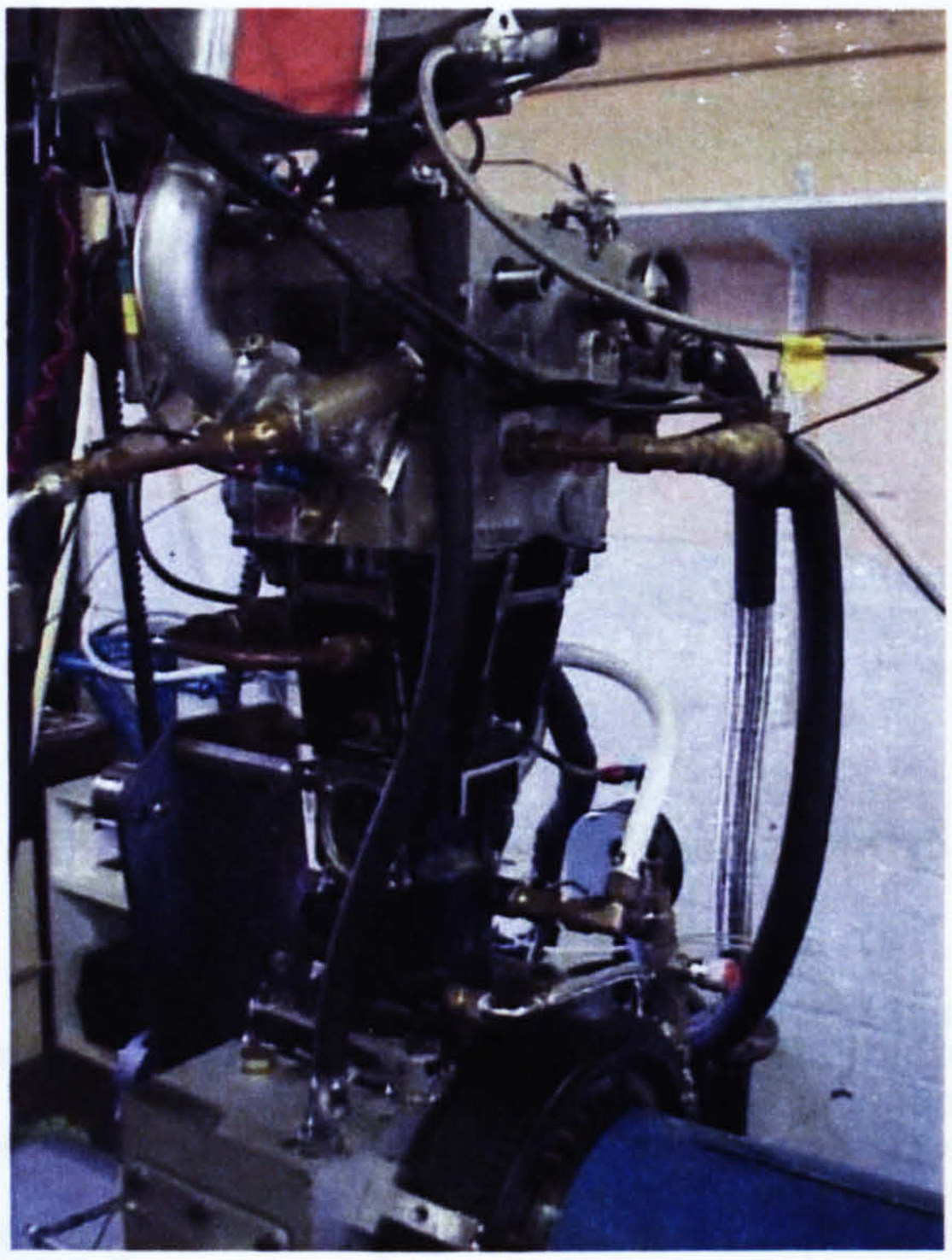

Figure 6-2: Complete Optical Engine

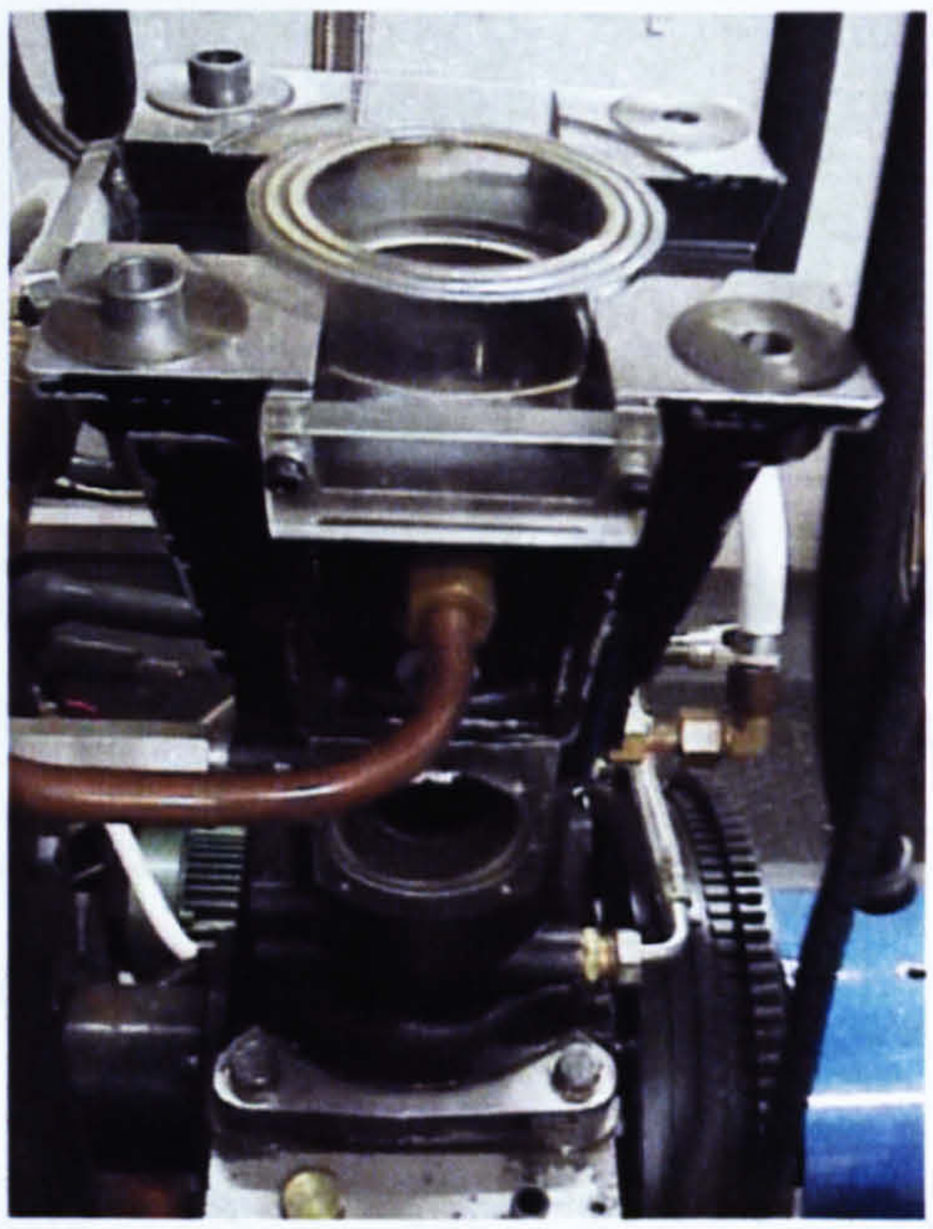

Figure 6-4: Engine block and fused silica crown

Figure 6-3: Elongated and hollow piston

Figure 6-5: Piston head

The engine has a 4-valve asymmetric pent-roof cylinder-head configuration to accommodate bigger inlet valves. One of the inlet valves is deactivated in order to create a swirl motion inside the cylinder. A spark plug is located at the centre of the roof line. A Bosch 70°/10° Swirl injector is located between the two intake valves (see *Figure 6-6*).

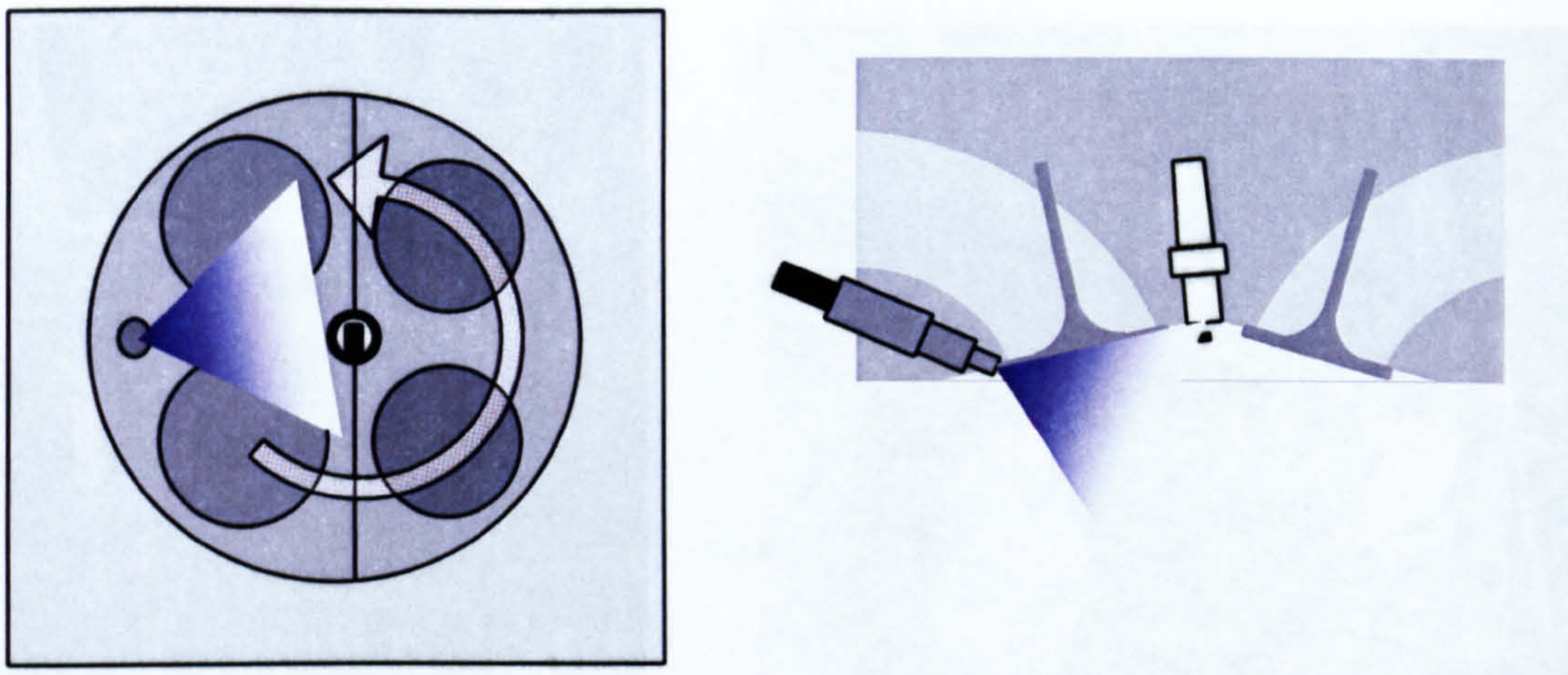

Figure 6-6: A view of the cylinder head configuration

Optical access in the cylinder is also possible through the fused silica annulus located between the engine block and the cylinder head. The 2 triangular sections of the cylinder-head also have fused silica inserts for optical access in the pent-roof region of the combustion chamber.

Air enters the engine by passing through an air filter, an intake duct, a throttle body and finally an inlet plenum (see *Figure 6-8*). The entire length of the intake manifold is heated to 40°C using heating mats. The manifold pressure is measured in the inlet plenum. An additional injector (the calibration injector) is mounted approximately 1m upstream of the intake. This allows to create a charge that is homogenously mixed before entering the cylinder. This system was designed by Berckmüller and O'Young, in 1996, but was not published before 2000 (Kelman et al.). Ipp et al. (1999) used the same air intake system for their FAR-LIF experiments.

The tracer/fuel mixture is stored in a tank and is pressurised in two stages before reaching the injector. First, the tanks are pressurised to 3bar using Nitrogen. The fuel is then delivered to the high pressure fuel pump. The 3-piston type pump is mounted on the top of the cylinder head and is belt-driven from the intake cam-shaft. The pressurised fuel is then fed into a pressure regulator before being sent to the injector (see *Figure 6-7*).

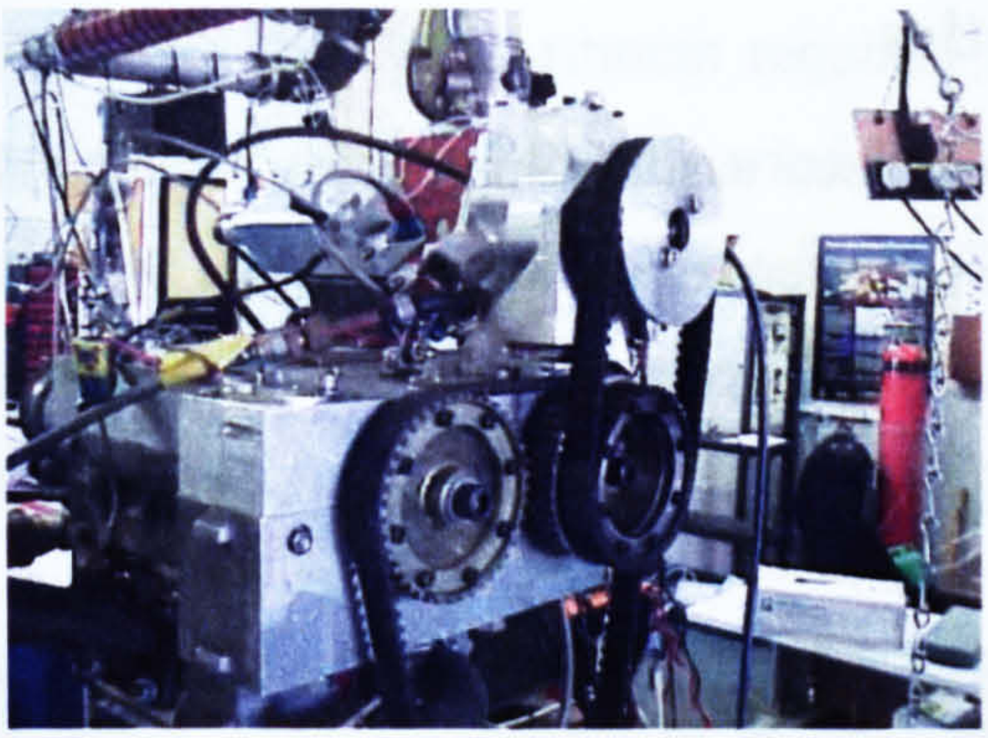

Figure 6-7: Fuel Pump and Pressure Regulator

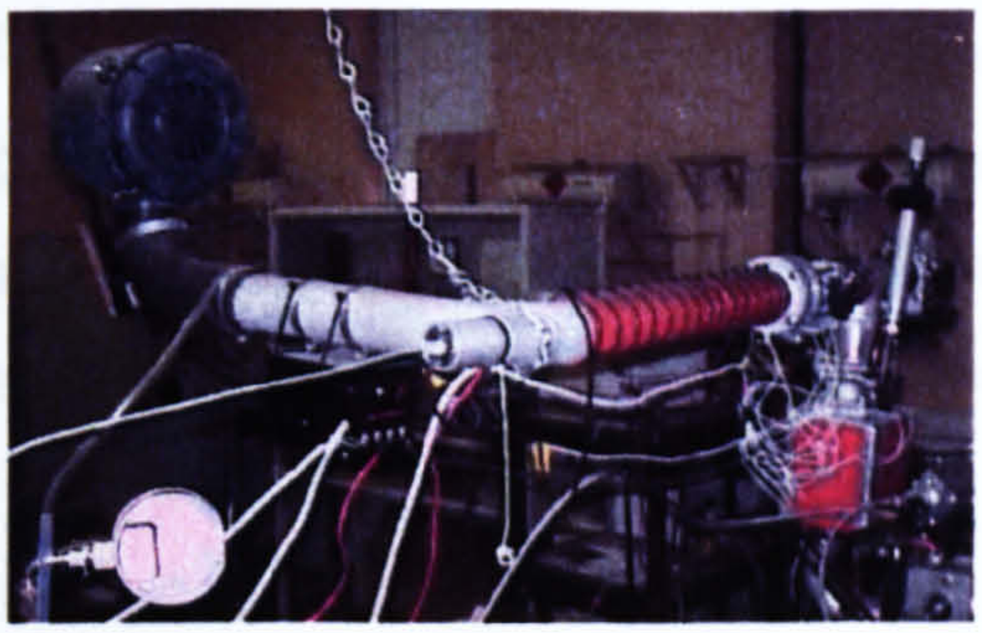

Figure 6-8: Air filter, intake, plenum chamber and calibration injector

The engine is mounted on an English Electric dynamometer regulated by a Saftronics controller to provide constant speed, which was 1000 rpm for this set of experiments. The engine speed is regulated to a pre-set value by the controller of the dynamometer on which the engine is mounted.

The engine's cylinder head is water cooled and its coolant is preheated to 70°C. The engine block is cooled by cold water. The oil is circulated from the crank-case to the cylinder-head via an independent electrical pump. The operating pressure is 40psi.

The engine was designed for early GDI development work and was adapted here for good optical access. This piston geometry compromised the mixing process. The first task consisted in finding 2 operating points: one in the early injection/homogeneous mode, and another in the late injection/lean/stratified mode. The conditions are summarised in *Table 6-1*. The crank angle reference (0°CA) is the compression/combustion top dead centre. 360°CA is the exchange TDC.

	Early injection (Homogeneous)	**Late injection (Stratified)**
SOI	420°CA	670°CA
Injection duration	1.85ms	1.80ms
Ignition	702°CA	702°CA
ΔP	340mbar	20mbar
λ	1	~3

Table 6-1: Operating points for the GDI engine

6.1.2. Laser and Light Sheet Optics

A Spectra Physics PIV 400 Nd:YAG laser was used as the illumination source. The laser emits at 1064nm. Doubling crystals allow to generate 532nm and 266nm light. For the LSD and AFR-LIF experiments, the fuel was excited using the 4th harmonic (266nm) whilst the 2nd harmonic (532nm) was chosen to carry out the PIV measurements.

A laser sheet was formed inside the cylinder to image the fuel in the central plane of the combustion chamber. A vertical sheet coming through the piston was used to illuminate the whole chamber, including the pent-roof, in order to visualise the fuel around the sparkplug at time of ignition.

At the exit of the laser, the beam was redirected with two dichroic mirrors (266nm or 532nm depending on the experiment) so that it was perpendicular to the engine, horizontal and pointing at the middle of the 45° mirror located under the cylinder axis. The laser sheet was then formed using a combination of 3 fused silica lenses: a spherical lens of 2m focal length thinned the beam to less than 500µm inside the engine. Two cylindrical lenses then expanded the beam in one direction to form a sheet of approximately 5cm in width. The sheet was then directed into the cylinder via the 45° mirror.

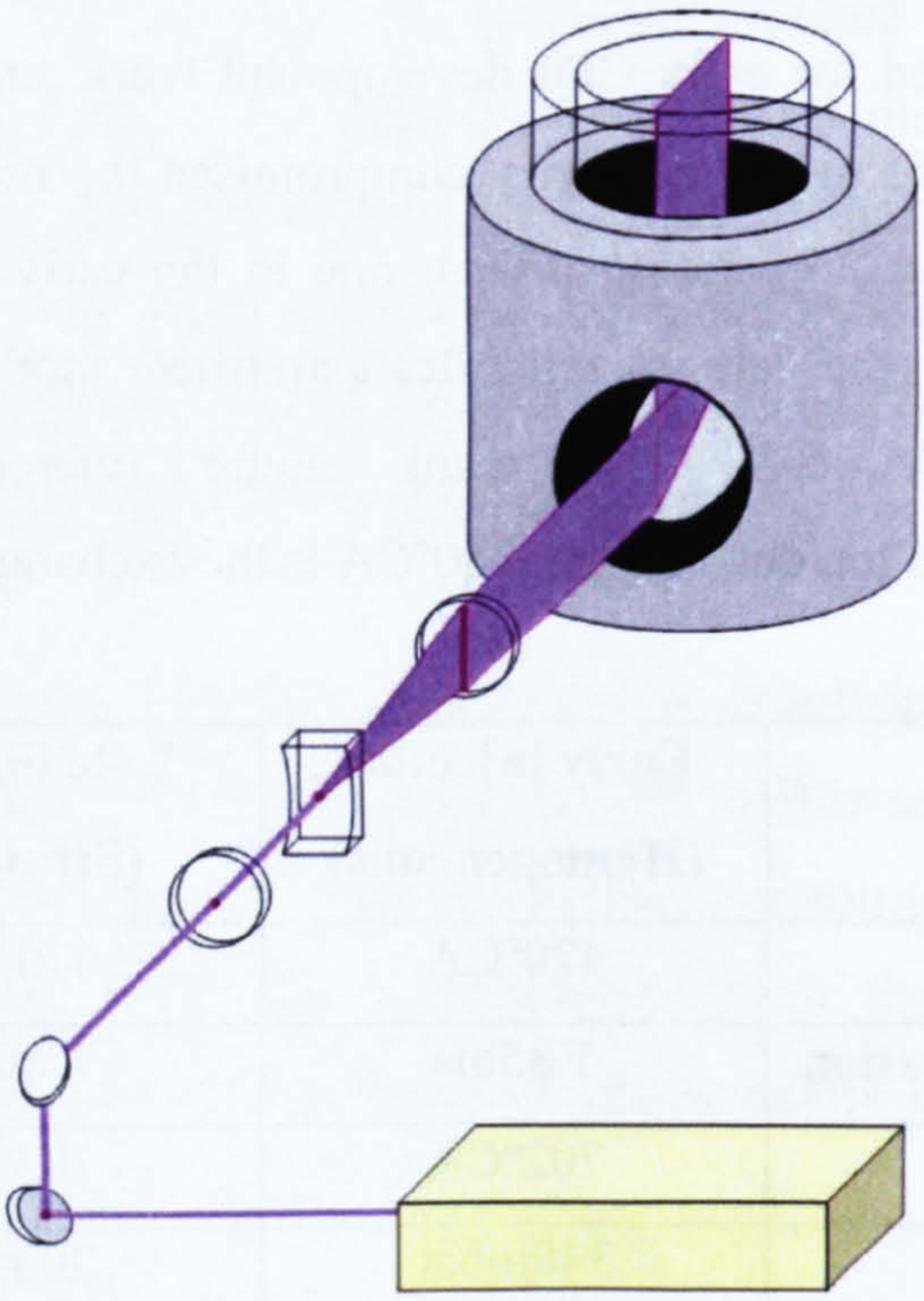

Figure 6-9: Sheet-forming Optics

The laser sheet's adjustment required the removal of the cylinder head. A target was positioned over the annulus window. It was set against the two cylinder head guides, used as reference, and had markings for several positions left and right of the central plane. The laser sheet position was fine adjusted using the 2nd dichroic mirror and the rotary mount of the 2nd cylindrical lens.

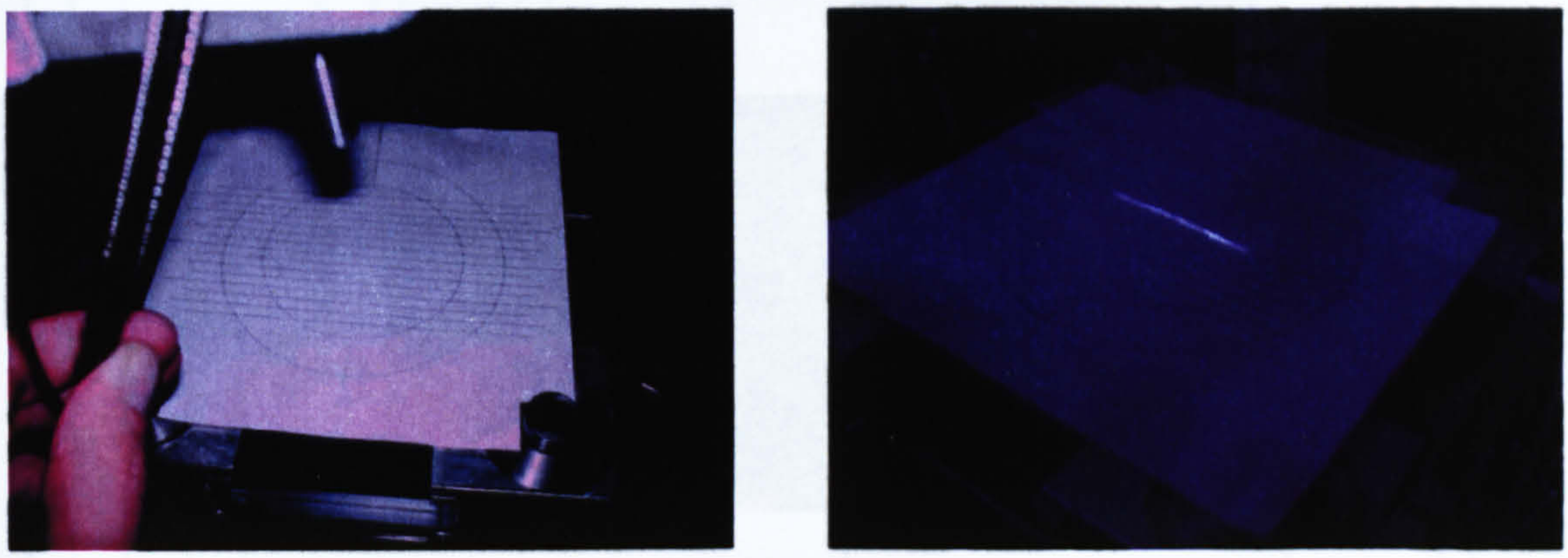

Figure 6-10: Laser sheet target and illumination

6.1.3. Spatial Calibration

To determine the resolution and the position of the images, a calibration plate containing regularly spaced white crosses on a black background was used to calibrate the CCD chip. A plate similar to the laser target, with a circular hole cut out, enabled the insertion of the plate inside the cylinder and to position it at the same location as the laser sheet (see *Figure 6-11*).

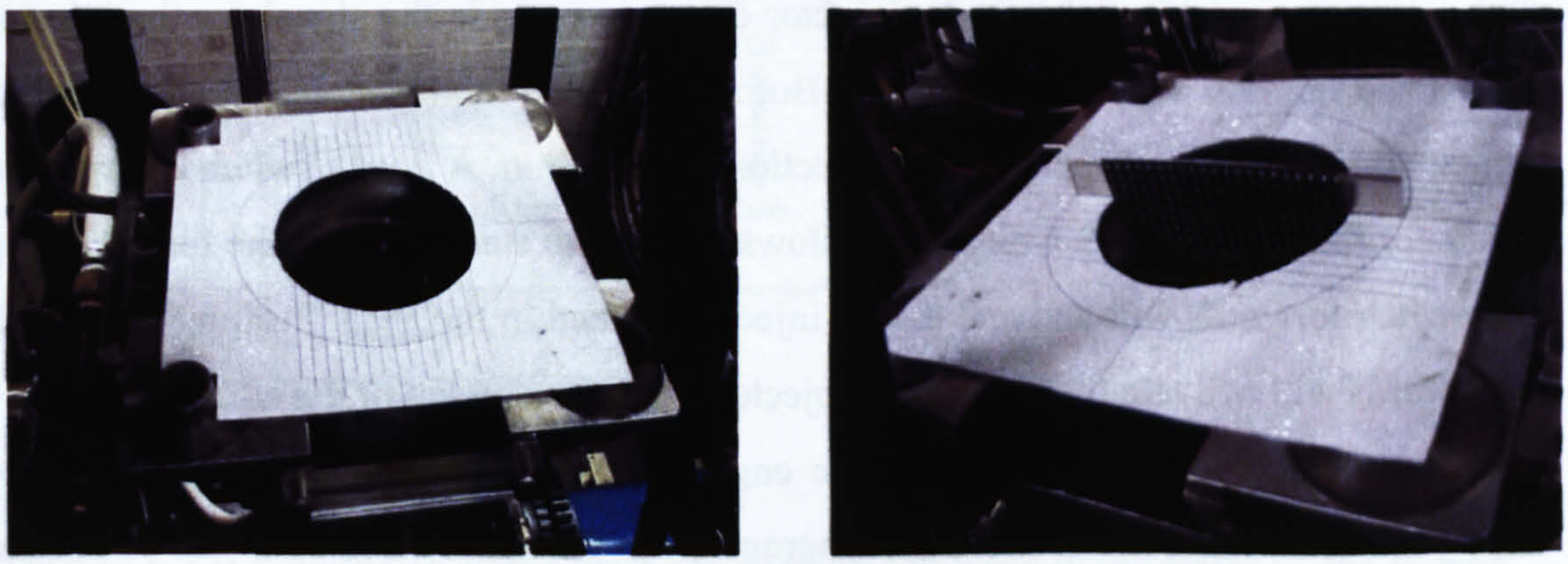

Figure 6-11: Positioning plate and Calibration plate

6.1.4. Timing and Synchronising for the Experiment

The timing and synchronisation is schematically represented in *Figure 6-13*.The engine is the experiment master. The dynamometer keeps the engine at a constant speed. A Kistler type 2612B sensor situated at the end of the crankshaft provides a 1 pulse / ºCA signal, and an optical sensor with a single tooth disk on the exhaust camshaft provides a 1 pulse / 2 rev signal (see *Figure 6-12*).

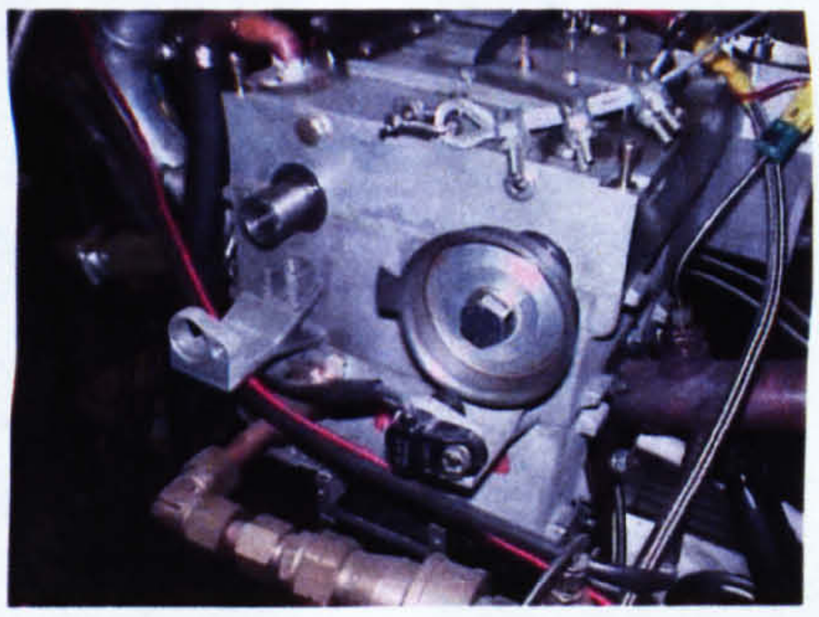

Figure 6-12: The cam sensor and single tooth

These signals are fed into the engine management box. This box allows the user to set:

- the crank angle for start of injection (SOI)
- the injection duration (in ms)
- the crank angle for ignition
- the crank angle for the laser trigger

Every 4-stroke cycle, the engine management box outputs an injection, an ignition and a laser-trigger signal.

The injection signal is fed into the injector driver to provide the signal for the injector whilst the ignition signal is amplified. Both signals are then sent into a Control Box which allows the user to activate the injection and ignition. A 2-way switch controls the spark for the ignition. A 3-way switch allows the user to start injecting the fuel. Pushing the switch forwards will activate the DI injector located in the head. Pushing the switch backwards will activate the calibration injector located upstream of the air intake.

The laser-trigger signal supplied by the engine management box is amplified before being used to trigger the computer's Programmable Timing Unit (PTU). The PTU runs the laser, intensifier (IRO) and camera (CCD). The imaging software used was DaVis6.2 by LaVision.

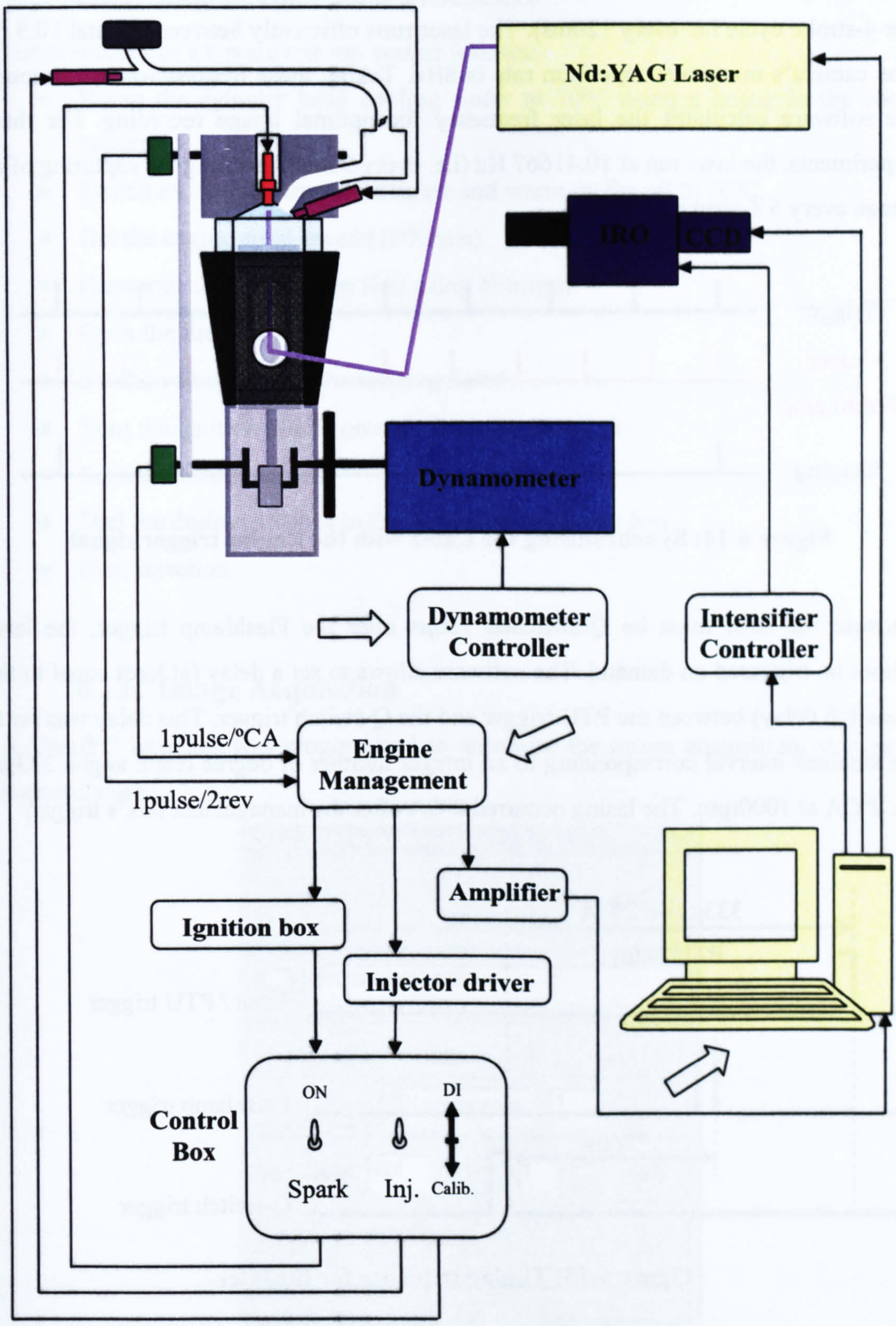

Figure 6-13: Schematic of the instrumentation for laser diagnostics in the engine

At 1000 rpm, the management box is sending the computer a signal at 8.33Hz (1 signal per 4-stroke cycle i.e. every 120ms). The laser runs efficiently between 9.5 and 10.5 Hz The camera's maximum repetition rate is 8Hz. Taking these frequencies into account, the software calculates the laser frequency for optimal image recording. For these experiments, the laser ran at 10.41667 Hz (i.e. every 96ms), enabling the capturing of an image every 5 4-stroke cycles.

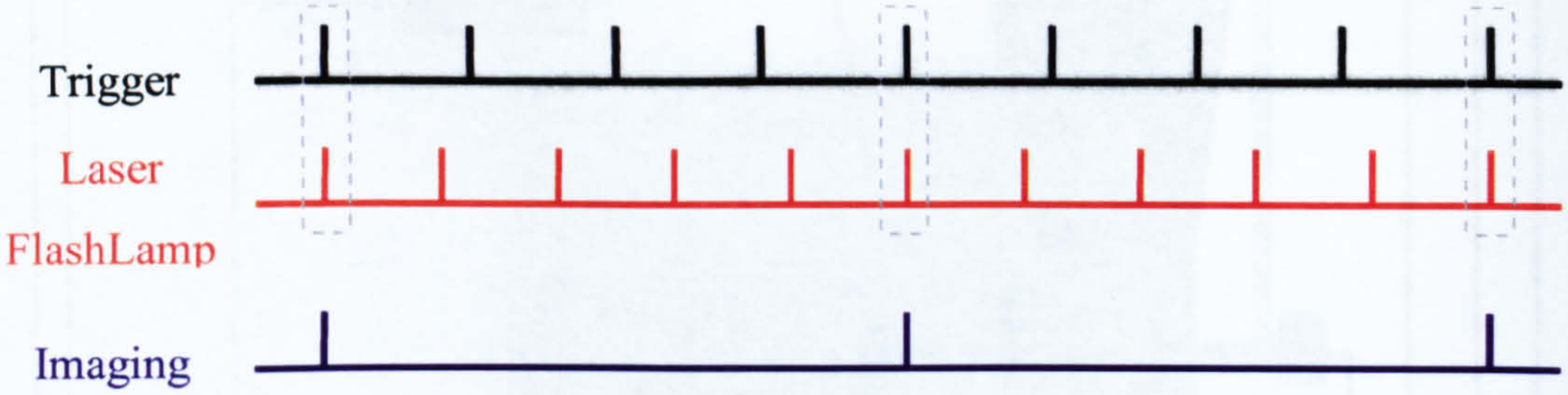

Figure 6-14: Synchronising the Laser with the Engine trigger signal

Because the laser must be Q-switched 186µs after the Flashlamp trigger, the laser cannot be triggered on demand. The software allows to set a delay (at least equal to the Q-switch delay) between the PTU trigger and the Q-switch trigger. This delay was set to the smallest interval corresponding to an integer number of degree crank angle: 333µs, i.e. 2°CA at 1000rpm. The lasing occurred 2°CA after the management box's trigger.

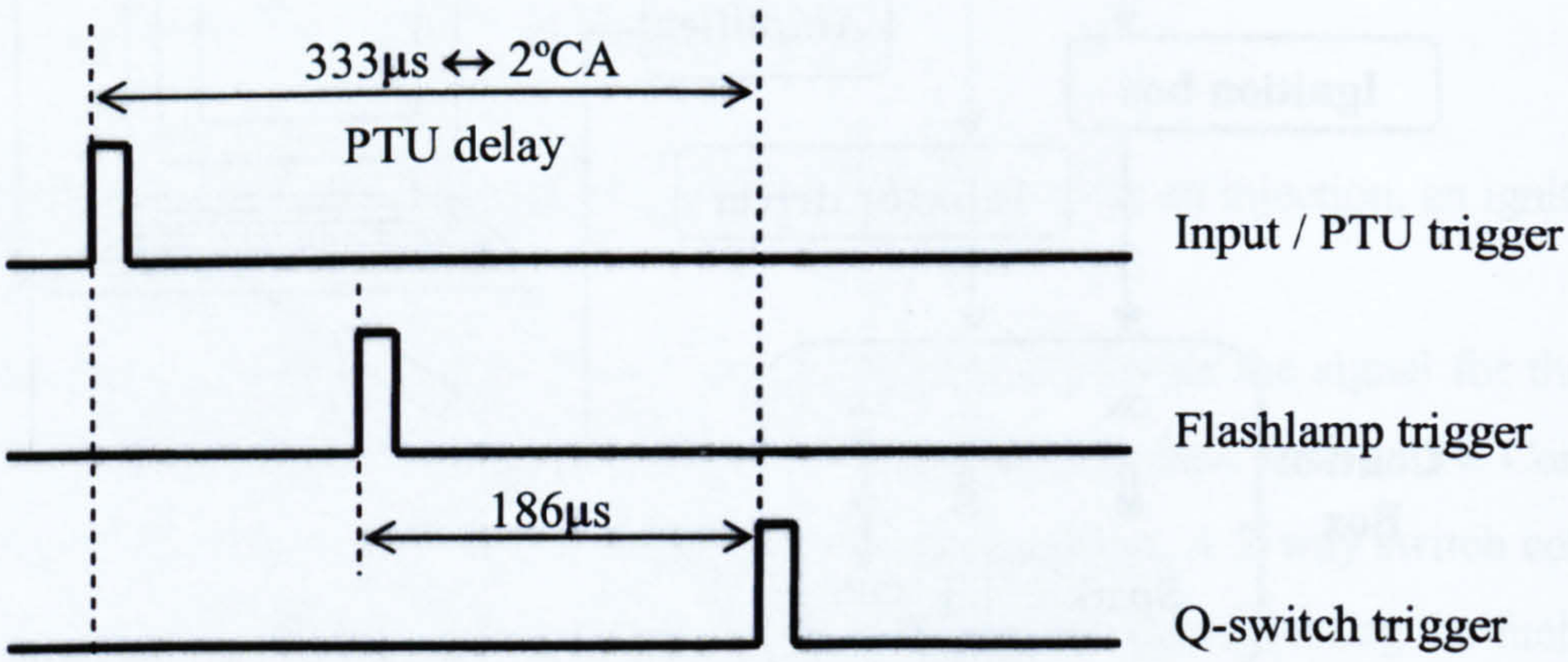

Figure 6-15: Timing sequence for the laser

The repetition rate of the camera (8Hz), combined with the laser frequency (10Hz) do not allow high-speed imaging. Instead, many images were recorded at the same crank angle over many cycles. This was repeated at different crank angle positions.

6.1.5. Engine Operation Procedure

The procedure of a typical test run was as follows:

- Warm the cylinder head cooling water to 70°C using a heater in the coolant system
- Switch on the oil pump to circulate and warm up the oil to 70°C.
- Get the engine up to speed (1000rpm)
- Pressurise the fuel tank to 3bar using Nitrogen
- Open the fuel line
- Set the voltage to the Pressure regulator
- Turn the ignition switch on and check for the spark
- Set the throttle position
- Dial the desired settings in the engine management box
- Start injection

6.1.6. Image Acquisition

A User/PC interface was programmed to automate the image acquisition, storage and nomenclature.

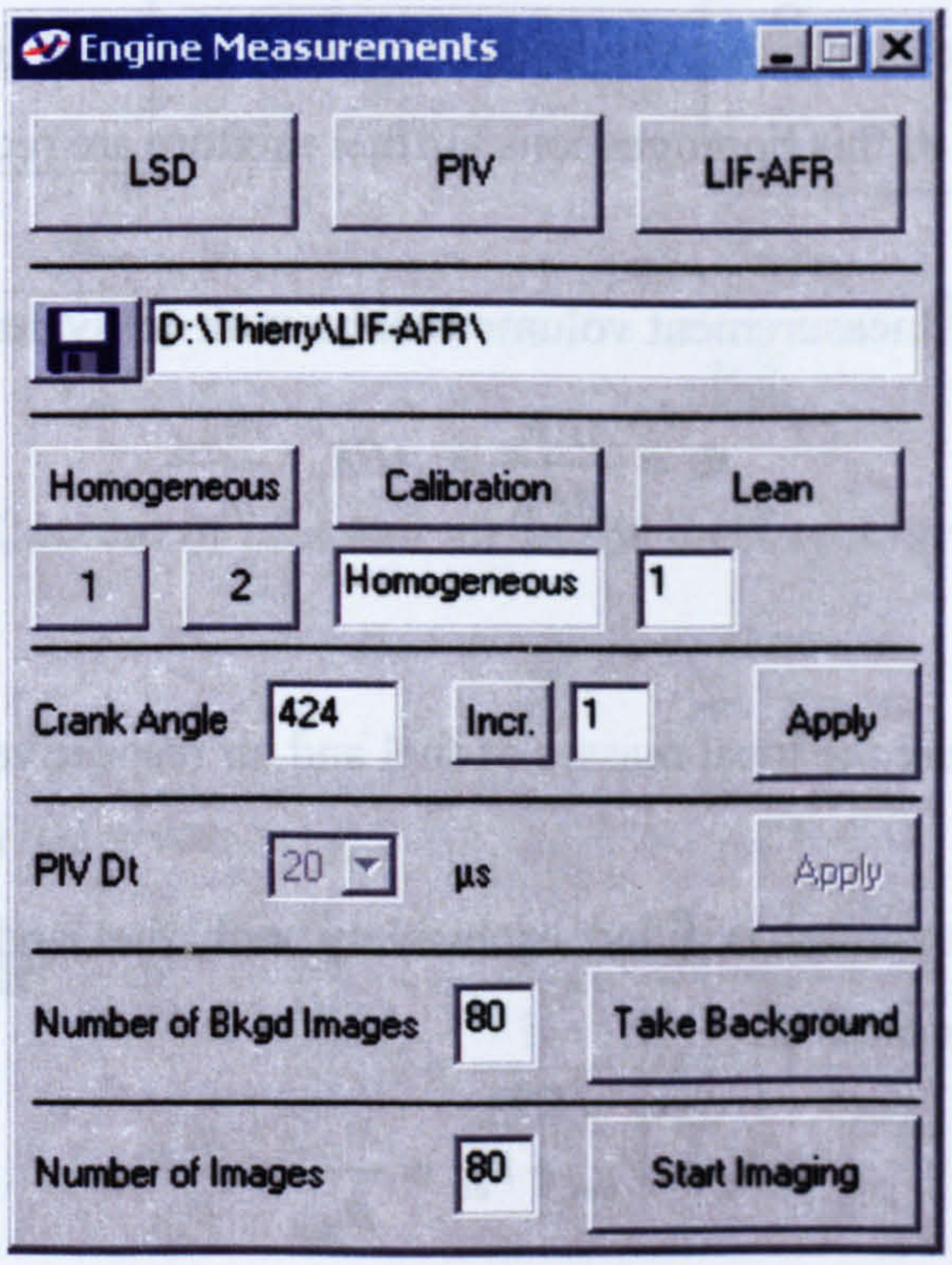

Figure 6-16: User-PC interface for the measurements

6.2. LIF measurements for Equivalence ratio

Equivalence ratio measurements were performed to compare the evolution of fuel distribution and stoichiometry for the early and late injection modes. A mixture of 20% Pentanone in Iso-Octane was used. The stoichiometric equation for the combustion of 1 mole in air is:

$$\left(\frac{4}{5}\cdot C_8H_{18}+\frac{1}{5}\cdot C_5H_{10}O\right)+\frac{115}{10}\cdot\left(O_2+3.76\cdot N_2\right)\rightarrow\frac{37}{5}\cdot CO_2+\frac{41}{5}\cdot H_2O+3.76\cdot\frac{115}{10}\cdot N_2$$

Equation 6-1: Combustion of 20% 3-Pentanone – 80% Iso-Octane in air

The stoichiometric AFR for this fuel mixture is $AFR_{st} = 14.5$.

6.2.1. Measuring equivalence ratio using LIF

The idea of the experiments is to perform two sets of LIF measurements. The 1st set, referred to as *DI* (Direct Injection) consists in recording (at a specific crank angle) the fluorescence of fuel that is directly injected into the cylinder using the injector located in the cylinder head. In the 2nd measurement set, referred to as *Cal* (Calibration), fuel is injected in the intake duct using the injector located upstream of the air-intake and the fluorescence images of this homogeneous air/fuel mixture are recorded.

In both cases, a local measurement volume will have an equivalence ratio of:

$$\Phi=\frac{AFR_{st}}{AFR}=AFR_{st}\cdot\frac{m_{fuel}}{m_{air}}$$

Equation 6-2

where m_{fuel} and m_{air} are the local masses of fuel and air respectively.

Assuming that the cylinder is filled exclusively with fuel and air, the measurement volume (V_T) can be written as:

$$V_T=V_{fuel}+V_{air}=\frac{m_{fuel}}{\rho_{fuel}}+\frac{m_{air}}{\rho_{air}}$$

Equation 6-3

Combining *Equation 6-2* and *Equation 6-3*, the measurement volume is:

$$V_T = m_{fuel} \cdot \left(\frac{1}{\rho_{fuel}} + \frac{1}{\rho_{air}} \cdot \frac{AFR_{st}}{\Phi} \right) = \frac{1}{\Phi} \cdot m_{fuel} \cdot \frac{AFR_{st}}{\rho_{air}} + \frac{m_{fuel}}{\rho_{fuel}}$$

Equation 6-4

This measurement volume for the Calibration and DI experiments are identical. This can be written as:

$$\frac{1}{\Phi^{Cal}} \cdot m_{fuel}^{Cal} \cdot \frac{AFR_{st}}{\rho_{air}} + \frac{m_{fuel}^{Cal}}{\rho_{fuel}} = \frac{1}{\Phi^{DI}} \cdot m_{fuel}^{DI} \cdot \frac{AFR_{st}}{\rho_{air}} + \frac{m_{fuel}^{DI}}{\rho_{fuel}}$$

Equation 6-5

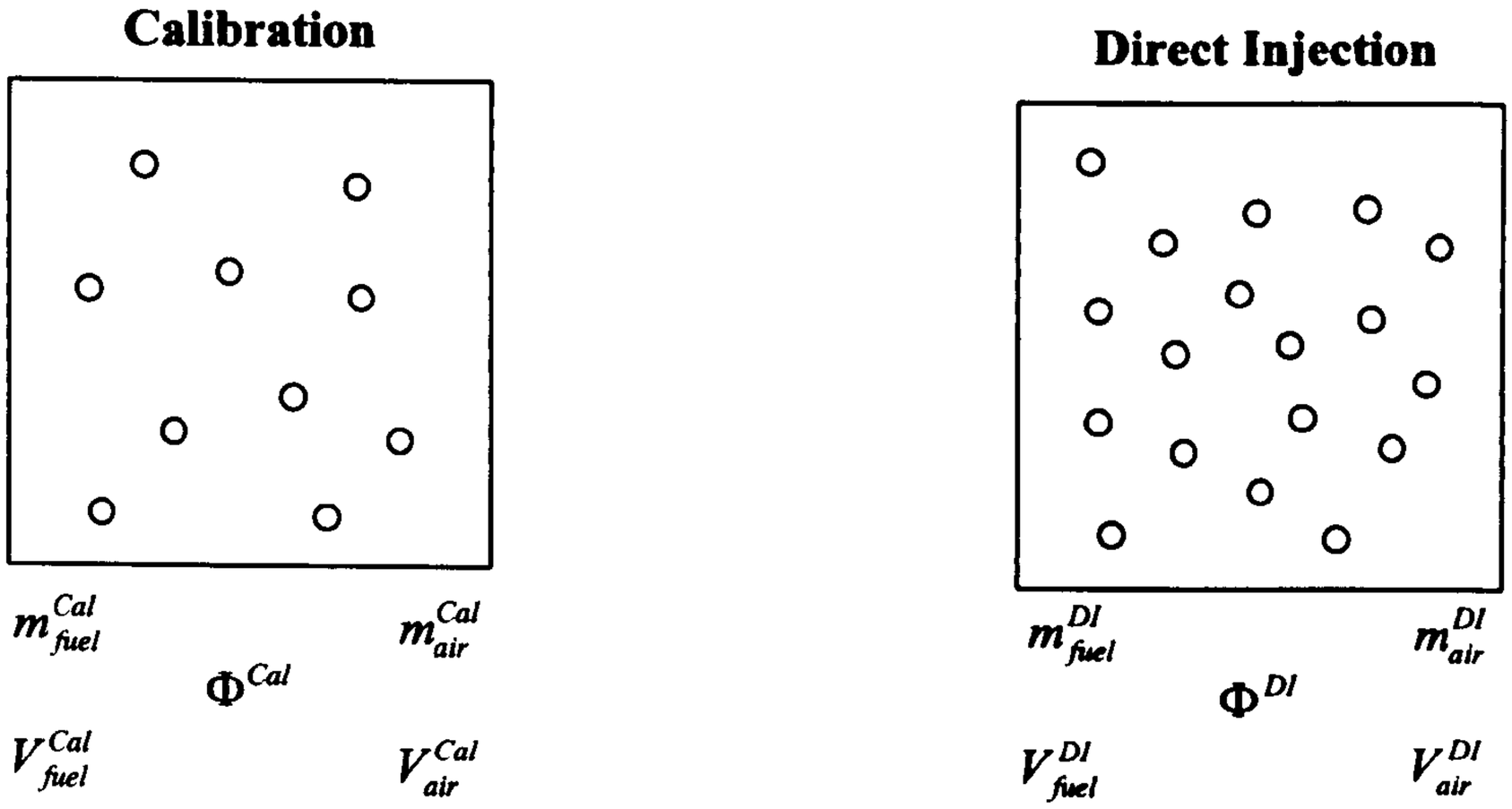

Figure 6-17: Content of fuel and air in the local measurement volume

Rearranging *Equation 6-5* gives:

$$\Phi^{DI} = \Phi^{Cal} \cdot \frac{m_{fuel}^{DI}}{m_{fuel}^{Cal}} \cdot \frac{1}{1 + \frac{1}{AFR_{st}} \cdot \frac{\rho_{air}}{\rho_{fuel}} \cdot \left(1 - \frac{m_{fuel}^{DI}}{m_{fuel}^{Cal}} \right)}$$

Equation 6-6

If a fluorophore that is not quenched by Oxygen is added to the fuel, its fluorescence signal is given by:

$$I_f = C \cdot I_{laser} \cdot \eta \cdot f(P,T) \cdot n_{tracer}$$

Equation 6-7

where C is a proportionality constant, I_{laser} is the local laser intensity, η is the collection efficiency of the detection system, n_{tracer} is the amount of tracer and $f(P,T)$ is the fluorescence yield of the tracer at a given pressure (P) and temperature (T).

When the fuel is fully vaporised, the amount of tracer is proportional to the amount of fuel. In terms of mass of fuel (m_{fuel}), the fluorescent intensity can be written as:

$$I_f = C' \cdot I_{laser} \cdot \eta \cdot f(P,T) \cdot m_{fuel}$$

Equation 6-8

If the LIF measurements are performed using the DI injector, the local fluorescent intensity will be:

$$I_f^{DI} = C' \cdot I_{laser} \cdot \eta \cdot f\left(P^{DI}, T^{DI}\right) \cdot m_{fuel}^{DI}$$

Equation 6-9

If calibration measurements are performed by injecting a homogenous charge using the calibration injector, the local fluorescent intensity can be expressed as:

$$I_f^{Cal} = C' \cdot I_{laser} \cdot \eta \cdot f\left(P^{Cal}, T^{Cal}\right) \cdot m_{fuel}^{Cal}$$

Equation 6-10

Dividing *Equation 6-9* by *Equation 6-10* gives the local ratio of mass:

$$\frac{m_{fuel}^{DI}}{m_{fuel}^{Cal}} = \frac{I_f^{DI}}{I_f^{Cal}} \cdot \frac{f\left(P^{Cal}, T^{Cal}\right)}{f\left(P^{DI}, T^{DI}\right)}$$

Equation 6-11

Combining *Equation 6-6* and *Equation 6-11* gives the equivalence ratio as a function of the fluorescent intensities, the calibration stoichiometry and the fluorescence yields:

$$\Phi^{DI} = \Phi^{Cal} \cdot \frac{I_f^{DI}}{I_f^{Cal}} \cdot \frac{f\left(P^{Cal}, T^{Cal}\right)}{f\left(P^{DI}, T^{DI}\right)} \cdot \frac{1}{1 + \frac{1}{AFR_{st}} \cdot \frac{\rho_{air}}{\rho_{fuel}} \cdot \left(1 - \frac{I_f^{DI}}{I_f^{Cal}} \cdot \frac{f\left(P^{Cal}, T^{Cal}\right)}{f\left(P^{DI}, T^{DI}\right)}\right)}$$

Equation 6-12

6.2.2. Experimental setup

The fluorescence images were recorded using a 12bit Flowmaster3 CCD camera, coupled to a gated IRO image intensifier with a Halle *f* 2 100mm achromatic fused silica lens. A BG4 filter in front of the lens selected the fluorescence. To avoid damage to the lens/intensifier/camera system in case the quartz annulus exploded, a broadband (BB) UV-enhanced mirror was used to reflect the fluorescence at 90° before entering the imaging system.

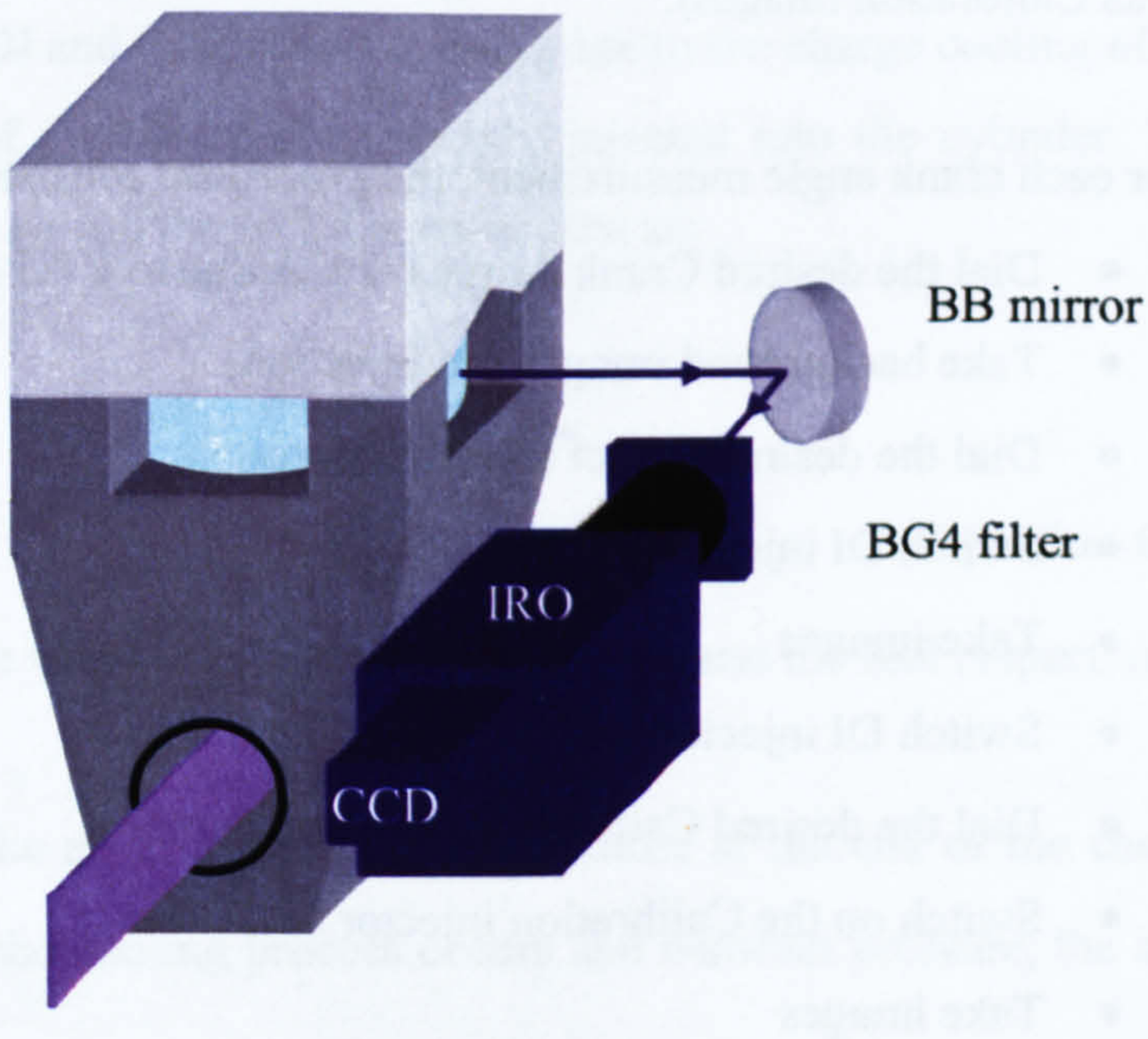

Figure 6-18: Imaging Setup for the Equivalence Ratio measurement

6.2.3. Measurement procedure

The first task consisted in determining the fuel injection duration of the calibration injector for the two throttle positions. The stoichiometry setting for the DI and Calibration run was matched as best as possible in order to obtain similar flame and therefore wall temperatures.

The calibration run requires the mixture to ignite in order to obtain a correct reading from the Lambda sensor. In the late injection case, the engine operated with a lean stratified mixture with an overall equivalence ratio Φ=0.33 (AFR of ~45). A homogeneous mixture will not ignite at this value of AFR. Thus, the mixture was leaned out as much as possible without reaching the misfire limit.

For the early direct injection case, the engine operated with a stoichiometric throttled air-fuel mixture. The calibration injection duration was adjusted to meet the same stoichiometry.

At each crank angle of interest, 2 sets of 80 LIF images were recorded. The first set consisted of images of the direct injection (referred to as DI images), the second set consisted of images from a homogeneous mixture of known equivalence ratio. (referred to as Calibration images).

For each crank angle measurement, the procedure consisted in:

- Dial the desired Crank Angle (-2°CA due to PTU delay)
- Take background images (no injection)
- Dial the desired Direct Injection duration
- Switch DI injector on
- Take images
- Switch DI injector off
- Dial the desired Calibration injection duration
- Switch on the Calibration injector
- Take images
- Switch Calibration injector off
- Repeat for other Crank Angles

Equation 6-12 is obtained by assuming that the laser intensities in the DI measurement and its corresponding Calibration measurement are identical. By alternating a DI and a Calibration measurement, the fluctuation of laser power with time was minimised.

	Early Injection		Late Injection	
	DI	**Calibration**	**DI**	**Calibration**
Injection duration	1.80ms	2.3ms	1.85ms	3.30ms
λ	1	1	~3	1.55
ΔP	340mbar		20mbar	

Table 6-2: Operating Parameters for the equivalence ratio measurements

6.2.4. Fluorescence yield correction

Obtaining equivalence ratio images requires crank-angle resolved determination of the thermodynamic in-cylinder conditions, in order to account for variations in fluorescence yield for the DI and Calibration image.

The differences between the DI and Calibration cycle is due to the charge cooling effect caused by the vaporisation of the fuel that is directly injected into the cylinder. The energy exchange between the air and the fuel can be written as:

$$m_{air} \cdot \Delta H_{air} = -m_{fuel} \cdot \Delta H_{fuel}$$

Equation 6-13

where ΔH_{air} and ΔH_{fuel} are the variation of enthalpy for the air and the fuel respectively.

If the initial temperature of the air is T_{air}^{i} and the temperature at the end of the charge cooling is T^{f}, assuming that the cooling process occurs and constant pressure, the air's change in enthalpy is:

$$\Delta H_{air} = c_{p,air} \cdot \left(T^{f} - T_{air}^{i}\right)$$

Equation 6-14

where $c_{p,air}$ is the specific heat of the air.

6.2.4.1. Early injection case

When direct injection occurs during the intake stroke, even though the injected fuel is in the super cooled regime, it will evaporate until it saturates the air. The partial pressure of the fuel at 25°C is a 10th of the total pressure (P_{fuel}^{sat}=0.06bar). Because the volume of air is 50 times that of the fuel when running at stoichiometric conditions, the fuel can therefore totally vaporise. The initial and final pressure and temperature conditions of the fuel are $\left(P_{fuel}^{i}, T_{fuel}^{i}\right)$ and $\left(P_{fuel}^{sat}, T^{f}\right)$ respectively.

The change in the enthalpy of the fuel can be decomposed as shown in *Figure 6-19*. This enables to write it as:

$$\Delta H_{fuel} = \Delta^{v} H_{fuel} + c_{p,fuel_{gas}} \cdot \left(T^{f} - T_{fuel}^{i}\right)$$

Equation 6-15

where $c_{p,fuel}$ is the specific heat of the fuel and $\Delta^{v}H_{fuel}$ is the heat of vaporisation of the fuel.

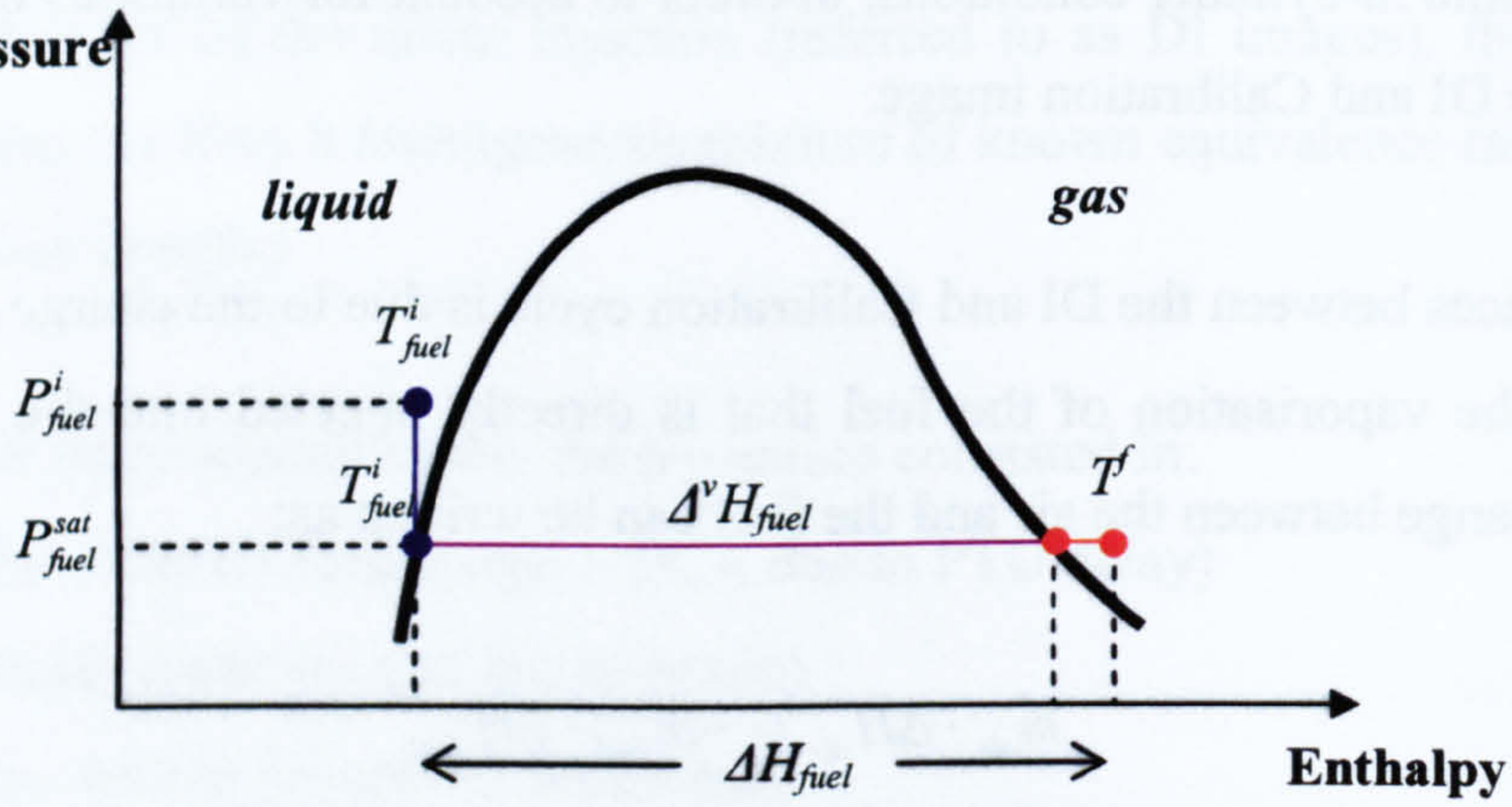

Figure 6-19: Enthalpy change for early injection

By introducing the AFR, the final temperature is given by:

$$T^{f} = \frac{AFR \cdot c_{p,air} \cdot T_{air}^{i} + c_{p,fuel_{gas}} \cdot T_{fuel}^{i} - \Delta^{v} H_{fuel}}{AFR \cdot c_{p,air} + c_{p,fuel_{gas}}}$$

Equation 6-16

The charge cooling was found to be 20°C and the thermodynamic values were taken at 30°C (see *Table 6-3*). The temperature of the charge was calculated assuming an isentropic compression (see *Figure 6-21*).

	Iso-Octane	3-Pentanone	Fuel
$c_{p,gas}$ **(J/g.K)**	2.3	1.6	2.2
$\Delta^v H$ **(J/g)**	300	440	328

Table 6-3: Thermodynamic values at 30°C for the early injection case

6.2.4.2. Late injection strategy

In the case of late injection (670°CA, i.e., 50° BTDC), the in-cylinder pressure and temperature at the end of the intake stroke are identical for the DI and Calibration cases: 0.980bar and 40°C.

The variation between the cycles occurs at 670°CA when the direct injection of fuel causes the charge cooling in the compression stroke. The change in enthalpy can be decomposed as shown in *Figure 6-20* :

$$\Delta H_{fuel} = m_{fuel} \cdot \left[c_{p,fuel_{liq}} \cdot \left(T^{i}_{fuel} - T^{sat}_{fuel} \right) + \Delta^{v} H_{fuel} + c_{p,fuel_{gas}} \cdot \left(T^{sat}_{fuel} - T^{f} \right) \right]$$

Equation 6-17

where $c_{p,fuel_{liq}}$ and $c_{p,fuel_{gas}}$ are the specific heats of the fuel in the liquid phase and gas phase respectively.

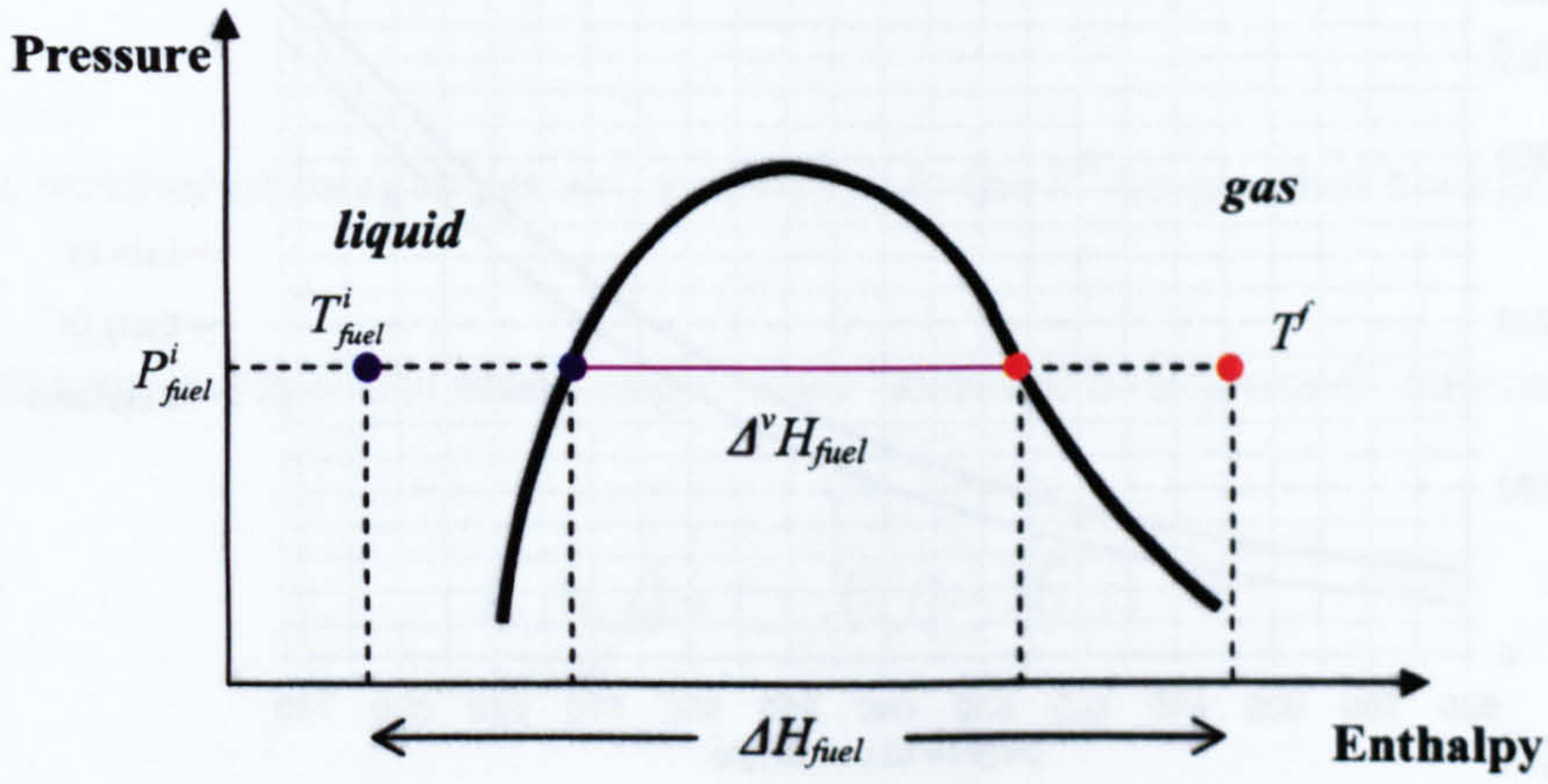

Figure 6-20: Change in enthalpy for late injection

Introducing the AFR, the final temperature is:

$$T^f = \frac{AFR \cdot c_{p,air} \cdot T^i_{air} - c_{p,fuel_{liq}} \cdot T^i_{fuel} + \left(c_{p,fuel_{gas}} - c_{p,fuel_{liq}}\right) \cdot T^{sat}_{fuel} - \Delta^v H_{fuel}}{AFR \cdot c_{p,air} + c_{p,fuel_{gas}}}$$

Equation 6-18

Pressure and temperature were plotted against Degree Crank Angle (°CA) to determine the in-cylinder conditions. At the start of injection, they are P=5bar and T=220°C. The temperature drop was 17°C. The thermodynamic values were therefore taken at 210°C and can be found in *Table 6-4*. The injection lasted approximately 15°CA: the fuel imposed a temperature drop of 1°C per crank angle. This temperature drop was implemented in the isentropic compression for each crank angle.

	Iso-Octane	3-Pentanone	Fuel
$c_{p,liq}$ (J/g.K)	3.5	2.3	3.3
$c_{p,gas}$ (J/g.K)	2.9	2.0	2.75
$\Delta^v H$ (J/g)	170	250	183
T^{sat} (°C)	160	160	160

Table 6-4: Thermodynamic values for the late injection case

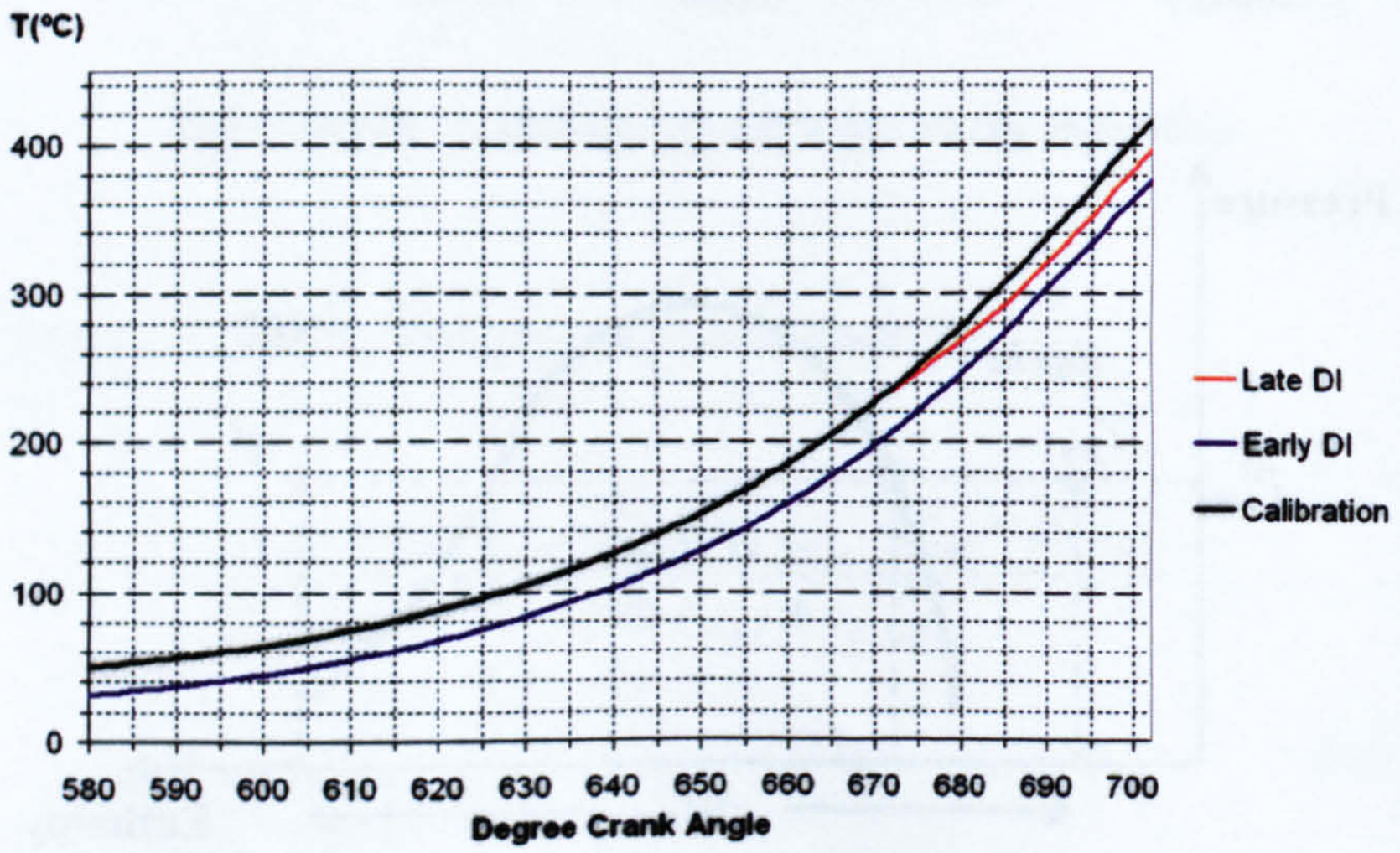

Figure 6-21: In-cylinder Temperatures during the compression stroke

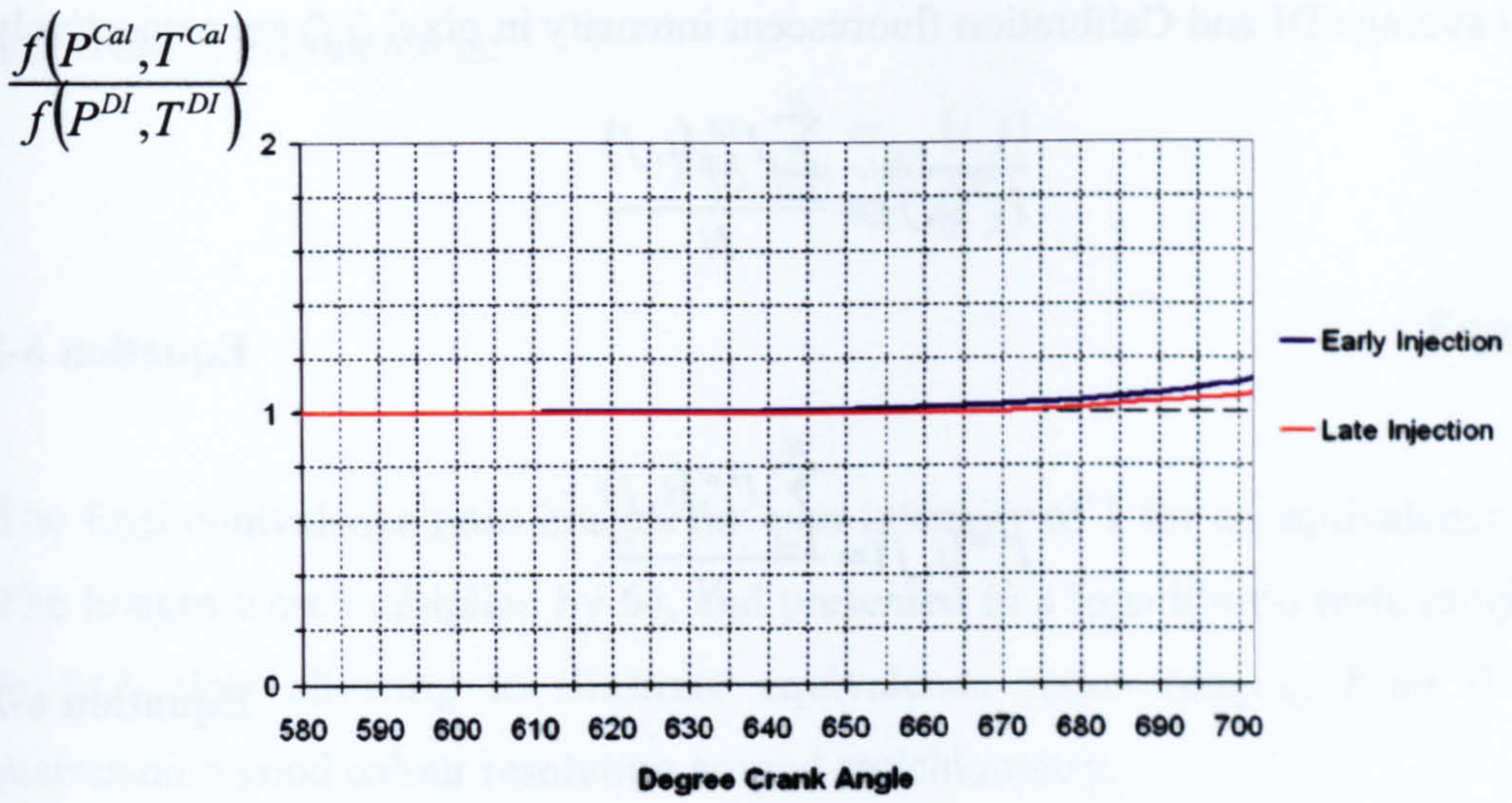

Figure 6-22: Ratio of fluorescence yield during the compression stroke

Figure 6-22 shows a maximum increase of the fluorescence yield ratio by 10% for the ignition crank angle. However, the calculations do not take into account heat input from the cylinder walls, therefore the charge cooling was overestimated. This suggests an overestimation of the increase of the fluorescence yield ratio. For the image processing, the ratio was therefore assumed constant and set to unity.

6.2.5. Image Processing

For each crank angle, the average background image was calculated as:

$$\overline{B(i,j)} = \frac{\sum_{k=1}^{N} B_k(i,j)}{N}$$

Equation 6-19

where N is number of images per set, and $B_k(i,j)$ is the k^{th} single shot background image

The raw images at a specific crank angle were "average background" subtracted:

$$I_{f,k}(i,j) = I_{raw,k}(i,j) - \overline{B(i,j)}$$

Equation 6-20

The local average DI and Calibration fluorescent intensity in pixel (i,j) are respectively:

$$\overline{I_f^{DI}(i,j)} = \frac{\sum_{k=1}^{N} I_{f,k}^{DI}(i,j)}{N}$$

Equation 6-21

$$\overline{I_f^{Cal}(i,j)} = \frac{\sum_{k=1}^{N} I_{f,k}^{Cal}(i,j)}{N}$$

Equation 6-22

The local single-shot equivalence ratio is given by:

$$\Phi_k^{DI}(i,j) = \Phi^{Cal} \cdot \frac{I_{f,k}^{DI}(i,j)}{\overline{I_f^{Cal}(i,j)}} \cdot \frac{1}{1 + \frac{1}{AFR_{st}} \cdot \frac{\rho_{air}}{\rho_{fuel}} \cdot \left(1 - \frac{I_{f,k}^{DI}(i,j)}{\overline{I_f^{Cal}(i,j)}}\right)}$$

Equation 6-23

The average equivalence ratio is expressed as an average of mass, and therefore as an average of intensities:

$$\overline{\Phi^{DI}(i,j)} = \Phi^{Cal} \cdot \frac{\overline{I_f^{DI}(i,j)}}{\overline{I_f^{Cal}(i,j)}} \cdot \frac{1}{1 + \frac{1}{AFR_{st}} \cdot \frac{\rho_{air}}{\rho_{fuel}} \cdot \left(1 - \frac{\overline{I_f^{DI}(i,j)}}{\overline{I_f^{Cal}(i,j)}}\right)}$$

Equation 6-24

The standard deviation is then defined as:

$$\sigma_{\Phi^{DI}}(i,j) = \sqrt{\frac{\sum_{k=1}^{N} \left(\overline{\Phi^{DI}(i,j)} - \Phi_k^{DI}(i,j)\right)^2}{N}}$$

Equation 6-25

The relative fluctuation is:

$$F(i,j) = \frac{\sigma_{\Phi^{DI}}(i,j)}{\Phi^{DI}(i,j)}$$

Equation 6-26

The final equivalence ratio images have an intensity of 1 for an equivalence ratio of 1. The images were multiplied by 64, and presented in a logarithmic scale ranging from 0 to 512, thus allowing to illustrate equivalence ratios ranging from 0 to 8 and maintaining good colour resolution around stoichiometry.

The images for the equivalence ratio fluctuation were multiplied by 64 and were presented on a linear scale ranging from 0 to 124, to illustrate variations up to 200%.

Following Pages:

Figure 6-23: Equivalence ratio and its fluctuations (in%) in the vertical plane in the centre of the combustion chamber. Early Injection (SOI at 420°CA) and Late Injection (SOI at 670°CA). 360°CA is the exhaust/inlet TDC and O°/720°CA is the compression/combustion TDC.

Early Injection

SOI 420°CA

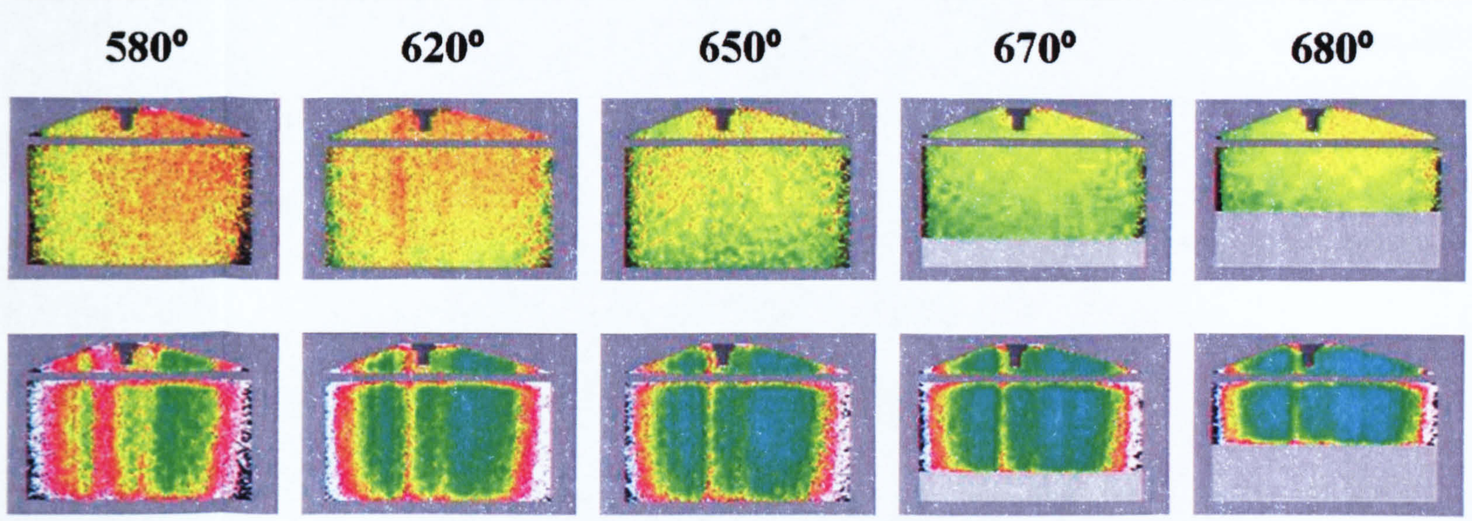

Late Injection

SOI 670°CA

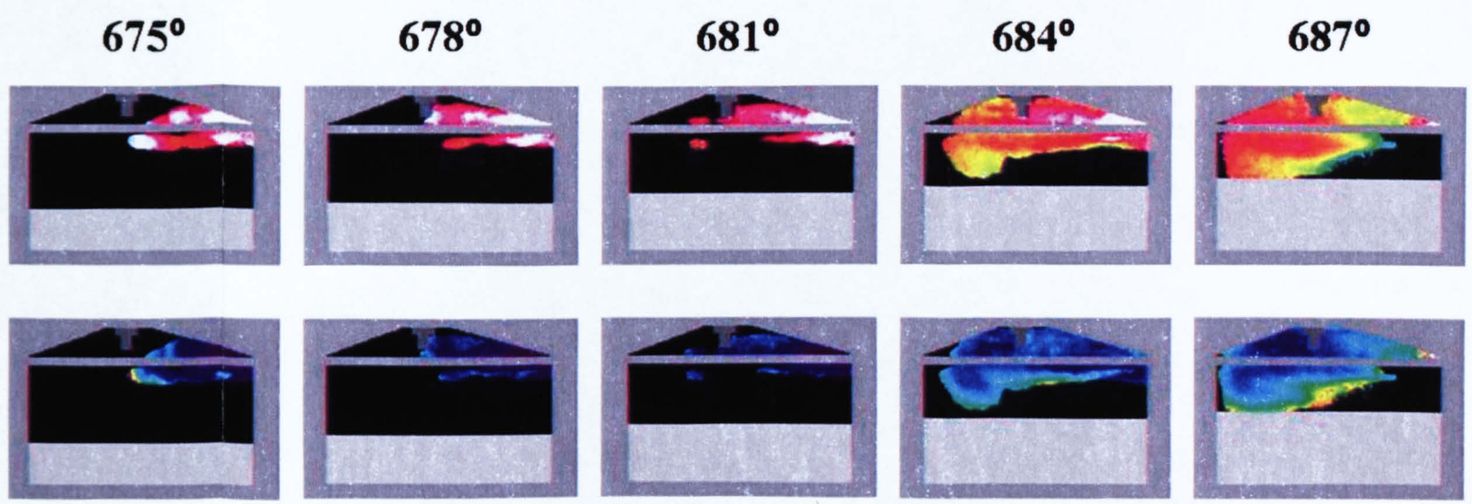

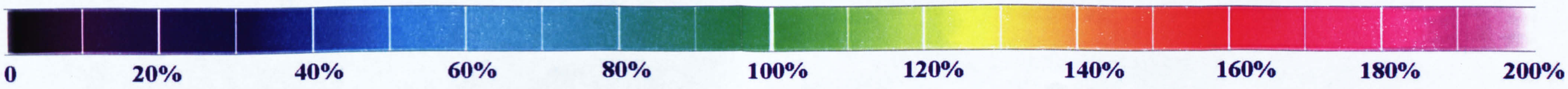

Equivalence Ratio

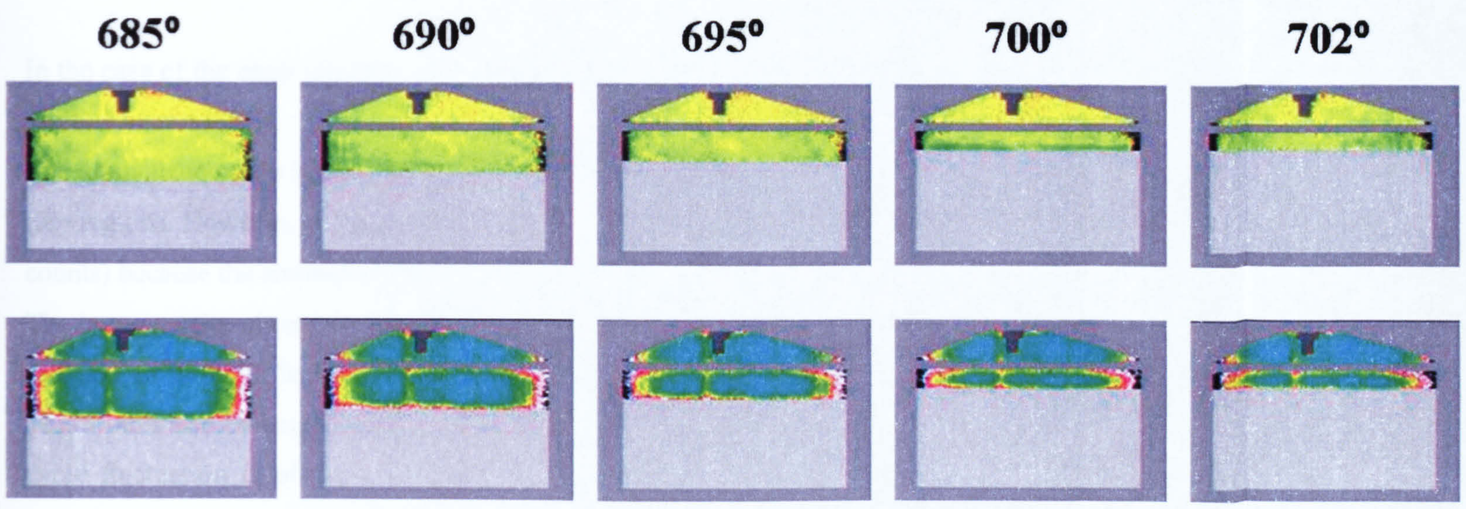

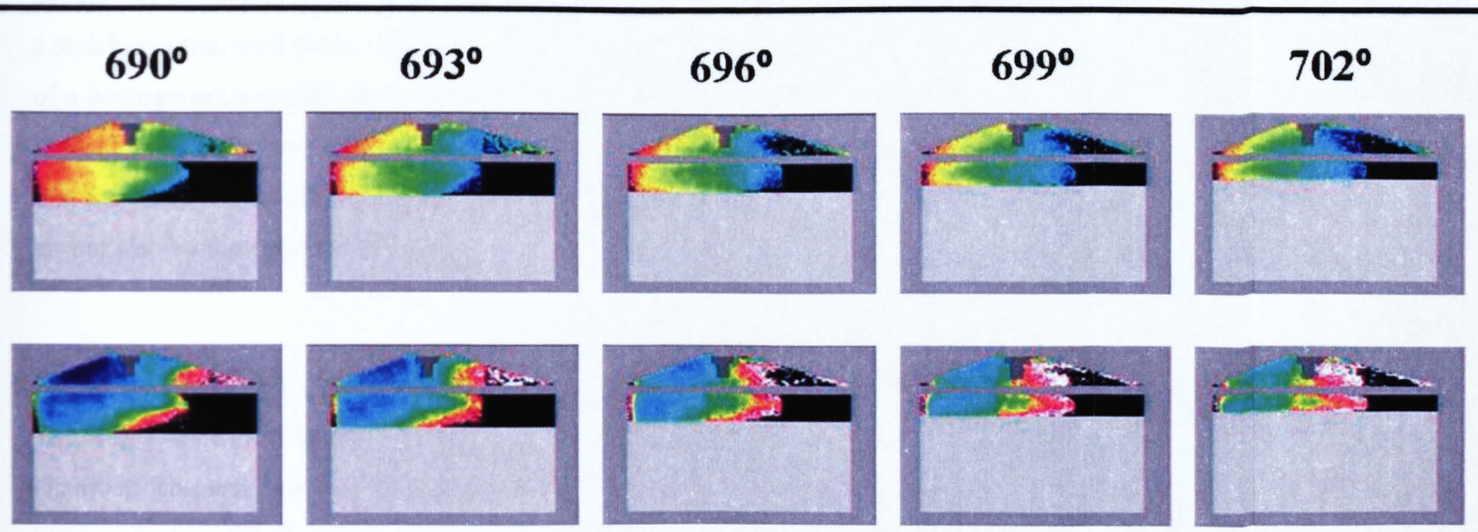

6.2.6. Results

6.2.6.1. Early Injection

The images show vertical structure caused by low laser power regions in the laser sheet (and therefore high SNR). This was due to combustion material deposits on the piston crown window.

In the case of the early injection, the images show a homogeneous and stoichiometric mixture after 650°CA.

The equivalence ratio images obtained at 580°CA (40° ABDC) and 640°CA indicate rich regions. However, at these piston positions, the fluorescence signal was low (20 counts) because the amount of fuel per unit volume is low.

The homogeneity observed at 650°CA (i.e. ~50°CA before ignition) suggests that the fuel and air will still have sufficient time to mix at full load (6 to 7 times the speed). This would also be helped by the increase in turbulence at higher rpm. The cycle-to-cycle fluctuation is of the order of 60%. This value is slightly high, and can be explained by the low signals throughout the experiment.

In this early injection mode, there were no misfires and the flame was blue indicating a stoichiometric, well premixed flame. Therefore, the images were expected to be that of a homogeneous stoichiometric mixture. Had the fluorescence yield correction been applied, the results would have become inconsistent. This further agrees with the idea that the energy input to vaporise the fuel is not only supplied through cooling of the air but also by the cylinder walls.

6.2.6.2. Late Injection

The late injection images show a collapsed spray shooting across the combustion chamber. The early part of the injection shows a very rich mixture ($\Phi>5$) with very little cycle-to-cycle fluctuation. This indicates that the early part of the injection is very stable and can be explained by the high kinetic energy of the ballistic liquid fuel. At the end of the injection (687°CA) a stoichiometric mixture appears at the bottom edge of the spray. This region corresponds to the location in the spray where the

fuel/air interface is the largest. The mixing in that region is also the highest and is indicated by the higher fluctuations (although the higher fluctuations can also be attributed to low signals and high signal-to-noise ratio). After the end of the injection, the cloud of fuel is entrained towards the cylinder wall on the exhaust side. The cycle-to-cycle fluctuations increase, indicating that the mixture is in the gas phase and is prone to fluctuations from in-cylinder air motion. The cloud is stratified: it has very fuel-rich region nearest to the exhaust side, and an increasingly diluted mixture towards the sparkplug.

At time of ignition, the rich fuel cloud has travelled beyond the spark plug, and has disappeared from the optical access. A small stoichiometric mixture is present at the top left of the spark plug, but the mixture around the spark plug is mainly lean. The part of the combustion chamber closest to the injector is ultra lean.

Advancing the time of ignition or retarding the start of injection would locate the ignitable mixture closer to the spark plug. However, in the ideal stratified mixture, the ignitable pocket is the richest region, and the neighbouring air/fuel cloud should be stoichiometric. In this late injection strategy, the ignitable pocket is surrounded by an even richer mixture on one side and a leaner mixture on the other. This results in the production of a sooty flame in the rich region and unburnt hydrocarbons in the other. Another solution could consist in putting the spark plug between the exhaust valves, opposite to the injector and retarding the time of ignition. This would give the rich cloud some additional mixing time, and reduce the equivalence ratio to a more appropriate value (~1.1-1.2) for ignition.

In these conditions, the engine misfired and the flame was yellow, indicating rich regions and that the charge was not well premixed.

The excess air played an important role in keeping the temperature of the burnt gases down: the exhaust temperature stabilised at around 300°C. This allowed to run the engine continuously, whereas in the early/homogenous injection, the exhaust temperatures would exceed 400°C, and injection had to be stopped after 40 images in order not to damage the engine.

6.3. LSD measurements

6.3.1. Experimental Setup

The LSD technique was applied to the engine in the early and late injection modes. The tracer system that gave the best results in the previous study was used: 3-Pentanone (0.5%) mixed with 3-Hexanone (1.5%) in Iso-Octane (98%).

Simultaneous LIF and Mie scatter images were recorded using the same optical set-up as the measurements performed in the pressure vessels: a 4-mirror system and a 12 bit Flowmaster3 CCD camera, coupled to a gated IRO image intensifier with a Halle *f* 2 100mm achromatic fused silica lens. A combination of two ND filters (3 and 0.3) was in the Mie scatter path to attenuate the signal to the same order of magnitude as the fluorescence signal. A BG4 filter was in the LIF path to eliminate residual 266nm and 532nm light. Because the images section was wider than it was high, the camera was mounted at 90° to the IRO to optimise the separation of the PLIF and Mie Scatter image on the two halves of the CCD chip (see *Figure 6-24*).

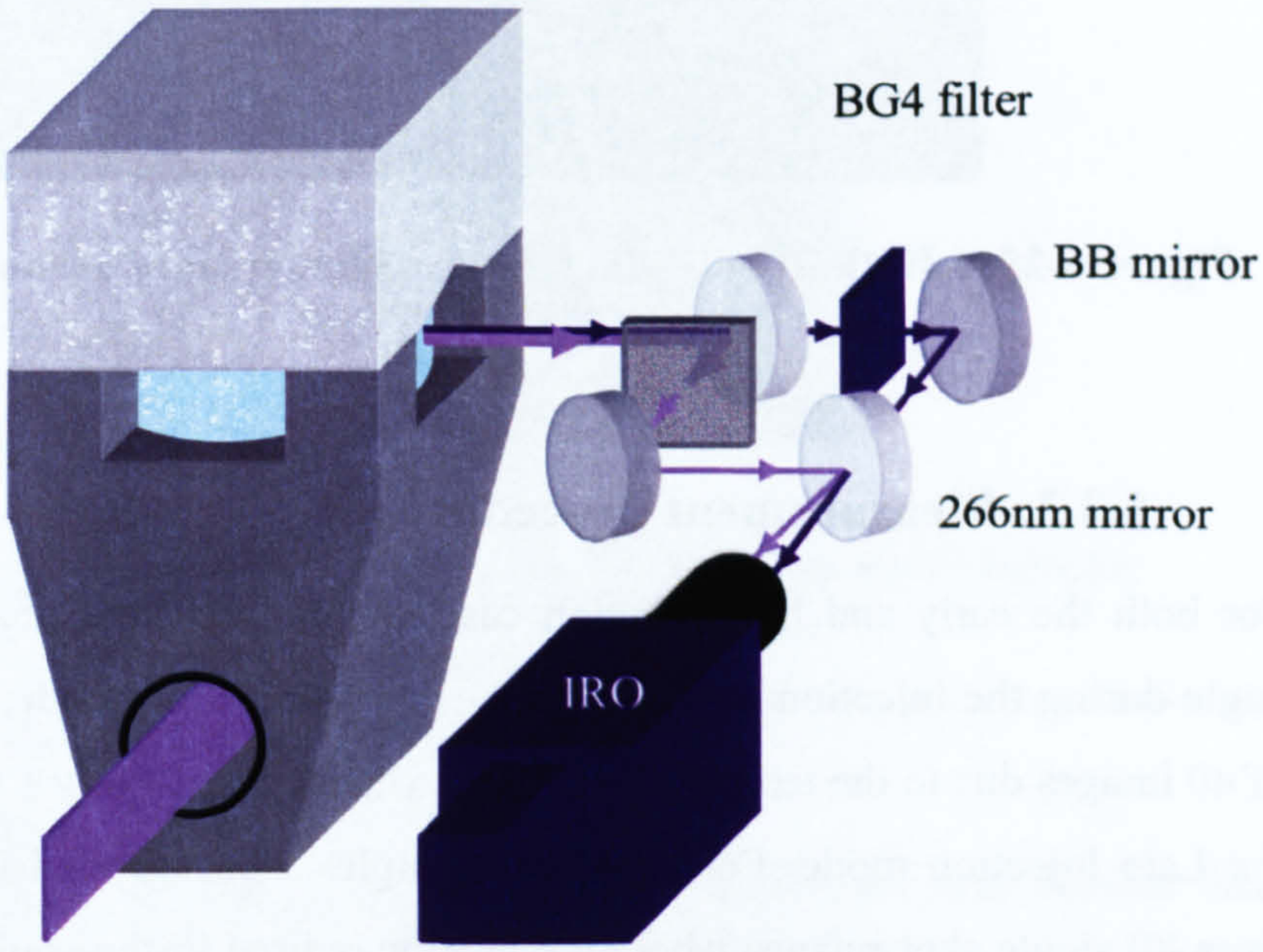

Figure 6-24: Imaging Setup for the LSD technique

6.3.2. Spatial Calibration

A calibration plate with crosses placed at 4mm intervals was used. The ND filter in the Mie scatter path attenuated the intensity of the Mie scatter signal by a factor of 10^3. Because the laser power was low, an acceptable Mie scattering image of the calibration plate was difficult to obtain. This proved to be the major difficulty in applying the technique. The light sheet used to illuminate the calibration plate required extremely fine adjustments and an average of 2000 images was necessary to obtain a suitable calibration image for the image-correction algorithm.

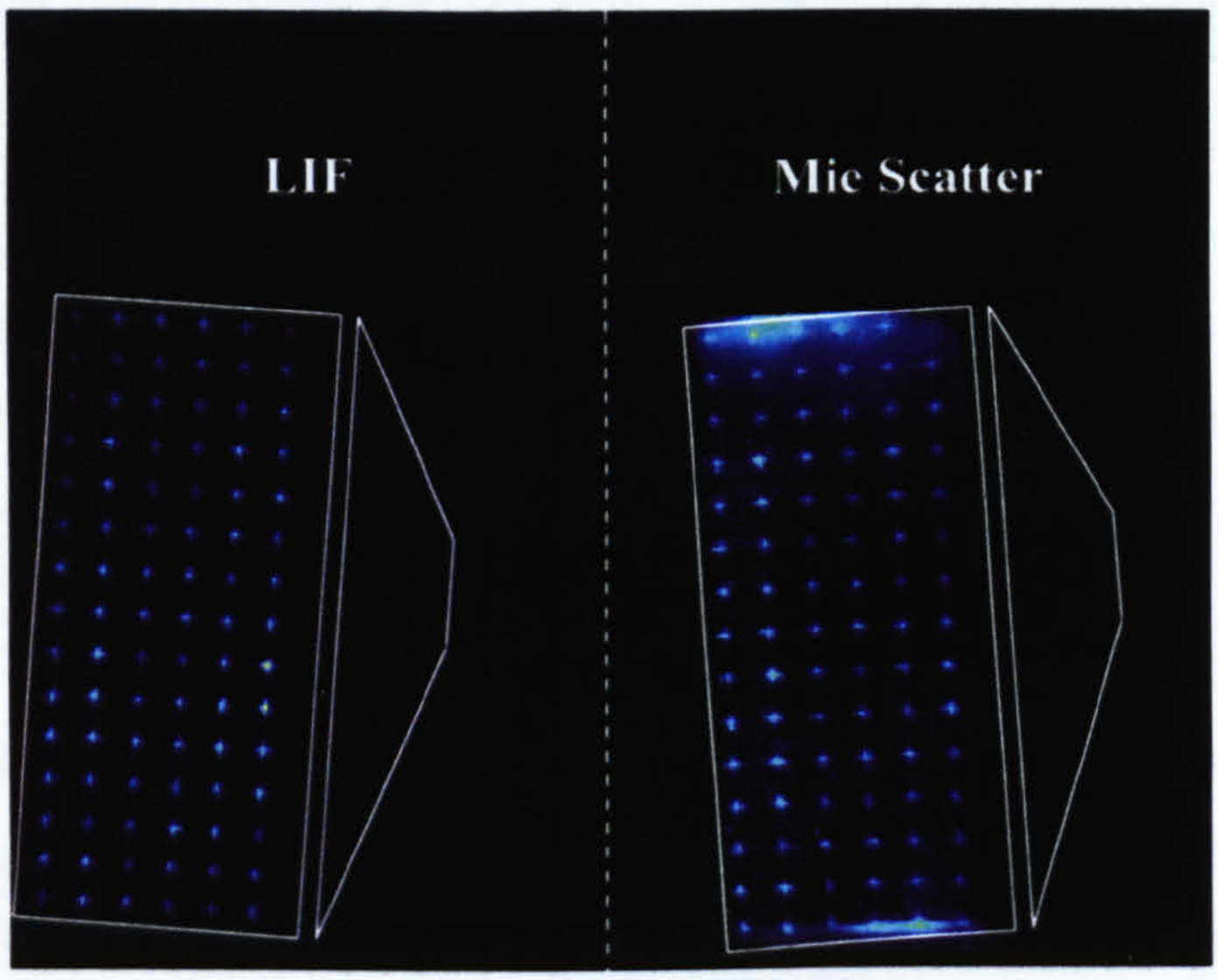

Figure 6-25: LIF (left) and Mie scatter (right) images of the calibration plate

6.3.3. Measurement procedure

For both the early and late injection case, 80 images were recorded at each crank angle during the injection duration. In the Early Injection mode, this required 2 runs of 40 images due to the temperature of the exhaust gases. Only 1 run was necessary in the Late Injection mode. For each crank angle, a background image was averaged from 80 single shot images where the laser was fired in the engine without injecting fuel.

The laser sheet was positioned at the centre of the combustion chamber. The triggering scheme for the laser, intensifier and camera was the same as the equivalence ratio measurements.

6.3.4. Image Processing

The images were processed to obtain average and rms data for the PLIF and Mie scatter images.

The images were background subtracted. An additional spray-induced background was subtracted (typically 2 to 5 counts). The images were then corrected for position. The LSD images were obtained by dividing the corrected average image of PLIF by the corrected average image of the Mie scatter.

SMD images were then determined by multiplying the LSD image by a Calibration constant. Due to the similarities between the injector present in the engine (Bosch swirl 70°/10°) and the injector used in the pressure vessels (Bosch swirl 70°/0°), it was assumed that both would yield similar SMDs. The LSD images were therefore calibrated using the SMD values of from the 70°/0°.

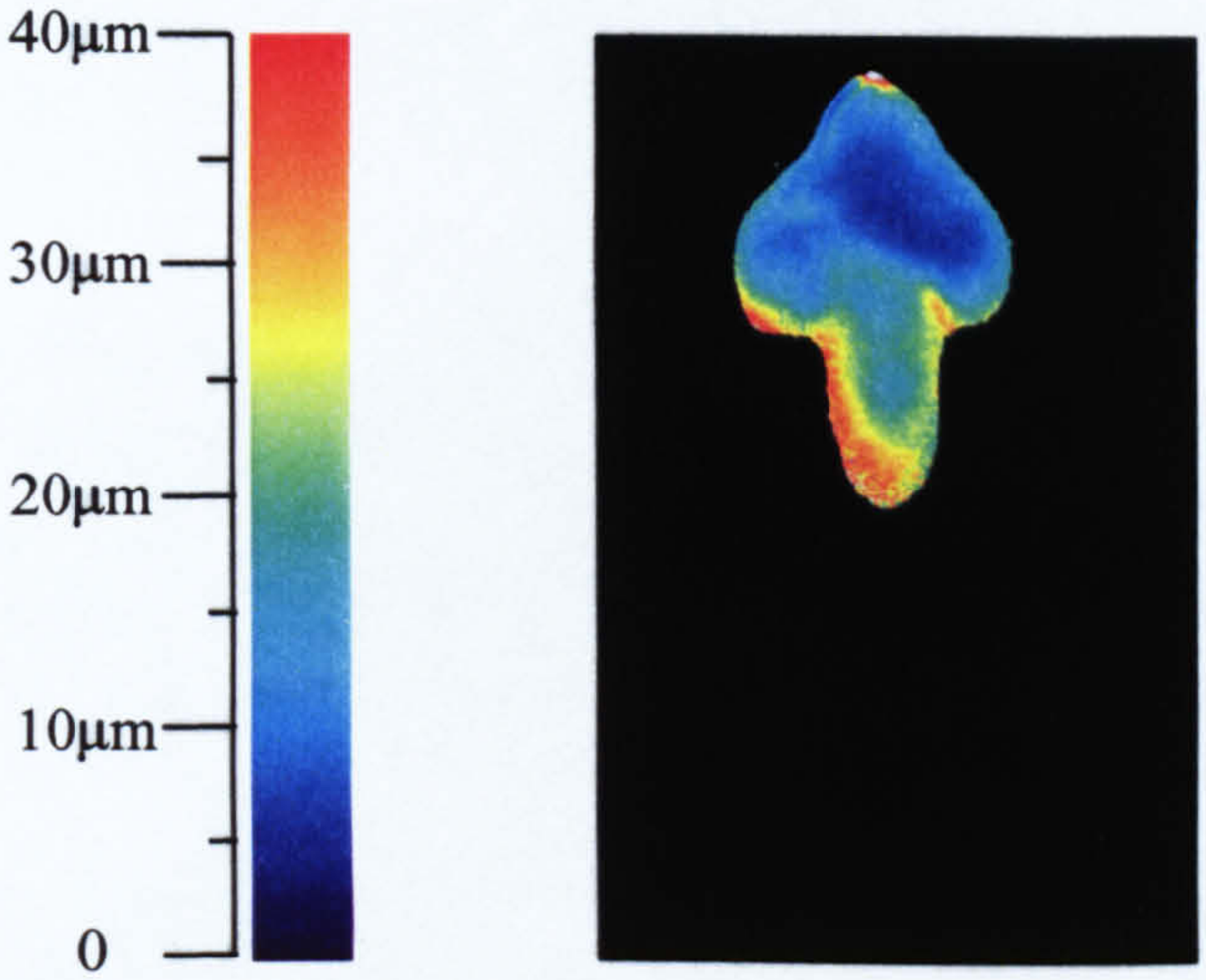

Figure 6-26: SMD image from the 70°/0° Bosch Swirl Injector

Following pages:

Figure 6-27: Early Injection (SOI: 420°CA) - LIF and Mie scatter images (Average and Rms) presented in a logarithmic scale. The SMD image is a calibrated LSD image presented in linear scale.

Figure 6-28: Late Injection (SOI: 670°CA) - LIF and Mie scatter images (Average and Rms) presented in a logarithmic scale. The SMD image is a calibrated LSD image presented in linear scale.

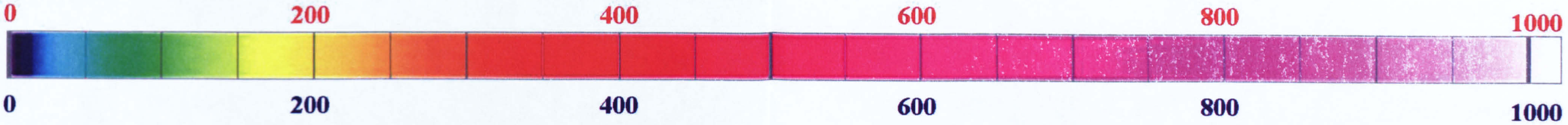
0
200
400
600
800
1000
0
200
400
600
800
1000

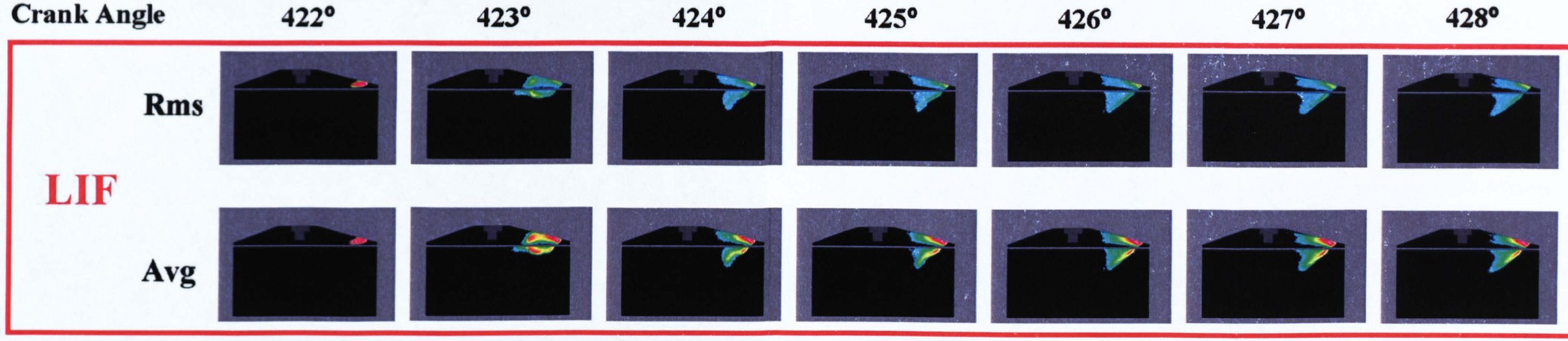
Crank Angle
422°
423°
424°
425°
426°
427°
428°
LIF
Rms
Avg

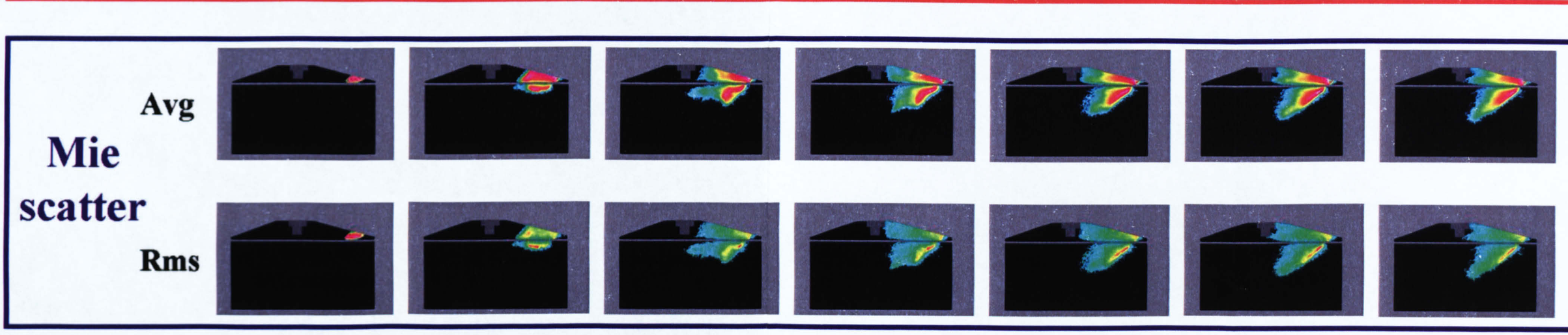
Mie scatter
Avg
Rms

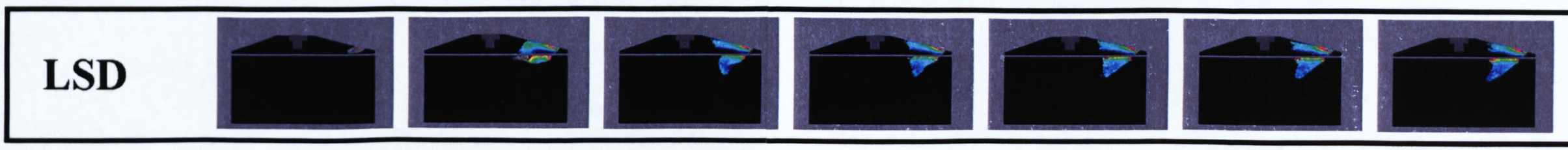
LSD


0
10μm
20μm
30μm
40μm

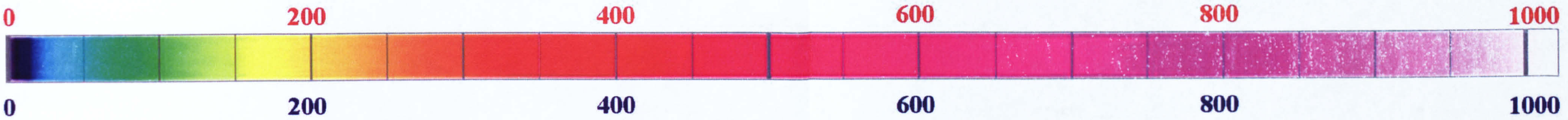

429° 430° 431° 432° 433° 434° 435° Crank Angle

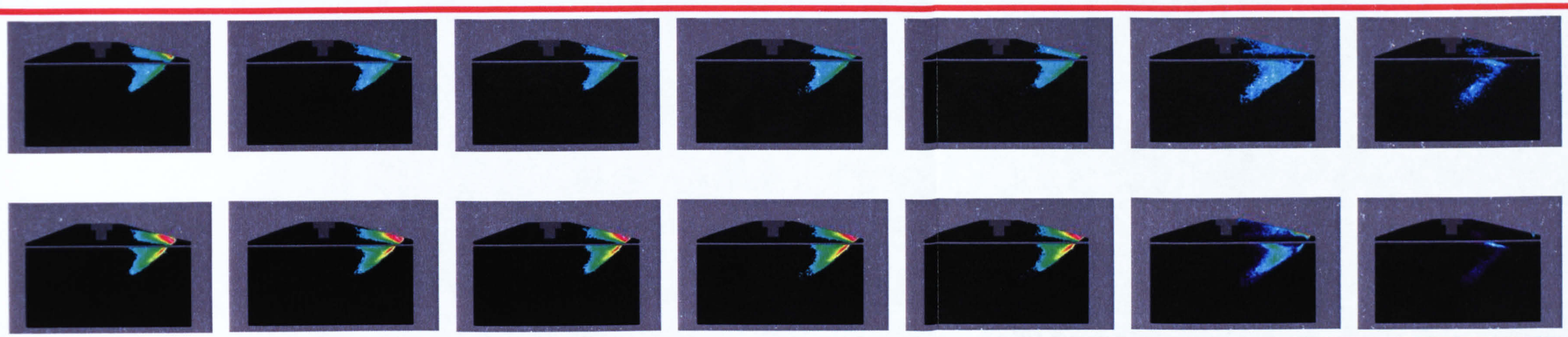

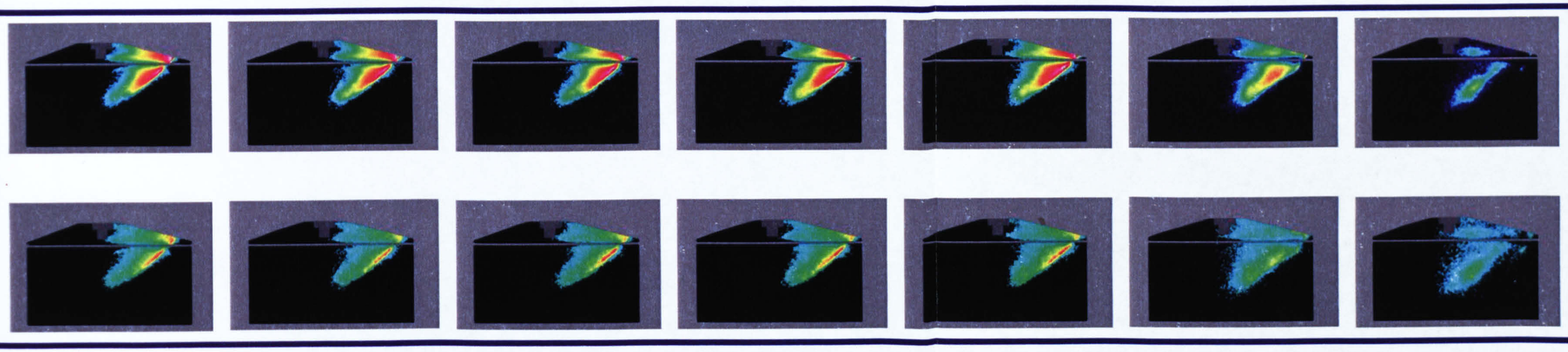

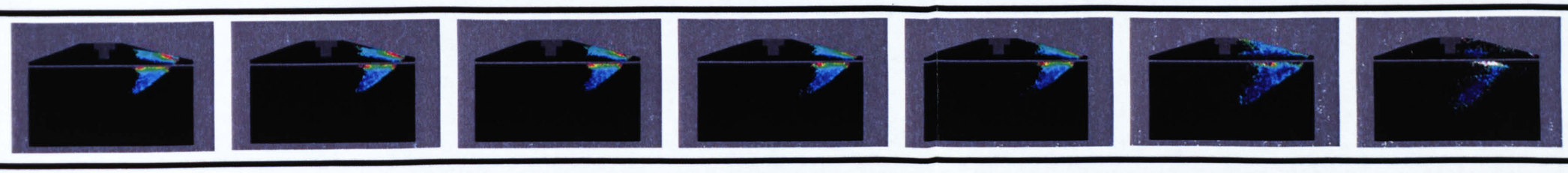

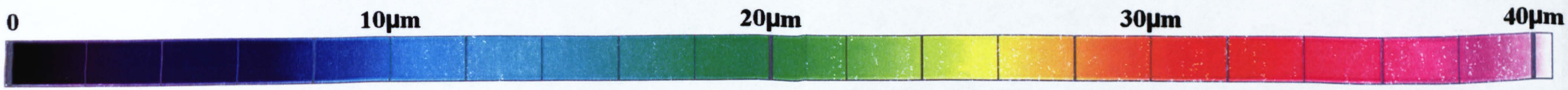

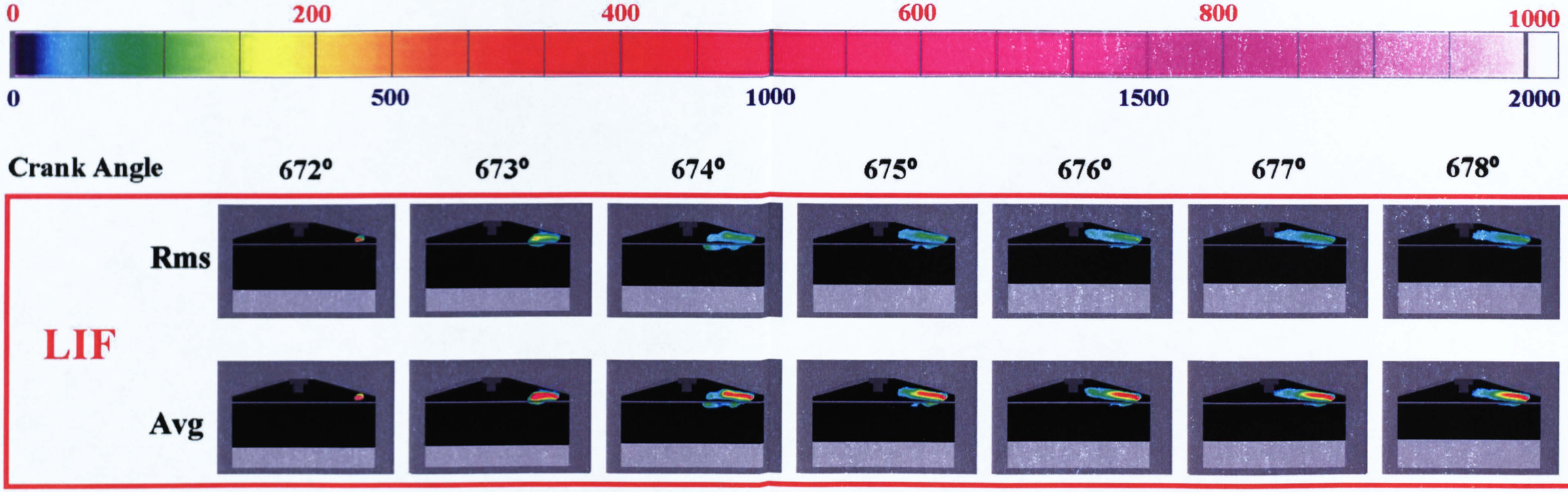
0
200
400
600
800
1000
0
500
1000
1500
2000
Crank Angle
672°
673°
674°
675°
676°
677°
678°
LIF
Rms
Avg
Mie scatter
Avg
Rms
LSD
0
10μm
20μm
30μm
40μm

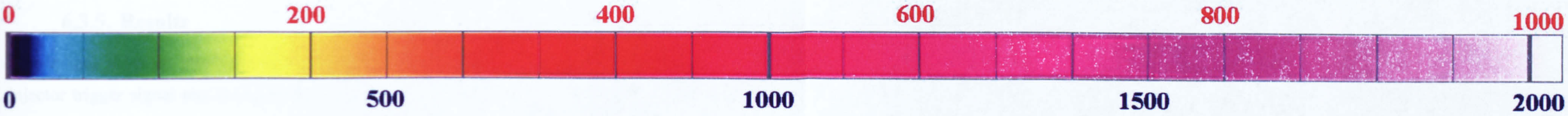

679° 680° 681° 682° 683° 684° 685° Crank Angle

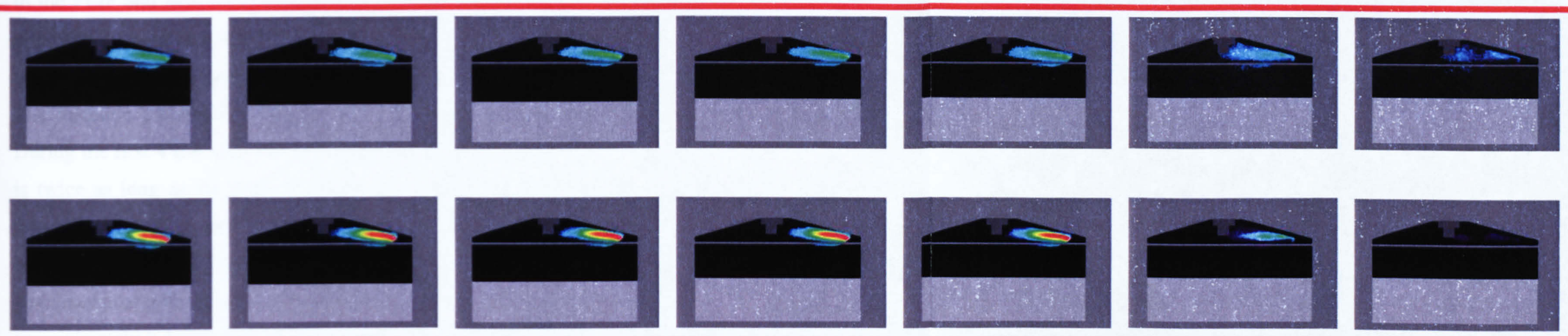

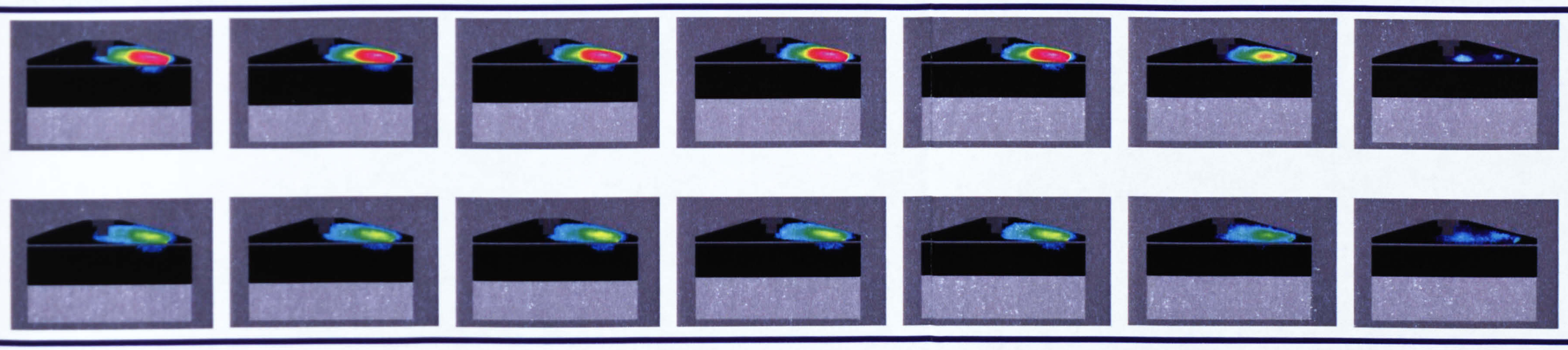

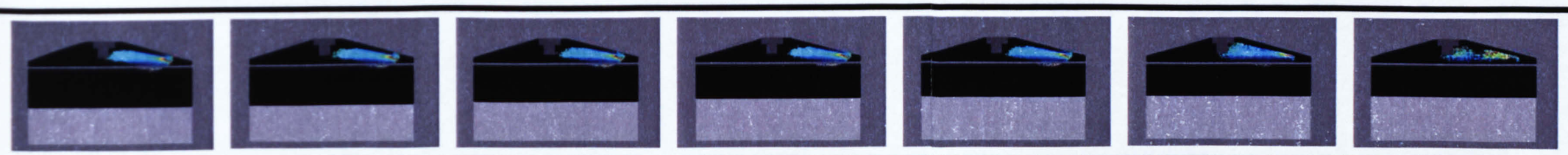

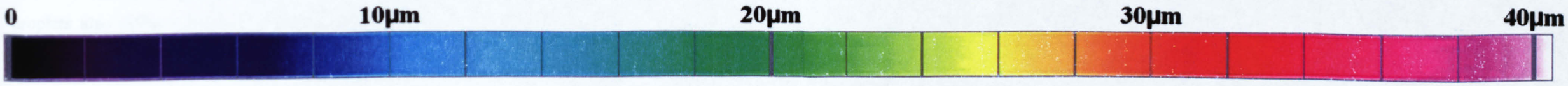

6.3.5. Results

The images show an injector delay corresponding to 2°CA (i.e. 0.33μs) between the injector trigger signal and the actual start of injection (or Optical Start Of Injection – OSOI).

At 1000rpm, an injection duration of 1.8ms represents 11°CA. However, the intensities in the PLIF and Mie scatter images only start reducing 12°CA after OSOI. At 13°CA after OSOI, there is no more fuel at the injector tip, indicating that the injector closes within 2°CA. That suggests that the injector opens fully within 2°CA.

The injection process for both the early and late strategies shows 3 distinct phases. During the first 4°CA after OSOI, the spray is in a transient phase. This transient phase is twice as long as the needle lift. The variation of the fuel passage causes the fuel pressure to oscillate and these oscillations are not immediately attenuated when the injector is fully open. The fuel exiting the injector at this early phase has no common characteristics with the later part of the spray. It is referred to as "pre-spray". It takes approximately 0.66ms for the spray to fully develop. From 4°CA to 11°CA after OSOI, the injection is in steady state and the spray geometry is unchanged: as the injector closes, the cone angle is unchanged.

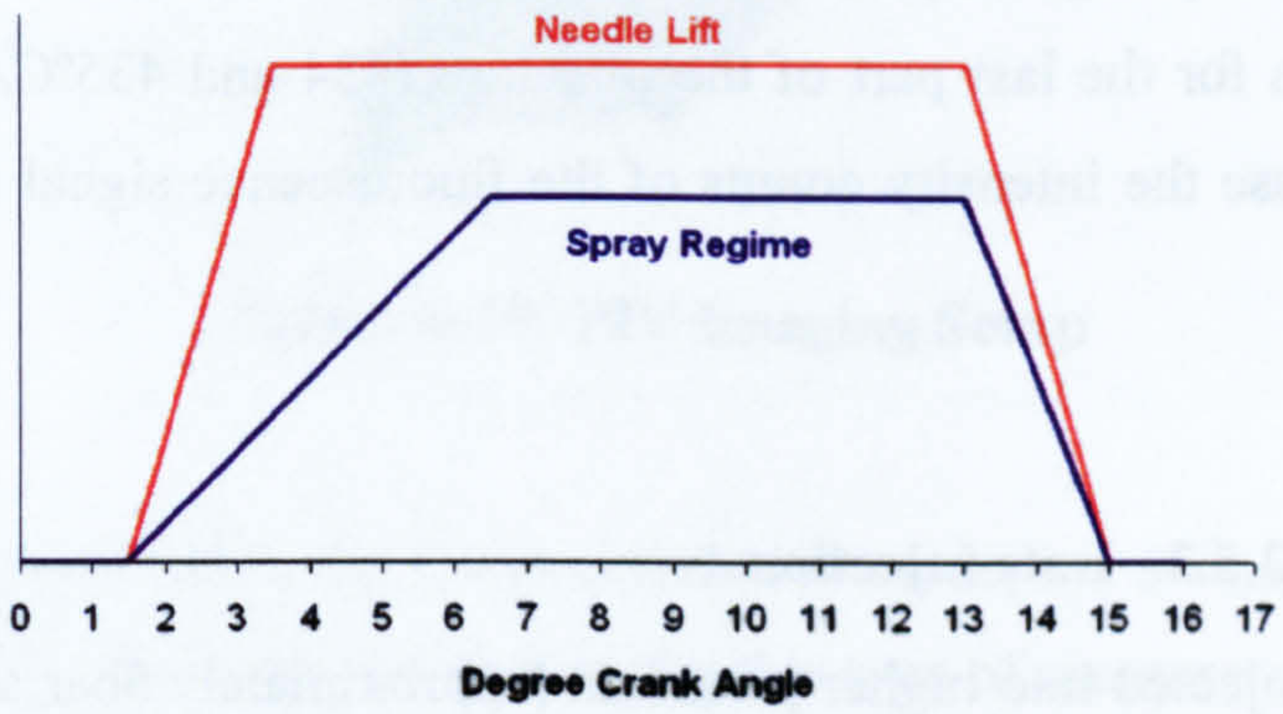

Figure 6-29: Injector Opening and Spray Regime

When the spray is fully developed, the fluorescence signal remains constant even though there is an increasing amount of fuel present inside the cylinder. This can be explained by the conical nature of the spray, whereby the number of droplets per unit volume decreases as they travel away from the injector tip. The evaporation of these droplets also diffuses mass outside the sheet. Eventually, the fluorescence from the diluted tracer is below the detection threshold of the intensifier/camera system.

6.3.5.1. Early Injection

For this injection strategy, the cone angle of the fully developed spray is 70°.

At the start of the injection (422°CA), the SMDs are very high. These values are inaccurate, because the fuel is likely to be present in ligaments and the LSD technique only applies to spherical droplets.

In these conditions, the fuel temperature is below boiling point. Therefore the evaporation process requires the presence of unsaturated air.

At 423°CA, most of the pre-spray has SMD values around 20μm. The droplet sizes at the edge of the spray in the near nozzle region are twice as high.

At 424°CA, the spray has started to open up, therefore enhancing evaporation: the droplet sizes have decreased to around 15μm.

Beyond 425°CA, when the spray is established, the droplet sizes around the nozzle are 30μm). The proximity of the cylinder head limits the motion and availability of air for the top part of the spray, therefore compromising the mixing and evaporation. On the other hand, the bottom part of the spray benefits from almost unlimited amounts of unsaturated air, and no boundary conditions. This results in higher SMDs at the top (15μm) compared to the bottom (10μm). Furthermore, the swirling motion of the spray drives the larger droplets towards the edge of the spray. This further contributes to the high SMDs in the top edge (18μm).

The SMD values for the last part of the injection (434 and 435°CA) are unfortunately unreliable, because the intensity counts of the fluorescence signal are too low to yield accurate data.

6.3.5.2. Late injection

As the spray is injected into higher pressures (approximately 5bar at 670°CA), the cone angle collapses to 30°. This feature is common to swirl injectors and is explained by the breaking down of the swirling motion due to the increased density of the air. The reduced centrifugal force homogenises the droplet distribution and the SMDs within the spray are approximately 13μm. This collapse of the spray increases the density of the droplets and therefore reduces the air/fuel mixing.

The droplet sizes around the nozzle (35μm) are identical to the early injection case.

6.4. PIV Measurements

6.4.1. Experimental Setup

Mie scatter PIV was applied to the optical engine using a 532nm light sheet. The fuel consisted of Iso-Octane only.

The images were captured on a FlowMaster3 Camera coupled to a Nikon *f* 4 50mm lens. A 532nm filter was installed on the end of the lens to select the Mie scattering. A broadband mirror reflected the signal at 90º.

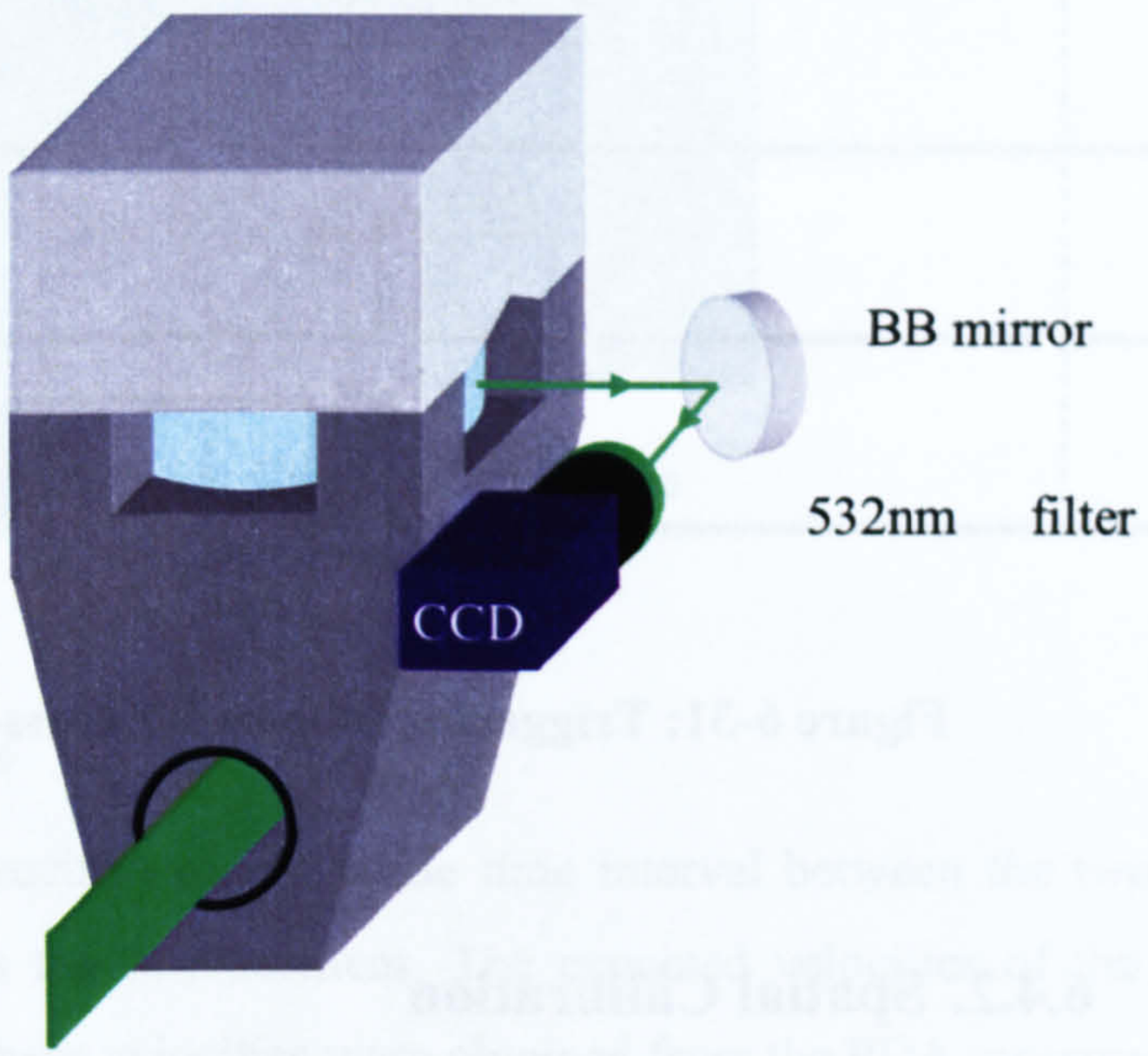

Figure 6-30: PIV Imaging Setup

The images were recorded in the Cross-correlation mode, i.e. 2 images per frame. The triggering scheme for the laser and camera for this type of measurement is illustrated in *Figure 6-31*. In this mode, the camera exposure is fixed to 10μs for the 1st frame and 125ms for the 2nd frame at the end of which both frames are read out to the computer. The camera trigger is such that the first lasing occurs at the end of the 1st frame.

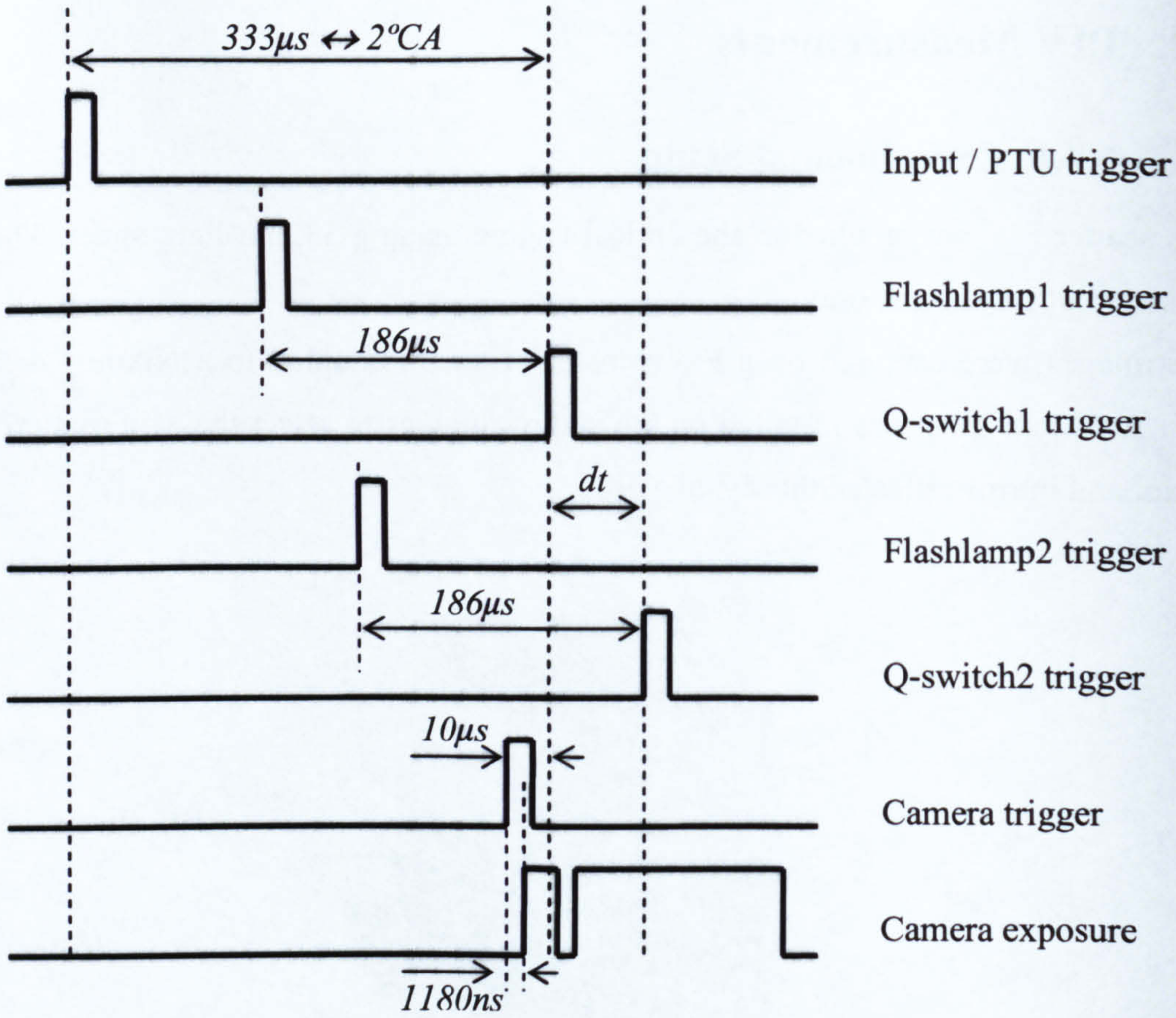

Figure 6-31: Triggering scheme for cross-correlation PIV

6.4.2. Spatial Calibration

Usually, PIV is applied to flow measurements, where the flow is seeded with low density particles. The cross-correlation is then accurate because the intensities in the interrogation window have distinct intensity peaks. In the case of fuel velocity measurements, the fuel acts as the seed and can be extremely dense (see *Figure 6-32*).

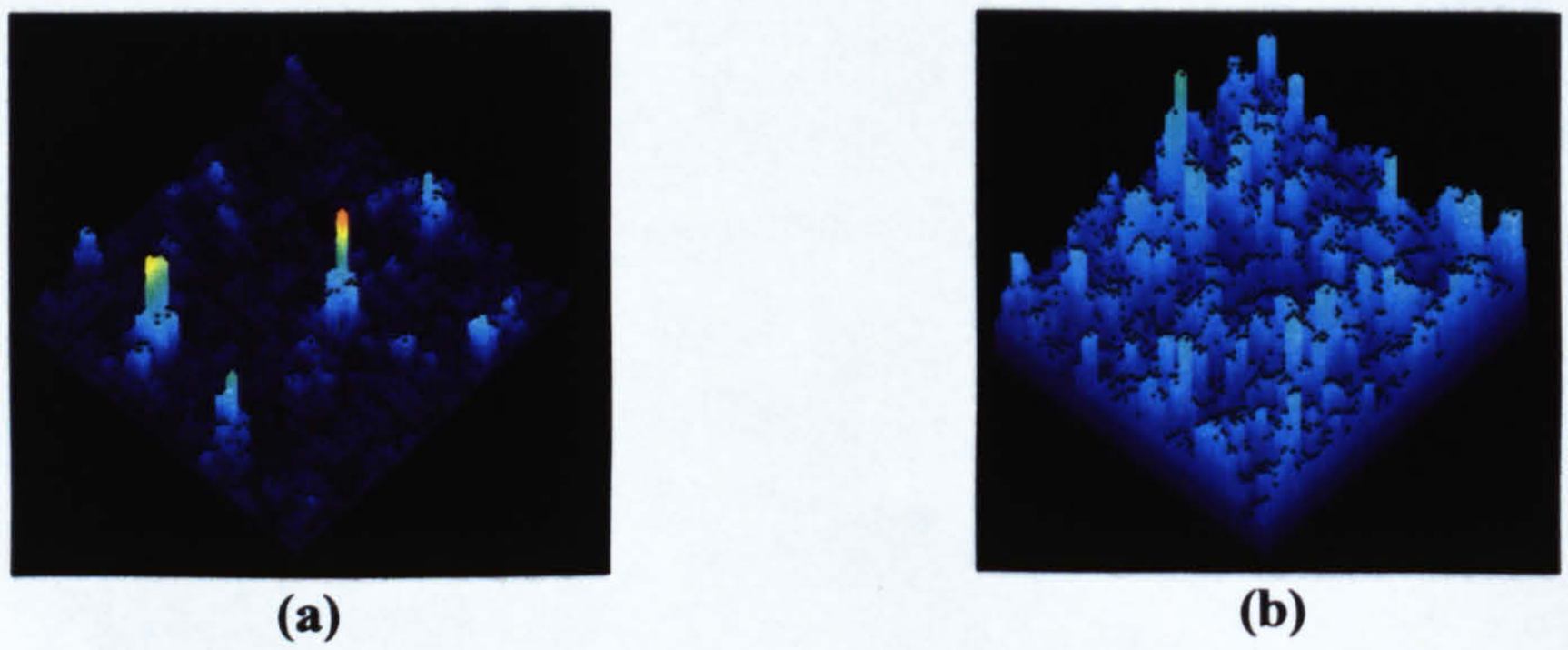

(a) **(b)**

Figure 6-32: Interrogation regions of the spray – non dense (a) and dense (b)

For the cross-correlation to be successful, the image resolution must be such that structure can be resolved. The spray was magnified as much as possible whilst maintaining it entirely within the camera frame. The focusing of the camera and the spatial calibration of the combustion chamber was performed by illuminating the calibration plate with a flashlamp. The resolution was 30μm per pixel.

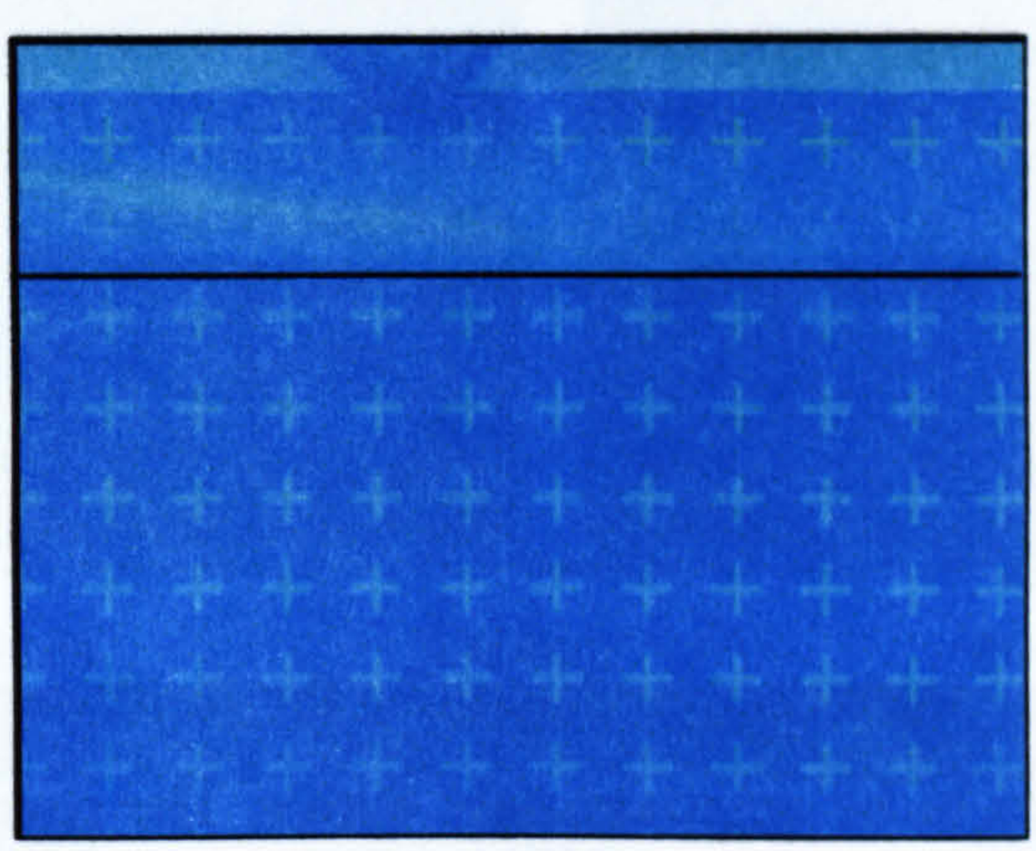

Figure 6-33: Calibration Image

6.4.3. PIV Settings

For a fixed resolution, the crucial variable is the time interval between the two laser shots (*dt*), because it defines the displacement. The expected velocities of the spray ranged from 1m/s to 80m/s (these velocities were obtained from the PDA measurements with the 70°/0° Bosch swirl injector). *Table 6-5* shows the pixel displacement for various speeds, at various values of *dt*.

Velocity / *dt*	1m/s	5m/s	10m/s	20m/s	50m/s	80m/s
05μs	0.2	0.8	1.7	3.3	8.3	13.3
10μs	0.3	1.7	3.3	6.7	16.7	26.7
15μs	0.5	2.5	5.0	10.0	25.0	40.0
20μs	0.7	3.3	6.7	13.3	33.3	53.3

Table 6-5: Displacements in pixels for various velocities and *dt*

For each crank angle, 100 double-frame images were recorded for 3 different *dt*s: 5, 10 and 20μs. Before each set of 100 images, a background image was averaged from 100 single shot images where the laser was fired in the engine without injecting fuel.

The images were background subtracted and corrected. To reduce computing time, the images were masked, so that vectors would only be calculated in the region where the spray was present.

The individual images were then processed with different interrogation window sizes with single passes (64×64 and 32×32), constant window-size multipasses (64×64 and 32×32) and adaptive multipasses (64×64 then 32×32).

6.4.4. Results

The Mie scatter images were used to determine the displacement of the pre-spray. Its velocity was calculated to be approximately 80m/s. The results that gave the closest velocity values were obtained with a *dt* of 5μs.

The spray density is the main reason for this result. Many droplets are travelling in slightly different directions. By setting a short time interval, their displacement is kept low and similar: the peak in the cross-correlation indicates this displacement. For longer time intervals, the displacements of the numerous droplets will be different and the peak observed in the cross-correlation will not correspond to any physical displacement.

Amongst the results obtained with *dt*=5μs, the best match was obtained using a constant window size multipass with a 32×32 interrogation region and a 50% overlap.

The single shot vector fields obtained in *Figure 6-34* illustrate the problems caused by high density: in both the early and late injection cases, the vectors obtained in the very dense region around the nozzle are incorrect. Also, some regions of the image have patches where velocity data are incorrect, or could not be determined at all. These patches with incorrect data vary from one image to another. Therefore, the averaging of the single shot vector fields gives an ensemble idea of the spray velocities, but the velocities obtained in the denser parts of the spray, where the data are ambiguous, are likely to be underestimated.

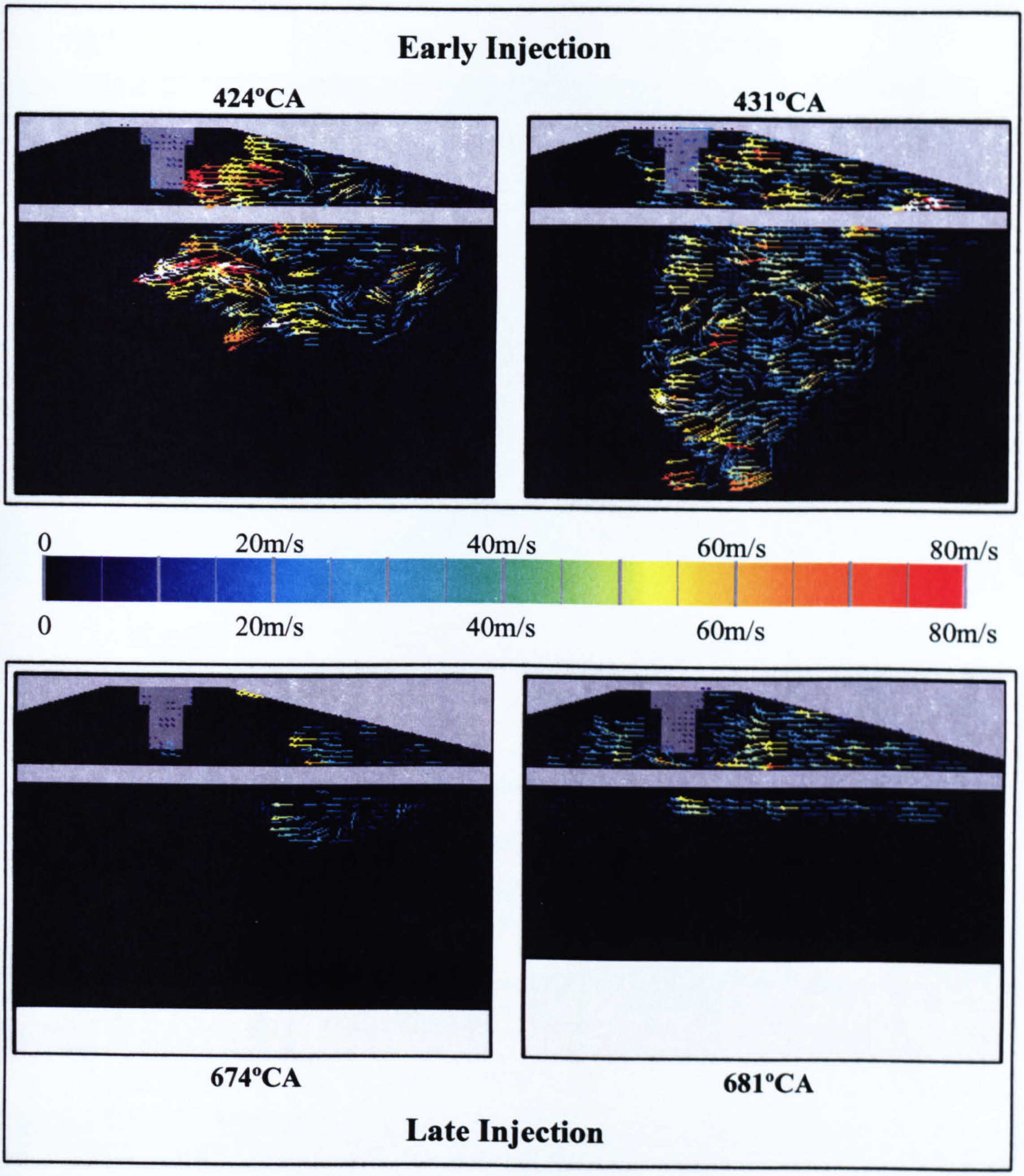

Figure 6-34: Single Shot PIV Images (32×32), 2-pass

Following pages:

Figure 6-35: Velocities and corresponding Average Mie scatter images for the Early and Late injection cases. The vector fields are presented with a grey scale Mie scatter image in the background.

Early Injection

SOI 420°CA

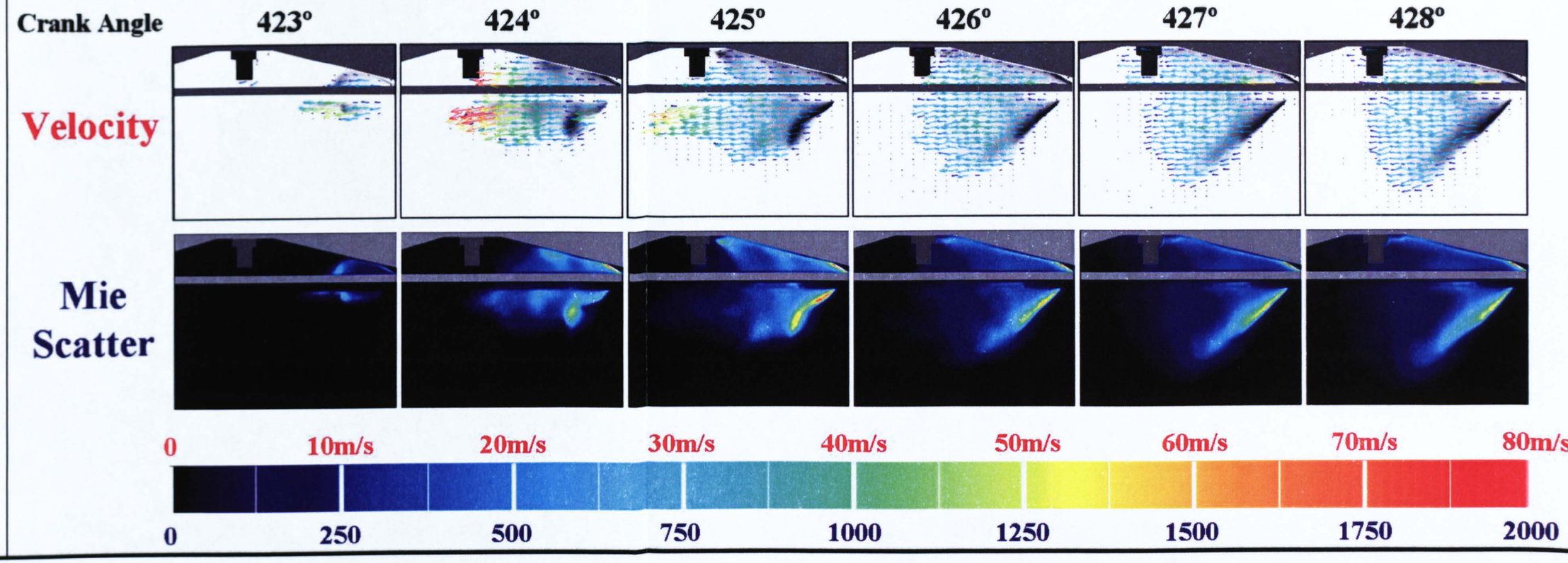

Late Injection

SOI 670°CA

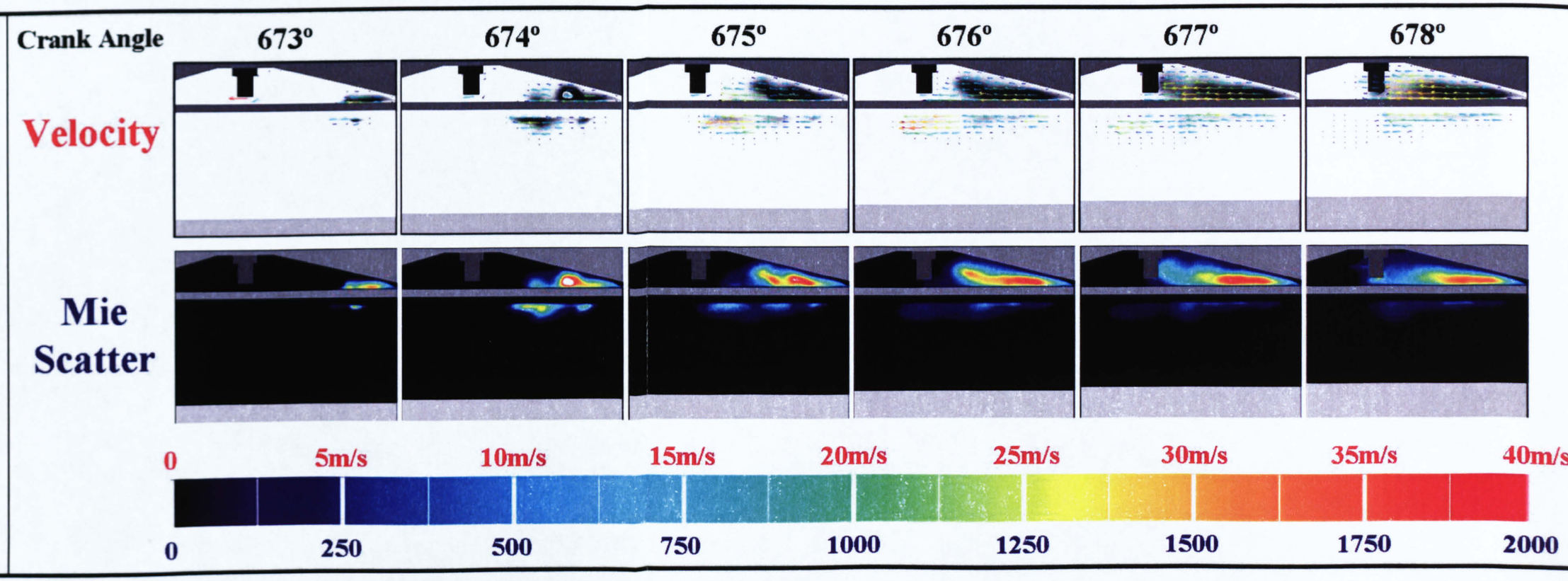

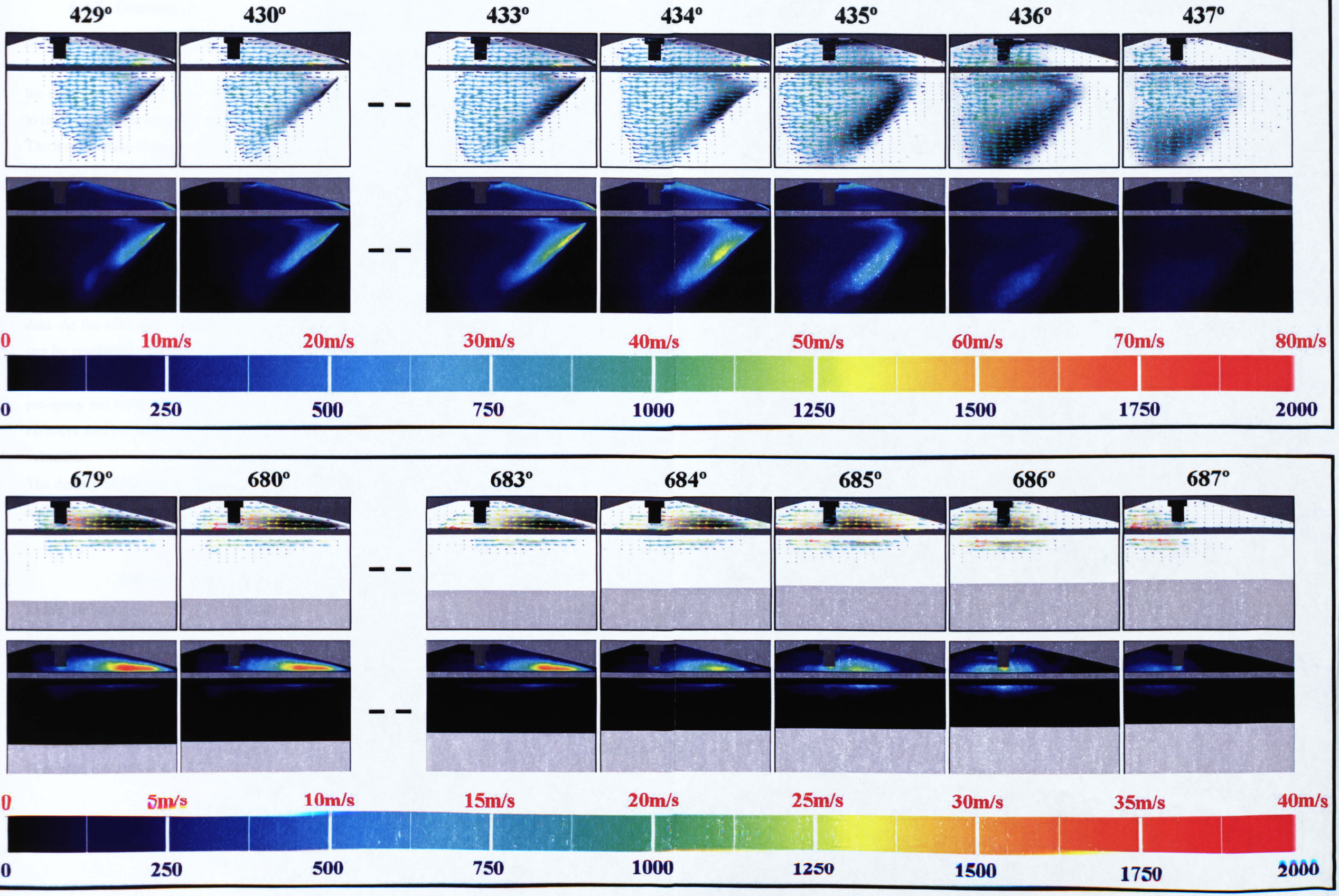
429°
430°
433°
434°
435°
436°
437°
0
10m/s
20m/s
30m/s
40m/s
50m/s
60m/s
70m/s
80m/s
0
250
500
750
1000
1250
1500
1750
2000
679°
680°
683°
684°
685°
686°
687°
0
5m/s
10m/s
15m/s
20m/s
25m/s
30m/s
35m/s
40m/s
0
250
500
750
1000
1250
1500
1750
2000

6.4.5. Discussion

Even though different regions of the instantaneous vector fields show ambiguous results, the averaged vector fields in the less dense regions agree with the evolution of the spray given by the crank-angle resolved Mie scatter images. This can be attributed to the high number of images used in the calculation.

The lens aperture is set so that the high density (therefore brightest) regions of the spray illuminate the CCD to the maximum of 4000 counts. However, this limits the resolution in the less dense part of the spray, where the intensity can be 500 times lower.

6.4.5.1. Early injection

At 423°CA, the spray is very dense and the resolution is too low too obtain reliable PIV data. As the cone angle starts to widen, the spray become more dilute and the structure can be resolved in the less dense regions. At 424°CA, the pre-spray is the least dense part of the spray, and its velocity is 80m/s. The velocities of the droplets following the pre-spray are lower, typically 30 to 40m/s. This phenomenon is expected because the effective fuel passage is smaller as the needle just begins to lift, therefore giving higher velocities.

The density of the fuel present beyond the spark plug is too low to obtain a sufficiently high Mie scatter signal and the velocities are therefore inaccurate.

6.4.5.2. Late Injection

In the late injection mode, the collapsing of the spray increases the density, and the PIV measurements cannot provide accurate data until the cone angle has opened sufficiently (675°CA). The velocities throughout the injection range typically between 20 and 30m/s. They are lower than the ones obtained for the early injection because the higher pressure increases the collision rate between air and fuel molecules. This induces a lower spray penetration which is clearly visible on the Mie scatter image at 676°CA. However, the fuel speeds are still high, and the fuel is projected past the spark plug.

6.5. Summary

Three measurement techniques were applied to the optical engine to characterise the spray and mixture formation process for two different injection strategies.

These results showed that direct injection during the intake stroke gave a wide spray which facilitated the air/fuel mixing to give a homogeneous premixed charge at time of ignition, as a PFI engine would.

When the fuel was injected in the later phase of the compression stoke, the spray gave similar droplet sizes. However, the collapse of the cone angle reduced the air/fuel mixing. This poor mixing created a fuel stratification. The low mixing time resulted in an inadequate stratified charge for "clean" combustion: at the time of ignition, there remained a rich region next to an ignitable pocket, and the latter was not at the appropriate location. The reduced evaporation also implies that more fuel was in the liquid phase and was able to maintain a high velocity. One method to reduce the penetration and avoid the fuel going past the spark plug could consist in injecting smaller droplets. They would evaporate faster, thus reducing the speed of the fuel cloud. This would also increase the mixing. The optimal start of injection would likely be a function of load (i.e. injection duration) and engine speed, and could be determined with LIF imaging.

PART IV

CONCLUSION, REFERENCES AND APPENDICES

Chapter 7

Conclusion

In order to meet the new emissions legislation, the automotive industry is having to refine the operation of its petrol engines. The GDI concept is a promising technology: it offers the opportunity of increased efficiency through unthrottled operation. However, the realisation of this concept is critically dependent on the in-cylinder mixture formation, especially in the late injection/lean operation mode. Ideally, this would require a precise stratification of the in-cylinder fuel-air mixture in 3 distinct zones: an ignitable pocket located at the spark plug, surrounded by a stoichiometric mixture of fuel and air, encompassed by air. High pressure injection and piston bowl geometries were early attempts to redirect the spray and stratify the air-fuel mixture. Air-guided systems improved the system by limiting wall wetting. However, the future seems to be in the spray-guided systems: the realisation of GDI concept strongly depends on the advances in injector technology.

The GDI sprays have become very refined. Due to the elevated injection pressures, the atomisation is improved, the particle sizes are much smaller and the mass flux is increased. These sprays are very fine and dense. The idea behind this project was to develop a tool that could be applied to these sprays for rapid 2-D characterisation. This involved applying Phase Doppler Anemometry (PDA), Planar Laser-Induced Fluorescence (PLIF) and the Laser-Sheet Dropsizing (LSD) technique to denser sprays in harsher environments, where these tools are at the limit of their validity.

The study lead to three important results.

Firstly, an optimal tracer system was determined for the application of the PLIF technique for liquid-phase measurements. It uses the combination of two ketones (3-

Pentanone and 2-Hexanone) which have opposite evaporative behaviours when mixed with Iso-Octane. This limits the differential evaporation. The low concentrations of these tracers gives a good volume-dependent fluorescence signal in the liquid phase, whilst retaining reasonable signal intensities. Ketones also have the advantage of not being quenched by Oxygen, therefore enabling the use of this tracer system for realistic IC engine studies.

Secondly, the LSD and PDA techniques were applied to a GDI spray in a pressure vessel for realistic in-cylinder conditions, ranging from supercooled to superheated environments. The comparison of the results demonstrated several problems which can be improved.

The PDA technique suffers from multiple occupancy of droplets in these very dense sprays. Higher laser power and smaller measurement volume can increase the accuracy.

The study also showed that the LSD technique provided good quantitative data at atmospheric conditions. In highly evaporative conditions, the technique still gave reliable SMD data for the early stages of the injection where evaporation was not dominant, but was limited afterwards by vapour-phase contribution to the fluorescence signal. This could be resolved in non-quenching environments by using Exciplex tracer systems and the appropriate filter to eliminate entirely the vapour phase from the collected fluorescence. On the other hand, the comparison of a two-phase LIF signal and liquid-phase Mie scatter signal can provide an indication of the evaporation rate.

Discrepancies between the results obtained with the PDA and LSD techniques were also attributed to 2 issues. The first is the d^2 dependence assumption of the Mie scattering signal. For small droplets, the proportion of scattered light at 90° can vary substantially for different diameters. Perhaps another observation angle would yield a better surface dependence of the Mie scatter signal. Second, multiple scattering will contribute additional intensity to both fluorescence and Mie scattering signals. This surplus of light is not related to the local dropsize distribution. However, this effect is probably of second order as the LSD technique uses a ratio of signals. The quantification of multiple scattering is currently under investigation.

In low evaporating regimes, the LSD technique therefore has the overall advantage of being a 2-D measurement technique, and will yield data with a maximum error of 30% in dense parts of the spray where PDA data is totally unreliable. If the spray evaporates

quickly, PLIF by itself is an appropriate tool for following the air-fuel mixture, because short droplet lifetimes limit the 2-phase flow behaviour of the spray.

Lastly, 3 diagnostics (PIV, PLIF and LSD technique) were applied in an optical GDI engine. First, it demonstrated the application of the LSD technique in an engine. The major difficulty proved to be the spatial calibration of the two images when using a single camera. Secondly, the study of the spray's behaviour and the location of the fuel highlighted the important issues that the GDI concept faces: the stratification was at the wrong location because the fuel maintained ballistic speed for too long. By reducing the droplet diameters, the fuel would vaporise and therefore slow down much faster, enabling the formation of the cloud at the spark plug. Most importantly, the equivalence ratio measurements allowed the determination of the location and stoichiometry of the air-fuel mixture. This suggests that stratification can be achieved with small droplet spray-guided systems. It is now up to the injector manufacturers to provide such technology.

References

Aizu, Y., Durst, F., Gréhan, G., Onofri, F. and Xu, T.H. (1993) *PDA system without Gaussian beam defects*, Proc. of 3rd Int. Congress on Optical Particle Sizing, Yokohama, August, pp. 461-470.

Arcoumanis, C. and Enotiadis, A.C. (1991) *In-Cylinder Fuel Distribution in a Port-Injected Model engine using Rayleigh Scattering*, Experiments and Fluids, vol. 11, pp. 375-387.

Arnold, A., Becker, H., Suntz, R., Monkhouse, P. and Wolfrum, J. (1990) *Flame Front Imaging in an IC Engine Simulator by Laser Induced Fluorescence of Acetaldehyde*, Optical Letters vol. 15, no.15, pp. 831-833.

Bachalo, W.D. (1980) *Method for measuring the size and velocity of spheres by dual-beam light scatter interferometry*, Applied Optics, vol. 19, 3, pp. 363-370.

Bachalo, W.D. and Houser, M.J. (1984) *Development of the phase/Doppler spray analyser for liquid drop size and velocity characterization*, AIAA, Paper no. 84-1199.

Baritaud, T.A. and Heinze, T.A. (1992) *Gasoline Distribution Measurements with PLIF in a SI-Engine*, SAE Paper 922355.

Berkmüller, M., Tait, N.P., Locket, R.D., Greenhalgh, D.A., Ishii, K., Urata, Y., Umiyama, H. and Yoshida, K. (1994) *In-Cylinder Crank-Angle-Resolved Imaging of Fuel Concentration in a Firing SI Engine Using Planar Laser-Induced Fluorescence*, 25th Symposium (International) on Combustion/ The Combustion Institute, pp. 155-156.

Berkmüller, M. (1996) *A study of Mixture Formation in a Lean Burn Research Engine Using Laser Fluorescence Imaging*, Ph.D. Thesis, Cranfield University, School of Mechanical Engineering.

Berrocal, E., Meglinski, I.V. and Jermy, M.C. (2005) *A new model for light propagation in highly inhomogeneous polydisperse turbid media with applications in spray diagnostics*, submitted in Optics Express.

Bohren, C.F. and Huffman, D.R. (1983) *Absorption and scattering of light by small particles*, Wiley Interscience Publication.

Charalampous, G., Hardalupas, Y. and Taylor, A.M.K.P. (2004) *Optimisation of the Droplet Sizing Accuracy of the combined Scattering (Mie)/ Laser Induced Fluorescence (LIF) technique*, Proc. 12th Int. Symp. on Application of Laser Techniques to Fluid Mechanics.

Chemical Rubber Co. (2001) *Handbook of Chemistry and Physics*, 81st edition, CRC Press.

Clerk, D. (1921) *Cylinder Actions in Gas and Gasoline Engines*, SAE Journal, vol. 8, p. 523.

Conwell, P.R., Barber, P.W. and Rushforth, C.K. (1984) *Resonant Spectra of Dielectric Spheres*, J. Opt. Soc. AM. A, vol. 1, no. 1, pp. 62-67.

Davy, M.H., Williams, P.A. and Anderson, R.W. (2000) *Effects of fuel composition on Mixture Formation in a firing Direct-Injection Spark-Ignition (DISI) engine: an experimental study using Mie-scattering and planar laser-induced fluorescence (PLIF) techniques*, SAE Paper 2000-01-1904.

Davy, M., Williams, P., Han, D. and Steeper, R. (2003) *Evaporation Characteristics of the 3-pentanone/isooctane binary system*, Experiments in Fluids, vol. 35, pp. 92-99.

Demtröder, W. (1982) *Laser Spectroscopy*, Springler-Verlag.

Dibble, R.W. and Hollenbach R.E. (1981) *Laser Rayleigh thermometry in turbulent flames*, Proc. of 18th Int. Symp. on Combustion, p. 1489.

Domann, R. and Hardalupas, Y. (2000) *Evaluation of the Planar Droplet Sizing (PDS) Technique*, 8th Int. Conf. On Liquid Atomization and Spray Systems.

Domann, R. (2002) *Characterisation of Spray Unsteadiness*, Ph.D. Thesis, Imperial College of Science, Technology and Medicine, University of London.

Domann, R. and Hardalupas, Y. (2003) *Quantitative Measurement of Planar Droplet Sauter Mean Diameter in sprays using Planar Droplet Sizing*, Particle & Particle Systems Characterization, vol. 20, pp. 209-218.

Drake, M.C., Fansler, T.D., Solomon, A.S. and Szekely, G.A. Jr. (2003) *Piston Fuel Films as a Source of Smoke and Hydrocarbon Emissions form a Wall-Controlled Spark Ignited Direct-Injection Engine*, SAE Paper 2003-01-0547.

Durst, F. and Zaré, M. (1975) *Laser Doppler measurement in two phase flows, in the Accuracy of Flow Measurements by the Laser Doppler Method*, Proc. of the LDA Symposium, pp. 403-429.

Durst, F., Meling, A. and Whitelaw, J.H. (1981) *Principles and Practise of Laser Doppler Anemometry*, 2nd edition, Academic Press.

Durst, F., Tropea, C. and Xu, T.-H. (1994) *The slit effect in phase Doppler anemometry*, Proc. Of the 2nd Int. Conf. on Fluid Dynamic Measurement and its Applications, X. Shen and X. Sun, eds, pp. 38-43.

Durst, F., Brenn, G. and Xu, T.-H. (1997) *A review of the development and characteristics of planar phase-Doppler anemometry*, Measurement Science and technology, no. 8, pp. 1203-1221.

Espey, C., Dec, J.E., Litzinger T.A., and Santavicca, D.A. (1997) *Planar Laser Rayleigh Scattering for Quantitative Vapor-Fuel Imaging in a Diesel Jet*, Combustion and Flame, vol. 109, pp. 65-86.

Felton, P.G., Mantzaras, J., Bomse, D.S. and Woodlin, R.L. (1988) *Initial Two-Dimensional Laser-Induced Fluorescence Measurements of OH Radicals in an Internal Combustion Engine*, SAE Paper 881633.

Felton, P.G., Bracco, F.V. and Bardsley, M.E.A. (1993) *On the Quantitative Application of Exciplex Fluorescence to Engine Sprays*, SAE Paper 930870.

Frank, R.M. and Heywood, J.B. (1991) *The Effect of Piston Temperature on Hydrocarbon Emissions from a Spark-Ignited Direct-Injection Engine*, SAE Paper 910558.

Frieden, D. and Sick, V. (2003) *A two-tracer LIF strategy for quantitative oxygen imaging in engines applied to study the influence of skip-firing on in-cylinder oxygen contents of an SIDI engine*, SAE Technical Paper Series 2003-01-1114.

Fröba, A.P., Rabenstein, F., Münch, K.-U. and Leipertz, A. (1998) *Mixture of Triethylamine (TEA) and Benzene as a New Seeding Material for the Quantitative Two-Dimensional Laser-Induced Exciplex Fluorescence Imaging of Vapor and Liquid Fuel Inside SI Engines*, Combustion and Flame, vol. 112, pp. 199-209.

Fuchs, R., Krenzer, L. and Gaube, J. (1984) *Excess properties of binary mixtures composed of a polar component and an alkane*, Ber. Bunsenges Phys. Chem., vol. 88, pp. 642-649.

Fujikawa, T., Hattori, Y. and Akihama, K. (1997) *Quantitative 2-D Fuel Distribution Measurements in an SI Engine Using Laser-Induced Fluorescence with Suitable Combination of Fluorescence Tracer and Excitation Wavelength*, SAE Paper 972944.

Gatowski, J.A. and Heywood, J.B. (1985) *Effects of Valve Shrouding and Squish on Combustion in a SI-Engine*, SAE Paper 852093.

Ghandi, J.B. and Felton, P.G. (1996) *On the Fluorescence Behaviour of Ketones at High Temperature,* Experiments in Fluids, vol. 21, pp. 143-144.

Glantsching, W.J. and Chen, S.-H. (1981) *Light Scattering from Droplets in the Geometrical Optics Approximation*, Applied Optics, vol. 20, no. 14, pp. 2499-2509.

Glover, A.R., Skippon, S.M. and Boyle, R.D. (1995) *Interferometric Laser Imaging for Droplet Sizing: a method for droplet size measurement in sparse dense sprays*, Applied Optics, vol. 34, pp. 8409-8421.

Gréhan, G., Gouesbet, G., Naqwi, A. and Durst, F. (1992) *Trajectory ambiguities in Phase Doppler systems: use of polarizers and additional detectors to suppress the effect*, Proc. of 6th Int. Symposium on Applications of Laser Techniques to Fluid Mechanics, Lisbon.

Grossmann, F., Monkhouse, P.B., Ridder, M., Sick, V. and Wolfrum, J. (1996) *Temperature and Pressure Dependences of the Laser-Induced Fluorescence of Gas-Phase Acetone and 3-Pentanone*, Applied Physics B, vol. 62, pp. 249-253.

Haddad, O. and Denbratt, I. (1991) *Turbulence Characteristics of Tumbling Air Motion in 4-Valve SI-Engines and their Correlation with Combustion Parameters*, SAE Paper 910478.

Hall, M.J. and Bracco, F.V. (1987) *A Study of Velocities and Turbulence Intensities Measured in Firing and Motored Engines*, SAE Paper 870453.

Hammond, D.C. (1981) *Deconvolution technique for line-of-sight optical scattering measurement in axi-symmetric sprays*, Applied Optics, vol. 20, no. 3, p. 493-499.

Han, D. and Steeper, R. (2002) *Examination of Iso-Octane/Ketone mixtures for Quantitative LIF Measurements in a DISI Engine*, SAE Paper 2002-01-0837.

Hardalupas, Y., Taylor, A.M.K.P., Whitelaw, J.H., Ishii, K., Mitano, H. and Urata, Y. (1995) *Influence of Injection Timing on In-Cylinder Fuel Distribution in a Honda VTEC-E Engine*, SAE Paper 950507.

Hentschel, W., Homburg, A., Ohmstede, G., Müller, T. and Grünefeld, G. (1999) *Investigation of Spray Formation of DI Hollow-Cone Injectors Inside a Pressure Chamber and a Glass Ring Engine by Multiple Optical Techniques*, SAE Paper 1999-01-3660.

Hesselbacher, K.H., Anders, K. and Frohn, A. (1991) *Experimental investigation of Gaussian beam effects on the accuracy of a droplet sizing method*, Applied Optics, vol. 30, pp. 4930-4935.

Heywood, J.B. (1988) *Internal Combustion Engine Fundamentals*, McGraw-Hill.

Hill, S.C. and Benner, R.E. (1988) *Morphology-dependent resonances*, Chapter in "Optical effects associated with small particles", Advanced Series in Applied Physics, vol. 1, World Scientific Publishing Co.

Hill, S.C., Saleheen, H.I., Barnes, M.D., Whitten, W.B. and Ramsey, J.M. (1996) *Modelling fluorescence collection from single molecules in microspheres: effect of position, orientation and frequency*, Applied Optics, vol. 35, no. 31, pp. 6278-6288.

Horie, K., Hishizawa, K., Ogawa, T., Akazaki, S. and Miura, K. (1992) *The Development of a High Fuel Economy and High Performance Four-Valve Lean Burn Engine*, SAE Paper 920455.

Inoue, T., Matsushita, S., Nakanishi, K. and Okano, H. (1993) *Toyota Lean Combustion System – 3rd Generation System*, SAE Paper 930873.

Ipp, W., Egermann, J., Schmitz, I., Wagner, V. and Leipertz, A. (2001) *Quantitative Bestimmung desLuftverhältnisses in einem optisch zugänglichen Motor mit Benzindirekteinspritzung*, Proc. of Direkteinspritzung im Ottomotor III, pp.110-129.

Iwamoto, Y., Danno, Y., Hirako, O., Fukui, T. and Murikami, N. (1992) *The 1.5 Liter Vertical Vortex Engine*, SAE Paper 920670.

Jermy, M.C. and Greenhalgh, D.A. (2000) *Planar dropsizing by elastic and fluorescence scattering in sprays too dense for phase Doppler measurements*, Applied Physics B, vol. 71, pp. 1-8.

Johnston, S.C. (1979) *Precombustion Fuel/Air Distribution in a Stratified charge Engine using Laser Raman Spectroscopy*, SAE Paper 790433.

Joyce, J.R. (1949) *The Atomization of Liquid Fuels for Combustion*, J. Inst. Fuel, vol. 22, no. 124, pp. 150-156.

Karl, G., Abthoff, J., Bargende, M., Kemmler, R., Kühn, M. and Bubeck, G. (1996) *Thermodynamische Analyse eines direkteinspritzenden Ottomotors*, Proc. of Wiener Motoren Symposium, pp. 200-234.

Karlsson, R.B. and Heywood, J.B. (2001*) Piston Fuel Film Observations in an Optical Access GDI Engine*, SAE Paper 2001-01-2022.

Keck, J.C., Heywood, J.B. and Noske, G. (1987) *Early Flame Development and Burning Rates in Spark Ignition Engines and their Cyclic Variability*, SAE Paper 870164.

Kelman, J.B. and Masri, A.R. (1994) *Quantitative Imaging of temperature and OH in turbulent diffusion flames by using a single laser source*, Applied Optics, vol. 33, no. 18, pp. 3992-3999.

Kelman, J.B., Sherwood, G., O'Young, F., Berckmüller, M., Jermy, M.C., Masri, A.R. and Greenhalgh, D.A. (2000) *Pulsed laser imaging in practical combustion systems from 2D to 4D*, Proc. of SPIE vol. 4076.

Kiyota, Y., Akishino, K. and Ando, H. (1992) *Concept of Lean Combustion by Barrel-Stratification*, SAE Paper 920233.

Knapp, M., Beushausen, V., Hentschel, W., Manz, P., Grünefeld, G. and Andresen, P. (1997) *In-cylinder mixture formation analysis with spontaneous Raman scaterring applied to a mass production SI engine*, SAE Paper 970827.

Knight, J.C., Driver, H.S.T. and Robertson, G.N. (1992) *Non-linear scattering from liquid droplets*, research articles, South African Journal of Science, vol. 88, pp. 162-166.

Koboyashi, T., Kawagushi, T. and Maeda, M. (2000) *Measurement of Spray Flow by an Improved Interferometric Laser Imaging Droplet Sizing (ILIDS) System*, Proc. of 10th Int. Symp. Applications of Laser Techniques to Fluid Mechanics, Lisbon.

Koch, J.D. and Hanson, R.K. (2003) *Temperature and excitation wavelength dependencies of 3-pentanone absorption and fluorescence for PLIF applications*, Applied Physics B, vol. 76, pp. 319-324.

König, G., Anders, K. and Frohn, A. (1986) *A new light-scattering technique to measure the diameter of periodically generated moving droplets*, J. Aerosol Sci., vol. 17, pp. 157-167.

Kornmesser, C., Müller, T., Beuhausen, V., Hentschel, W. and Andresen, P. (2001) *Applicability of different exciplex tracers and model fuels for investigation of mixture formation in direct injection gasoline engines*, Proc. of 5th Int. Symp. On Diagnostics and Modeling of Combustion in Internal Combustion Engines (COMODIA 2001).

Lauwenz, W., Kohler, J., Meier, F., Stolz, W., Wirth, R., Bloss, W.H., Maly, R.R., Wagner, E. and Zahn, M. (1992) *Quantitative 2-D measurements of Ait/Fuel Ratios Duing the Intake Stroke in a Transparent SI Engine*, SAE Paper 922320.

Law, C. (1982) *Recent Advances in droplet Vaporisation and combustion*, Prog. Energy Combustion. Sci., vol. 8, pp. 171-201.

Le Coz, J.F. (1992) *Cycle-to-Cycle Correlations between Flow Field and Combustion Initiation in a SI-Engine*, SAE Paper 920517.

Le Coz, J., Catalano, C. and Baritaud, T. (1994) *Application of Laser-Induced Fluorescence for Measuring the Thickness of Liquid films on Transparent Walls*, Proc. of 7th Int. Symposium of Laser Techniques to Fluid Mechanics.

Le Gal, P. (1999) *Development of a Laser Sheet Dropsizing Technique for Sprays*, Ph.D. Thesis, Cranfield University, School of Mechanical Engineering.

Lee, D.W. (1939) *A Study of Air Flow in an Engine Cylinder*, NACA Report no. 653.

Li, J., Matthews, R.D., Stanglmaier, R.H., Roberts, C.E. and Anderson, R.W. (1999) *Further Experiments on The Effect of In-Cylinder Wall Wetting on the HC Emissions from Direct Injection Gasoline Engines*, SAE Paper 1999-01-3661.

Li, J., Theis, J.R., Goralski, C.T., Kudla, R.J., Watkins, W.L. and Hurley, R.H. (2001) *Sulfur poisoning and desulfation of the lean NOx trap*, SAE Future Transportation Technology Conference and Exposition.

Liou, T.M. and Santavicca, D.A. (1983) *Cycle Resolved Turbulence Measurements in a Ported Engine with and without Swirl*, SAE Paper 830419.

Longwell, J.P. (1943) *Fuel Oil Atomization*, D.Sc. Thesis, MIT.

Maeda, M., Kawaguchi, T. and Hishida, K. (2000) *Novel interferometric measurement of size and velocity distributions of spherical particles in fluids flows*, Meas. Sci. Technol. 11 no. 12, pp. 13-18.

Maeda, M., Kawaguchi, T., Akaska, Y., Kurosawa, R. and Hishida, K. (2003) *Novel Simultaneous Planer Measurement and Application of Droplet Size, Velocity Vector, Number Density and Vapor Concentration in Spray by ILIDS and LIF Techniques*, Proc. of IEA-TLM.

Malanowski, S. and Anderko, A. (1992) *Modelling Phase Equilibria: Thermodyamic Background and Practical Tools*, Wiley.

Matsumoto, Y. (2004) *The Spray Guided Concept for the second Generation of Gasoline Direct Injection*, SAE Paper 20045040.

Melton, L.A. (1983) *Spectrally separated fluorescence emissions for diesel fuel droplets and vapour,* Applied Optics, vol. 22, no. 14, pp. 2224-2226.

Melton, L.A. and Verdieck, J.F. (1985) *Vapor/Liquid Visualization of Fuel Sprays, Combustion Science and Technology*, vol. 42, pp. 217-222.

Melton, L.A. (1993) *Exciplex-Based Vapor/Liquid Visualization Systems Appropriate for Automotive Gasoline,* Applied Spectroscopy, vol. 47, no. 6, pp. 782-786.

Metghalchi, M. and Keck, J.C. (1982) *Burning Velocities of Mixtures of Air with Methanol, Iso-Octane and Indolene at high Pressure and Temperature*, Combustion and Flame 48, pp. 191-210.

Mie, G. (1908) *Beitrage zur Optik trüber Medien speziel kolloidaler Metallösungen*, Annual Physics, vol. 25, pp. 377-445.

Miles, P.C. (1999) *Raman line imaging for spatially and temporally resolved mole fraction measurements in internal combustion engines,* Applied Optics, vol. 38, no. 9.

Miles, P. and Diligan, M. (1996) *Quantitative In-Cylinder Fluid Composition Measurements Using Broadband Spontaneous Raman Scattering*, SAE Paper 960828.

Nino, E., Gadjeczko, B.F. and Felton, P.G. (1993) *Two-Colour Particle Image Velocimetry in an Engine With Combustion*, SAE Paper 930872.

Neij, H., Johansson, B. and Aldén, M. (1994) *Development and demonstration of 2-D LIF for studies of mixture preparation in SI engines*, Combustion and Flame, vol. 99, pp. 449-457.

Ossler, F. and Aldén, M. (1997) *Measurement of picosecond laser induced fluorescence from gas-phase 3-pentanone and acetone: Implications to combustion diagnostics*, Applied Physics B 64, pp. 493-502.

Pajot, O. (2000) *Étude expérimentale de l'influence de l'aérodynamique sur le comportement et la structure du front de flamme dans les conditions d'un moteur à allumage commandé*, Ph.D. Thesis, Université d'Orleans (France).

Pajot, O. and Mounaïm-Rouselle, C. (1998) *Droplet Sizing by Interferometric Method Based on Mie scatter in an IC Engine*, Proc. of 9th Int. Symp. On Applications of Laser Techniques to Fluid Mechanics, Lisbon.

Park, S., Cho, H., Yoon, I. and Min, K. (2002) *Measurement of droplet size distribution of gasoline direct-injection spray by droplet generator and planar image technique*, Measurement Science and Technology, vol. 13, pp. 859-864.

Pischinger, S. and Heywood, J.B. (1988) *A Study of Flame Development and Engine Performance with Breakdown Ignition Systems in a Visualization Engine*, SAE Paper 880518.

Quader, A.A. (1974) *Lean Combustion and the Misfire Limit in SI Engines*, SAE Paper 741055.

Quader, A.A. (1976) *What Limits Lean Operation in SI-Engines – Flame Initiation or Flame Propagation ?*, SAE Paper 760760.

Reboux, J., Puechberty, D. and Dionnet, F. (1994) *A New Approach of Planar Laser Induced Fluorescence Applied to Fuel/Air Ratio Measurement in the Compression Stroke of an Optical S.I. Engine*, SAE Paper 941988.

Reid, R.C., Prausnitz, J.M. and Poling, B.E. (1987) *The Properties of Liquids and Gases*, McGraw-Hill.

Reeves, M. (1995) *Particle Image Velocimetry Applied to Internal Combustion Engine In-Cylinder Flows*, D.Phil. Thesis, Loughborough University of Technology.

Reuss, D.L., Adrian, R.J., Landreth, C.C., French, D.T. and Fansler, T.D. (1989) *Instantaneous Planar Measurements of Velocity and Large Scale Vorticity and Strain Rate in an Engine Using Particle Image Velocimetry*, SAE Paper 890616.

Rhodes, D.B. and Keck, J.C. (1985) *Laminar Burning Speed Measurements of Indolene-Air-Diluent Mixtures at High Pressures and Temperatures*, SAE Paper 850047.

Sankar, S.V., Inenaga, A.S. and Bachalo, W.D. (1992) *Trajectory dependent scattering in phase Dopller interferometry: minimizing and eliminating sizing errors*, 6th Int. Symp. on Applications of Laser Techniques to Fluid Mechanics, Paper 12.2.

Sankar, S.V., Robart, D.M. and Bachalo, W.D. (1996) *A Planar Droplet Sizing Technique for Spray Characterization*, ILASS Paper.

Sankar, S.V., Robart, D.M. and Bachalo, W.D. (1997) *A planar droplet sizing technique for spray characterization*, Proc. of 9th annual conference on liquid Atomization and Spray Systems.

Sandquist, H., Lingren, R. and Denbratt, I. (2000) *Sources of Hydrocarbon Emissions from a Direct injection Stratified Charge Spark Ignition Engine*, SAE Paper 2000-01/1906.

Seitzman, J.M., and Hanson, R.K. (1993) *Comparison of excitation techniques for quantitative fluorescence imaging of reacting flows*, AIAA Journal, vol. 31, no. 3, pp. 513-519.

Serpengüzel, A., Swindal, J.C., Change, R.K. and Acker, W. (1992) *Two-dimensional imaging of sprays with fluorescence, lasing and stimulated Raman scattering*, Applied Optics, vol. 31, no. 18, pp. 3543- 3551.

Shaw, B.T., Hoult, D.P. and Wong, V.W. (1992) *Development of Engien Lubricant Film Thickness Diagnostics Using Fiber Optics and Laser Fluorescence*, SAE Paper 920651.

Shimuzu, R., Seiichi., M., Furuno., S., Murayama, M. and Kojima., S. (1992) *Measurement of Air-Fuel Mixture Distribution in a Gasoline Engine using LIEF Technique*, SAE Paper 922356.

Simko, A.O., Choma, M.A. and Repko, L. (1972) *Exhaust Emission Control by the Ford Programmed Combustion Process : PROCO*, SAE Paper 720052.

Smart, A.E. and Ford, R.A.J. (1974) *Measurement of Thin Liquid Films by a Fluorescence Technique*, Wear, vol. 29, pp.41-47.

Stanglmaier, R.H., Li, J. and Matthews, R.D. (1999) *The Effect of In-Cylinder Wall Wetting Location on the HC Emissions from SI Engines*, SAE Paper 1999-01-0502.

Stojkovic, B.D. and Sick, V. (2000) *Evolution and impingement of an automotive fuel spray investigated with simultaneous Mie/LIF techniques*, Applied Physics, B 73, pp. 75-83.

Suntz, R., Becker, H., Monkhouse, P. and Wolfrum, J. (1988) *Two-Dimensional Visualization of the Flame Front in an Internal Combustion Engine Using Laser-Induced Fluorescence of OH Radicals*, Applied Physics B 47, pp. 287-283.

Swithenbank, J. (1976) *A laser diagnostic technique for the measurement of droplet and particle size distribution*, AIAA Paper 76-79.

Tait, N.P. (1994) *Development of Planar Laser Diagnostic Techniques for Fuel and Soot Imaging in Combustion Applications*, Ph.D. Thesis, Cranfield University, School of Mechanical Engineering.

Tait, N.P. and Greenhalgh, D.A. (1992) *2D Laser induced fluorescence imaging of parent fuel fraction in nonpremixed combustion*, Proc. of 24th Symp. (Int.) on Combustion, The Combustion Institute, pp.1621-1628.

Talley, D.G., McDonnell, V.G., Lee, S. and Samuelsen, G.S. (1996) *Accounting for laser sheet extinction in applying PLIF to sprays*, AIAA Paper 96-0469.

Thomas, E.R. and Eckert, C.A. (1984) *Prediction of limiting activity coefficients by a modified separation of cohesive energy density and UNIFAC*, Ind. Eng. Chem. Process Design Development, vol. 23, pp. 194-209.

Tropea, C., Xu, T.-H., Onofri, F., Gréhan, G., Haugen, P. and Stieglmeier, M. (1995) *Dual mode phase Doppler anemometer*, 4th Int. Congress on Optical Particle Sizing, Nuremberg, pp. 21-23.

Van de Hulst, H.C. (1957) *Light Scattering by Small Particles*, Wiley, New York, reprinted by Dover Publications, Inc., 1981.

Van de Hulst, H.C. and Wang, R.T. (1991) *Glare points*, Applied Optics, vol. 30, pp. 4755-4763.

Wigley, G. (1994) *Chapter in Optical Diagnostics for Flow Processes*, ed. Lading, L., Wigley, G. and Buchave, P., Plenum Press.

Wigley, G., Hargrave, G.K. and Heath, J. (1999) *A high Power, High Resolution LDA/PDA System Applied to Gasoline Direct Injection Sprays*, Part. Part. Syst. Char., vol. 16, pp. 11-19.

Wigley, G., Goodwin, M., Pitcher, G. and Blondel, D. (2002) *Imaging and PDA Analysis of a GDI Spray in the Near Nozzle Region*, Proc. of 11th Int. Symp. on Application of Laser Techniques to Fluid Mechanics.

Wilson, G.M. (1964) *A New Expression for the Excess Free Energy of Mixing*, J. Am. Chem. Soc., 86, pp. 127-130.

Wolff, D., Beushausen, V. and Andresen, P. (1995) *Ketones: Suitable tracer substances for quantitative LIF measurements in high pressure systems*, Proc. of 33rd Japanese Symp. Comb.

Yamakawa, M., Ishiki, S., Yoshizaki, T. and Nishida, K. (2001) *Measurement of Ambient Air motion of D.I. Gasoline Spray by LIF-PIV*, Proc. of 5th Int. Symp. on Diagnostics and Modelling of Combustion in Internal Combustion Engines (COMODIA).

Yeh, C.-N., Kamimoto, T., Kobori, S. and Kosaka, H. (1993a) *Fluorescence/scattering imaging technique for particle sizing in unsteady Diesel spray,* Transactions of the Japan Society of Mechanical Engineers, no. 93-0134, pp. 308-313.

Yeh, C.-N., Kosaka, H. and Kamimoto, T. (1993b) *A Fluorescence Imaging Technique for Instantaneous 2-D Measurement of Particle Size Distribution in a Transient Spray*, Proc. of the 3rd International Congress on Optical Particle Sizing, pp. 355-361.

Yeh, C.-N., Kosaka, H. and Kamimoto, T. (1996) *Measurement of Drop Sizes in Unsteady Dense Sprays,* Recent Advances in Spray Combustion: Spray Atomisation and Drop Burning Phenomena, vol. 1, ed. K. Kuo, AIAA Inc.

Yeh, Y. and Cummins, H.Z. (1964) *Localized Flow Measurements with He-Ne Laser Spectrometer*, Appl. Phys. Letter, vol. 4, pp. 176-181.

Young, M.B. (1981) *Cyclic Dispersion in the Homogeneous-Charge SI-Engine – a Literature Survey*, SAE Paper 810020.

Zhao, F.-Q., Taketomi, M., Nishida, K. and Hirorasu, H. (1993) *Quantitative Imaging of the Fuel Concentration in a SI Engine with Laser Rayleigh Scattering*, SAE Paper 932641.

Zhao, H. and Ladommatos, N. (1998) *Optical Diagnostics for In-Cylinder Mixture Formation Measurements in IC Engines*, Progress in Energy and Combustion Science, vol. 24, pp. 297-336.

Zimmer, L., Ikeda, Y., Domann, R. and Hardalupas, Y. (2002) *Simultaneous LIF and Mie scattering measurements for branch-like spray cluster in industrial oil burner*, AIAA 02-0340.

APPENDIX A

LIF and Mie Scatter images

Average fluorescence (LIF) and Mie scatter images obtained in the Pressure Vessel. For each (Pressure-Temperature) condition, the images at the five times after Start of Injection are illustrated.

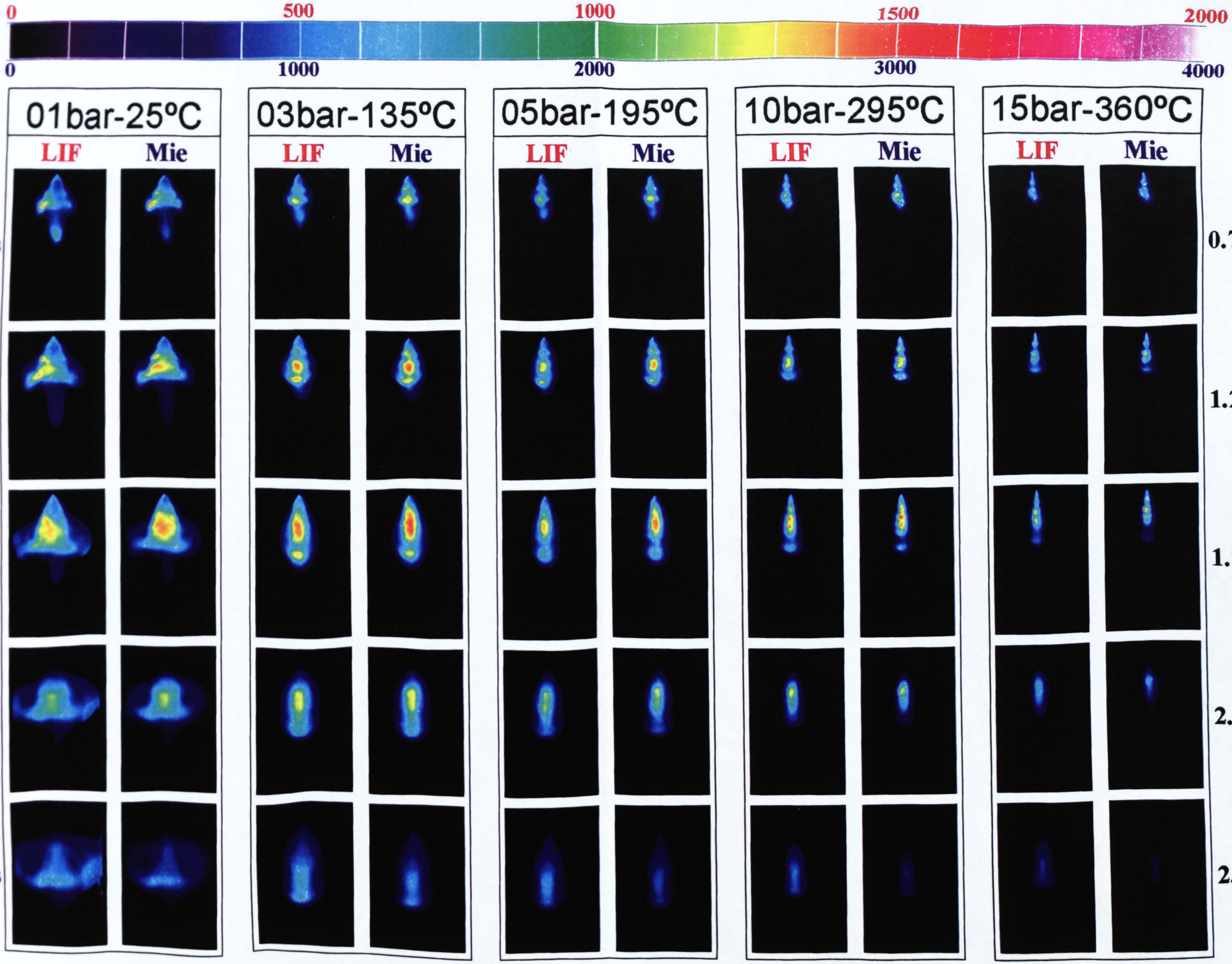
0
500
1000
1500
2000
0
1000
2000
3000
4000
01bar-25ºC
03bar-135ºC
05bar-195ºC
10bar-295ºC
15bar-360ºC
LIF
Mie
0.7ms
1.2ms
1.7ms
2.2ms
2.7ms

APPENDIX B

Time-resolved PDA results

SMD (μm)

0.7ms	0	4	8	12	16	20	24
5	0.0	10.5					
10	26.9	9.4	13.6				
15	26.2	0.0	17.7	19.8			
20	11.7	0.0	3.5	12.8	25.4	0.0	
25	12.7	17.4	17.1	17.2	20.4	0.0	0.0
30	12.7	17.8	36.4	59.1	23.3	0.0	0.0
35	18.0	16.6	33.9	34.3	0.0	0.0	0.0
40	32.2	25.3	39.9	0.0	0.0	0.0	0.0
45	27.9	29.3	2.5	0.0	0.0	0.0	
50	23.9	23.9	2.6	0.0	0.0		
55	17.4	0.0	0.0	0.0			
60	0.0	0.0	0.0				
65	0.0						
70							

Number of Droplets

0.7ms	0	4	8	12	16	20	24
5	0	1					
10	1	5	72				
15	2	0	16	20			
20	1	0	1	146	117	0	
25	22	19	117	100	20	0	0
30	70	257	36	7	12	0	0
35	84	224	23	1	0	0	0
40	108	125	4	0	0	0	0
45	73	52	5	0	0	0	
50	24	7	5	0	0		
55	1	0	0	0			
60	0	0	0				
65	0						
70							

1.2ms	0	4	8	12	16	20	24
5	0.0	15.8					
10	0.0	2.9	15.1				
15	0.0	0.0	15.6	15.2			
20	0.0	0.0	0.0	12.2	7.7	17.3	
25	0.0	0.0	16.3	10.6	10.7	15.6	0.0
30	0.0	2.8	17.3	15.9	17.4	16.3	0.0
35	15.4	18.2	17.3	20.3	20.7	20.9	0.0
40	12.3	13.3	16.1	24.5	0.0	0.0	0.0
45	17.6	15.9	19.2	0.0	30.7	0.0	
50	18.0	16.3	25.0	2.1	0.0		
55	26.6	25.8	31.7	2.6			
60	25.3	27.6	34.9				
65	33.7						
70							

1.2ms	0	4	8	12	16	20	24
5	0	25					
10	0	1	60				
15	0	0	27	147			
20	0	0	0	69	7	1	
25	0	0	6	18	22	30	0
30	0	1	10	53	93	240	0
35	45	47	90	37	38	33	0
40	87	140	170	2	0	0	0
45	114	176	102	0	2	0	
50	107	138	24	3	0		
55	75	75	19	1			
60	37	34	5				
65	11						
70							

1.7ms	0	4	8	12	16	20	24
5	0.0	13.0					
10	0.0	0.0	14.7				
15	0.0	0.0	16.2	16.4			
20	0.0	0.0	0.0	37.7	11.9	4.5	
25	0.0	0.0	14.2	15.4	8.7	7.5	0.0
30	0.0	0.0	17.0	13.6	3.2	20.9	0.0
35	0.0	0.0	18.5	15.5	16.5	18.5	14.1
40	17.7	16.6	17.5	17.6	18.8	19.6	19.2
45	16.5	15.4	15.4	22.8	24.1	27.9	
50	15.3	16.3	15.6	26.0	0.0		
55	16.0	15.9	19.4	32.0			
60	20.3	22.8	25.4				
65	24.1						
70							

1.7ms	0	4	8	12	16	20	24
5	0	5					
10	0	0	37				
15	0	0	30	8			
20	0	0	0	71	120	3	
25	0	0	13	35	91	32	0
30	0	0	36	38	15	3	0
35	0	0	1	33	68	161	3
40	2	2	30	130	91	77	1
45	76	103	200	41	1	1	
50	138	154	153	10	0		
55	133	156	116	4			
60	77	102	35				
65	40						
70							

2.2ms	0	4	8	12	16	20	24
5	6.3	10.9					
10	5.6	13.3	20.9				
15	7.7	9.3	17.4	36.2			
20	8.2	13.3	0.0	16.8	16.9	18.1	
25	10.4	15.5	13.9	36.7	11.2	7.9	0.0
30	0.0	15.7	14.9	12.2	7.8	10.1	0.0
35	0.0	13.6	14.8	12.1	17.6	21.2	1.9
40	0.0	17.6	18.9	13.1	14.9	16.8	22.2
45	0.0	0.0	21.0	18.0	18.1	19.7	
50	17.4	15.6	14.8	16.4	18.9		
55	14.3	15.4	15.0	18.4			
60	15.9	15.9	16.8				
65	19.2						
70							

2.2ms	0	4	8	12	16	20	24
5	370	5					
10	168	68	1				
15	118	40	19	1			
20	28	14	0	98	91	14	
25	12	27	91	116	96	106	0
30	0	5	38	65	114	22	0
35	0	1	28	41	12	3	1
40	0	1	17	27	56	117	1
45	0	0	1	79	313	188	
50	10	38	106	175	69		
55	92	120	201	90			
60	158	158	174				
65	130						
70							

2.7ms	0	4	8	12	16	20	24
5	7.1	13.2					
10	7.2	17.7	0.0				
15	6.5	10.7	18.4	0.0			
20	9.6	13.7	0.0	18.5	17.8	17.3	
25	11.1	12.0	15.4	15.2	13.8	11.9	0.0
30	13.0	14.4	14.5	12.0	11.5	10.4	2.8
35	16.3	14.6	12.6	16.8	6.1	12.8	0.0
40	12.8	16.0	16.6	16.9	4.1	1.1	0.0
45	11.9	15.0	16.5	16.6	12.8	18.9	
50	13.7	15.0	20.3	13.1	17.2		
55	16.9	18.9	18.0	16.1			
60	15.6	15.7	16.1				
65	17.6						
70							

2.7ms	0	4	8	12	16	20	24
5	510	1					
10	292	15	0				
15	278	8	3	0			
20	119	27	0	19	20	9	
25	143	170	141	130	108	138	0
30	92	87	121	138	105	84	1
35	50	70	67	100	180	8	0
40	32	33	61	40	66	1	0
45	14	29	52	41	46	34	
50	1	4	10	26	131		
55	1	3	19	165			
60	32	112	220				
65	128						
70							

APPENDIX C

Time-resolved PDF of TSI and Dantec data

Each line represents a measurement point (MP).

The PDF from TSI data is on the left and the PDF from Dantec data is on the right.

The colours indicate the time ASOI.

MP 1

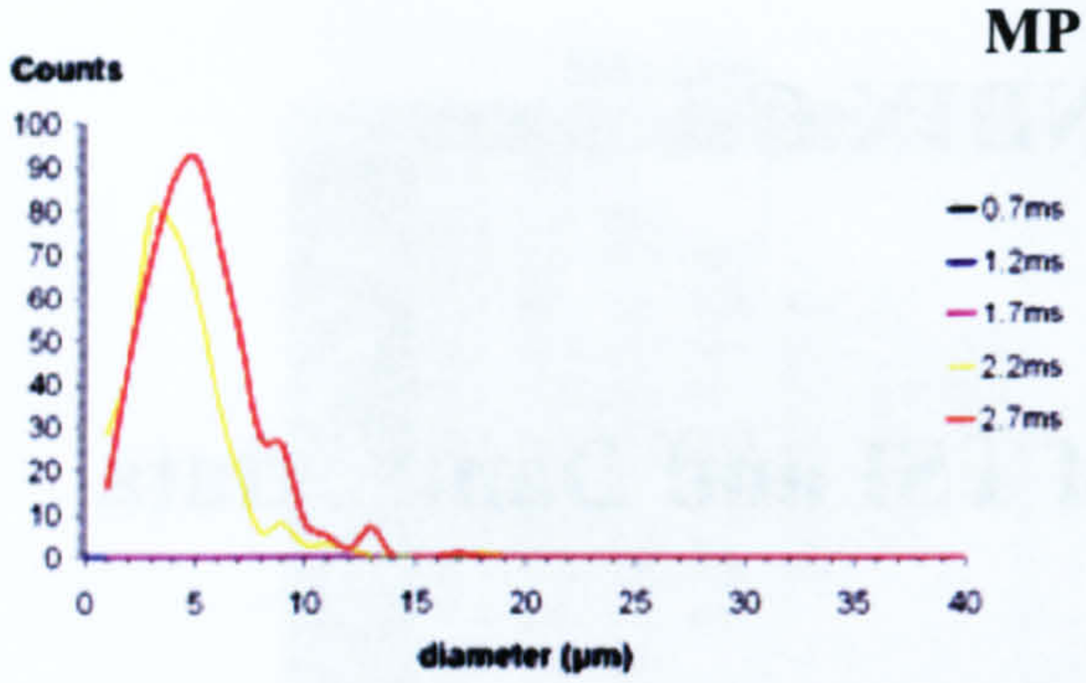

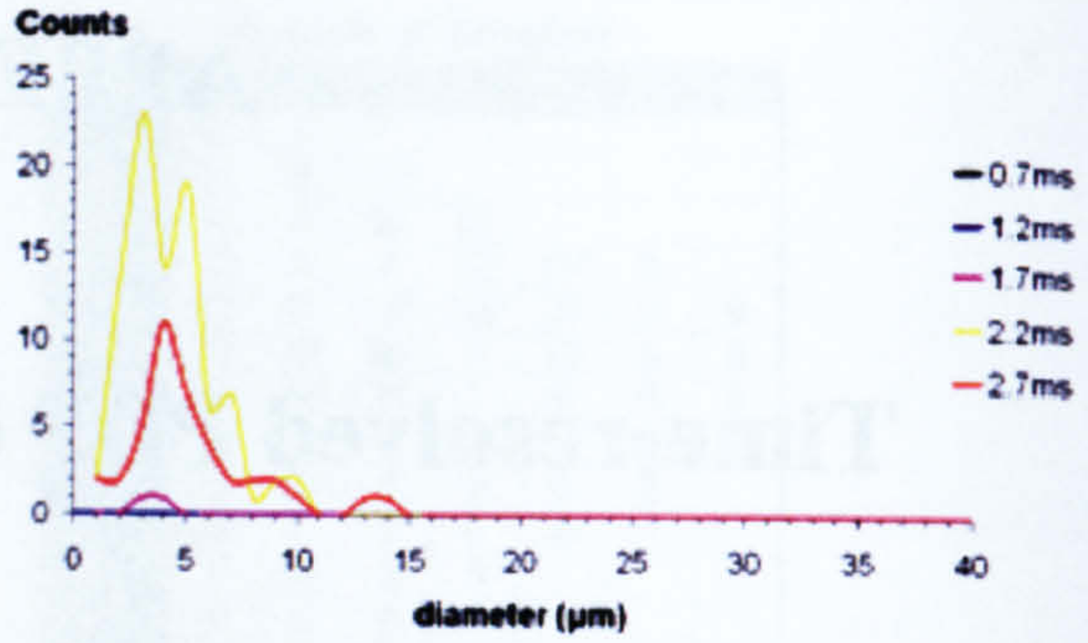

MP 2

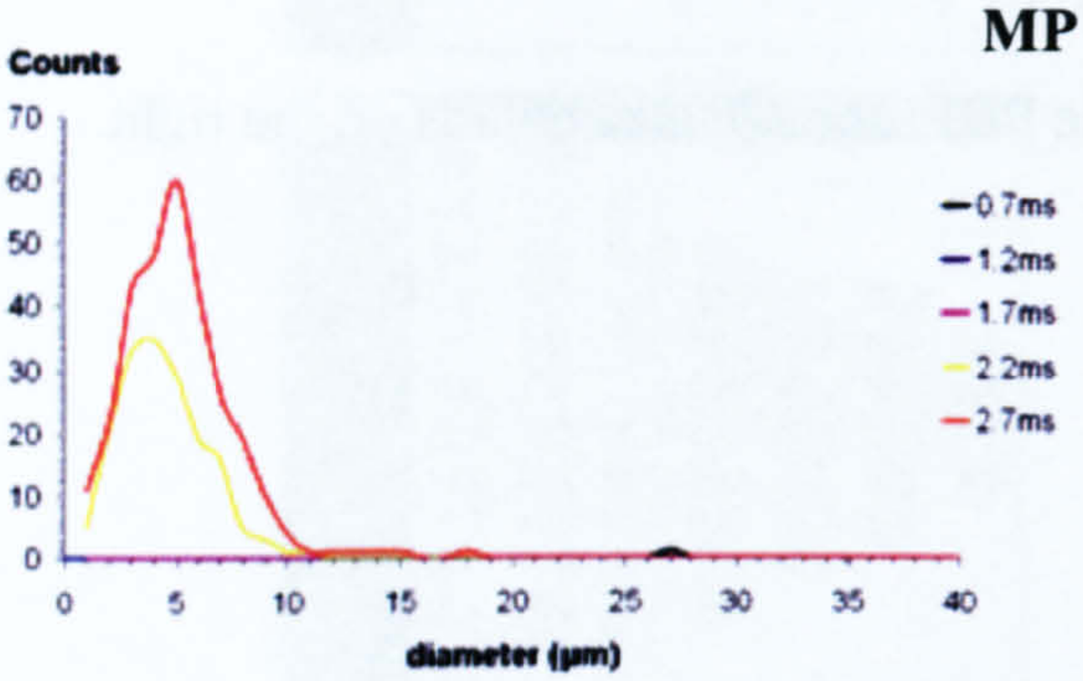

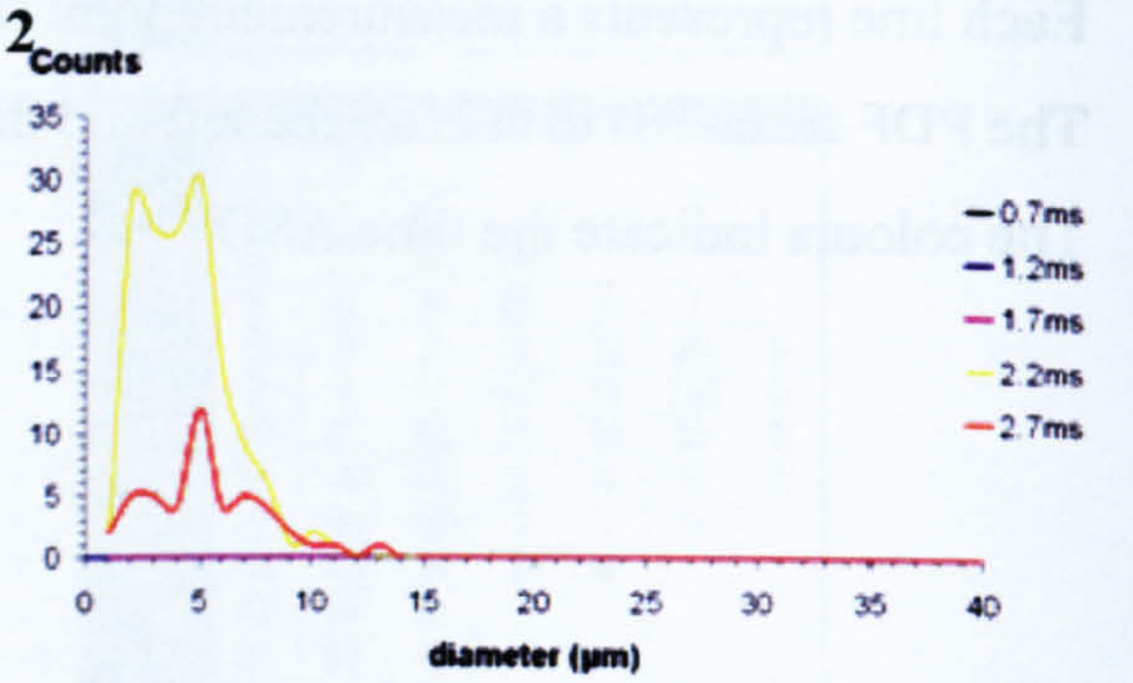

MP 3

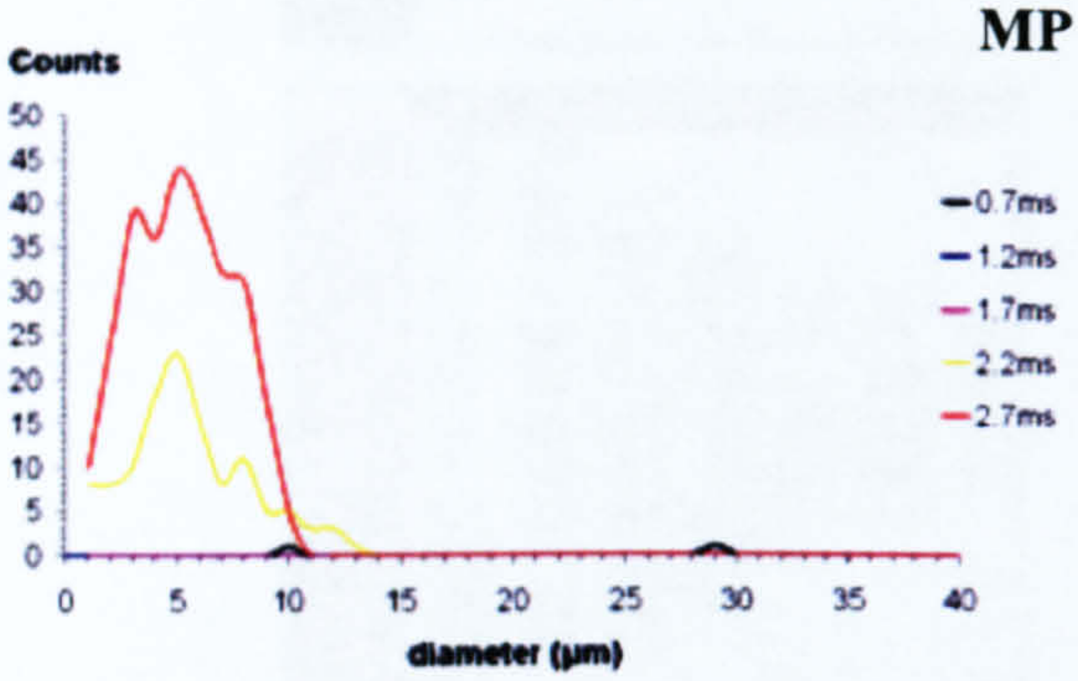

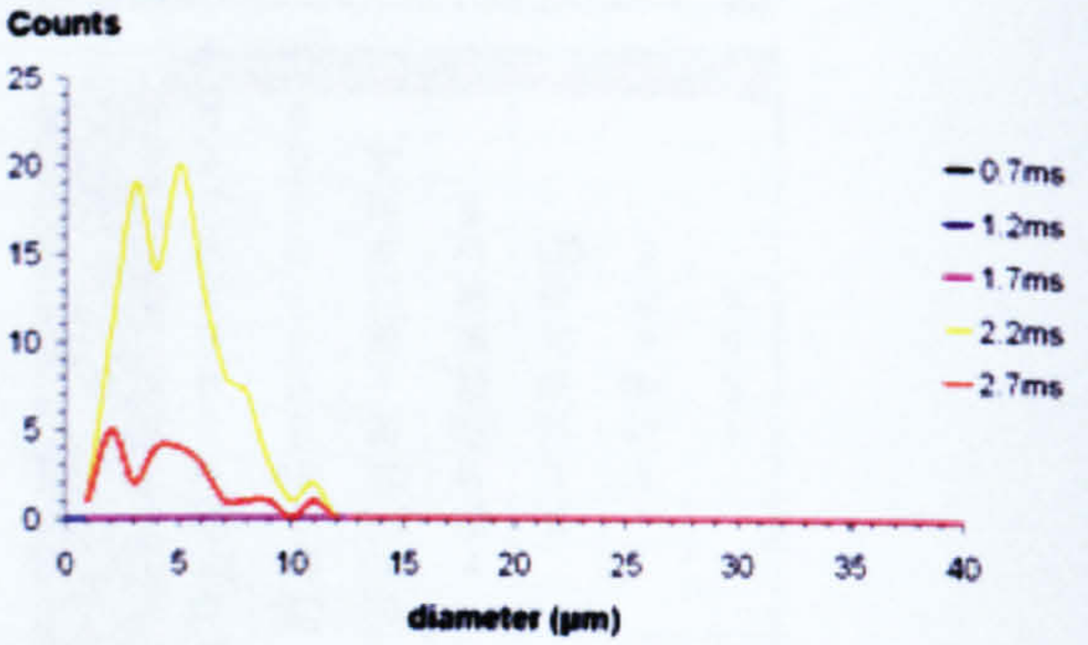

MP 4

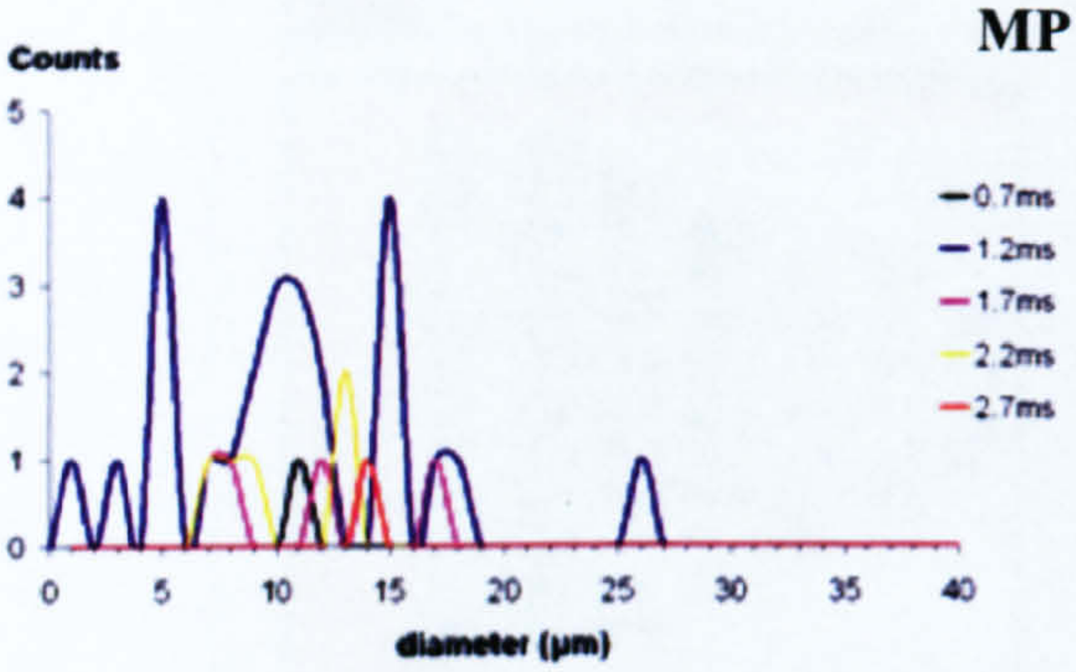

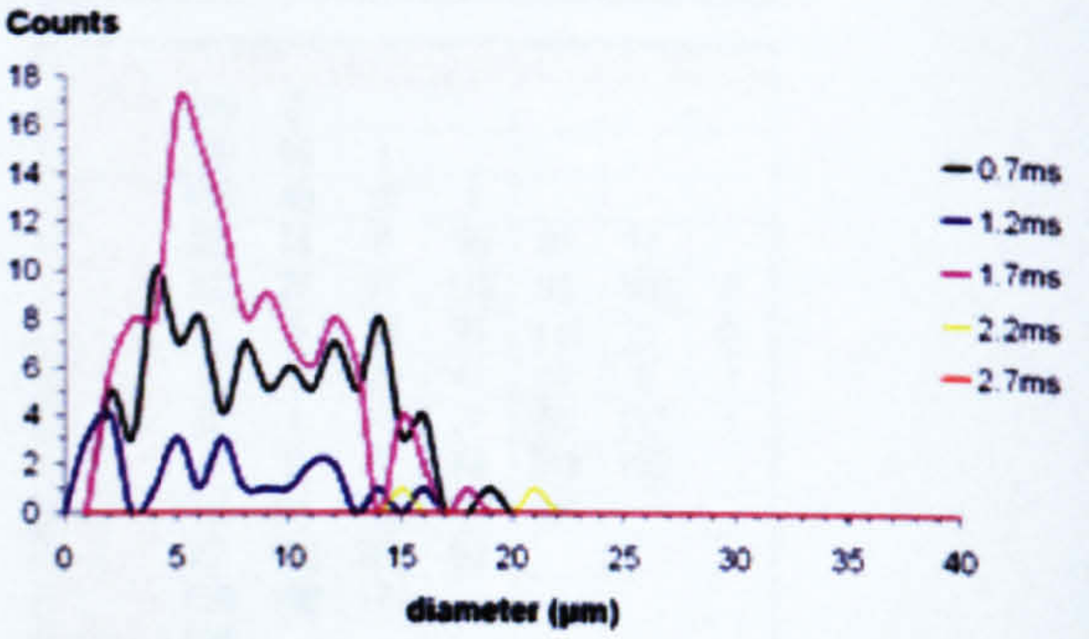

MP 5

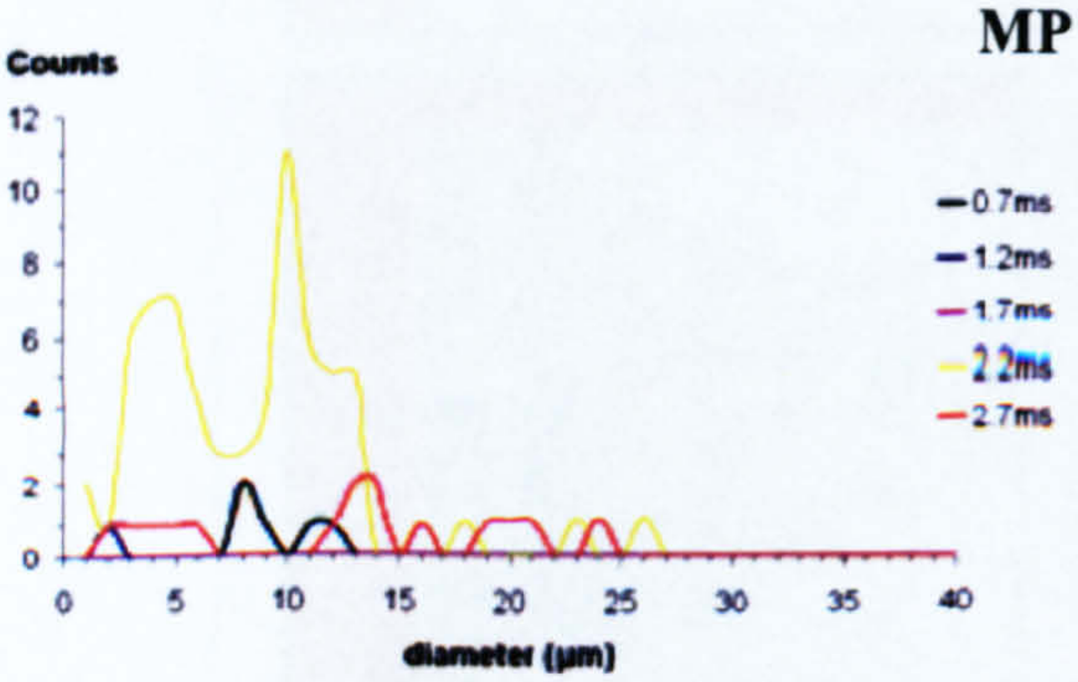

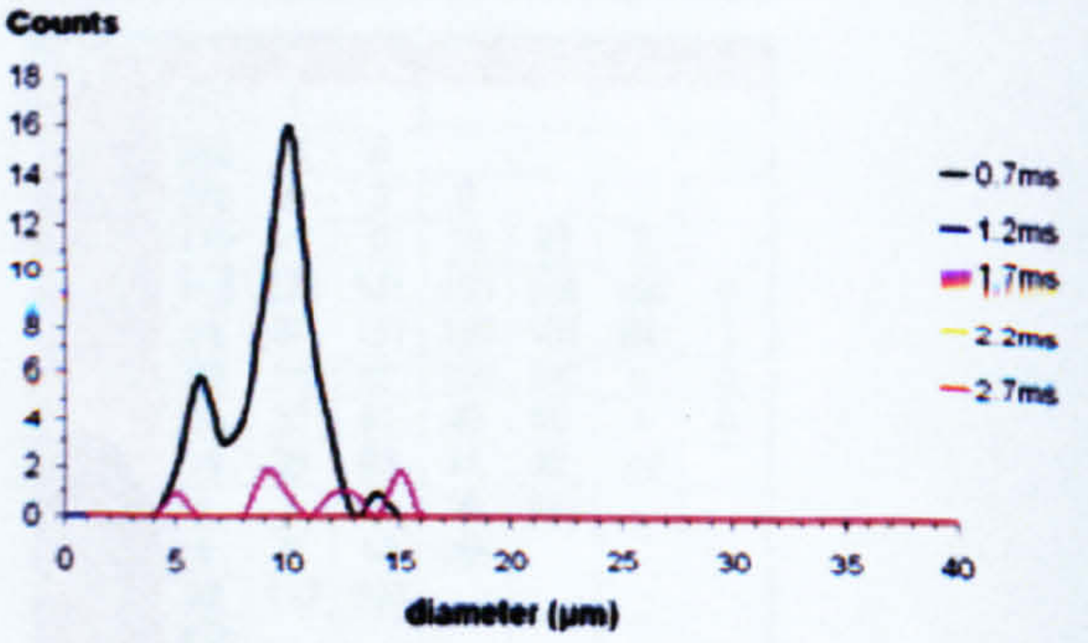

MP 6

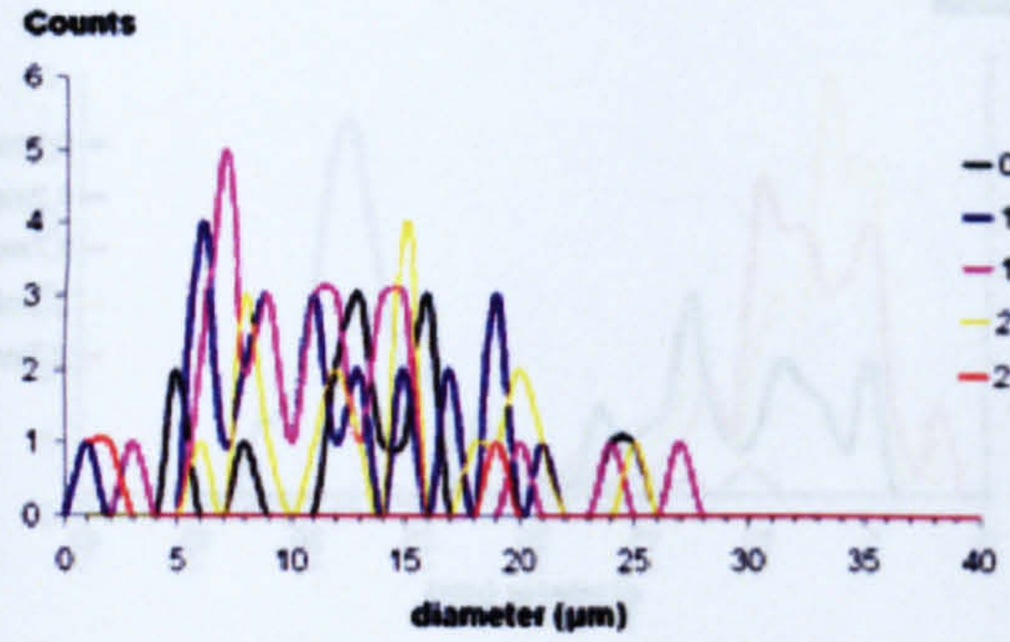

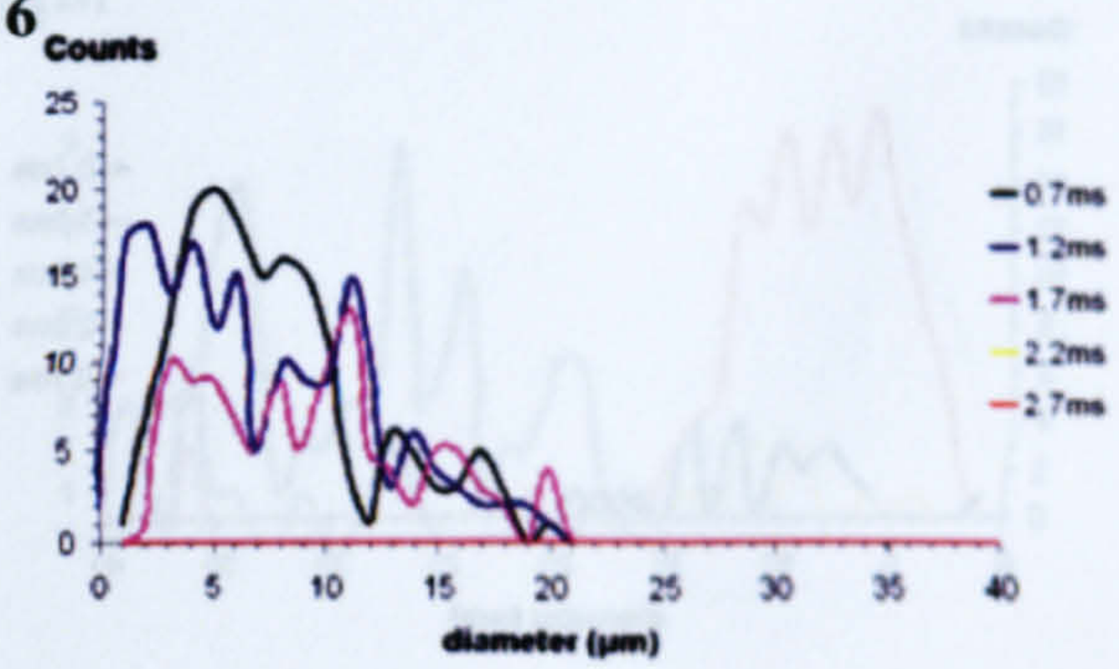

MP 7

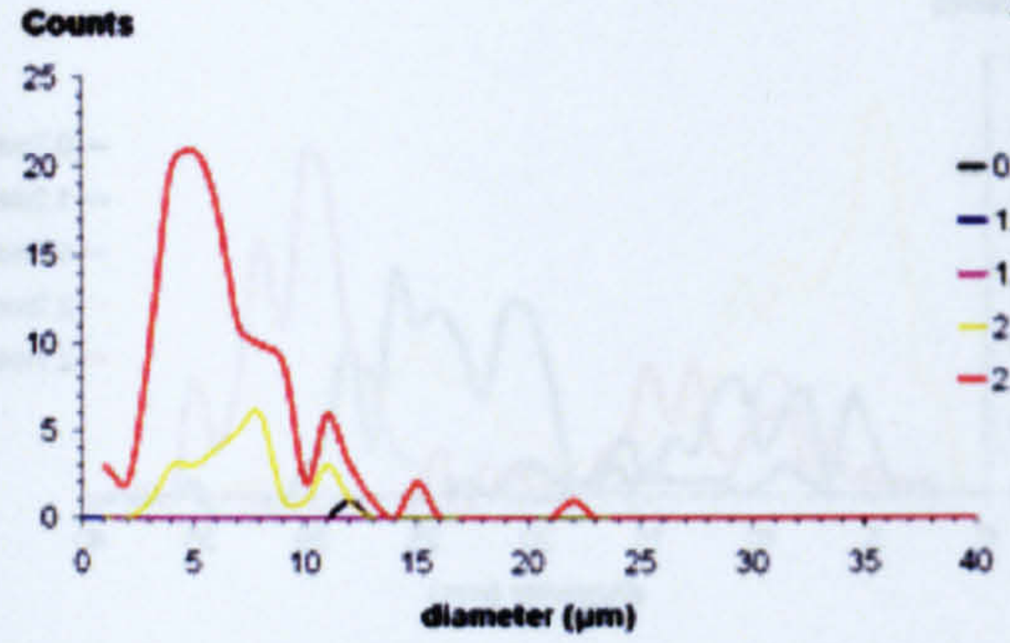

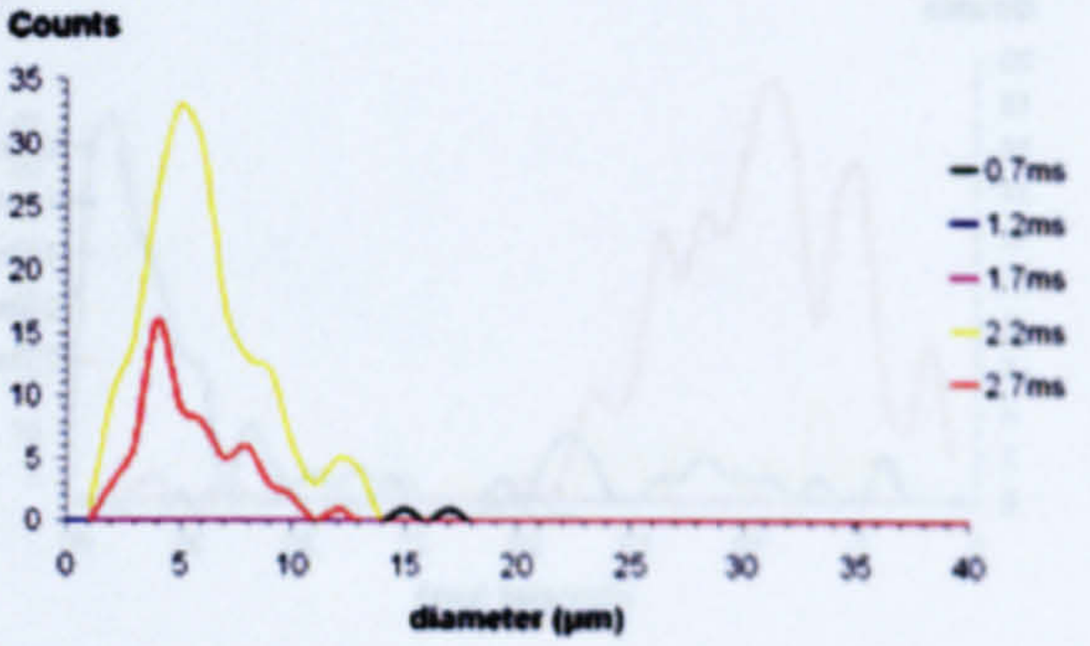

MP 8

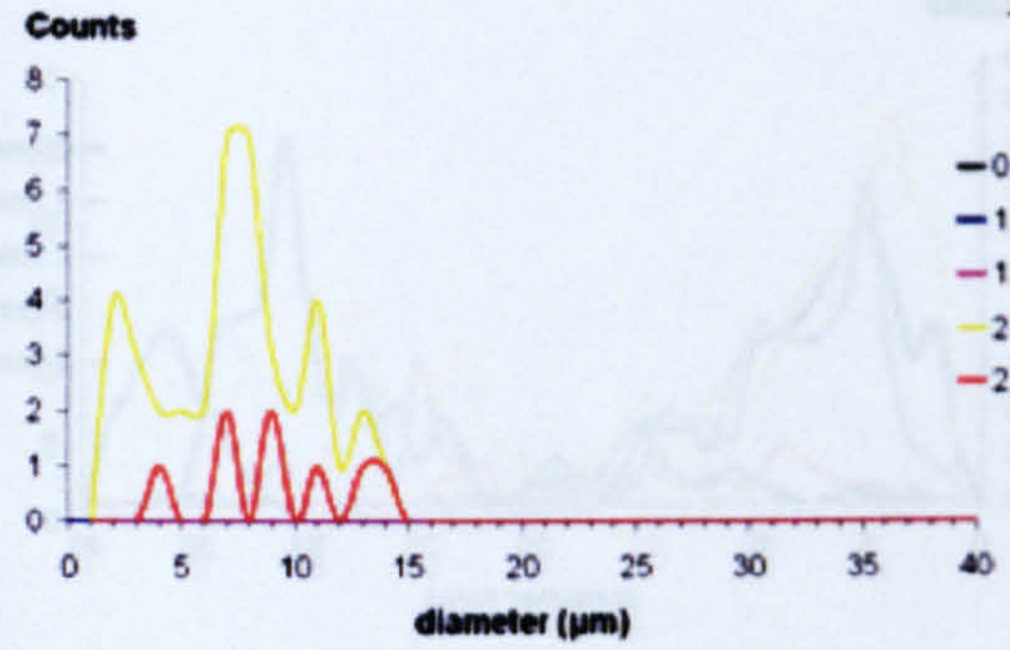

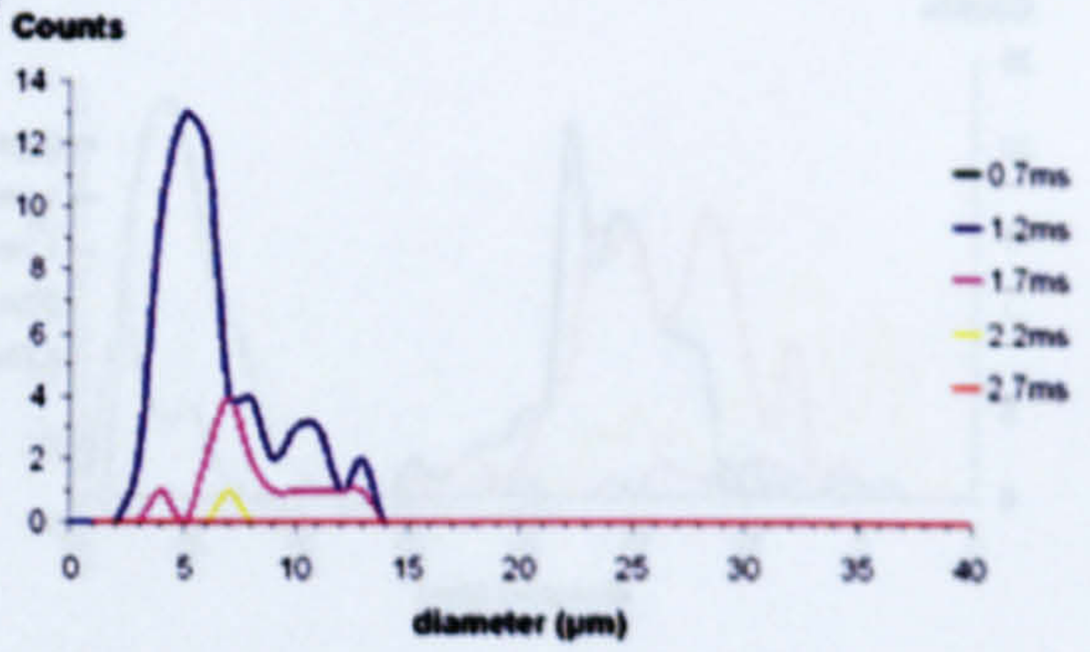

MP 9

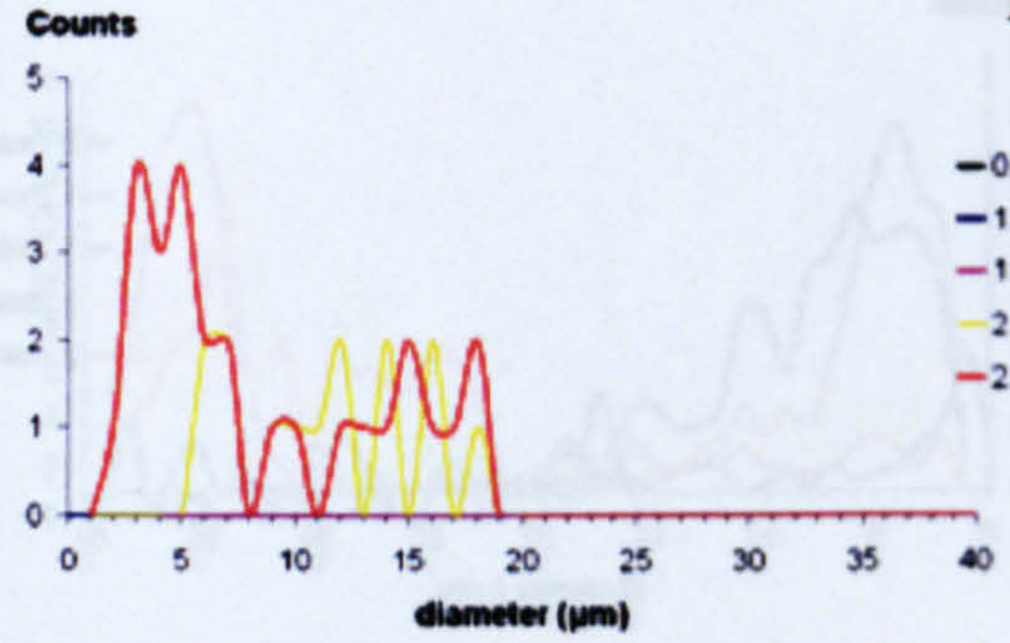

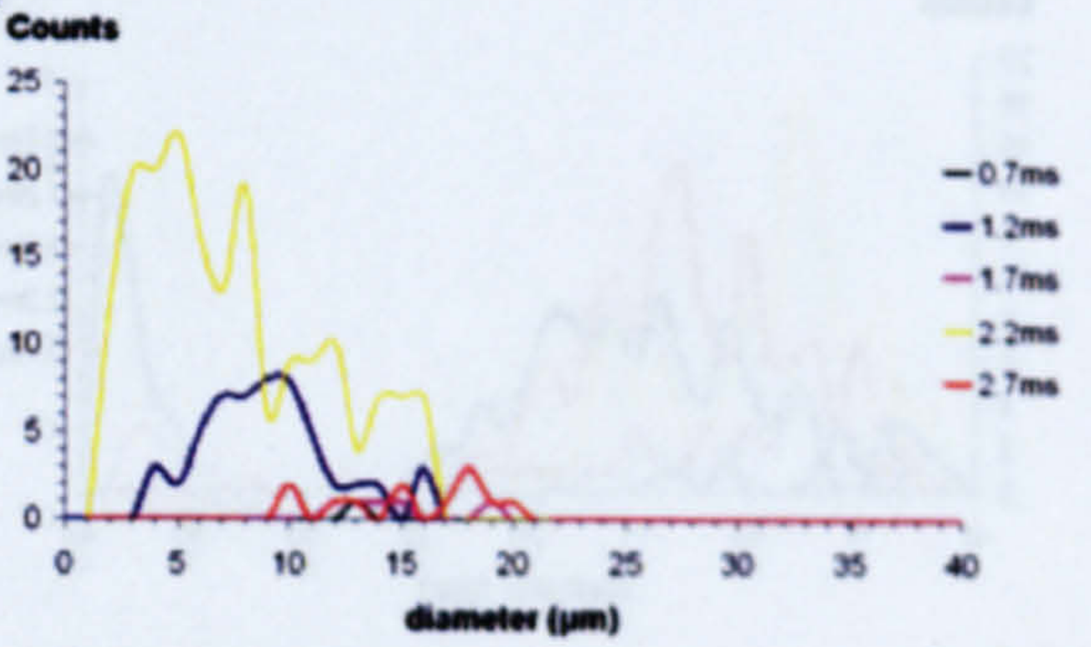

MP 10

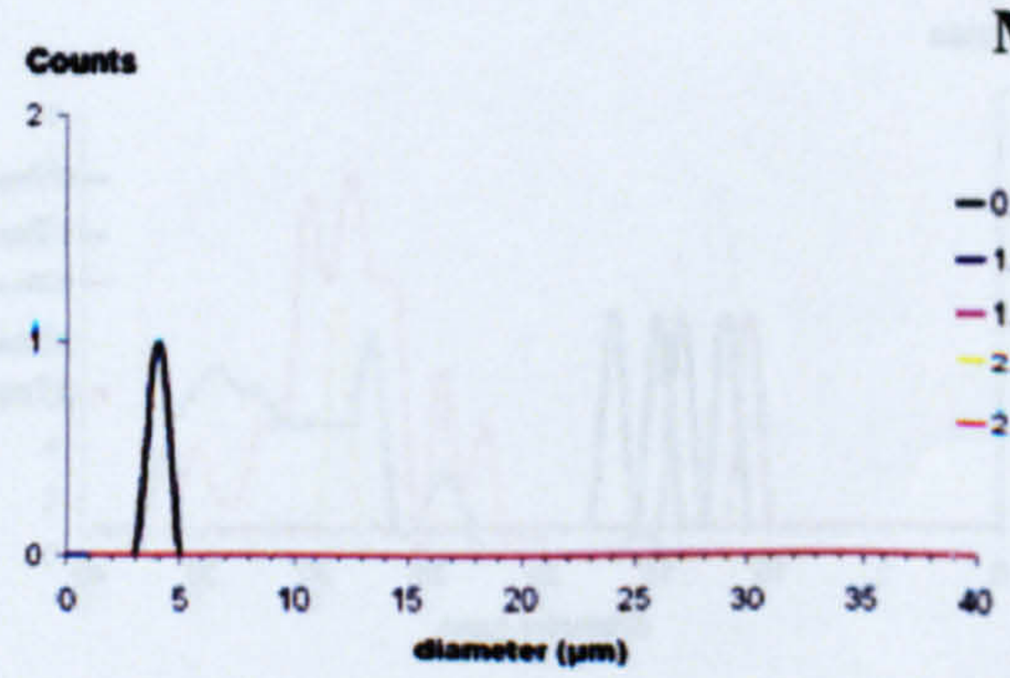

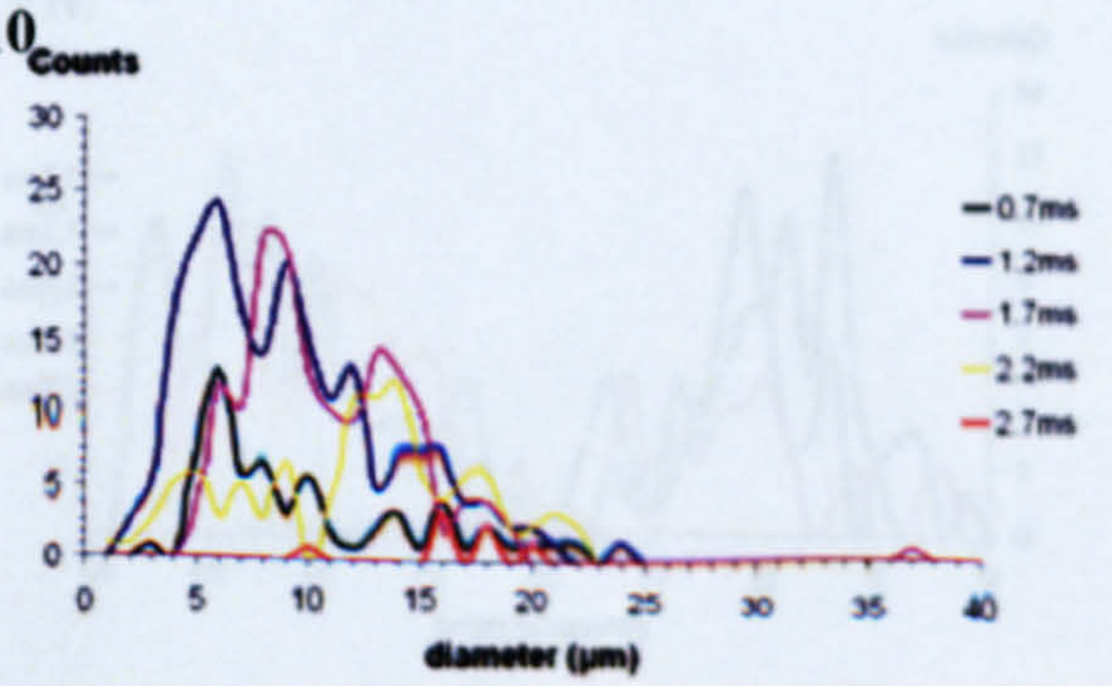

MP 11

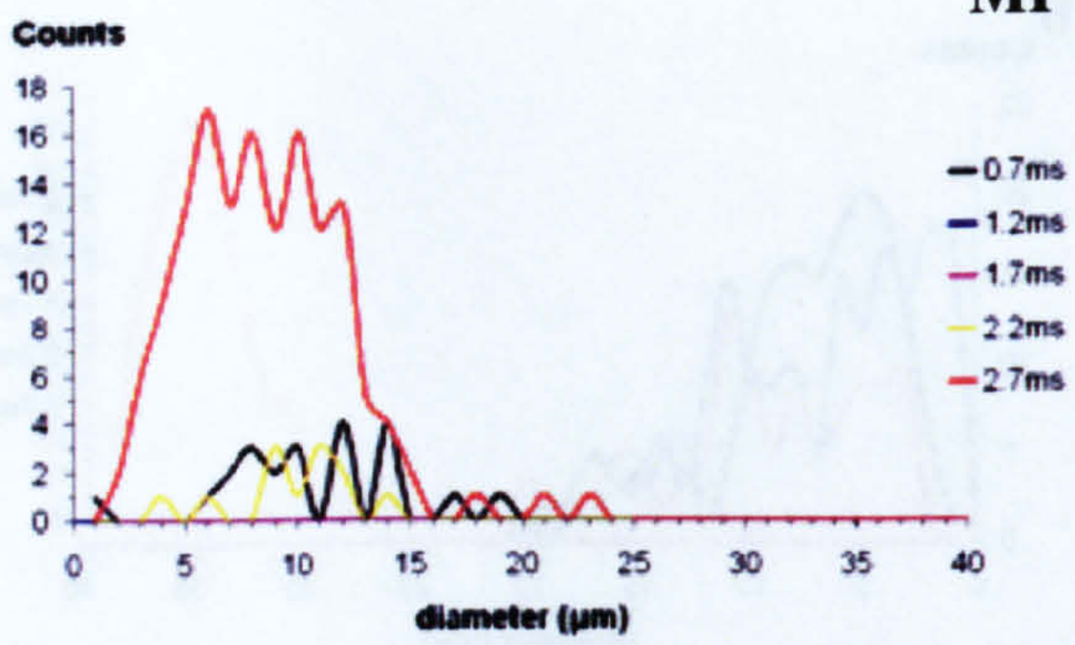

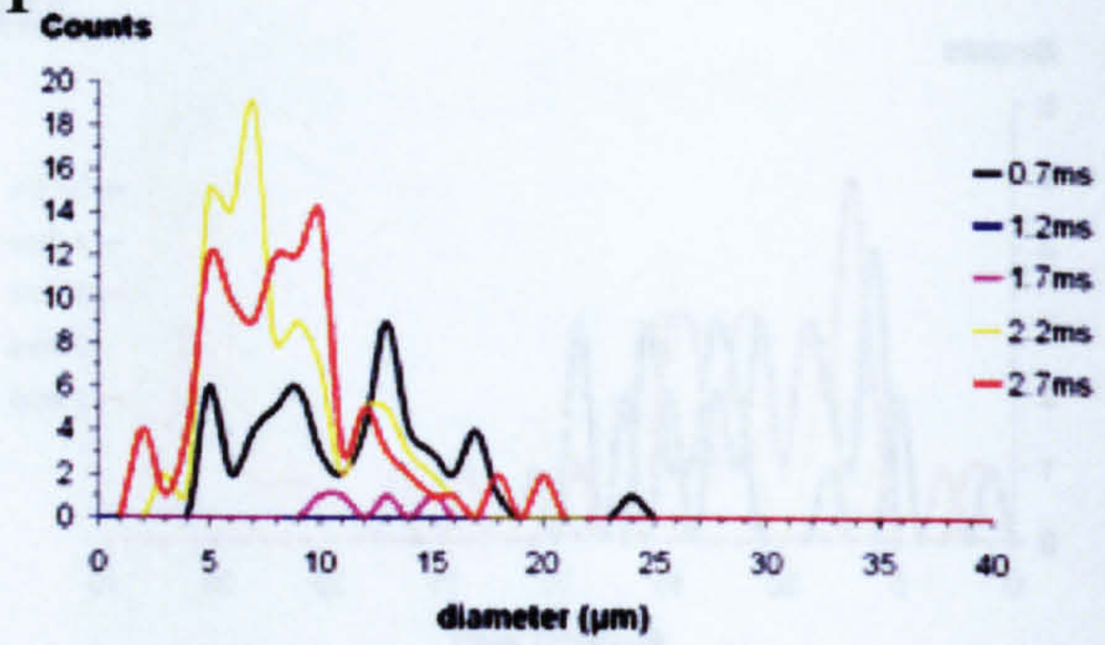

MP 12

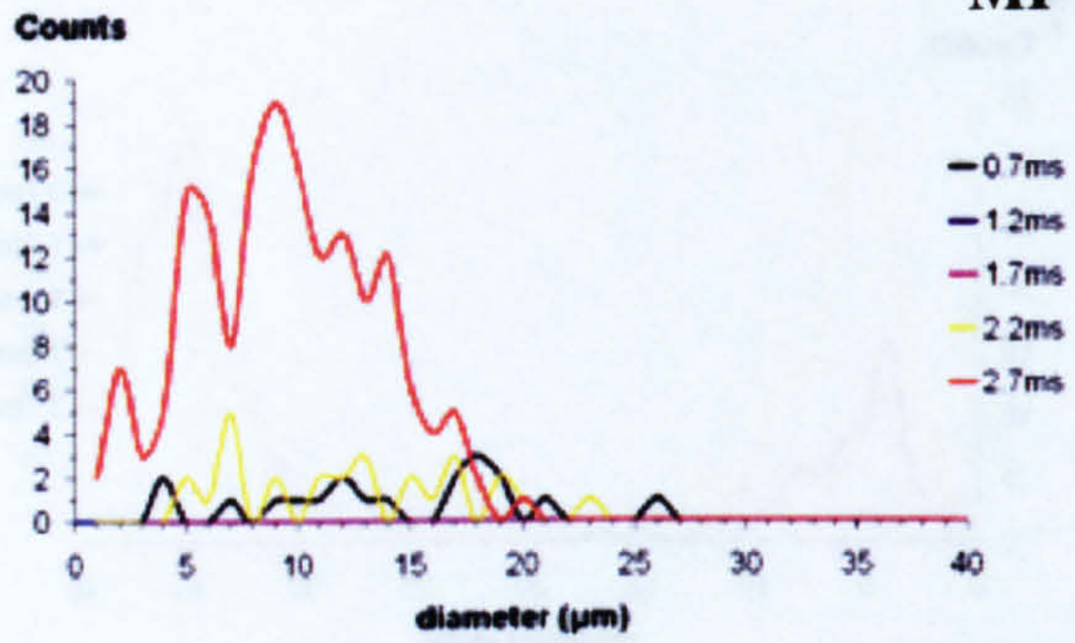

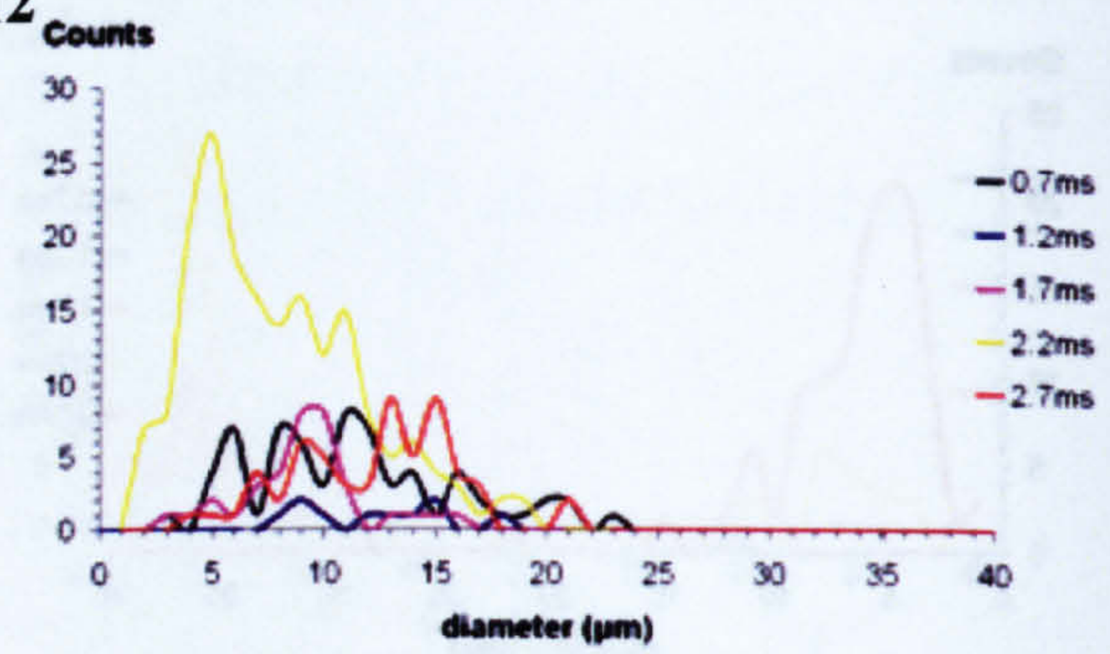

MP 13

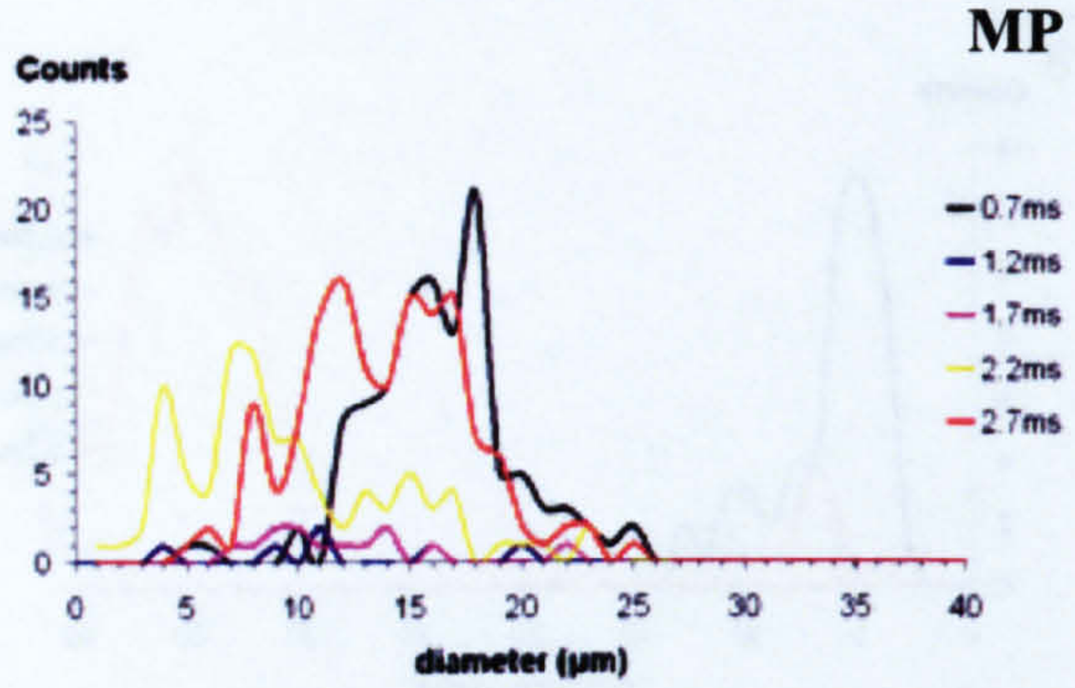

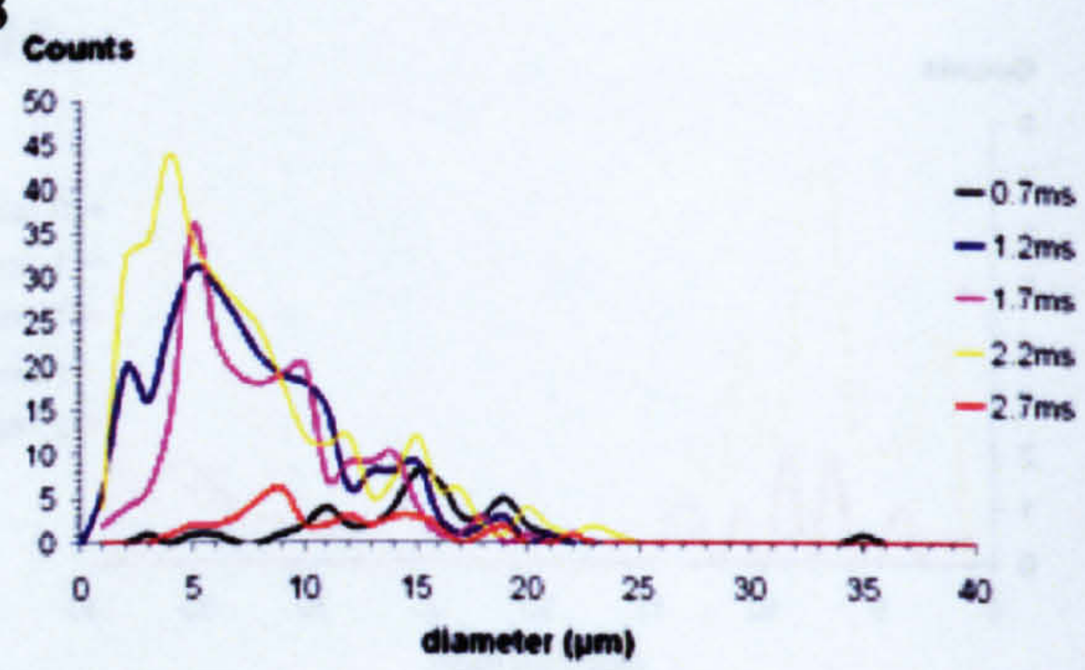

MP 14

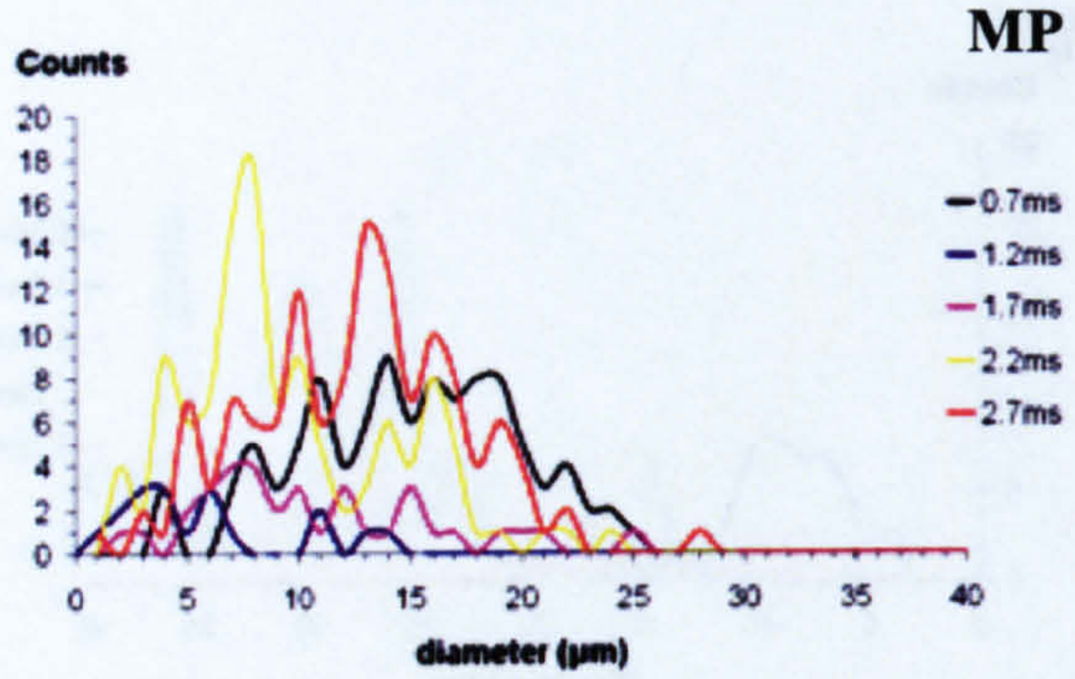

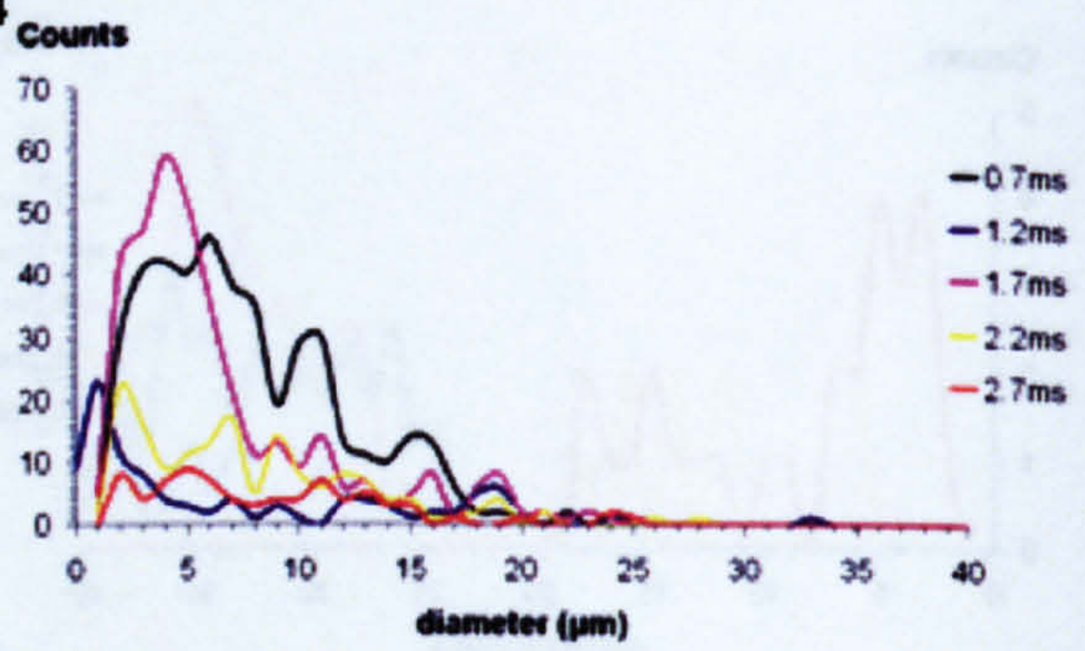

MP 15

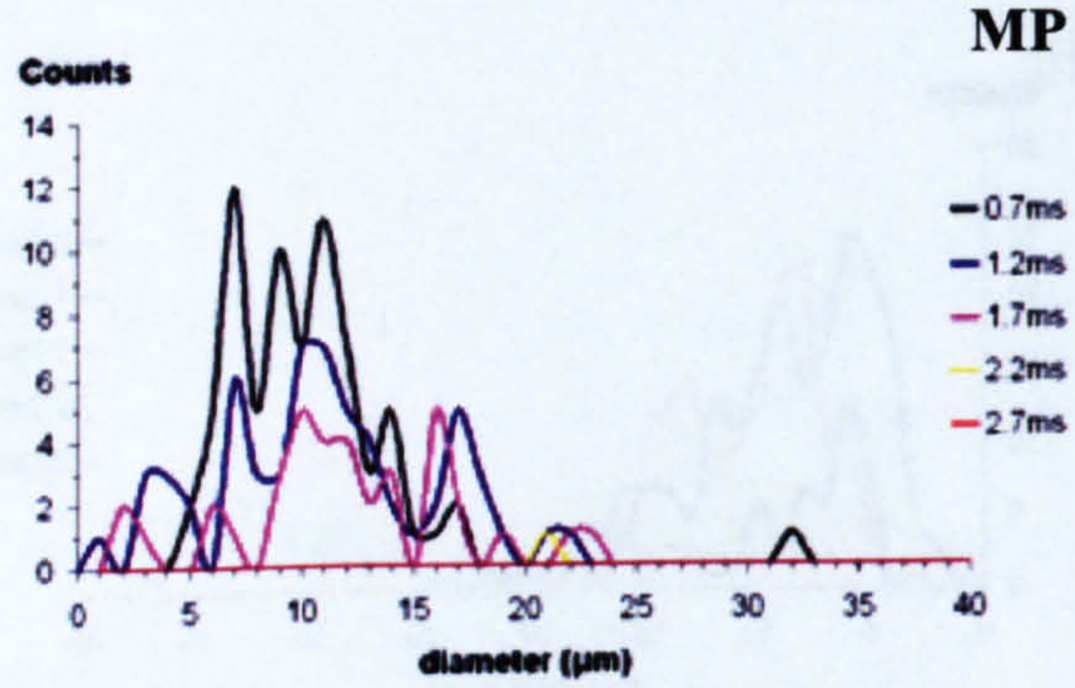

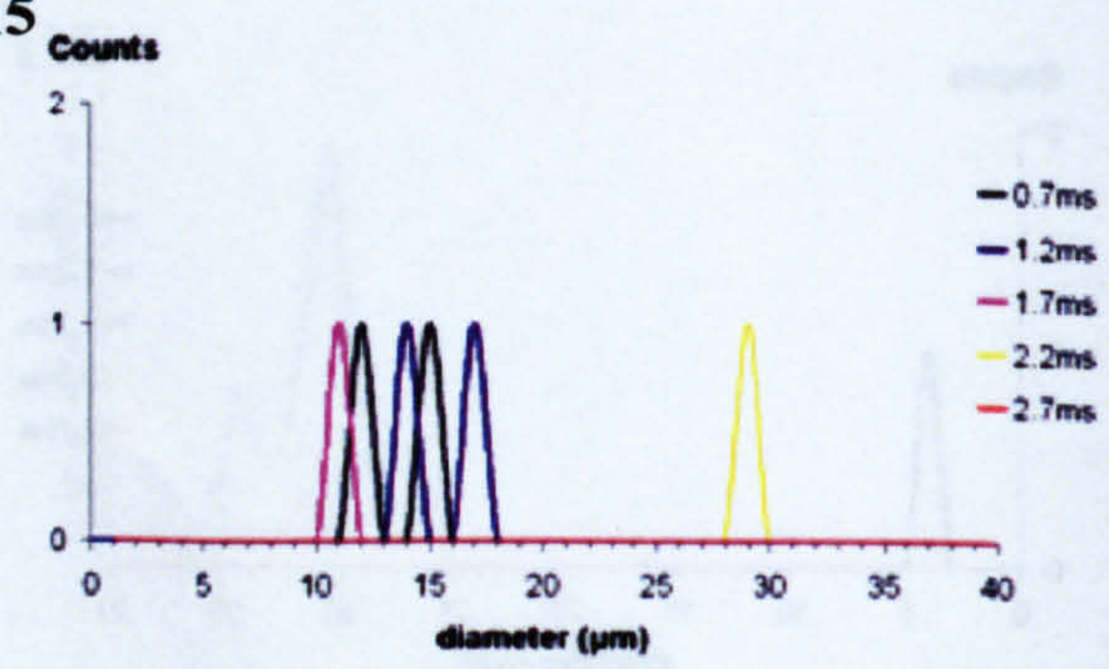

MP 16

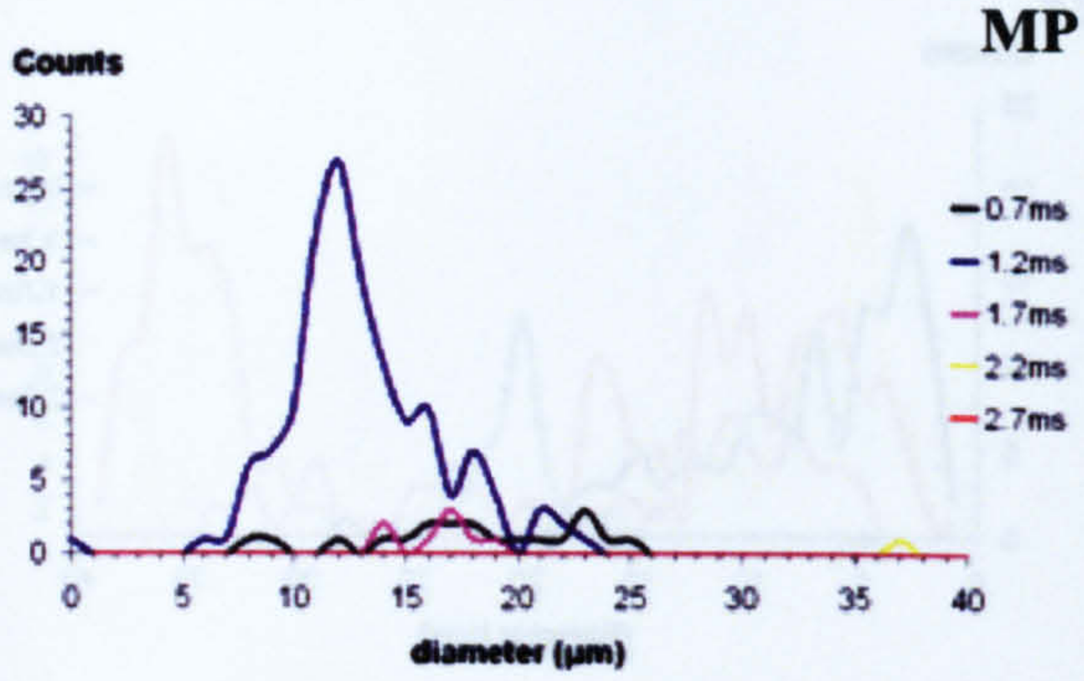

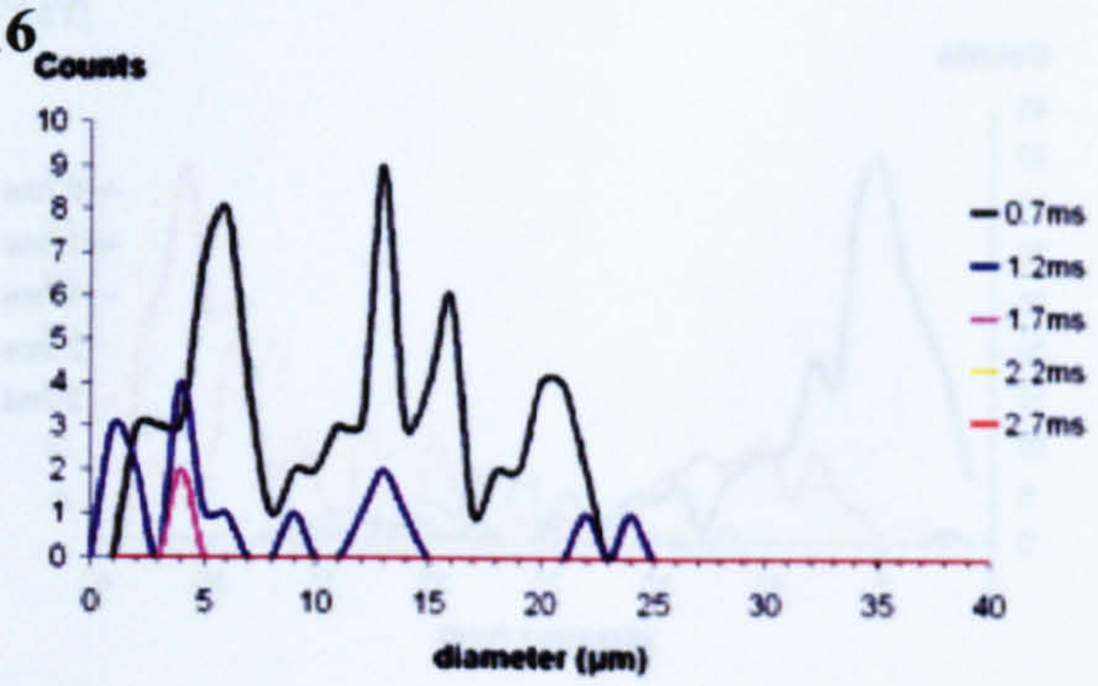

MP 17

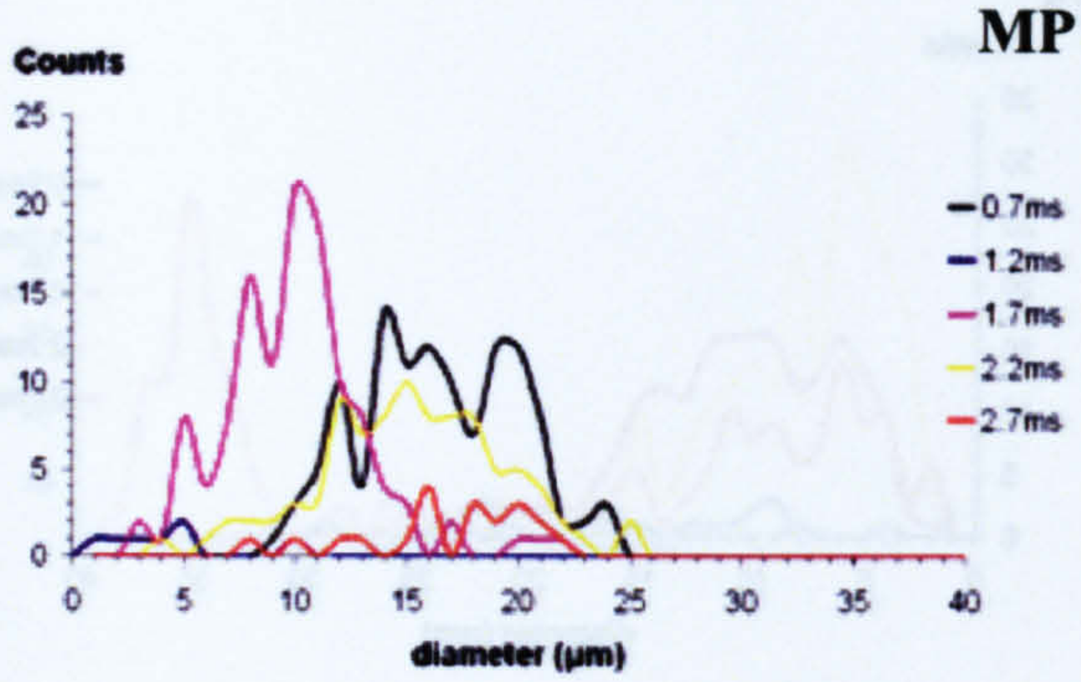

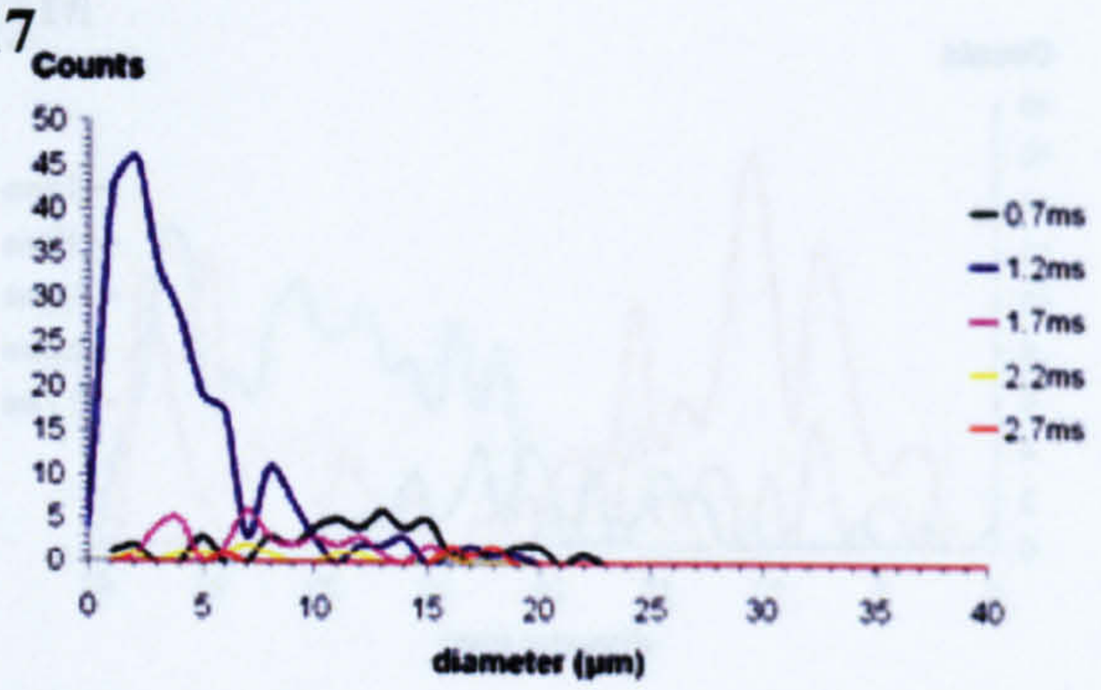

MP 19

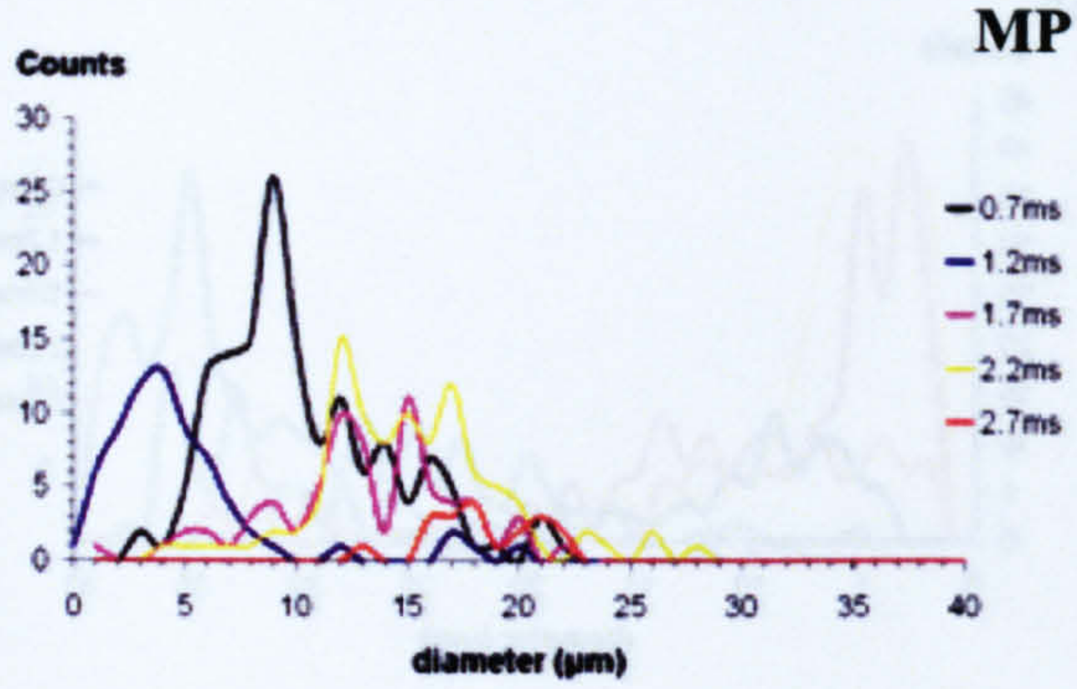

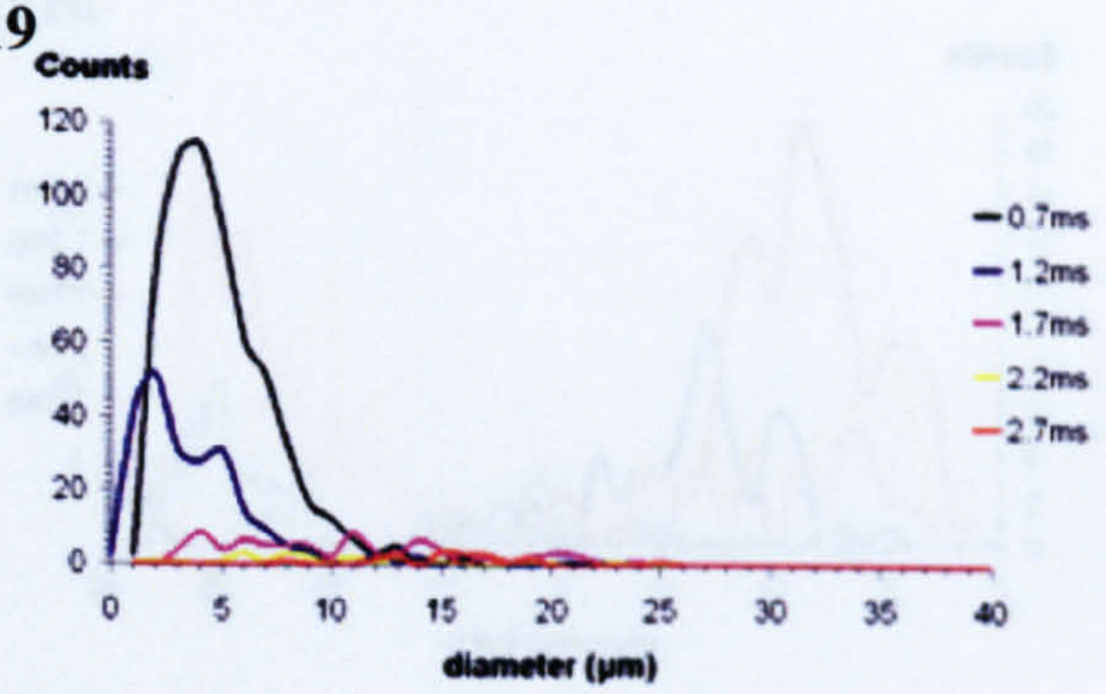

MP 20

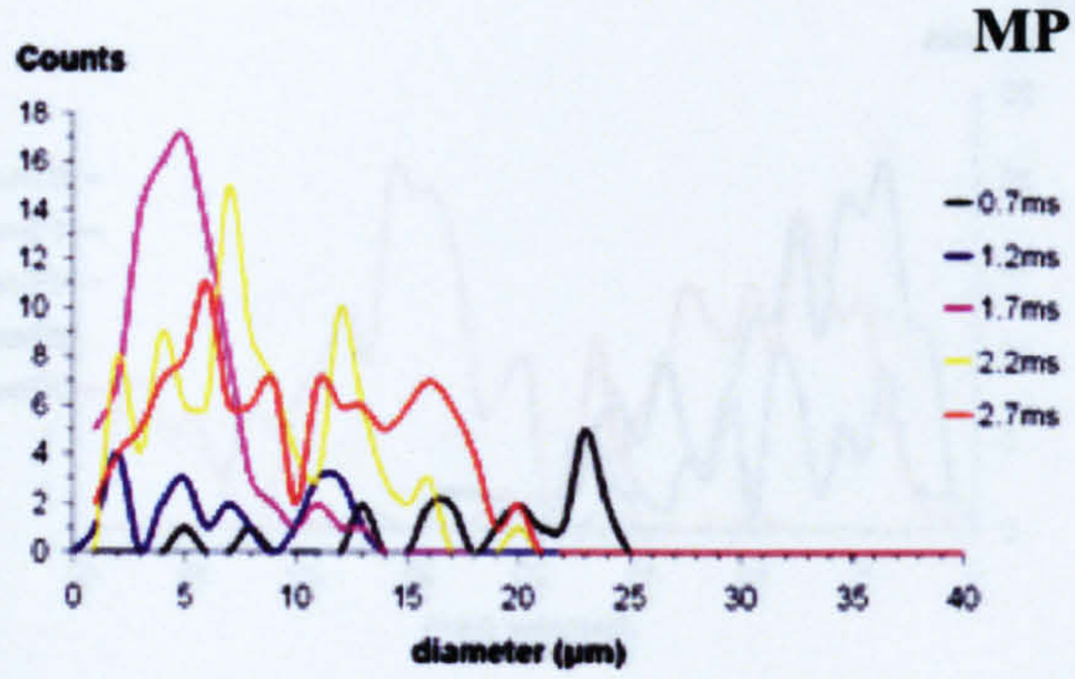

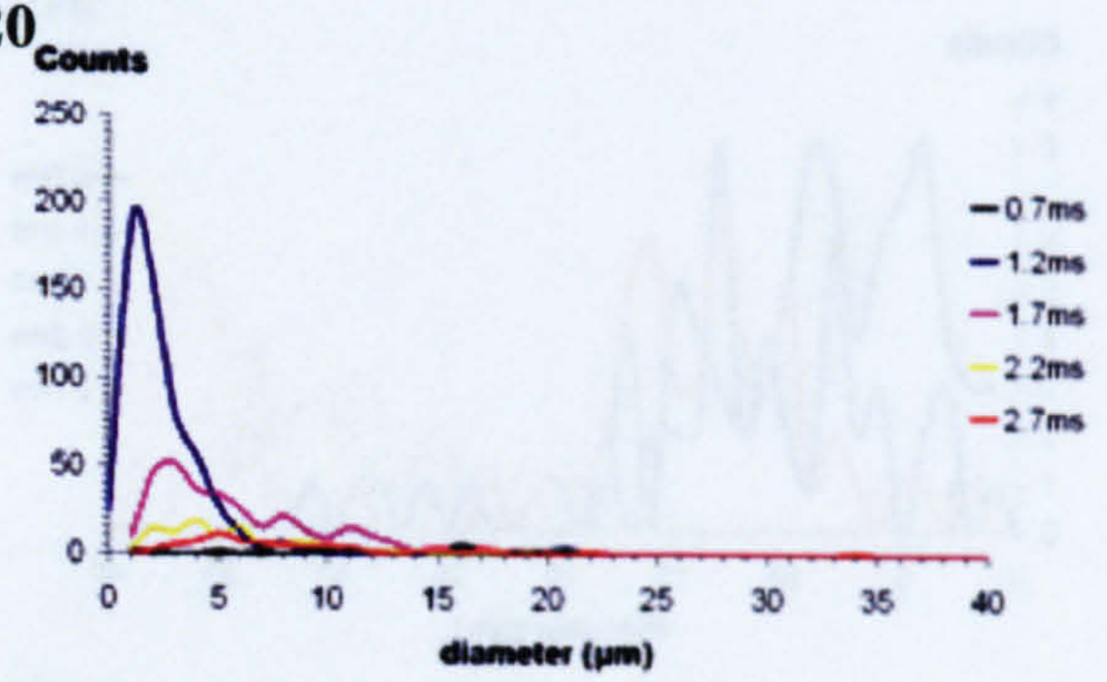

MP 23

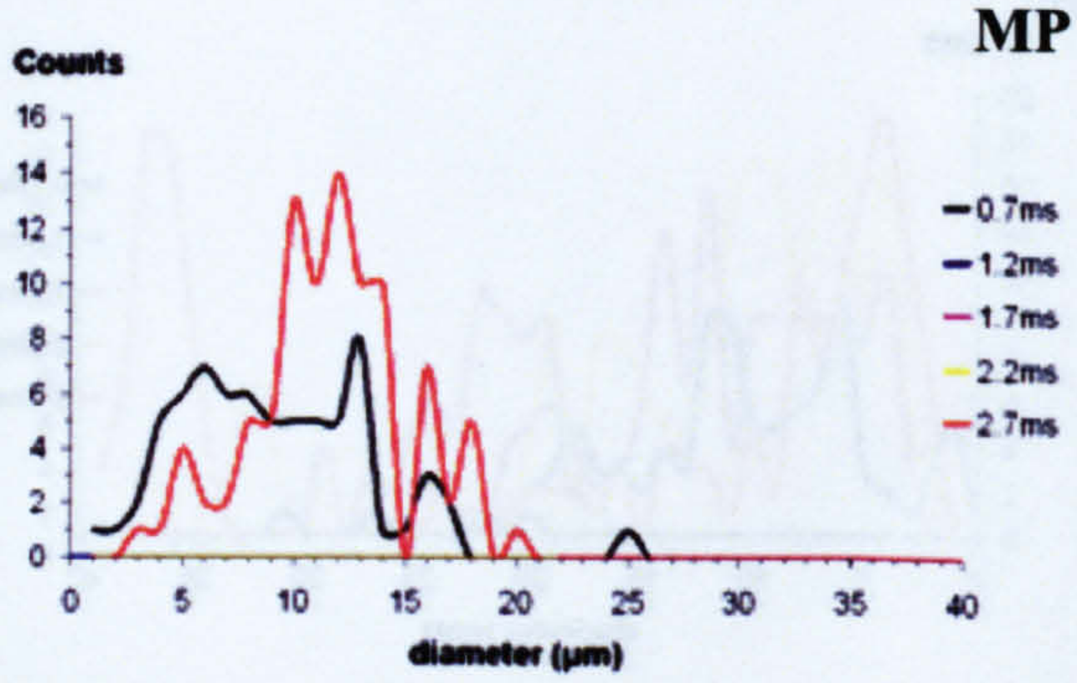

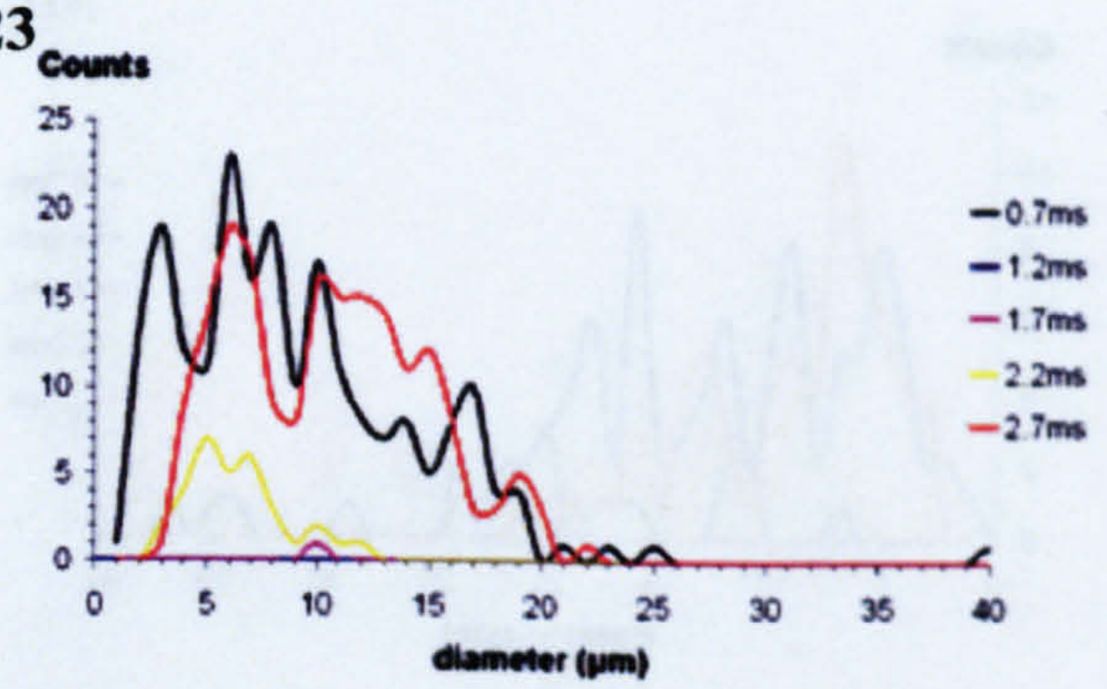

MP 24

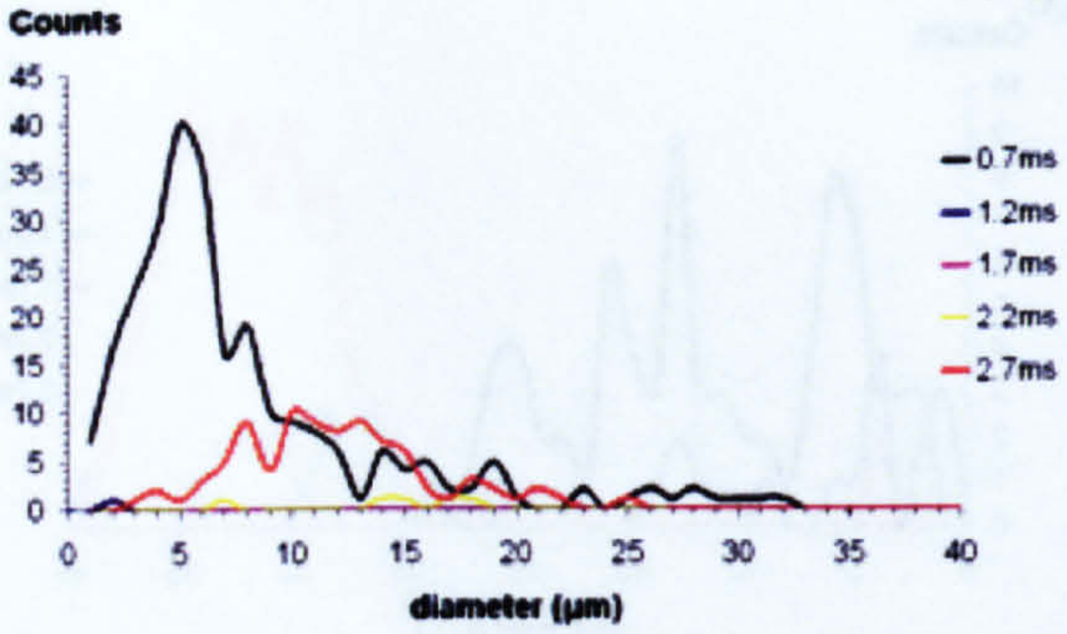

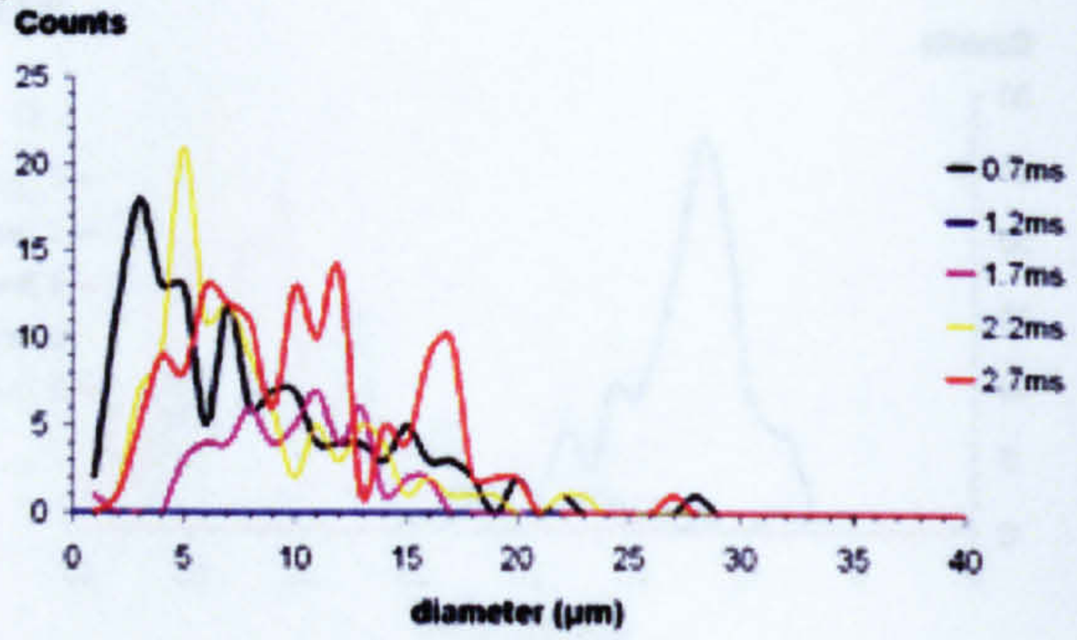

MP 25

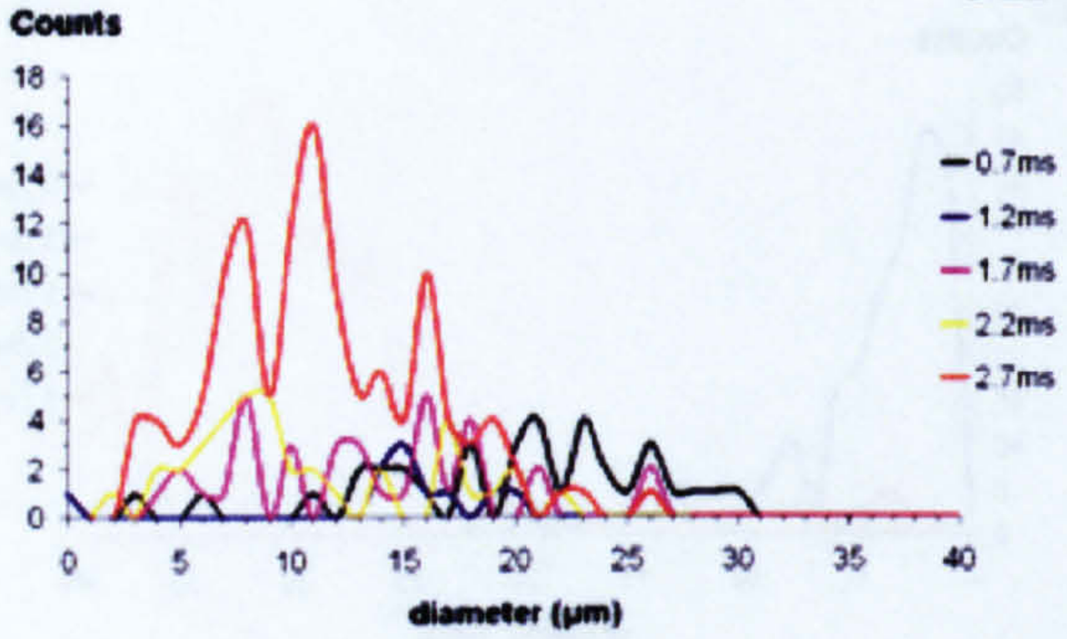

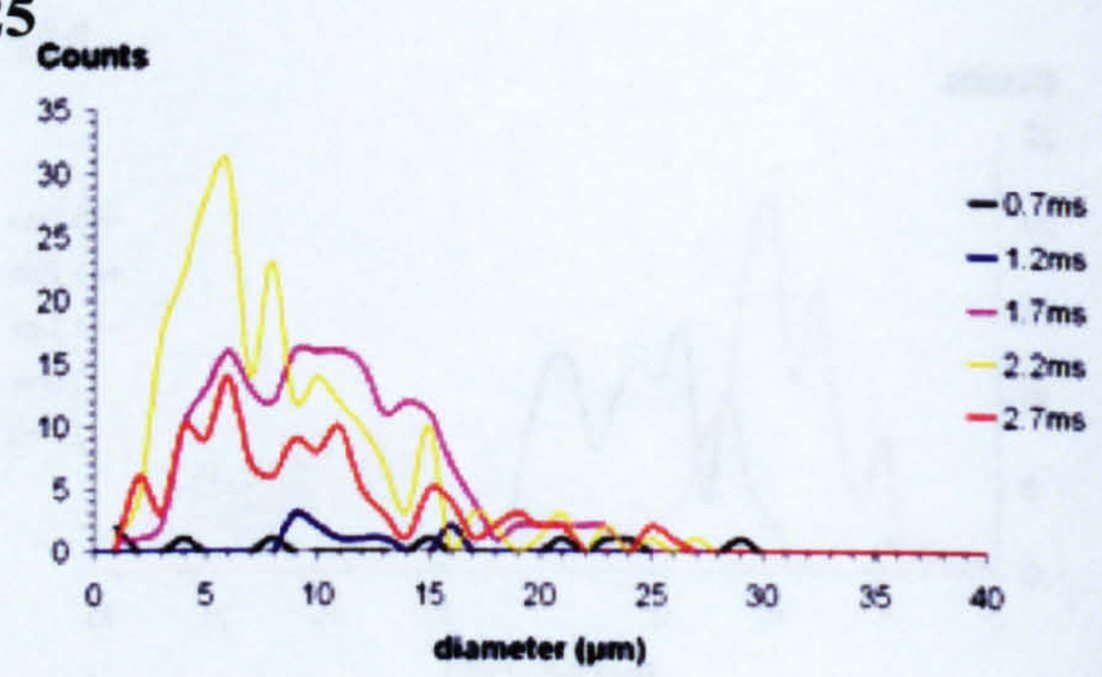

MP 26

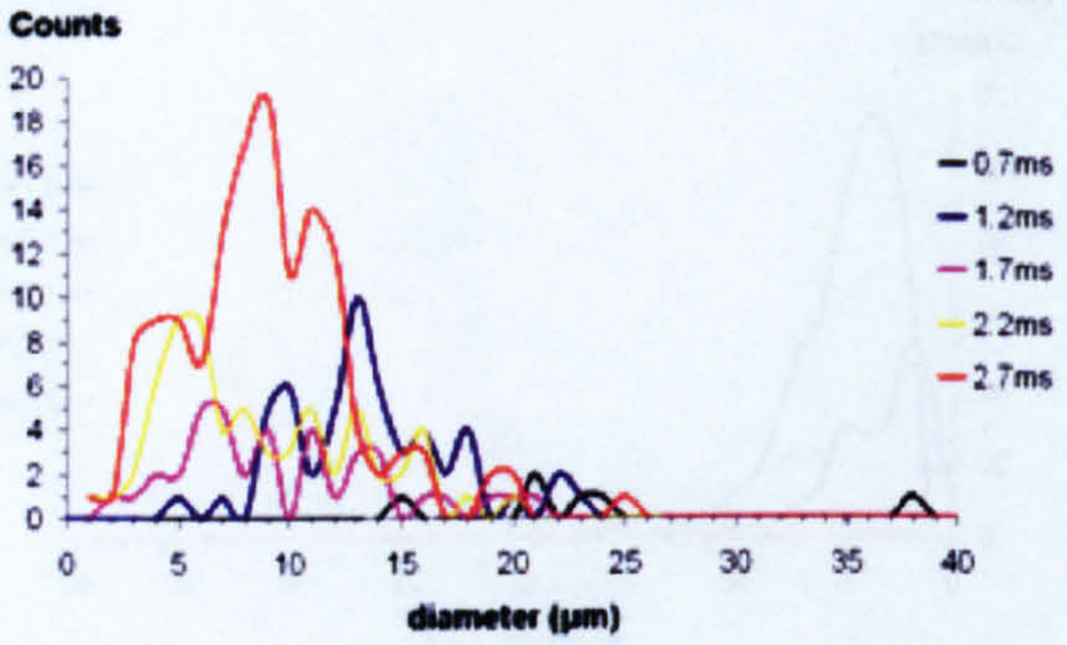

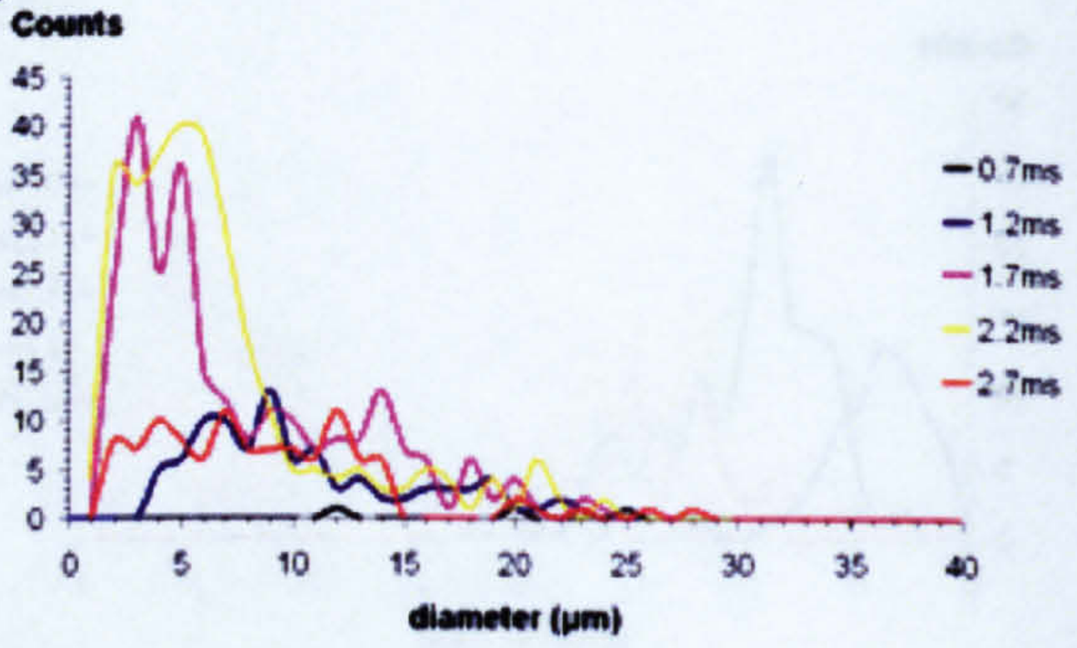

MP 29

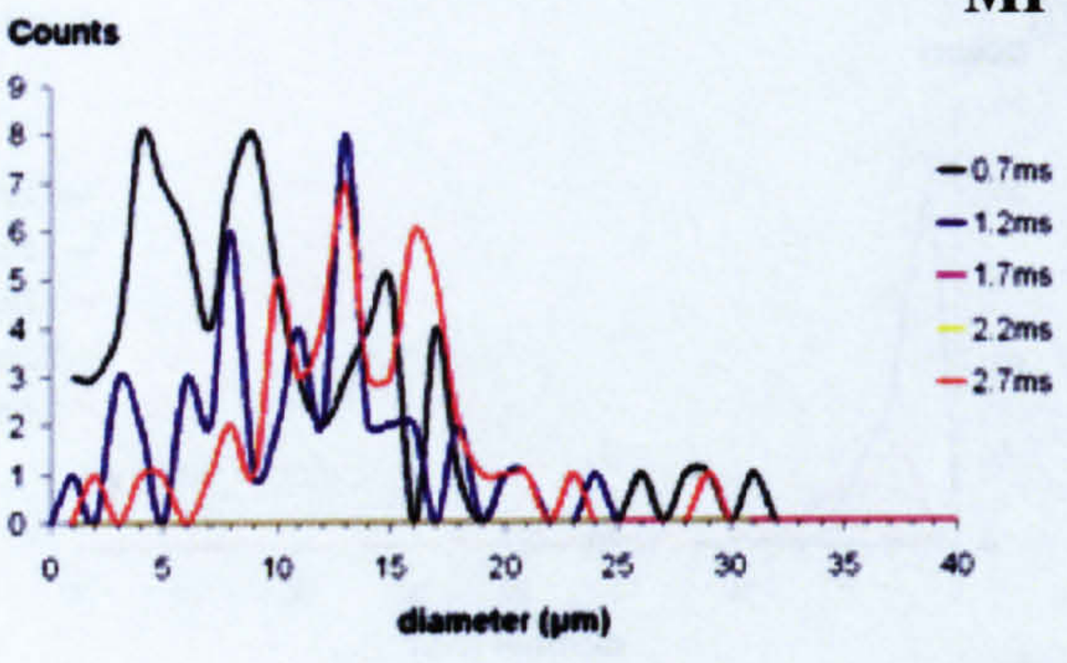

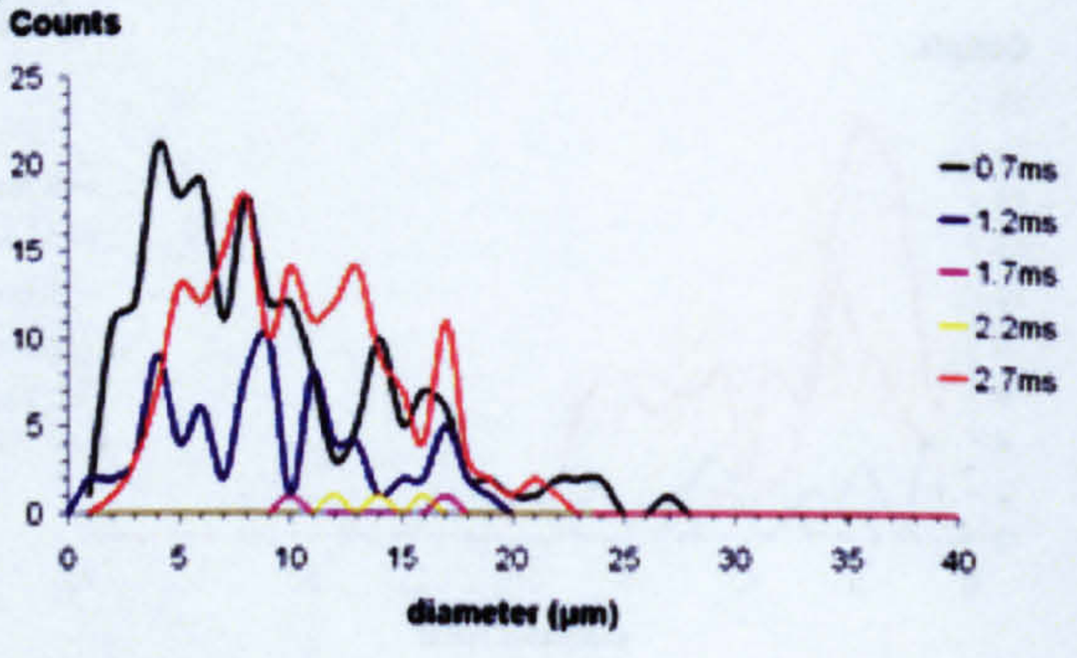

MP 30

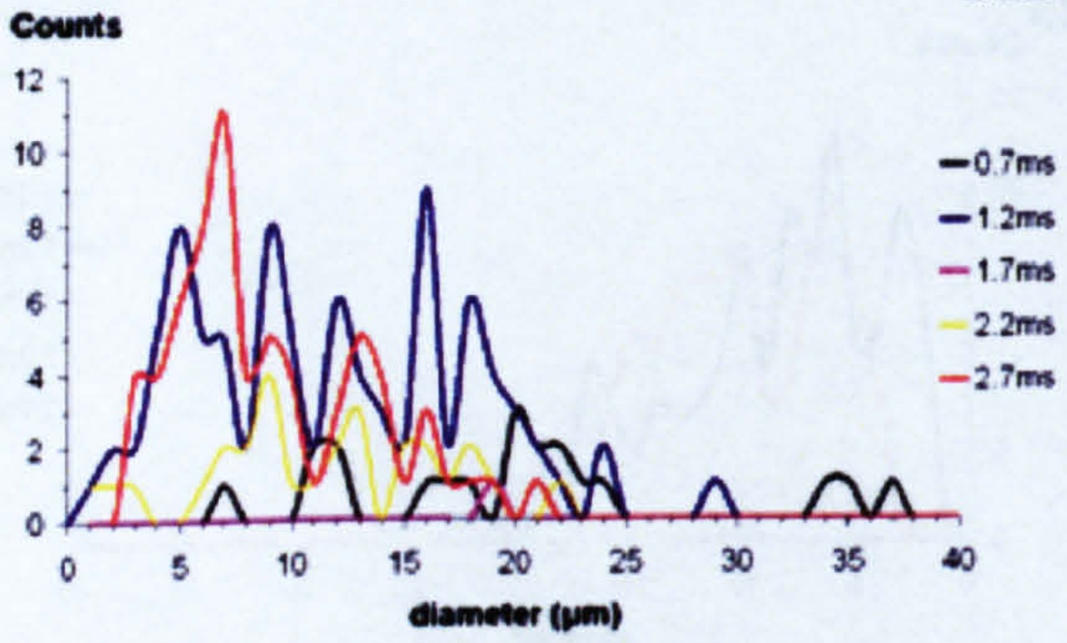

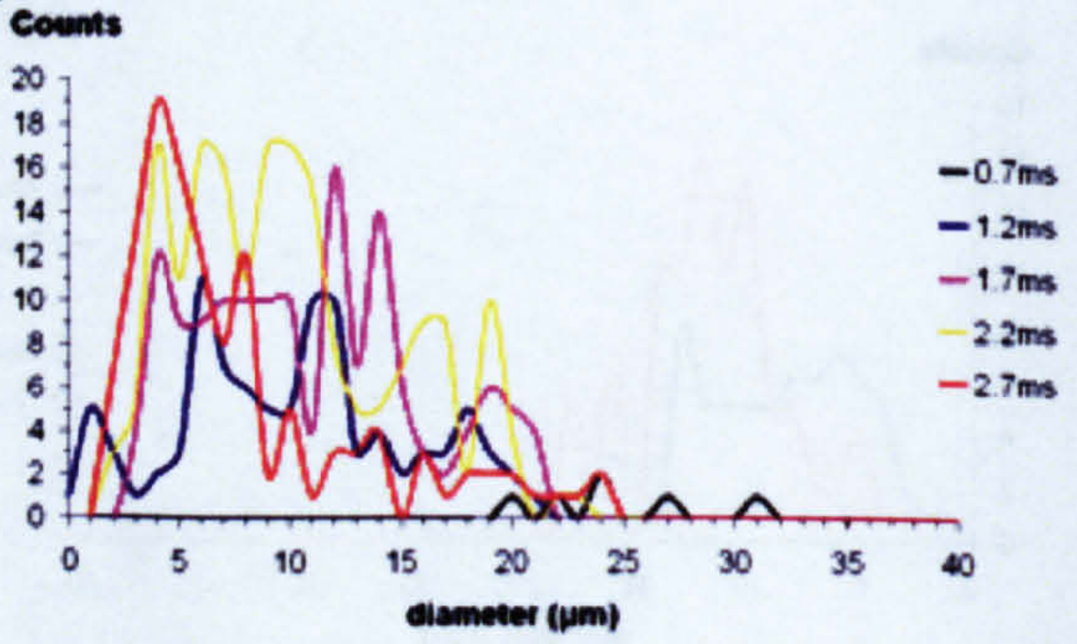

MP 31

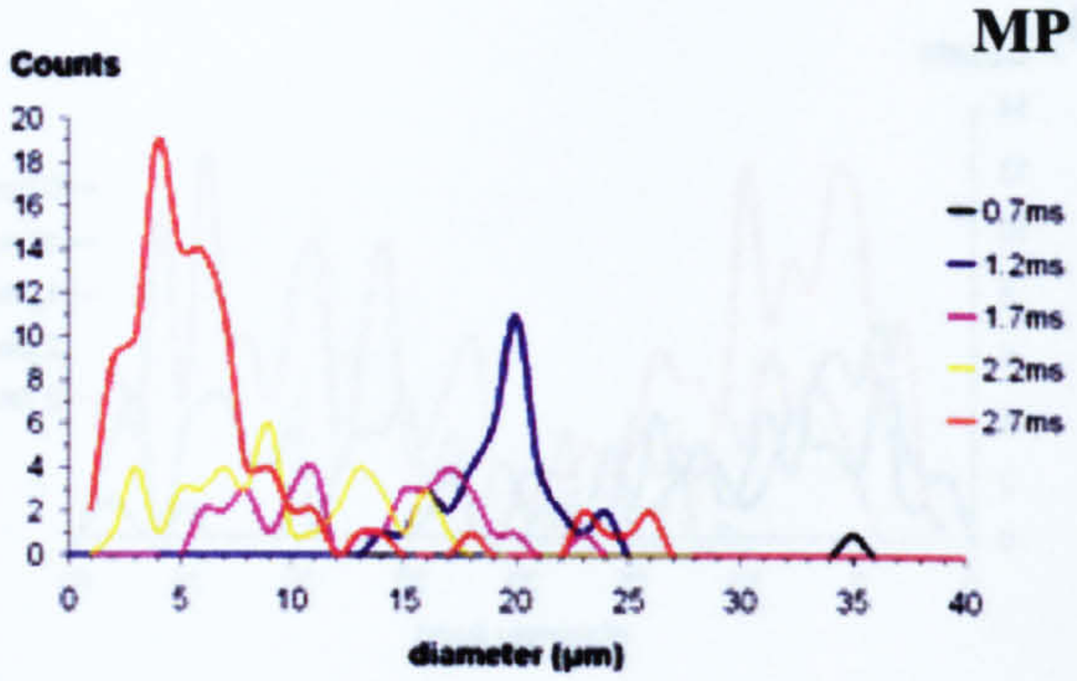

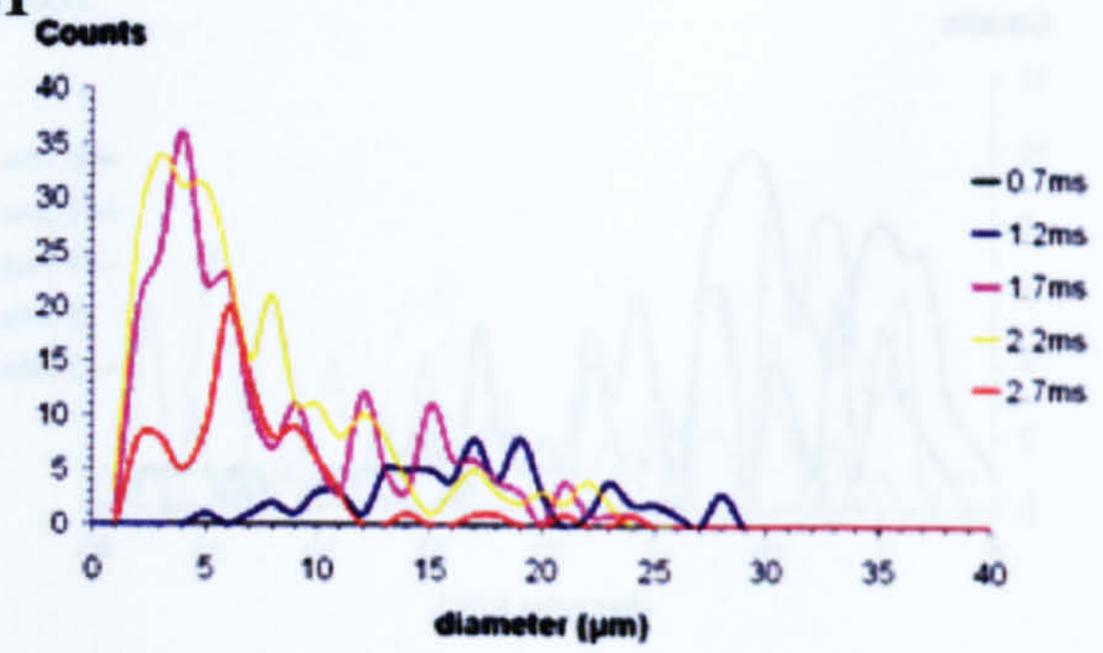

MP 32

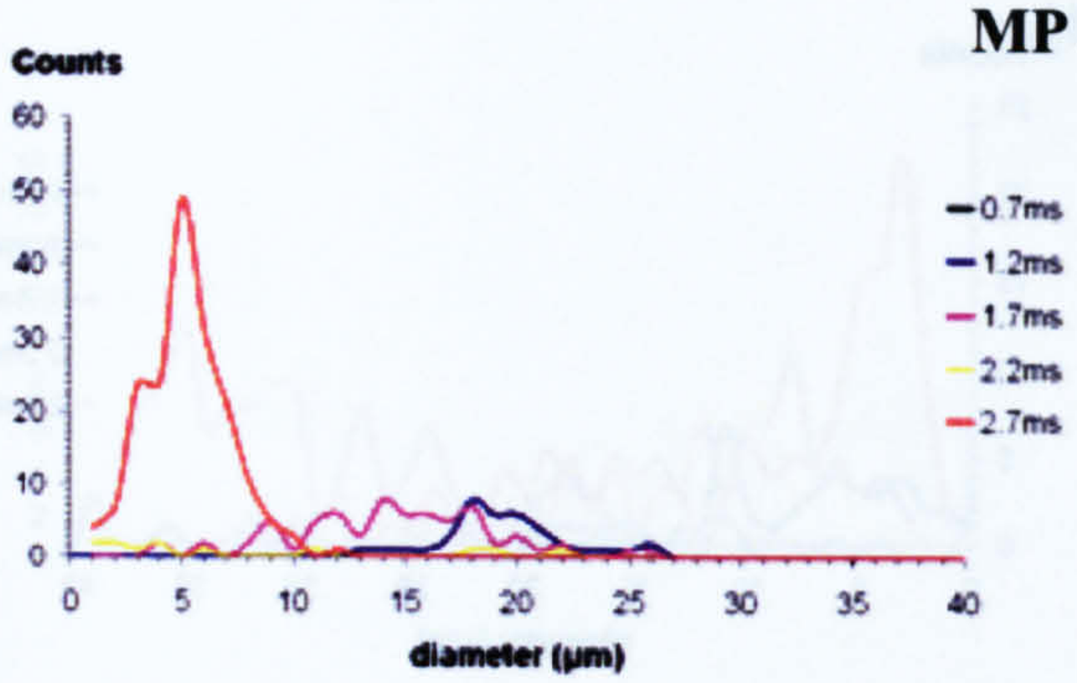

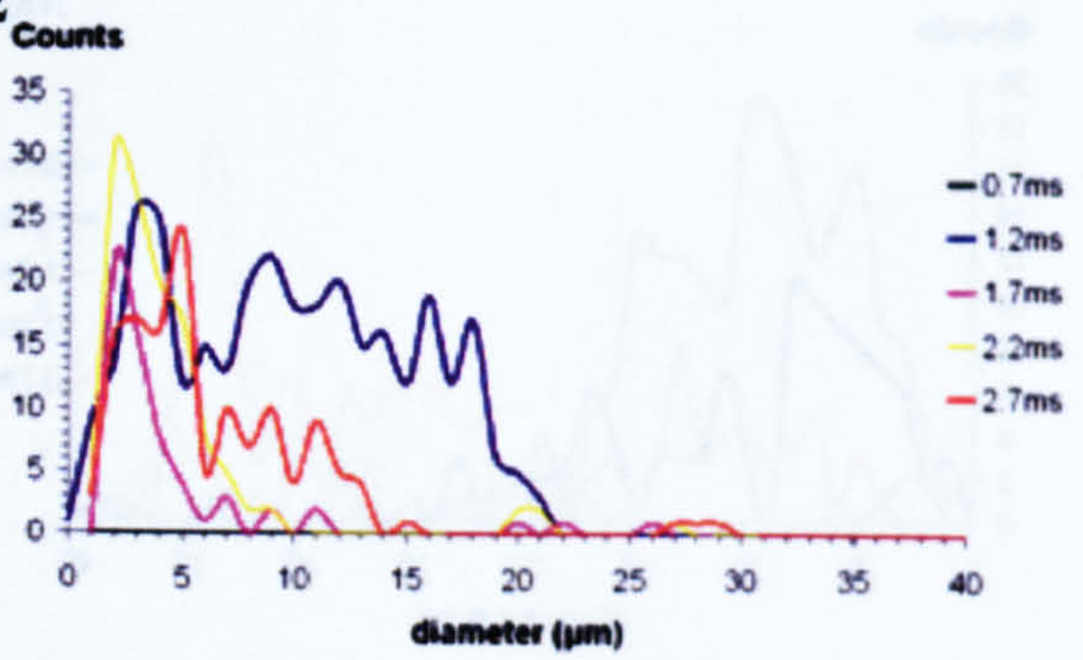

MP 34

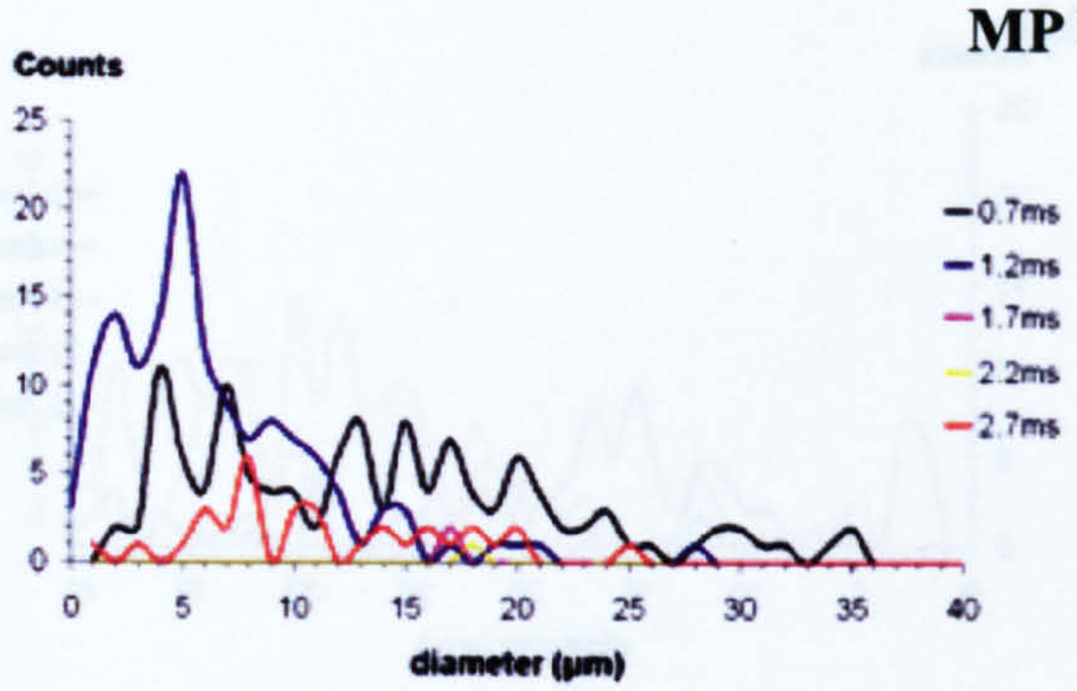

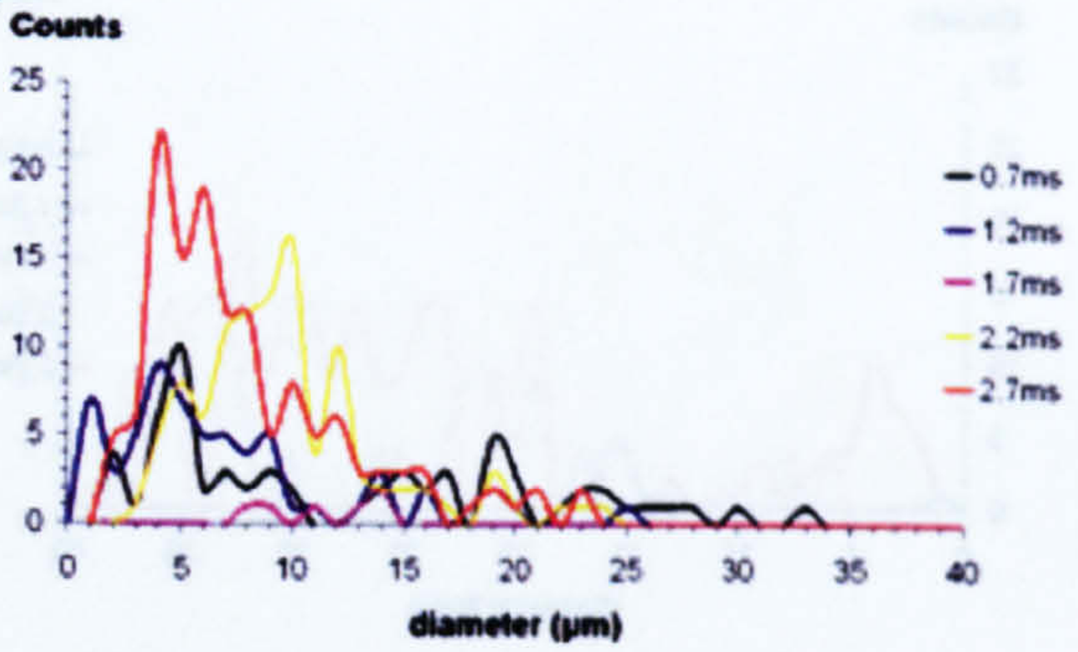

MP 35

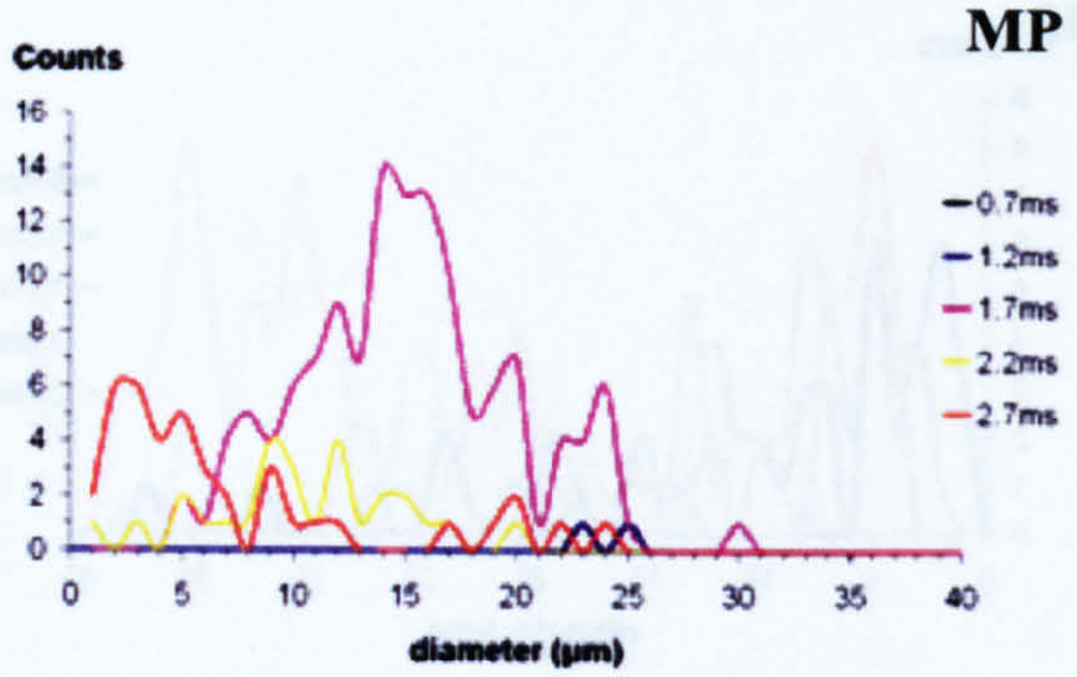

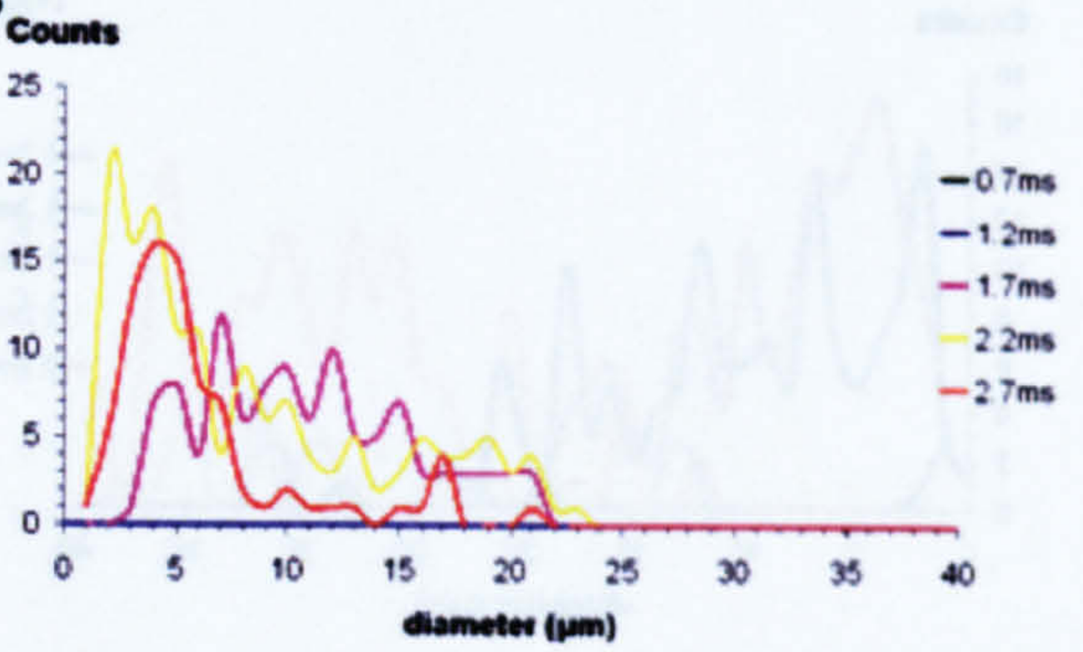

MP 36

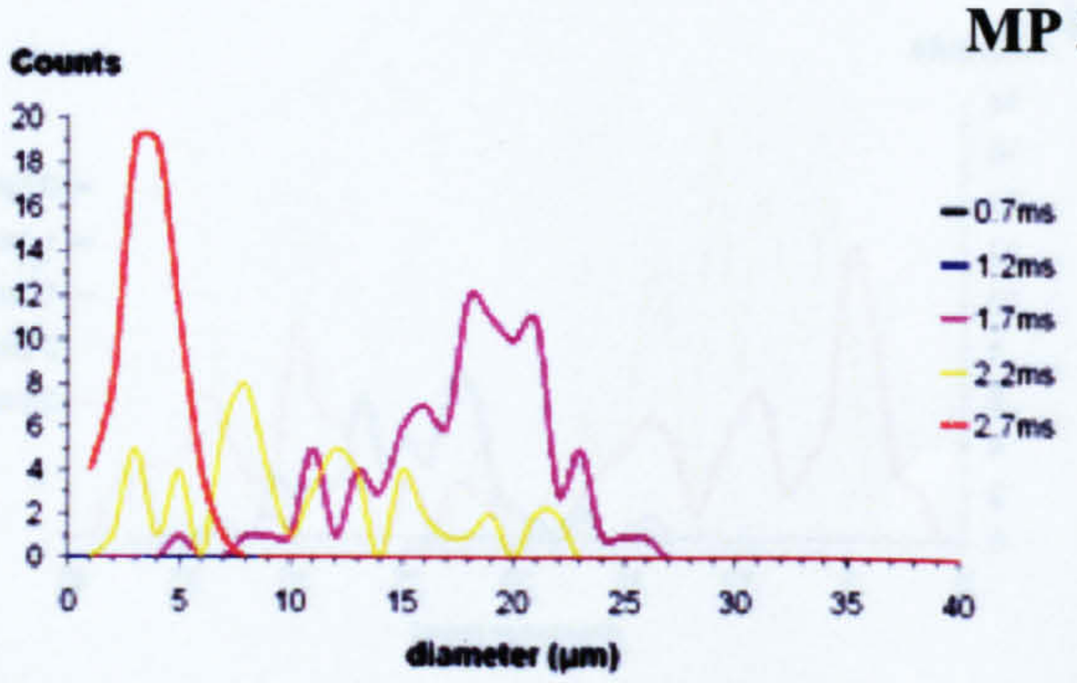

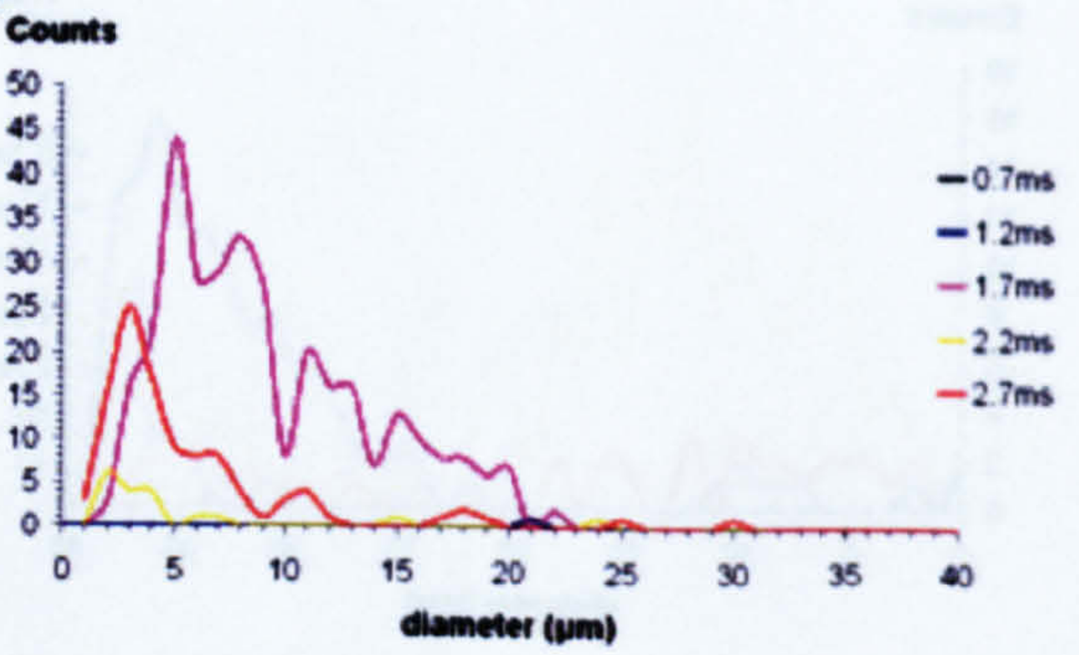

MP 39

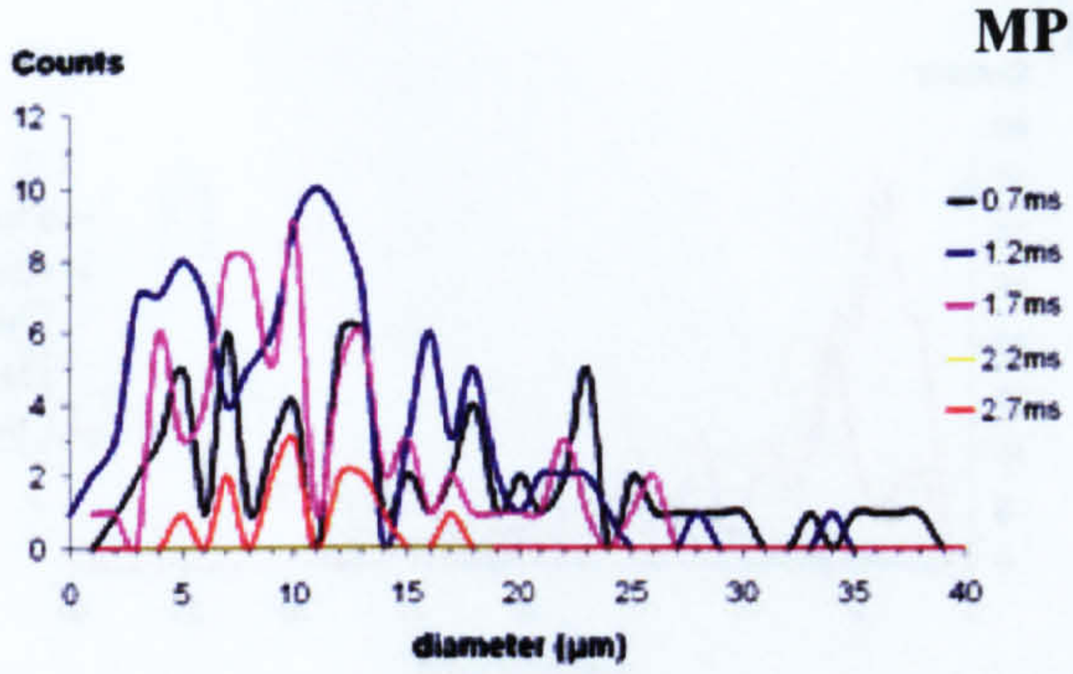

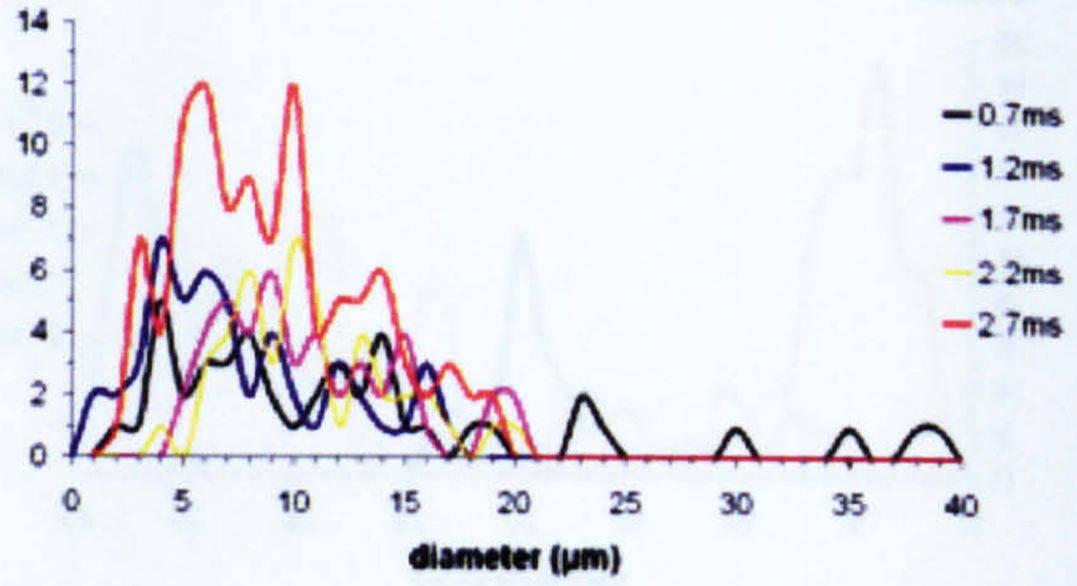

MP 40

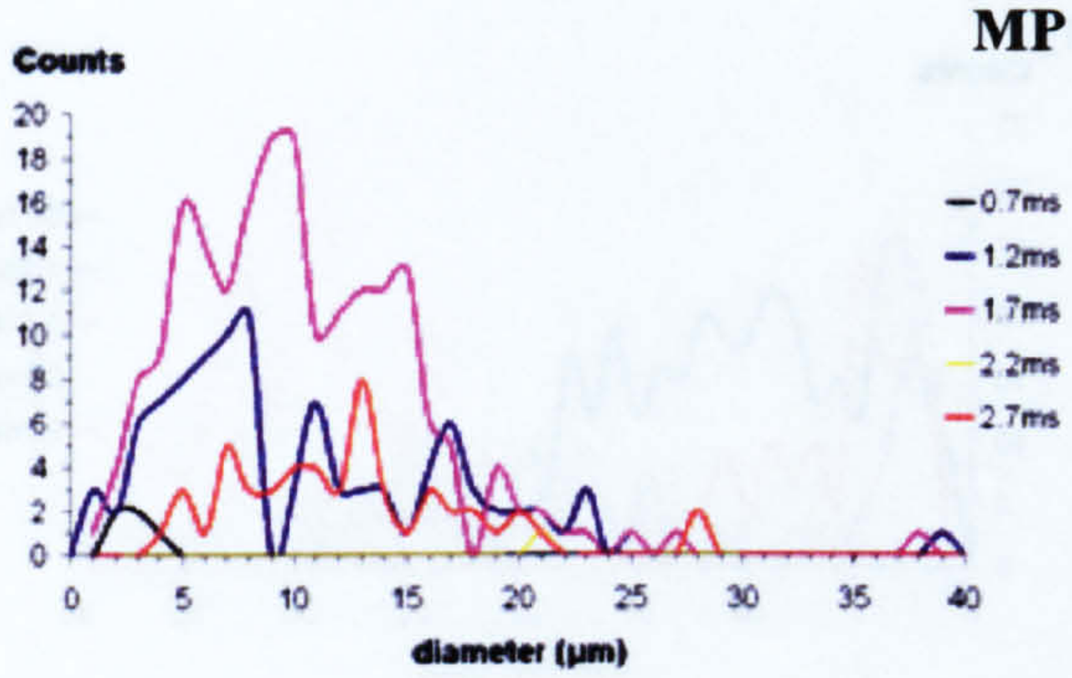

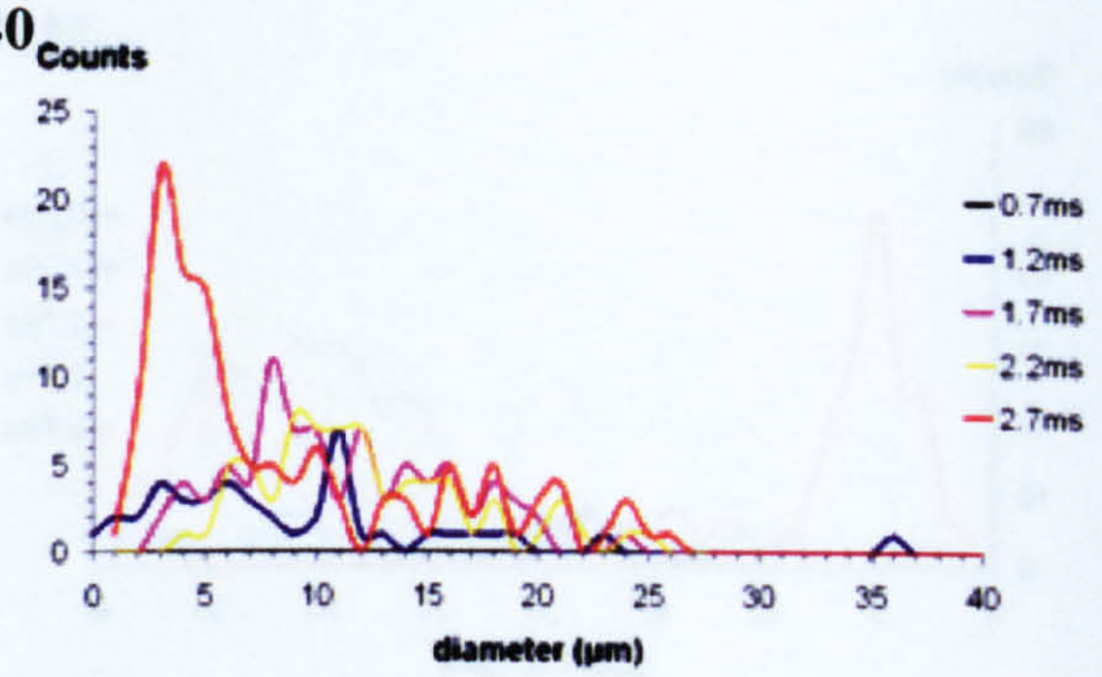

MP 41

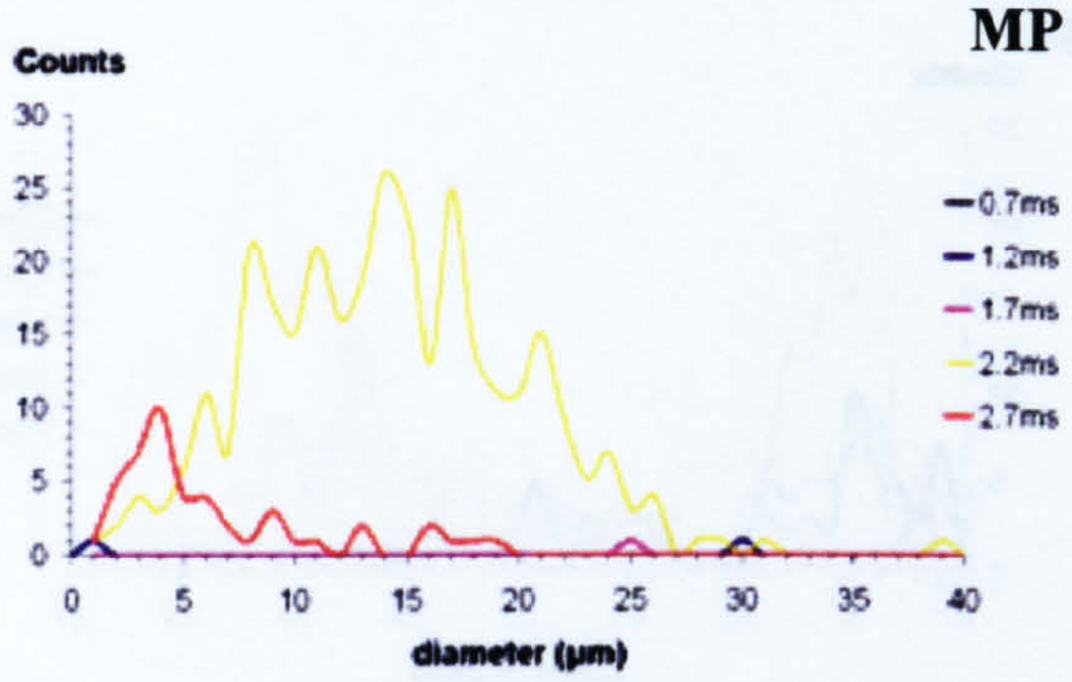

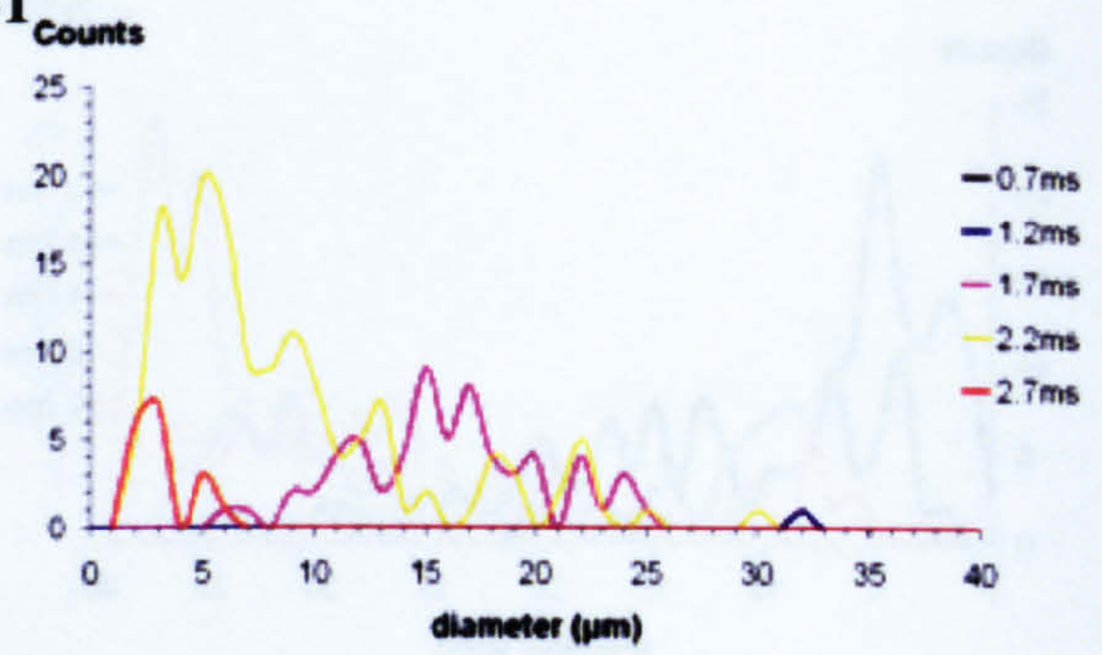

MP 43

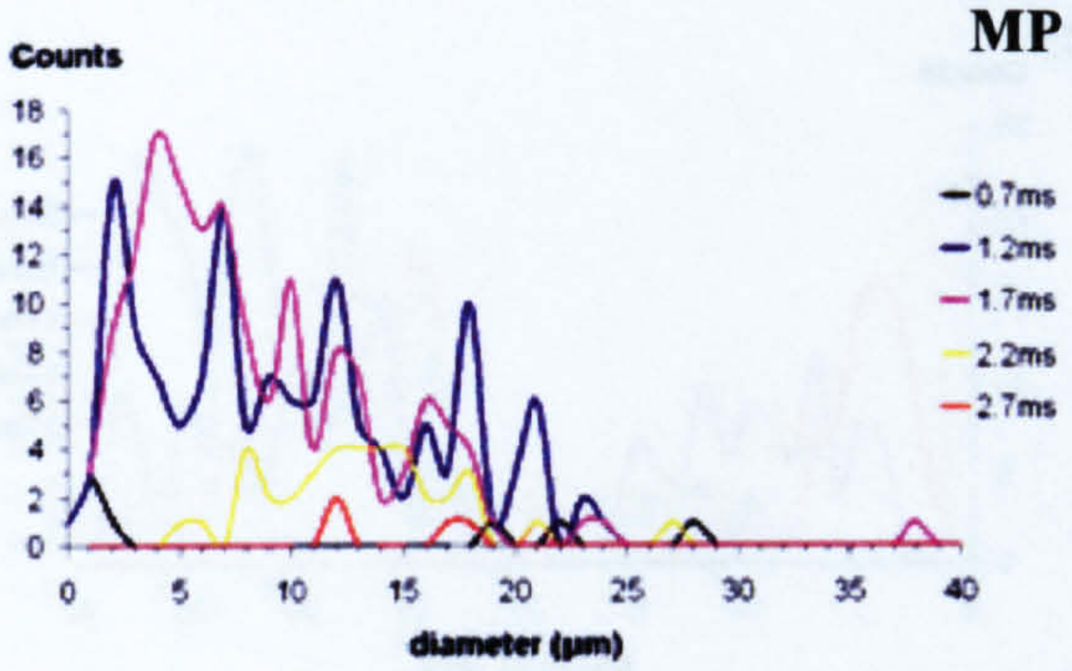

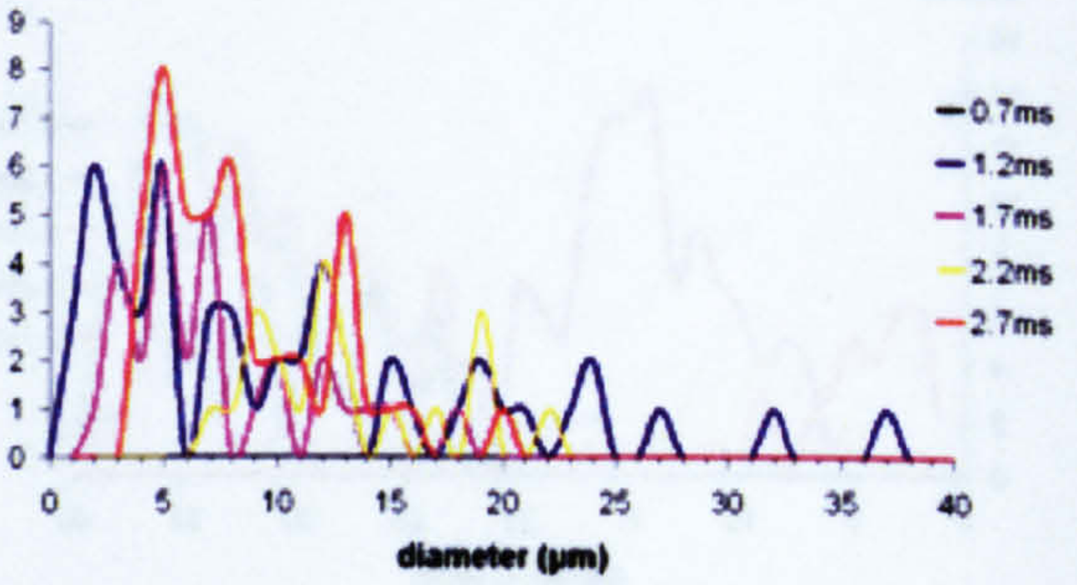

MP 44

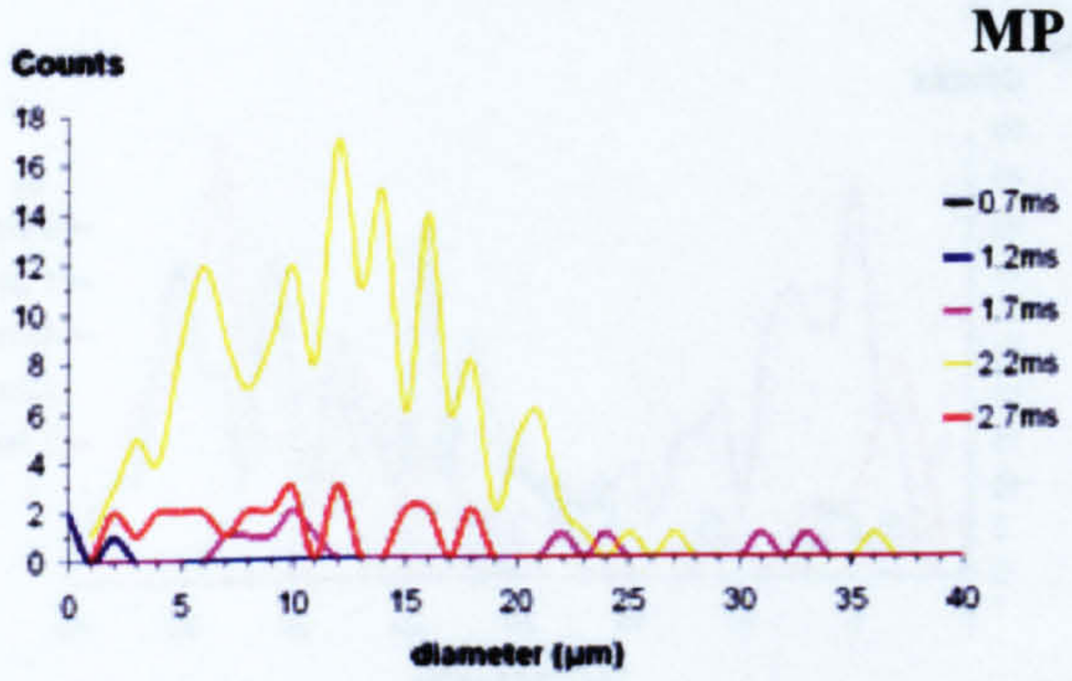

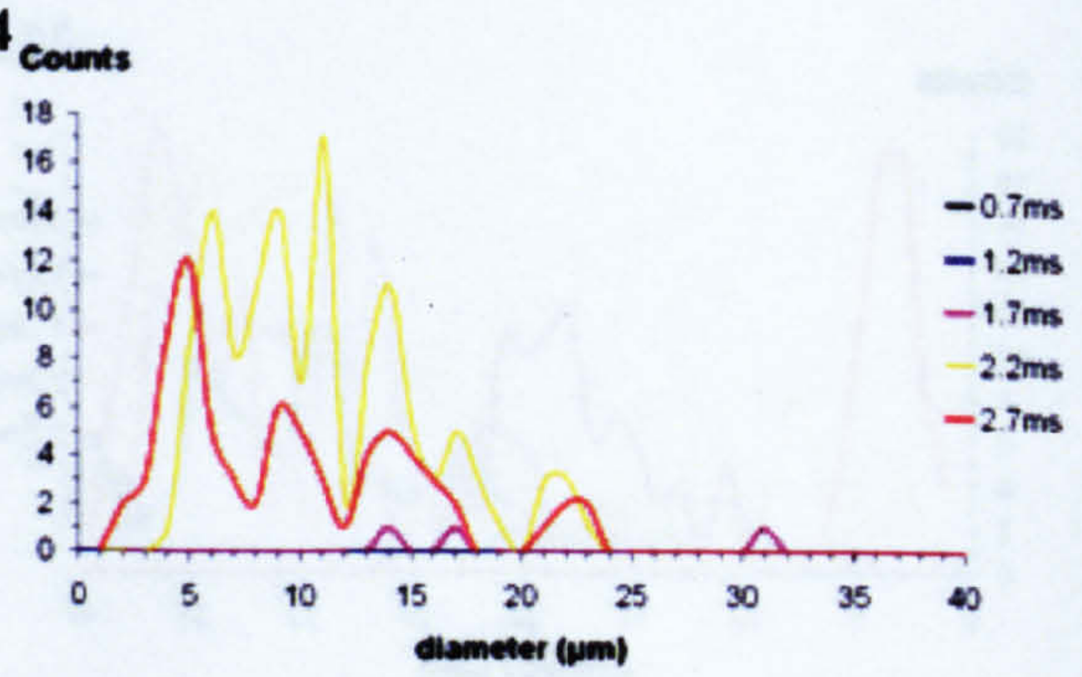

MP 45

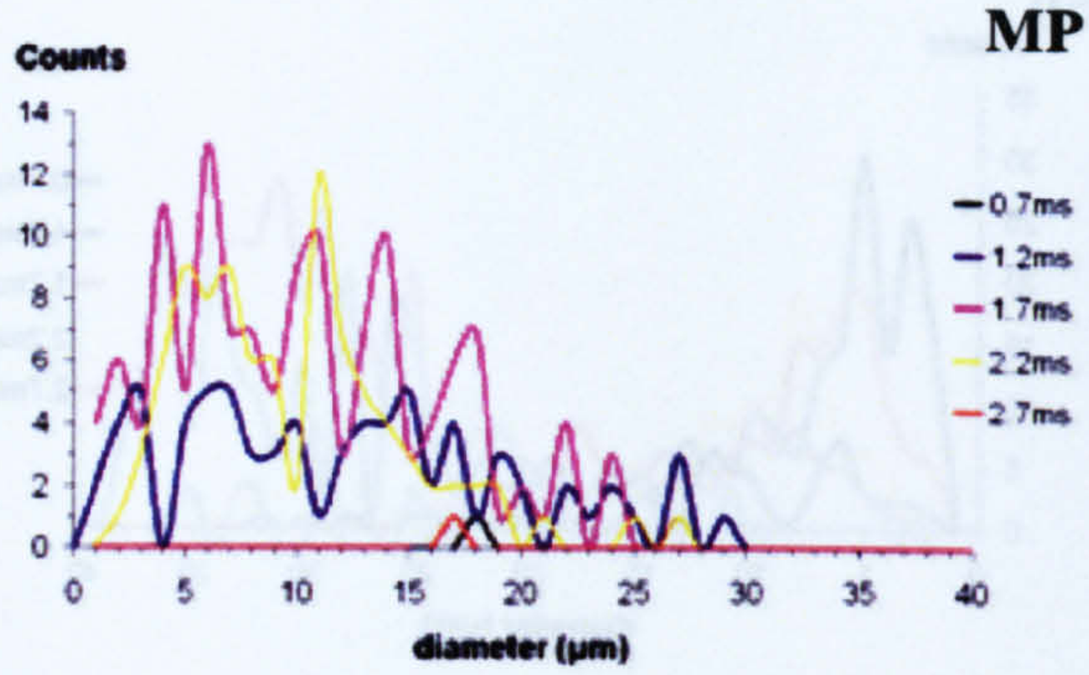

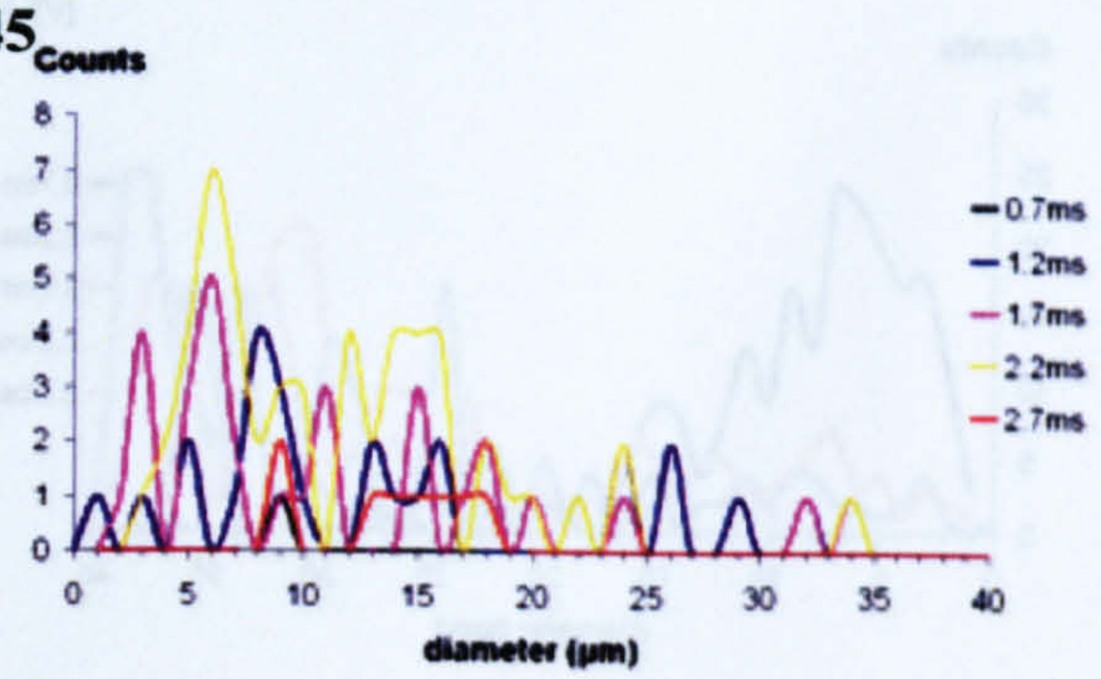

MP 46

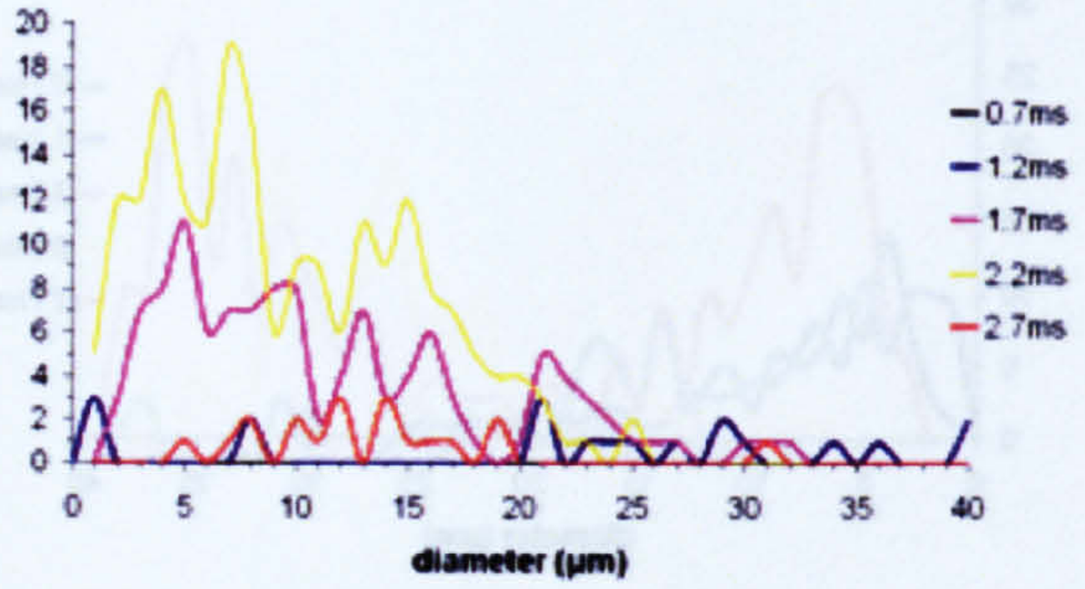

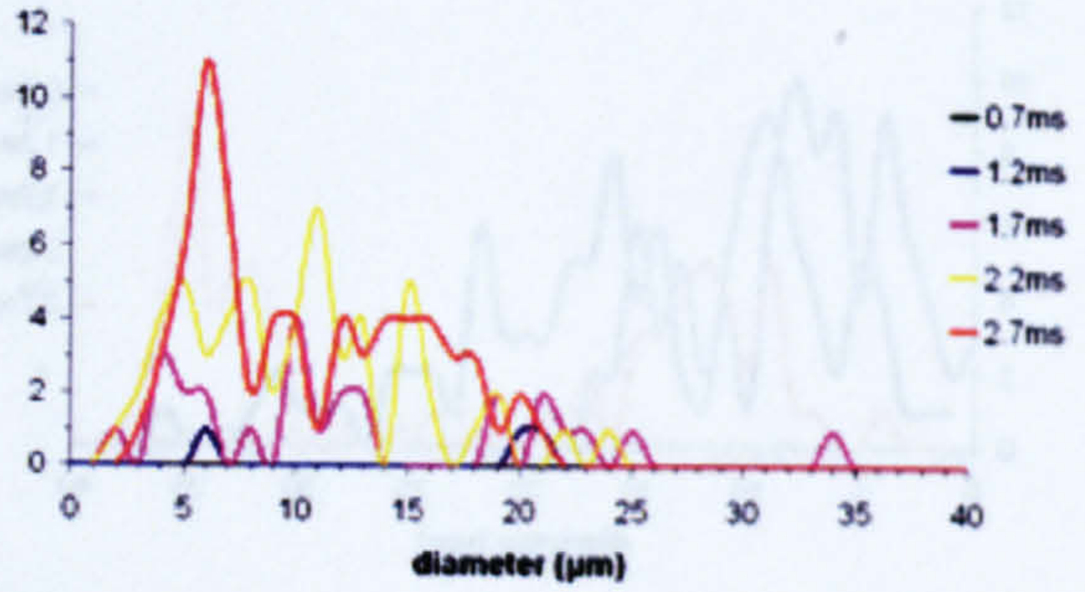

MP 47

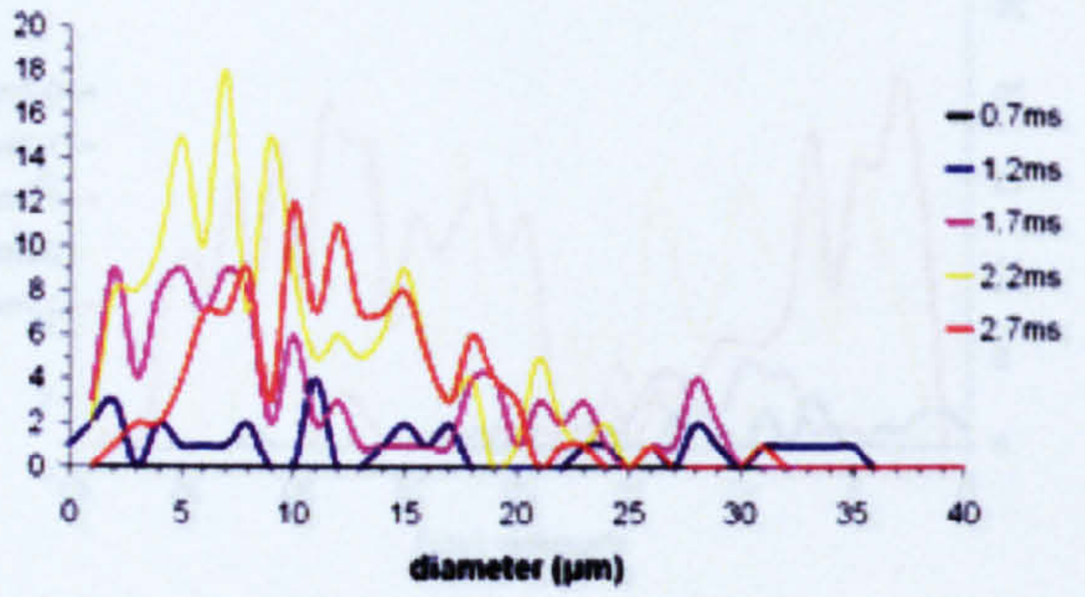

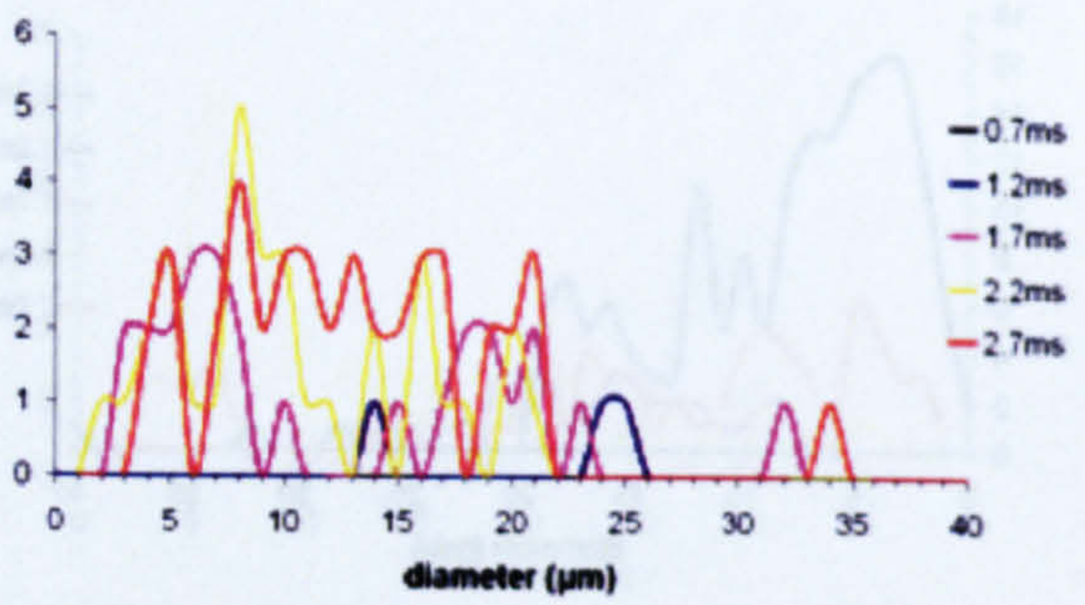

MP 48

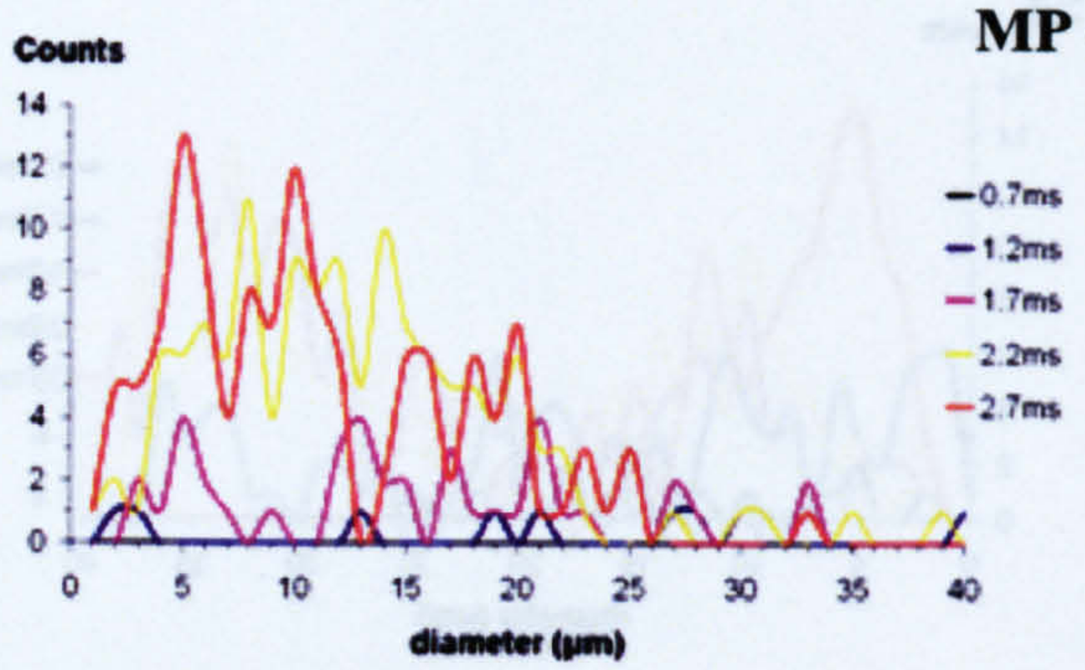

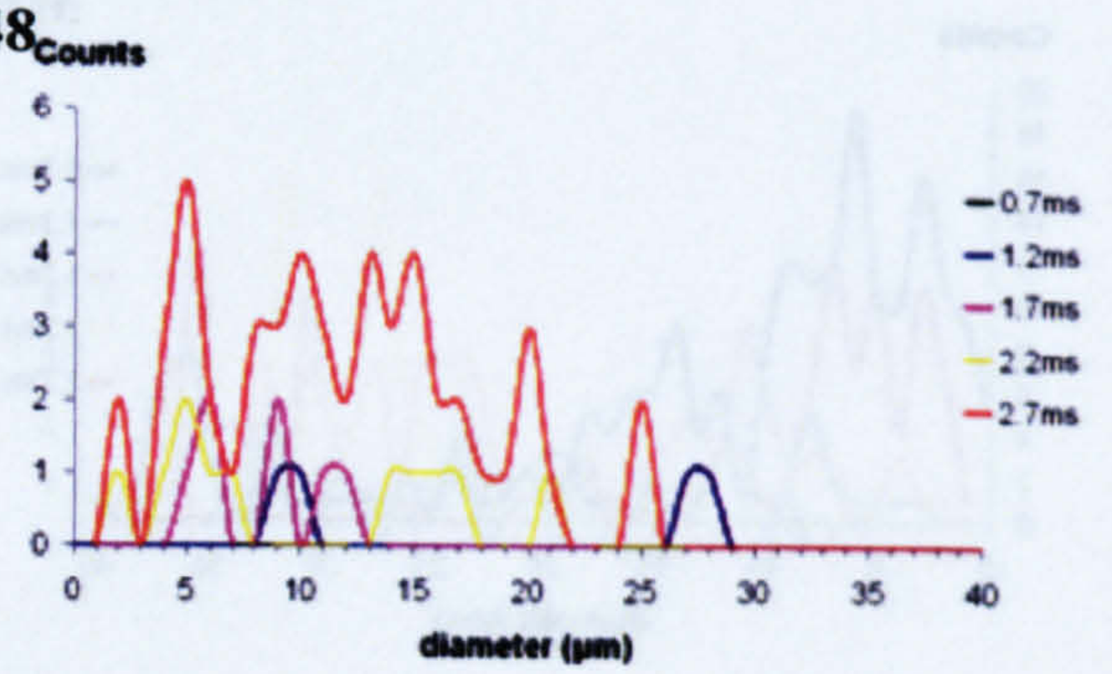

MP 49

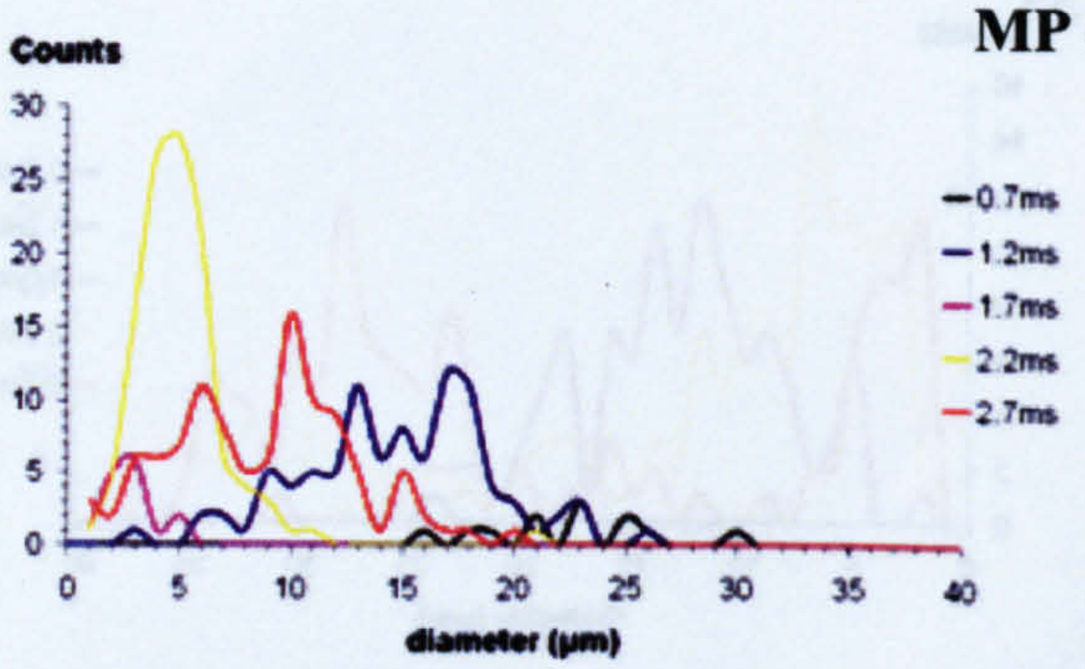

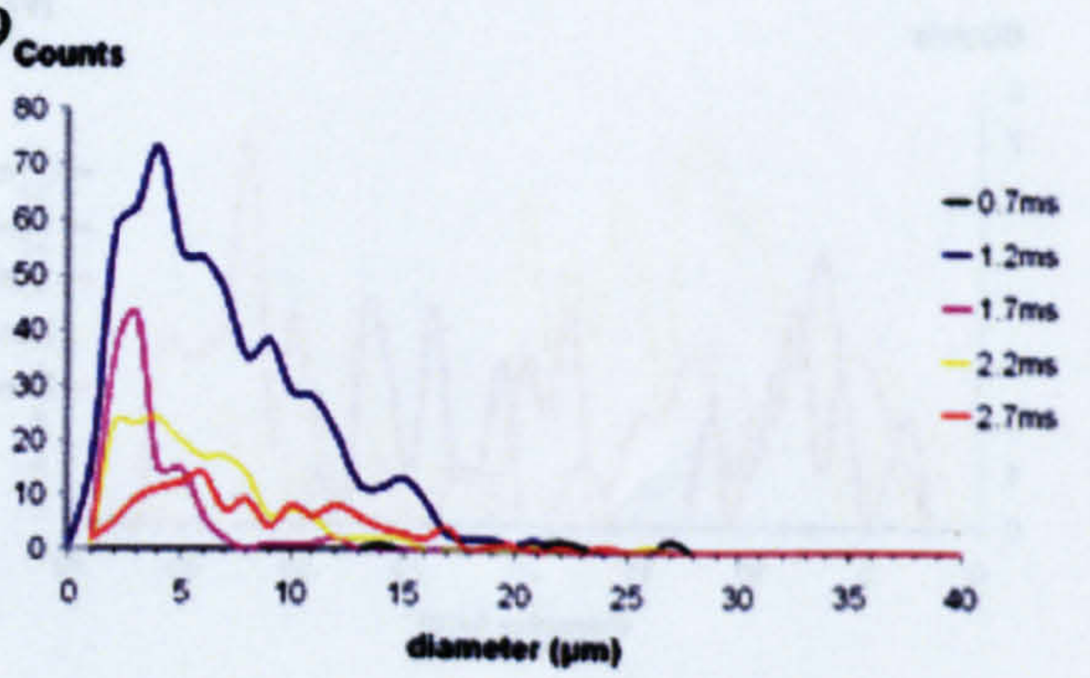

MP 50

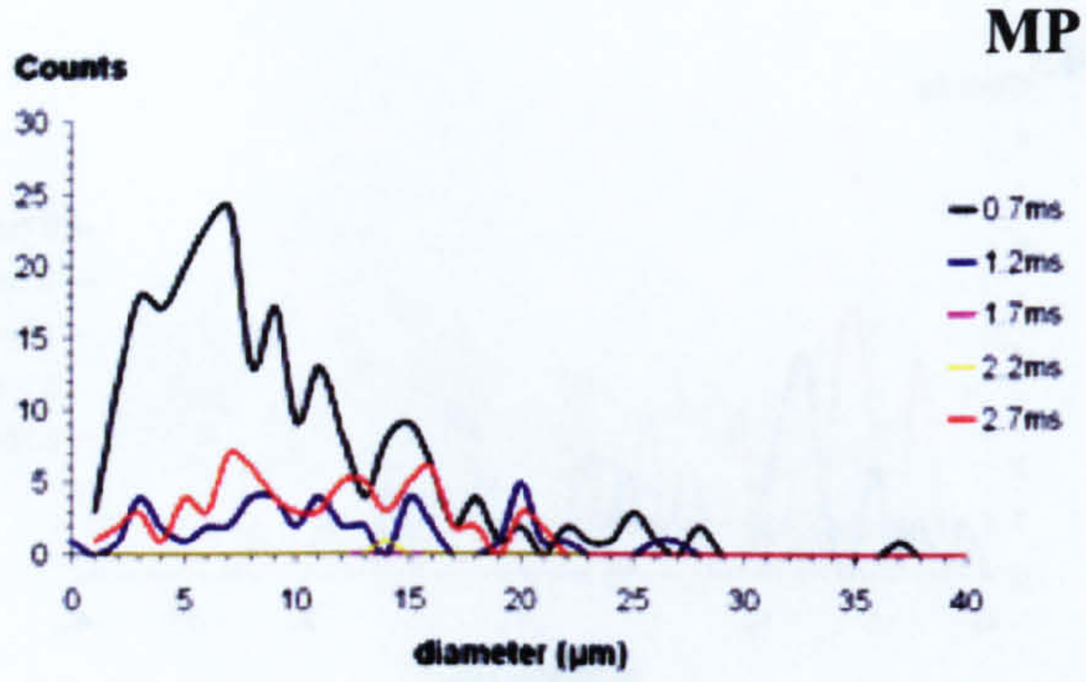

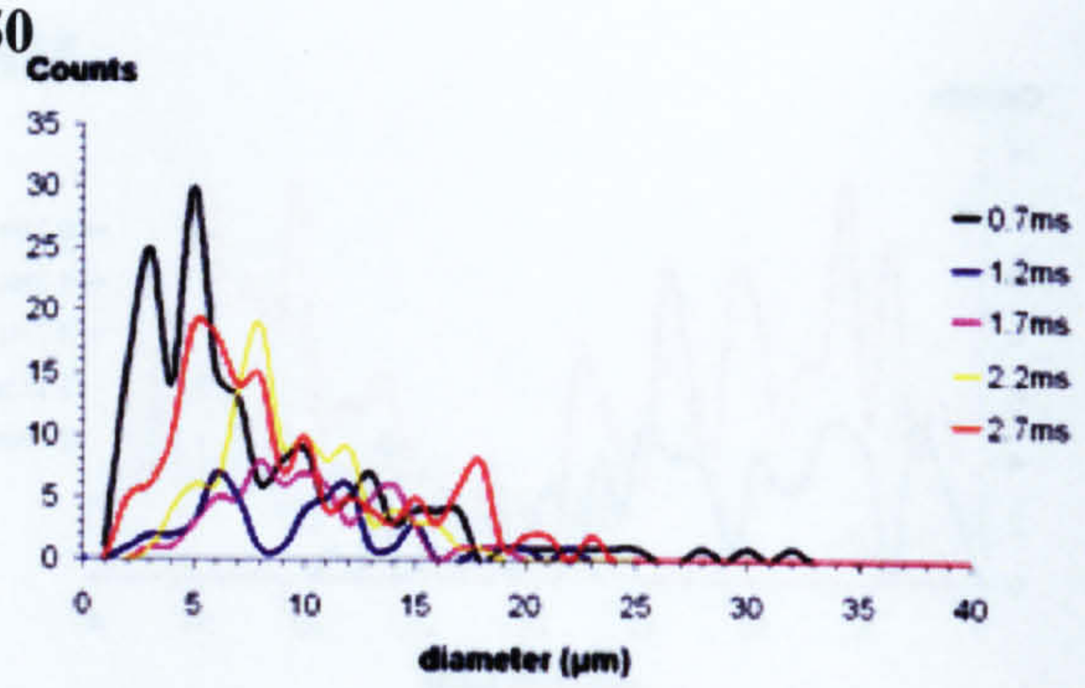

MP 52

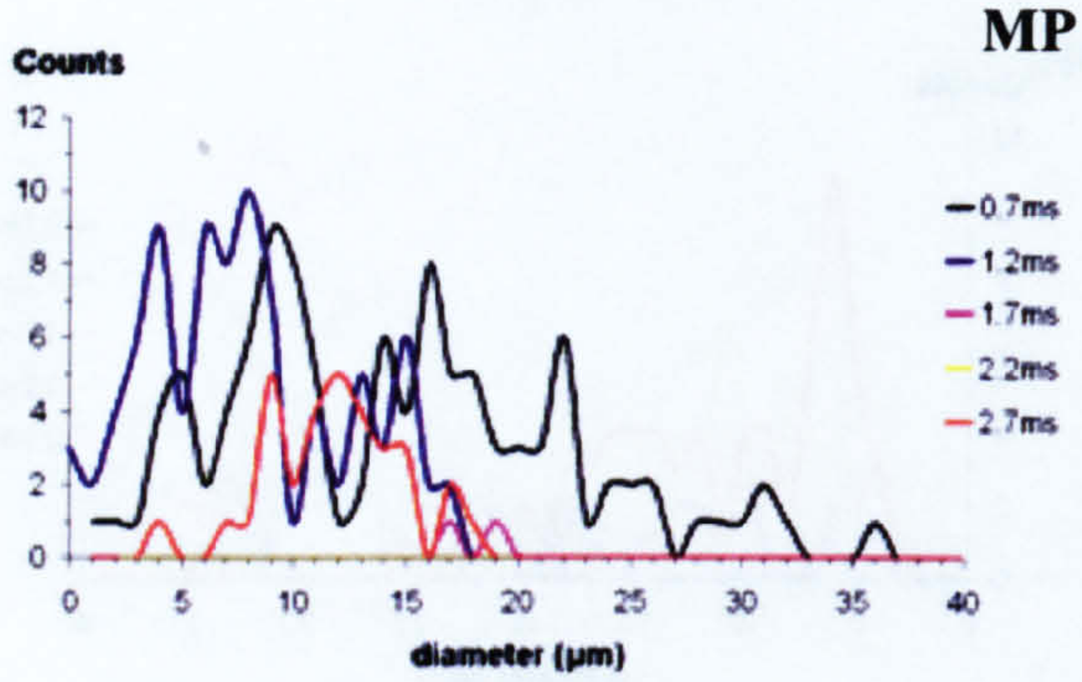

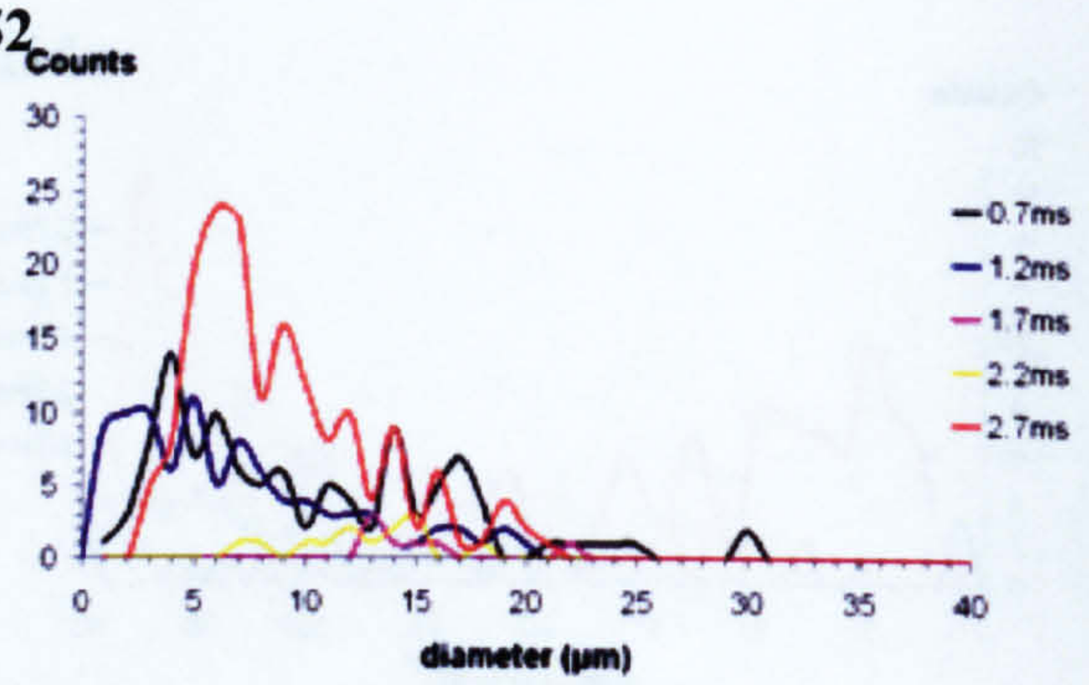

MP 53

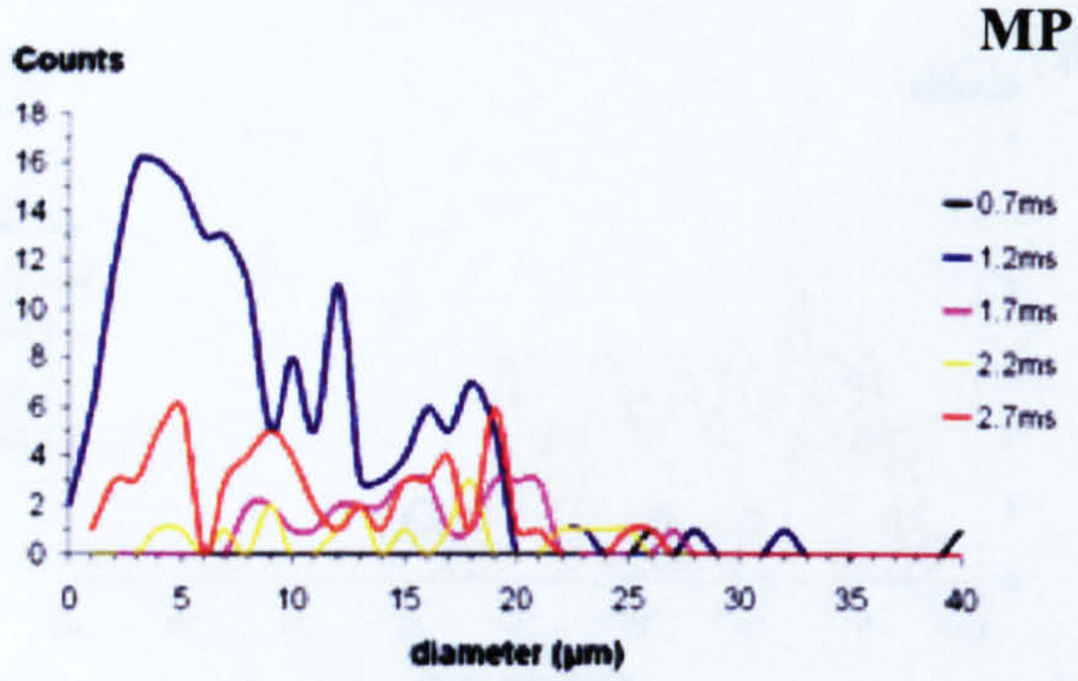

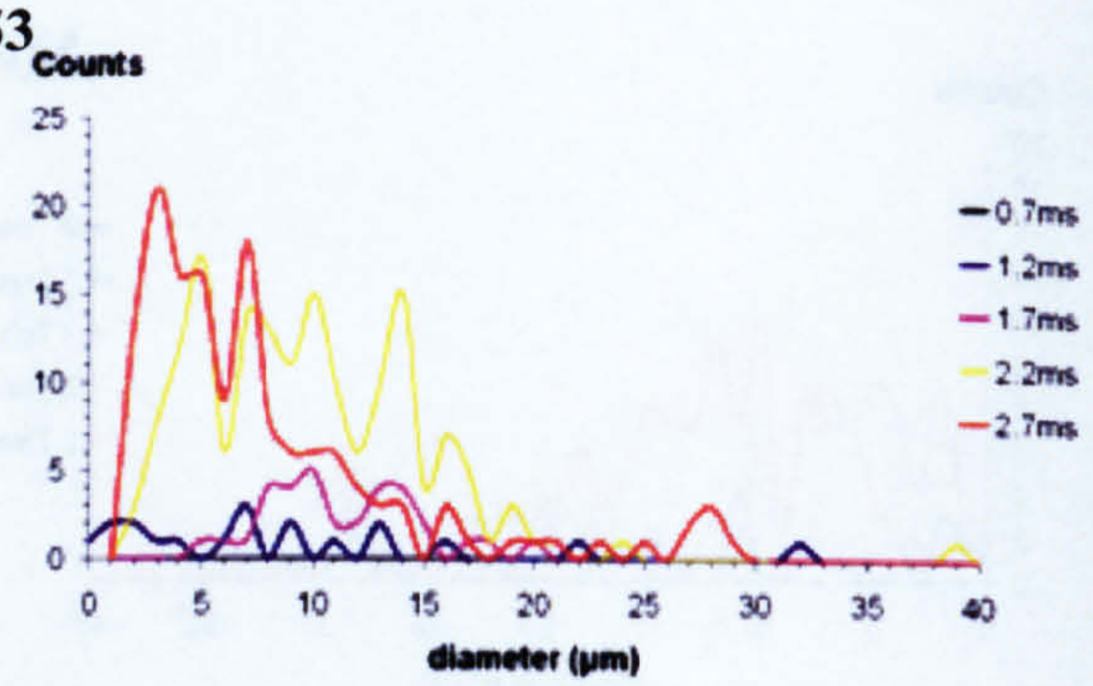

MP 54

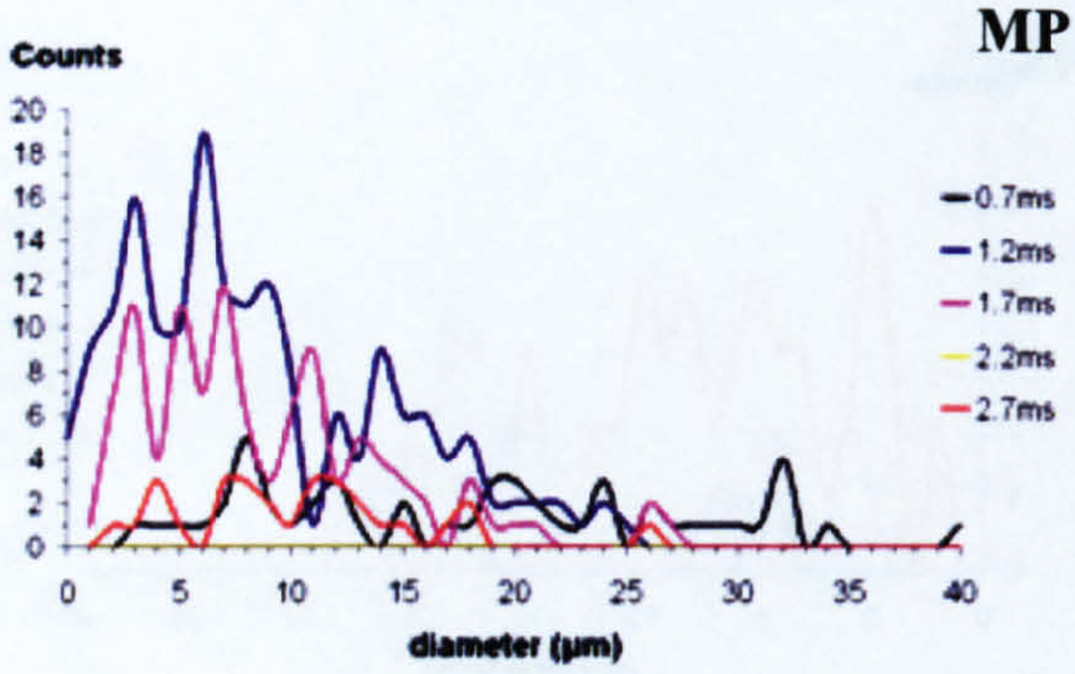

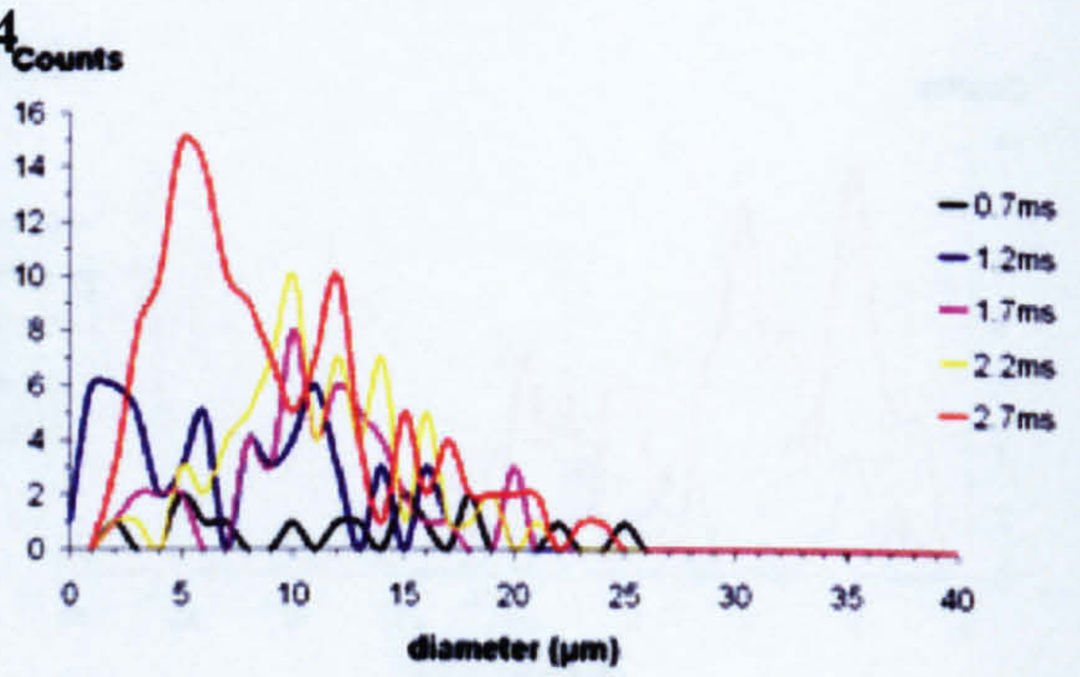

MP 55

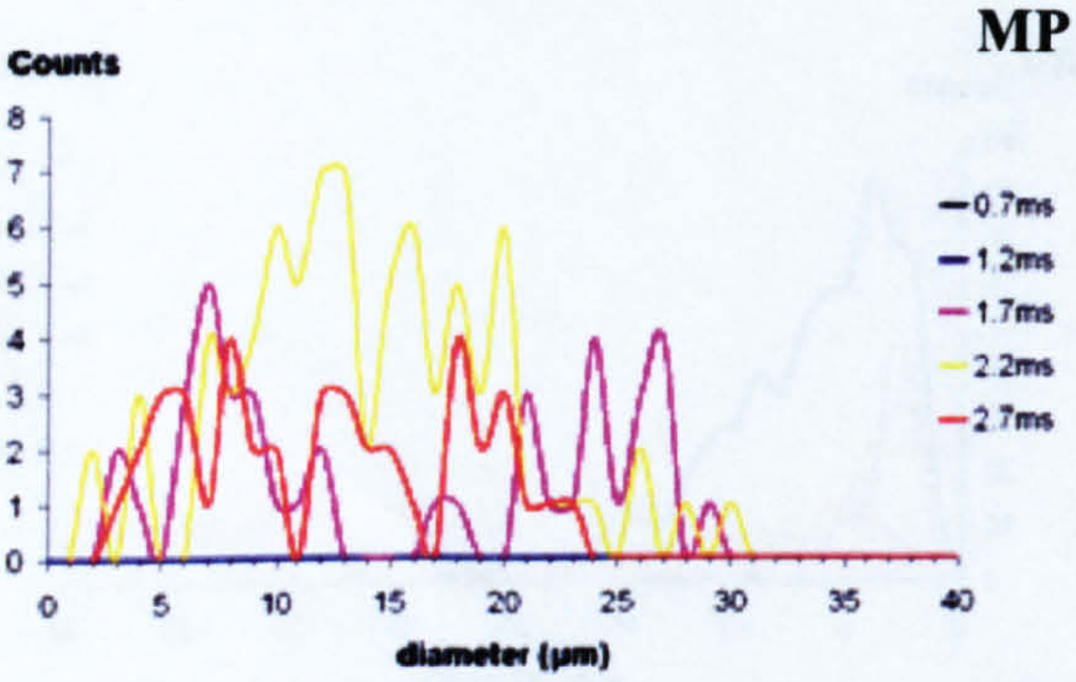

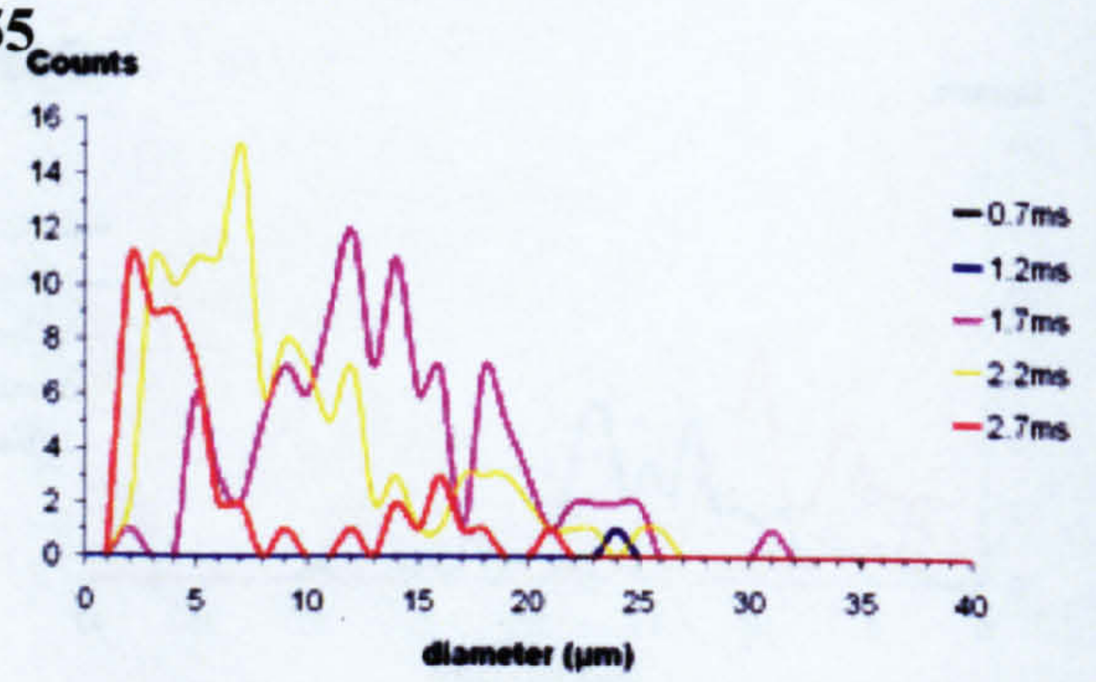

MP 56

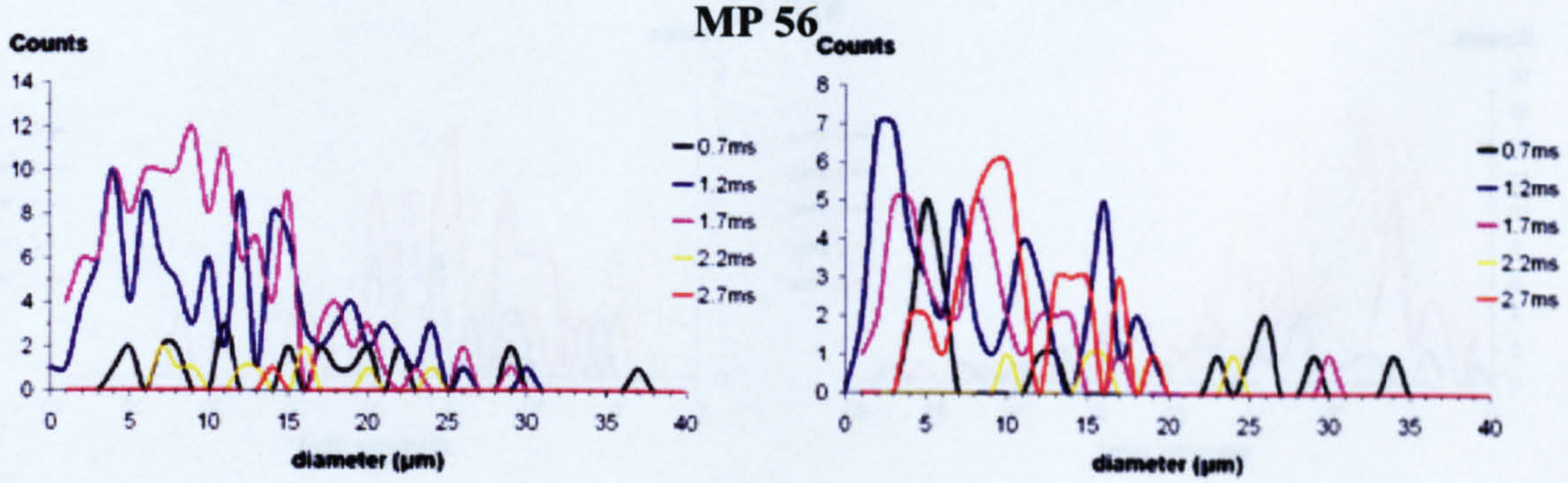

MP 57

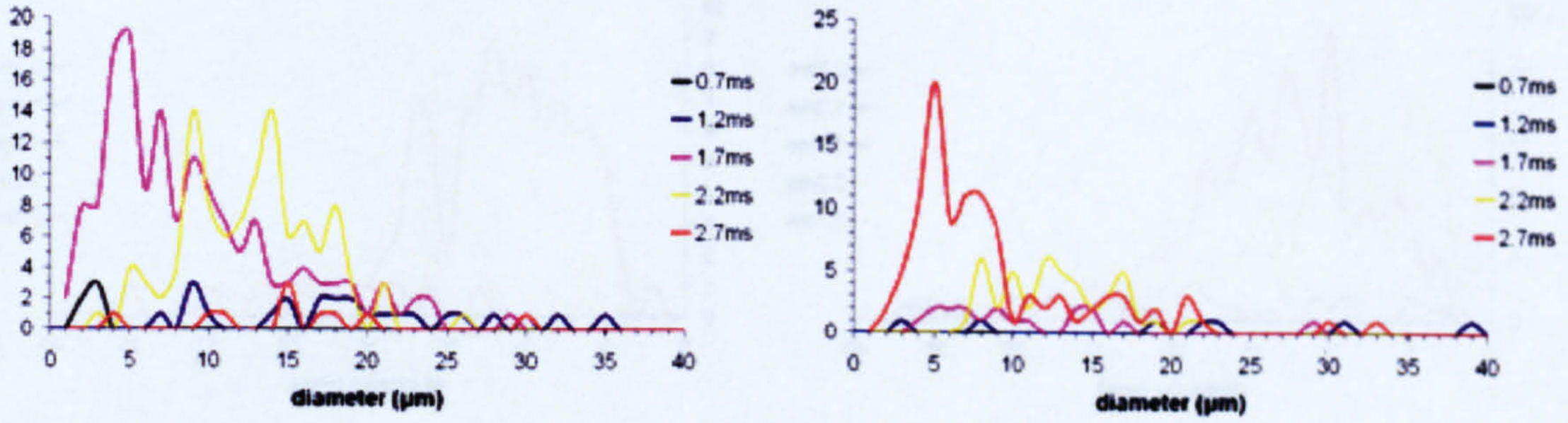

MP 58

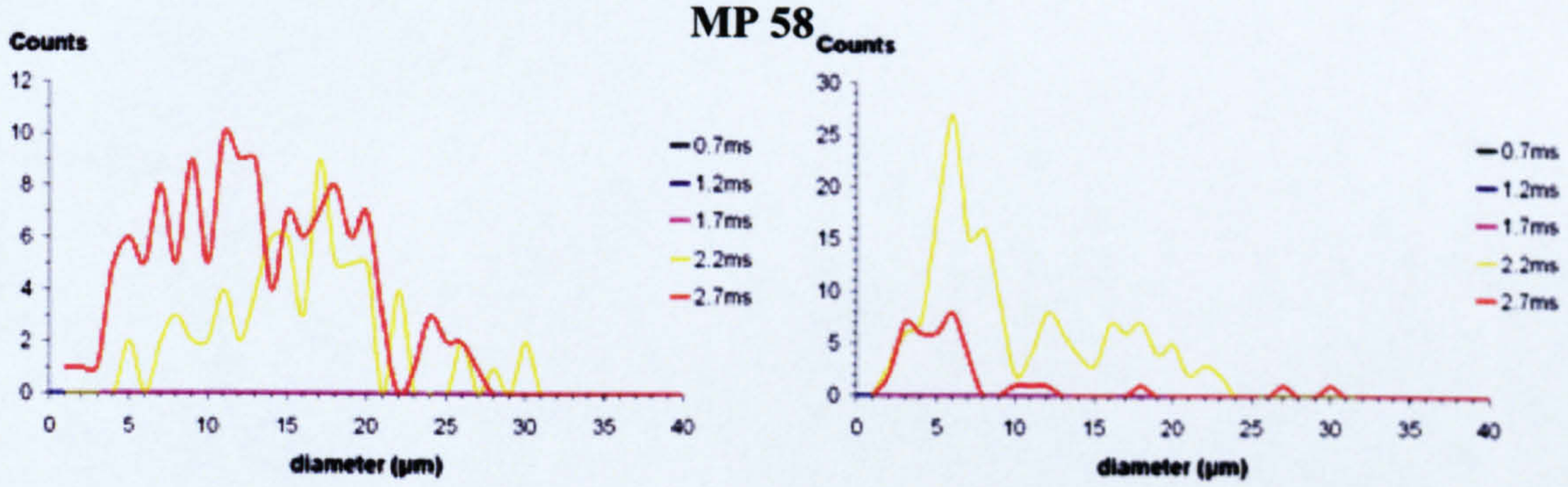

MP 59

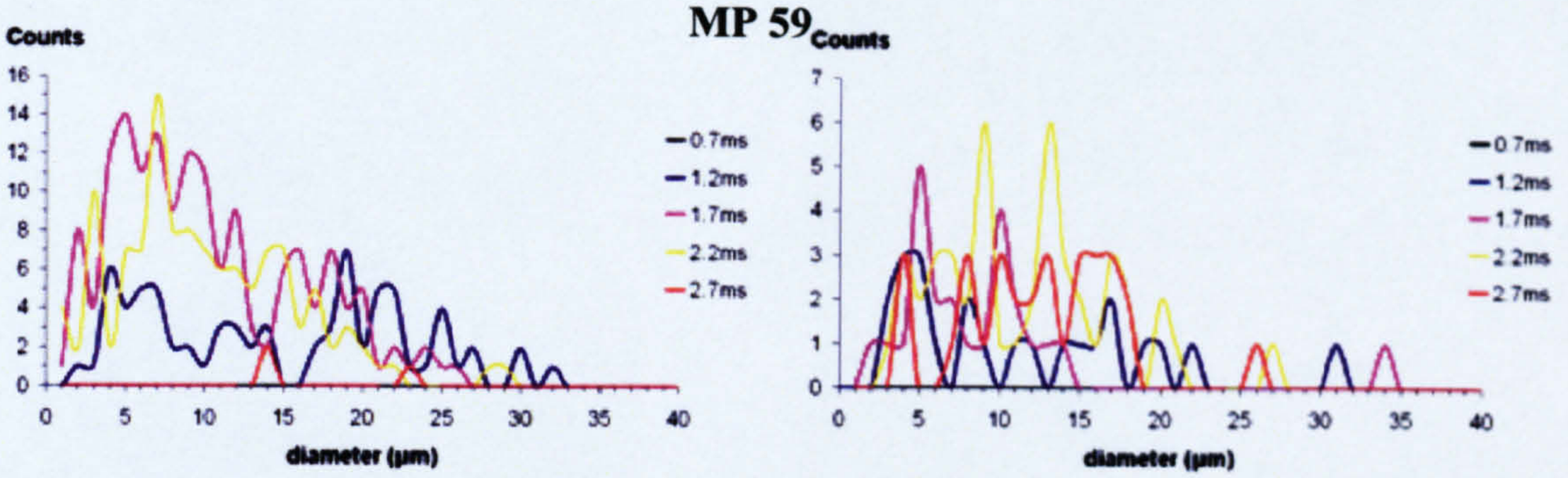

MP 60

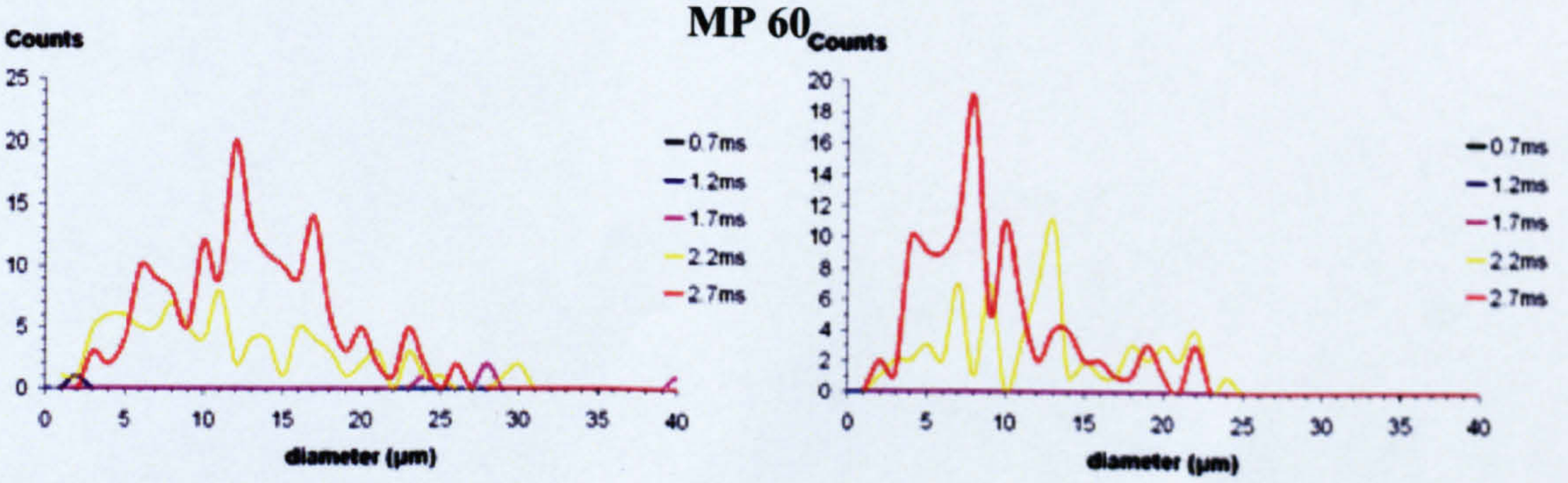

MP 61

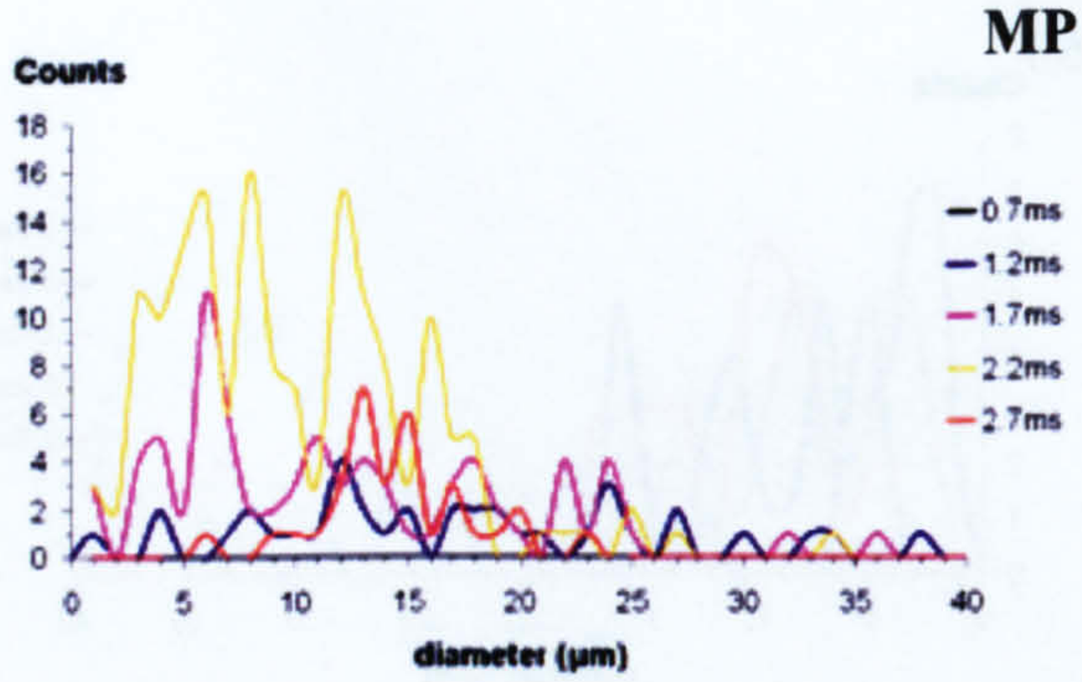
Counts
18
16
14
12
10
8
6
4
2
0
0
5
10
15
20
25
30
35
40
diameter (µm)
0.7ms
1.2ms
1.7ms
2.2ms
2.7ms

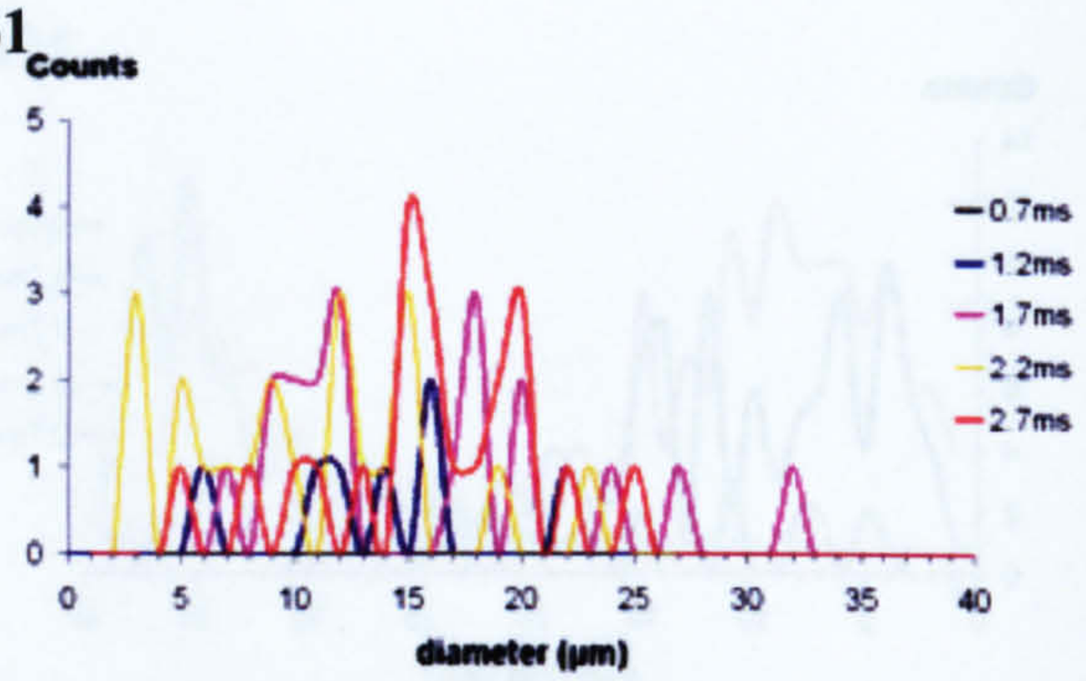
Counts
5
4
3
2
1
0
0
5
10
15
20
25
30
35
40
diameter (µm)
0.7ms
1.2ms
1.7ms
2.2ms
2.7ms

MP 62

Counts
25
20
15
10
5
0
0
5
10
15
20
25
30
35
40
diameter (µm)
0.7ms
1.2ms
1.7ms
2.2ms
2.7ms

Counts
10
9
8
7
6
5
4
3
2
1
0
0
5
10
15
20
25
30
35
40
diameter (µm)
0.7ms
1.2ms
1.7ms
2.2ms
2.7ms